ZAŠTITA MATERIJALA

G o d i n a LXV **B e o g r a d, 2024.** **B r o j 1**

Izdavač- Publisher: INŽENJERSKO DRUŠTVO ZA KOROZIJU, Beograd, Kneza Miloša 9/I, Tel/fax (011) 3860 - 867 i (011) 3230–028, E-mail:editor@idk.org.rs; idk@idk.org.rs, www.idk.org.rs, E-mail:caslav.lacnjevac@gmail.com

SADRŽAJ – CONTENT

SUIZDAVAČI

INSTITUT ZA TEHNOLOGJU NUKLEARNIH I DRIGIH MINERALNIH SIROVINA, BEOGRAD

UDRUŽENJE INŽENJERA SRBIJE ZA KOROZIJU I ZAŠTITU MATERIJALA

CRNOGORSKO DRUŠTVO ZA ZAŠTITU MATERIJALA

DONATORI

JP ELEKTROMREŽA SRBIJE, BEOGRAD
JKP DRUGI-OKTOBAR, VRŠAC
"NIS - FAM", KRUŠEVAC
GALFOS, BEOGRAD
PD DRINSKO LIMSKE ELEKTRANE, BAJINA BAŠTA
INSTITUT ZA PREVENTIVU, NOVI SAD
MAŠINSKI FAKULTET, BEOGRAD
TEHNOLOŠKO-METALURŠKI FAKULTET, BEOGRAD
TEHNIČKI FAKULTET, BOR
TEHNOLOŠKI FAKULTET, LESKOVAC
ALFA PLAM ad, VRANJE
„HELIOS“, DOMŽALE
ŠUMARSKI FAKULTET, BEOGRAD
AGRONOMSKI FAKULTET, ČAČAK
GRAĐEVINSKO-ARHITEKTONSKI FAKULTET, NIŠ
TEHNOSAM, SUBOTICA
"PITURA", NOVI BEOGRAD
UNIPROMET, ČAČAK
FAKULTET ZAŠTITE NA RADU, NIŠ
INSTITUT ZA VODOPRIVREDU „JAROSLAV ČERNI“, BEOGRAD
„GALVA“, KRAGUJEVAC
PERIĆ & PERIĆ, POŽAREVAC
HORIZONT PRES, BEOGRAD
VISOKA TEHNOLOŠKA ŠKOLA STRUKOVNIH STUDIJA, NOVI BEOGRAD
VISOKA STRUKOVNA ŠKOLA, NIŠ
VISOKA TEH. SKOLA STRUK. STUDIJA, NOVI SAD
INSTITUT ZA PUTEVE, BEOGRAD
IMPOL SEVAL, UŽICE
ALFATERM, ČAČAK
METALAC A.D., GORNJI MILANOVAC
SINVOZ DOO, ZRENJANIN

U finansiranju izdavanja časopisa "ZAŠTITA MATERIJALA" učestvuju:

MINISTARSTVO NAUKE, TEHNOLOŠKOG RAZVOJA I INOVACIJA REPUBLIKE SRBIJE

INŽENJERSKA KOMORA SRBIJE

CIP - Katalogizacija u publikaciji
Narodna biblioteka Srbije, Beograd

620.1
ZAŠTITA MATERIJALA = Materials Protection / glavni urednik: Časlav Lačnjevac), [Štampano izd.]. - God. 1, br. 1 (1953)-god. 22, br. 3/4 (1974) ; god. 23, br. 1 (1982). - Beograd: Inženjersko društvo za koroziju, 1953-1974; 1982- (Zemun : Akademska izdanja). - 29 cm

Dostupno i na: http://idk.org.rs. - Tromesečno. - Drugo izdanje na drugom medijumu:
Zaštita materijala (Online) = ISSN 2466-2585
ISSN 0351-9465 = Zaštita materijala
COBISS.SR-ID 4506626

EVROPSKA FEDERACIJA ZA KOROZIJU (EFC) SMATRA OVAJ ČASOPIS ZVANIČNOM PUBLIKACIJOM ZA OBJAVLJIVANJE IZVEŠTAJA I INFORMACIJA
EUROPEAN FEDERATION OF CORROSION (EFC) CONSIDERES THIS JOURNAL TO BE THE OFFICIAL PUBLICATION FOR PUBLISHING THE REPORTS AND INFORMATION

Redakcija: Beograd, Kneza Miloša 9/I, Tel/fax (011) 3860 - 867, i (011) 3230 - 028,E-mail: idk@idk.org.rs; www.idk.org.rs; E-mail: editor@idk.org.rs, www.zastita-materijala.org/index.php/home/issuse

Tekući račun: 205 - 24967 – 71, Komercijalna banka, Beograd; Časopis izlazi četiri puta godišnje

Rukopisi se ne vraćaju; Štampa: Akademska izdanja, Zemun

*Jelena D. Gojgić[1], Aleksandar M. Petričević[1], Mila N. Krstajić Pajić[1], Vladimir D. Jović[2]**

[1]*University of Belgrade, Faculty of Technology and Metallurgy, Belgrade, Serbia,* [2]*Retired from the University of Belgrade, Institute for Multidisciplinary Research, Belgrade, Serbia*

Scientific paper
ISSN 0351-9465, E-ISSN 2466-2585
https://doi.org/10.62638/ZasMat1039

Zastita Materijala 65 (1)
3 - 10 (2024)

Correct determination of the hydrogen evolution reaction parameters at Ni foam electrode modified by electrodeposited Ni-Sn alloy layer

ABSTRACT

The example of the procedure for the correct determination of the parameters of hydrogen evolution reaction (HER), the exchange current density (j_o) and relaxation time (τ_o) for intermediate (adsorbed hydrogen, H_{ads}) adsorption at modified porous Ni-based electrode are presented in this work. Such a procedure is applicable for the HER at all electrode materials. The value of j_o was obtained from the intercept at η = 0 mV from the η vs. log (R_{ct}^{-1}) dependence (η - overpotential), while the value of τ_o was obtained from the intercept at η = 0 mV from the logτ vs. η dependence. It was shown that for the correct determination of j_o and τ_o, it is necessary to correct applied η for the jR_s drop, by recording current density (j) for applied η and correcting it for jR_s.

***Keywords**: HER parameters, exchange current density, relaxation time, Ni-Sn alloy, Ni foam, 30% KOH*

1. INTRODUCTION

As one of the most investigated electrochemical reactions, the HER was the subject of many chapters and books by different authors, with some of them being cited here [1-6]. The mechanism and kinetics of the HER were mainly studied by Tafel plots analysis and electrochemical impedance spectroscopy (EIS) investigations. Since it was shown that by Tafel plots analysis it is not possible to determine the influence of overpotential on the electrosorption/electrodesorption of active intermediate [7] and that only EIS measurements can provide sufficient data for this process, in this introduction (as well as in the paper) only EIS results for the HER were considered [8-21].

The first theoretical treatment of the electrosorption / electrodesorption of active intermediate was presented in the work of R.D. Armstrong et al. [8], where the impedance of electrochemical reaction with an adsorbed intermediate without diffusion has been analyzed. At that time a constant phase element (*CPE*) had not yet been introduced in the literature and the equivalent circuit for intermediate adsorption (shown in Figure 1) was composed of the charge transfer resistance (R_{ct}) of the HER in series with the adsorption pseudocapacitance (C_p), and the charge transfer resistance of the electrodesorption of intermediate (R_p) connected in parallel. It was assumed that the rate of the formation of the intermediate is v_1, while the rate of its disappearance is v_2. In the steady-state $v_1 = v_2$ and the concentration of intermediate at the surface is given by equation

$$\frac{d\Gamma}{dt} = v_1 - v_2 \qquad (1)$$

while relaxation time (τ) is defined as

$$\tau = [\left(\frac{\partial v_2}{\partial \Gamma}\right)_E - \left(\frac{\partial v_1}{\partial \Gamma}\right)_E]^{-1} \qquad (2)$$

and

R_o (additional resistance at zero frequency) as

$$\frac{1}{R_o} = \tau[n_1 F \left(\frac{\partial v_1}{\partial \Gamma}\right)_E + n_2 F \left(\frac{\partial v_2}{\partial \Gamma}\right)_E]^{-1}[\left(\frac{\partial v_1}{\partial E}\right)_\Gamma - \left(\frac{\partial v_2}{\partial E}\right)_\Gamma] \qquad (3)$$

Where

n_1 is the number of electrons involved in the formation of one molecule of intermediate and n_2 is the number of electrons involved in its disappearance.

*Corresponding author: Vladimir D. Jović
E-mail: vladajovic@imsi.bg.ac.rs
Paper received: 12. 11. 2023.
Paper accepted: 01. 12. 2023.
Paper is available on the website: www.idk.org.rs/journal

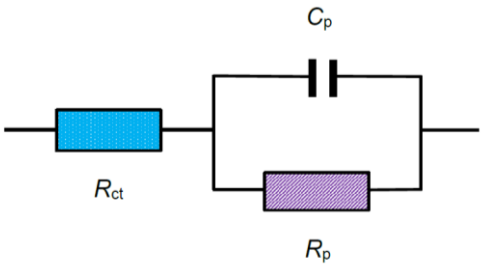

Figure 1. Equivalent circuit for the electrosorption / electrodesorption of active intermediate [8]

Slika 1. Ekvivalentno kolo za reakciju elektrosorpcije / elektrodesorpcije intermedijara [8]

By the analysis of the impedance of this equivalent circuit following equations were derived:

$$R_p = -\frac{R_{ct}^2}{R_0 + R_{ct}} \quad (4)$$

$$C_p = -\frac{R_0 \tau}{R_{ct}^2} \quad (5)$$

Detailed analysis of the obtained impedance equations predicted three general shapes of Nyquist plots [8]:

(1) R_0 >> R_{ct} – the equivalent circuit is reduced to the parallel connection of R_{ct} and C_{dl} producing one semi-circle;

(2) R_0 comparable to R_{ct} – if $R_{ct}C_{dl}$ << τ two semi-circles will appear on the Nyquist plot, one at high frequencies ($\omega \geq 1/R_{ct}C_{dl}$) corresponding to the parallel connection of R_{ct} and C_{dl} and another one at low frequencies ($\omega \leq 1/\tau$) corresponding to the parallel connection of R_p and C_p;

(3) R_0 << R_{ct} – producing complex shapes of Nyquist plots depending on the values of parameters.

In 1982 Harrington et al. [16] provided a detailed theoretical analysis for such a case considering the same equivalent circuit as that in Ref. [8] connected in parallel with the double layer capacitance (C_{dl}) by discussing the significance of the equivalent circuit elements on the behavior of a multi-step reaction with the adsorbed intermediate in the absence of diffusion control. The best example for this analysis was the HER. The total impedance was given by the equation

$$Z = \frac{1}{\left[R_{ct} + \frac{1}{\left(\frac{1}{R_p} + j\omega C_p\right)}\right]^{-1} + j\omega C_{dl}} \quad (6)$$

Where

R_{ct} is the charge transfer resistance of the HER, R_p is the charge transfer resistance of the electrodesorption step and/or recombination step, and C_p is the pseudo-capacitance of the electrosorbed species. The capacitance C_p was assumed to appear in combination with the resistor R_p.

There are in the literature only a few papers presenting experimentally obtained results for the parameters R_p and C_p [17-21]. In Ref. [17] the HER at a rotating Pt electrode was investigated in 0.5 M NaOH and 0.5 M H_2SO_4 by EIS measurements. Nyquist plots in both solutions were characterized by two semi-circles with the values of C_p being one order of magnitude higher than the values of C_{dl}, increasing with the overpotential, while R_p values decreased with the overpotential increase. Two semi-circles were also obtained for the EIS of HER on modified (Ni-Al-Cu-Cr) and pure Reney nickel electrode (Ni-Al) in 5.36 M KOH at 70 ^oC, with C_p increasing and R_p decreasing with the overpotential [18]. Kinetics and mechanism of the HER at electrodeposited Ni/$NiMoS_2$ electrode in 6 M KOH at 25 ^oC were also investigated by EIS measurements in the work of Castro et al. [19]. Again, two semi-circles in Nyquist plots were obtained, but the values of C_p and R_p as a function of overpotential were not presented. The same equivalent circuit (as that in Refs. [16] and [17]) was used to fit EIS results of the HER at Pd-Ni alloys in 0.5 M NaOH at 25 ^oC. Fitting results showed that the values of C_p and C_{dl} are comparable as a consequence of hydrogen absorption at the electrode surface reducing available electrode surface for the HER to only 10 % [20]. In Ref. [21] the HER was investigated in 0.1 M H_2SO_4 at a rough Pd rotating electrode. EIS results were fitted with the equivalent circuit presented in Figure 5, since all Nyquist plots were characterized with well-defined two semi-circles. It was shown that the value of C_p is practically independent of overpotential, with the value of $d\eta/d\log R_p$ being ~ 0.062 V dec^{-1}. Such behavior was explained by the fact that hydrogen adsorption does not follow Langmuir adsorption isotherm.

The procedure of interpretation of the experimental results and calculation of correct values of parameters for the HER at Ni-Sn coated Ni foam by the analysis of EIS results is presented in this work.

2. EXPERIMENTAL

2.1. Sample preparation

All solutions were made from p.a. chemicals (Sigma-Aldrich) in extra pure (18.2 MΩ) UV water (Smart2, Pure UV, TKA). Ni foam with average open pore size of 800 μm was used as a substrate

for electrdeposition. In order to remove oxide from the Ni surface Ni foam substrate was first soaked in acetone for 10 min. with ultrasonication. The next step was cleaning in 1.0 M HCl solution in an ultrasound bath for 10 min., while the final step was ultrasonication for 5 min. in deionized water. Pretreatment of Ni foam was performed at room temperature. Such sample was used for the electrodeposition of Ni-Sn alloy on it. The sample was made by the procedure shown in Figure 2 [22]. The foam was cut into dimensions 2 cm x 1 cm. Half of the foam (1 cm) was covered with the L-shaped Ni mesh 40 (2.5 cm x 1 cm) and pressed to provide good contact between the foam and Ni mesh 40. This part of the electrode, as well as part of Ni mesh, were isolated with Teflon tape (foil) in order to prevent contact with the electrolyte. The top of the Ni mesh was soldered for Ni wire and placed in a glass tube in such a way that electrolyte could not enter the tube.

The geometric surface area (S_g), as well as the real surface area (*RSA*), are presented in Table 1. The *RSA* was obtained by BET analysis (Brunauer–Emmett–Teller), where BET surface areas were measured by krypton adsorption at 77.3 K according to DIN ISO 9277 (Autosorb AS-1). The values given in Table 1 were obtained for pure Ni foam without Ni-Sn coating on the Ni foam [22].

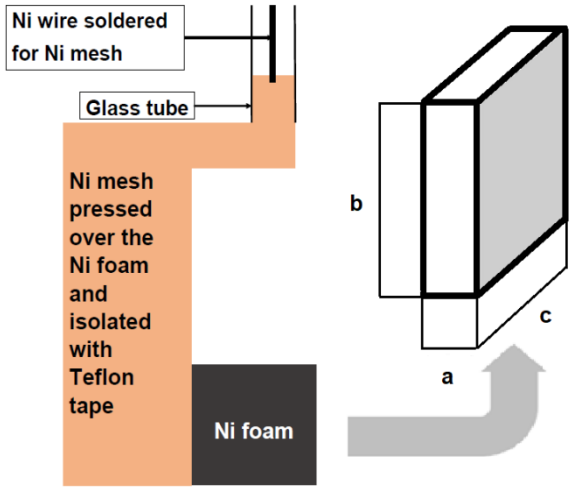

Figure 2. Schematic presentation of the Ni foam working electrode. Geometric electrode surface area was calculated by the equation: $S_g = 2ab + (a + 2b)\cdot c$ *[22]*

Slika 2. Shematski prikaz elektrode od Ni pene. Geometrijska površina elektrode je izračunata pomoću jednačine: $S_g = 2ab + (a + 2b)\cdot c$ *[22]*

Table 1. Geometric surface area (S_g) and the value of RSA for Ni foam

Tabela 1. Geometrijska površina elektrode (S_g) i vrednost realne površine elektrode (RSA) za Ni penu

Ni foam	Specification (cm^2/cm^3)	S_g (cm^2)	V (cm^3)	*RSA* (cm^2)	*RSA* / S_g
800 μm	83	3.16	0.282	23.406	7.41

The H-type electrochemical cell was used for the HER testing**.**

The Ni foams are commercially available as a mass product for different applications. Ni foam (Alantum) was used as a substrate for the electrodeposition of Ni-Sn alloy coating.

2.2. Electrodeposition of Ni-Sn alloy on Ni foam substrate

The electrodeposition of Ni-Sn coating on Ni foam substrate was performed by means of a potentiostat Interface 1010E (Gamry Instruments Inc.) at constant current density of j_{dep} = -40 mA cm^{-2} for 2000 s in the bath containing 0.6 M $K_4P_2O_7$ + 0.1 M $NiCl_2\cdot 6H_2O$ + 0.03 M $SnCl_2\cdot 2H_2O$ + 0.3 M NH_2CH_2COOH (pH 6.7) at the room temperature.

2.3. HER polarization curves

The HER polarization characteristic at the investigated electrode was tested in 30 % KOH solution at the temperature of 70 °C. The sample was first submitted to HER at a constant current density j = -300 mA cm^{-2} for 600 s (j was calculated using geometric surface area S_g – see Table 1). The polarization curves were recorded using linear sweep voltammetry (LSV) at the sweep rate of 1 mV s^{-1} by two procedures: (1) Without jR_s drop correction, starting from η = -50 mV and finishing at η = -110 mV; (2) Using current interrupt technique, starting from η = -20 mV up to the η at which the current reached maximum value of 1 A (limit of the potentiostat).

2.4. HER investigation by EIS

EIS measurements were performed in the same cell with the same potentiostat, using software EIS 300 (Gamry Instruments Inc.): amplitude 5 mV RMS, 20 points per decade, starting at 20 kHz and finishing at 0.01 Hz at four values of η: -50 mV, -70 mV, -90 mV and -110 mV. Before recording EIS results, sample was held at the potential of the EIS measurements for 100 s to establish a stable current density response. Fitting of the experimental results was carried out by

Echem Analyst software – EIS 300 (Gamry Instruments Inc.).

3. RESULTS AND DISCUSSION

3.1. Polarization curves for the HER

The polarization curve measured without jR_s correction and polarization curve corrected for jR_s for the HER at Ni-Sn/Ni foam 800 sample in 30 % KOH at 70 °C are shown in Figure 3.

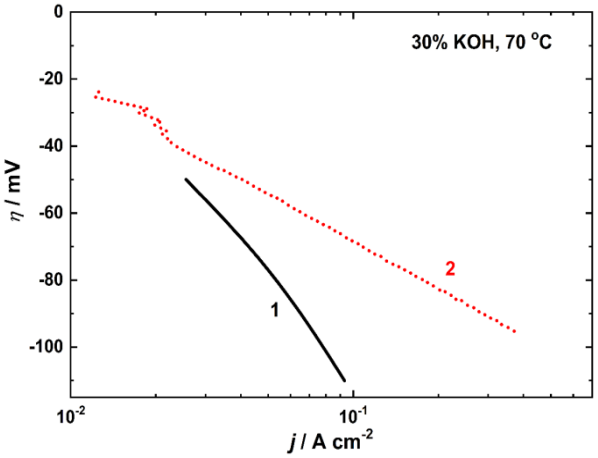

Figure 3. Polarization curves for the HER at investigated sample in 30 % KOH at 70 °C: (1) Without jR_s drop correction; (2) With jR_s drop correction using current interrupt technique

Slika 3. Polarizacione krive za izdvajanje vodonika na ispitivanoj elektrodi u 30 % KOH na temperaturi od 70 °C: (1) Bez korekcije za pad napona jR_s; (2) Sa korekcijom za pad napona jR_s

Curve 1 corresponds to the measurement without jR_s correction, while curve 2 represents the measurement with current interrupt jR_s correction. As can be seen, the same overpotential has been reached at a higher current density for the jR_s drop corrected curve.

3.2. HER investigation by EIS

Nyquist plots recorded at four overpotentials (-50 mV, -70 mV, -90 mV and -110 mV) are presented in Figure 4. All Nyquist plots are characterized by the presence of two semi-circles, one at high frequencies corresponding to the charge transfer and the other one at low frequencies, which could only be ascribed to the overpotential-dependence of the process of electrosorption / electrodesorption of H_{ads} intermediate. Those Nyquist plots were fitted with the equivalent circuit shown in Figure 5. The values of C_p were calculated using the equation [23,24]

$$C_p = \left[Y_p R_p^{(\alpha_p - 1)}\right]^{\frac{1}{\alpha_p}} \quad (7)$$

with Y_p being the constant of CPE_p and α_p exponent. Obtained values for R_{ct}, C_p and R_p were used for further calculation.

According to Armstrong et al. [8] marked part of the equivalent circuit presented in Figure 5 corresponds to the process of intermediate electrosorption / electrodesorption. Using obtained values for R_{ct}, C_p and R_p, the values of R_o and τ were calculated by the following equations:

$$R_o = \frac{-R_{ct}(1+R_p)}{R_p} \quad (8)$$

$$\tau = \frac{-C_p(R_{ct}^2)}{R_o} \quad (9)$$

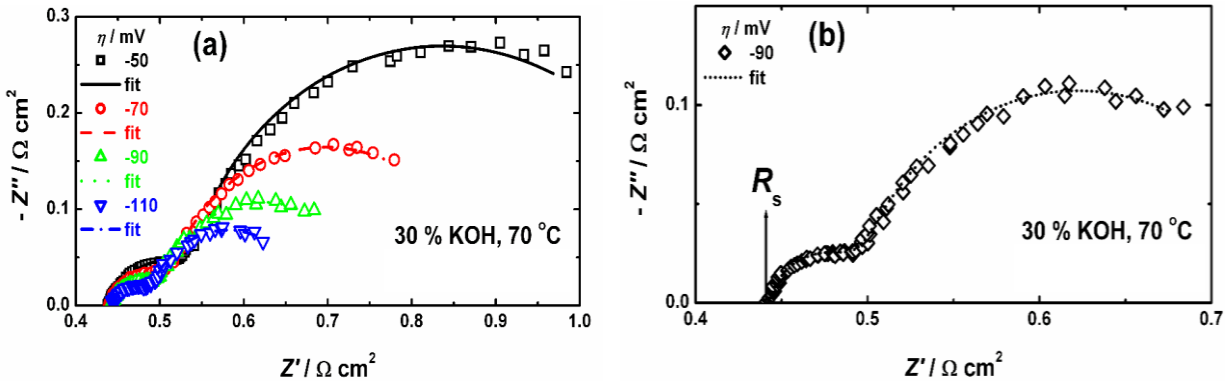

Figure 4. Nyquist plots recorded at different overpotentials in 30 % KOH at 70 °C. Squares, circles and triangles represent experimental points, while lines (solid, dotted, dashed and dash-dot) correspond to the fitting curves

Slika 4. Nyquist-ovi dijagrami registrovani pri različitim vrednostima prenapetosti u 30 % KOH na temperaturi od 70 °C. Kvadrati, krugovi i trouglovi predstavljaju eksperimentalne tačke, a linije (puna, tačkasta, isprekidana i tačka-crtica) odgovaraju krivama fitovanja

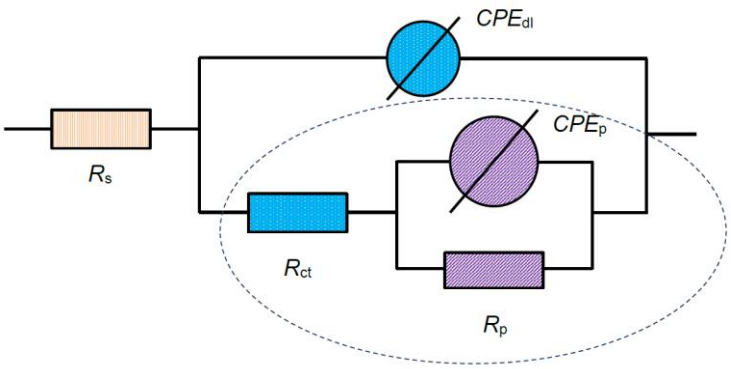

Figure 5. Equivalent circuit for fitting Nyquist plots presented in Figure 4: R_s – solution resistance; R_{ct} – charge transfer resistance; CPE_{dl} – constant phase element corresponding to double layer capacitance; CPE_p - constant phase element corresponding to adsorption pseudo capacitance and R_p - charge transfer resistance of the electrosorption / electrodesorption of intermediate

Slika 5. Ekvivalentno kolo za fitovanje Nyquist-ovih dijagrama prikazanih na slici 4: R_s – omski otpor elektrolita; R_{ct} – otpor razmene naelektrisanja; CPE_{dl} – konstantni fazni element koji odgovara kapacitetu dvojnog sloja; CPE_p - konstantni fazni element koji odgovara kapacitetu adsorpcije intermedijara; R_p - otpor razmene naelektrisanja pri electrosorpciji / electrodesorpciji intermedijara

As stated in the Section 2.4. before recording EIS results, sample was held at applied overpotential for 100 s to establish a stable current density response. Since the EIS measurements cannot be performed with jR_s drop compensation, the current density for each overpotential was recorded for 100 s, as shown in Figure 6. As can be seen after the initial decrease of the current density well-defined plateaus were established.

In order to obtain the values of η corrected for jR_s drop, the values of current density plateaus (j) were multiplied with the values of solution resistance (R_s) and subtracted from the applied overpotentials by the equation:

$$/\eta_{corr.}/ = /\eta/ - /jR_s/ \qquad (11)$$

In Table 2 are given the absolute values of j and R_s, as well as uncorrected and corrected overpotentials (η and $\eta_{corr.}$). Hence, it is obvious that the applied overpotential is higher than the corrected one, and this (corrected) value should be used for determining the real values of j_o and τ_o.

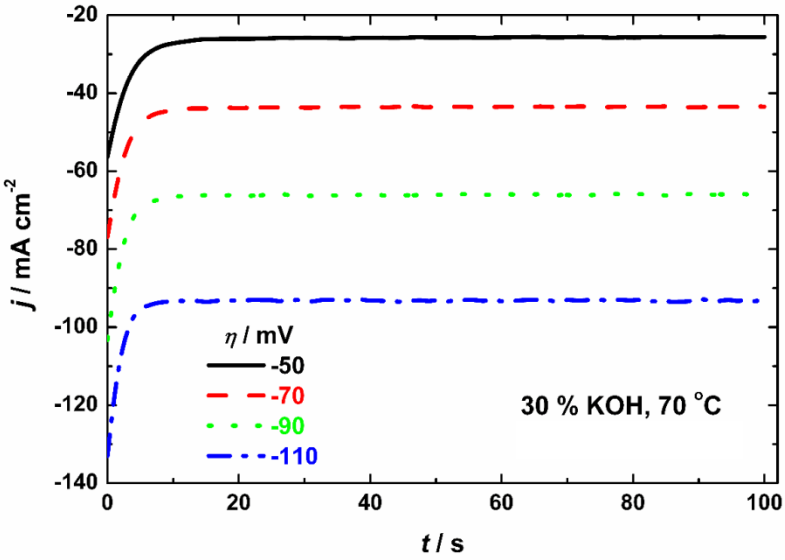

Figure 6. j vs. t responses for different values of η before the EIS measurements at these overpotentials

Slika 6. j -t odgovori pri različitim vrednostima prenapetosti pre impedansnih merenja na tim prenapetostima

Table 2. Applied (η) and corrected (η_{corr}) values of the overpotentials

Tabela 2. Zadate (η) i korigovane (η_{corr}) vrednosti prenapetosti

$\lvert\eta$ / V$\rvert$	R_s / Ω cm^2	$\lvert j$ / A cm$^{-2}\rvert$	$\lvert j R_s$ / V$\rvert$	$\lvert\eta_{corr}$ / V$\rvert$
0.05	0.43891	0.02559	0.01123	0.03959
0.07	0.43942	0.04346	0.0191	0.05233
0.09	0.44247	0.06591	0.06285	0.06285
0.11	0.44399	0.09303	0.0413	0.07163

In Figure 7(a) are presented η *vs.* log (R_{ct}^{-1}) and η_{corr} *vs.* log (R_{ct}^{-1}) dependences. It is obvious that the value of j_o(corr.) obtained from η_{corr} *vs.* log (R_{ct}^{-1}) dependence is much lower, and that particular value should be used for the correct determination of j_o. In Figure 7(b) are presented logτ *vs.* η_m and logτ *vs.* η_{corr} dependencies with τ_o and τ_o(corr.) corresponding to measured and correct values of τ, respectively. The values of j_o and j_o(corr.) were calculated using equation

$$j_o = \frac{RT}{zF}\frac{1}{R_{ct}^o} \qquad (11)$$

with $1/R_{ct}^o$ representing the intercept at the x axis for $\eta = 0$ (Figure 7(a)).

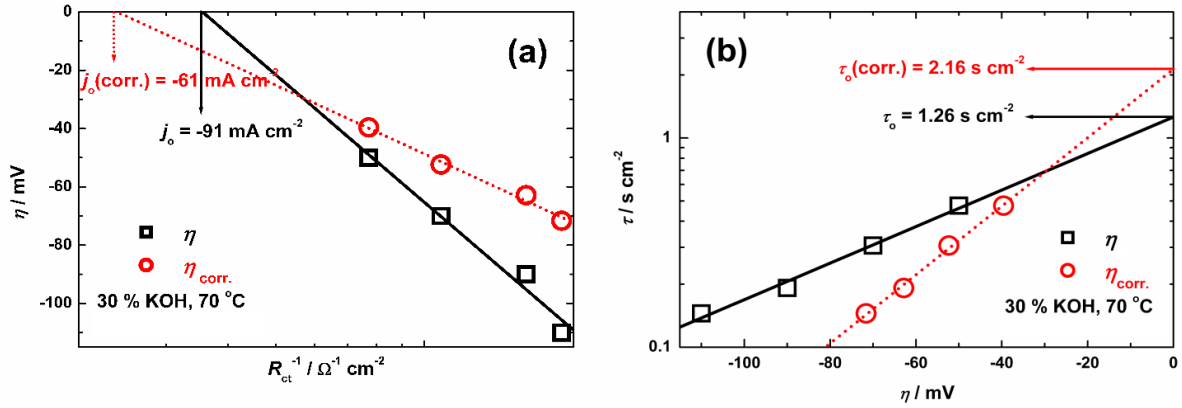

Figure 7. (a) η_m vs. log (R_{ct}^{-1}) and η_{corr} vs. log (R_{ct}^{-1}) dependences for the HER at investigated electrode in 30 % KOH at 70 °C. (b) logτ vs. η_m and logτ vs. η_{corr}

Slika 7. (a) η_m vs. log (R_{ct}^{-1}) and η_{corr} vs. log (R_{ct}^{-1}) za izdvajanje vodonika na ispitivanoj elektrodi u 30 % KOH na temperaturi od 70 °C. (b) logτ vs. η_m and logτ vs. η_{corr}

All obtained values correspond to the geometric surface area S_g. Assuming that the *RSA* for pure Ni foam and that covered with the Ni-Sn coating is the same, the values given in Figure 7 should be divided by 7.41 (see Table 1) in order to obtain values of j_o and τ_o expressed per real surface area.

4. CONCLUSIONS

In order to obtain correct values of the parameters of HER at any type of electrode materials, the exchange current density (j_o) and relaxation time (τ) for intermediate (H_{ads}) adsorption, the procedure explained in this work should be used. The value of j_o was obtained from the intercept at η = 0 mV from the η vs. log (R_{ct}^{-1}) dependence, and the value of τ_o was obtained from the intercept at η = 0 mV from the logτ vs. η dependence. It was shown that for the correct determination of j_o and τ_o, it is necessary to correct applied η for the jR_s drop, by recording current density (j) for applied η and correcting it for jR_s.

Acknowledgements

This work was supported by the Federal Ministry of Education and Research – Germany, through the WBC2019 call – project NOVATRODES 01DS21010 and by the Ministry of Science, Technological Development and Innovation of the Republic of Serbia, contract no. 451-03-47/2023-01/200135.

SPONSORED BY THE

Federal Ministry of Education and Research

5. REFERENCES

[1] S.Trasatti (1992) Electrolysis of Hydrogen Evolution: Progress in Cathode Activation, In: H. Gerischer, C.W. Tobias (Eds.), Advances in Electrochemical Science and Engineering, Wiley-VCH, Weinheim, p. 2–85.

[2] B.V.Tilak, P.W.T.Lu, J.E.Colman, S.Srinivasan (1981) Electrolytic Production of Hydrogen, In: Comprehensive Treatise of Electrochemistry, J.O'.M. Bockris, B.E. Conway, E. Yeager, R.E. White (Eds.), Vol. 2, Plenum Press, New York and London, p. 1-97.

[3] V.D.Jović, N.V.Krstajić, T.Rauscher (2023) Electrodeposited Ni-Based, Non-Noble Metal Cathodes for a Hydrogen Evolution Reaction in Alkaline Solutions, In: M.J. Acosta (Ed.), Advances in Energy Research, Vol. 39, Nova Science Publishers, Inc., New York, p. 97-184.

[4] A.Lasia (2003) Hydrogen evolution reaction, In: W. Vielstich, A. Lamm, H.A. Gasteiger (Eds.), Handbook of Fuel Cells – Fundamentals, Technology and Applications, Vol. 2, John Wiley & Sons, Ltd., Chichester, p 416-440.

[5] Noble-Metal-Free Electrocatalysts for Hydrogen Energy, Catalytic Science Series, Vol. 20, Q. Gao, L. Yang (Eds.), World Scientists, 2022.

[6] B.E.Conway, B.V.Tilak, in: D.D. Eley, H.Pines, P.B. Weisz (Eds.) (1992) Advances in Catalysis, vol. 38, Academic Press, Inc., San Diego, California, Ch. 1.

[7] H.Gerischer, W.Mehl, Z.Elektrochem (1955) Zum Mechanismus der kathodischen Wasserstoffabscheidung an Quecksilber, Silber und Kupfer, Z. Physic. Chem, 59, 1049-1059.

[8] R.D.Armstrong, M.Henderson (1972) Impedance plane display of a reaction with an adsorbed intermediate, J. Electroanal. Chem., 39, 81-90.

[9] S.-I. Pyun, T.-H.Yang (1996) Investigation of the HER at a 10 wt. Pd-dispersed C electrode using EIS, J. Appl. Electrochem., 26, 953-958.

[10] C.Hitz, A.Lasia (2001) Experimental study and modeling of impedance of the her on porous Ni electrodes, J. Electroanal. Chem., 50, 213-222.

[11] A.Lasia (2002) Applications of electrochemical impedance spectroscopy to hydrogen adsorption, evolution and absorption into metals, in: B.E. Conway, R.E. White (Eds.), Modern Aspects of Electrochemistry, no. 35, Kluwer Academic Publishers, New York, Boston, Dordrecht, London, Moscow, Ch. 1.

[12] B.Losiewicz, A.Budniok, E.Rowinski, E.Lagiewka, A. Lasia (2004) The structure, morphology and electrochemical impedance study of the hydrogen evolution reaction on the modified nickel electrodes, Int. J. Hydrogen Energy, 29, 145-157.

[13] L.Birry, A.Lasia (2004) Studies of the hydrogen evolution reaction on Raney nickel–molybdenum electrodes, J. Appl. Electrochem., 34, 735–749.

[14] B.E.Castro, R.H.Milocco (2005) Identifiability of sorption and diffusion processes using EIS: Application to the hydrogen reaction, J. Electroanal. Chem., 579, 113-123.

[15] A.Lasia (2019) Mechanism and kinetics of the hydrogen evolution reaction, Int.J.Hydrogen Energy, 44, 19484-19518.

[16] D.A.Harrington, B.E.Conway (1987) Ac impedance of faradaic reactions involving electrosorbed intermediates - I. Kinetic theory, Electrochim. Acta, 32, 1703-1712.

[17] L.Bai, D.A.Harrington, B.E.Conway (1987) Behavior of overpotential-deposited species in faradaic reactions - II. ac impedance measurements on H_2 evolution kinetics at activated and unactivated Pt cathodes, Electrochim. Acta, 32, 1713-1731.

[18] M.Okido, J.K.Depo, G.A.Capuano (1993) The Mechanism of Hydrogen Evolution Reaction on a Modified Raney Nickel Composite-Coated Electrode by AC Impedance, J. Electrochem. Soc., 40, 127-133.

[19] E.B.Castro, M.J. de Giz, E.R.Gonzalez, J.R.Vilche (1997) An electrochemical impedance study on the kinetics and mechanism of the hydrogen evolution reaction on nickel molybdenite electrodes, Electrochim. Acta, 42, 951-959.

[20] N.V.Krstajić, S.Burojević, Lj.M.Vračar (2000) The determination of kinetics parameters of the hydrogen evolution on Pd-Ni alloys by ac impedance, Int.J.Hydrogen Energy, 25, 635-641.

[21] D.Lin, A.Lasia (2017) Electrochemical impedance study of the kinetics of hydrogen evolution at a rough palladium electrode in acidic solution, J. Electroanal. Chem., 785, 190-195.

[22] J.D.Gojgić, A.M.Petričević, T.Rauscher, C.I. Bernäcker, T.Weißgärber, L.Pavko, R.Vasilić, M.N. Krstajić Pajić, V.D.Jović (2023) Hydrogen evolution at Ni foam electrodes and Ni-Sn coated Ni foam electrodes, Applied Catalysis A, General, 663, 119312

[23] C.H.Hsu, F.Mansfeld (2001) Technical Note: Concerning the Conversion of the Constant Phase Element Parameter Y_0 into a Capacitance, Corr. 57, 747-748.

[24] V.D. Jović (2022) Calculation of a pure double layer capacitance from a constant phase element in the impedance measurements, Zaštita Materijala, 63, 50-57.

IZVOD

PROCEDURA KOREKTNOG ODREĐIVANJA PARAMETARA REAKCIJE IZDVAJANJA VODONIKA NA ELEKTRODI OD Ni PENE MODIFIKOVANE ELEKTROHEMIJSKI ISTALOŽENOM Ni-Sn LEGUROM

Na primeru izdvajanja vodonika na Ni-Sn/Ni pena 800 elektrodi u ovom radu je prikazana procedura korektnog određivanja parametara ove reakcije, a to su: gustina struje izmene (j_o) i relaksaciono vreme adsorpcije intermedijara (τ) (H_{ads}). Vrednost j_o je određena iz odsečka za η = 0 mV zavisnosti η vs. log(R_{ct}^{-1}) (η - prenapetost), dok je vrednost τ_o određena iz odsečka za η = 0 mV zavisnosti logτ vs. η. Pokazano je da je za korektno određivanje ovih parametara neophodno korigovati gustinu struje pri svakoj zadatoj prenapetosti za vrednost omskog pada napona jR_s.

***Ključne reči**: Reakcija izdvajanja vodonika, gustina struje izmene, relaksaciono vreme, Ni-Sn legura, Ni pena, 30 % KOH*

Naučni rad
Rad primljen: 12.11.2023.
Rad prihvaćen: 01.12.2023.
Rad je dostupan na sajtu: www.idk.org.rs/casopis

Agha Inya Ndukwe

Federal University of Technology, Department of Materials & Metallurgical Engineering, Owerri, Imo State, Nigeria

Review paper
ISSN 0351-9465, E-ISSN 2466-2585
https://doi.org/10.62638/ZasMat1034

Zastita Materijala 65 (1)
11 – 21 (2024)

Corrosion inhibition of carbon steel by eucalyptus leaves in acidic media: An overview

ABSTRACT

This paper concerns the overview of previous studies on the corrosion and inhibition of carbon steel that is allowed to degrade in a corrosive medium by the extract of the eucalyptus plant, with an emphasis on the extract's adsorption behaviour. Many researchers have largely employed eucalyptus plant bark, oil, and leaf extracts to prevent the corrosion of mild steel in acidic environments under various temperature settings. According to the results, when the bark extract of the eucalyptus plant was added to HCl (5%) at a concentration of 900 ppm, the inhibitor's maximum efficiency was 98.2 %. The leaf extract, on the other hand, had the maximum inhibitory efficacy of 93.09 % at 600 mg/L extract concentration in the H_2SO_4 (0.5 M) medium. The extracts' potency was shown to diminish with increasing temperature. The mechanism for eucalyptus extract's protection of carbon steel from corrosion in diverse corrosive situations was largely associated with the adsorption of the extract's inhibitive components on the steel's surface to reduce the interaction between the metal and the corrosive surroundings. The majority of the reported inhibitive behaviour of the eucalyptus extract was consistent with the Langmuir adsorption isotherm model.

Keywords: *eucalyptus leaf-extract, inhibition efficiency, mild steel, Langmuir isotherm model, corrosion inhibition, carbon steel.*

1. INTRODUCTION

The breakdown of a metal as a result of its contact with its environment is known as corrosion [1]. Metal corrosion occurs as a result of its interaction with specific elements in the environment, resulting in the deterioration of metal's characteristics. This is a natural and unavoidable process [2]. Metal corrosion has several negative effects on human society's progress [3]. Alloys and metals, in particular, had shown a significant proclivity to corrode in the presence of acid. Certainly, metals are vulnerable to corrosion in acid solutions because the acid can target the metal's surface, dissolving it into its ions [4]. In addition, weldments also corrode in the presence of degrading environments [5,6].

Corrosion inhibition is one of the strategies used to reduce the impact of corrosion. In general, corrosion inhibitors are divided into two types: inorganic and organic [7]. Organic corrosion inhibitors (such as chromium-based inhibitors) can successfully prevent metal corrosion, but they also have drawbacks. Many chemical compounds, for example, are very poisonous and will cause significant environmental harm when used [8]. The use of aqueous extracts is favoured over organic extracts in theory because aqueous extracts, being inorganic inhibitors, include comparatively polar phytochemicals that allow stronger bonding with the metallic surface than the non-polar phytochemicals of organic extracts [9].

Environmentally friendly inhibitor as a replacement for chromate-based inhibitors is a long-standing endeavour by researchers to solve environmental challenges [10]. A lot of plant extracts have previously been reported as effective for inhibiting the corrosion of carbon steel in some corrosive media [11-21]. Extracts from different parts of the eucalyptus plant have been studied

*Corresponding author: Agha Inya Ndukwe
E-mail: agha.ndukwe@futo.edu.ng
Paper received: 18. 06. 2023.
Paper accepted: 12. 07. 2023.
Paper is available on the website: www.idk.org.rs/journal

and affirmed to be effective inhibitors to deter the corrosion of mild steel in different corrosive environments. A study to investigate the inhibitory behaviour of the oil obtained from the eucalyptus globulus leaves has been undertaken [22] It was reported that the application of the oil at 1.6 g/L gave the maximum inhibition efficiency of 89.03 % at room temperature. In addition, the inhibition efficiency was observed to reduce as the temperature increased from 298 to 338 K. The adsorption behaviour of the oil was found to be in sync with the Langmuir adsorption isotherm model. Different scholars have acknowledged the effectiveness of the eucalyptus plant extract as a natural material for inhibiting the corrosion of metal in acidic media [23,24].

This current work aims at studying recent developments on the corrosion and inhibition of carbon steel that are allowed to degrade in corrosive media by the extracts of the eucalyptus plant with the adsorption behaviour of the extract in perspective.

2. UNDERSTANDING CORROSION

Corrosion refers to the degradation process which is instigated between the metal or alloy and the exposed surrounding which invariably leads to the weakening of the physical and mechanical properties of the metal [25]. The degradation process can be in the form of an electrochemical or chemical process [26].

2.1. Electrochemical process

An electrochemical process causes corrosion. That is, corrosion often happens as a result of the attendant electrochemical half-cell processes rather than a metal reacting chemically with its surroundings directly [27]. A process in which electrons are transferred is referred to as an electrochemical reaction. The reaction also includes both oxidation and reduction. Because both processes are frequently coupled in one piece of metal, it is not always evident that corrosion is made up of a minimum of one chemical reaction and one reduction reaction [28].

2.1.1.Reactions in half a cell

When electrons only occur on one side of the reaction, the reaction is said to be a half-cell reaction. The half-cell reaction is an oxidation process if electrons are products (right side of the reaction). On the other hand, the half-cell reaction is a reduction process if electrons are reactants (on the left-hand side of the reaction) [27]. A half reaction (also known as a half-cell reaction) is the oxidation or reduction reaction portion of a redox reaction in chemistry [29].

2.1.2.What happens at the anodic half-cell

An anodic reaction results in metal loss, viz:

$$Fe(s) = Fe^{2+}(aq) + 2e^{-} \quad (1)$$

The reaction can be possible if there is a rise in the species' oxidation number, and the process produces electrons [27]. Figure 1 presents a graphical representation of these concepts.

2.1.3.Cathodic reaction half-cell

For the reaction to be cathodic, the given species must undergo a reduction in its oxidation number.

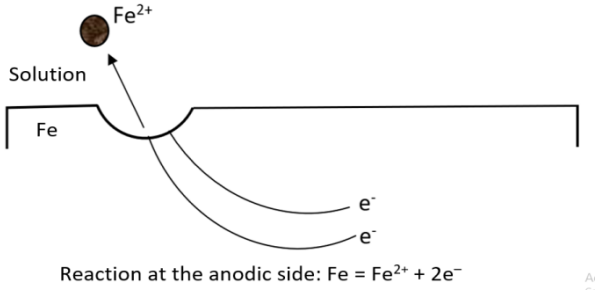

Figure 1. Schematic illustration of the dissolution of iron during anodic reaction [27]

Slika 1. Šematski prikaz rastvaranja gvožđa tokom anodne reakcije [27]

This results in the consumption of electrons at the cathodic region. A veritable instance is the decrease of 2 ions of hydrogen to give rise to one molecule of hydrogen gas [30]:

$$2H^{+}\,(aq) + 2e^{-} \rightarrow H_2\,(g) \quad (2)$$

A schematic representation of this reaction is shown in Figure 2.

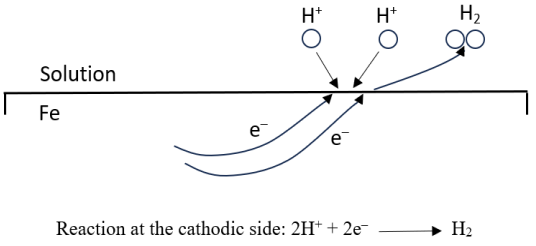

Figure 2. Schematic reaction at the cathodic region involving the evolution of hydrogen on Fe in an acid medium [27]

Slika 2. Šematska reakcija u katodnom delu koja uključuje izdvajanje vodonika na Fe u kiseloj sredini [27]

The reduction of dissolved oxygen to hydroxyl ions, which takes place in neutral or basic fluids, is another typical cathodic process [31].

$$O_2(g) + 2H_2O + 4e^{-} \rightarrow 4OH^{-}(aq) \quad (3)$$

2.2. Electrochemical studies

2.2.1. Potentiodynamic Polarization Analysis

The Potentiodynamic Polarization Measurement (PDP) is one of the most used DC electrochemical methods used in corrosion measurements. In PDPs, a broad range of potential is given to the test electrode as a consequence of which a sufficient current is produced. Depending on the polarization direction, this causes a dominating oxidation or reduction process to occur on the metal surface. One may derive the polarization curve by presenting the potential as a function of the current density (I) (or log I) at each measured point. The metal's propensity for corrosion and rate of corrosion under the conditions present may be calculated using the polarization curve (Tafel slope) [32]. The benefit of potentiodynamic polarization measurement can be seen in the ability to detect localized corrosion, the simplicity and speed with which the corrosion rate can be calculated, as well as the effectiveness of corrosion protection. However, in many cases, to calculate the Tafel slope, we must use data that are located further away from the corrosion potential, allowing us to take into account additional reactions that could result in significant errors in the calculated slope [32,33].

2.2.2. Impedance spectroscopy for electrochemistry

The electrochemical measuring technique (EIS) uses many frequencies of AC. Over a broad frequency range (from 1 MHz to 10 kHz), it detects the electrical resistance (impedance) of the metal/solution contact. The EIS data provide for the possibility of calculating the double layer's capacitance, solution resistance, and polarization resistance (low- and high-frequency regions). The corrosion rate is frequently determined using polarization resistance [32,34].

2.2.3. Weight-loss corrosion study

Of all the corrosion monitoring systems, the Weight Loss method is the most well-known and straightforward [35]. A sample of material (the coupon) is exposed to a process environment for a predetermined amount of time before being removed for analysis. Weight loss is the fundamental measurement that may be obtained from corrosion coupons; the corrosion rate is given as the weight loss over the exposure period. As a result of the corrosion coupon technique's ease of use, it serves as the standard method of measurement in many corrosion monitoring programs. The method is incredibly adaptable since weight loss coupons may be made from any alloy that is readily available in commerce. Moreover, a range of corrosion processes employs suitable geometric shapes [35]. The corrosion rate can be quantified using the method [36]:

$$rCorr = W_{loss}/A_{exp} \times T_{exp} \quad (4)$$

where,

$rCorr$ = rate of corrosion.

W_{loss} = difference between the initial and final weights.

A_{exp} = area of exposure.

T_{exp} = time of exposure.

The measure of the inhibition efficiency of corrosion studies can be quantified by using the relationship [37]:

$$I.Efficiency\ (\%) = ((rCorr_{un} - rCorr_{in}) / rCorr_{un}) \times 100 \quad (5)$$

Where,

$I.Efficiency\ (\%)$ = Efficiency in corrosion inhibition.

$rCorr_{un}$ = corrosion rate of the blank solution.

$rCorr_{in}$ = corrosion rate of the solution wherein the inhibitor had been added.

2.3. Surface characterization method utilized in corrosion studies

2.3.1. Atomic force microscopy (AFM)

The fundamental working tenet of the AFM is the accurate detection of forces operating at very small distances between a sharp probe tip and a sample surface [38]. The contact force of a corresponding physical quantity is preserved constantly by feedback loops when the probe tip is raster-scanned across the sample surface to accomplish imaging [38]. The following elements make up an AFM (Figure 3): (i) a scanner to precisely position the sample to the probe tip in three dimensions (x, y, and z); (ii) a force sensing element and the associated detection scheme; and (iii) control electronics and a computer to (a) operate scanners and other components; (b) record, display, and save data; and (c) operate feedback loops.

According to Baykara et al. [38], a laser beam deflector is used to detect the deflections of a micro-fabricated cantilever with an integrated probe tip, while a piezoelectric scanner is used to adjust the relative tip-sample location with picometer accuracy in three dimensions. Control electronics that are in charge of tip-sample placement, data collecting, and feedback loop functioning are driven by a computer. When doing dynamic AFM, the cantilever base is stimulated with an amplitude, which causes the probe tip to oscillate [38]. Several studies have employed AFM as one of the methods

to characterize the surface phenomena of metals in various corrosive environments [39].

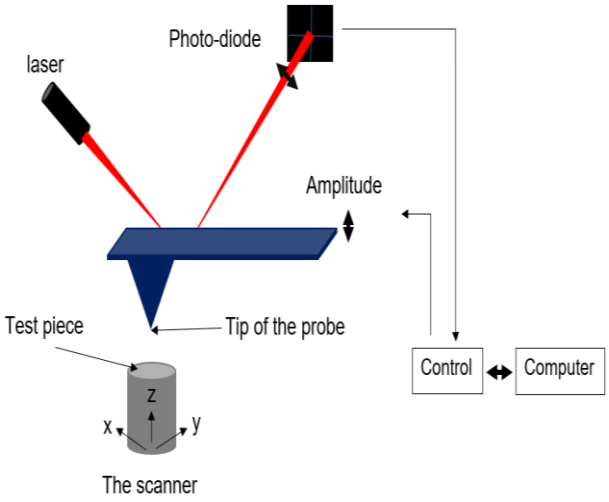

Figure 3. Diagram of a typical AFM setup [38]

Slika 3. Dijagram tipične AFM postavke [38]

2.3.2. Scanning Electron Microscopy

The scanning electron microscope (SEM) uses a focused stream of high-energy electrons to generate a variety of signals at the surface of solid objects. The signals originating from electron-sample interactions give information on the sample in addition to its external morphology (texture), chemical composition, crystalline structure, and orientation of its parts. The sample surface is typically selected for data collection, and a 2-dimensional image is produced to demonstrate the spatial variations in these parameters [40].

2.3.3. Transmission electron microscopy

To see the tiniest structures in materials, analysts utilize transmission electron microscopy (TEM). In contrast to optical microscopes, which rely on light in the visible spectrum, TEM can enlarge nanoscale structures by a factor of up to 50 million, revealing astonishing detail at the atomic scale [41]. This is because, when accelerated via a strong electromagnetic field, electrons may have a wavelength that is hundreds of orders of magnitude shorter (about 100,000 times smaller) than that of visible light, improving the resolution of a microscope by a wide margin. A high-intensity electron beam is propelled through an incredibly thin "electron transparent" material, usually less than 100 nm, to create a TEM picture. The beam of light is focused on the sample, distortions are reduced, and the resulting picture is magnified onto a phosphor screen or a specialized camera using a series of electromagnetic lenses and apertures positioned throughout the microscope's column [41].

2.4. Inhibitors that deter corrosion

There are several categories into which inhibitors might be placed. Adsorption inhibitors and film-forming inhibitors are the two primary categories.

2.4.1. Adsorption inhibitors

Adsorption inhibitors block ongoing electrochemical dissolution processes by forming a chemisorptive link with the metal surface. Chemical-type inhibitors make up the majority of organic inhibitors [27,42-43]. A schematic representation of an organic molecule with an electron pair on the nitrogen atom that is available for donation to the metal surface is shown in Figure 4 (a), for instance.

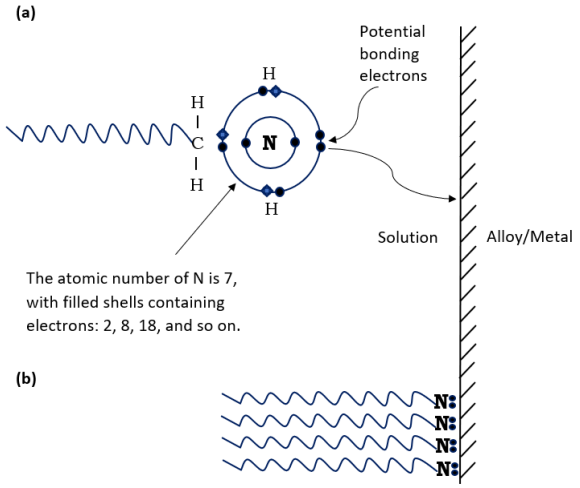

Figure 4. (a) The chemical absorption of an organic substance onto a metal surface. The symbols represent electrons from H or C atoms, whereas the solid black dots represent N atom electrons. (b) On the metal surface, a tightly packed monolayer forms [27].

Slika 4. (a) Hemijska apsorpcija organske supstance na metalnu površinu. Simboli predstavljaju elektrone iz H ili C atoma, dok pune crne tačke predstavljaju elektrone N atoma. (b) Na površini metala formira se čvrsto zbijeni monosloj [27].

Additionally, the hydrocarbon tails of the molecule are directed toward the solution and away from the interface such that an array of hydrophobic hydrocarbon tails forms on an adjacently adsorbed organic component, providing additional protection. As seen in Figure 4 (b), this hydrophobic network serves to keep water molecules and aggressive anions like Cl^- away from the metal surface [27].

2.4.2.Inhibitors of film formation

Passivating inhibitors and precipitation inhibitors are the two different manifestations of

film-forming inhibitors. Passivating inhibitors work by encouraging the development of a passive coating on the surface, as suggested by their name. There are oxidizing and non-oxidizing passivating inhibitors. In the process of oxidizing another molecule, oxidizing agents undergo reduction [43]. The chromate ion is reduced to Cr_2O_3 or $Cr(OH)_3$ on the metal surface when combined with iron or steel, producing a protective mixed oxide of chromium and iron. Chromates are common oxidizing inhibitors. Since oxidizing inhibitors are often adsorbed on the metal surface before being reduced and forming the passive layer, adsorption is also crucial in the case of these substances. To create the passive film, non-oxidizing passivation like benzoates, azelates, and phosphates also initially adsorb on the surface [27].

With precipitation inhibitors, a three-dimensional barrier layer is deposited on the metal surface as a result of a precipitation interaction between the cations of the corroding metal and the inhibitor. When the salt generated between the cations of the metal and the anions of the inhibitor exceeds its solubility product, a film of this nature forms. Examples of inhibitors of the precipitation type include phosphates and silicates. According to which partial electrochemical process is impacted, inhibitors can be categorized as anodic, cathodic, or mixed inhibitors. Chromate compounds, certain phosphates, and the majority of organic molecules are all examples of anodic, cathodic, and mixed inhibitors, respectively [27].

2.4.3. Mechanism of corrosion inhibition in acidic media

The research on the adsorption of inhibitors onto the surface of the metal has found that the efficiency of an inhibitor may be determined by quantifying the amount of extract adsorbed on the metal's surface. This development can manifest in the form reduction in the rate at which the metal corrodes. According to Shreir et al. [45], the adsorbed inhibitors can be directly measured using solution depletion, and radio-tracer detection techniques.

The adsorption behaviour of an inhibitor stipulates that corrosion may be prevented within the region of the metal’s surface that is already inundated with the adsorbed inhibitive materials. In essence, the level of inhibition is commensurate with the fraction of the metal surface that is covered by the adsorbed inhibitor [45].

2.4.4. Factors that influence the adsorption of the inhibitor species on alloys and metals

It has been reported that the adsorption of the inhibitor species on alloys and metals is dependent on the metal’s surface charge, the structure of the inhibitor and the functional group, interaction of the inhibitor with water and adsorbed inhibitor species [45].

The attraction (electrostatic) interactions between the charges (ionic) on the adsorbed materials and the charge (electric) on the alloy at the solution/metal contact might cause adsorption. Whenever the potential, compared to the zero-charge potential is in the positive direction, the anions are favourably adsorbed and when it is more negative, cations are more likely to be adsorbed.

The bonding between the inhibitor species and the metal surfaces can be formed by the transfer of electrons. Transition metals are more favoured for this kind of relationship because of low energy and vacant electron orbitals. For the functional groups containing groups VI and V of the periodic table, it has been discovered that bond formation with stronger coordination (leading to stronger adsorption) occurs by these elements with descending value of electronegativity [45].

2.4.5. Interaction of the inhibitor with water and adsorbed inhibitor species

In the first instance, the metal surfaces in solutions (aqueous) are covered with adsorbed water molecules. When inhibitor molecules are adsorbed on the metal's surface, water molecules are displaced off the metal's surface. On the other hand, the increase in the adsorbed surface coverage may lead to the interaction among the adsorbed species. This reaction may either be repulsive or attractive. Repulsive reactions can exist between molecules containing charges thereby leading to poor adsorption of the inhibitor on the surface of the metal. Conversely, attractive interactions can occur between molecules that contain excessive hydrocarbons. An increase in van der Waals's attractive force between adjoining molecules makes for stronger adsorption at maximum coverage.

Through electrochemical retardation, the adsorbed inhibitor can react to form a product, which in turn can be protective. The nature of the inhibition, occasioned by the introduction of the inhibitive material into a corrosive system is referred to as primary inhibition, whereas that of the reaction product is secondary inhibition [45].

2.4.6. Inhibitors' effect on corrosion reactions

The corrosion process at the anode of an acid-containing solution involves the release of metal ions from the metal surface into the corrosive medium, whereas, at the cathode, hydrogen ions are discharged, resulting in the generation of hydrogen gas. In an acidic environment, the

presence of an inhibitor may entail the decrease of one or both cathodic and anodic processes [46].

2.5. Adsorption isotherm

Several models have been established to explain the adsorption behaviour of experimental data. The current study is largely in agreement with the Langmuir adsorption isotherm model.

2.5.1.Langmuir adsorption isotherm model

The Langmuir isotherm model hinges on the assumption that under constant thermodynamic conditions, the adsorbate exhibits the behaviour of an ideal gas. In addition, the adsorption of the adsorbate is considered the interaction between an empty sorption area and the adsorbate gaseous molecule under chemical reaction conditions. The formula for the Langmuir isotherm is stated thus [47]:

$$\theta_{ads} = \frac{K_q^r \rho_r}{1+K_q^r \rho_r} \quad (6)$$

where,

θ_{ads} = fraction of material located at the adsorption area.

$\mathrm{K_q^r}$ = equilibrium constant of the adsorbate.

ρ_r = partial pressure of the adsorbate.

2.5.2. Freundlich adsorption isotherm

The Freundlich adsorption isotherm may be used to define an exponential energy distribution that surrounds a heterogeneous surface [48,49]. It gives a clear explanation of the relationship between the inhibitor concentration in a liquid that is in touch with a metal's surface and the inhibitor concentration there. The Freundlich adsorption isotherm model's mathematical formulation is as follows [48]:

$$\theta_{Cor} = K_{Frd} C_{ad}^{1/n_{it}} \quad (7)$$

where,

θ_{Cor} = The quantity of metal absorbed per gram of the adsorbent at equilibrium.

K_{Frd} = Freundlich isotherm constant (mg/g).

n_{it} = the level of absorption.

C_{ad} = equilibrium adsorbate concentration (mg/L).

2.5.3Temkin Adsorption Isotherm

The linearity in the decline of adsorption heat with surface coverage is demonstrated by Temkin's adsorption isotherm. The model is used as an example to show how the interactions between the adsorbent and adsorbate uniformly distribute binding energy. Because it explains the interactions that take place in the adsorbed layer, the Temkin adsorption model stands out from all the other models that have been previously given. In mathematics, it is expressed as [47,48]:

$$\theta_{rCorr} = B_{sp}\, InA_{Tm} + B_{Sp}\, InC_{in} \quad (8)$$

$$B_{Sorp} = \frac{RT}{b_{Tm}} \quad (9)$$

where,

θ_{rCorr} = the percentage of surface covering.

B_{Sp} = constant heat of sorption (J/mol).

A_{Tm} = Temkin isotherm equilibrium binding constant (l/g).

C_{in} = concentration of inhibitors.

R = standard gas constant (8.314J/mol/K).

T = absolute degree of heat.

b_{Tm} = Temkin's constant for isotherm.

2.6. The Eucalyptus Plant

Eucalyptus (genus Eucalyptus), a massive genus comprising around 660 species of shrubs and tall trees in the Myrtaceae family, is indigenous to Australia, Tasmania, and neighbouring islands [50].

Eucalyptus grow swiftly, and some species can reach great heights. In Victoria and Tasmania, the huge gum tree, or mountain ash (Eucalyptus regnans), grows to a height of roughly 90 metres (300 feet) with a girth of 7.5 metres (24.5 feet). Many species shed their dead outermost layer of bark in flakes or ribbons regularly, but others have thick, textured bark. The leathery leaves hang obliquely or vertically, and the majority of species are evergreen [50].

Photography 1. The leaves of the eucalyptus plant [50]

Fotografija 1. Listovi biljke eukaliptusa [50]

When the bloom grows, the petals stick together to form a cap. The capsule fruit, which contains numerous minute seeds, is surrounded by a woody cup-shaped receptacle [50].

3. AN OVERVIEW OF PREVIOUS WORK ON THE INHIBITION OF CARBON STEEL IN VARIOUS CORROSIVE ENVIRONMENTS BY THE LEAF EXTRACTS OF THE EUCALYPTUS PLANT

Many studies have employed eucalyptus plant extracts to lower the rate of corrosion of metals in acidic conditions. Table 1 summarizes the greatest inhibition efficiency achieved, as well as the corresponding inhibitor concentration.

Eucalyptus leaf extract has been used to prevent mild steel corrosion in hydrochloric acid solutions [51]. Following the addition of 800 ppm eucalyptus leaf extract, the corrosion rate fell from 0.93 μA/cm^2 to 0.25 μA/cm^2 after 5 hours. The maximal inhibitory efficiency was roughly 88%. The leaf extract's adsorption behaviour was shown to be consistent with the Langmuir isotherm model, while the polarization analysis demonstrated that the eucalyptus leaf extract influenced a mixed-type inhibitive behaviour. In a separate research, Abdulkhaleq [53] used eucalyptus camaldulens leaves to prevent corrosion of low-carbon steel in HCl (3M) media at various study temperatures ranging from 25 to 55 ^{0}C. After 46 hours of adding 8 g/L of the leaf extract, the maximal inhibitory effect of 91% was obtained. Furthermore, the efficiency of the inhibitory mechanism was found to rise as the concentration of the plant extract increased. The explanation for this development was linked to the adsorption of the extract's inhibitive elements on the surface of the mild steel to prevent additional corrosive environment attacks on the steel. In essence, the plant leaf extract's adsorption behaviour was determined to correspond with the Langmuir adsorption isotherm model.

Table 1. Summary of corrosion inhibition of mild steel in the corrosive environment by Eucalyptus plant extracts

Tabela 1. Rezime inhibicije korozije mekog čelika u korozivnoj sredini ekstraktima biljaka eukaliptusa

Inhibited material	Study Environment	Study Method (s)	Part of the plant used	Maximum Inhibition Efficiency Attained (%)	Extract Concentration	Adsorption	Ref.
MS	HCl (1 M)	EIS, PDP	Leaf	88	800 ppm	Langmuir	[52]
LCS	HCl (3 M)	WL	Leaf	91	8g/L	Langmuir	[53]
MS	HCl (5 %)	WL, EIS, PDP	Bark	98.2	900 ppm	Langmuir	[54]
CS	H_2SO_4 (1 M)	WL, PDP, EIS	Leaf	84	1.5 g/L	Langmuir	[55]
MS	H_2SO_4 (0.5 M)	PDP, EIS	Leaf	91	0.4 mol/L	Langmuir	[56]
	H_2P_4 (0.5 M)	EIS, PDP		78	0.2 mol/L		
LCS	H_2SO_4 (0.5 M)	Tafel, WL, EIS	Leaf	93.09	600 mg/L	Langmuir	[57]
CS	HCl (2 M)	WL	Leaf	91.56	0.08g/mL	Langmuir	[58]
	HCl (4 M)			85.68			
MS	NaCl	EIS, PDP	Leaf + Zn^+	90	600 ppm Zn^+ + 200 ppm of the extract 5.0g/L	Langmuir	[59]
MS	HCl (0.1 M)	WL	Bark	97.86		Langmuir	[60]
MS	HCl (0.5 M)	EIS, Tafel	Oil (essential)	91.1	-	Langmuir	[61]
LCS	H_2SO_4 (1 M)	WL	Leaf	84	120 ml	-	[62]
	H_2SO_4 (0.5 M)			86			
	H_2SO_4 (1.5 M)			75			

The bark extract of the eucalyptus plant has been researched for its ability to preserve mild steel against corrosion in HCl (5%) solution [54]. At 900 ppm concentration of the extract in an acidic medium, an inhibitory effect of 98.2% was found. Furthermore, the inhibitive disposition of eucalyptus bark extract was discovered to be mixed-type and consistent with the Langmuir isotherm model.

The use of eucalyptus globulus leaf extract to minimize carbon steel corrosion in H_2SO_4 (1 M) media has been explored [55]. The addition of 1.5 g/L of methanolic leaf extract of the eucalyptus plant in the aforementioned corrosive solution resulted in a maximum inhibitory efficacy of 84%. The inhibitive properties were discovered to be of the mixed kind and consistent with the Langmuir adsorption isotherm model. The adhesion of the extract on the surface of the carbon steel was thought to be the preventative mechanism that the leaf extract utilized to prevent corrosion, hence minimizing the aggressive response between the

corrosive solution and the steel. In a similar work, Haldhar et al. [57] evaluated the use of eucalyptus globulus leaf extract to prevent corrosion of low-carbon steel in H_2SO_4 (0.5 M). After adding 600 mg/L of the plant's leaf extract, the inhibition effectiveness reached 93.09%. The adsorption characteristic of the plant extract was discovered to be consistent with the Langmuir adsorption isotherm model.

Abdel-Gaber et al. [56] investigated the use of eucalyptus leaf extract to suppress mild steel corrosion in both phosphoric (H_2PO_4) and sulphuric acid solutions. The addition of the extract to both acidic solutions lowered the rate of mild steel deterioration as the extract concentration increased. After adding 0.4 and 0.2 mol/L of eucalyptus leaf extracts to the corrosive media, the impedance (electrochemical) findings indicated 91 % and 78 %, respectively. The more persistent contact between the mild steel surface and the eucalyptus extract was credited with the leaf extract being more successful in preventing the corrosion of mild steel immersed in H_2SO_4 (1 M) than in H_2PO_4 (1 M). Physical adsorption was identified as the mechanism for the inhibitory process. Furthermore, the adsorption behaviour of the extract was discovered to correspond with Temkin and kinetic thermodynamic isotherm models.

A study has been conducted to reduce the deterioration of carbon steel in the H_2SO_4 (2 M and 4 M) medium [58]. At 20 ^{0}C, the maximal inhibition efficiencies after the addition of 0.08 g/L of the extract were 91.56 % and 85.68 % for the H_2SO_4 (2 M) and H_2SO_4 (4 M) solutions, respectively. The effectiveness of the leaf extract was observed to increase with increasing extract concentration but decrease with increasing temperature. In addition, the extract's adsorption disposition agreed with the Langmuir isotherm model. In another work, the inhibitive impact of the synergy of zinc ions (divalent) and eucalyptus plant leaf extract on mild steel corrosion in NaCl solution was investigated [59]. After 48 hours, the inhibitive materials combined in the following proportions: zinc ions (600 ppm) and eucalyptus leaf extract (200 ppm) achieved the greatest inhibition efficacy of 90 %. Additionally, the analytical analysis demonstrated that the adsorption mechanism that exists between the inhibitors is dependent on the acceptor-donor system.

Gupta et al. [60] used the bark of the eucalyptus plant to prevent mild steel corrosion in HCl (0.1 M). The presence of the inhibitor lowered the corrosion rate of mild steel in the acidic medium, but the inhibition efficacy decreased as the temperature increased. The greatest inhibitory efficiency reported was 97.86 %. In another work, Gualdron et al. [61] employed eucalyptus oil to prevent mild steel corrosion in HCl (0.5 M). Eucalyptus oil was determined to be a mixed-type inhibitor with a maximum inhibition effectiveness of 91.1%. In addition, Abdal-nabi et al. [62] studied the protection against corrosion of low-carbon steel using eucalyptus leaf extract at different sulphuric acid concentrations (1 M, 0.5 M, and 1.5 M). The inhibition efficiency dropped as the temperature increased from 25 to 60 ^{0}C, with the inhibition efficiencies dropping to 86 – 67 %, 84 – 59 %, and 75 – 52 % for 0.5 M H_2SO_4, 1 M H_2SO_4, and 1.5 M H_2SO_4 solutions, respectively.

4. IDENTIFIED GAPS IN KNOWLEDGE AND RECOMMENDATIONS

The review of previous studies on the use of the extracts of the eucalyptus plant to prevent the corrosion of mild steel in various acid concentrations has revealed the following gaps in knowledge:

1. It is true that different parts of the eucalyptus plant have been reported to give high values of inhibition efficiencies, but the combination of the parts to inhibit the corrosion of steel is yet to be adequately explored. Further studies to understand the influence of the synergy of the plant's parts to avert corrosion are recommended.
2. There is limited knowledge in the exploration of the active constituents of the eucalyptus extracts that were responsible for the inhibition process. Further studies are encouraged to identify in specific terms the active materials in the eucalyptus extract that inhibit corrosion.
3. There is a lack of predictive models that can forecast the corrosion rate of mild steel in the absence and presence of the eucalyptus plant. Further studies should be intensified in this direction.

5. CONCLUSION

After reviewing previous studies on the use of eucalyptus extracts to hinder the corrosion of carbon steels in several corrosive media, the following conclusions can be drawn:

1. The adsorption behaviour of the leaf and bark extracts of the eucalyptus plant were found to be of mixed type and predominantly obey the Langmuir adsorption isotherm model.
2. The inhibition efficiencies of the examined eucalyptus extracts were found to increase with concentration while their effectiveness was principally reported to reduce with a temperature rise.
3. The mechanism for the protection of the carbon steel from corrosion in different corrosive media by the eucalyptus extract was largely linked to the adherence of the inhibitive constituents of the extract on the surface of the steel to reduce the interaction between the metal and the corrosive surrounding.

6. REFERENCES

[1] N.Al-Akhras, Y.Mashaqbeh (2021) Potential Use of Eucalyptus Leaves as Green Corrosion Inhibitor of Steel Reinforcement, J. of Building Engineering, 35, 101848. https://doi.org/10.1016/j.jobe.2020. 101848

[2] B.Tan, J. He, S. Zhang, C. Xu, S. Chen, H. Liu, W. Li (2021) Insight into anti-corrosion nature of Betel leaves water extracts as the novel and eco-friendly inhibitors, *Journal of colloid and interface science*, *585*, 287–301. https://doi.org/10. 1016/j.jcis.2020.11.059

[3] L.Guo, B.Tan, W.Li, W., Q.Li, X.Zheng, I.B.Obot (2021) Banana leaves water extracts as inhibitor for X70 steel corrosion in HCl medium, *Journal of Molecular Liquids*, *327*, 114828, https://doi.org/10. 1016/j.molliq.2020.114828

[4] S.Z.Salleh, A.H.Yusoff, S.K.Zakaria, M.A.A.Taib, A.Abu, A.Seman, M.Masri, M.Mohamad, S.Mamat, S.Ahmad, S.Sobri, A.Ali, P.T.Teo (2021) Plant extracts as green corrosion inhibitor for ferrous metal alloys: A review, *Journal of Cleaner Production*, *304*, 127030, https://doi.org/10. 1016/ j.jclepro.2.021.127030

[5] A.I.Ndukwe, J.U.Anaele (2023) Corrosion of duplex stainless-steel weldments: A review of recent developments. Structural integrity and life. 23(3), 307–317.

[6] A.I.Ndukwe, N.E.Dan, J.U.Anaele, P.C.Agu (2023). Recent findings on corrosion of ferritic stainless steel weldments: a review. J. Materials Protection, 64(4), 372-283. https://doi.org/ 10. 5937/zasmat2304372N

[7] X.Zuo, W.Li, W.Luo, X.Zhang, Y.Qiang, J.Zhang, H.Li, B.Tan (2021) Research of Lilium brownii leaves extract as a commendable and green inhibitor for X70 steel corrosion in hydrochloric acid. *J. of Molecular Liquids*, *321*, 114914, https://doi.org/10.1016/ j.molliq.2020.114914

[8] B.Tan, B.Xiang, S.Zhang, Y.Qiang, L.Xu, S.Chen, J.He (2021) Papaya leaves extract as a novel eco-friendly corrosion inhibitor for Cu in H_2SO_4 medium, *Journal of colloid and interface science*, *582*(Pt B), 918–931, https://doi.org/ 10.1016/j.jcis.2020.08.093

[9] S.H.Alrefaee, K.Y.Rhee, C.Verma, M.Quraishi, E.E.Ebenso (2021) Challenges and advantages of using plant extract as inhibitors in modern corrosion inhibition systems: Recent advancements, *Journal of Molecular Liquids*, *321*, 114666, https://doi.org/10.1016/j.molliq.2020.114666

[10] M.Shahini, M.Ramezanzadeh, G.Bahlakeh, B. Ramezanzadeh (2021) Superior inhibition action of the Mish Gush (MG) leaves extract toward mild steel corrosion in HCl solution: Theoretical and electrochemical studies, *J. of Molecular Liquids*, *332*, 115876, doi.org/10.1016/ j.molliq.2021.115876

[11] M.EL-Zekred, A.Nofal, K.Shalabi, A.Fouda (2021) Ficus carica extract as environmentally friendly inhibitor for the corrosion of L-80 carbon steel in 0.5 M H_2SO_4 media, *J. of the Indian Chemical Society*, *98*(9), 100128, https://doi.org/10.1016/j.jics. 2021. 1001282

[12] A.I.Ndukwe (2022) Green inhibitors for corrosion of metals in acidic media: a review, AJME, 20(2), 36–50, https://ajme.ro/ PDF_AJME_2022_2/L5.pdf

[13] A.I.Ndukwe, C.N.Anyakwo (2018) Deterring the corrosion of mild steel in sulphuric acid medium by the leaf-paste of landolphia dulcis, A paper presented at the school of engineering technology conference and exhibition of the Akanu Ibiam Federal Polytechnic Unwana, Paper no: 2037018, p. 401 – 417.

[14] A.I.Ndukwe, S.O.Ihuoma, C.Akuwudike, D.O. Oluehi, F.A.Akaneme, E.U.Chibiko (2023) Predictive model for the corrosion inhibition of mild steel in 1.5 m HCl by the leaf-juice of Carica papaya. Journal Materials Protection, 64(4), 413-423. doi: 10.5937/zasmat2304413N

[15] C.N.Anyakwo, A.I.Ndukwe (2016) Corrosion inhibition of mild Steel in sulphuric acid by the leaf-juice of tridax procumbens plant. A paper presented at the school of engineering technology conference and exhibition of the Akanu Ibiam Federal Polytechnic Unwana. Paper no: 1056016, pp. 501-508.

[16] A.I.Ndukwe, C.N.Anyakwo (2017) Predictive model for corrosion inhibition of mild steel in HCl by crushed leaves of clerodendrum splendens, *IRJET*, 4(2), 679-688, https://irjet.net/archives/V4/i2/IRJET-V4I2129.pdf

[17] A.I.Ndukwe, C.N.Anyakwo (2017) Modelling of corrosion inhibition of mild steel in sulphuric acid by thoroughly crushed leaves of voacanga Africana (apocynaceae), *AJER*, 6(1), 344-356, https://www. ajer.org/papers/v6(01)/ZX060344356.pdf

[18] A.I.Ndukwe, C.N.Anyakwo (2017) Corrosion inhibition model for mild steel in sulphuric acid by crushed leaves of clerodendrum splendens (verbenaceae), *IJSEAS*, 3(3), 39-49, http://ijseas.com/volume3/v3i3/ijseas20170305.pdf

[19] C.N.Anyakwo, A.I.Ndukwe (2017) Mathematical model for corrosion inhibition of mild steel in hydrochloric acid by crushed leaves of tridax procumbens (asteraceae), *International journal of science and engineering investigations.,* 6(65), 81-89, http://www.ijsei.com/papers/ijsei-66517-13.pdf

[20] C.N.Anyakwo, A.I.Ndukwe (2017) Prognostic model for corrosion-inhibition of mild steel in hydrochloric acid by crushed leaves of voacanga Africana, *International journal of computational and theoretical chemistry*, 2(3), 31–42, https://www. sciencepublishinggroup.com/journal/paperinfo?journalid=228&doi=10.11648/j.ijctc.20170503.12

[21] Q.Wang, X.Wu, H.Zheng, L.Liu, Q.Zhang, A.Zhang, Z.Yan, Y.Sun, Z. Li, X.Li (2023) Evaluation for Fatsia japonica leaves extract (FJLE) as green corrosion inhibitor for carbon steel in simulated concrete pore solutions, *Journal of Building Engineering*, *63*, 105568, https://doi.org/10. 1016/ j.jobe.2022.105568

[22] M.Bathily, B.Ngom, M.Mbengue, D.Gassama (2023) Evaluation of the inhibitory action of essential oil from Eucalyptus globulus leaves on the corrosion of mild carbon steel in 1M HCl medium, Ovidius University Annals of Chemistry, 34(1) 1-7, https://doi.org/10.2478/auoc-2023-0001

[23] S.Bilgiç (2022) Plant extracts as corrosion inhibitors for mild steel in H_2SO_4 and H_3PO_4 media – Review II, Int. J. Corros. Scale Inhib., 11(1), 1–42, doi: 10.17675/2305-6894-2022-11-1-1

[24] A.J.Mwakalesi (2022) Corrosion inhibition of mild steel in sulphuric acid solution with tetradenia riparia leaves aqueous extract: kinetics and thermodynamics, https://www.suaire.sua.ac.tz/ handle/ 123456789/4240

[25] J.J.Moore, E.A.Boyce, M.J.Brooks, B.Perry, P.J.Sheridan (1999) Chemical Metallurgy (2nd ed.), p. 338-343, 372-375. London: Butterworths.

[26] B.Brycki, I.H.Kowalczyk, A.Szulc, O.Kaczerewska, M.Pakiet (2018) Organic Corrosion Inhibitors. Corrosion Inhibitors, Principles and Recent Applications,https://www.intechopen.com/chapters/58695

[27] E.McCafferty (2010) Introduction to Corrosion Science. New York: Springer.

[28] A.Kehr (2022) Corrosion Electrochemistry: The 6 Electrochemical Reactions Involved in Corrosion, Accessed from: https://www.corrosionpedia. com/ 2/1430/corrosion-101/corrosion-electrochemistry-electrochemical-reactions-during-the-corrosion-process

[29] Half-reaction (2023) In *Wikipedia*. Accessed from https://en.wikipedia.org/wiki/Half-reaction

[30] R.Buchanan, E.Stansbury (2012) Electrochemical Corrosion. *Handbook of Environmental Degradation of Materials (Second Edition)*, p.87-125, https://doi.org/10.1016/B978-1-4377-3455-3.00004-3

[31] I.Crossland (2011) Development and use of metal containers for the disposal of radioactive wastes, *Handbook of Advanced Radioactive Waste Conditioning Technologies*, 363-394, https://doi.org/ 10.1533/9780857090959.2.363

[32] J.Telegdi, A.Shaban, G.Vastag (2018) Biocorrosion—Steel. *Encyclopedia of Interfacial Chemistry*, p.28-42. https://doi.org/10.1016/B978-0-12-409547-2.13591-7

[33] S.U.Rahman, A.Ogwu (2020) Corrosion and Mott-Schottky probe of chromium nitride coatings exposed to saline solution for engineering and biomedical applications. Advances in Medical and Surgical Engineering, p.239-265. https://doi.org/10.1016/B978-0-12-819712-7.00013-9

[34] N.Meddings, M.Heinrich, F.Overney, J.Lee, V.Ruiz, E.Napolitano, S.Seitz, G.Hinds, R.Raccichini, M.Gaberšček, J.Park (2020) Application of electrochemical impedance spectroscopy to commercial Li-ion cells: A review. *Journal of Power Sources*, *480*, 228742. https://doi.org/10.1016/ j.jpowsour.2020.228742

[35] Introduction to Corrosion Monitoring (n.d.) What is Corrosion Monitoring? Accessed from https://www.alspi.com/ introduction.htm

[36] A.I.Ndukwe, C.N.Anyakwo (2017) Modelling of corrosion inhibition of mild steel in hydrochloric acid by crushed leaves of sida acuta (malvaceae), *THEIJES*, 6(1), 22-33, https://www.theijes.com/ papers/vol6-issue1/Version-3/D0601032233.pdf

[37] A.I.Ndukwe, C.N.Anyakwo (2017) Predictive corrosion-inhibition model for mild steel in sulphuric acid (H_2SO_4) by leaf-pastes of sida acuta plant, *Journal of civil, construction and environmental engineering,* 2(5), 123-133, https://www. sciencepublishinggroup. com/journal/paperinfo? journalid=617&doi=10.11648/j.jccee.20170205.11

[38] M.Baykara, U.Schwarz (2017) Atomic Force Microscopy: Methods and Applications. *Encyclopedia of Spectroscopy and Spectrometry (Third Edition)*, p.70-75. https://doi.org/10.1016/ B978-0-12-409547-2.12141-9

[39] K.Shinato, F.Huang, Y.Jin (2020) Principle and application of atomic force microscopy (AFM) for nanoscale investigation of metal corrosion. *Corrosion Reviews*, *38*(5), 423-432. https://doi. org/10.1515/corrrev-2019-0113

[40] S.Swapp (2017) Scanning Electron Microscopy (SEM), Geochemical Instrumentation and Analysis, accessed from: https://serc.carleton.edu/18401

[41] Transmission Electron Microscopy (n.d.) What is Transmission Electron Microscopy? accessed from: https://www.nanoscience.com/techniques/transmission-electron-microscopy/#:~:text=Transmission%20 electron%20microscopy%20(TEM)%20is,up%20to %2050%20million%20times

[42] D.D.Ebbing, S.D.Gammon (1996) General chemistry. *Energy*, *2*(2), 2-13.

[43] A.Yurt, B.Duran, H.Dal (2014) An experimental and theoretical investigation on adsorption properties of some diphenolic Schiff bases as corrosion inhibitors at acidic solution/mild steel interface, *Arabian Journal of Chemistry*, *7*(5), 732-740, https://doi.org/10.1016/j.arabjc.2010.12.010

[44] C.Monticelli (2018) Corrosion Inhibitors, Encyclopedia of Interfacial Chemistry, 164-171, https://doi.org/10.1016/B978-0-12-409547-2.13443-2

[45] L.L.Shreir, R.A.Jarman, G.T.Burstein (2000) Corrosion volume 2: corrosion control. 17:40 – 17:46. London: Planta Tree

[46] G.Palanisamy (2019) Corrosion Inhibitors. Corrosion Inhibitors. https://www.intechopen. com/ chapters/64392

[47] A.M.Langmuir (2023) Langmuir adsorption isotherm model. Accessed from: https://en. wikipedia.org/ wiki/Langmuir_adsorption_model

[48] A.I.Ndukwe, N.E.Dan, J.U.Anaele, C.C.Ozoh, K. Okon, P.C.Agu (2023). A review of the inhibition of mild steel corrosion by papaya and neem extracts. J. Materials Protection, 64(3), 274-282. https://doi.org/10.5937/zasmat2303274N

[49] A.O.Dada, A.P.Olalekan, A.M.Olatunya, O.Dada (2012) Langmuir, Freundlich, Temkin and Dubinin–Radushkevich Isotherms Studies of Equilibrium Sorption of Zn2+ Unto Phosphoric Acid Modified Rice Husk. Journal of Applied Chemistry., 3, 38-45. https://doi.org/10.9790/5736-0313845

[50] T.Britannica (2023) Editors of Encyclopaedia (2023, May 10). eucalyptus. Encyclopedia Britannica. https://www.britannica.com/plant/ Eucalyptus

[51] P.L.Eucalyptus. Retrieved 6-16-2023 from https://pixabay.com/photos/eucalyptus-leaf-plant-floral-2086785/

[52] A.Dehghani, G.Bahlakeh, B.Ramezanzadeh (2019) Green Eucalyptus leaf extract: A potent source of bio-active corrosion inhibitors for mild steel, *Bioelectrochemistry*, *130*, https://doi.org/10. 1016/j.bioelechem.2019.107339

[53] G.L.Abdulkhaleq (2023) The Inhibitive Effect of Eucalyptus Camaldulenis Leaves Extracts on the corrosion of low carbon steel in Hydrochloric Acid, Journal of Engineering and Sustainable Development, 17(3), 169–185, Retrieved from https://jeasd.uomustansiriyah.edu.iq/index.php/jeasd/article/view/1009

[54] J.Aslam, M.Mobin, Huda, A.Aslam, R.Aslam (2023) Corrosion inhibition performance of multi-phytoconstituents from *Eucalyptus* bark extract on mild steel corrosion in 5% HCl solution. *Int. J. Environ. Sci. Technol.,*20, 2441–2454, https://doi.org/10.1007/s13762-022-04152-5

[55] M.Tezeghdenti, L.Dhouibi, N.Etteyeb (2015) Corrosion Inhibition of Carbon Steel in 1 M Sulphuric Acid Solution by Extract of *Eucalyptus globulus* Leaves Cultivated in Tunisia Arid Zones. *J. Bio Tribo Corros,* 1, 16-24, https://doi.org/10.1007/s40735-015-0016-x

[56] A.M.Abdel-Gaber, H.T.Rahal, F.T.Beqai (2020) Eucalyptus leaf extract as a eco-friendly corrosion inhibitor for mild steel in sulfuric and phosphoric acid solutions. Int J Ind Chem, 11, 123–132, https://doi.org/10.1007/s40090-020-00207-z

[57] R.Haldhar, D.Prasad (2020) Corrosion Resistance and Surface Protective Performance of Waste Material of *Eucalyptus globulus* for Low Carbon Steel. *J. Bio Tribo Corros,* 6, 48-56, https://doi.org/10.1007/s40735-020-00340-3

[58] L.Ghalib, H.J.M.Al Jaaf, H.A.Abdulghani (2021) Temperature effect on the efficiency of Eucalyptus Camaldulensis leaves in the acid corrosion of carbon steel, *Materials Today: Proceedings*, *42*, 2475-2481. https://doi.org/10.1016/j.matpr.2020.12.566

[59] M.M.Tabatabaei, G.Bahlakeh, A.Dehghani, B. Ramezanzadeh, M.Ramezanzadeh (2019) Combined molecular simulation, DFT computation and electrochemical studies of the mild steel corrosion protection against NaCl solution using aqueous Eucalyptus leaves extract molecules linked with zinc ions, *J. of Molecular Liquids*, *294*, 111550, https://doi.org/10.1016/j.molliq.2019.111550

[60] D.K.Gupta, L.Awasthi, A.K.Das, B.Yadav, A.Ghimire, A.P.Yadav (2020) Corrosion Inhibition Effect of Acidic Extract of Bark of Eucalyptus Globulus on Mild Steel, *Tribhuvan University Journal*, *35*(1), 1–10, https://doi.org/10.3126/tuj.v35i1.35828

[61] A.F.Gualdrón, E.N.Becerra, D.Y.Peña, J.C. Gutiérrez, H.QBecerra (2013) Inhibitory effect of Eucalyptus and Lippia Alba essential oils on the corrosion of mild steel in hydrochloric acid. J. Mater. Environ. Sci., 4(1), 143-158, https://www.jmaterenvironsci.com/Document/vol4/vol4_N1/19-JMES-353-2013-Gualdron.pdf

[62] S.M.Abdal-nabi, S. M.Mahdi (2022) Inhibition Effect of Eucalyptus leaf extract on low carbon steel in dilute H_2SO_4 acid at room and high temperatures. International Journal of Mechanical Engineering, 7(1), 2247-2254, https://kalaharijournals.com/resources/261280/IJME_7.1_272.pdf

IZVOD

INHIBICIJA KOROZIJE UGLJENIČNOG ČELIKA LIŠĆEM EUKALIPTUSA U KISELOJ SREDINI: PREGLED

Ovaj rad se bavi pregledom prethodnih studija o koroziji i inhibiciji ugljeničnog čelika kome je dozvoljeno da se razgradi u korozivnom medijumu ekstraktom biljke eukaliptusa, sa naglaskom na adsorpcionom ponašanju ekstrakta. Mnogi istraživači su uglavnom koristili koru, ulje i ekstrakte listova eukaliptusa kako bi sprečili koroziju mekog čelika u kiselim sredinama pod različitim temperaturnim uslovima. Prema rezultatima, kada je ekstrakt kore biljke eukaliptusa dodat u HCl (5%) u koncentraciji od 900 ppm, maksimalna efikasnost inhibitora iznosila je 98,2 %. Ekstrakt lista je, s druge strane, imao maksimalnu inhibitornu efikasnost od 93,09 % pri koncentraciji ekstrakta od 600 mg/L u medijumu H_2SO_4 (0,5 M). Pokazalo se da potencija ekstrakata opada sa povećanjem temperature. Mehanizam za zaštitu ugljeničnog čelika ekstrakta eukaliptusa od korozije u različitim korozivnim situacijama bio je u velikoj meri povezan sa adsorpcijom inhibitivnih komponenti ekstrakta na površini čelika kako bi se smanjila interakcija između metala i korozivne okoline. Većina prijavljenih inhibitivnih ponašanja ekstrakta eukaliptusa bila je u skladu sa modelom izoterme Langmuir adsorpcije.

Ključne reči: *ekstrakt lista eukaliptusa, efikasnost inhibicije, meki čelik, model Langmuirove izoterme, inhibicija korozije, ugljenični čelik*

Pregledni rad

Rad primljen: 18.06.2023.

Rad prihvaćen: 12.07.2023.

Rad je dostupan na sajtu: www.idk.org.rs/casopis

Susai Rajendran[1,2], Abdulhameed Al-Hashem[3], Arjunan Krishnaveni[4], Little Jewelcy Arockiaraj[1], Gurmeet Singh[5], Caslav Lacnjevac[6], Murugan Naga Jothi[7], Pooviah Shanthy[7]*

[1]Department of Chemistry, Corrosion Research Centre, St. Antony's College of Arts and Sciences for Women, Dindigul-624005 (Mother Teresa Women's University,Kodaikanal, India), [2]Adjunct Professor, Centre for Nanoscience and Technology, Pondicherry University, Puducherry, India, [3]Petroleum Research Centre, Kuwait Institute for Scientific Research, Kuwait, [4]PG Department of Chemistry, Yadava College Madurai, Tamil Nadu, India, [5]Vice Chancellor, Pondicherry University, Puducherry, India, [6]Faculty of Agriculture, University of Belgrade, Serbia, [7]Deparetment of Chemistry, Sri Meenakshi Government Arts College for Women (A,) Madurai, India

Scientific paper
ISSN 0351-9465, E-ISSN 2466-2585
https://doi.org/10.62638/ZasMat1040

Zastita Materijala 65 (1)
22 - 34 (2024)

Corrosion inhibition by fruit extracts -Inhibition of corrosion of mild steel in simulated concrete pore solution prepared in sea water by an aqueous extract of apple juice- A Case study

ABSTRACT

*The inhibition efficiency of an aqueous extract of apple juice in controlling corrosion of mild steel immersed in **simulated concrete pore solution (**SCPS) prepared in sea water, has been evaluated by weight loss method. Langmuir adsorption isotherm has been investigated. The mechanistic aspect of corrosion inhibition has been investigated by Electrochemical impedance spectra (AC impedance spectra). The protective film has been analysed by Fluorescence spectroscopy, FTIR spectroscopy and AFM. The SCPS system offers 60% inhibition efficiency to mild steel immersed in sea water. In presence of apple juice extract the inhibition efficiency increases as the concentration of the extract increases. When 10 ml of extract is added, 85% inhibition efficiency is obtained. Electrochemical impedance spectra (AC impedance spectra) reveal that a protective film is formed on the metal surface. In the presence of inhibitor system, charge transfer resistance value increases, impedance value increases, phase angle value increases whereas double layer capacitance value decreases as expected. The FTIR spectral study reveals that the protective film consists of complexes consisting of iron-active principles of the apple juice extract. AFM study reveals that when the inhibition efficiency increases the roughness of the surface decreases or in other words the smoothness of the system increases.*

Keywords: *corrosion inhibition, mild steel I, simulated concrete pore solution ,sea water , an aqueous extract of apple juice, electrochemical studies, FTIR, Fluorescence spectroscopy, AFM.*

1. INTRODUCTION

Corrosion is the process of slowly eating up metals by gas and water vapours present in the atmosphere due to the formation of certain compounds like oxide, sulphide, carbonate, etc. Corrosion is a natural spontaneous and thermo-dynamically stable process. Corrosion cannot be prevented even though the rate of corrosion can be controlled. There are several methods of controlling corrosion. One such method is use of inhibitors. Corrosion inhibitors are chemical molecules used in small quantities to control corrosion by adsorption on the metal surface or by blanketing effect. Once chromates were used as corrosion inhibitors. But due to environmental toxicity use of chromates were avoided. This being the new trend and need of the hour many researchers are going for extracts of (aqueous, alcoholic etc.,) natural products. This is due to the facts they are less toxic or non toxic, less expensive and readily available . Chemically speaking the extracts contain many active ingredients. These molecules have polar atoms such as oxygen, sulphur , nitrogen and aromatic rings. Some molecules (β-carotene for example) have conjugated dienes also. Hence electron transfer from these molecules to the metal ions (Fe^{2+} for example) generated during the corrosion process is easy. Under these conditions metal-inhibitor complexes are formed on the anodic sites of the metal surface. Thus the corrosion process is controlled. Moreover the plant extract contains many active ingredients. Hence there is

*Corresponding author: Susai Rajendran
E-mail: susairajendran@gmail.com
Paper received: 09. 07. 2023.
Paper accepted: 28. 07. 2023.
Paper is available on the website: www.idk.org.rs/journal

chance of synergistic effect also. Both anodic reaction and cathodic reactions are controlled, simultaneously. That is the plant extracts act as mixed type of inhibitors and electron pumpers.

Various parts of the natural products, such as leaves, barks, roots and fruits can be used as corrosion inhibitors. In the present study, the use of extracts of some fruits is discussed. A case study is also presented. That is “Inhibition of corrosion of mild steel in simulated concrete pore solution prepared in sea water by an aqueous extract of apple juice” is presented. The use of extracts of fruits as corrosion inhibitors is summarized in Table 1.

Table 1. Use of extracts of fruits as corrosion inhibitors

Tabela 1. Upotreba ekstrakta voća kao inhibitora korozije

S.No	Metal/medium	Name of fruirt	Methods	Findings	Ref
1	mild steel in acidic environment	red dragon fruit (Selenicereus costaricensis) waste peel extracts	Thermodynamic studies. as activation energy (Ea) and changes in enthalpy (ΔHo) and entropy (ΔSo)	97% IE.	1
2	mild steel in 0.5 M HCl pickling environment	Microwave-assisted extraction of Swietenia macrophylla fruit shell	of weight loss (WL), electrochemical (potentiodynamic polarization and AC impedance spectroscopy) and scanning electron microscopy (SEM) techniques	Weight loss results suggest that, the protection efficiency enhances with a rise in the amount of Swietenia macrophylla fruit shell extract and decreases with an increase in the corrosive solution temperature. Mixed type of inhibitor	2
3	low carbon steel in NaCl electrolyte	mulberry fruit (Morus nigra L.) extracts incorporated hybrid (GPTMS-TEOS) composite silanol coatings	electrochemical impedance spectroscopy, electrochemical noise measurement and potentiodynamic polarization. FTIR, contact angle measurement, energy dispersive X-ray spectroscopy (EDX),SEM	The corrosion inhibition efficiencies obtained were 85.57% and 81.37% for hybrid coatings doped with mulberry ethanol extract and water extract, respectively.	3
4	Pitting Potential Improvement of 304 Stainless Steel in Hydrochloric Acid Solution	Terminalia bellirica Fruit Extract	potentiodynamic polarization curves,	95% IE. Langmuir adsorption isotherm	4
5	stainless steel corrosion during acid washing in a multistage flash desalination plant	orange peel extract	Electrochemical methods, quantum chemical calculations,	Langmuir adsorption isotherm	5
6	Mild Steel in Hydrochloric Acid. 0.25 M HCl	Extractfromthe Pericarp of the fruit Tamarindus indica (Tamarind)	scanning electron microscopy and energy-dispersive x-ray spectroscopy. UV-visible spectrum and IR spectrum.	mixed type of inhibitor.	6
7	low carbon steel in H2SO4 solution	grapefruit essential oil extracts	Standard deviation data	above 95 % inhibition	7
8	steel in industrial media	Tomato pomace extract	electrochemical methods, weight loss assay. SEM and AFM	98% IE. Quantum-chemical calculations.	8

9	Carbon Steel in an Acidic Medium	Wild Lycium ferocissimum Miers Fruit Extract. (phenolic extract)	potentiodynamic polarization (PDP), electrochemical impedance spectroscopy (EIS), and weight loss method.	80 % IE.	9
10	Aluminium Alloy in Acidic Medium	Aqueous Extract of Punica Granatum Fruit Peel	potentiodynamic polarization and electrochemical impedance spectroscopy techniques.SEM. FTIR	Langmuir adsorption isotherm.	10

Extracts of various fruits [1-10] have been used as corrosion inhibitors.

Metals: Extracts of various fruits [1-10] have been used as corrosion inhibitors to control various metals and alloys such as mild steel [1-3,6,7,9], stainless steel [4,5,8] and aluminium [10].

Medium: Corrosion of metals have been prevented by flower extracts in various media such as acid [1,2, 4-7,9,10] and sodium chloride [3] medium.

Flowers: Extracts of various flowers such as red dragon fruit[1], Swietenia macrophylla fruit shell [2], mulberry fruit [3], Terminalia bellirica Fruit[4], orange peel extract[5], Tamarind[6], grapefruit[7], Tomato pomace extract[8], Wild Lycium ferocissimum Miers Fruit[9] and Punica Granatum Fruit Peel[10].

Methods: Various methods have been used to control the corrosion process. Weight loss method [2,8] and electrochemical methods[2-5,8-10] have been employed.

Surface analysis of protective films: Methods such as SEM [2,3,6,8,10], FTIR [3,6,10], AFM [8] and EDX [3,6] have been used for this purpose.

Contact angle measurements have not been used to study the hydrophobic nature of the protective film.

Case study

Title: "Inhibition of corrosion of mild steel in simulated concrete pore solution prepared in sea water by an aqueous extract of apple juice"

2. EXPERIMENTAL

Preparation of mild steel specimens

Mild steel specimens of dimensions 1.0 cm x 4.0 cm x 0.2 cm were polished to a mirror finish and degreased with trichloroethylene.

Weight loss method

Mild steel specimens in triplicate were immersed in 100 ml of the simulated concrete pore solution (SCPS) prepared in sea water in the absence and presence of an aqueous extract of apple juice , for a period of one day. The weight of the specimens before and after immersion was determined using a Shimadzu balance, model AY62. The corrosion products were cleaned with Clarke's solution. The corrosion rate was calculated using the following equation.

$$\text{Corrosion rate} = (W/AT)\ \text{mdd}$$

Where

W = loss in weight (mg)

A = surface area of the specimen (dm^2)

T = period of immersion (days)

The corrosion rate is expressed in mdd units [mdd = mg/(dm^2) (day)]

The inhibition efficiency was calculated using the relation.

$$\text{Inhibition efficiency} = [(CR_1 - CR_2)/CR_1] \times 100\ \%$$

Where

CR_1 = corrosion rate in the absence of inhibitor

CR_2 = corrosion rate in the presence of inhibitor.

Electrochemical study

AC impedance spectra (Electrochemical Impedance Spectra - EIS)

In the present work, corrosion resistance of mild steel immersed in various test solutions were measured by Electrochemical Impedance Spectra - EIS. The experiments were done at room temperature. Electrochemical Impedance Spectra were recorded in a CHI- electrochemical work station with impedance model 660A. It was provided with iR compensation facility. A three-electrode cell assembly was used. Mild steel was used as working electrode. Platinum was used as counter electrode and saturated calomel electrode (SCE) was used as reference electrode. From Electrochemical Impedance Spectra, corrosion parameters such as charge transfer resistance (Rt), double layer capacitance value (Cdl) and impedance log (Z/Ohm) value were calculated.

Surface characterization study

FTIR

The FTIR spectra were recorded in a Perkin Elmer 1600 series spectrophotometer with resolving power of 4 cm^{-1}.

Atomic force microscopy (AFM)

The mild steel specimens immersed in various test solutions for one day were taken out, rinsed with double distilled water, dried and subjected to the surface examination. The surface morphology measurements of the mild steel surface was carried out by atomic force microscopy (AFM) using SPM Veecodi Innova connected with the software version V7.00 and the scan rate of 0.7 Hz.

3. RESULTS AND DISCUSSION

The inhibition efficiency of an aqueous extract of apple juice in controlling corrosion of mild steel immersed in SCPS prepared in sea water has been evaluated by weight loss method. Langmuir adsorption isotherm has been investigated, The mechanistic aspect of corrosion inhibition has been investigated by Electrochemical impedance spectra (AC impedance spectra). The protective film has been analyzed by Fluorescence spectroscopy, FTIR spectroscopy and AFM.

Weight loss method

The inhibition efficiency of an aqueous extract of apple juice in controlling corrosion of mild steel immersed in SCPS prepared in sea water has been evaluated by weight loss method. Three mild steel specimens were immersed in SCPS prepared in sea water in the absence and presence of an aqueous extract of apple juice extract. The corrosion rates and inhibition efficiencies are given in Table 2.

Table 2 . Corrosion rate and inhibition efficiency of mild steel immersed in SCPS prepared in sea water in the absence and presence of apple juice obtained by weight loss method

Tabela 2. Brzina korozije i efikasnost inhibicije mekog čelika uronjenog u SCPS pripremljen u morskoj vodi u odsustvu i prisustvu soka od jabuke dobijenog metodom gubitka težine

System	Corrosion rate, mdd	IE, %	surface coverage θ	C/θ
Sea water	20.86	-	-	-
SCPS	8.34	60	0.60	0
SCPS + extract 2ml	7.30	65	0.65	3.1
SCPS + extract 4ml	6.47	69	0.69	5.8
SCPS + extract 6ml	5.01	76	0.76	7.9
SCPS + extract 8ml	4.17	80	0.80	10.0
SCPS + extract 10ml	3.13	85	0.85	11.8

It is observed from Table2 that as the concentration of apple juice (C ml) increases, the corrosion rate decreases and inhibition efficiency increases and surface coverage (θ = IE%/100) increases.

Langmuir adsorption isotherm

The Langmuir adsorption isotherm is used to describe the equilibrium between adsorbate and adsorbent system, where the adsorbate adsorption is limited to one molecular layer at or before a relative pressure of unity is reached.

There are the three assumptions of the Langmuir isotherm. They are the adsorption consists entirely of a monolayer at the surface; (2) there is no interaction between molecules on different sites and each site can hold only one adsorbed molecule; (3) the heat of adsorption does not depend on the number of sites and is equal for all sites.

SCPS + Apple juice system

A plot of C vs C/ $\boldsymbol{\theta}$ gives a straight line (Table 3, Figure 1). This indicates that Langmuir adsorption isotherm is obeyed. The R^2 value is very high (0.989). The adsorption consists entirely of a monolayer of the ingredients of apple juice (Figure 1) the metal surface.

Table 3 . Data for Langmuir adsorption isotherm
Tabela 3. Podaci za Langmuir-ovu adsorpcionu izotermu

C, ml of extract	C/ $\boldsymbol{\theta}$
0	0
2	3.1
4	5.8
6	7.9
8	10.0
10	11.8

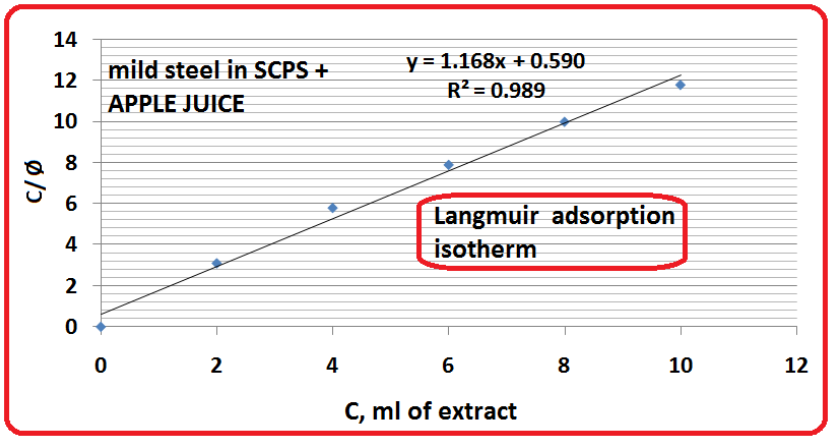

Figure 1. Langmuir adsorption isotherm for apple juice system

Slika 1. Langmuir-ova adsorpciona izoterma za sistem soka od jabuke

Analysis of AC impedance spectra

AC impedance spectra have been used to confirm the formation of protective film on the metal surface. If a protective film is formed on the metal surface, charge transfer resistance (R_t) increases, double layer capacitance value (C_{dl}) decreases and impedance log (Z/Ohm) value increases (Figure 2).

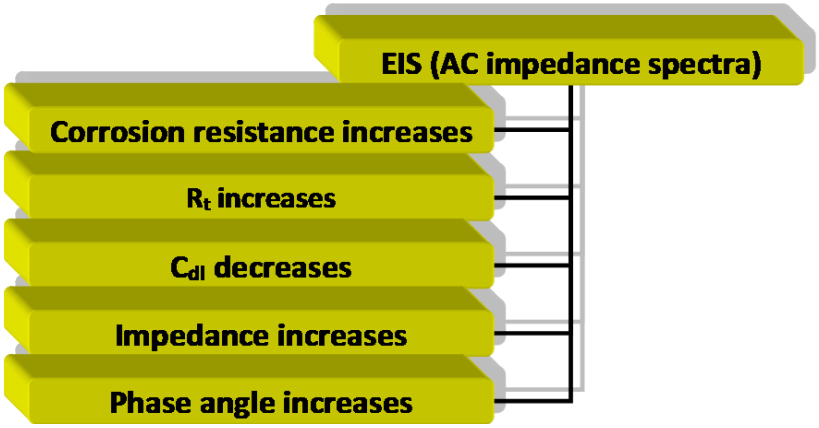

Figure 2. Corrosion parameters obtained from AC impedance spectra (Principles of AC impedance spectra)

Slika 2. Parametri korozije dobijeni iz spektra impedanse naizmenične struje (Principi spektra impedanse naizmenične struje)

The AC impedance spectra (Nyquist plots and Bode plots) of mild steel immersed in various test solutions are shown in Figures (3-5). The corrosion parameters, namely, charge transfer resistance (R_t), double layer capacitance (C_{dl}), and impedance values are given in Table 3.

It is observed that when mild steel is immersed is sea water, the charge transfer resistance is 42.7 Ohmcm^2. The C_{dl} value is 1.19 x 10^{-7} F/cm^2. The impedance value is 1.671 [log(Z/Ohm)] .

It is further inferred that when mild steel in immersed in SCPS, the charge transfer resistance increases from 42.7 Ohmcm^2 to 50.04 Ohmcm^2. The C_{dl} value decreases from 1.19 x 10^{-7} x 10^{-7} F/cm^2 to 1.02 x 10^{-7} A/cm^2. The impedance value increases from 1.671 to 1.741. It is interesting to observe that when apple juice is added to SCPS system,the charge transfer resistance increases from 42.7 Ohmcm^2 to 55.8 Ohmcm^2. The C_{dl} value decreases from 1.19 x 10^{-7} x 10^{-7} F/cm^2 to 0.91 x 10^{-7} A/cm^2. The impedance value increases from 1.671 to 1.828.

From all these experimental data, the following useful conclusions are scientifically drawn from the principles of AC impedance spectra. When mild steel is immersed in SCPS prepared in sea water the corrosion resistance of mild steel increases. When apple juice is added to SCPS prepared in

sea water the corrosion resistance of mild steel further increases. It is interpreted that in the presence of SCPS, the increase in corrosion is due to the formation of $CaCO_3$ and CaO . The increase in corrosion protection in the presence of apple juice is due to the fact that in the presence of apple juice, the ingredients present in apple juice, namely, Quercetin, Epicatechin, Procyanidin B2 and Caffeic acid have been deposited on the metal surface resulting in the formation iron-active ingredient complexes formed on the anodic sites of the metal surface (Schema 1).

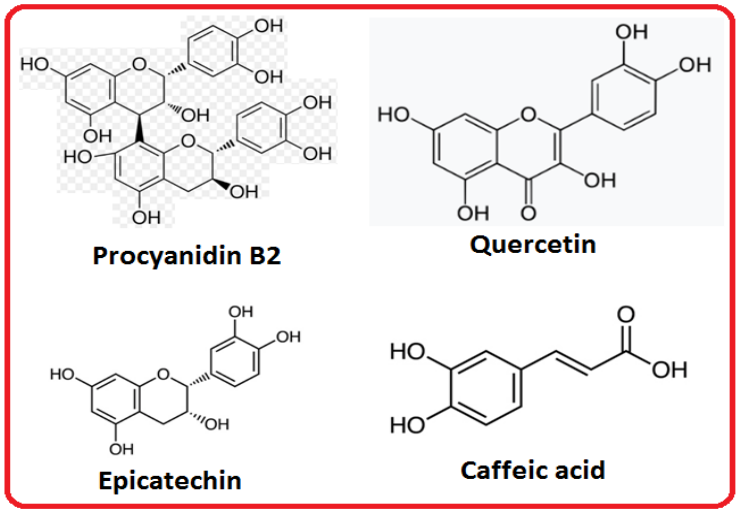

Scheme 1: Phenolic compounds present in apples

(Quercetin, Epicatechin, Procyanidin B2, Caffeic acid)

Shema 1. Fenolna jedinjenja prisutna u jabukama

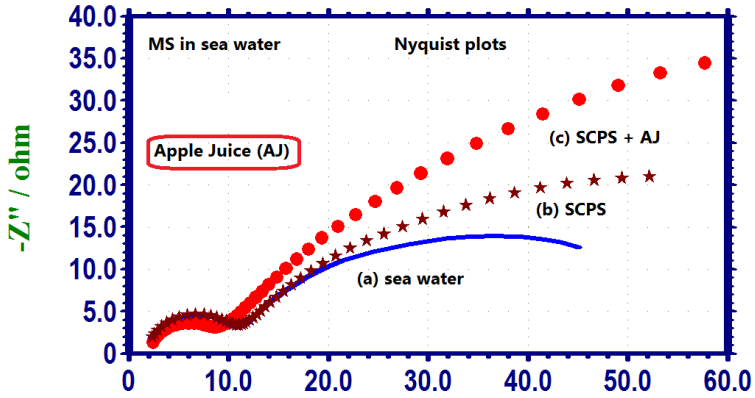

Figure 3. Nyquist plots of mild steel immersed in various test solutions. (a) sea water; (b) SCPS prepared in sea water (c) SCPS + apple juice

Slika 3. Nyquist-ove krive mekog čelika uronjenog u različita testna rešenja: (a) morska voda; (b) SCPS pripremljen u morskoj vodi, (c) SCPS + sok od jabuke

Table 4. Corrosion parameters of mild steel (MS) immersed in simulated concrete pore solution prepared in sea water, in the absence and presence of inhibitor, an aqueous extract of apple [apple juice (AJ)] obtained by the impedance spectra

Tabela 4. Parametri korozije mekog čelika (MS) uronjenog u simulirani rastvor pora betona pripremljen u morskoj vodi, u odsustvu i prisustvu inhibitora, vodeni ekstrakt jabuke [sok od jabuke (AJ)] dobijen spektrom impedanse

System	Rt, Ohmcm^2	Cdl,F/cm^2	Impedance, [log(Z/Ohm)]
sea water	42.7	1.19 x 10^{-7}	1.671
SCPS	50.04	1.02 x 10^{-7}	1.741
SCPS + AJ	55.8	0.91 x 10^{-7}	1.828

Equivalent circuit diagram for various systems

The equivalent circuit for various systems is shown in Figure 4. This is in accordance with the shape of the corresponding Nyquist plot, wherein two time constants are noticed. The one in the high frequency region is obvious. The one in the low frequency region is less obvious. This type of Nyquist plot is characteristic of film formation and film breaking.

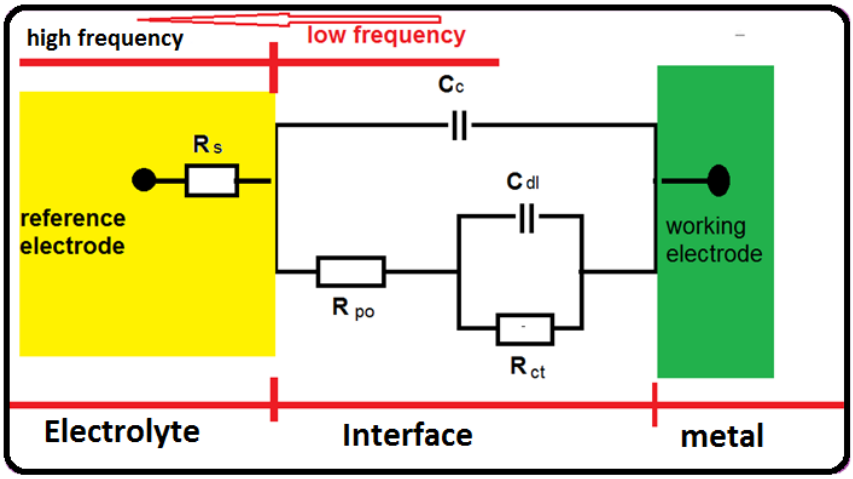

Figure 4. Equivalent circuit diagram for failed coating (Film formation and film breaking)

Slika 4. Ekvivalentna šema za neuspeli premaz (formiranje filma i pucanje filma)

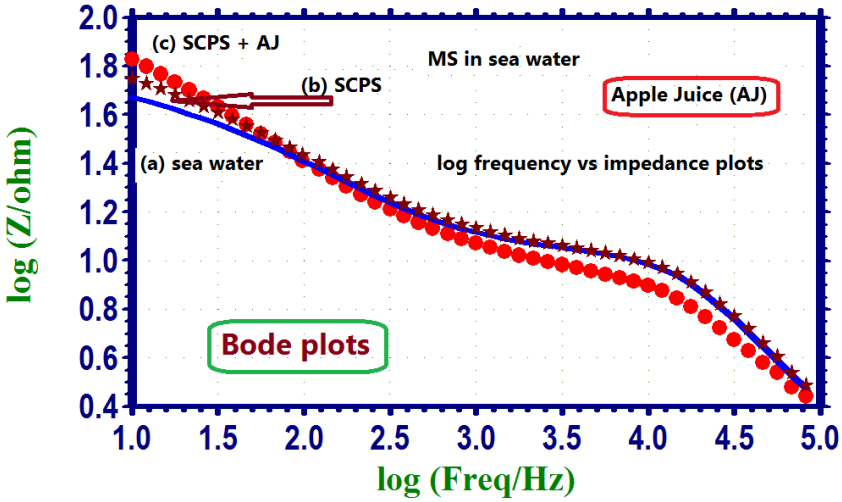

Figure 5. Bode plots of mild steel immersed in various test solutions. (a) sea water; (b) SCPS prepared in sea water (c) SCPS + apple juice

Slika 5. Bode-ove krive mekog čelika uronjene u različita testna rešenja. (a) morska voda; (b) SCPS pripremljen u morskoj vodi (c) SCPS + sok od jabuke

Analysis of FTIR spectra

The active principles of an aqueous extract of apple juice are **Quercetin, Epicatechin, Procyanidin B2, Caffeic acid** (Scheme 1). The main functional groups are phenolic –OH, carbonyl group C=O and ether -O- group. A few drops of an aqueous extract of apple juice were dried on a glass plated. A solid mass was obtained. The FTIR spectrum (KBr) of this solid mass is shown in Figures 6,7. The various stretching frequencies are given in Table 5. The FTIR spectrum (KBr) of the protective film formed on the metal surface after immersion in the solution containing SCPS and apple extract for one day is shown in Figures 8,9,10. The various stretching frequencies are given in Table 5.

Table 5. Stretching frequencies of various functional groups

Tabela 5. Frekvencije istezanja različitih funkcionalnih grupa

Details	solid mass obtained from apple extract	film formed on metal surface
-OH stretching	3403.72 cm^{-1}	3429 cm^{-1}
C-H stretching	2928	2924
C=O stetching	1637.78	1636
O-H bending, carboxylic acid	1408.3	1452
C-H bending, 1,2-disubstituted	779.07	763
C-H bending, aromatic compound	2095.14	Disappeared
phenol O-H bending	1384, 1408	1384, 1452
ether C-O-C stretching	1058.8	1037

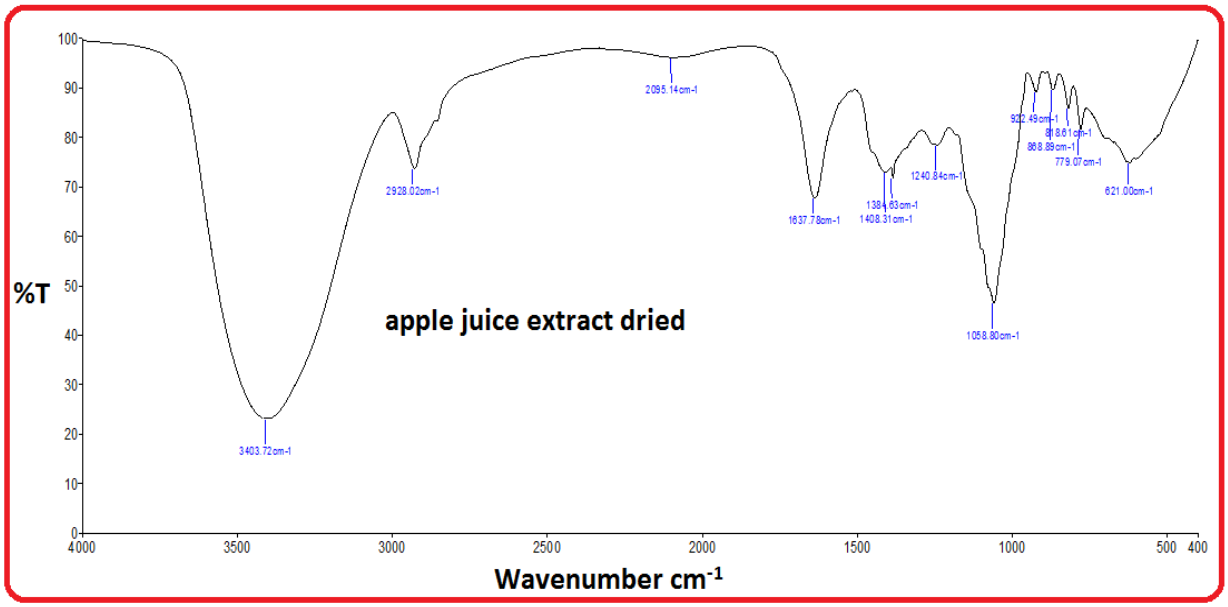

Figure 6. FTIR spectrum of of apple juice extract dried on a glass plate

Slika 6. FTIR spektar ekstrakta soka od jabuke osušenog na staklenoj ploči

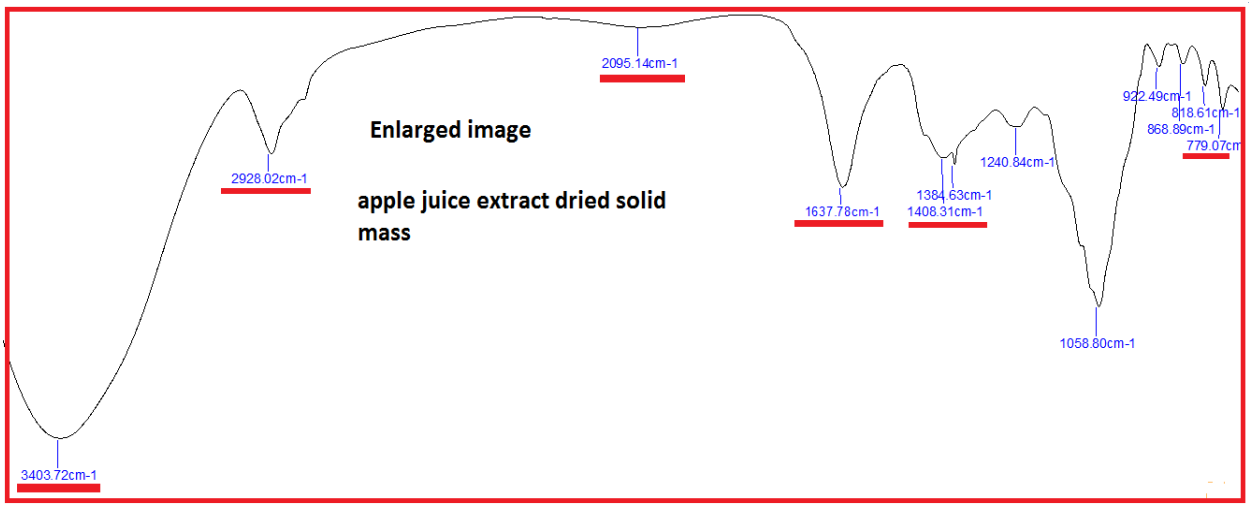

Figure 7. FTIR spectrum of of apple juice extract dried on a glass plate (Enlarged image)

Slika 7. FTIR spektar ekstrakta soka od jabuke sušenog na staklenoj ploči (uvećana slika)

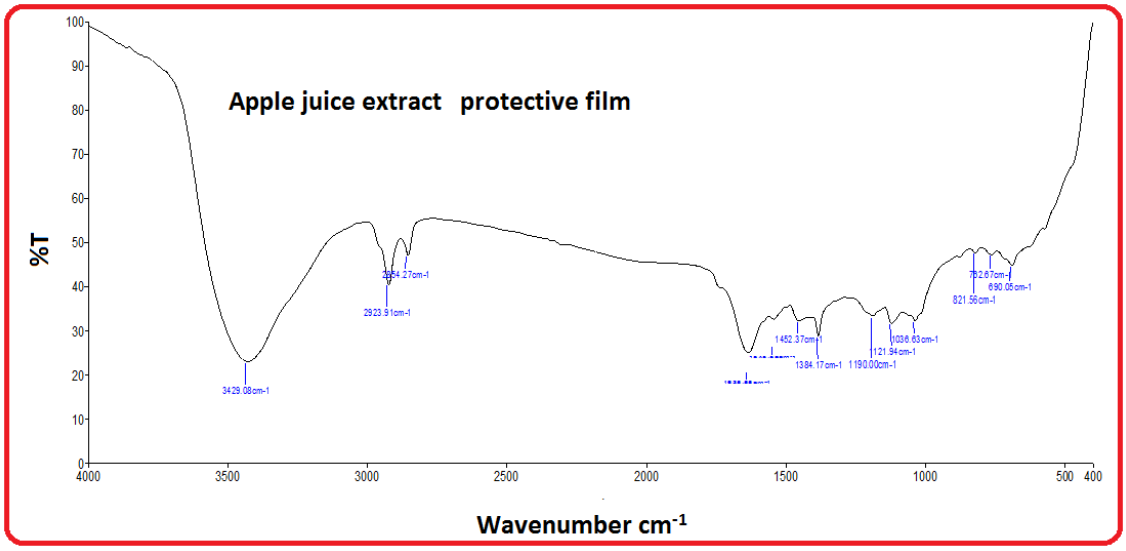

Figure 8. FTIR spectrum (KBr) of protective film.

Slika 8. FTIR spektar (KBr) zaštitnog filma

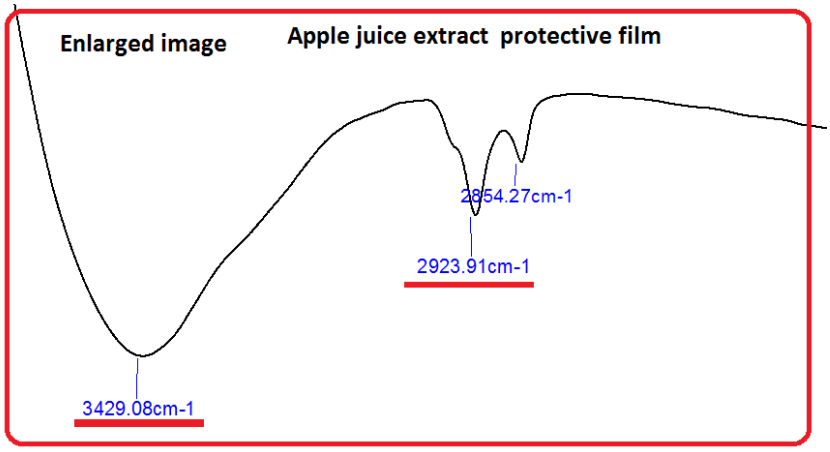

Figure 9. FTIR spectrum (KBr) of protective film(Enlarged image)

Slika 9. FTIR spektar (KBr) zaštitnog filma (uvećana slika)

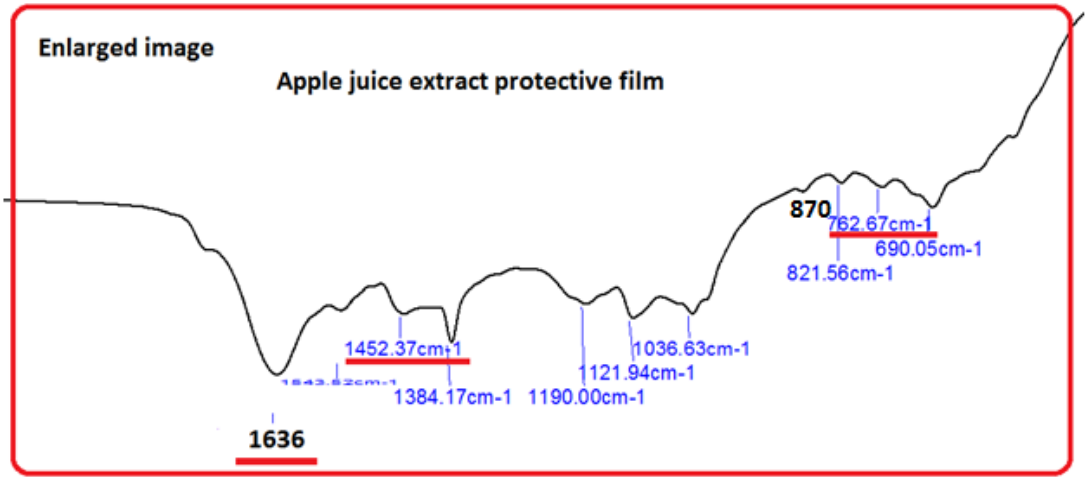

Figure 10. FTIR spectrum(KBr) of protective film (Enlarged image)

Slika 10. FTIR spektar (KBr) zaštitnog filma (uvećana slika)

It is observed from the Table 5 that the Fe^{2+} ions on the metal surface, generated during corrosion process on the metal surface, have coordinated with the polar groups of the active ingredients of the apple juice such as phenolic O-H , C-O-C , and aromatic pi electrons, resulting in the formation of a protective film on the metal surface. This film is responsible for corroion protection.

The peaks at 1452 cm^{-1}, 870 cm^{-1} and 762 cm^{-1} 690 are due to calcium oxide and calcium carbonate formed on the metal surface [11,12].

Luminescence spectra

Luminescence spectra have been used in corrosion inhibition studies. Apple juice extract is mixed with ferrous sulphate solution to prepare a complex consisting of Fe^{2+}-active principles of the ingredients of apple juice. Luminescence spectrum (λ_{ex} = 300nm) of this solution was recorded. A peak appears at 305 nm.

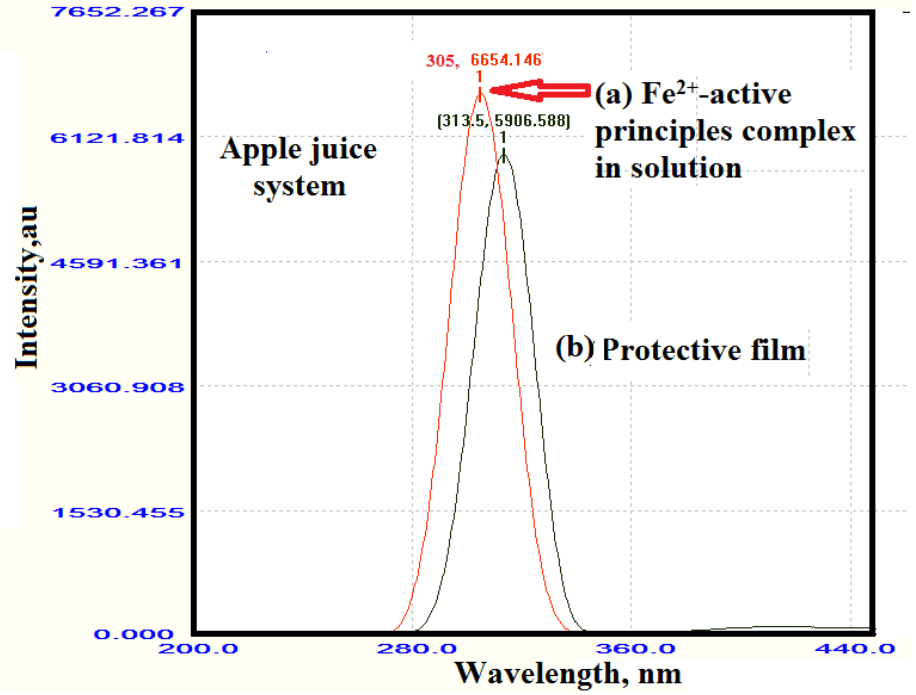

Figure 11. Fluoresence spectra of SCPS + Apple juice

Slika 11. Fluorescentni spektri SCPS + sok od jabuke

Luminescence spectrum (λ_{ex} = 300nm) of the protective film formed on the metal surface after immersion in the solution consisting of SCPS and apple juice for a period of one day is shown in Figure 11. A peak appears at 313.5 nm. This peak very closely matches with the previous peak at 305nm. Thus it is confirmed that the protective film consists of Fe^{2+}-active principles of the ingredients of apple juice. It is noted that there is decrease in the intensity of the peak. This is due to the fact that in the solid state there is restriction in the movement of electrons.

ANALYSIS OF AFM

Atomic force microscopy is used widely in corrosion inhibition study. The roughness of the metal surface can be investigated and measured for three systems, namely polished metal (system A), polished metal immersed in the blank solution(SCPS) (system-B) and polished metal immersed in the inhibitor system (SCPS + Apple juice) (system C) (Fig. 12-14).The average roughness (Ra), RMS roughness (Rq) and maximum peak -to -valley height can be derived from AFM images. In general, for the three systems, A, B and C the average roughness is in following order A>B>C. This indicates that a protective film is formed on the metal surface and hence corrosion inhibition efficiency increases for system B and system C. The average roughness decreases as the corrosion inhibition efficiency increases. The high value of the average roughness for polished metal (system A) may be due to the formation of iron oxide formed on the metal surface. As the smoothness increases the inhibition efficiency increases. 2D images and 3D images are produced in AFM study (Fig. 12-14). Section analysis is another aspect of AFM.

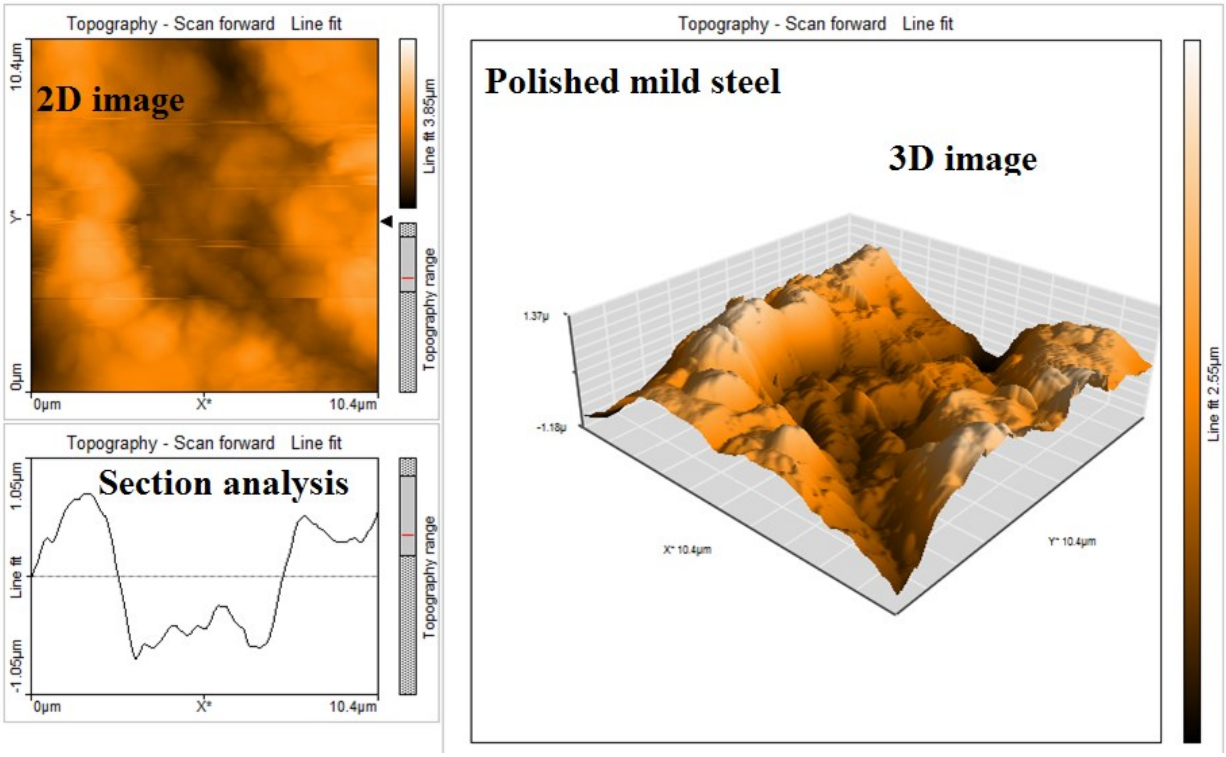

Figure 12. Polished mild steel

Slika 12. Polirani meki čelik

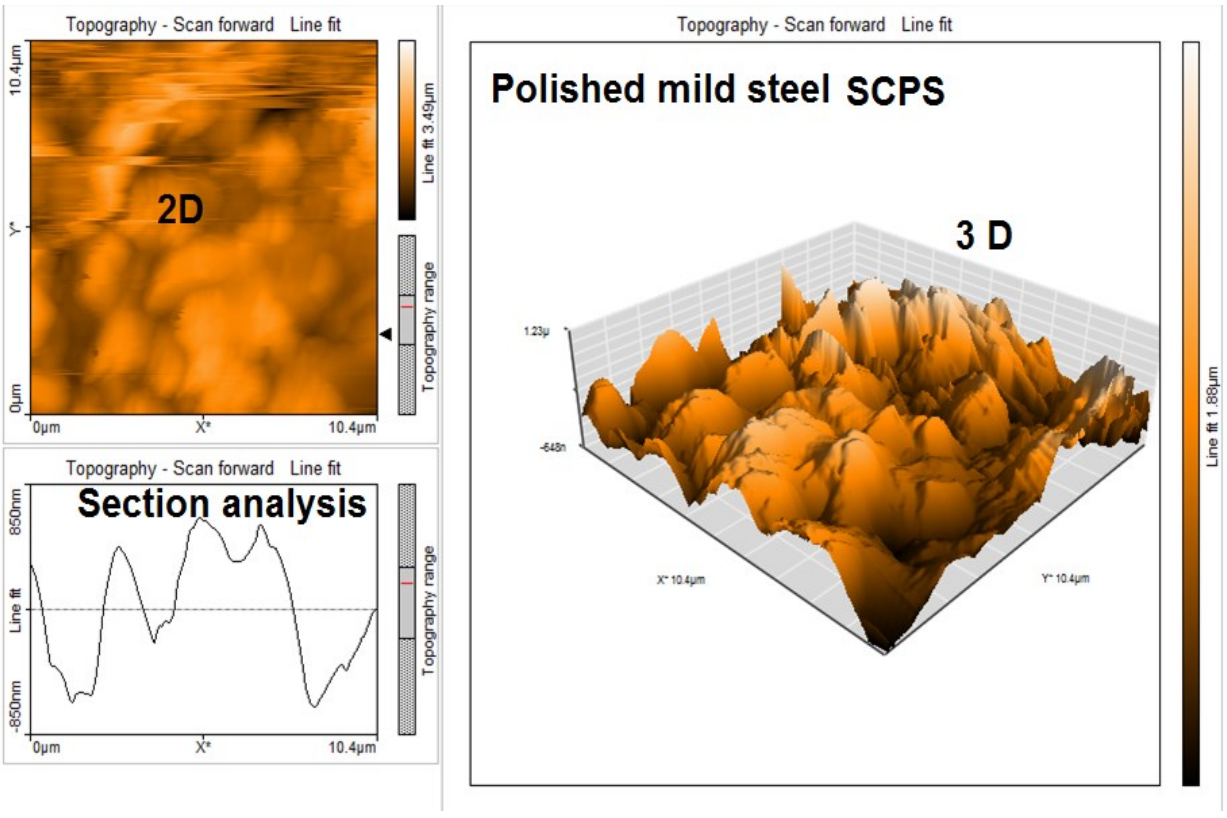

Figure 13. Polished mild steel immersed in SCPS

Slika 13. Polirani meki čelik uronjen u SCPS

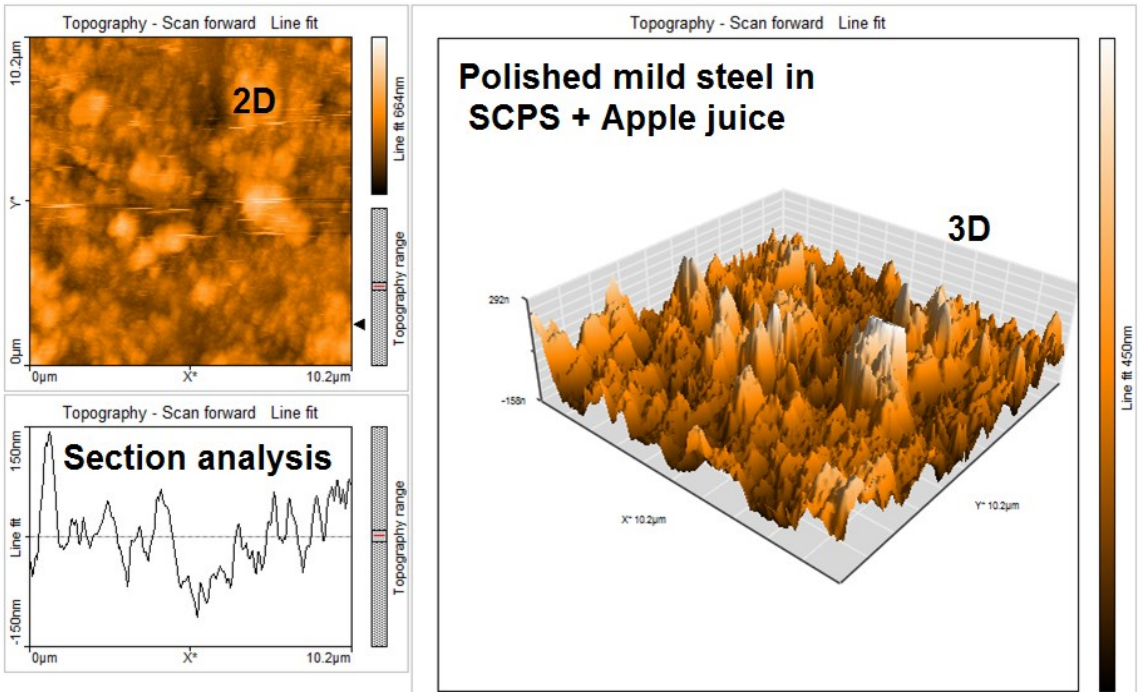

Figure 14. Polished mild steel immersed in SCPS +Apple juice

Slika 14. Polirani meki čelik uronjen u SCPS + sok od jabuke

Table 6: AFM parameters of various surfaces

Tabela 6. AFM parametri različitih površina

Samples	RMS (R_q) Roughness (nm)	Average (R_a) Roughness (nm)	Maximum peak – to valley– height (nm)
Polished mild steel (Control)	422.76 nm	396.01nm	1290.5nm
Mild Steel immersed in SCPS	239.13nm	205.74nm	973.88nm
Mild steel immersed in SCPS + Apple juice	91.984nm	69.477nm	415.76nm

4. CONCLUSIONS

The inhibition efficiency SCPS prepared in sea water in controlling corrosion of mild steel immersed in SCPS prepared in sea water has been evaluated by weight loss method. Langmuir adsorption isotherm has been investigated, The mechanistic aspect of corrosion inhibition has been investigated by Electrochemical impedance spectra (AC impedance spectra). The protective film has been analysed by Fluorescence spectroscopy, FTIR spectroscopy and AFM.

The SCPS system offers 60% inhibition efficiency to mild steel immersed in sea water.

In presence of apple juice extract the inhibition efficiency increases as the concentration of the extract increases

When 10 ml of extract is added, 85% inhibition efficiency is obtained.

Electrochemical impedance spectra (AC impedance spectra) reveal that a protective film is formed on the metal surface.

In the presence of inhibitor system , charge transfer resistance value increases, impedance value increases, phase angle value increases whereas double layer capacitance value decreases as expected.

The FTIR spectral study reveals that the protective film consists of complexes consisting of iron-active principles of the apple juice extract.

AFM study reveals that when the inhibition efficiency increases the roughness of the surface decreases or in other words the smoothness of the system increases.

5. REFERENCES

[1] R.R.Macadangdang (2022) Corrosion inhibition, adsorption behaviour, and thermodynamic studies of red dragon fruit (Selenicereus costaricensis) waste peel extracts on mild steel in acidic environment, Indian Journal of Chemical Technology, 29(2), 201-206.

[2] M.Hegde, S.P.Nayak, N.Raghavendra (2023) Microwave-assisted extraction of Swietenia

macrophylla fruit shell and its application in corrosion inhibition for mild steel in 0.5 M HCl pickling environment, Sadhana - Academy Proceedings in Engineering Sciences, 48(1), 10-19.

[3] N.A.A.Mohamad Azran, T.S.Hamidon, S.S.Azahar, M.H.Hussin (2023) Corrosion-resistant mulberry fruit (Morus nigra L.) extracts incorporated hybrid (GPTMS-TEOS) composite silanol coatings for low carbon steel protection, Journal of Sol-Gel Science and Technology, 105(3), 34-747.

[4] S.Sutthiruangwong, C.Wongpaiboon, N.Sritha, N.Anukulkich (2023) Pitting Potential Improvement of 304 Stainless Steel in Hydrochloric Acid Solution by Terminalia bellirica Fruit Extract, Metals, 13(2), 262-271.

[5] N.A.Barghout, A.El Nemr, B.A.Abd-El-Nabey, S.Ragab, N.O.Eddy (2023) Use of orange peel extract as an inhibitor of stainless steel corrosion during acid washing in a multistage flash desalination plant, Journal of Applied Electrochemistry, 53(2), 379-399.

[6] V.Pinto, G.M.Pinto, L.D.Kateel, A.Thomas (2023) Green Approach to Corrosion Inhibition of Mild Steel in Hydrochloric Acidusing Extractfromthe Pericarp of the fruit Tamarindus indica (Tamarind), Biointerface Research in Applied Chemistry, 13(6), 544-553.

[7] R.Tolulope Loto, E.Alagbe, A.Busari (2023) Data analysis of the corrosion protection behavior of ginger, tea tree and grapefruit essential oil extracts on low carbon steel in H_2SO_4 solution, Materials Today: Proceedings, 80, 1408-1412.

[8] V.Vorobyova, M.Skiba, K.Andrey (2022) Tomato pomace extract as a novel corrosion inhibitor for the steel in industrial media: The role of chemical transformation of the extract and proinhibition effect, Journal of Molecular Structure, 1264, 133155.

[9] H.Fadhil, F.Mraihi, P.M.T.Ayadi, P.J.K.Cherif (2022) Anticorrosive Performance of Wild Lycium ferocissimum Miers Fruit Extract on Carbon Steel in an Acidic Medium, Chemistry Select, 7(23), e202104297.

[10] M.Sahraoui, M.Boulkroune, A.Chibani, Y.Larbah, A.Abdessemed (2022) Aqueous Extract of Punica Granatum Fruit Peel as an Eco-Friendly Corrosion Inhibitor for Aluminium Alloy in Acidic Medium, Journal of Bio- and Tribo-Corrosion, 8(2), 54-65.

[11] https://webbook.nist.gov/cgi/cbook.cgi?ID=C471341&Mask=80

[12] https://www.google.com/search?q=calcium+oxide+ftir+spectrum&oq=CALCIUM+OXIDE+FTIR&aqs=chrome.0.0i512j69i57j0i22i30l5j0i390i650l3.17005j0j15&sourceid=chrome&ie=UTF-8#imgrc=ckSMvRnoGH_-bM

IZVOD

INHIBICIJA KOROZIJE VOĆNIM EKSTRAKTIMA - INHIBICIJA KOROZIJE MEKOG ČELIKA U SIMULIRANOM RASTVORU PORA BETONA PRIPREMLJENOM U MORSKOJ VODI VODENIM EKSTRAKTOM SOKA OD JABUKE - STUDIJA SLUČAJA

Efikasnost inhibicije vodenog ekstrakta soka od jabuke u kontroli korozije mekog čelika uronjenog u rastvor simuliranih betonskih pora (SCPS) pripremljen u morskoj vodi, procenjena je metodom gubitka težine. Istražena je Lengmirova izoterma adsorpcije. Mehanički aspekt inhibicije korozije je istražen spektrima elektrohemijske impedanse (AC impedance spectra). Zaštitni film je analiziran fluorescentnom spektroskopijom, FTIR spektroskopijom i AFM. SCPS sistem nudi efikasnost inhibicije od 60% za meki čelik uronjen u morsku vodu. U prisustvu ekstrakta soka od jabuke efikasnost inhibicije se povećava kako se koncentracija ekstrakta povećava. Kada se doda 10 ml ekstrakta, postiže se 85% efikasnost inhibicije. Spektri elektrohemijske impedanse (AC impedance spectra) otkrivaju da se na površini metala formira zaštitni film. U prisustvu inhibitornog sistema, vrednost otpora prenosa naelektrisanja se povećava, vrednost impedanse raste, vrednost faznog ugla se povećava dok vrednost kapacitivnosti dvojnog sloja opada prema očekivanjima. FTIR spektralna studija otkriva da se zaštitni film sastoji od kompleksa koji se sastoje od gvožđe aktivnih supstanic ekstrakta soka od jabuke. AFM studija otkriva da kada se efikasnost inhibicije poveća, hrapavost površine se smanjuje ili drugim rečima, glatkoća sistema se povećava.

***Ključne reči**: inhibicija korozije, meki čelik, simulirani rastvor pora betona, morska voda, vodeni ekstrakt soka od jabuke, elektrohemijske studije, FTIR, fluorescentna spektroskopija, AFM.*

Naučni rad

Rad primljen :09.07.2023.

Rad prihvaćen: 28.07.2023.

Rad je dostupan na sajtu: www.idk.org.rs/casopis

Siska Prifiharni[1], Amalia Rizky Sabila[2], Gadang Priyotomo[1], Arini Nikitasari[1], Rahayu Kusumastuti[1], Siti Musabikha[1], Rahma Nisa Hakim[1], Yanyan Dwiyanti[2], Bening Nurul Hidayah Kambuna[2]*

[1]National Research and Innovation Agency, Research Center of Metallurgy, Tangerang Selatan, Indonesia, [2]University of Sultan Ageng Tirtayasa, Departement of Metallurgy, Cilegon, Indonesia

Scientific paper
ISSN 0351-9465, E-ISSN 2466-2585
https://doi.org/10.62638/ZasMat1006

Zastita Materijala 65 (1)
35 - 44 (2024)

Electrochemical analysis of corrosion inhibition shallot leaf (*Allium cepa*) extract on mild steel in acidic medium at different immersion times

ABSTRACT

Plant derivatives as eco-friendly corrosion inhibitors are currently greatly interested in much research. Shallot leaf (Allium cepa) was utilized in 0.1M HCl as a corrosion inhibitor of mild steel. The functional groups present in the macerated extract were subsequently identified using an FTIR test. Electrochemical tests such as tafel polarization and EIS were carried out to determine the corrosion inhibition performance of shallot leaf extract on the SS400 steel. The results of the electrochemical analysis show that shallot leaf extract can inhibit mild steel up to 94% at a concentration of 500 ppm. Furthermore, the addition of SLE reduces surface damage of mild steel, which can be seen by SEM.

Keywords: *Corrosion inhibitor, plant extract, shallot leaf extract, carbon steel, immersion time*

1. INTRODUCTION

Mild steel is frequently used as structural steel due to its remarkable mechanical qualities and inexpensive cost. However, it suffers corrosion attacks in acidic environments commonly used in industrial processes such as oil and gas pipelines, chemical processing, paper, textile, refining, etc [1]. Corrosion leads to various losses, including decreased metal service life, safety, human life, cost, and material conservation [2]. Hydrochloric acid (HCl) is a common acid used in the energy industry, particularly oil and gas, for a variety of purposes, including well stimulation, well completion, and well cleaning. It is most often used for acidizing, which is the process of pumping acid into the well to dissolve rock and increase permeability. HCl is also used in well acidizing to remove damage to the wellbore caused by drilling, completion, or production [3].

However, if mild steel is continuously exposed to an environment containing hydrochloric acid (HCl), it will undergo corrosion. Various corrosion inhibitors can be used to stop mild steel from corroding in HCl surroundings. These inhibitors create a protective coating on the metal, blocking any acid from coming into contact with the steel's surface [4].

Inhibitors are generally classified into organic and inorganic, commercially available, and utilized in industrial settings. On the other hand, commercial synthetic inorganic inhibitors are harmful to the environment [5]. Even though organic inhibitors prevent corrosion, many of these substances are created through chemical processes. These technologies have a limited range of applications since they are prohibitively expensive and environmentally harmful [6]. The use of affordable, environmentally friendly chemicals is a hot topic.

Additionally, it has been stated that these compounds work incredibly effectively to safeguard metals in acidic situations [7]. As a result, environmentalists are concerned about the safety of corrosion inhibitors to the environment. Hence, numerous scientists are paying attention to creating green corrosion inhibitors.

Organic inhibitors contain antioxidant compounds that can delay, slow, or stop oxidation by donating electrons. Inhibitors can boost corrosion inhibition with electronegative components such as Oxygen, Sulfur, Nitrogen, and Phosphorus, as well as through the conjugation of double or triple bonds and the presence of aromatic rings [8,9]. Corrosion inhibitors can physically adsorb to the metal

*Corresponding author: Siska Prifiharni
E-mail: siska.prifiharni@brin.go.id
Paper received: 18. 07. 2023.
Paper accepted: 21. 08. 2023.
Paper is available on the website: www.idk.org.rs/journal

surface and prevent any interaction with the corrosive solution, or they can chemically react with the surface of the metal to stop corrosion.

Various recent studies have developed a green organic compound that can be obtained from plant extracts such as fruit [10], leaves [11], stem [12], flowers [13,14], seed [15], peel [16] which have shown has high efficiency as a corrosion inhibitor in acidic media. Shallot (*Allium cepa*) has active compounds in flavonoids and phenolic content that capture free radicals to release hydrogen atoms from their hydroxyl groups [17,18]. The highest total flavonoid content is found in shallot leaves when compared to 62 other common plants [19]. The total flavonoid content in leeks of 2720.5 mg/kg ranked first and was followed by Semambu leaves, cayenne pepper, black tea, papaya and guava plants [20]. Flavonoids and phenolics can be used as corrosion inhibitors to protect carbon steel from an aggressive environment and prevent corrosion [21,22]. From this explanation, shallot leaves have the potential to be used as an organic inhibitor. In addition, research has never been conducted on the use of shallot leaf extract (SLE) as an evironmetal friendly corrosion inhibitor. Therefore, this study was conducted to determine the effect of shallot leaf extract on the corrosion phenomenon of mild steel in an acidic solution, namely 0.1 M HCl solution.

2. EXPERIMENTAL SECTION

2.1. Preparation Of Mild Steel

SS400 mild steel was the material chosen for this study, which has the following composition: C:0.19%wt.; Mn: 0.3%wt.; P: 0.009%wt.; S: 0.009%wt.; Si: 0.15%wt.; Ni: 0.11%wt.; Cu: 0.014%wt.; Zn: 0.01%wt.; Al: 0.02%wt.; Fe: Remaining. Mild steel was cut into 10 × 10 × 10 mm^3 dimensions and embedded with resin for the electrochemical experimental procedure. The surface sections of the metals were abraded using sandpapers of various grit levels before each experiment (240, 400, 600, 800, 1000, and 1200).

2.2. Extraction of Shallot Leaves

The extraction of the shallot leaves begins with drying the shallots at room temperature. Shallots are then reduced in size by cutting them. After that, the maceration process was carried out: soaking the shallots in 96% ethanol for four days. The obtained filtrate was then filtered from the residue with filter paper (Whatman No. 44), and the solvent was then evaporated over the course of three days inside an oven at 100°C. The solid waste was then gathered, kept, and employed as an inhibitor (SLE) in several studies in an acidic media.

2.3. Fourier Transform Infrared Spectroscopy (FTIR)

The functional groups contained in the shallot extract were tested using FTIR. The analysis was carried out with the FTIR test instrument. The procedure was performed by homogenizing shallot leaf extract with KBr powder. After that, the mixture is made in pellets or pills and ready for analysis.

2.4. Total Phenolic Content

Total phenol analysis was initiated by making gallic acid master liquor and sample preparation. A master solution of gallic acid was produced by dissolving 1 mg of the acid into 1 mL of methanol (1000 g/mL). Each tube received 25, 50, 100, 150, and 200 L of the master solution by pipetting. To prepare the sample, dissolve 4 mg of the dry sample extract in 4 mL of 1000 g/mL methanol.

The Folin Ciocalteau method with gallic acid as a standard was used to determine the total phenolic content of the extract. The regression equation from the calibration curve obtained was used to represent the total phenolic content of the extract as gallic acid equivalent in mg/g extract. Pipette 25, 50, 100, 150, and 200 mL of Gallic acid standard solutions or a 250 mL sample solution into separate test tubes. Add 7.5 mL of distilled water and 0.5mL of Follin Ciocalteau to each test tube, then shake them. After allowing the mixture to rest for 8 minutes, add 1.5 mL of 20% Na2CO3 to each test tube and mix thoroughly. Set aside for two hours at room temperature before continuing. A wavelength of 765 nm was used to measure absorption. The measurements were carried out twice to ensure the phenol obtained was equal to gallic acid (mg/gr extract).

2.5. Tafel Polarization

Tafel measurements were conducted at 0.6 mV/s in a potential range of -0.25 to +0.25 V, using a GAMRY PCI4G750-50090 potentiostat testing equipment. This electrochemical analysis was completed with a three-electrode cell in the solution, having a platinum counter electrode, calomel reference electrode and a mild steel abrasively prepared working electrode. By extrapolating the Tafel curves, we were able to obtain data such as corrosion potential (E_{corr}), cathodic Tafel slope (β_c) and corrosion current density (i_{corr}). Next, using Eq. 1, the current density of corrosion was applied for determining the inhibition efficiency [15].

$$\eta\,(\%) = \frac{i^0_{corr} - i_{corr}}{i^0_{corr}}\, x\, 100\% \qquad (1)$$

Where

i^0_{corr} is corrosion current density without addition of inhibitor and i_{corr} is current after addition of inhibitor.

2.6. Electrochemical Impedance Spectroscopy

The EIS measurement was conducted with a frequency range between 300,000 Hz to 0.1 Hz using the Gamry instrument, and a Nyquist plot was used to represent EIS data. A fitting line from a practical equivalent circuit measures the impedance parameter. The surface coverage was calculated from corrosion charge transfer resistance using the following equation [15]:

$$\theta\ (\%) = \frac{R_{ct} - R_{ct}^{0}}{R_{ct}}\ x\ 100\% \qquad (2)$$

Where

R_{ct}^{0} is charge transfer resistance without inhibitor and R_{ct} is charge transfer after the addition of inhibitors.

3. RESULTS AND DISCUSSION

3.1. Ftir Analysis

The functional organic compounds that were present in the SLE were identified using the FTIR assay. The results of the FTIR experiment result in a graph that shows tiny peaks in a certain wavelength range, which may indicate the existence of several groups. Figure 1 shows the FTIR results of shallot leaf extract.

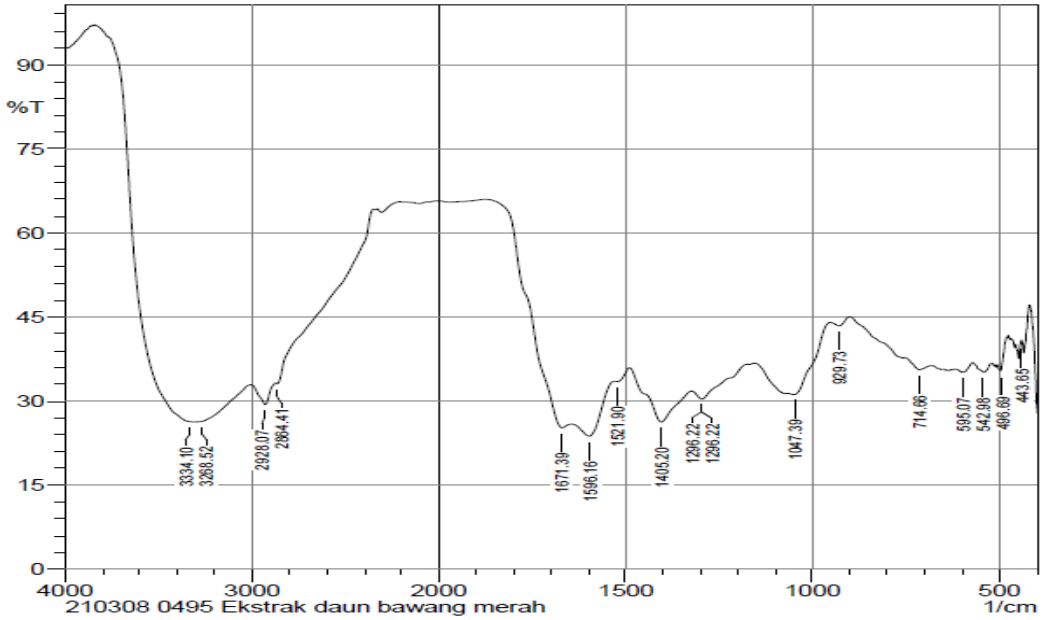

Figure 1. FTIR graph of SLE

Slika 1. FTIR grafik SLE

From the results of this analysis, it can be analyzed for the groups of functions contained in the shallot leaf extract. the functional groups detected in shallot leaf extract are C-H alkyne and alkane and aromatic at 1405.2 cm^{-1}, C-O and C-N bonds carboxyl at 1296.22 cm^{-1}, NO2 and C=C aromatic at 1521.9 cm^{-1}, O-H and N-H groups at 334.1 cm^{-1}[23]. The SLE had N, C, and OH groups, all of which belonged to the alkaloids carboxyl groups, according to the FTIR data. The SLE had polyphenol and flavonoid compounds since they contained aromatic components and phenol.

3.2. Total Phenolic Content

The total phenol content is expressed in EAG (gallic acid equivalent), a unit for defining the number of milligram equivalents of the gallic acid compound from one gram of sample. The total phenol test results showed that the tested shallot leaf extract has a total phenol content of 5.535 mgEAG/g extract.

3.3. Tafel Polarization

Figure 2 depicts Tafel polarization's outcome shallot leaf extract at various immersion times and inhibitor concentrations. The increase of SLE concentration to 500 ppm resulting high inhibition efficiency that reaches 94 percent at 60 min of immersion, as shown in table 2. At 500 ppm corrosion current of SLE decreases from 752.9 µA cm^{-2} to 107.7 µA cm^{-2} (0 min), from 793.3 µA cm^{-2} to 60,90 µA cm^{-2} (30 min), and from 802,4 to 46,74 µA cm^{-2} (60 min). The corrosion current density and corrosion rate of mild steel decreases when concentration of the SLE inhibitor increases, resulting in higher efficiency inhibition. The

deposited corrosion inhibitor molecule on the metal surface formed a protective barrier at the metal interface, protecting the metal surface from the acidic media and reducing the metal's corrosion rate [24,25].

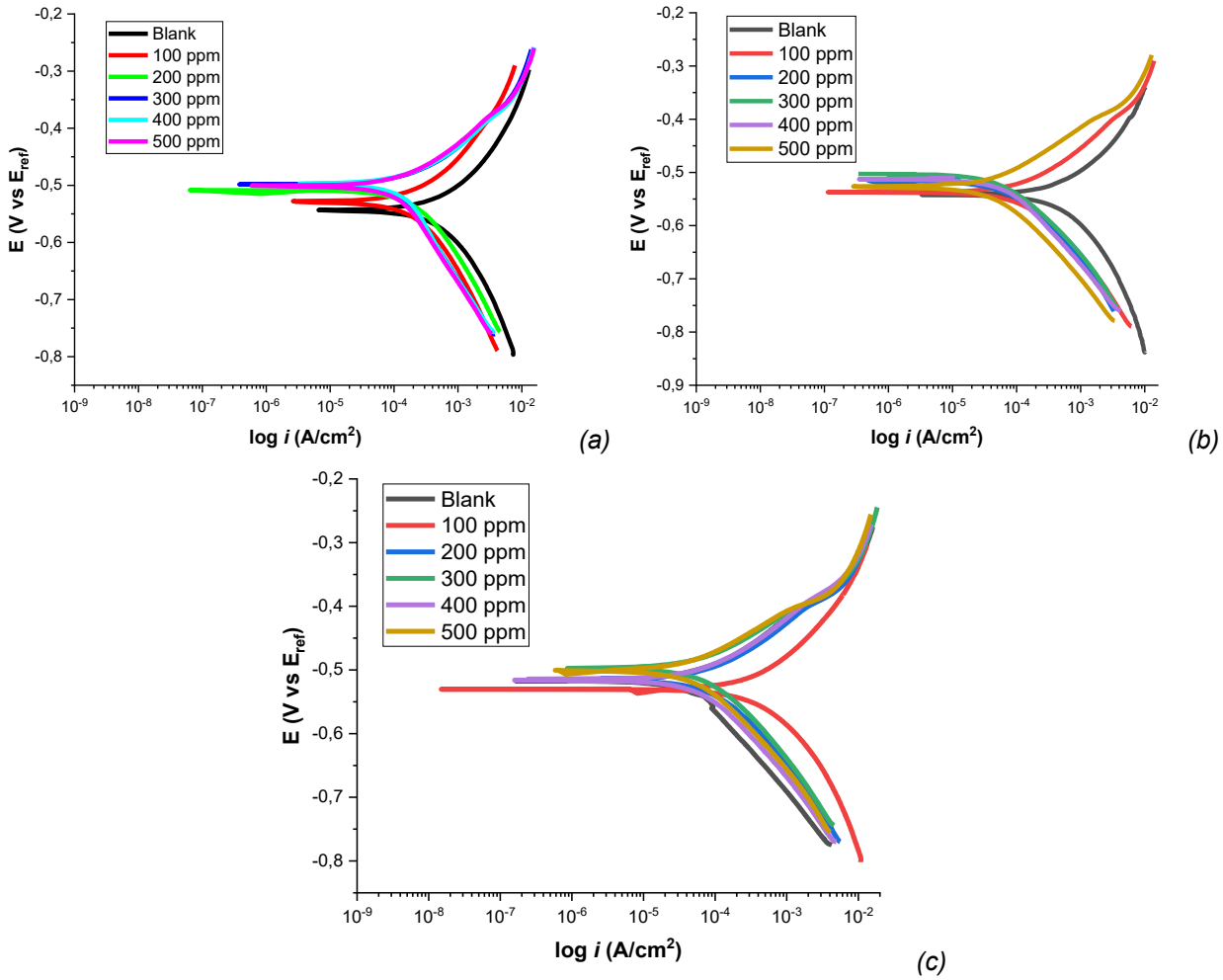

Figure 2. Tafel polarization of mild steel in the absence and presence of SLE in 0.1 M HCl after immersion (a) 0 minutes, (b) 30 minutes, (c) 60 minutes

Slika 2. Tafel-ove krive mekog čelika u odsustvu i prisustvu SLE u 0,1 M HCl nakon potapanja (a) 0 minuta, (b) 30 minuta, (c) 60 minuta

Corrosion potential slightly increases with adding SLE if it is compared to the blank. SLE addition reduces anodic dissolution and blocks oxidation reactions by preventing reaction sites that become active on the steel surface [26], showing that adding inhibitors to the solution reduces both cathodic and anodic currents without modifying the mechanism [27,28]. It has been reported that if the corrosion potential movement from blank to anodic or cathodic directions is more significant than 85 mV is categorized as an anodic or cathodic inhibitor. In this report, the greatest movement of E_{corr} value was 45.5 mV indicating that inhibitor SLE is a mixed-type inhibitor.

Table 1 shows the current density (i_{corr}) and corrosion rate of mild steel decrease after 30 and 60 minutes of immersion. The decrease in current density as well as corrosion rate indicates that SLE has a great inhibitor effectiveness and durability in film inhibition [29]. The inhibitor efficiency rises at the longer immersion time up to 94.2% in 500 ppm of SLE. The immersion period will also give the antioxidant compound molecules of the shallot leaf extract and the SS400 steel enough time to adsorb or inhibit one another and create a film or monolayer layer on the steel surface [30]. Figure 3 examines the influence of concentration on changing the corrosion potential and decreasing current density to reduce corrosion rate and increase inhibition efficiency.

Table 1. Electrochemical parameters of SLE

Tabela 1. Elektrohemijski parametri SLE

Immersion Time (min.)	Concentration (ppm)	β_c (V/decade)	E_{corr} (mV)	i_{corr} (μA/cm^2)	CR (mpy)	η (%)
0	0	0.2347	-544.8	752.9	344.9	0
	100	0.2116	-530.2	279.4	128.0	62.89
	200	0.1932	-508.3	255.1	116.9	66.10
	300	0.1744	-580.8	116.5	53.37	84.52
	400	0.1735	-499.3	112.1	51.36	85.11
	500	0.1717	-503.0	107.7	49.33	85.70
30	0	0.2318	-541.9	793.3	363.4	0
	100	0.1588	-538.5	184.9	84.69	76.70
	200	0.1567	-515.4	70.19	50.96	85.98
	300	0.1441	-501.5	85.55	39.19	89.21
	400	0.1398	-512.7	70.99	32.52	91.05
	500	0.1409	-528.7	60.90	27.90	92.32
60	0	0.2125	-530.4	802.4	367.6	0
	100	0.1486	-515.3	131.3	60.17	83.63
	200	0.1479	-497.5	108.4	49.65	86.49
	300	0.1378	-516.0	77.31	35.42	90.36
	400	0.1365	-500.6	70.71	32.39	91.19
	500	0.1311	-517.1	46.74	21.41	94.17

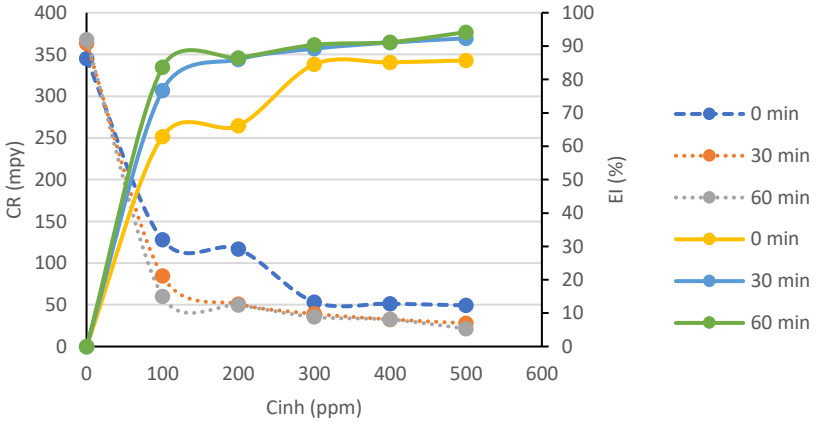

Figure 3. Graph of the effect of concentration on corrosion rate and inhibition efficiency

Slika 3. Grafikon uticaja koncentracije na brzinu korozije i efikasnost inhibicije

3.4. Electrochemical Impedance Spectroscopy (EIS)

The EIS tests create Nyquist curves which to learn more about the phenomena carried on by adding XME inhibitors at the metal/electrolyte contact. EIS test was carried out at various concentrations and immersion periods both without and with the addition of inhibitors. The Nyquist curve is typically depicted as a semicircle, showing the difference between the real and imaginary impedance values. Figure 4 displays the Nyquist curve for this study. EIS data were measured between 300 kHz and 0.1 Hz in frequency. A primary Randles-type electrical circuit will simulate a Nyquist curve derived from the test findings.

The semicircular Nyquist diameter can be assumed as an inhibitor's capacity to prevent corrosion. The larger the curve's radius indicates the greater charge transfer resistance (R_{ct}). Semicircular Nyquist diameter grows more significant with the SLE inhibitor presence and increases as SLE concentration rises. Likewise, increased immersion time will make an enormous semicircular diameter Nyquist curve. The fitting line from EIS was used the Randles model editor, which is shown in Figure 5, to determine the solution resistance (R_u), charge transfer resistance (R_{ct}), and double-layer capacitance (C_{dl}). The resistance parameters of SLE on SS400 steel are shown in Table 3.

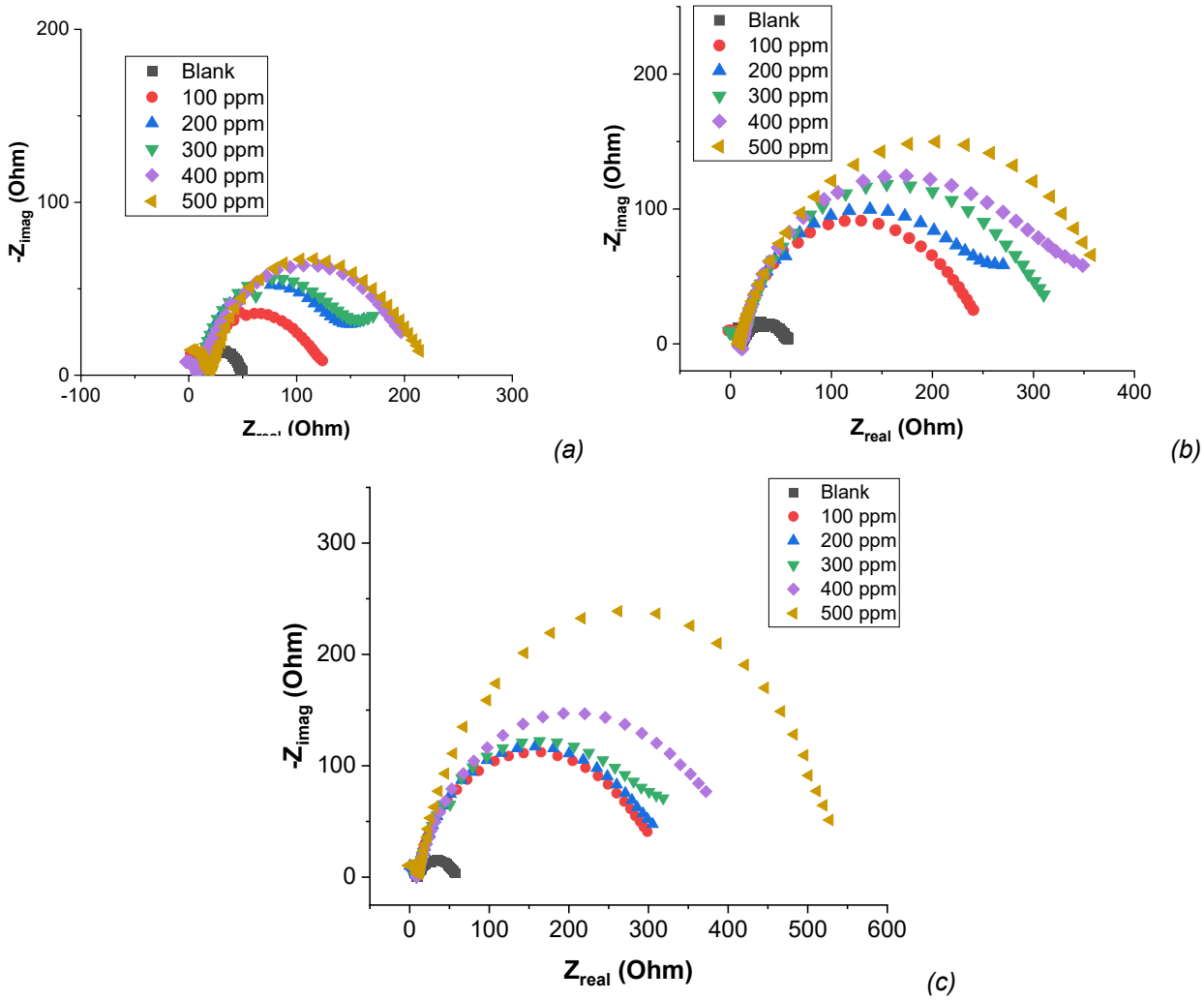

Figure 4. Nyquist plot of mild steel in various concentration of SLE in 0.1 M HCl after immersion (a) 0 minutes, (b) 30 minutes, (c) 60 minutes

Slika 4. Nyquist-ove krive mekog čelika u različitim koncentracijama SLE u 0,1 M HCl nakon potapanja (a) 0 minuta, (b) 30 minuta, (c) 60 minuta

The observation from Table 2 shows that the Rct value increases by increasing SLE concentration and the longer immersion duration of the steel in the solution. Because of resistance in a layer on the electrode's surface, R_{ct} rises, causing a drop in potential and a fall in corrosion rate. After adding SLE, a barrier will form on the metallic surface, preventing electrons or ions from passing. It shows that as the inhibitor concentration rises, inhibitor molecules that adsorb to the surface of the steel increase resulting in increasing the steel's resistance to charge transfer only by inhibiting active sites on the metal [31]. An increase in R_{ct} value affects better inhibition efficiency, calculated using eq.2. Table 2 also shows that increasing immersion increases the R_{ct} value. Excellent surface coverage was obtained after a longer immersion time of 60 minutes, improving the inhibitor's efficiency. This trend suggests that SLE molecules adsorbed to the metal/solution interface create a long-term protective barrier, inhibiting the molecules from adhering to the metal surface and, thus, shielding it from corrosive attack. Plant extracts, including *syzygium cumini* [32], rosa canina [33], esfan seed [34], and dardagan fruit [29] also exhibit this behavior.

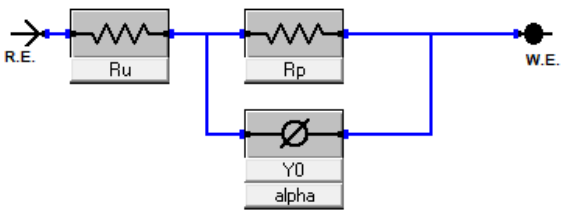

Figure 5. An equivalent circuit model was used in this study

Slika 5. Model ekvivalentnog kola korišćen u ovoj studiji

Table 2. The fitted data of EIS result in concentration and immersion time variations

Tabela 2. Dobijeni podaci EIS-a pri varijacijama koncentracije i vremena uranjanja

Immersion Time (minute)	Conc. (ppm)	R_u (ohm)	R_{ct} (ohm)	Y^0 (10^4)	n	C_{dl} (μF)	θ (%)
0	0	9.543	42.14	4.38	0.73	97	0.00
	100	9.807	115.5	3.02	0.72	80	63.52
	200	8.274	153.4	1.24	0.77	37	72.53
	300	8.286	162.1	1.11	0.77	33	74.00
	400	8.272	198.0	1.05	0.75	29	78.72
	500	13.26	210.9	1.18	0.70	24	80.02
30	0	9.252	49.56	6.17	0.69	131	0.00
	100	6.862	244.7	1.52	0.81	70	79.75
	200	8.976	268.8	0.95	0.82	43	81.56
	300	8.029	313,8	0.93	0.81	40	84.21
	400	9.304	346.9	0.80	0.80	33	85.71
	500	9.003	392.2	0.81	0.78	31	87.36
60	0	8.485	51.07	12.05	0.58	401	0.00
	100	9.313	301,6	1.26	0.82	390	83.07
	200	6.466	323.6	1.85	0.79	388	84.22
	300	8.727	330.4	3.82	0.82	382	84.54
	400	9.019	404.0	1.04	0.80	297	87.36
	500	7.404	527.9	0.45	0.92	162	90.33

From Table 2, the results demonstrate clearly that double-layer capacitance (C_{dl}) decreases as R_{ct} values increase. The C_{dl} value gradually decreases as inhibitor concentration increases, showing that the adsorption of corrosion inhibitor leads to the dielectric constant being reduced, thickening the electric double-layer at the metal/electrolyte interface [35].

3.5. Surface Characterization

The surface of corrosion inhibitors of SLE was characterized by SEM. The carbon steel was soaked in 0.1M HCl in the blank and with the addition of 500 ppm SLE for 24 hours at room temperature. Figure 6 shows the smoother surface on the steel was found after adding of 500 ppm of SLE. On the other hand, pitting corrosion can occur and the surface of carbon steel without the presence of SLE seems rough. The rough surface of the metal without inhibitors indicates that the surfaces formed a corrosion product from the interaction between metal and electrolyte. The addition of SLE increases the homogeneity of the surface and minimizes the roughness of the steel substrate. Surface smoothness is produced when a layer of protective Fe^{2+} complex and shallot leaf extract is formed on the metal surface, reducing the carbon steel corrosion rate [36,37].

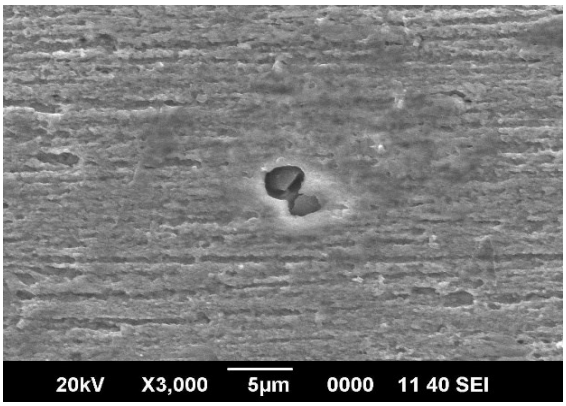

(a)

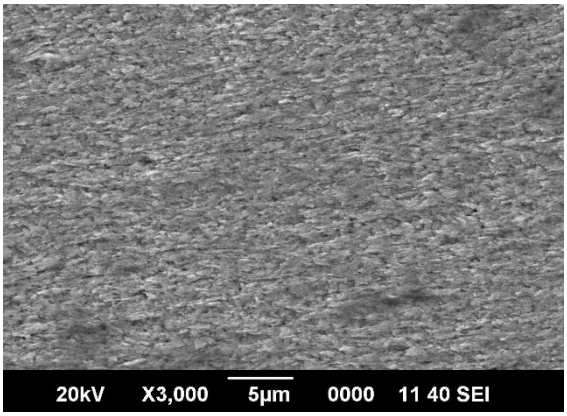

(b)

Figure 6. SEM morphology of carbon steel (a) blank and (b) after the addition of 500 ppm SLE

Slika 6. SEM morfologija ugljeničnog čelika (a) blanko i (b) nakon dodavanja 500 ppm SLE

3.6. Proposed Inhibition Mechanism

Potentiodynamic polarization and EIS observed a greater efficiency at higher concentrations of corrosion inhibitors. Thus, the mechanism and efficiency of inhibition are dependent on inhibitor concentration. The difference in immersion time on mild steel also gives another effect on the adsorption of the inhibitor. During the first step of immersion, the plant extract components were adsorbed onto the steel surface. The process can lead to the formation of a barrier layer that protects the metal surface from damaging the HCl environment. The inhibitor molecules keep adhering to the metal surface, producing a thicker protective layer as the immersion duration lengthens. This may result in a decrease in the corrosion rate and an improvement in the effectiveness of the inhibitor. However, due to the aggressive environment and prolonged immersion times, the inhibitor molecules may begin to desorb from the metal surface. This may cause the inhibition efficiency to drop and the rate of corrosion to rise [38]. Figure 7 provides an illustration of the potential SLE adsorption process on the surface of mild steel.

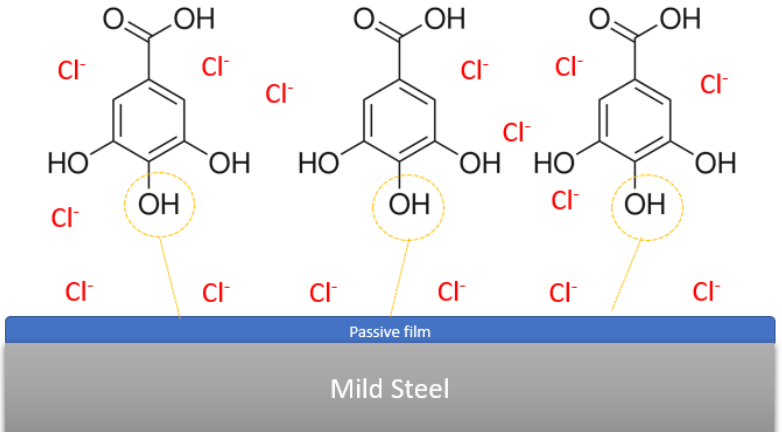

Figure 7. Possible adsorption mechanism process of SLE onto mild steel surface

Slika 7. Mogući proces mehanizma adsorpcije SLE na površini od mekog čelika

4. CONCLUSION

In this study, ethanol extracted an eco-friendly corrosion inhibitor from shallot leaf and evaluated using electrochemical and surface analysis in 0.1 M HCl. Tafel polarization of carbon steel shows a decrease in corrosion rate after the addition of SLE with 94% inhibition effectiveness after 60 minutes of immersion. The polarization test also showed that SLE acted as a mixed-type inhibitor. SEM morphology of metal surface showed that the inhibitor adsorption of SLE significantly decreases the surface damage of mild steel.

Conflict of interest

All of the authors declare there is no conflict of interest.

Acknowledgment

Thanks to the Research Center of Metallurgy, National Research and Innovation Agency, for fully funding this research and providing the laboratory.

5. REFERENCES

[1] X.Joy Pradeep, J.Sathiyabama (2021) A study on corrosion inhibition of Carbon steel in well water by Oxalis corniculata L. Leaves extract, Mater. Today. Proc., 47, 154–158. doi: 10.1016/j.matpr.2021.04.031.

[2] M.Finšgar, J.Jackson (2014) Application of corrosion inhibitors for steels in acidic media for the oil and gas industry: A review, Corros. Sci., 86, 17–41. doi: 10.1016/j.corsci.2014.04.044.

[3] X.Zuo, W. Li, W.Luo, X.Zhang, Y. Qiang, J.Zhang, H.Li, B.Tan (2021) Research of Lilium brownii leaves extract as a commendable and green inhibitor for X70 steel corrosion in hydrochloric acid, J. Mol. Liq., 321 114914. doi: 10.1016/j.molliq.2020.114914.

[4] C.G.Dariva, A.F.Galio (2016) Corrosion inhibitors: Principles, mechanisms and applications, in: M. Aliofkhazraei (Ed.), Developments in Corrosion Protection, Intech Open, book, p.365–379. doi: 10.5772/57255.

[5] N.Chaubey, P.Savita, A.Qurashi, D.S.Chauhan, M.A.Quraishi (2021) Frontiers and advances in green and sustainable inhibitors for corrosion applications: A critical review, J. Mol. Liq., 321, 115085, doi: 10.1016/j.molliq.2020.114385.

[6] S.Chitra, I.M.Chung, S.H.Kim, M.Prabakaran (2019) A study on anticorrosive property of phenolic components from Pachysandra terminalis against low carbon steel corrosion in acidic medium, Pigment. Resin. Technol., 48, 389–396. doi: 10.1108/PRT-09-2018-0095.

[7] D.Lakshmi, S.Rajendran, J.Sathiyabama (2016) Corrosion Inhibition by Phenols – An Overview, Int. j. nano corros. sci. eng., 3, 1–18.

[8] A.P.S.Kaban, A.Ridhova, G.Priyotomo, B.Elya, A. Maksum, Y.Sadeli, T.Aditiyawarman, R.Riastuti, J.W.Soedarsono (2021) Development of White Tea Extract As Green Corrosion Inhibitor in Mild Steel Under 1 M Hydrochloric Acid Solution, East. -Eur. J. Enterp., 2, 6–20. doi: 10.15587/1729-4061. 2021.224435.

[9] A.A.Olajire (2017) Corrosion inhibition of offshore oil and gas production facilities using organic compound inhibitors - A review, J. Mol. Liq., 248, 775–808. doi: 10.1016/j.molliq.2017.10.097.

[10] E. de B.Policarpi, A.Spinelli (2020) Application of Hymenaea stigonocarpa fruit shell extract as eco-friendly corrosion inhibitor for steel in sulfuric acid, J. Taiwan. Inst. Chem. Eng., 116, 215–222. doi: 10.1016/j.jtice.2020.10.024.

[11] A.A.Khadom, A.N.Abd, N.A.Ahmed (2018) Xanthium strumarium leaves extracts as a friendly corrosion inhibitor of low carbon steel in hydrochloric acid: Kinetics and mathematical studies, S. Afr. J. Chem. Eng., 25, 13–21. doi: 10.1016/j.sajce.2017.11.002.

[12] E.Honarmand, H.Mostaanzadeh, M.H. Motaghedifard, M.Hadi, M.Khayadkashani (2017) Inhibition effect of opuntia stem extract on corrosion of mild steel: a quantum computational assisted electrochemical study to determine the most effective components in inhibition, Prot. Met. Phys. Chem., 53, 560–572. https://doi.org/10.1134/S207020511703008X.

[13] A.Dehghani, G.Bahlakeh, B.Ramezanzadeh, M. Ramezanzadeh (2019) Potential of Borage flower aqueous extract as an environmentally sustainable corrosion inhibitor for acid corrosion of mild steel: Electrochemical and theoretical studies, J. Mol. Liq., 277, 895–911. doi: 10.1016/j.molliq.2019.01.008.

[14] A.Rajendran, C.Karthikeyan (2012) The Inhibitive Effect of Extract of Flowers of Cassia Auriculata in 2 M HCl on the Corrosion of Aluminium and Mild Steel, Int. J. Plant Res. 2, 9–14. doi: 10.5923/ j.plant.20120201.02.

[15] H.Hassannejad (2018) A. Nouri, Sunflower seed hull extract as a novel green corrosion inhibitor for mild steel in HCl solution, J. Mol. Liq., 254, 377–382. doi: 10.1016/j.molliq.2018.01.142.

[16] L.L.Liao, S.Mo, H.Q.Luo, N.B.Li (2018) Corrosion protection for mild steel by extract from the waste of lychee fruit in HCl solution: Experimental and theoretical studies, J. Colloid. Interface. Sci., 520, 41–49. doi: 10.1016/j.jcis.2018.02.071.

[17] N.Marefati, N.Eftekhar, M.Kaveh, J.Boskabadi, F. Beheshti, M.H.Boskabady (2018) The Effect of Allium cepa Extract on Lung Oxidant, Antioxidant, and Immunological Biomarkers in Ovalbumin-Sensitized Rats, Med. Princ. Pract.., 27, 122–128. doi: 10.1159/000487885.

[18] S.Masood, A.Rehman, M.A.Ihsan, K.Shahzad, M. Sabir, S.Alam, W.Ahmed, Z.H.Shah, F.Alghabari, A. Mehmood, G.Chung (2023) Antioxidant potential and α-glucosidase inhibitory activity of onion (Allium cepa L.) peel and bulb extracts, Braz. J. Biol., 83, 1–9. doi: 10.1590/1519-6984.247168.

[19] V. Lanzotti (2006) The analysis of onion and garlic, J. Chromatogr. A., 1112, 3–22. doi: 10.1016/ J. CHROMA.2005.12.016.

[20] K.H.Miean, S.Mohamed (2001) Flavonoid (myricetin, quercetin, kaempferol, luteolin, and apigenin) content of edible tropical plants, J. Agric. Food. Chem., 49, 3106–3112. doi: 10.1021/ JF000892M.

[21] A.A.Rahim, E.Rocca, J.Steinmetz, M.J.Kassim, R. Adnan, M.Sani Ibrahim (2007) Mangrove tannins and their flavanoid monomers as alternative steel corrosion inhibitors in acidic medium, Corros. Sci., 49, 402–417. doi: 10.1016/j.corsci.2006.04.013.

[22] K.W.Tan, M.J.Kassim (2011) A correlation study on the phenolic profiles and corrosion inhibition properties of mangrove tannins (Rhizophora apiculata) as affected by extraction solvents, Corros. Sci., 53, 569–574. doi: 10.1016/j.corsci. 2010.09.065.

[23] A.B.D.Nandiyanto, R.Oktiani, R.Ragadhita (2019) How to read and interpret ftir spectroscope of organic material, Indones. J. Sci. Technol., 4, 97–118. doi: 10.17509/ijost.v4i1.15806.

[24] N. el Hamdani, R.Fdil, M.Tourabi, C.Jama, F. Bentiss (2015) Alkaloids extract of Retama monosperma (L.) Boiss. seeds used as novel eco-friendly inhibitor for carbon steel corrosion in 1 M HCl solution: Electrochemical and surface studies, Appl. Surf. Sci., 357, 1294–1305. doi:10.1016/ j.apsusc. 2015.09.159.

[25] M.Ramezanzadeh, G.Bahlakeh, Z.Sanaei, B. Ramezanzadeh (2019) Corrosion inhibition of mild steel in 1 M HCl solution by ethanolic extract of eco-friendly Mangifera indica (mango) leaves: Electrochemical, molecular dynamics, Monte Carlo and ab initio study,Appl.Surf. Sci., 463, 1058–1077. doi: 10.1016/j.apsusc.2018.09.029.

[26] P.E.Alvarez, M.V.Fiori-Bimbi, A.Neske, S.A. Brandán, C.A.Gervasi (2018) Rollinia occidentalis extract as green corrosion inhibitor for carbon steel in HCl solution, J. Ind. Eng. Chem., 58, 92–99. doi: 10.1016/j.jiec.2017.09.012.

[27] S.Kadapparambil, K.Yadav, M.Ramachandran, N. Vi.Selvam (2017) Electrochemical investigation of the corrosion inhibition mechanism of Tectona grandis leaf extract for SS304 stainless steel in hydrochloric acid, Corros., 35. 111–121. doi: 10.1515/corrrev-2016-0074/machinereadablecitation/ris.

[28] J.P.Flores-De Los Ríos, M.Sánchez-Carrillo, C.G. Nava-Dino, J.G.Chacón-Nava, J.G.González-Rodríguez, E.Huape-Padilla, M.A.Neri-Flores, A. Martínez-Villafañe (2015) Opuntia ficus-indica extract as green corrosion inhibitor for carbon steel in 1M HCl solution, J. Spectrosc., 2015, ID 714692. doi: 10.1155/2015/714692.

[29] A.Sedik, D.Lerari, A.Salci, S.Athmani, K.Bachari, H. Gecibesler, R.Solmaz (2020) Dardagan Fruit extract as eco-friendly corrosion inhibitor for mild steel in 1 M HCl: Electrochemical and surface morphological studies, J. Taiwan. Inst. Chem. Eng., 107, 189–200. doi: 10.1016/j.jtice.2019.12.006.

[30] A.Dehghani, G.Bahlakeh, B.Ramezanzadeh, M. Ramezanzadeh (2019) Potential of Borage flower

aqueous extract as an environmentally sustainable corrosion inhibitor for acid corrosion of mild steel: Electrochemical and theoretical studies, J. Mol. Liq., 277, 895–911. doi: 10.1016/j.molliq.2019.01.008.

[31] J.Aldana-González, A.Espinoza-Vázquez, M. Romero-Romo, J.Uruchurtu-Chavarin, M.Palomar-Pardavé (2019) Electrochemical evaluation of cephalothin as corrosion inhibitor for API 5L X52 steel immersed in an acid medium, Arab. J. Chem., 12, 3244–3253. https://doi.org/10.1016/j.arabjc. 2015. 08.033.

[32] R.Riastuti, G. Mashanafie, V.Rizkia, A.Maksum, S. Prifiharni, A.Kaban, G.Priyotomo, J.Soedarsono (2022) Effect of syzygium cumini leaf extract as a green corrosion inhibitor on API 5l carbon steel in 1M HCL, East. -Eur. J. Enterp., 6, 30–41. doi: 10.15587/1729-4061.2022.267232.

[33] Z.Sanaei, M.Ramezanzadeh, G.Bahlakeh, B. Ramezanzadeh (2019) Use of Rosa canina fruit extract as a green corrosion inhibitor for mild steel in 1 M HCl solution: A complementary experimental, molecular dynamics and quantum mechanics investigation, J. Ind. Eng. Chem., 69, 18–31. doi: 10.1016/j.jiec.2018.09.013.

[34] M.T.Majd, M.Ramezanzadeh, B.Ramezanzadeh, G. Bahlakeh (2020) Production of an environmentally stable anti-corrosion film based on Esfand seed extract molecules-metal cations: Integrated experimental and computer modeling approaches, J. Hazard. Mater., 382, 121029. doi: 10.1016/ j.jhazmat.2019.121029.

[35] [H.L.Y.Sin, A. Abdul Rahim, C.Y.Gan, B.Saad, M.I. Salleh, M.Umeda (2017) Aquilaria subintergra leaves extracts as sustainable mild steel corrosion inhibitors in HCl, Measurement., 109, 334–345. doi: 10.1016/j.measurement.2017.05.045.

[36] A. R. Shahmoradi, M. Ranjbarghanei, A. A. Javidparvar, L. Guo, E. Berdimurodov, B. Ramezanzadeh (2021) Theoretical and surface/electrochemical investigations of walnut fruit green husk extract as effective inhibitor for mild-steel corrosion in 1M HCl electrolyte, J. Mol. Liq., 338, 116550. doi: 10.1016/j.molliq.2021.116550.

[37] Q.Wang, H.Zheng, L. Liu, Q. Zhang, X. Wu, Z.Yan, Y.Sun, X. Li (2022) Insight into the anti–corrosion behavior of Reineckia Carnea leaves extract as an eco–friendly and high–efficiency corrosion inhibitor, Ind. Crops. Prod., 188 A, 115752 doi: 10.1016/j.indcrop.2022.115640.

[38] B. Liao, Z. Luo, S. Wan, L. Chen (2023) Insight into the anti-corrosion performance of Acanthopanax senticosus leaf extract as eco-friendly corrosion inhibitor for carbon steel in acidic medium, J. Ind. Eng. Chem., 117, 238–246. doi: 10.1016/J.JIEC. 2022. 10.010.

IZVOD

ELEKTROHEMIJSKA ANALIZA INHIBICIJE KOROZIJE EKSTRAKTA LISTA SHALLOT *(Allium cepa)* NA MEKOM ČELIKU U KISELOJ SREDINI PRI RAZLIČITIM VREMENIMA POTARPANJA

Biljni derivati kao ekološki prihvatljivi inhibitori korozije su trenutno veoma zainteresantni za mnoga istraživanja. List SHALLOT (Allium cepa) je korišćen u 0,1 M HCl kao inhibitor korozije mekog čelika. Funkcionalne grupe prisutne u maceriranom ekstraktu su naknadno identifikovane korišćenjem FTIR testa. Sprovedeni su elektrohemijski testovi kao što su Tafel polarizacija i EIS da bi se odredio učinak inhibicije korozije ekstrakta lista Shallot na SS400 čeliku. Rezultati elektrohemijske analize pokazuju da ekstrakt lista Shallot može inhibirati meki čelik do 94% u koncentraciji od 500 ppm. Štaviše, dodatak SLE smanjuje površinsko oštećenje mekog čelika, što se može videti pomoću SEM.

Ključne reči: *inhibitor korozije, biljni ekstrakt, ekstrakt lista ljutike, ugljenični čelik, vreme potapanja.*

Naučni rad
Rad primljen: 18.07.2023.
Rad prihvaćen: 21.08.2023.
Rad je dostupan na sajtu: www.idk.org.rs/casopis

*Snežana Marković[1], Bojana Radojković[2], Bore Jegdić[2], Aleksandar Jovanović[3], Jovica Stojanović[3], Milan Trumić[1], Vaso Manojlović[4]**

[1]University of Belgrade, Technical Faculty in Bor, Bor, Serbia, [2]University of Belgrade, Institute for Chemistry, Technology and Metallurgy, Belgrade, Serbia, [3]Institute for Technology of Nuclear and Other Mineral Raw Materials, Belgrade, Serbia, [4]University of Belgrade, Faculty of Technology and Metallurgy, Belgrade, Serbia

Scientific paper
ISSN 0351-9465, E-ISSN 2466-2585
https://doi.org/10.62638/ZasMat998

Zastita Materijala 65 (1)
45 - 53 (2024)

Corrosion behavior of high- and low-chromium steel grinding balls in chloride solution

ABSTRACT

The corrosion behaviour of three types of alloys (two low-alloy carbon steel and one stainless iron with ~15 wt.% Cr), in a solution which simulates seawater (3% NaCl solution, pH 8.1) was tested. Tested samples are used to make steel (iron) balls applied in mils for grinding copper and other ore. The corrosion tests were performed using three electrochemical methods, at room temperature in the presence of atmospheric oxygen. The linear polarization resistance (LPR) method, electrochemical impedance spectroscopy (EIS) method, and linear sweep voltammetry (LSV) method were applied. Based on measurements by LPR and EIS methods (as non-destructive methods), the value of polarization resistance (R_p) was determined and the general corrosion rate (v_{corr}) of the examined samples was calculated. The obtained values of the general corrosion rate can be used to calculate the service life of steel (iron) balls under exploitation conditions (seawater). The appearance of the surface after linear sweep voltammetry (LSV) measurement showed the presence of localized corrosion (pits were formed) of the tested samples, especially stainless iron, and the LSV method is not suitable for the determination of the general corrosion rate of tested samples in seawater. This form of corrosion occurs at high anodic polarizations, during performing LSV measurements.

Keywords: *Low-alloy Steel, Stainless Iron, Electrochemical Corrosion, LPR, EIS, LSV, Seawater*

1. INTRODUCTION

Steel balls used for grinding copper and other ores during exploitation are exposed to intense wear and corrosion. Corrosion processes are very important considering that steel balls and ore are in contact with seawater. The procedure for determination of the level of synergetic action wear and corrosion is analysed in the ASTM G119 standard [1].

In seawater, during electrochemical corrosion, on the steel surface, two electrochemical reactions (anodic and cathodic) occur simultaneously. The anodic reaction is the dissolution of the metal (steel), i.e. the transition of metal ions into the solution. The cathodic reaction is the reduction of oxygen dissolved in seawater. The oxygen present in the seawater removes electrons from the metal surface, ensuring the transition of the metal atom to the ionic state.

*Corresponding author: Vaso Manojlović
E-mail: v.manojlovic@tmf.bg.ac.rs
Paper received: 14. 09. 2023.
Paper accepted: 12. 10. 2023.
Paper is available on the website: www.idk.org.rs/journal

In accordance with the heterogeneous theory of electrochemical corrosion, the places where the anodic and cathodic reactions take place on the metal surface are separated and the flow of electrons in the metal is necessary for the occurrence of the corrosion processes. Such a separation of anodic and cathodic reactions is energetically favourable. General corrosion is characterized by a uniform reduction in metal thickness, without significant localized attack. During the occurrence of general corrosion, the anodic and cathodic sites are replaced, as a result of which the dissolution of the steel is approximately the same over the entire surface of the metal [2].

A quantitative indicator of general corrosion is its corrosion rate. The rate of corrosion can be determined in the exploitation conditions [3, 4], at corrosion stations [4-6], based on mass loss of the specimens before and after corrosion tests [7-9], in the different chambers such as a chamber with neutral salt spray, a chamber with acid-salt spray [10], etc. The mentioned methods require a long time to obtain appropriate results. The rate of general corrosion is presented by the depth of the

corrosion into metal for a certain period and is most often expressed in mm year^{-1}.

In the last decades, electrochemical methods have been increasingly used to determine the corrosion rate of metals. As a result of electrochemical measurements, the polarization resistance and corrosion current density are obtained, on which value of the corrosion rate can be calculated.

In this work, the rate of general corrosion of three types of alloys (two low-alloyed carbon steels and one stainless iron with ~ 15 wt.% Cr) was determined. The tests were performed in a slightly alkaline 3% NaCl solution (pH 8.1), which simulates seawater, using several electrochemical methods. The electrochemical polarization resistance (LPR) method [11-14], the electrochemical impedance spectroscopy (EIS) method [15-18], and the linear sweep voltammetry (LSV) method [19-22], were applied.

With increasing the concentration of NaCl in the solution up to 3%, the solution conductivity increases. At the same time, the rate of steel corrosion also increases. On the other hand, at higher concentrations of NaCl, the solubility of the atmospheric oxygen decreases and the corrosion rate decreases [23]. Accordingly, the highest corrosion rate of the steel is in a 3% NaCl solution. This is the reason for the application of a 3% NaCl solution for performing experiments in this study.

Before the electrochemical corrosion measurements, the specimens (steel) were kept in the tested solution (3% NaCl solution, pH 8.1) for a certain time, at an open circuit potential, until a stable value of that potential was established. The open circuit potential is known as the mixed potential or corrosion potential for a given metal/electrolyte system. Corrosion potential is a basic indicator of the state of the corrosion system and it is a basis for subsequent electrochemical corrosion tests using the aforementioned methods.

The corrosion potential value can be used independently of other electrochemical measurements, as in the case of determining the condition of steel reinforcement in concrete. Steel reinforcement in concrete that is in a passive state has a corrosion potential value that is several hundred millivolts more positive than reinforcement that is in an active state, i.e., corroding reinforcement [24]. Also, the value of the corrosion potential of metals and alloys in a corrosive environment is used to predict the occurrence of galvanic corrosion [25-27]. A large number of different applications of corrosion potential measurement are summarized in the ASTM G215 standard [28] and literature [29, 30].

This paper aims to consider the possibility of determining the general corrosion rate of steel in a 3 % NaCl solution using different electrochemical methods. Also, based on the obtained values for the corrosion rate, the goal is to predict the reduction of the wall thickness of the steel balls (which are used for grinding copper or other ore), as well as the determination of the service life of the steel (iron) balls under the specified exploitation conditions.

2. MATERIALS AND METHODS

2.1. Materials

The chemical composition of the tested samples was determined by the optical emission spectrometer for metal analysis, Belec lab 3000s (Belec Spectrometric Opto-Elektronik GmbH, Germany) and is given in Table 1. S1 is casted steel, and contains < 0.1% chromium, S2 is steel in a wrought state and contains ~ 0.5% chromium, while S3 is casted iron and contains ~ 15 wt.% chromium. For the steels (iron) to be stainless, the chromium content must be greater than ~ 12 wt. %. Accordingly, S3 is stainless cast iron, because the carbon content in this sample is 2.56 wt. %.

Table 1. Chemical composition of the tested samples (wt.%)

Tabela 1. Hemijski sastav ispitanih uzoraka (mas. %)

	C	Si	Mn	P	S	Cu	Cr	Ni	Mo	Fe
S1	0.445	0.355	0.765	0.013	0.035	0.17	0.08	0.048	0.08	Rest
S2	0.74	0.42	0.667	0.008	0.005	0.049	0.51	0.033	0.013	Rest
S3	2.56	0.61	0.483	0.03	0.024	0.055	15.14	0.11	0.03	Rest

Table 2 lists the hardness values (HB), measured on a Brinell hardness testing machine. The Brinell hardness test was measured by pressing a hard steel ball (5 mm) into tested specimens with a 750 kg force for 20 seconds (AMSLER, Switzerland) and then measuring the size of the indentation by optical microscopy. The hardness value is the highest for S3 (iron with the highest concentration of carbon and chromium), and the lowest for the steel with the lowest concentration of carbon and chromium (steel S1). The hardness of steel S2 is higher than for S1, due

to its hardening structure formed during steel ball rolling.

Table 2. The hardness of the tested samples (HB)

Tabela 2. Tvrdoća ispitivanih uzoraka (HB)

	HB
S1	285
S2	547
S3	555

Before the electrochemical corrosion measurements, test specimens were cut from steel (iron) balls (the diameter of the balls was ~70 mm), and then successively grinded with grind paper with a fineness of 400 grit to 1000 grit. The specimens were washed with distilled water and dried. Until the beginning of the corrosion measurements, the specimens were kept in a desiccator.

A test solution (3% NaCl solution, pH 8.1) which simulates seawater was made using bi-distilled water and analytical grade NaCl. Natural seawater has a pH of 8.1 due to the presence of dissolved basic minerals, such as various carbonates. During the Industrial Revolution, due to the presence of acid rain, the pH value of seawater decreased from 8.2 to 8.1.

2.2. Linear polarization resistance (LPR)

The LPR method was used to determine the value of polarization resistance (R_p) of the tested samples in a corrosive environment (3% NaCl solution, pH 8.1). The R_p value is inversely proportional to the corrosion current density (j_{corr}), and the corrosion rate (v_{corr}). The steel in the solution was polarized in a narrow potential range (E = ± 10 mV) concerning the corrosion potential (E_{corr}), starting from the cathodic to the anodic potential values, and the corresponding current (j) was registered. The applied potential sweep rate was 0.5 mV s^{-1}. The polarization resistance was determined as the slope of the experimental curve E–j, at the corrosion potential. Based on the experimentally determined R_p value, the corrosion current density, and general corrosion rate of the samples were calculated.

2.3. Electrochemical impedance spectroscopy (EIS)

The EIS method also allows the determination of the value of the polarization resistance (R_p). A small amplitude alternating potential (± 10 mV vs. E_{corr}) was applied to the tested steel in the test solution. The range of applied frequencies (f) was from 100 000 Hz to 0.01 Hz. Based on the value of electrochemical impedance at very high and very low frequencies, the value of polarization resistance (R_p) was determined. The corrosion current density and the corrosion rate were calculated on the base measured R_p values.

The corrosion current density (j_{corr}) was calculated based on the value of the polarization resistance (R_p), using the Stern–Geary equation [31, 32]:

$$j_{corr} = B/R_p \quad (1)$$

Where

B is a constant that depends on the value of the anodic (b_a) and cathodic (b_c) Tafel slopes:

$$B = b_a \cdot b_c/(2.3 \cdot (b_a + b_c)) \quad (2)$$

Tafel slopes can be determined experimentally, by forming polarization Tafel diagrams, or their values can be taken from the literature [11]. For carbon steel in seawater, the value of the constant B is ~ 25 mV. Therefore, the corrosion current density (j_{corr}) is:

$$j_{corr} = 25\ mV/R_p \quad (3)$$

The corrosion rate of the tested samples (v_{corr} in mm yr^{-1}) was calculated using Faraday law, based on the obtained value of the corrosion current density (j_{corr} in µA cm^{-2}), in accordance with the ASTM G102 standard [32]:

$$v_{corr} = 0.01166 \cdot j_{corr} \quad (4)$$

2.4. Linear sweep voltammetry (LSV)

Tafel diagrams are obtained by this method. The steel in the 3% NaCl solution was polarized in the potential range E = ± 0.250 V in relation to the corrosion potential (E_{corr}) and the corresponding value of the current density (j) was registered. The applied potential sweep rate was 0.5 mV s^{-1}. From the obtained polarisation diagrams (E–log j), the corrosion current density (j_{corr}) was determined by extrapolation of the Tafel region of the anodic polarization curve to the corrosion potential (E_{corr}).

All electrochemical tests were performed using a potentiostat/galvanostat BioLogic SP-200, in a 3% NaCl solution (pH 8.1). Tests were performed at room temperature, in the presence of atmospheric oxygen.

The tests were carried out in a classical three-electrode electrochemical cell with a saturated calomel electrode (SCE) as a reference electrode and a Pt grid as an auxiliary electrode. The working electrode was the tested specimens, with a working surface of 1 cm^2. Before starting the electrochemical measurements, each specimen was held in the test solution for a certain time at the open circuit potential (up to 1 h), until a relatively stable corrosion potential (E_{corr}) was established.

2.5. Optical microscopy

The morphology of the surface of tested samples after polarization measurements (linear sweep voltammetry (LSV) method) was analysed by applying optical microscopy Carl Zeiss-Jena, JENAPOL-U polarizing microscope for reflected and transmitted light. The microscope was outfitted with a "Carl Zeiss AxioVision SE64 Rel. 4.9.1." software package, a "Multiphase" module, and an "Axiocam 105 color" camera.

3. RESULTS AND DISCUSSION

3.1. Corrosion potential (E_{corr})

The tested specimens were kept in a 3% NaCl solution at an open circuit potential until a relatively stable corrosion potential was established. In the initial period of exposure, there was a relatively rapid decrease in the value of the corrosion potential (Figure 1).

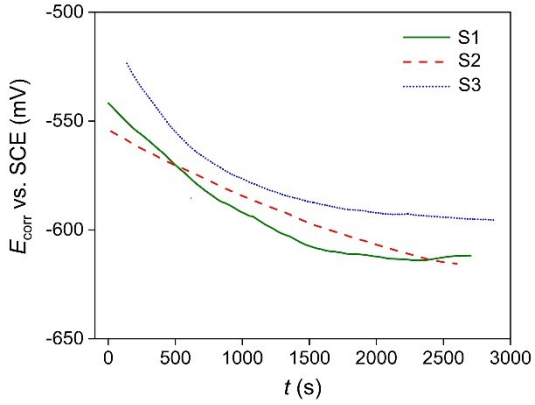

Figure 1. Time dependence of the corrosion potential for samples S1, S2, and S3

Slika 1. Zavisnost korozionog potencijala od vremena za uzorke S1, S2 i S3

The decrease in the value of the corrosion potential of the tested samples can be explained by the gradual activation of the steel surface due to the action of chloride ions.

The value of the corrosion potential established at the end of the test period (> 2500 s) for S1 and S2 is approximately the same and amounts to ~ -615 mV, while in the case of S3, the value of the corrosion potential was more positive and amounted to ~ -585 mV. The more positive value of the corrosion potential for S3 is a consequence of the higher chromium content in that sample (~ 15 wt.% Cr), i.e. the presence of a passive film on its surface.

3.2. LPR measurements

The linear polarization resistance (LPR) method is a widely used electrochemical method for determining the corrosion rate of steel and other metals and alloys as well as protective systems (corrosion inhibitors and organic and inorganic coatings). Corrosion monitors that are usually used to determine the value of general corrosion and the tendency to pitting corrosion in an on-field environment are based on the LPR method.

Figure 2a-c shows the polarization diagrams *E-j* obtained by the LPR measurements. The slope of the curve ($\Delta E/\Delta j$) on the corrosion potential (E_{corr}) corresponds to the value of the polarization resistance (R_p). The value of polarization resistance for S1 is the lowest and the highest for S3 (Figure 2 and Table 3). The highest value R_p for S3 as can be expected is a consequence of a higher amount of chromium (~15 wt.% Cr).

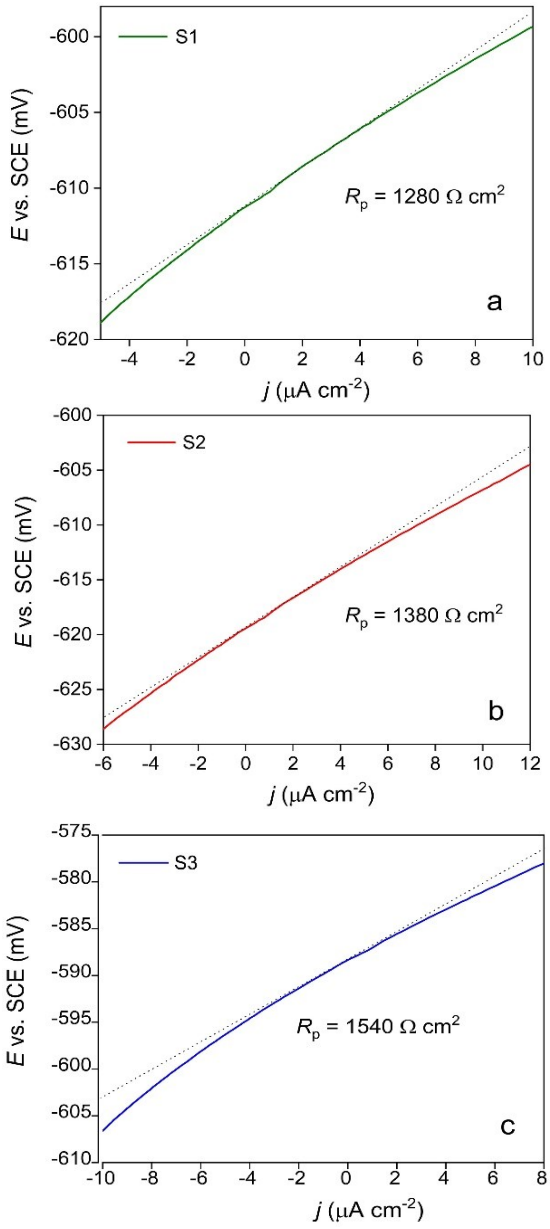

Figure 2. LPR diagrams for samples: a) S1, b) S2, and c) S3

Slika 2. LPR dijagrami za uzorke: a) S1, b) S2 i c) S3

Based on the experimental values for the polarization resistance (R_p), the corrosion current density (j_{corr}) was calculated using Equation (3). The corrosion current density is directly proportional to the corrosion rate (v_{corr}). The corrosion rate was calculated using Equation (4).

3.3. EIS measurements

Electrochemical impedance spectroscopy (EIS) has been successfully applied to the study of corrosion systems during the previous few decades and today it is considered a reliable and precise method for studying the corrosion process and determining the corrosion rate. An important advantage of this method is the possibility of applying signals of small amplitudes, which negligiblely disturb the tested metal surface.

Figure 3 summarizes the Nyquist diagrams obtained by the EIS measurements for S1, S2 and S3 in 3% NaCl solution (pH 8.1). The INSET of Figure 3 shows the Equivalent Electrical Circuit (EEC) which can be applied for the analyses of the corrosion system (tested samples/NaCl solution). On the EEC the polarization resistance is presented by R_p, the Constant Phase Element is presented by CPE, and the electrolyte resistance by R_e. The Constant Phase Element (CPE) was introduced instead of the capacity of the double layer on the surface of the tested steels (C_{dl}). The CPE contains all the microstructural inhomogeneities of the examined steel surface, such as surface roughness and segregation of alloying elements [16].

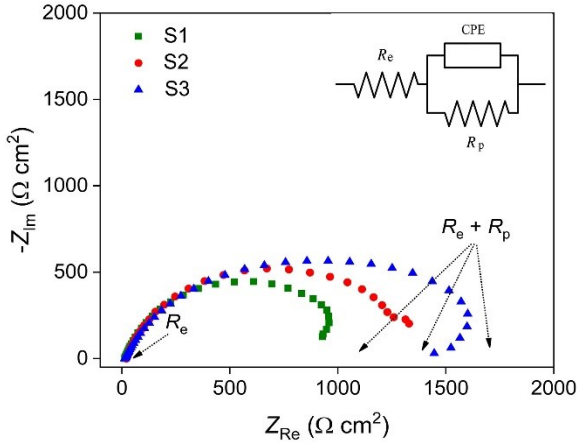

Figure 3. Nyquist diagrams obtained by the EIS method for S1, S2, and S3. INSET: Equivalent Electrical Circuit (EEC)

Slika 3. Najkvistovi dijagrami dobijeni primenom EIS metode za čelik 1, čelik 2 i čelik 3. UMETNUTO: Ekvivalentno Električno Kolo (EEC)

The larger the diameter of the semicircle on the Nyquist diagrams (Figure 3), the higher the value of the polarization resistance (R_p), that is, the greater the steel resistance to general corrosion. In the case of stainless iron (S3), the largest semicircle diameter was obtained on the Nyquist diagram.

The Nyquist plot gives the dependence of the real impedance component (Z_{Re}) and the imaginary impedance component (Z_{Im}) in linear coordinates. The electrolyte resistance value is R_e ~ 10 Ω cm^2 (Figure 3 and Figure 4a). On the right side of the Nyquist diagram, the total resistance $R_e + R_p$ is shown. Therefore, the values of polarization resistances (R_p) are ~ 1100 Ω cm^2, ~ 1400 Ω cm^2, and ~1700 Ω cm^2, for S1, S2 and S3 respectively. The values of the corrosion current density were calculated using Equation (3), and corrosion rate values using Equation (4).

Figure 4a shows a summary of the Bode modulus diagrams obtained using the EIS method for the tested samples. The Bode modulus diagram represents the dependence of the impedance modulus (Z_{Mod}) on the applied frequency (f) in logarithmic coordinates.

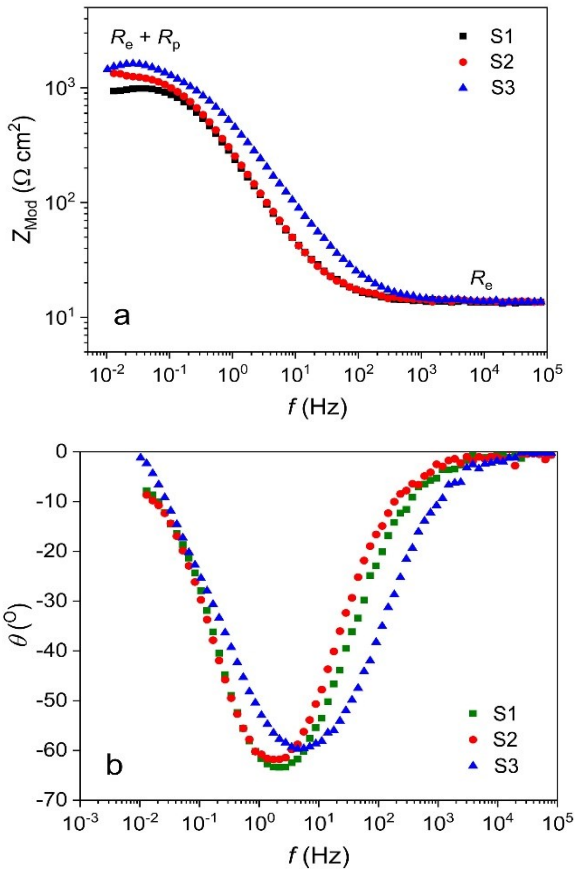

Figure 4. Bode diagrams obtained using the EIS method a) Bode modulus, and b) Bode phase diagrams, for samples S1, S2, and S3

Slika 4. Bodeovi dijagrami dobijeni primenom EIS metode a) Bode moduo, i b) Bode fazni dijagram, za uzorke: S1, S2 i S3

The Bode modulus diagrams at relatively high frequencies (from 10^3 to 10^5 Hz) are related to the electrolyte resistance (R_e), which remains constant during the measurements (R_e ~ 10 Ω cm^2). For intermediate frequency values (10^3 to 10^{-1} Hz) the Bode modulus curves for S1 and S2 overlap, while the curve for S3 (stainless cast iron) is shifted towards higher impedance values. The shift of the Bode modulus curve towards higher impedance values is also a consequence of the higher chromium content (~15 wt.% Cr) and the presence of a passive layer on the surface of that stainless iron. The plateau at low frequencies corresponds to the value of polarization resistance (R_e + R_p).

Figure 4b shows a summary of the Bode phase diagrams for the tested samples. The Bode phase diagram shows the dependence of the phase angle (Θ) on the logarithm of the frequency (f). The frequency at which some corrosion reaction takes place can be determined. Also, deeper interpretations of corrosion processes on the metal surface can be performed. The shape of the Bode phase diagrams for the tested samples in 3% NaCl solution (Figure 4b) indicates the existence of only one time constant, i.e. existence of one peak on the phase diagrams. The corresponding Equivalent Electrical Circuit is shown in the INSET of Figure 3.

Table 3. Summarized results of LPR and EIS methods for the tested samples

Tabela 3. Sumirani rezultati LPR i EIS metoda za ispitane čelike

	LPR		EIS	
	R_p (Ω cm^2)	v_{corr} (mm yr^{-1})	R_p (Ω cm^2)	v_{corr} (mm yr^{-1})
S1	1280	0.23	1100	0.26
S2	1380	0.21	1400	0.21
S3	1540	0.19	1700	0.17

Table 3 lists the values of polarization resistance (R_p), measured using the LPR and EIS method, as well as the values of the corrosion rate (v_{corr}), calculated using equation (4).

3.4. Linear sweep voltammetry (LSV)

Applying the LSV method, the value of the corrosion current density (j_{corr}) was determined. The value of the corrosion rate (v_{corr}) can be directly calculated by applying the Faraday law, based on corrosion current density. The disadvantage of the LSV method is relatively large polarizations (usually ± 0.25 V), and as a result, there is a significant perturbance in the metal surface (the tested samples), so the LSV method is considered a destructive method.

Summarised Tafel diagrams (obtained in a 3% NaCl solution, pH 8.1) for the tested samples are shown in Figure 5. The corrosion current density (j_{corr}) was determined by extrapolation of the anodic Tafel regions on the corrosion potential (E_{corr}). The corrosion current density value j_{corr} = 38 μA cm^{-2}, 27 μA cm^{-2}, and 23 μA cm^{-2} for S1, S2, and S3, respectively. Based on the corrosion current density, the corrosion rate (v_{corr}) can be calculated, provided that the steel corrodes uniformly.

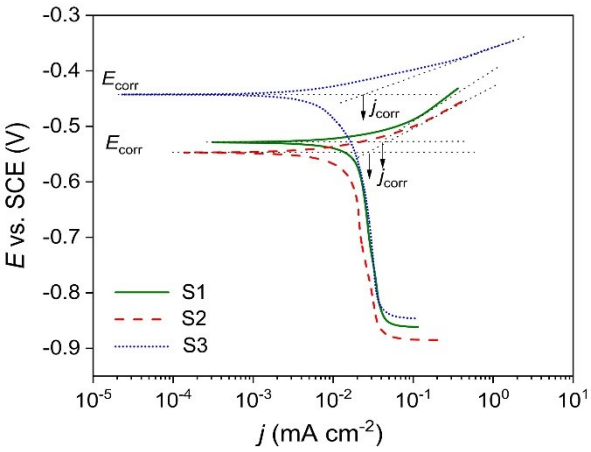

Figure 5. Tafel diagrams for samples: S1, S2, and S3, in a 3 %NaCl solution (pH 8.1).

Slika 5. Tafelovi dijagrami za uzorke: S1, S2 i S3, dobijeni u rastvoru 3% NaCl (pH 8,1).

3.5. Appearance of the surface of the samples after polarization measurements

Figure 6 shows the appearance of the steel surface after performing linear sweep voltammetry (LSV) measurements. The application of this electrochemical method involves relatively high anodic polarizations (± 0.25 V) so that intense dissolution of the steel surface can occur during testing. Dissolution of the steel surface is incomparably less when tests are performed using the LPR or EIS method.

Localized corrosion (pitting corrosion) occurred in all tested samples, after anodic polarization in a 3% NaCl solution applying the LSV method. In the case of S1 as casted steel, the pits are significantly larger than in the case of S2 (rolled steel). In the case of stainless iron (cast S3), the formed pits are of very large dimensions (several hundred micrometres) and have the form of pits with a so-called lacy cover (Figure 6). The passive film on the surface of S3 (stainless cast iron because this steel contains 15.14 wt.% Cr and 2.56 wt.% C), in a solution containing a high concentration of chloride ions (3% NaCl solution), is not stable enough under anodic polarizations, so pits are formed. Pits are formed at favourable places in the microstructure of the tested stainless steel, such as the boundaries

of MnS inclusions with the surrounding matrix, as well as on the other inhomogeneities, as liquations on the steel surface [33].

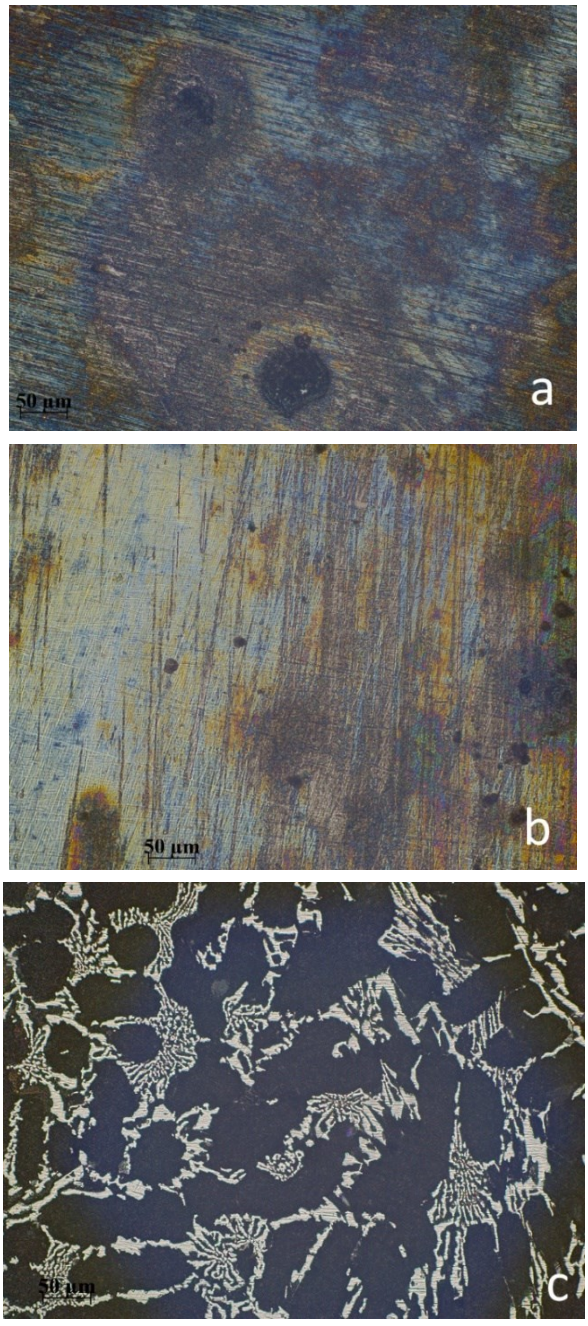

Figure 6. Appearance of samples surface after polarization measurements a) S1, b) S2, and c) S3

Slika 6. Izgled površine uzoraka nakon polarizacionih merenja: a) S1, b) S2 i c) S3

During the polarization measurements (LSV method), localized forms of corrosion (pitting corrosion) occurred, so the obtained values of the corrosion current density (j_{corr}) cannot be used to calculate the general corrosion rate (v_{corr}) of the tested samples.

4. CONCLUSION

The corrosion behaviour of different types of steel and iron that can be potentially used for making steel balls in copper and other ore grinding mills in the presence of seawater was analysed. Two steels are low-alloy carbon steels (S1 as cast, and S2 as rolled), while the third (S3) is stainless cast iron, containing ~15.14 wt.% Cr and 2.56 wt.% C. Three electrochemical methods were used to determine the corrosion rate: the linear polarization resistance (LPR) method, the electrochemical impedance spectroscopy (EIS) method and the linear sweep voltammetry (LSV) method.

Based on the results of the LPR and EIS methods (as non-destructive methods), the value of polarization resistance (R_p) was determined, and then, using the Stern-Gary equation and Faraday law, the general corrosion rate (v_{corr}) of the samples was calculated.

The obtained values for the general corrosion rate (v_{corr}) can be used to predict the service life of the steel balls in the exploitation conditions (seawater).

Using the linear sweep voltammetry (LSV) method, the corrosion current density (j_{corr}) was determined, which can be used to directly calculate the general corrosion rate (v_{corr}), using Faraday law. However, during the linear sweep voltammetry testing at relatively high anodic polarizations, localized forms of corrosion occur, such as pitting corrosion. Therefore, this method is not suitable for calculating the general corrosion rate.

Characteristic microphotographs (which show the presence of localized forms of corrosion, such as pitting corrosion) were obtained for the tested steels after performing the linear sweep voltammetry (LSV) measurements.

Acknowledgements

This study was financially supported by the Ministry of Science, Technological Development and Innovation of the Republic of Serbia (Grant No. 451-03-47/2023-01/200026 and 451-03-47/2023--01/200135).

5. LITERATURE

[1] Standard Guide for Determining Synergism Between Wear and Corrosion: ASTM G119-2009. https://doi.org/10.1520/G0119-09.

[2] E.McCafferty (2010) Introduction to Corrosion Science, Springer, New York

[3] L.Yang (2021) Techniques for corrosion monitoring, Cambridge, England

[4] R.Baboian (2005) ASTM Corrosion Tests and Standards: Application and Interpretation, second ed., ASTM International

[5] Standard Guide for Conducting Corrosion Tests in Field Applications, ASTM G4-2014. https://doi.org/10.1520/G0004-01R14.

[6] Standard Practice for Conducting Atmospheric Corrosion Tests on Metals, ASTM G50-2015. https://doi.org/10.1520/G0050-10R15.

[7] K.Chiang, T.Mintz (2021) Gravimetric techniques, in Techniques for corrosion monitoring,Edited by L.Yang, Cambridge, England, p.239-254.

[8] Standard Guide for Laboratory Immersion Corrosion Testing of Metals, ASTM G31-2012. https://doi.org/10.1520/G0031-12A.

[9] Standard Practice for Exposure of Metals and Alloys by Alternate Immersion in Neutral 3.5 % Sodium Chloride Solution, ASTM G44-2013. https://doi.org/10.1520/G0044-99R13.

[10] Corrosion tests in artificial atmospheres-Salt spray tests: ISO 9227-2017.

[11] F.Mansfeld (1976) The Polarisation Resistance Technique for Measuring Corrosion Currents, in Advances in Corrosion Science and Technology, Vol. 6, Edited M.G.Fontana and R.W.Staehle, Plenum Press, New York and London, p.163-262.

[12] J.R.Scully (2000) Polarization resistance methods for determination of instantaneous corrosion rates, Corrosion, 56(2), 199-218. https://doi.org/10.5006/1.3280536

[13] Standard Test Method for Conducting Potentiodynamic Polarization Resistance Measurements, ASTM G59-2014. https://doi.org/10.1520/G0059-97R14.

[14] R.G.Kelly, J.R.Scully, D.W.Shoesmith, R.G. Buchheit (2002) Electrochemical Techniques in Corrosion Science and Engineering, Marcell Dekker, New York

[15] M.E.Orazem, B.Tribollet (2017) Electrochemical Impedance Spectroscopy, John Wiley &Sons, New Jersey

[16] R.Srinivasan, F.Fasmin (2021) An Introduction to Electrochemical Impedance Spectroscopy, Taylor & Francis Group, New York

[17] F.Mansfeld (2006) Electrochemical Impedance Spectroscopy, in Analytical Methods in Corrosion Science and Engineering, Edited By P. Marcus and F. Mansfeld, Taylor & Francis Group, p.463-505.

[18] Standard Practice for Verification of Algorithm and Equipment for Electrochemical Impedance Measurements, ASTM G106-2015. https://doi.org/10.1520/G0106-89R15.

[19] S. Papavinasam (2021) Electrochemical polarization techniques for corrosion monitoring, Techniques for corrosion monitoring, Edited by L.Yang, Cambridge, England, p.45-75.

[20] E. Heitz (2006) DC Electrochemical Methods, in Analytical Methods, in Corrosion Sciencen and Engineering, Edited By P.Marcus and F.Mansfeld, Taylor & Francis Group, p.435-462.

[21] F. Mansfeld (2003) Electrochemical methods of corrosion testing, in: ASM Handbook, Vol. 13A, Corrosion: Fundamentals, Testing and Protection, ASM International, p.446-462.

[22] E.E.Stansbury, R.A. Buchanan (2000) Fundamentals of Electrochemical Corrosion, ASM International, Materials Park, Ohio

[23] E. Bardal (2004) Corrosion and protection, Springer, London, Berlin, New York

[24] Standard Test Method for Corrosion Potentials of Uncoated Reinforcing Steel in Concrete, ASTM-C876-2009. https://doi.org/10.1520/C0876-09.

[25] Standard Guide for Development and Use of a Galvanic Series for Predicting Galvanic Corrosion Performance, ASTM G82-2014. https://doi.org/10.1520/ G0082-98R14.

[26] Standard Test Method for Measurement of Corrosion Potentials of Aluminum Alloys1ASTM G69-2012. https://doi.org/10.1520/G0069-12.

[27] Test Method for Standard Test Method for Evaluating the Potential for Galvanic Corrosion for Medical Implants, ASTM F3044-2014. https://doi.org/ 10.1520/F3044-14.

[28] Standard Guide for Electrode Potential Measurement, ASTM G215-2016.https://doi.org/10.1520/G0215-16.

[29] B.V.Jegdić, B.M.Bobić, M.Bošnjakov (2017) Relationship between corrosion potential and different corrosion forms of metals, alloys and theirs welded joints - part I, Welding and Welded Structures, 62(2), 65-76. https://doi.org/10.5937/zzk1702065J

[30] B.V.Jegdić, B.M. Bobić, B.M. Radojković (2018) Relationship between corrosion potential and different corrosion forms of metals, alloys and theirs welded joints - part II, Welding and Welded Structures, 63(2), 53-63. https://doi.org/10.5937/zzk1802053J

[31] M.Stern, A.L.Geary (1957) Electrochemical polarization. I. A theoretical analysis of the shape of the polarization curves, Journal of The Electrochemical Society, 104(1), 56-63. https://doi.org/10.1149/1.2428473

[32] Standard Practice for Calculation of Corrosion Rates and Related Information from Electrochemical Measurements, ASTM G102-2015.

[33] B.Radojković, B.Jegdić, J.Pejić, D.Marunkić, A.Simović, S.Eraković-Pantović (2023) Influence of nitrogen content on the pit formation and pit propagation in the welded joints of X5CrNi18-10 stainless steel, Materiales Corrosion (accepted). https://doi.org/10.1002/maco.202314120

IZVOD

KOROZIONO PONAŠANJE ČELIČNIH KUGLICA ZA MLEVENJE SA VISOKIM I NISKIM SADRŽAJEM HROMA U RASTVORU HLORIDA

Ispitivano je koroziono ponašanje tri vrste legura (dva nisko-legirana ugljenična čelika i jedan uzorak je nerđajuće gvožđe sa ~15% Cr), u rastvoru koji simulira morsku vodu (3% rastvor NaCl, pH 8,1). Ispitani uzorci se koriste za proizvodnju čeličnih kugli koje se primenjuju u mlinovima za mlevenje bakarnih i drugih ruda. Koroziona ispitivanja su izvedena primenom tri elektrohemijske metode, na sobnoj temperaturi u prisustvu atmosferskog kiseonika. Korišćene su metoda linearne polarizacione otpornosti (LPR), metoda elektrohemijske impedansne spektroskopije (EIS) i metoda linearne promene potencijala (LSV). Na osnovu merenja LPR i EIS metodama (kao nerazarajućim metodama), određena je vrednost polarizacione otpornosti (R_p), a zatim je izračunata vrednost brzine opšte korozije (v_{kor}) ispitivanih uzoraka. Dobijene vrednosti za brzinu opšte korozije se mogu koristiti za izračunavanje veka trajanja kugli u uslovima eksploatacije (morska voda). Izgled površine ispitivanih uzoraka nakon izvođenja LSV metode pokazao je prisustvo lokalizovane korozije (formirane su jamice, pitovi) na ispitivanim uzorcima, posebno na nerđajućem gvožđu. Prema tome, LSV metoda nije pogodna za određivanje brzine opšte korozije ispitivanih čelika u morskoj vodi. Ovaj oblik korozije javlja se pri visokim anodnim polarizacijama tokom izvođenja LSV merenja.

Ključne reči: *Nisko-legirani čelik, nerđajuće gvožđe, elektrohemijska korozija, LPR, EIS, LSV, morska voda*

Naučni rad

Rad primljen: 14.09.2023.

Rad prihvaćen: 12.10.2023.

Rad je dostupan na sajtu: www.idk.org.rs/casopis

Vijayalakshmi Arumugam, Sowmiya Chandrasekar*

Research department of physics, Sri Vasavi college Erode, Tamil Nadu, India

Scientific paper
ISSN 0351-9465, E-ISSN 2466-2585
https://doi.org/10.62638/ZasMat1000

Zastita Materijala 65 (1)
54 - 62 (2024)

Reinforce the surface properties of domestic garbage activated carbon by low temperature plasma accustomed in energy storage applications

ABSTRACT

Since activated carbon is a highly porous material with a sizable internal surface area, it is simple to adsorb a wide range of substances when used in energy storage devices, sewage treatment, water purification, catalyst, food processing and other applications. This work focuses on the viability of using mixed fruit peels as a precursor for the carbonization process with physical activation to produce activated carbon. The Phase confirmation was examined using X-ray diffraction (XRD). Fourier transform infrared spectrometer (FTIR) concludes the functional groups present in mixed fruit peels activated carbon. Field emission scanning electron microscopy (FESEM) was used to analyze the morphological makeup and textural traits of the activated carbon that was produced. Energy Dispersive X-Ray Analysis (EDX) shows the elemental composition of nano powdered carbon. Raman spectroscopy confirms the presence of graphene that appears at 1580cm^{-1}. Electrochemical Impedance Spectroscopy (EIS) and Nyquist plot in order to evaluate the conductivity performance over the frequency range of 1μHz to 10 kHz, measurements were used.

Carbon yield analysis were conducted and analyzed. Wettability of the mixed fruit peels were examined using contact angle. The Mixed Fruit peels activated carbon were subjected to low temperature plasma to increase its surface properties, The outcomes were evaluated, and the charge transfer resistance and the polarization resistance for air plasma treatment is 1.43 and 0.2 ohms. Hydrophilic nature is occurred when treated with air plasma. According to these findings, air plasma treatment of mixed fruit peel activated carbon improves its surface characteristics, making it suitable for electrode in energy storage applications.

Keywords: *Mixed fruit peels, physical activation, low temperature plasma, surface modification, Nano powder*

1. INTRODUCTION

The ever-growing demand for sustainable solutions has led to an increasing focus on the utilization of natural resources and waste materials. In this pursuit, researchers and innovators have turned their attention to the vast potential hidden within fruit peels, recognizing them as a rich source of valuable compounds and fibers. Among these advancements, the emergence of mixed fruit peels activated carbon stands out as a promising development that not only addresses the issue of waste management but also offers numerous applications in diverse fields [1,2]. This revolutionary material, derived from a combination of discarded fruit peels and advanced activation techniques, has garnered attention as an eco-friendly alternative to conventional activated carbon [3]. With its exceptional adsorption properties, mixed fruit peels activated carbon has the potential to revolutionize industries such as water purification, energy storage, and environmental remediation, contributing to a greener and more sustainable future [4]. Fruit peels, until recently, were largely considered as waste products resulting from the consumption of fruits. Fruit peels, consisting of a complex matrix of cellulose, hemicellulose, lignin, and various bioactive compounds, possess unique chemical and physical properties that make them an attractive raw material for activated carbon

Corresponding author: Vijayalakshmi Arumugam
E-mail: kavijayalakshmi@yahoo.com
Paper received: 28. 09. 2023.
Paper accepted: 20. 10. 2023.
Paper is available on the website: www.idk.org.rs/journal

production[5]. By diverting these peels from landfills and transforming them into activated carbon, not only reduce waste accumulation but also contribute to a circular economy by reusing a valuable resource that would otherwise go to waste. Due to its extraordinarily high surface area and purity, which activated carbons were directly related to the performance in the preferred electrode material in capacitors, batteries, and a variety of advanced batteries [6,7].

Plasma surface modification: The objective of Plasma surface treatment is to enhance the surface characteristics without compromising the bulk qualities, which is typically challenging to achieve through conventional methods[8]. Plasma treatment, as depicted in (Fig. 1), generates a greater number of free radicals, ions, and electrons, making it a promising approach for improving energy storage systems. The interactions between plasma species and the surface facilitate various energy and matter exchange processes, offering a wide range of options for modifying the surface.

Consequently, this technique enhances the properties of different materials and expands their applications in electrochemical systems[9]. Plasma modification serves multiple purposes, including the creation of functional groups that interact with other groups, alteration of surface free energy, and prevention of corrosion [10]. These modifications result in improved resistance, changes in interface nature and morphology, impurity removal, and the formation of cross-linking between molecules. The adhesion, bonding, and chemical inertness are also enhanced through these processes [11].

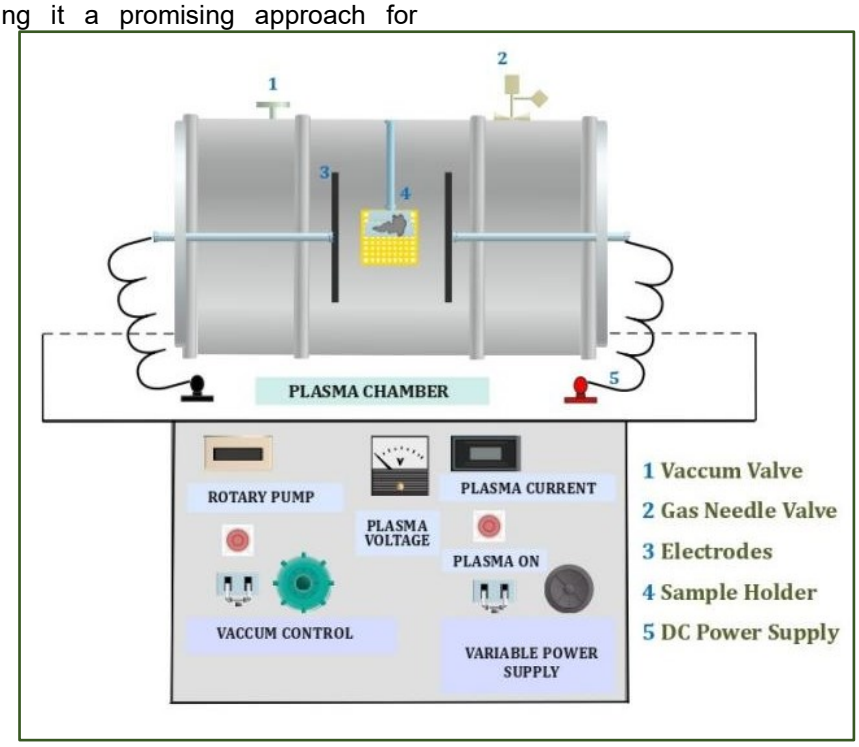

Figure 1. Schematic diagram of plasma chamber

Slika 1. Šematski dijagram plazma komore

Porous electrodes have a substantially higher surface area than conventional electrodes in capacitors, activated carbon has proven excellent properties and can be used in energy storage devices allows them to store much more energy. Activated carbon also enhances the adsorption properties [7,12,13]. To achieve high energy density for such devices, high capacitance materials must be used. In order to boost the energy density of these devices without reducing their power capacity, research efforts are currently concentrated upon the development of electrode materials and electrolytes. The use of electroactive materials in carbon-based electrodes is also gaining popularity as a means to boost the amount of energy that can be stored in such a device. Low temperature plasma treatment improves the properties and surface of the carbon material without altering its fundamental nature.

2. MATERIALS AND METHODS.

The garbage from mixed fruit peels (MFP) is created by physical processes. The fruit peels from apple, pomegranate, papaya, mango and

muskmelon were obtained from a nearby local fruit market. The peels were cleaned with tap water first, then with distilled water. They were then set for drying in direct sunlight, and after seven days, the dried peels were stored for synthesis. Carbonization and activation are the two processes that was used in the processing of synthesis. The dried peels were carbonized in an air muffle furnace (KEMI-KMF-1S) for two hours at 300°C, then well ground and maintained for 30 minutes at 400°C for activation in an air muffle furnace. Obtained mixed fruit peel activated carbon was labeled as MFPAC and it was subject to characterization.

In this study, a DC glow discharge cold plasma, which is suitable for heat-sensitive materials, was used. A stainless-steel chamber measuring 30 cm in diameter and 50 cm in length serves as the DC glow discharge plasma reactor for the experiment. Two aluminum electrodes were placed within the chamber, six centimeters apart and symmetrically arranged perpendicular to the axis. A vacuum pump was used to initially suction the chamber down to a pressure of 0.03 mbar. By modulating the gas input using a controlled needle valve and monitoring it with a Pirani gauge, the necessary low pressure was maintained.

Figure 2. Synthesis of Mixed fruit peel activated carbon

Slika 2. Sinteza mešovitog aktivnog uglja od kore voća

X Ray diffraction – XRD (XPERT-PRO with CuK radiation) is used to analyze the nature of the sample and the particle size. Functional groups were identified by Fourier-transform infrared spectroscopy - FTIR (SHIMADZU FTIR-8400S). Field emission scanning electron microscopes - FE-SEM (VEGA3, TESCAN (Czech Republic)) analyze the morphological character of the activated carbon and the porosity of the material. Energy-dispersive X-ray spectroscopy - EDX (BURKER Nano, GmbH, D-12489(Germany)) confirms the presence of element in the activated carbon. Raman analysis (WiTec alpha 300, Germany) shows the existence of two bands (D and G band). Electrochemical Impedance Spectroscopy - EIS confirms, resistivity of the material. Hydrophobic and hydrophilic nature is identified by wetting angle.

3. RESULTS AND DISCUSSION

This section presents the experimental findings about the elements, functional groups, functional morphology, resistivity and nature of the activated mixed fruit peels.

In order to calculate the carbon yield fifteen grams of dried peels were carbonized and activated. A yield of 82% was achieved. Using (Eq. 1), the carbon yield percentage is calculated.

$$Yield\ (in\ \%) = (\ Quantity\ of\ activated\ carbon / Quantity\ of\ raw\ material) * 100 \quad (1)$$

3.1. XRD Analysis

In the Figure 3 XRD spectrum of untreated MFP, air plasma MFP and oxygen plasma MFP were presented. A few sharp peaks are visible in the XRD profile in the range of 10° - 80° at an angle 2θ. In this investigation, crystalline carbon makes up the majority of the product. The pyrolysis reaction was finished as a result[14] The peak at 2θ value was 28.3°, which is evidence that this could be the carbon structure of graphite[15]. Its crystalline nature is represented by the peak 2θ range at 40.41°[16]. MFPAC that has been plasma-treated gains intensity without altering its nature or structure. (Fig. 3) illustrates that MFPAC treated with air plasma has a higher intensity than MFPAC treated with oxygen plasma[17]. The grain size of the air plasma treated MFPAC is 26.75nm.

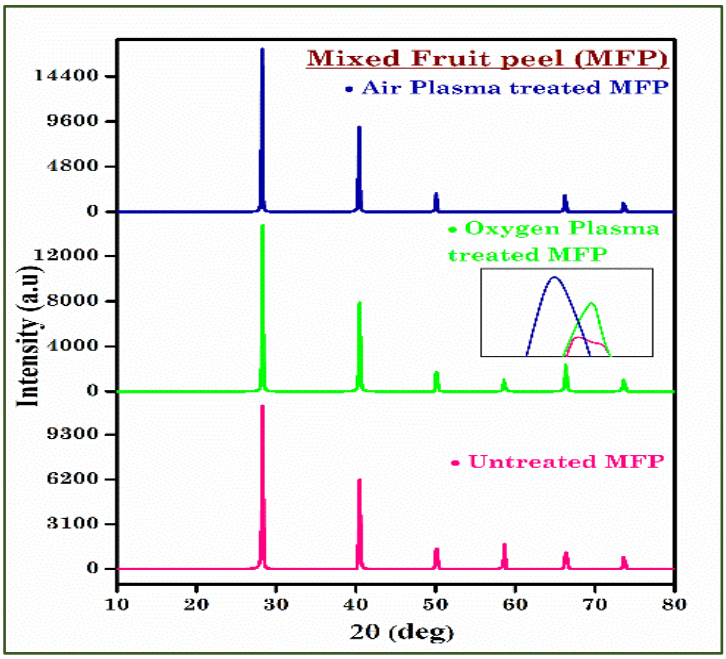

Figure 3. XRD of Untreated, Air plasma treated and oxygen plasma treated MFPAC

Slika 3. XRD netretiranog, vazdušnom plazmom tretiranog i MFPAC tretiranog plazmom kiseonikom

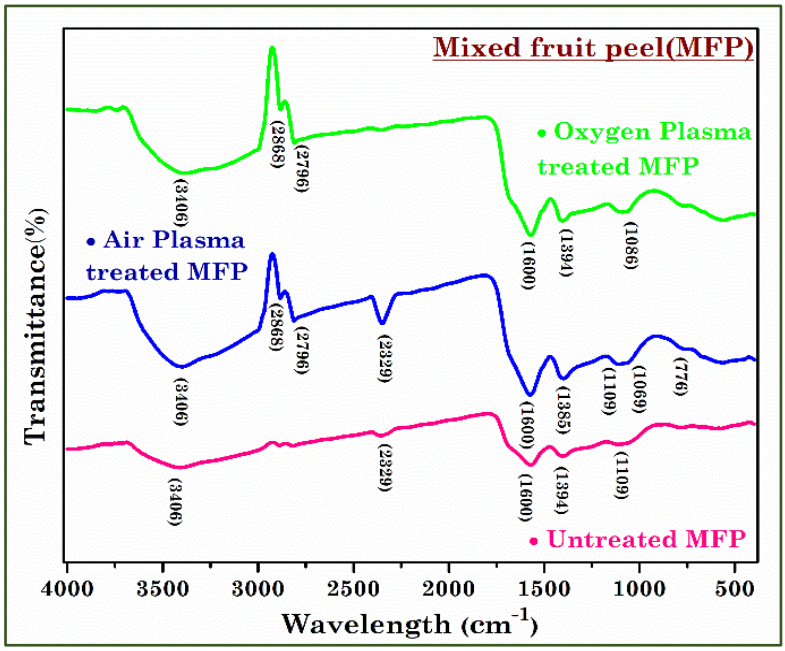

Figure 4. FTIR of Untreated, Air plasma treated and oxygen plasma treated MFPAC

Slika 4. FTIR netretiranog, MFPAC tretiranog vazdušnom plazmom i kiseoničkom plazmom

3.2. FTIR evaluation

By using FTIR analysis, functional groups of obtained materials can be observed. The results are presented in (Fig. 4) and cover the 400 cm^{-1} to 4000 cm^{-1} range. Band at 1109 cm^{-1} in the untreated MFPAC spectrum could be assigned to the C-O group, while band at 1394 cm^{-1} indicate C-H bending. Bands between 1600 cm^{-1} and 2344 cm^{-1}, could be assigned to C=C stretches due to presence of aromatic rings. The band at 3406 cm^{-1} indicates the function group O-H. The emergence of a new functional group follows the plasma treatment that increases wettability. At 776 cm^{-1} and 2796 cm^{-1}, the C-H group's peaks were found. The C-O group might have produced the peak ranges at 1069 cm^{-1} and 1109 cm^{-1}. Moreover, the aromatic ring bond has C=C stretch that varies between 1385 cm^{-1}, 1600 cm^{-1}, and 2344 cm^{-1}[18], while the, bend at 2869 cm^{-1} suggest C-H bending [19,20]. The band at 3406 cm^{-1} serve as a representation of the function group O-H [21].Around 2329 cm^{-1}, two different bands that represent the carboxylic group that can be found in the O-H band can be seen [22]. According to the results, activated carbon that has been treated with air plasma contains hydroxylic and carbonyl functional groups.

3.3. SEM Analysis

The porous structure of the materials can be seen in (Fig.5), together with morphological study of the MFPAC. The activated carbon that has undergone plasma treatment demonstrates that it has more porous structure [17], [23,24]. MFPAC that has been air plasma treated is quite porous than untreated and oxygen plasma treated activated carbon, which will lead to increase in surface area. EDX confirms the presence of oxygen and carbon in all EDX spectra.

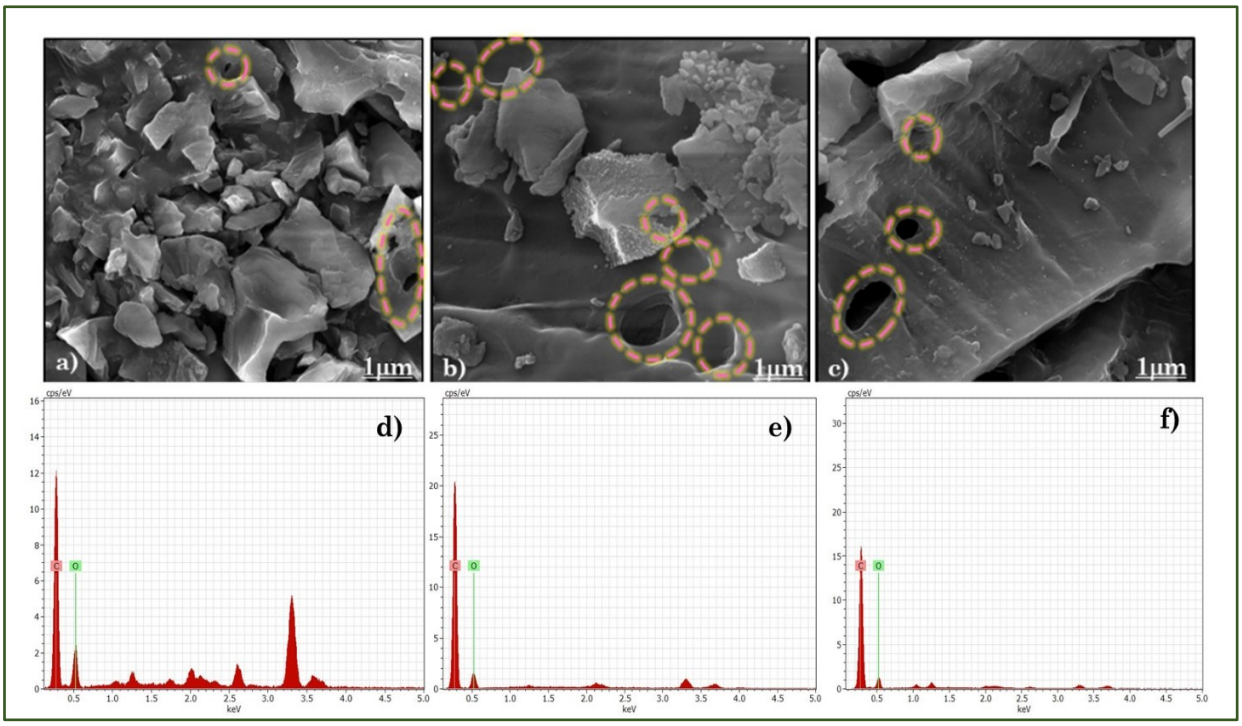

Figure 5. FE-SEM of a) Untreated, b) Air plasma treated, c) oxygen plasma treated MFPAC. d) EDX of Untreated, e) Air plasma treated, f) oxygen plasma treated MFPAC

Slika 5. FE-SEM od a) neobrađenog, b) tretiranog vazdušnom plazmom, c) MFPAC tretiranog kiseoničkom plazmom. d) EDX neobrađenog, e) tretiranog vazdušnom plazmom, f) MFPAC tretiranog kiseoničkom plazmom

3.4. Raman Spectroscopy

Both untreated and plasma-treated MFPAC were analyzed using the Raman spectroscopy, and the obtained spectra are presented in Fig. 6. Two bands are dominant: D-Band, at 1394cm^{-1} and the G-Band, at 1512cm^{-1}. The disordered carbon structure is linked to the D-Band. In contrast, the G-Band is connected to the graphitic or ordered lattice of carbon. The sp^3 hybridized disordered carbon phase appears by the D-band, whereas the sp^2 hybridized graphitic carbon phase is represented by the G-band. The defect with the sample's sp^2 carbon network, which may exist in either a C=C aromatic structure [24].

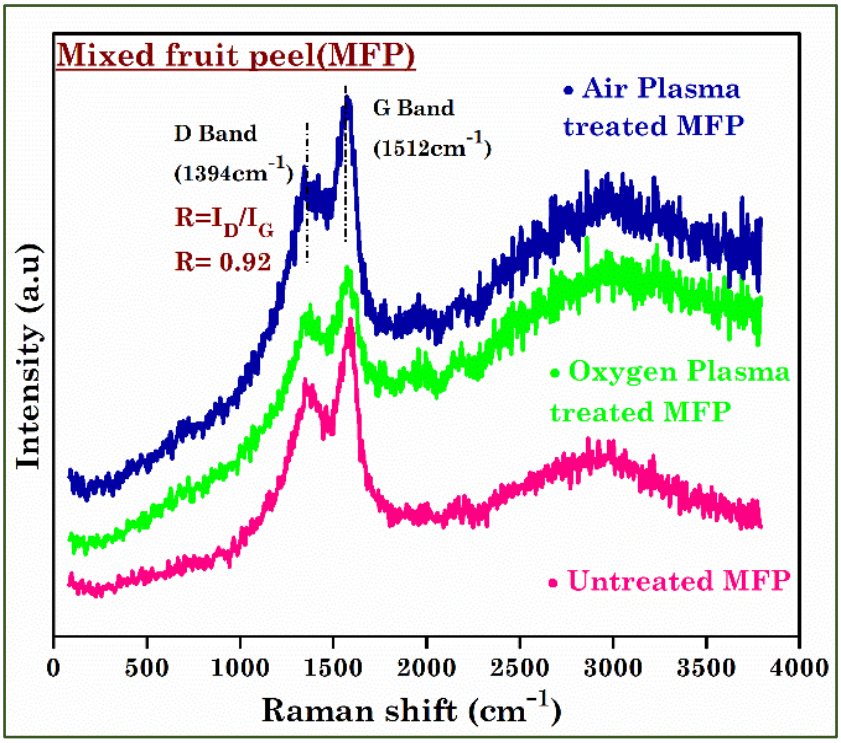

Figure 6. Raman spectra of Untreated, Air plasma treated and oxygen plasma treated MFPAC

Slika 6. Ramanski spektri netretiranog, obrađenog vazdušnom plazmom i MFPAC tretiranog plazmom kiseonikom

The MFPAC was subjected to the plasma treatment which result in the increases in the intensity which evidently shows by the intensity ratio (I_D/I_G)[25]. The Raman spectra characteristics that it has the amorphous nature with the intensity ratio of I_D/I_G for the untreated MFPAC is 0.82 and for Oxygen plasma treated MFPAC is 0.87, then for Air plasma treated MFPAC is 0.92. (Fig. 6) indicates the Raman shift of untreated, oxygen and air plasma treated MFPAC.

3.5. Impedance analysis

The MFPAC, EIS Nyquist plot in order to evaluate the conductivity performance over the frequency range of 1μHz to 10 kHz, measurements were used. For each sample, the EIS measurement reveals a semicircle shape. Which includes the real Z' and imaginary Z" components. (Fig. 7) shows the characteristics of the Polarization Resistance (Rs) and the Charge-Transfer Resistance (Rct). According to the graphs, linear shapes display at low frequencies (Polarization Resistance) and semicircular shapes at high frequencies (Charge-Transfer Resistance). The diameter of the semicircle at high frequencies represents the charge transfer resistance at the electrode-electrolyte interface [26].

The Polarization resistance is 0.2 ohms and the charge transfer resistance is 1.76 ohms for the untreated MFPAC and for air plasma treatment the polarization resistance and the charge transfer resistance are 0.2 and 1.43 ohms thus for Oxygen plasma treatment the polarization resistance and the charge transfer resistance are 0.2 and 1.43 ohms. Thus due to the hydrophobic nature of the plasma treated materials the resistance is lowering due the surface modification[27].

3.6. Contact angle analysis

The surface wettability of MFPAC is assessed using contact angle measurement. The wetting angle of MFPAC is shown in (Fig. 8). The MFPAC that has been plasma treated is hydrophilic in nature, while the untreated MFPAC has an angle of 114°, which is hydrophobic. When comparing the air and oxygen plasma treated MFPAC, the air plasma treated carbon has a higher level of wetness and has an angle of 16° and 61° for oxygen plasma treated carbon. This demonstrates that air plasma treated MFPAC has higher wettability than oxygen plasma treated and untreated MFPAC[28].

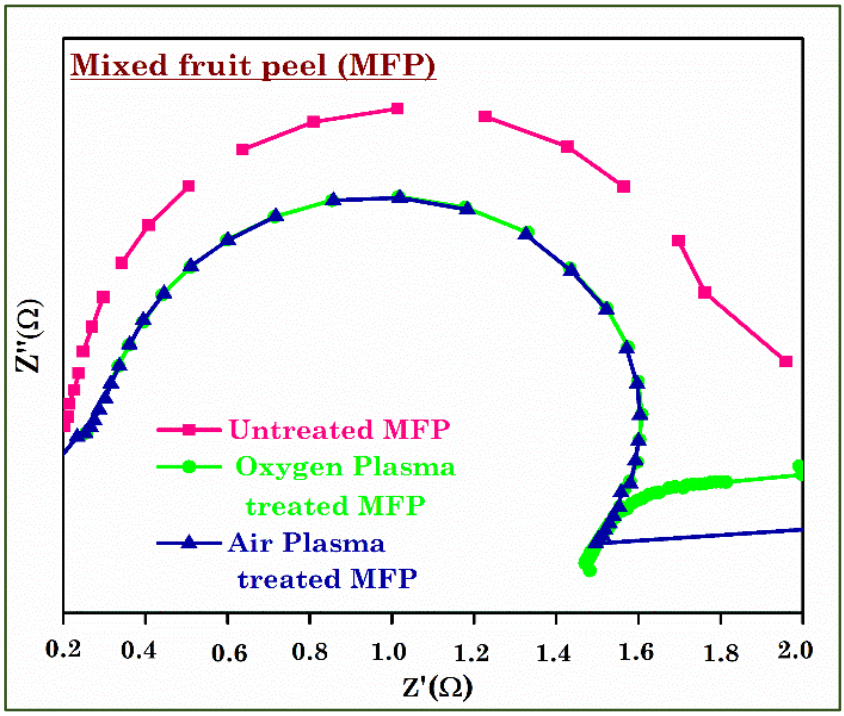

Figure 7. EIS of Untreated, Air plasma treated and oxygen plasma treated MFPAC

Slika 7. EIS netretiranog, vazdušnom plazmom tretiranog i MFPAC tretiranog plazmom kiseonikom

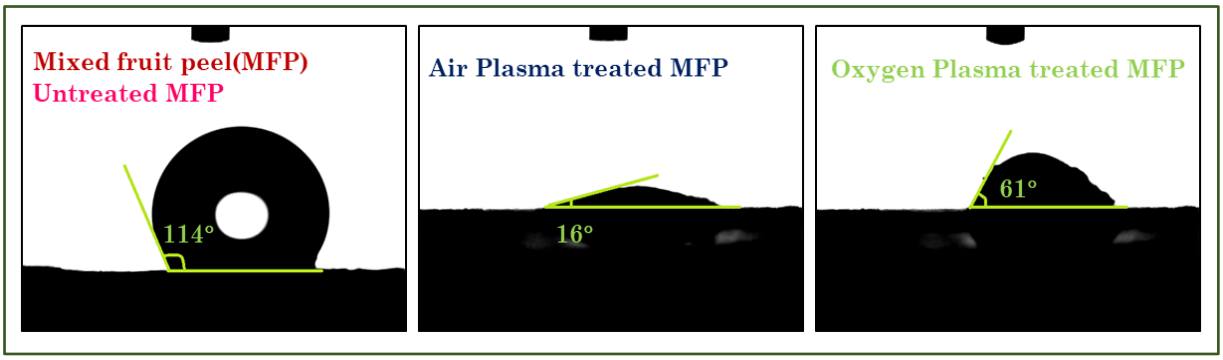

Figure 8. Contact angle of Untreated, Air plasma treated and oxygen plasma treated MFPAC

Slika 8. Kontaktni ugao netretiranog, obrađenog vazdušnom plazmom i MFPAC tretiranog kiseoničkom plazmom

These qualities have led to the high intensity of air plasma treated (MFPAC), which has been detected in XRD analysis. According to IR spectroscopy, MFPAC that has been treated with air plasma has improved bonding, which results in better pore structure. Additionally, the air plasma treated MFPAC has a more increased porosity structure in comparison to oxygen plasma treated and untreated mixed fruit peels. Raman spectra reveal that MFPAC treated with air plasma has the highest ratio of intensity. EIS explains the benefits of good conductance for MFPAC treated with air plasma. The wettability of MFPAC treated with air plasma has increased. According to these findings, air plasma treatment of MFPAC improves its surface characteristics, making it suitable for electrode in energy storage applications.

4. CONCLUSION

The emergence of Air plasma treated MFPAC presents a sustainable and eco-friendly solution to energy storage applications. By harnessing the inherent value of discarded fruit peels, this material offers good porous properties for air plasma exposed activated carbon that can be harnessed across various industries, from water and air purification to energy storage remediation. MFPAC shows promise in energy storage applications,

particularly in supercapacitors, because of its large surface area and good electrical conductivity. As we strive for a greener and more sustainable future, MFPAC stands as a testament to the potential hidden within nature's bio waste, unlocking new possibilities for a circular economy and a healthier planet.

5. REFERENCES

[1] K.F.Azlan Zahari, U.K.Sahu, T.Khadiran, S.N.Surip, Z.A.ALOthman, A.H.Jawad (2022) "Mesoporous Activated Carbon from Bamboo Waste via Microwave-Assisted K2CO3 Activation: Adsorption Optimization and Mechanism for Methylene Blue Dye. Separations, 9(12), 390. doi: 10.3390/separations9120390.

[2] J.B.Njewa, E.Vunain, T.Biswick (2022) Synthesis and Characterization of Activated Carbons Prepared from Agro-Wastes by Chemical Activation J Chem, vol. 2022, ID 9975444 doi: 10.1155/2022/9975444.

[3] P. D. Pathak, S.A.Mandavgane, B.D.Kulkarni (2015) Fruit peel waste as a novel low-cost bio adsorbent. Reviews in Chemical Engineering, 31(4), 361–381, doi: 10.1515/revce-2014-0041.

[4] K.Surya, M.S.Michael (2021) Hierarchical porous activated carbon prepared from biowaste of lemon peel for electrochemical double layer capacitors. Biomass Bioenergy, 152, 106175, doi: 10.1016/j.biombioe.2021.106175.

[5] M. A.Fayza S.Hashem, Kh. M Al-qahtani,F.Foziah, Al-Fawzan (2016) Comparative Study on Activated Carbon Prepared from Various Fruit Peels. Fayza S Hashem, Khairia M Al-qahtani, Foziah F Al-Fawzan, Mashael Alshabanat, 5(3), 2750–2759, doi: 10.15680/IJIRSET.

[6] A.Ehsani, H.Parsimehr (2020) Electrochemical Energy Storage Electrodes via Citrus Fruits Derived Carbon: A Minireview. Chemical Record, 20(8), 820–830, doi: 10.1002/tcr.202000003.

[7] H.Rustamaji, T.Prakoso, H.Devianto, P. Widiatmoko, W.H.Saputera (2022) Urea nitrogenated mesoporous activated carbon derived from oil palm empty fruit bunch for high-performance supercapacitor. J Energy Storage, 52, 104724, doi: 10.1016/J.EST.2022.104724.

[8] R.K.Gupta, M.Dubey, P.Kharel, Z.Gu, Q.H.Fan (2015) Biochar activated by oxygen plasma for supercapacitors. J Power Sources, 274, 1300–1305, doi: 10.1016/j.jpowsour.2014.10.169.

[9] W.M.Chang, C.C. Wang, C.Y.Chen (2015) Plasma Treatment of Carbon Nanotubes Applied to Improve the High Performance of Carbon Nanofiber Supercapacitors. Electrochim Acta, 186, 530–541, doi: 10.1016/j.electacta.2015.11.038.

[10] C.Saka (2018) Overview on the Surface Functionalization Mechanism and Determination of Surface Functional Groups of Plasma Treated Carbon Nanotubes. Crit Rev Anal Chem, 48(1), 1–14, doi: 10.1080/10408347.2017.1356699.

[11] R.Wolf, A.C.Sparavigna (2010) Role of Plasma Surface Treatments on Wetting and Adhesion. Engineering, 02(06), 397–402, doi: 10.4236/eng. 2010.26052.

[12] S.A.Gupta et al (2022) Adsorption isotherm studies of Methylene blue using activated carbon of waste fruit peel as an adsorbent. Mater Today Proc, 57, 1500–1508, doi: 10.1016/J.MATPR.2021.12.044.

[13] W. Saadi, S.Rodríguez-Sánchez, B. Ruiz, S. Najar-Souissi, A. Ouederni, E. Fuente (2022) "From pomegranate peels waste to one-step alkaline carbonate activated carbons. Prospect as sustainable adsorbent for the renewable energy production. J Environ Chem Eng, 10(1), 107010, doi: 10.1016/J.JECE.2021.107010.

[14] M.T.Amin, A. A.Alazba, M.Shafiq (2018) Removal of Copper and Lead using Banana Biochar in Batch Adsorption Systems: Isotherms and Kinetic Studies. Arab J Sci Eng, 43(11), 5711–5722, doi: 10.1007/s13369-017-2934-z.

[15] E.S.Ngankam, L. Dai-Yang, B. Debina, A.Baçaoui, A. Yaacoubi, A.N.Rahman (2020) Preparation and Characterization of Magnetic Banana Peels Biochar for Fenton Degradation of Methylene Blue. Materials Sciences and Applications, 11(06), 382–400, doi: 10.4236/msa. 2020.116026.

[16] V.Balasubramanian, T.Daniel, J.Henry, G. Sivakumar, K.Mohanraj (2020) Electrochemical performances of activated carbon prepared using eggshell waste. SN Appl Sci, 2(1), 62-69. doi: 10.1007/s42452-019-1921-2.

[17] K.A.Vijayalakshmi, K.Vignesh, N.Karthikeyan (2015) Synthesis and surface characterization of bamboo charcoal carbon using low temperature plasma treatment. Materials Technology, 30(A2), A99–A103, doi: 10.1179/17535557A15Y. 000000005.

[18] M. D. Mehare, A. D.Deshmukh, S.J.Dhoble (2021) Bio-waste lemon peel derived carbon based electrode in perspect of supercapacitor. Journal of Materials Science: Materials in Electronics, 32(10), 14057–14071, doi: 10.1007/s10854-021-05985-5.

[19] B.Smith (2018) Infrared spectral interpretation: A systematic approach," Infrared Spectral Interpretation: A Systematic Approach., book, Pub. Location,Boca Raton, p.1–304, doi: 10.1201/9780203750841.

[20] D.Ramutshatsha-Makhwedzha, A. Mavhungu, M. L. Moropeng, R.Mbaya (2022) Activated carbon derived from waste orange and lemon peels for the adsorption of methyl orange and methylene blue dyes from wastewater. Heliyon, 8(8), e09930, doi: 10.1016/j.heliyon.2022.e09930.

[21] S. Saveetha, K. A.Vijayalakshmi (2022) Influence of Low temperature Plasma on activated bamboo charcoal employed in energy storage system., 16(1001), 12–22, doi: 10.37896/jxu16.6/002

[22] T.V.Nagalakshmi, K.A.Emmanuel, Ch.Suresh Babu, Ch.Chakrapani, P.P.Divakar (2015) Preparation of Mesoporous Activated Carbon from Jackfruit PPI-1 Waste and Development of Different Surface Functional Groups. International Letters of

Chemistry, Physics and Astronomy, 54, 189–200, doi: 10.18052/www.scipress.com/ilcpa.54.189.

[23] K. A.Vijayalakshmi, S.Saveetha (2020) Enhancing the dielectric properties of activated bamboo charcoal under the exposure of DC glow discharge plasma. Mater Today Proc, 43, 1456–1459, doi: 10.1016/j.matpr.2020.09.298.

[24] C.K.Ranaweera, P.K.Kahol, M.Ghimire, S.R. Mishra, R.K.Gupta (2017) Orange-Peel-Derived Carbon: Designing Sustainable and High-Performance Supercapacitor Electrodes. C (Basel), 3(4), 25-37, doi: 10.3390/c3030025.

[25] O.Kazak, Y.R.Eker, H. Bingol, A.Tor (2017) Novel preparation of activated carbon by cold oxygen plasma treatment combined with pyrolysis. Chemical Engineering Journal, 325(1), 564-575, doi: 10.1016/j.cej.2017.05.107.

[26] P.Wang, Q.Wang, G.Zhang, H.Jiao, X.Deng (2015) Promising activated carbons derived from cabbage leaves and their application in high-performance supercapacitors electrodes. J. of Solid State Electroch., 20(2), 319-325. doi: 10.1007/s10008-015-3042-1.

[27] G. Ghanashyam, H. K.Jeong (2021) Plasma treated carbon nanofiber for flexible supercapacitors. J Energy Storage., 40, 102806, doi: 10.1016/j.est.2021.102806.

[28] Y.C.Hong, D. H. Shin, S. C.Cho, H.S.Uhm (2006) Surface transformation of carbon nanotube powder into super-hydrophobic and measurement of wettability. Chem Phys Lett., 427(4–6), 390–393, doi: 10.1016/j.cplett.2006.06.033.

IZVOD

OJAČANA POVRŠINSKA SVOJSTVA AKTIVNOG UGLJA IZ KUĆNOG OTPADA POMOĆU PLAZME NISKE TEMPERATURE KOJA SE KORISTI U APLIKACIJAMA ZA SKLADIŠTENJE ENERGIJE

Pošto je aktivni ugalj visoko porozan materijal sa značajnom unutrašnjom površinom, lako je adsorbovati širok spektar supstanci kada se koristi u uređajima za skladištenje energije, tretmanu otpadnih voda, prečišćavanju vode, katalizatorima, preradi hrane i drugim primenama. Ovaj rad se fokusira na održivost upotrebe mešanih kora voća kao prekursora za proces karbonizacije sa fizičkom aktivacijom za proizvodnju aktivnog uglja. Fazna potvrda je ispitana korišćenjem rendgenske difrakcije (XRD). Infracrveni spektrometar sa Furijeovom transformacijom (FTIR) zaključuje funkcionalne grupe prisutne u mešanom aktivnom uglju od kore voća. Skenirajuća elektronska mikroskopija polja (FESEM) je korišćena za analizu morfološkog sastava i teksturnih osobina aktivnog uglja koji je proizveden. Energetska disperzivna rendgenska analiza (EDX) pokazuje elementarni sastav nano praškastog ugljenika. Ramanova spektroskopija potvrđuje prisustvo grafena koji se pojavljuje na 1580cm^{-1}. Korišćena su elektrohemijska impedansna spektroskopija (EIS) i Nyquist-ovi dijagrami u cilju procene performansi provodljivosti u opsegu frekvencija od 1μHz do 10 kHz.

Sprovedena je i analizirana kolicina prinosa ugljenika. Vlaženje kore mešanog voća je ispitivano primenom kontaktnog ugla. Aktivni ugalj za mešane voćne kore je podvrgnut plazmi niske temperature da bi se povećala svojstva površine. Rezultati su procenjeni, a otpor prenosa naelektrisanja i otpor polarizacije za tretman vazdušnom plazmom je 1,43 i 0,2 oma. Hidrofilna priroda se javlja kada se tretira vazdušnom plazmom. Prema ovim nalazima, tretman vazdušnom plazmom mešanog aktivnog uglja od kore voća poboljšava njegove površinske karakteristike, čineći ga pogodnim za elektrode u aplikacijama za skladištenje energije.

Ključne reči: *Mešane voćne kore, fizička aktivacija, niskotemperaturna plazma, modifikacija površine, Nano prah.*

Naučni rad

Rad primljen: 28.09.2023.

Rad prihvaćen: 20.10.2023.

Rad je dostupan na sajtu: www.idk.org.rs/casopis

*Dipsikha Bhattacharya**

Adamas University, Department of Chemistry, School of Basic and Applied Sciences, Kolkata, India

Scientific paper
ISSN 0351-9465, E-ISSN 2466-2585
https://doi.org/10.62638/ZasMat1041

Zastita Materijala 65 (1)
63 - 72 (2024)

Development of hyaluronate tethered magnetic nanoparticles for targeted anti-cancer drug delivery

ABSTRACT

Despite the tremendous progress in understanding the molecular basis of the disease, cancer still remains one of the leading causes of deaths. Recently, advances in nanotechnology are rapidly enabling the development of novel, multifunctional materials with combined cancer specific targeting, therapeutic and diagnostic functions within a single nanocomplex (NP) that address the shortcomings of traditional disease diagnostic and therapeutic agents. Among the myriad of nanocarriers, magnetic nanoparticles (MNPs) have sparked extensive promise as novel theranostic applications as these MNPs can be directly targeted to the diseased cells with effective therapeutic efficiency. For this, these MNPs should be modified with some highly biocompatible polymers (specially polysaccharides) exhibiting the cancer targeting properties that can strongly interact with receptors expressed on the target cancer to facilitate accurate detection of the specific cancer and enhanced delivery to the target site while reducing unintended tside effects. Over the last few years, many groups have reported hyaluronic acid (HA) as the targeting agent as it directly delivers targeted MNPs to CD44 overexpressed cancer cells. In most of the cases, doxorubicin (DOX) has been used as the anticancer drug as it is largely utilized for treating a broad spectrum of cancers. In our work, we have designed a novel, intravenously injectable, CD44 receptor targeted MNP formulation, where the HA moiety of MNPs facilitate easy detection of cancer cells via receptor specific interactions, DOX can regress the cancer cells with simultaneous imaging efficacy. This theranostic MNPs led to the formation of novel nanoformulation, capable of performing concomitant detection, regression and imaging in in vitro CD44 over expressing cancer cells.

Keywords: *Multifunctional, MNP, Hyaluronic acid, Doxorubicin, CD44.*

1. INTRODUCTION

From last few decades, cancer, a complex, multifactorial disease are threatening human health by causing high mortality and recurrence rates [1]. The major drawbacks in chemotherapy are the poor intratumoral drug penetration and distribution, which can lead to serious off-target side effects and toxicities[2]. Another associated challenge in chemotherapy is the development of multidrug resistance (MDR) by tumor cells, which also reduced efficacy of drugs[3,4]. Therefore, it's important to create new methods for the precise identification of early-stage cancer and for targeted therapies that can only treat cancer with high dosages of lethal medications with minimal cytotoxicity to normal cells [5,6]. Recently nanotechnology provides an alternative strategy to overcome MDR by adopting various conceivable approaches to solve this issue. The increased permeability and retention (EPR) effect has been used to demonstrate that nanoparticles can passively accumulate in malignancies [7,8]. Among many multifunctional nanomedicines, magnetic nanoparticles (MNPs) have emerged as promising multifunctional nanoprobes because of their enhanced capability of delivering therapeutic agents (therapeutic drugs, DNA and small interfering RNA) to the targeted lesions along with their MR based diagnostic imaging efficiency [9-11]. Currently, a huge research impetus has been introduced to fabricate actively targeted MNPs with multiple imaging, detection and delivery functions through conjugating cancer specific “targeting” molecule to the surface of MNPs [12]. Many molecular targeting agents such as various

*Corresponding author: Dipsikha Bhattacharya
E-mail: dipsikha.chem@gmail.com
Paper received: 28. 09. 2023.
Paper accepted: 20. 10. 2023.
Paper is available on the website: www.idk.org.rs/journal

antibodies, peptides, naturally occurring polysaccharides, folic acid (FA) have been used in targeted drug delivery systems [13,14]. Among the natural polymers as cancer specific targeting agents, anionic glycosoaminoglycans such as hyaluronic acid (HA), its nonsulfated form has attracted striking interest not only due to their biodegradability, lower toxicity but also their contribution to the formation of extracellular constituent of connective tissues [15,16]. The main target molecule of HA is the antigen CD44 It is a breast cancer cell-surface glycoprotein antigen and is well known for its particular affinity for hyaluronic acid (HA) [17,18]. It is a multipurpose cell-surface molecule that has a role in the pathological characteristics of cancer cells, including cell proliferation, differentiation, migration, angiogenesis, and chemokines. Additionally, CD44 is known to be a marker for cancer stem cells, a subpopulation of cancer cells with the ability to self-renew. Hence, HA has been frequently utilized as a targeting moiety to detect CD44 receptors, which are available at low levels on epithelial, hematopoietic and neuronal cells and at elevated levels in various carcinomas, melanomas, lymphomas, colorectal, and lung tumor cells [15]. In recent times, the field of self-assembled HA carriers with CD44 targeting efficacy has attracted emerging attention as these nanocarriers can imbibe both the hydrophobic and hydrophilic therapeutics exploiting their amphiphilic nature [19-24]. In most of the cases, doxorubicin (DOX) molecules has been used as the anticancer drug as it is largely utilized for treating a broad spectrum of cancers. The main purpose of the present work is to develop a CD44 targeted HA-tethered nanotherapeutics with combined cancer specific targeting, diagnostic imaging and therapeutic efficiency for cancer specific drug delivery and noninvasive treatment monitoring. In order to overcome the intricate modification steps, we have prepared targeted DOX entrapped HA tethered MNPs where simple electrostatic interactions as well as chemical conjugation (as represented in Figure 1) was adopted for conjugating amine functionalities of Polyethylene imine (PEI) stabilized MNPs with carboxyl groups of HA groups. The DOX molecules are entrapped inside the self-assembled HA-MNP nanoparticles by the combined hydrophobic and the ionic interactions to construct a CD44 receptor targeted nanoprobes with targeting, imaging and therapeutic property. This theranostic pro drug with HA, DOX, Fluorescent dyes and MNPs led to the formation of novel nanoformulation, capable of performing concomitant detection, regression and imaging in in vitro CD44 over expressing cancer cells. These CD44 targeted formulations were extensively evaluated in CD44 over expressing cancer cells while extensive crosschecking with normal cells.

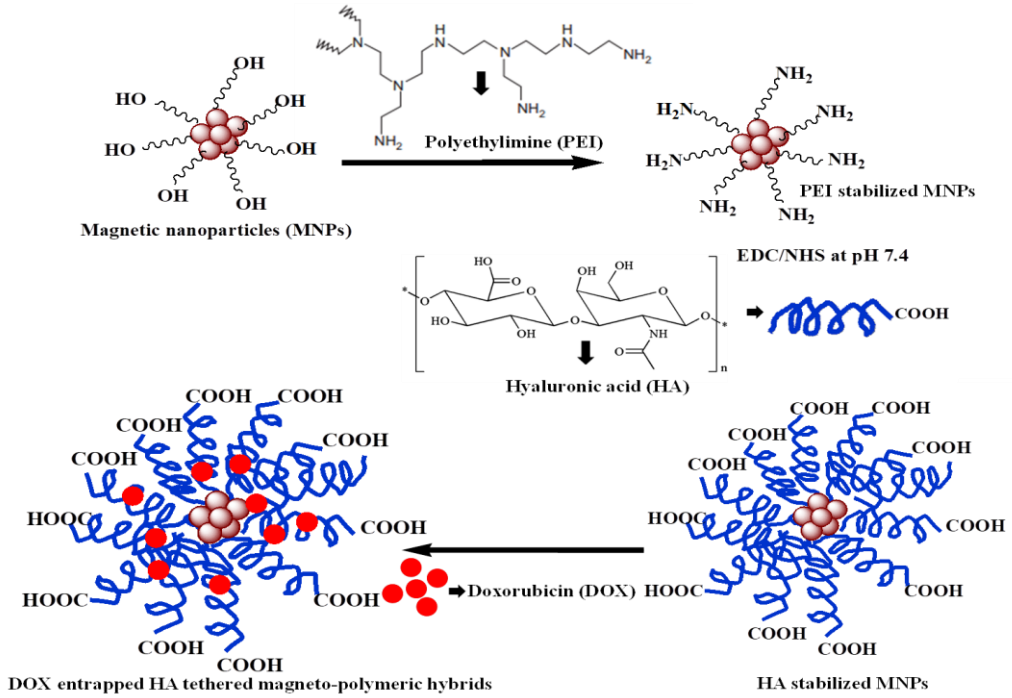

Figure 1. Schematic representation of synthesis of PEI functionalized MNPs followed by targeting with HA and DOX loading

Slika 1. Šematski prikaz sinteze PEI funkcionalizovanih MNP-a nakon čega sledi ciljanje sa HA i DOX opterećenjem

2. MATERIALS AND METHODS

2.1. Materials

Ferric chloride ($FeCl_3$), ferrous sulphate ($FeSO_4.7H_2O$), branched poly-(ethylenimine) (PEI, 25 kDa), hyaluronic acid (HA), N-hydroxy-succinimide (NHS), and 1-[3-(dimethylamino)-propyl] The following items were acquired from Sigma-Aldrich Chemicals in the United States: 3-ethyl carbodiimide hydrochloride (EDC), rhodamine isothiocyanate (RITC), doxorubicin, 4-6-diamidino-2-phenylindole (DAPI), propidium iodide (PI), RNase, and 3-(4,5-dimethylthiazol-2-yl)-2,5-Vacuum distillation was used to clean up commercially available dimethyl sulfoxide (DMSO) and N, N-dimethyl formamide (DMF), then dried 1, 4-dioxane was distilled over salt. We bought chloroform ($CHCl_3$) from Merck in Germany. Minimum essential medium (MEM) and foetal bovine serum were purchased from Hyclone in the United States and Himedia in India, respectively.

2.2. Methods

Synthesis of amine functionalized PEI-MNPs and HA targeted PEI-MNPs

Highly hydrophilic, biocompatible MNPs were synthesized using the standard controlled co-precipitation approach of using Fe^{2+} and Fe^{3+} (1:2 ratio) in presence of branched PEI according to our previously reported procedure[25,26]. In brief, a mixture of 0.324 g of $FeCl_3$ and 0.278 g of $FeSO_4.7H_2O$ were dissolved in 40 ml deoxygenated Milli-Q water containing 2 mg/ml of branched PEI in a three neck flask with a magnetic stirrer and an argon flow. To this, ammonium hydroxide (5 ml) was added drop wise and the mixture was stirred for 4 h at 70ºC. After completion of the reaction, these PEI-MNPs were recovered using magnetic separation, dialysis followed by freeze drying. Hyaluronic acid tethering to PEI-MNPs was carried out via EDC/NHS chemistry according to a reported procedure with little modification [27]. In a typical synthesis, a total of 100 mL of PBS, 0.15 g of HA, 0.1 g of EDC.HCl, and 0.6 g of NHS were added. Dilute NaOH was used to keep the pH between 8 and 10. Using EDC (100 mg, 0.48 mM) and NHS (56 mg, 0.48 mM) for 4 hours in the dark, the carboxyl group was activated. Subsequently, it was mixed with the aqueous dispersion of 150 mg of PEI-MNPs, and the final mixture was agitated overnight at RT. The HA-PEI-MNPs were finally retrieved after being magnetically concentrated, multiple times washed with Milli Q water, and PBS.

Development of anticancer drug entrapped HA-PEI-MNPs

After the successful development of MNP nanocarriers, doxorubicin (DOX), the anticancer drug, was entrapped inside these HA-PEI-MNPs with the weight ratio of 1:10. The red-colored solution was gently swirled for 36 hours at 25ºC in the dark. The resultant solution was then dialyzed against double distilled water while being stirred for 24 hours and having at least five water changes to get rid of undesirable components. To get DOX, the dialyzed solution was lyophilized in a speed vacuum for 24 hours. To get DOX, the dialyzed solution was lyophilized in a speed vacuum for 24 hours loaded HA-PEI-MNPs [28]. For evaluation of the loading and entrapment of the drug, 2 mg amount of DOX loaded nanoparticles were dissolved in 10 ml of Milli-Q water under stirring condition and absorbance of the drug was checked using standard UV-Vis and Fluorescence microscopy. It was degraded for 24 h in 10 ml of PBS: water mixture (1:1) under gentle shaking and the absorbance of the solution was measured at 480 nm. The amount of DOX entrapped inside this MNPs was determined using a previously drawn calibration curve of the drug using different concentrations. All the measurements were performed in triplicate.

$$\textit{Drug Loading } (DL) = \frac{DOX \times 100}{MNP + DOX} \qquad (1)$$

Entrapment Efficiency

$$(EE) = \frac{\textit{Amount of actual DOX loaded in MNPs}}{\textit{Amount of total DOX taken for entrapment}} \qquad (2)$$

To investigate the release of DOX, 10 mg of DOX-HA-PEI-MNPs were dispersed in 10 ml PBS solution and was placed in a dialysis bag at different pH values i.e. 7.4 (molecular weight cut-off of 12 kDa). The bags were suspended in 50 ml PBS solution at pH 7.4 and shaken for 5 days at 200 rpm. At selected time intervals, 1 ml of the sample was taken and replaced by an equal volume of fresh PBS. By spectrophotometrically analysing the solution's absorbance at 480 nm collected at predetermined intervals, the amount of released DOX was determined [26]. After being measured, and the samples that were obtained for sampling were added back to the receiver solution. A standard curve of a free drug solution was used to calculate the percentage of released drug. Three independent experiments' means and standard deviations were used to express the data.

Preparation of RITC labelled HA-PEI-MNPs (fluorescent conjugates of 1 and 2).

For the fluorescent labelling, a fraction of the previously stated HA-Poly-MNPs were covalently coupled using the amine groups with the highly fluorescent molecule rhodamine isothiocyanate (RITC) for the fluorescent labelling according to the previous reported literature [26].

The characterization of nanoparticles

Transmission electronic microscopy was used to observe the nanoparticles' size and form (TEM, JEOL-2100). The nanoparticles were dissolved in deionized water and subjected to a 10-minute ultrasonic process for the TEM investigation. The solution was then dropped onto a copper grip that had been carbon-coated before the pictures were taken and air-dried [29]. Image J software was used to analyse the average particle size. The MNPs' alteration was controlled by FTIR spectra in the range 500–4000cm^{-1}.

Cell lines and cytotoxicity studies.

The biocompatibility of the HA-PEI-MNPs and cytotoxicity of DOX–HA–PEI-MNPs was evaluated by a standard MTT [3-(4, 5-dimethylthiazol-2-yl)-2,5-diphenyltetrazolium bromide] assay. Two types of cells cultivated for in vitro experiments were A549 (Lung Carcinoma Cell Line for adenovirus) and HaCaT (immortalized human keratinocyte), which were acquired from the National Centre for Cell sciences (NCCS), Pune, India.Trypsinized cells were adjusted to a concentration of 1×10^5 cells per ml and plated in 96 well flat bottom culture plates for the cytotoxicity assay. (180 ml per well) and were incubated with DOX–HA–PEI-MNPs for 24 h at 37ºC in a humidified 5% CO_2 incubator [30]. Cell toxicity was measured by the MTT colorimetric procedure. Mean and standard deviation for the triplicate wells were reported.

Intracellular uptake studies by Confocal imaging and Prussian blue staining

The internalization and intracellular distribution of HA-PEI-MNPs were observed by fluorescence microscopic imaging. The PEI-MNPs and HA-PEI-MNPs were incubated with A549 cells. The cells (1×10^6 cells/well) were treated with 1 mg/ml of nanoconjugates in the culture for 4 h, the culture media were removed, and the cells were washed three times with PBS. The cells were then stained with DAPI for 10 min at room temperature and observed by fluorescence microscopy [26]. For the concentration dependent uptake via Prussian Blue staining, 1×10^6 cells was seeded in each wells for 24 h and were incubated with 25µg/ml of non-targeted PEI-MNPs and dose dependent concentrations of 5, 10, 20 and 25 µg/ml of targeted HA-PEI-MNPs for 4h respectively. After the incubation period, these wells were washed with PBS to remove any free nanoparticles. Cells were fixed for 40 minutes using 4% paraformaldehyde (Sigma-Aldrich). The cells were washed three times with PBS, counterstained with neutral red (0.02%) (Sigma-Aldrich), and subsequently observed by an inverted optical microscope [31,32].

Cell cycle analysis.

For the evaluation of the therapeutic efficacy of the DOX–HA–PEI-MNPs, time dependent cell-cycle analysis was performed in A549 cells. Cells (1×10^5) were treated with 10 µg free DOX, 25 µg HA-PEI-MNPs and the same concentrations of DOX-HA-PEI-MNPs for 0 hr, 30 min, 1 hr and 2 hrs at 37ºC. Cells were harvested and fixed in ethanol with a 70% alcohol content. The cells were then washed with ice-cold PBS (10 mM, pH 7.4), resuspended in 200 l of PBS, and incubated at 37 oC for 1 h in the dark with 20 l of DNA intercalating dye PI (1 mg/ml) and 20 l of DNAase free RNase. The hypochromic sub-diploid staining characteristics of the cells were used to identify apoptotic cells. Using a Becton-Dickinson FACS Calibur Flow Cytometer and Cell Quest software, the DNA histogram was examined to determine the distribution of cells in various cell-cycle phases.

DAPI staining for nuclear morphology study.

For visualization of A549 cells, the cell nucleus was stained with DAPI. The DAPI staining was performed to corroborate the apoptotic effect of DOX entrapped MNPs on A549 cells. For this, A549 cells were treated with HA-PEI-MNPs (control set) and (5, 10, 20 and 25 µg/ml) of DOX–HA–PEI-MNPs for 24 h at 37ºC. After this, cells were fixed with 3.7% formaldehyde for 15min, permeabilized with 0.1 percent Triton X-100 and dyed for 5 minutes at 37 degrees with 1 g/ml DAPI. After being cleaned with PBS, the cells were analysed using fluorescence microscopy (Olympus IX 70).

Statistical Analysis

One-way ANOVA was used to assess the statistical significance of differences (p 0.05) between the groups tested.

3. RESULTS AND DISCUSSIONS

HA-MNPs with superparamagnetic properties are synthesised from the step up chemistry of PEI-MNPs followed by the successful modification with Hyaluronic acid which is represented in Scheme 1. First, NH_2 functionalized highly stable, water-dispersible MNPs were synthesized through a standard co-precipitation technique using PEI as the stabilizing as well as surface anchoring agent. Further, HA was used as a CD44 receptor specific targeting agent to introduce targeting efficacy on the PEI-MNPs and the carboxylic acid groups in HA molecules were covalently conjugated with the ample NH_2 functionalities of PEI-MNPs through standard carbodimide activation approach. Therefore, the carboxyl groups of the HA molecules were conjugated to the amine group on the surface of NH_2-MNPs via the formation of amide bonds (HA-MSNs) [33,34]. Both of these

PEI-MNPs and HA-PEI-MNPs were labelled with RITC by covalent linking utilizing some of the residual surface amine groups [25]. The structure of PEI-MNPs and HA-PEI-MNPs was observed by transmission electron microscopy (TEM) analysis. As indicated in Figure 2(A-B), it was confirmed that before modification through HA, the size of the PEI-MNPs were in between 5-7 nm whereas after modification with high molecular weight HA, these HA-PEI-MNPs showed a size enhancement around 7 nm showing the size in the range of 15-17 nm. It authenticates their successful modification with PEI as well as HA as shown in Figure 2(A-B). The particle sizes of these functionalized MNPs were also checked by Dynamic Light Scattering technique i.e DLS. The hydrodynamic diameters (HDs) of these PEI-MNPs and HA-PEI-MNPs were observed at 85±10 nm and 205±10 nm (Table 1) with poly dispersity index (PDI) 0.25 and 0.28 of indicating larger diameters observed from TEM. This discrepancy is due to the fact that TEM measures the size of the NP core under vaccum, while the hydrodynamic diameter is a measure of the size of the core and the total hydrated coating in solution[35].

The surface charges of these nanoconjugates also show the +45.7 and -27.8 mV confirming the successful functionalization with NH_2 groups of PEI and –COOH groups of HA molecules. The decrease of zeta potential of the MNPs from +45.7 to -27 indicates the free amine groups of PEI-MNPs should be protonated and hence positive charged at neutral pH while after modification with HA, as HA is negatively charged –COOH groups and –CONH groups due to covalent bonding, this rendered HA-PEI-MNPs bearing negative zeta potential [36,37]. The successful functionalization with HA was confirmed by Fourier transform infrared (FTIR) spectroscopy. The FTIR spectra of HA-PEI-MNPs (Figure 2D) have shown all the peaks at 3470 cm^{-1}, 2936 cm^{-1}, 2856 cm^{-1}, 1358 cm^{-1}, 1230 cm^{-1}, 1057 cm^{-1} and 560 cm^{-1} indicating the presence of NH2, O-H, C-H, C-O, NH-CO and Fe-O stretching vibrations, respectively [38].

Table 1. Hydrodynamic (HD) size and zeta potential of the PEI-MNPs and HA-PEI-MNPs at physiological pH.

Tabela 1. Hidrodinamička (HD) veličina i zeta potencijal PEI-MNP i HA-PEI-MNP pri fiziološkom pH.

Nanoparticles	Size (nm)	Poly dispersity index (PDI)	Zeta potential (mV)
PEG-NH_2-MNPs	85±10	0.25	+45.7
HA-PEI-MNPs	205±6	0.28	-27.8

3.1. Therapeutic efficiency, Potential Cytotoxicity and Receptor Mediated Internalization analysis

Despite the powerful anti-cancer actions of doxorubicin (DOX), its non-specific side effects led to the creation of DOX loaded HA targeted nanocarriers to enable tumor-specific targeting. According to UV-vis spectrophotometry used in this investigation, the DOX loading and entrapment efficiency of DOX-HA-PEI-MNPs was around 6.2 percent and 82 percent [26,39]. According to a prior publication, DOX molecules can be loaded inside nanocarriers using both covalent pH-sensitive bonding and hydrophobic/ionic interactions [40-42]. In our situation, the combination hydrophobic and hydrogen bonding interactions between DOX molecules led to the entrapment of DOX in HA-PEI-MNPs. and carboxyl groups of HA-PEI-MNPs as previously reported from our group [26]. As shown in Figure 2C, the release of DOX molecules from DOX-HA-PEI-MNPs at pH 7.4 shows a sustained release of 25% within 24 h indicating the successful entrapment as well as sustained release of therapeutics at physiological pH.

From the cytotoxicity assay as shown in Figure 2(E-F), the cellular toxicity values of DOX-HA-PEI-MNPs along with free DOX molecules were examined in healthy HaCaT and target cancer cells (A549 cells: high CD44 expression) for 24 h with cell proliferation kit. As HaCaT cells has low CD44 expression, DOX-HA-PEI-MNPs shows almost 80% cell viability in comparison to free drug in normal HaCaT cells while in A549 cells with high CD44 expression, DOX-HA-PEI-MNPs indicates higher cytotoxicity compared to free drug molecules. Thus, due to the targeted internalization in A549 cells, the DOX-HA-PEI-MNPs shows enhanced toxicity indicating their efficiency over bulk DOX molecules. To authenticate the targeted CD44 receptor mediated internalization of RITC-HA-PEI-MNPs labelled over RITC-PEI-MNPs, confocal laser scanning microscopy was used and these nanoconjugates were incubated with A549 cells for 4 h which was shown in Figure 3(A-B). Compared with the internalization of RITC-PEI-MNPs demonstrated in Figure 3(A), HA targeted nanoconjugates (as shown in Figure 3B) showed enhanced red fluorescence intensity indicating higher internalization of RITC-HA-nanoconjugates due to the CD44 receptor mediated endocytosis of HA-PEI-MNPs [43,44]. The dose dependent intracellular uptake of HA-PEI-MNPs was investigated using Prussian Blue staining in shown in Figure 3(C-G). According to the images shown, the HA-PEI-MNPs show enhanced cell uptake when same concentrations of A549 cells was

incubated with increasing concentrations from 5, 10, 20 and 25 µg/ml Figure 3(D-G). It was evident that due to the CD 44 receptor mediated internalization, HA-PEI-MNPs exhibited enhanced intracellular uptake as compared to PEI-MNPs of the same concentration.

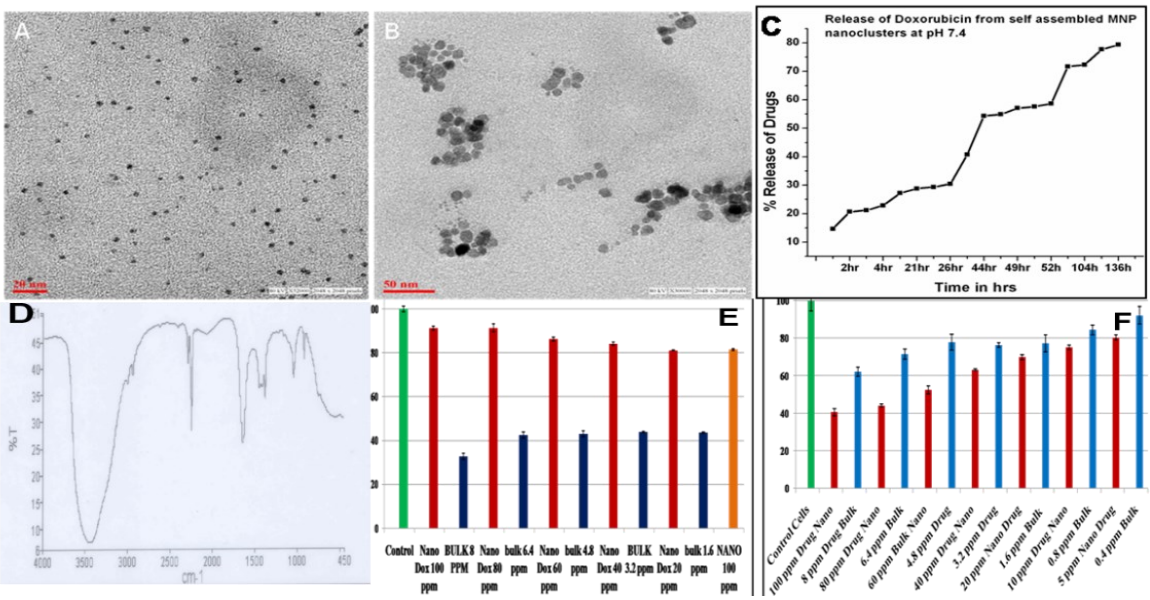

Figure 2. (A-B) TEM images of PEI-MNPs and HA-PEI-MNPs, C) DOX release from DOX-HA-PEI-MNPs, D) FT-IR spectrum of HA-PEI-MNPs. (E-F) MTT assays of DOX-HA-PEI-MNPs in HaCaT and A549 cells

Slika 2. (A-B) TEM slike PEI-MNP i HA-PEI-MNP, C) Oslobađanje DOX iz DOX-HA-PEI-MNP, D) FT-IR spektar HA-PEI-MNP, (E-F) MTT testovi DOX-HA-PEI-MNP u HaCaT i A549 ćelijama

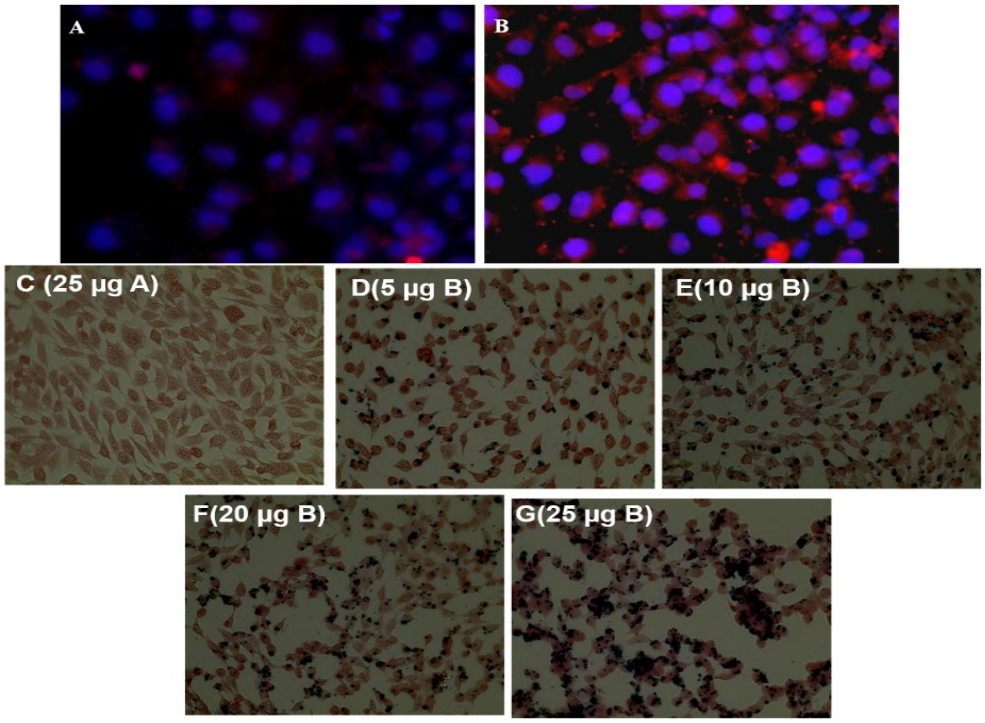

Figure 3. (A-B) Intracellular uptake of PEI-MNPs and HA-PEI-MNPs in A549 cells. (C-G) Intracellular uptake by Prussian Blue Staining of C) 25 µg/ml of PEI-MNPs D) to G) 5, 10, 20 and 25 µg/ml of HA-PEI-MNPs

Slika 3. (A-B) Intracelularno preuzimanje PEI-MNP i HA-PEI-MNP u A549 ćelijama. (C-G) Intracelularno preuzimanje pruskom plavim bojenjem od C) 25 µg/ml PEI-MNP D) do G) 5, 10, 20 i 25 µg/ml HA-PEI-MNP

Propidium iodide (PI) and DAPI staining have been used to analyse the cell cycle and undertake DNA fragmentation studies, or apoptosis studies, to further assess the anti-proliferative effect of DOX-HA-PEI-MNPs on A549 cells. From the DNA fragmentation study using increasing concentration of DOX–HA-PEI-MNPs (5, 10, 20 and 25 µg/ml) as represented in Figure 4(A-B), it was indicative that with increasing concentration there was substantial nuclei fragmentation, including membrane blebbing, condensed nuclei, and the development of apoptotic bodies.

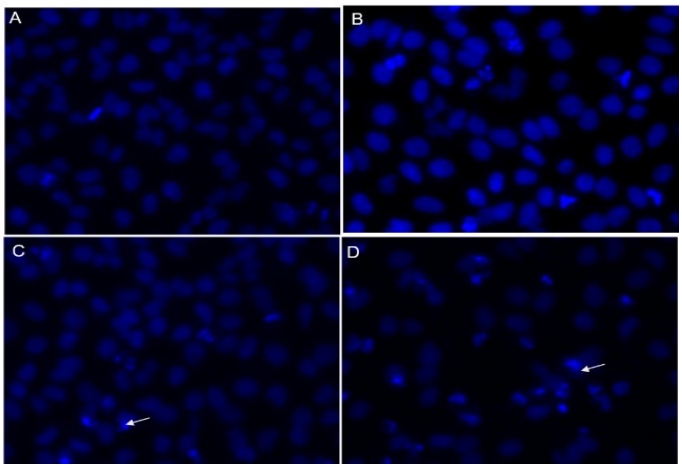

Figure 4. (A-D) DOX-HA-PEI-MNPs were used to evaluate apoptosis by examining the morphological changes in cell nuclei using fluorescence microscopy following DAPI labelling. For 24 hours, DOX-HA-PEI-MNPs were administered to A549 cells at concentrations of (A) 5 g/ml, (C) 10 g/ml, (D) 20 g/ml, and (E) 25 g/ml. Apoptotic nuclei are shown by arrows

Slika 4. (A-D) DOX-HA-PEI-MNP-ovi su korišćeni za procenu apoptoze ispitivanjem morfoloških promena u ćelijskim jezgrima korišćenjem fluorescentne mikroskopije nakon obeležavanja DAPI. Tokom 24 sata, DOX-HA-PEI-MNP su davani ćelijama A549 u koncentracijama od (A) 5 g/ml, (C) 10 g/ml, (D) 20 g/ml i (E) 25 g/ ml. Apoptotična jezgra su prikazana strelicama

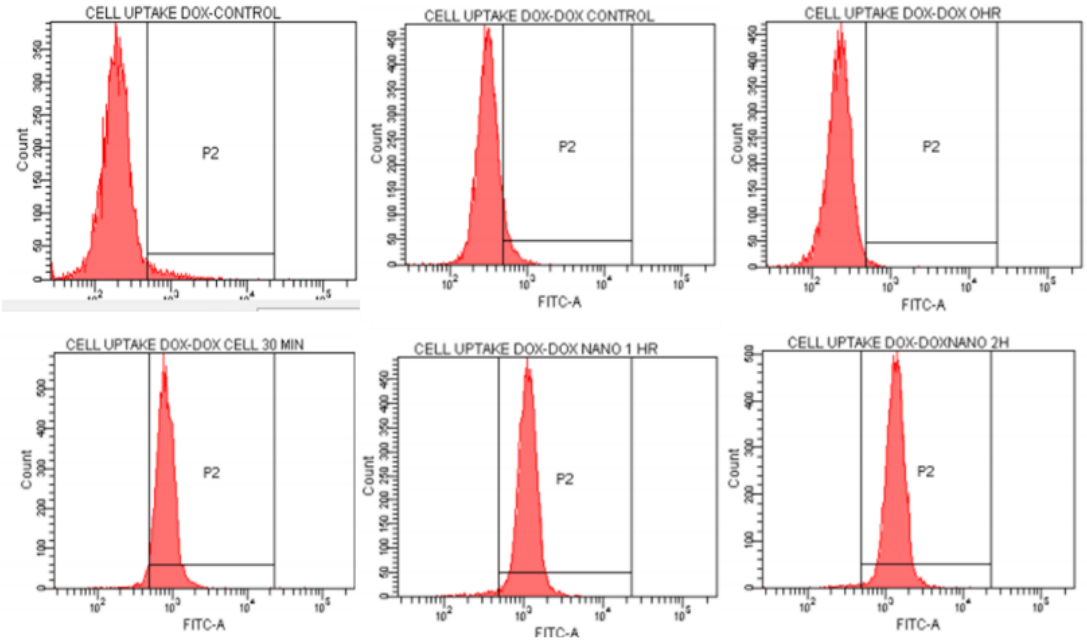

Figure 5. Flow-cytometric analysis of cell cycle phase distribution. Distribution of A549 cells treated with (A) HA-targeted nanoparticles (B) DOX only (C) 25 µg/mL of DOX-HA-MNPs for 0 hr (D) 25 µg/mL of DOX-HA-MNPs for 0.5 hr (E) 1 hr (F) 2 hrs

Slika 5. Protočna citometrijska analiza distribucije faza ćelijskog ciklusa. Distribucija ćelija A549 tretiranih sa (A) HA ciljanim nanočesticama (B) samo DOX (C) 25 µg/mL DOX-HA-MNP tokom 0 sati (D) 25 µg/mL DOX-HA-MNP tokom 0,5h (E) 1 sat (F) 2h

It was also evident that as the concentration of DOX-Poly-FA-MFNPs increased, the number of apoptotic nuclei increased as well (apoptotic nuclei shown by arrow in the Figure 4).This observation was fully supported by cell cycle analysis shown in Figure 5 where only HA-PEI-MNPs with highest concentration (25 μg/ml) has no apoptotic effect while increasing concentrations of DOX–HA-PEI-MNPs showed the maximum cell intensification at the G2/M phase [45], exhibiting cell cycle arrest in the same phase. Therefore, these DOX-HA-PEI-MNPs inhibited the growth of A549 cells by arresting cell cycle progression at the G2/M phase and followed to apoptosis or cell death.

4. CONCLUSIONS

In summary, we successfully fabricated DOX entrapped CD 44 receptor targeted HA-PEI-MNPs with combined cancer specific targeting and optical imaging by a facile preparation method. TEM images showed that these HA targeted nanoconjugates are highly dispersed and as they are intricately designed for the drug delivery applications, they should especially be taken up by cancer cells as opposed to normal cells. According to in vitro biological investigations, the DOX-HA-PEI-MNPs can deliver a single nanoconstruct with exceptional efficacy for locating and eliminating cancer cells.The DOX-HA-PEI-MNPs could efficiently deliver DOX to the tumor tissues, and gradually destroy CD44 receptor expressing cells compared to the free drug. Although further studies are needed, the various studies described in this manuscript indicate that the DOX-HA-PEI-MNPs represent an attractive nanocarrier that should have great potential for the treatment of cancer.

Acknowledgements

The authors are grateful to DST Nano Mission as well as Adamas University for providing financial support for this work.

5. REFERENCES

[1] M.Maluccio, A.Covey (2012) Recent progress in understanding, diagnosing, and treating hepatocellular carcinoma; CA Cancer J Clin., 62, 394-399.

[2] S.Senapati, A.K.Mahanta, K.Sunil, P.Maiti (2018) Controlled drug delivery vehicles for cancer treatment and their performance; Signal Transduct Target Ther., 3, 7-26.

[3] L.Gan, L.Zhenjiang, S.Chao (2018) Obesity linking to hepatocellular carcinoma: A global view; Biochim Biophys Acta Rev Cancer., 1869, 97-102.

[4] C.Sun, J.S.Lee, M.Zhang (2008) Magnetic nanoparticles in MR imaging and drug delivery; Adv. Drug Deliv. Rev., 60, 1252-1265.

[5] M.E.Davis, Z.Chen, D.M.Shin (2008) Nanoparticle therapeutics: an emerging treatment modality for cancer; Nat. Rev. Drug Discov., 7, 771-782.

[6] O.Veiseh, J.W.Gunn, M.Zhang (2010) Design and fabrication of magnetic nanoparticles for targeted drug delivery and imaging; Adv. Drug Deliv.Rev., 62, 284-304.

[7] H.Maeda, J.Wu, T.Sawa, Y.Matsumura, K.Hori (2000) Tumor vascular permeability and the EPR effect in macromolecular therapeutics: a review; J Control Release; 65, 271-284.

[8] H.Maeda, T.Sawa, T.Konno (2001) Mechanism of tumor-targeted delivery of macromolecular drugs, including the EPR effect in solid tumor and clinical overview of the prototype polymeric drug SMANCS; J. Control Release., 74, 47-61.

[9] J.W.M.Bulte, D.L.Kraitchman (2004) Iron oxide MR contrast agents for molecular and cellular imaging; NMR Biomed., 17, 484-499.

[10] J.H.Lee, Y.M.Huh, Y.Jun, J.Seo, J.Jang, H.T.Song, S.Kim, E.J.Cho, H.G.Yoon, J.S.Suh, J.Cheon (2007) Artificially engineered magnetic nanoparticles for ultra-sensitive molecular imaging. Nat. Med., 13, 95-99.

[11] Y.Pineiro, M.González Gómez, L. de Castro, A. Arnosa Prieto, A.García, P.S.Gudiña, R.Puig, J. Teijeiro, C.Yáñez-Vilar, S.J.Rivas (2020) Hybrid Nanostructured magnetite nanoparticles: from bio-detection and theragnostics to regenerative medicine. Magnetochemistry, 6, 4-31.

[12] A.Angelopoulou, A.Kolokithas-Ntoukas, C.Fytas, K. Avgoustakis (2019) Folic Acid-Functionalized, Condensed Magnetic Nanoparticles for Targeted Delivery of Doxorubicin to Tumor Cancer Cells Overexpressing the Folate Receptor. ACS Omega, 4, 22214-22227.

[13] S.D.Jo, S.H.Ku, Y.Y.Won, S.H.Kim, I.C.Kwon (2016) Targeted Nanotheranostics for Future Personalized Medicine: Recent Progress in Cancer Therapy; Theranostics, 6, 1362-1377.

[14] Z.Fang, X.Li, Z.Xu, F.Du, W.Wang, R.Shi, D.Gao (2019) Hyaluronic acid-modified mesoporous silica-coated superparamagnetic Fe3O4 nanoparticles for targeted drug delivery; International Journal of Nanomedicine, 14, 5785-5797.

[15] L.J.Lapcik, L.Lapcik, S.S.De, J.Demeester, P. Chabrecek (1998) Hyaluronan Preparation, Structure, Properties, and Applications; Chem. Rev., 98, 2663-2684.

[16] B.P.Toole (2004) Hyaluronan: from extracellular glue to pericellular cue; Nat. Rev. Cancer, 4, 528-539.

[17] Y. Lee, H. Lee, Y.B. Kim, J. Kim, T. Hyeon, H. Park, P.B. Messersmith, T.G. Park (2008) Bioinspired Surface Immobilization of Hyaluronic Acid on Monodisperse Magnetite Nanocrystals for Targeted Cancer Imaging; Adv Mater, 20, 4154-4157.

[18] H.Ponta, L.Sherman, P.A.Herrlich (2003) CD44: from adhesion molecules to signalling regulators; Nat Rev Mol Cell Biol, 4, 33-45.

[19] H.J.Chung, H.Lee, K.H.Bae, Y.Lee, J.Park, H.Cho, J.Y.H.Park, R.Langer, D.Anderson, T.G.Park (2011)

Facile Synthetic Route for Surface-Functionalized Magnetic Nanoparticles: Cell Labelling and Magnetic Resonance Imaging Studies. ACS Nano, 5, 4329-4336.

[20] K.Y.Choi, K.H.Min, J.H.Na, K.Choi, K.Kim, J.H. Park, I.C.Kwon, S.Y.Jeong (2009) Self-assembled hyaluronic acid nanoparticles for active tumor targeting; J Mater Chem, 19, 106-114.

[21] H.J. Cho, H.Y. Yoon, H. Koo, S.H. Ko, J.S. Shim, J.H. Lee, K. Kim, I.C. Kwon, D.D. Kim (2011) Self-assembled nanoparticles based on hyaluronic acid-ceramide (HA-CE) and Pluronic® for tumor-targeted delivery of docetaxel. Biomaterials, 32, 7181-7190.

[22] W. Park, K.S.Kim, B.C.Bae, Y.H. Kim, K. Na (2010) Cancer cell specific targeting of nanogels from acetylated hyaluronic acid with low molecular weight. Eur J Pharm Sci, 40, 367-375.

[23] T.Gong, Z.Dong, Y. Fu, T.Gong, L.Deng, Z.Zhang (2019) Hyaluronic acid modified doxorubicin loaded Fe_3O_4 nanoparticles effectively inhibit breast cancer metastasis. J. Mater. Chem. B, 7, 5861-5872.

[24] L. Song, Z. Pan, H. Zhang, Y. Li, Y. Zhang, J. Lin, G. Su, L. Xie, Y. Li, Z. Ho (2017) Dually folate/CD44 receptor-targeted self-assembled hyaluronic acid nanoparticles for dual-drug delivery and combination cancer therapy. J Mater Chem B., 5, 6835-6846.

[25] D. Bhattacharya, M.Das, D.Mishra, I. Banerjee, S. K. Sahu, T. K Maiti, P. Pramanik (2011) Folate receptor targeted, carboxymethyl chitosan functionalized iron oxide nanoparticles: a novel ultradispersed nanoconjugates for bimodal imaging. Nanoscale, 3, 1653 -1662.

[26] D.Bhattacharya, B.Behera, S.K.Sahu, R. Ananthakrishnan, T.K.Maity, P.Pramanik (2016) Design of dual stimuli responsive polymer modified magnetic nanoparticles for targeted anti-cancer drug delivery and enhanced MR imaging. New J. Chem., 40, 545-557.

[27] B. Gupta, B.K. Poudel, H.B. Ruttala, S. Regmi, S. Pathak, M. Gautam, S. Jin, J.H. Jeong, H.G. Choi, S. K. Ku, C. S. Yong, J. O. Kim (2018) Hyaluronic acid-capped compact silica-supported mesoporous titania nanoparticles for ligand-directed delivery of doxorubicin. Acta Biomaterialia, 80, 364--377.

[28] S. Wang, J. Zhang, Y. Wang, M. Chen (2016) Hyaluronic acid-coated PEI-PLGA nanoparticles mediated co-delivery of doxorubicin and miR-542-3p for triple negative breast cancer therapy. Nanomedicine, 12, 411-420.

[29] K. Kim, K. Kim, J. H. Ryu, H. Lee (2015) Chitosan-catechol: a polymer with long-lasting mucoadhesive properties. Biomaterials, 52, 161-170.

[30] S. Wen, H. Liu, C. Hongdong, M. Shen, X. Shi (2013) Targeted and pH-responsive delivery of doxorubicin to cancer cells using multifunctional dendrimer-modified multi-walled carbon nanotubes. Adv. Healthcare Mater, 2, 1267-1276.

[31] A.M. Reddy, B.K. Kwak, H.J. Shim (2010) In vivo Tracking of Mesenchymal Stem Cells Labeled with a Novel Chitosan-coated Superparamagnetic Iron Oxide Nanoparticles using 3.0T MRI. J Korean Med Sci., 25, 211-219.

[32] J. Krejci, J. Pachernik, A. Hampl, P. Dvorak (2008) In vitro labelling of mouse embryonic stem cells with SPIO nanoparticles. Gen Physiol Biophys, 27, 164-173.

[33] J. Y. Jeong, E.H. Hong, S. Y. Lee, J.Y. Lee, J. H. Song, S. H. Ko, J. S. Shim, S. Choe, D. D. Kim, H.J. Ko, H. J. Cho (2017) Boronic acid-tethered amphiphilic hyaluronic acid derivative-based nanoassemblies for tumor targeting and penetration. Acta Biomater, 53, 414-426.

[34] M. Ashrafizadeh, S. Mirzaei, M.H. Gholami, F. Hashemi, A. Zabolian, M. Regi, K. Hushmandi, A. Zarrabi, N.H. Voelcker, A. Reza Aref, M. Hamblin, R. Varma, R. S. Samarghandian, S. Arostegi, I.J. Alzola, M. Prem Kumar, A.Thakur, V. K. Nabavi, N. Makvandi, P. Tay, F. R. Orive, (2021) Hyaluronic acid-based nanoplatforms for Doxorubicin: A review of stimuli-responsive carriers, co-delivery and resistance suppression. Carbohydrate Polymers, 272, 118491-118521.

[35] H.A. Chen, Y.J. Lu, B. S. Dash, Y. K. Chao, J. P. Chen (2023) Hyaluronic Acid-Modified Cisplatin-Encapsulated Poly(Lactic-co-Glycolic Acid) Magnetic Nanoparticles for Dual-Targeted NIR-Responsive Chemo-Photothermal Combination Cancer Therapy. Pharmaceutics., 15, 290-314.

[36] J. Dou, Y.Mi, S.Daneshmand, M.H.Majd (2022) The effect of magnetic nanoparticles containing hyaluronic acid and methotrexate on the expression of genes involved in apoptosis and metastasis in A549 lung cancer cell lines. Arabian Journal of Chemistry., 15,104307.

[37] H.C.Wu, T.W.Wang, S.Y.Hsieh, J.S.Sun, P.L.Kang (2016) Targeted Delivery of Hyaluronan-Immobilized Magnetic Ceramic Nanocrystals. J. Biomed. Nanotechnol, 12, 103-113.

[38] M.D.Zhao, J.L.Cheng, J.J.Yan, F.Y.Chen, J.Z. Sheng, D.L.Sun, J.Chen, J.Miao, R.J.Zhang, C.H. Zheng, H.F.Huang (2016) Hyaluronic acid reagent functional chitosan-PEI conjugate with AQP2-siRNA suppressed endometriotic lesion formation. Inter. J. Nanomed., 11, 1323-1336.

[39] Z.Chai, C.Teng, L.Yang, L.Ren, Z.Yuan, S. Xu, M. Cheng, Y.Wang, Z.Yan, C.Qin, X. Han, L.Yin (2020) Doxorubicin delivered by redox-responsive Hyaluronic Acid–Ibuprofen prodrug micelles for treatment of metastatic breast cancer. Carbohydrate Polymers, 245, 116527-116545.

[40] Y.L.Su, J.Wang, H.Z.Liu (2002) Formation of a Hydrophobic Microenvironment in Aqueous PEO−PPO−PEO Block Copolymer Solutions Investigated by Fourier Transform Infrared Spectroscopy. J. Phys. Chem. B, 106, 11823-11828.

[41] S. Liu, Y.Zhao, M. Sen. Y. Hao, X. Wu, Y. Yao, Y. Li, Q. Yang. (2022) Hyaluronic acid targeted and pH-responsive multifunctional nanoparticles for chemo-photothermal synergistic therapy of atherosclerosis. J. Mater. Chem. B. 10, 562-570.

[42] Z. Luo, Y.Dai, H.Gao (2019) Development and application of hyaluronic acid in tumor targeting

drug delivery. Acta Pharmaceutica Sinica B., 9, 1099-1112.

[43] H.Urakawa, S.Tsukushi, H.Sugiura (2014) Neoadjuvant and adjuvant chemotherapy with doxorubicin and ifosfamide for bone sarcomas in adult and older patients. OncolLett., 8, 2485-2488.

[44] X.Pang, Z.Lu, H.Du, X.Yang, G.Zhai (2014) Hyaluronic acid-quercetin conjugate micelles: Synthesis, characterization, in vitro and in vivo evaluation. Colloids Surf B Biointerfaces., 123, 778-786.

[45] Y.H.Ling, A.K. el-Naggar, W.Priebe, R.Perez-Soler (1996) Cell cycle-dependent cytotoxicity, G2/M phase arrest, and disruption of p34cdc2/cyclin B1 activity induced by doxorubicin in synchronized P388 cells. Mol. Pharmacol., 49, 832-841.

IZVOD

RAZVOJ MAGNETNIH NANOČESTICA VEZANIH HIJALURONATOM ZA CILJANU ISPORUKU LEKOVA PROTIV RAKA

Uprkos ogromnom napretku u razumevanju molekularne osnove bolesti, rak i dalje ostaje jedan od vodećih uzroka smrti. Nedavno, napredak u nanotehnologiji ubrzano omogućava razvoj novih, multifunkcionalnih materijala sa kombinovanim ciljanim, terapeutskim i dijagnostičkim funkcijama za rak u okviru jednog nanokompleksa (NP) koji se bavi nedostacima tradicionalnih dijagnostičkih i terapeutskih agenasa za bolesti. Među bezbroj nanonosača, magnetne nanočestice (MNP) su izazvale veliko obećanje kao nove terapeutske primene jer ovi MNP mogu biti direktno ciljani na obolele ćelije sa efikasnom terapijskom efikasnošću. Za ovo, ovi MNP-ovi bi trebalo da budu modifikovani nekim visoko biokompatibilnim polimerima (posebno polisaharidima) koji pokazuju svojstva ciljanja raka, koja mogu snažno da interaguju sa receptorima eksprimiranim na ciljnom karcinomu kako bi se olakšalo tačno otkrivanje specifičnog raka i poboljšana isporuka na ciljno mesto uz smanjenje neželjene nuspojave. Tokom poslednjih nekoliko godina, mnoge grupe su prijavile hijaluronsku kiselinu (HA) kao sredstvo za ciljanje jer direktno isporučuje ciljane MNP u ćelije raka sa prekomernom ekspresijom CD44. U većini slučajeva, doksorubicin (DOKS) je korišćen kao lek protiv raka jer se u velikoj meri koristi za lečenje širokog spektra karcinoma. U našem radu, dizajnirali smo novu, intravenozno injekcionu, CD44 receptor ciljanu MNP formulaciju, gde HA deo MNP-a, olakšava lako otkrivanje ćelija raka putem interakcija specifičnih za receptor, DOKS može regresirati ćelije raka uz istovremenu efikasnost snimanja. Ovi teranostički MNP-i doveli su do formiranja nove nanoformulacije, sposobne da sprovede istovremenu detekciju, regresiju i snimanje u in vitro CD44 preko ekspresije ćelija raka.

Ključne reči: *multifunkcionalno, MNP, hijaluronska kiselina, doksorubicin, CD44.*

Naučni rad

Rad primljen: 28.09.2023.

Rad prihvaćen: 20.10.2023.

Rad je dostupan na sajtu: www.idk.org.rs/casopis

Nkemakolam Chinedu Izuwa, Stanley Toochukwu Ekwueme, Ndubuisi Uchechukwu Okereke, Onyebuchi Ivan Nwanwe, Nnaemeka Princewill Ohia

Federal University of Technology, Department of Petroleum Engineering, Owerri (FUTO), Nigeria

Scientific paper
ISSN 0351-9465, E-ISSN 2466-2585
https://doi.org/10.62638/ZasMat1009

Zastita Materijala 65 (1)
73 - 85 (2024)

Comparative analysis of geothermal binary ORC systems: performance and environmental considerations for CO_2 and water as geofluids

ABSTRACT

This study considers the process simulation of geothermal binary Organic Rankine Cycle (ORC) systems which utilizes CO_2 and water as geofluids for electricity generation. The simulation was performed using Hysys v11 software by using Peng Robinson's fluid property package. Two dry working fluids including isopentane and n-pentane, were used. The effects of geofluid temperature and working fluid mass flowrate on power generation, as well as the maximum pressure of working fluids were evaluated. The result showed that power generation increases with higher geofluid temperature due to enhanced heat transfer. Isopentane outperformed n-pentane, attributed to its superior thermodynamic properties. CO_2 showed better performance as geofluid than water highlighting its superiority, observed in the increased power generation. The unique characteristics of CO_2 enable efficient heat transfer at lower temperatures, making it an environmentally friendly and effective choice. Contrarily, the use of water as a geofluid poses some implications for local ecosystems and water resources. From an environmental perspective, CO_2 shows greater potential for reduced environmental impact, which aligns with the transition to cleaner energy sources. However, the economic considerations suggest a trade-off, as CO_2 projects may entail higher upfront costs compared to water-based systems. Regulatory factors and economic feasibility, therefore, play a crucial role in the choice of geofluid for geothermal power generation.

Keywords: *Geofluid, working fluid, ORC, renewable energy*

1. INTRODUCTION

In recent times, there has been increasing pressure to raise the proportion of renewable energy sources in electricity generation. This push has opened up opportunities for the development of geothermal energy in regions that were previously deemed unviable for this purpose [1].

Global concerns such as climate change, ozone layer depletion, rising electrical energy demand, and diminishing fossil fuel reserves have driven advancements in renewable energy technology. While wind and solar farms are gaining popularity, they are subject to weather-dependent operation [2]. Consequently, they require collaboration with traditional power plants and the advancement of energy storage solutions, including the exploration of underground caverns and fuel cell technology [3,4]. On the other hand, biomass combustion, hydroelectric, and geothermal power plants offer relatively stable or cyclical renewable energy [5] However, biomass power plants, despite their potential for compact construction, necessitate substantial quantities of low-energy feedstocks, often requiring significant land areas, unless utilizing waste materials. Hydroelectric power plants, in turn, can cause notable environmental contamination of local water sources [6]. Geothermal power plants stand out for their minimal surface impact on the environment. They extract heat energy by drilling deep into the earth [7].

Geothermal energy serves various purposes, including electricity and heat generation, combined heat and power applications, and space heating and cooling. It is broadly categorized into three temperature ranges: high temperature (above 150°C), intermediate temperature (between 90°C and 150°C), and low temperature (below 90°C)

*Corresponding author: Izuwa, N.C.
E-mail: Stanleyekwueme@yahoo.com
Paper received: 21. 09. 2023.
Paper accepted: 07. 10. 2023.
Paper is available on the website: www.idk.org.rs/journal

resources [8]. These applications can be classified into power generation and direct use [9].

Geothermal power plants fall into three types: flash, dry-steam, and binary, each suitable for different temperature ranges. Flash and dry-steam technologies are employed with higher temperature sources (above 180°C), while binary plants utilize lower temperature sources (from lower than 180°C) [9]. Globally, flash, dry-steam, and binary technologies comprise 58%, 26%, and 15% of the market, with emerging technologies constituting 1% of facilities [9].

The flash technology is well-established and used when the geothermal fluid contains both liquid and vapor phases at the wellhead, typically above 180°C [10]. In this method, the geothermal fluid undergoes a direct cycle: it is flashed to separate steam, which then drives a steam turbine before being condensed. The plant design depends on the geothermal fluid's composition, often containing salts and non-condensable gases (NCG) [10]. Treatment of the fluid, including NCG extraction for proper condenser operation, is essential. Depending on chemical composition, NCG may undergo further treatment or be released into the environment. Geothermal fluids can have varying chemical compositions, often including CO_2, H_2S, and sometimes hydrocarbons [9].

Binary cycle technology employs two separate cycles: a geothermal loop and a power cycle (ORC or Kalina cycle). This approach is commonly used for liquid sources or medium-low-temperature resources (typically 100-170°C) [11]. A significant benefit of the binary cycle is the enclosed geothermal fluid loop, which prevents environmental pollution by containing potential pollutants and reinjecting them underground. In ORC binary geothermal power plants, organic working fluids are used [10].

Several research has been conducted on the performance of different working fluids in Organic Rankine Cycle (ORC) systems, Pasetti et al. [12] investigated decomposition temperatures for n-butane, toluene, and n-pentane, with toluene remarkably stable at around 400°C, n-pentane stable below 315°C, and n-butane stable near 290°C. Notably, n-butane (R600), n-pentane, cyclopentane, hexamethyldisiloxane (MM), and toluene demonstrate higher thermal stability, making them suitable for geothermal solar hybrid applications. However, the existing literature lacks extensive analysis of these working fluids in such hybrid systems.

Ashouri et al. [13] investigated a small-scale ORC coupled with a parabolic trough solar collector in Tehran, favouring benzene for net electric efficiency. However, they didn't consider the impact of the Solar Heat Transfer Fluid on working fluid performance.

Salman et al. [14] conducted research comparing n-butane (R600), R236ea, R245fa, and n-hexane as working fluid using solar heat fluid in Aspen Plus software. They showed that n-butane possesses superior thermal efficiency at 13.55% within the 70°C–90°C range. However, their study did not consider the analysis of the impact of solar heat fluid on organic working fluid performance, as well as pump power requirements and network output. Additionally, they analyzed R245fa with a high Global Warming Potential (GWP) of 1030.

Najjar and Qatramez [15] studied various working fluids for ORC power generation using a geothermal temperature source of 200°C–260°C. Their study identified R11 with the highest net power output (24.89 MW) and efficiency (18.76%), however, its high GWP (4750) makes it unsuitable for ORC applications.

Wang et al. [16] compared small ORC systems powered by solar, using R245fa, R134a, and isobutane as working fluids. Their results showed that a thermal-driven pump solar system outperforms the conventional system for residential use. In another study, Wang et al. [17] performed a thermodynamic economic analysis of a solar-powered ORC, they showed that isobutane as the optimal working fluid for small-scale systems.

Song et al. [18] studied geothermal ORC systems and found that low critical temperature working fluids perform better when superheated, but higher critical temperature fluids degrade when superheated. In a subsequent study, Song et al. [19] performed a thermodynamic and financial analysis of carbon dioxide-ORC systems for hybrid geothermal and solar electricity generation, they concluded that the hybrid systems are superior.

2. GEOTHERMAL ENERGY

Geothermal energy refers to the energy harnessed from the internal heat of the earth. It represents a sustainable and renewable alternative to fossil fuels, which makes it attractive. Geothermal energy source is particularly well-suited for providing consistent base-load power due to its minimal variability [20]. Geothermal energy has various applications which includes both electricity and heat generation, being utilised for combined heat and power needs, as well as space heating and cooling requirements [21].

The advantages of geothermal energy are substantial. Geothermal power plants can reliably be operated for over 7000 hours annually, contributing to the stability of power grids [21]. With proper reservoir management, these power plants

can have an extended operational lifespan. However, it is worthwhile to note that reservoir water balance management is critical for ensuring sustainable and effective geothermal power plant operation [2].

Numerous studies centred around the modelling of geothermal power plants, principally focuses on two key aspects: power generation and reinjection facilities [2]. The former relates to the production wells and the closed power cycle, while the latter involves compressor trains and reinjection wells. Among various technologies, the Organic Rankine Cycle (ORC) technology emerges as highly compatible with "closed cycle reservoirs". ORCs show great promise for the conversion of low-temperature geothermal heat into power [2].

2.1. Organic Rankine Cycle (ORC) Systems

The successful exploitation of geothermal resources lies in the efficiency of the technologies adapted to its operation. Power production technologies of the geothermal plants are classified as flash, dry-steam and binary types. Flash and dry-steam types use geothermal sources with higher temperatures (i.e., minimum 220 ^{o}C). On the other hand, binary plants utilize sources that have lower temperatures (i.e., from 100 ^{o}C to 220 ^{o}C) [9].

A critical example of binary cycle turbine for geothermal turbine system is organic Rankine cycle (ORC). ORC have demonstrated capacity to convert low-temperature geothermal fluids to electricity. However, the efficiency of the system is reported to be around 13%. In ORC system, organic working fluids are used, these fluids are basically refrigerants or hydrocarbons [22].

It has been reported that the performance of ORC is largely dependent on the working fluid used. Therefore, choice of organic working fluid is critical and imperative and should be carefully done. The choice of working fluids for Organic Rankine Cycle (ORC) systems is influenced by a range of factors including health, safety, economics, environmental considerations, and thermodynamic properties [23]. The environmental and safety aspects of potential working fluids encompass flammability, toxicity, Global Warming Potential (GWP), and Ozone Depletion Potential (ODP). Organic working fluids, for instance, should possess a GWP below 150 and an absence of ODP [22].

In the selection of an ideal ORC working fluid favourable parameters such as low specific volume, liquid specific heat, viscosity, flammability, toxicity, ODP, GWP, and cost should be considered Bahrami, et al., [22] Moreover, process characteristics like high efficiency, latent heat, density, molecular weight, suitable thermal stability limits, compatibility with turbine materials and lubricating oil, non-corrosiveness, non-inflammability, and moderate heat exchanger pressures are important [24]. Saturated vapor specific volume is indicative of condenser size, tied to initial system costs. Higher saturation pressure (>100 kPa) prevents gas infiltration, which can reduce system efficiency. A working fluid with high latent heat and density is preferred to optimize output power in a combined cycle.

Working fluids can be categorized into three types: isentropic fluids, dry fluids, and wet fluids, based on the slope of the T-s saturation curve during expansion [25]. Wet fluids have a negative slope, isentropic fluids have a vertical slope, and dry fluids have a positive slope. Water is an example of a wet fluid, while dry fluids include many hydrocarbon gases like propane, butane, pentane, and hexane. Isentropic fluids include toluene and R245fa etc [9].

Water has been largely utilised for large-scale fossil fuel-fired Rankine cycle plants, particularly at high temperatures, but its limitations become significant at lower temperatures. Organic fluids, derived from petroleum, exhibit lower evaporation energy compared to water, requiring less heat for vaporization [23]. Their thermodynamic and chemical characteristics eliminate the need for superheating. Unlike water, most organic fluids result in superheated vapor through a turbine during isentropic expansion, avoiding two-phase mixtures and simplifying turbine and cycle design [24]. Dry working fluids are preferable for ORC use due to erosion concerns associated with droplets from wet fluid expansion. Isentropic fluids, due to their higher GWP, are becoming less favoured [23].

The steady-state energy models for the ORC system are given below

$$\sum \dot{m}_{in} = \sum \dot{m}_{out} \quad (1)$$

$$\sum Q + \sum \dot{m}_{in} h_{in} = \sum W + \sum \dot{m}_{out} h_{out} \quad (2)$$

$$W_{net} = W_{turbine} - W_{pump} \quad (3)$$

$$W_{turbine} = \dot{m}_f (h_{in} - h_{out}) \quad (4)$$

where

$\dot{m}$ (kg /s) is the mass flow rate

h is the specific enthalpy of the system's working fluid streams, (kJ/kg)

Q represent the heat energy passing via the component boundaries, (Watts)

W is the work energy passing via the component boundaries, (Watts).

W_{net} is the network, Watts

$W_{turbine}$ is the turbine work, Watts

W_{pump} is the pump work, Watts

$\dot{m}_f$ is the mass flow rate,

h_{in} is the specific enthalpy at the turbine entry

h_{out} is the specific enthalpy at the exit of the turbine

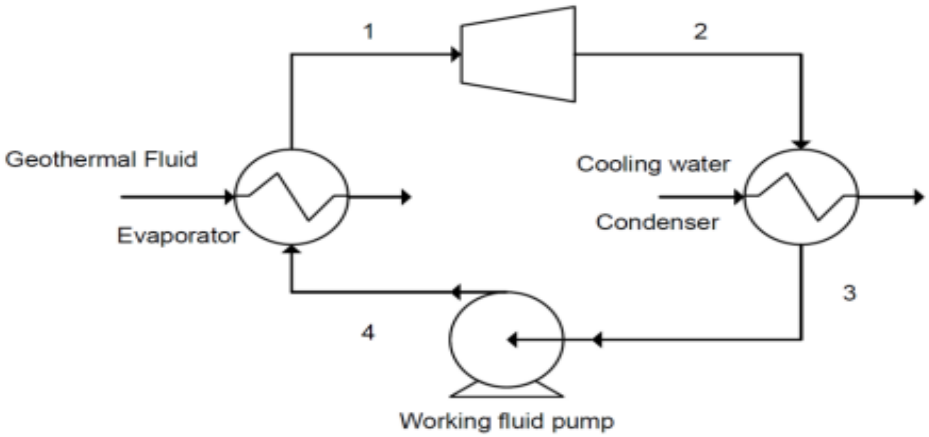

Figure 1. The working principle of the ORC system

Slika 1. Princip rada ORC sistema

Figure 1 describes the working principle of the ORC system.

The binary organic Rankine cycle (ORC) for generation of electricity using geothermal fluids is adequately similar to the conventional binary ORC process. The slight difference is the exclusion of the heat generator where the heat is generated. For the geothermal ORC, the geofluid is a hot fluid from the geothermal wells. The geothermal reservoir acts as the source of heat. As can be observed in figure 1, the geothermal fluid from the well is sent to the evaporator where superheated vapours are generated. usually, fluids with low boiling points are used as working fluids so that they can be easily vapourized. These working fluids gets vapourized upon moderate or low temperature heating by the geothermal fluid [22]. The working fluid is pumped from to the evaporated where it extracts the heat from the geofluid and vapourizes. The vapourized working fluid is sent to the turbine where its heat causes its expansion and is used to rotate the turbine blades generating electricity. The working fluid after being extracted of its heat leaves the turbine at lower temperature and pressure and goes to the condenser where it is cooled. The cooled working fluid is pumped back to the evaporator to continue the cycle. Meanwhile, the cooled geofluid is injected back into the well [23].

3. METHODS

The methods comprise the process modelling and simulation of binary geothermal system. The heat source is from abandoned oil and gas wells. Geothermal heat is mined using water and supercritical CO_2 as geofluid. The ORC system for electricity generation consists of binary plant modelled with isopentane and n-pentane as working fluids. The geofluids recovered from the well via the wellheads were sent to the ORC system. The process modelling and simulation is summarized using the block diagram given below.

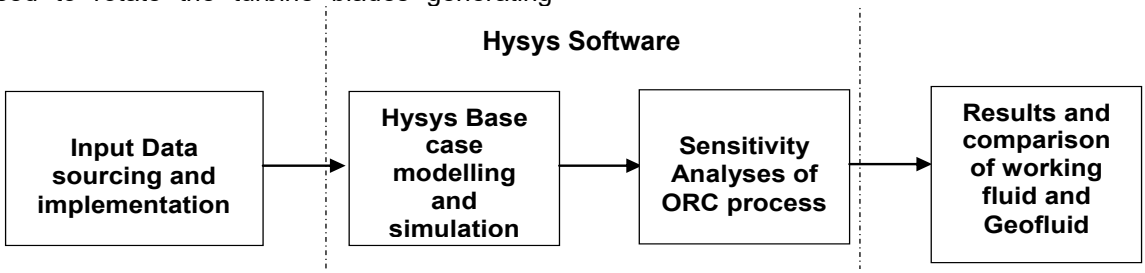

Figure 2. Simulation Process Block Diagram

Slika 2. Blok dijagram procesa simulacije

3.1. Input data

The input data comprises the thermodynamic the fluid parameters comprising the temperature, pressure and mass flowrate of the geofluids and the working fluids, the process components parameters, and operating conditions of the ORC system.

The input data is given in Table 1.

Table 1. Input data for process simulation
Tabela 1. Ulazni podaci za simulaciju procesa

Parameter	Value
Turbine isentropic efficiency	75%
Turbine polytropic efficiency	74%
Pump Adiabatic efficiency	75%
Ambient temperature	20°C
Water Mass Flowrate (Base)	80 kg/s
Water inlet temp (Base)	100°C
Water Inlet Pressure (Base	10 bars
CO_2 Mass Flowrate (Base)	80 kg/s
CO_2 inlet temp (Base)	100°C
CO_2 Inlet Pressure (Base	20 Mpa
Working fluid inlet temperature	36.1°C
Working fluid inlet pressure	20 bars
Working fluid mass flowrate (Base)	10 kg/s
Working Fluids	Isopentane, n-pentane
Geofluids	Water, CO_2

3.2. Process Simulation

The process was modelled using Aspen Hysys V11 software. The fluid property package used in the process was Peng Robinson's property package. The main process Hysys process components used includes the heat exchangers which were used to model the evaporators, the expander which was used to model the turbine, the air cooler which was used to model the condenser, and the pump. Two heat exchangers in series were used in the modelling. This was required to maximize the heat extraction from the geofluid. The process flow diagram (PFD) for the ORC process simulated in Hysys is given in figure 3.

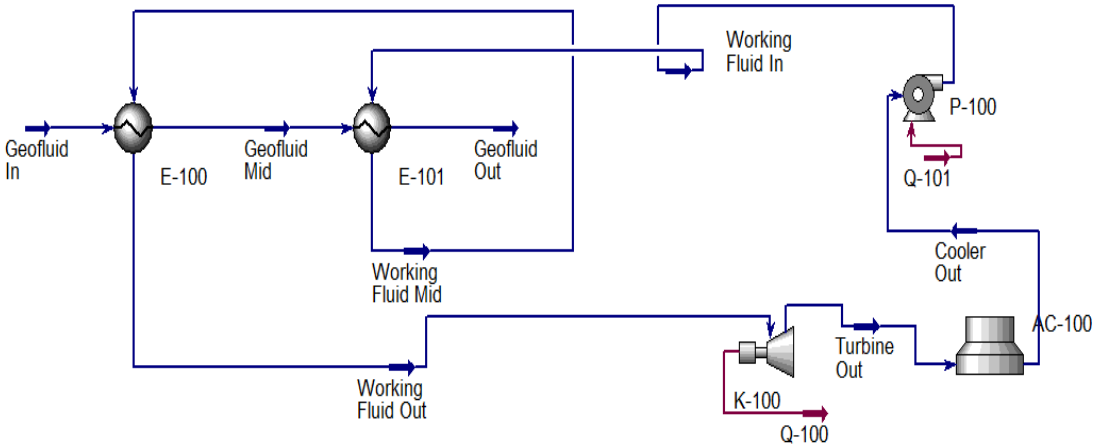

Figure 3. Process flow diagram (PFD) of the geothermal binary ORC system
Slika 3. Dijagram toka procesa (PFD) geotermalnog binarnog ORC sistema

Following figure 3, the geofluid coming from the well enters into HEX1 (E-100) and subsequently to HEX2 (E-101). The working fluid pumped into the heat exchangers extracted heat both from HEX2 and HEX1 and then exits HEX1 towards the turbine. At the turbine, the vapourized working fluid caused expansion which was used to rotate the turbine producing electricity. The electrical power was measured in kW at the turbine outlet. The working fluids exits the turbine at lower temperature and pressure and goes to the air cooler where it is cooled and then pumped back to the HEXs to continue the cycle. The Geofluid out from the outlet of HEX2 is injected back into the well and the cycle continues.

3.3. Sensitivity

The process model described above were conducted at base case and at varying process parameters highlighting the sensitivity of the process. Sensitivity analyses were conducted to investigate the effect of geofluid temperature, and working fluid flowrate. These formed the independent variables. The output results of the sensitivity included the electrical power generated and the max working fluid pressure. The two working fluids modelled were isopentane and n-pentane. These sensitivities were performed using water and CO_2 as geofluid-

4. RESULTS

Results of simulations are given and discussed in this section.

4.1. Results using water as geofluid

4.1.1. Effects of temperature on power generated

For water as geofluid, the effect of geofluid temperature on the electrical power produced using isopentane and n-pentane as working fluid is shown in figure 4.

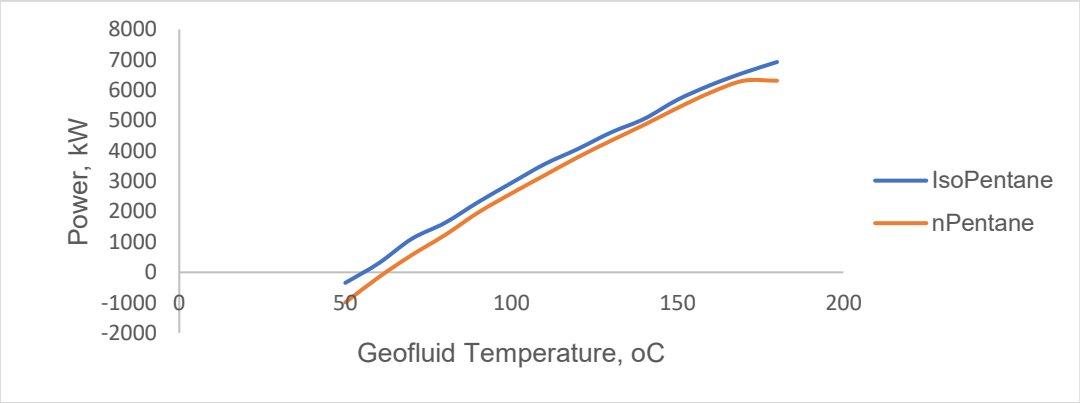

Figure 4. Effect of geofluid temperature on power produced using water as geofluid at 80 kg/s

Slika 4. Uticaj masenog protoka na proizvodnju energije korišćenjem vode kao geofluida na 100 °C

From figure 4, it can be seen that for both isopentane and n-pentane working fluids, the power produced increased as the water temperature is increased. This is expected as increase in temperature increases the thermal capacity of the geofluid, thus increasing its heat transfer to the working fluid for power production at the turbines. Furthermore, it can be observed that the use of isopentane working fluid resulted to higher electrical power generation at the turbine than n-pentane working fluid. Moreover, n-pentane showed negative power production when geofluid temperature was 60 °C while negative power production was observed for isopentane when the temperature of the water was 50 °C. it is seen that isopentane can handle lower temperatures than n-pentane at same operating conditions.

From the chart, at 80 kg/s mass flowrate of working fluid, the outlet power production from the turbine corresponding to isopentane and n-pentane working fluids at geofluid temperature of 180°C are 6924.8 kW and 6308 kW respectively. At this condition, it is seen that the use of isopentane as working fluid increased the power production by 9.8%.

4.1.2. Effects of geofluid temperature on maximum pressure of working fluid for water geofluid

The maximum pressure denotes the range of operability for the working fluid used at the process conditions specified. Figure 4 shows the maximum pressure for isopentane and n-pentane working fluids corresponding to varying temperature of water geofluid investigated.

From figure 5, it can be seen that isopentane showed higher maximum pressure than n-pentane. These pressures affect the outlet temperature of the working fluid from the evaporator. At higher operable pressures, the working fluids exits the evaporator with higher temperatures which translates to higher power production. this highlights the advantage of isopentane as a better working fluid than n-pentane. However, as can be seen from the char, at lower geofluid temperature, the differences in pressures between the two fluids widens.

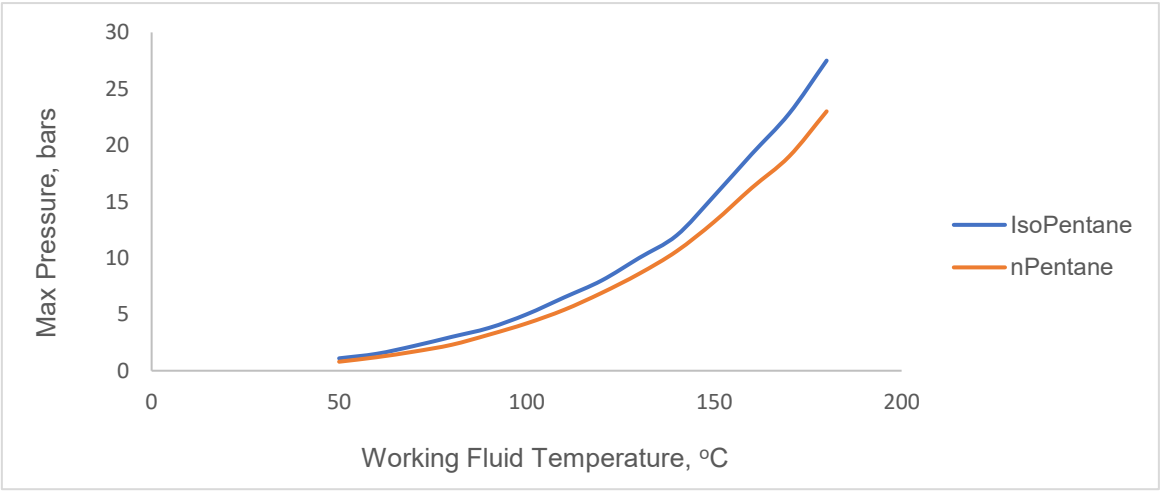

Figure 5. Maximum working fluid outlet pressure for water geofluid

Slika 5. Maksimalni izlazni pritisak radne tečnosti za vodeni geofluid

4.1.3. Effect of working fluid flowrate on power produced

The effect of the mass flowrate of the working fluids on the electrical power output of the turbine is given in this section.

The mass flowrates investigated were within the range of 1 to 100 kg/s at 100 °C. From figure 6, it can be seen that the mass flowrate of the working fluids yielded linearly proportionate increase with power production for both isopentane and n-pentane working fluids. Power increased as mass flowrate of working fluid increased. However, the rate of increase in power for isopentane was higher than that of n-pentane at corresponding mass flowrate of working fluids. Moreover, the nominal differences in the power produced relative to the mass flowrates of the working fluids increased progressively as the mass flowrate increased although their percentage increased remained constant. For instance, at mass flowrate of 10 kg/s, the power generated using isopentane and n-pentane were 367.8 kW and 324.6 kW respectively which gave a nominal and percentage difference of 43.14 kW and 13.29% respectively. also, at mass flowrate of 100 kg/s, the power generated using isopentane and n-pentane were 3677.6 kW and 3246.3 kW respectively which gave a nominal and percentage difference of 431.4 kW and 13.29% respectively.

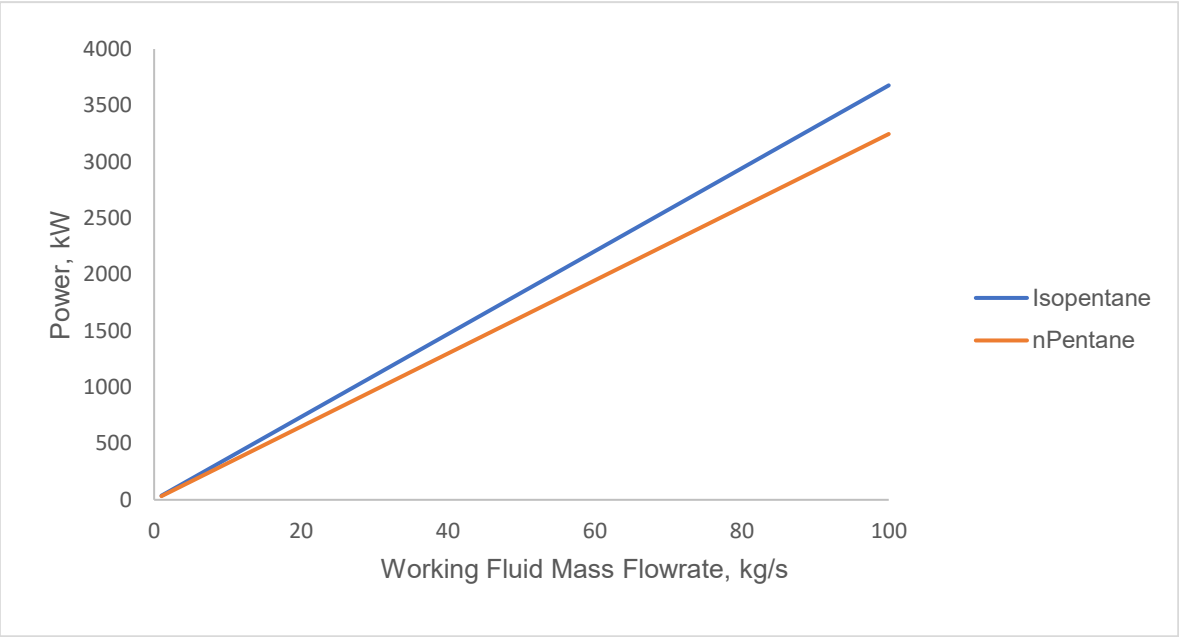

Figure 6. Effect of mass flowrate on power production using water as geofluid at 100°C

Slika 6. Uticaj masenog protoka na proizvodnju energije korišćenjem vode kao geofluida na 100°C

4.2. Results using CO_2 as geofluid

4.2.1. Effects of temperature on power generated

The effect of CO_2 geofluid temperature on the turbine outlet power generation is shown in Figure 7.

It is quickly observed from figure 7 that for CO_2 geofluid system, isopentane serves as a better working fluid than n-pentane demonstrated in the power produced relative to temperature. The power produced for both isopentane and n-pentane increased with increasing geofluid temperature. However, isopentane showed higher power output corresponding to each temperature increase compared to n-pentane. furthermore, it can be seen from the chart, that CO_2 geofluid enable low-temperature binary system. Maximum operable temperature of the CO_2 geofluid was observed at 110°C. This implies that the usage of CO_2 as geofluid includes temperature ranges not greater than 110°C. At higher temperature, the process system. Moreover, isopentane showed better characteristics as a working fluid than n-pentane visible in the power generation. At 80 kg/s mass flowrate of working fluid, the outlet power production from the turbine corresponding to isopentane and n-pentane working fluids at geofluid temperature of 110°C are 3738.4 kW and 3448 kW respectively. At this condition, it is seen that the use of isopentane as working fluid increased the power production by 8.4%.

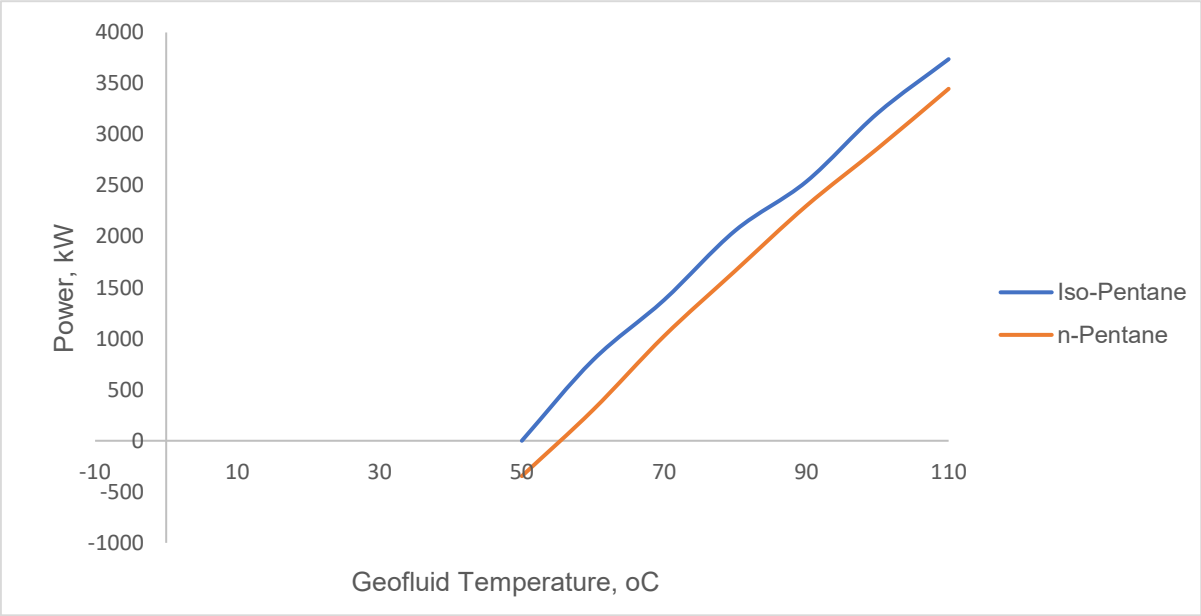

Figure 7. Effect of geofluid temperature on power produced using CO_2 as geofluid at 80 kg/s

Slika 7. Uticaj temperature geofluida na snagu proizvedenu korišćenjem CO_2 kao geofluida pri 80 kg/s

4.2.2. Effects of geofluid temperature on maximum pressure of working fluid for CO_2 geofluid

Figure 8 shows the maximum pressure for isopentane and n-pentane working fluids corresponding to varying temperature of CO_2 geofluid investigated.

From figure 8, it can be seen that isopentane showed higher maximum pressure than n-pentane when used with CO_2 geofluid. At higher operable pressures, the working fluids exits the evaporator with higher temperatures which translates to higher power production. This shows the advantage of isopentane as a better working fluid than n-pentane. However, as can be seen from the chart, at lower geofluid temperature, the differences in pressures between the two fluids widens.

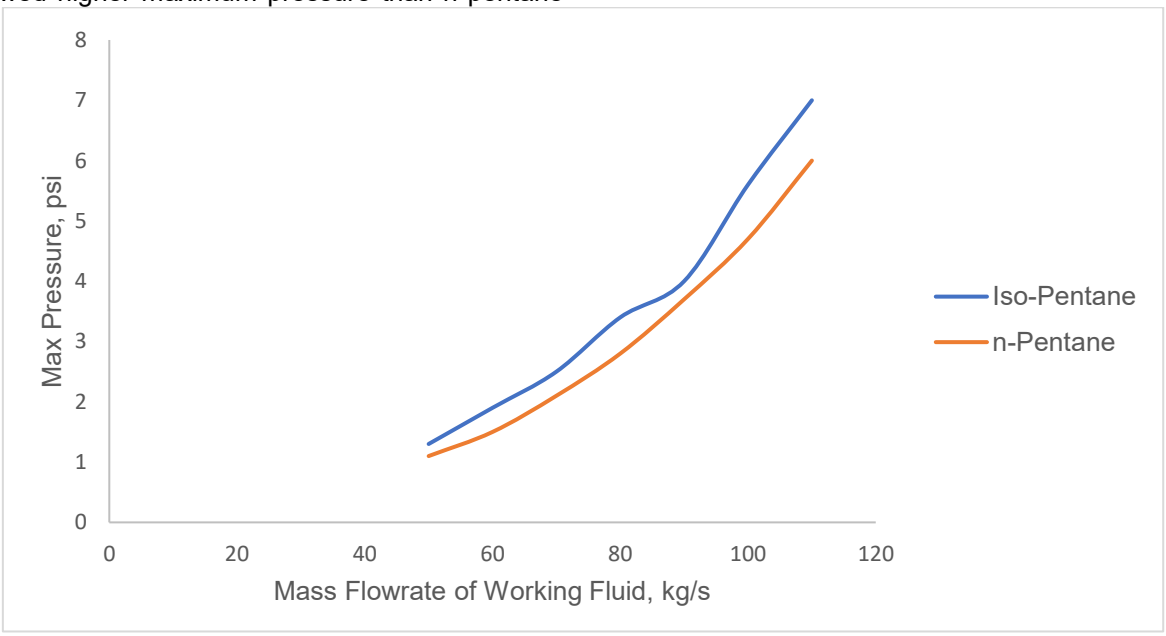

Figure 8. Maximum Working Fluid Outlet Pressure for Water geofluid

Slika 8. Maksimalni izlazni pritisak radne tečnosti za vodeni geofluid

4.2.3. Effect of Working Fluid Flowrate on Power Produced

The effect of the mass flowrate of the working fluids on the electrical power output of the turbine is given in this section.

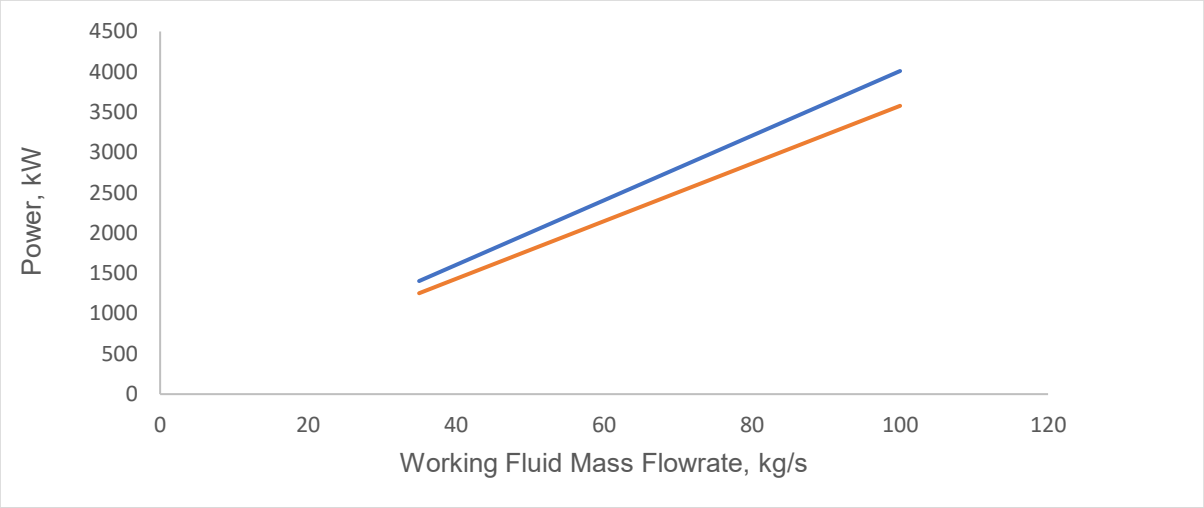

Figure 9. Effect of mass flowrate on power production using CO_2 as geofluid at 100 °C

Slika 9. Uticaj masenog protoka na proizvodnju energije korišćenjem CO_2 kao geofluida na 100 °C

From figure 9, it can be observed that the power produced increased linearly with mass flowrate for both isopentane and n-pentane working fluids. However, the power generated for isopentane working fluid was higher than that of n-pentane at corresponding mass flowrates. At mass flowrate of 10 kg/s, the power generated using isopentane and n-pentane were 4009.7 kW and 3577.9 kW respectively. This gave a nominal and percentage difference of 43.18 kW and 12.07 % respectively. Furthermore, at mass flowrate of 100 kg/s, the power generated using isopentane and n-pentane were 3677.6kW and 3246.3kW respectively which gave a nominal and percentage difference of 431.4 kW and 12.07 % respectively

4.2.4. Comparison of Water and CO_2 as geofluids

Comparison of the simulation results is made relative to water and CO_2 as geofluids.

Figure 9 shows the effect geofluid temperature on power production using water and CO_2 geofluids.

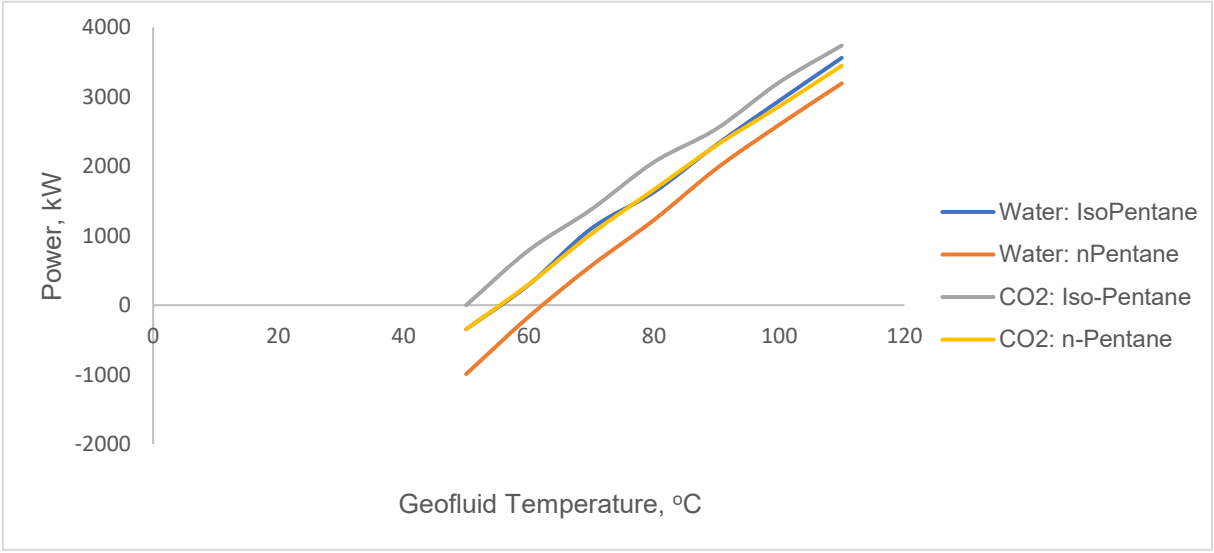

Figure 10. Effect of Geofluid on power production using water and CO_2 geofluids

Slika 10. Uticaj Geofluida na proizvodnju energije korišćenjem vode i CO_2 geofluida

From figure 10, it can be observed that the power produced from CO_2 geofluid is significantly higher than that of water at all geofluid temperatures. This was observed for both isopentane and n-pentane working fluids respectively. The comparison was made for geofluids temperatures within the range of 50 ^oC to 110 ^oC. This was necessary since the CO_2 geofluid showed maximum temperature operability at 110 ^oC. At 110 ^oC, the power produced using water geofluid at 80kg/s mass flowrate are 3560.8 kW and 3193.6 kW for isopentane and n-pentane working fluids respectively while the power produced at the same conditions for CO_2 geofluids are 3738.4 kW and 3448 kW for isopentane and n-pentane working fluids respectively. CO_2 geofluid showed 5% and 8% higher power generation than water for isopentane and n-pentane working fluids respectively. CO_2 proves a better geofluid than water for geothermal heat exploitation for low-temperature geothermal systems.

CO_2 has been selected as geofluid to its high compressibility, expansivity and low viscosity in comparison to water. However, CO_2 is feasible at lower temperatures, transferring geothermal heat more efficiently than water. Using CO_2 as working fluid fosters the utilization of low-temperature geothermal systems enabling the widespread adoption of the renewable resource.

4.3. Discussion

The study presented the modelling of a binary Organic Rankine Cycle (ORC) system used for electricity generation using geothermal fluids. Heat from a geothermal reservoir to generate power using water and CO_2 as the heat extraction fluids (geofluids). The geothermal fluid is sent to an evaporator where it heats the working fluid, causing it to vaporize and subsequently to produce electricity in the turbine. Two working fluids, isopentane and n-pentane, were considered, and simulations were conducted using both water and CO_2 as geofluids. A complete thermodynamic modelling and simulation of the process was conducted in Aspen Hysys. The process, environmental and economic aspect of the study are discussed.

4.3.1. Process Consideration

From the results on the effects of geofluid temperature on power generation, it was observed that power generation increased with higher geofluid temperature. This aligns with the basic principles of thermodynamics. As the geofluid temperature rises, it carries more thermal energy, leading to increased heat transfer to the working fluid in the evaporator. This results in higher vaporization and subsequently greater expansion in the turbine, generating more power. This phenomenon is well-established in heat-to-power conversion processes.

Furthermore, it was observed that isopentane showed higher power generation compared to n-pentane at all geofluid temperatures. The results can be attributed to the distinct thermodynamic properties of isopentane and n-pentane. Isopentane has higher boiling point, specific heat capacity, and vaporization than n-pentane. These characteristics contribute to its superior performance enhancing its ability to absorb heat from the geofluid, resulting in more efficient vaporization and expansion in the turbine.

It was also observed that Isopentane could handle lower temperatures than n-pentane. The ability of isopentane to handle lower temperatures ranges highlights its usage in the design and exploitation of wider range of geothermal resources.

It was observed that Isopentane generally exhibited higher maximum pressure than n-pentane, indicating a better performance in terms of operability. Higher maximum pressures indicate the working fluid's capacity to expand more in the turbine, which translates to greater mechanical work done, hence higher power output. Furthermore, higher pressure allowed the working fluid to exit the evaporator at higher temperatures, resulting in higher power generation.

Furthermore, it was observed from the results that power generation increased linearly with the mass flow rate of the working fluids. Higher mass flowrates of the working fluids translate to higher heat energy extraction from the geofluid resulting to increased power generation. Isopentane had a higher rate of increase in power compared to n-pentane at the same mass flow rate which as has been demonstrated highlights its much-enhanced thermodynamic properties.

CO_2 geofluid performed better than water geofluid in terms of power generation across various geofluid temperatures. CO_2 possess higher compressibility and expansivity, lower viscosity compared to water, which makes it a more efficient heat transfer fluid. The maximum operable temperature for CO_2 geofluid which was observed at 110°C suggests that CO_2 is well-suited for low-temperature geothermal systems. Thus, CO_2 characteristics as a geofluid enable the utilization of low-temperature geothermal resources. Due to its specific heat capacity and compressibility, CO_2 can efficiently transfer heat at the lower temperatures.

4.3.2. Environmental Considerations

The results indicate that CO_2 can lead to higher power generation and efficiency in low-temperature geothermal systems. This is important when environmental consideration is paramount, as increased process efficiency translates to higher power output from the same amount of heat. This potentially reduces the need for additional heat extraction, thus minimizing the environmental impact on geothermal reservoirs. Furthermore, the use of CO_2 as geofluid in geothermal systems aligns with the broader goals of reducing greenhouse gas emissions and transitioning to cleaner energy sources. The thermodynamic properties of CO_2 contribute to better heat transfer between the geothermal reservoir and the working fluid, potentially reducing the need for aggressive reservoir stimulation thus inducing positive implications for maintaining reservoir integrity and minimizing induced seismicity potentially widespread with water as geofluid.

On the other hand, while water is a natural choice for geofluid, its extraction and reinjection could have local environmental effects. Altering the temperature and pressure of the geothermal reservoir can affect the subsurface ecosystem, potentially impacting local ecosystems and water resources. Water might not be as efficient as CO_2 in low-temperature geothermal systems, which could lead to a higher environmental footprint. Extracting more water from the reservoir to achieve the desired power output might have greater ecological consequences.

4.3.3. Economic Considerations

In terms of economics, while the potentials of CO_2 for higher power output translates to more revenue from electricity sales, CO_2 project has more complex designs requiring higher upfront investment and operational costs than water. Also, the use of water as geofluid has reduced uncertainty during project implementation. Water extraction and reinjection regulations can vary by region. If local regulations favour water use over CO_2, this might influence the economic feasibility of geothermal projects. However, the characteristics of CO_2 for low-temperature geothermal resource exploitation expands the potential for geothermal power generation, maximizing resource utilization and potentially attracting more investment. Thorough economic investigation of CO_2 and water as geofluid in geothermal resource extraction would aid decision process in the choice of the geothermal heat extraction fluid.

5. CONCLUSION

This study presented a comprehensive analysis of a binary Organic Rankine Cycle (ORC) system for electricity generation using geothermal fluids as heat sources and hydrocarbon fluids as working fluids. Isopentane and n-pentane were used as the working fluid for binary system turbine electricity generation. The study focused on the comparison between water and CO_2 as geofluids, assessing their impacts on power generation, efficiency, and operability.

Base on process considerations from the simulation performed, both isopentane and n-pentane geofluids exhibited thermodynamic behaviour that showed theoretical correlations. Higher geofluid temperatures led to increased power generation, attributed to the greater heat transfer and subsequent vaporization of the working fluid in the evaporator. Isopentane consistently outperformed n-pentane due to its better thermodynamic properties, resulting in higher power output and broader operational temperature range.

CO_2 as a geofluid demonstrated significant advantages, highlighting its potential as a more efficient heat transfer medium compared to water. The unique characteristics of CO_2, such as high compressibility, expansivity, and low viscosity, translated to higher power generation. This is particularly significant for enabling the utilization of low-temperature geothermal resources, which is critical for sustainable geothermal energy development.

Environmental considerations highlighted CO_2's alignment with clean energy goals, contributing to reduced emissions and better reservoir management. Additionally, CO_2's potential for lower seismic impact due to enhanced heat transfer characteristics is a positive aspect in terms of reservoir integrity and induced seismicity.

Economically, the choice between CO_2 and water as geofluids involves a trade-off. While CO_2 presents the potential for higher power output and revenue generation, it also entails more complex system designs and potentially higher upfront investments. Water, being a well-established geofluid, offers simpler project implementation and operational advantages but might have limitations in terms of efficiency and resource utilization. Further research on economic evaluations were suggested as it is essential to fully determine the feasibility and sustainability of using CO_2 as a geofluid for geothermal heat extraction.

6. REFERENCES

[1] A.Sowiżdżał, W.Górecki, M.Hajto (2020) Geological conditions of geothermal resource occurrences in Poland. *Geological Quarterly*, *64*(1), 185-196.

[2] P.Ziółkowski, R.Hyrzyński, M.Lemański, B.Kraszewski, S.Bykuć, S.Głuch, J.Badur (2021) Different design aspects of an Organic Rankine Cycle turbine for electricity production using a geothermal binary power plant. *Energy Conversion and Management*, *246*, 114672.

[3] P.Ziółkowski, T.Kowalczyk, M.Lemański, J.Badur (2019) On energy, exergy, and environmental aspects of a combined gas-steam cycle for heat and power generation undergoing a process of retrofitting by steam injection. *Energy Conversion and Management*, *192*, 374-384.

[4] R.Hyrzyński, P.Ziółkowski, S.Gotzman, B.Kraszewski, T.Ochrymiuk, J.Badur (2021) Comprehensive thermodynamic analysis of the CAES system coupled with the underground thermal energy storage taking into account global, central and local level of energy conversion. *Renewable Energy*, *169*, 379-403.

[5] J.Badur, M.Lemański, T. Kowalczyk, P. Ziółkowski, S. Kornet (2018) Zero-dimensional robust model of an SOFC with internal reforming for hybrid energy cycles. *Energy*, *158*, 128-138.

[6] M.Kantorek, K.Jesionek, S.Polesek-Karczewska, P.Ziółkowski, M.Stajnke, J.Badur (2021) Thermal utilization of meat-and-bone meal using the rotary kiln pyrolyzer and the fluidized bed boiler–The performance of pilot-scale installation. *Renewable Energy*, *164*, 1447-1456.

[7] A.Wachowicz-Pyzik, A.Sowiżdżał, L.Pająk, P.Ziółkowski, J.Badur (2020) Assessment of the Effective Variants Leading to Higher Efficiency for the Geothermal Doublet, Using Numerical Analysis–Case Study from Poland (Szczecin Trough). *Energies*, *13*(9), 2174.

[8] X.Dai, L.Shi, W.Qian (2019) Thermal stability of hexamethyldisiloxane (MM) as a working fluid for organic Rankine cycle. *International Journal of Energy Research*, *43*(2), 896-904.

[9] P.Niknam, L.Talluri, D.Fiaschi, G.Manfrida (2021) Sensitivity analysis and dynamic modelling of the reinjection process in a binary cycle geothermal power plant of Larderello area. *Energy*, *214*, 118869.

[10] A.Sowizdzal (2018) Geothermal energy resources in Poland–Overview of the current state of knowledge. *Renewable and Sustainable Energy Reviews*, *82*, 4020-4027.

[11] M.Kaczmarczyk, B.Tomaszewska, L.Pająk (2020) Geological and thermodynamic analysis of low enthalpy geothermal resources to electricity generation using ORC and Kalina cycle technology. *Energies*, *13*(6), 1335.

[12] M.Pasetti, C.Invernizzi, P.Iora (2014) Thermal stability of working fluids for organic Rankine cycles: An improved survey method and experimental results for cyclopentane, isopentane and n-butane. *Applied Thermal Engineering*, *73*(1), 764-774.

[13] M.Ashouri, M.Ahmadi, M.Feidt (2014) Performance analysis of organic Rankine cycle integrated with a parabolic through solar collector. In *Conference paper. The 4th World Sustainability Forum*.

[14] M.Salman, J.Hennessy, H.Li (2017) Evaluating the Organic Rankine Cycle (Orc) for Heat to Power. Book, Publication: Malardalens Universitet.

[15] Y.Najjar, A.Qatramez (2019) Energy utilisation in a combined geothermal and organic Rankine power cycles. International Journal of Sustainable Energy, 38(9), 831-848.

[16] R.Wang, L.Jiang, Z.Ma, A.Gonzalez-Diaz, Y.Wang, A.Roskilly (2019) Comparative analysis of small-scale organic Rankine cycle systems for solar energy utilisation. *Energies*, *12*(5), 829.

[17] Y.Wang, J.Song, M.Chatzopoulou, N.Sunny, M.Simpson, J.Wang, C.Markides (2021) A holistic thermoeconomic assessment of small-scale, distributed solar organic Rankine cycle (ORC) systems: Comprehensive comparison of configurations, component and working fluid selection. *Energy Conversion and Management*, *248*, 114618.

[18] J.Song, P.Loo, J.Teo, C.Markides (2020) Thermo-economic optimization of organic Rankine cycle (ORC) systems for geothermal power generation: A comparative study of system configurations. *Frontiers in Energy Research*, *8*, 6.

[19] J.Song, Y.Wang, K.Wang, J.Wang, C.Markides (2021) Combined supercritical CO2 (SCO2) cycle and organic Rankine cycle (ORC) system for hybrid solar and geothermal power generation: Thermoeconomic assessment of various configurations. *Renewable Energy*, *174*, 1020-1035.

[20] A.Sowiżdżał, B.Papiernik, G.Machowski, M.Hajto (2013) Characterization of petrophysical parameters of the Lower Triassic deposits in prospective location for Enhanced Geothermal System (central Poland). *Geological Quarterly*, *57*, 729-744.

[21] K.Barse (2014) *Design and optimization of organic rankine cycle for low temperature geothermal power plant*. The University of North Dakota.

[22] M. Bahrami, F. Pourfayaz, A. Kasaeian (2022) Low global warming potential (GWP) working fluids (WFs) for Organic Rankine Cycle (ORC) applications. *Energy Reports*, *8*, 2976-2988.

[23] H.D.Venomhata, P.Oketch, B.Gathitu, P. Chisale (2023) Working fluid selection for the geothermal-solar hybrid cycle at Olkaria II power plant in Kenya. *Heliyon*, *9*(1), 1-15.

[24] C.Choudhari, S.Sapali (2017) Performance investigation of natural refrigerant R290 as a substitute to R22 in refrigeration systems. *Energy Procedia*, *109*, 346-352.

[25] B.Kępińska (2019) Geothermal energy use—Country update for Poland, 2016–2018. In *European Geothermal Congress*.

IZVOD

KOMPARATIVNA ANALIZA GEOTERMALNIH BINARNIH ORC SISTEMA: PERFORMANSE I RAZMATRANJA ŽIVOTNE SREDINE ZA CO_2 I VODU KAO GEOFLUIDE

Ova studija razmatra simulaciju procesa geotermalnih binarnih sistema organskog Rankinovog ciklusa (ORC) koji koriste CO_2 i vodu kao geofluide za proizvodnju električne energije. Simulacija je izvedena korišćenjem softvera Hisis v11 korišćenjem Peng Robinsonovog paketa fluidnih svojstava. Korišćene su dve suve radne tečnosti uključujući izopentan i n-pentan. Ocenjeni su uticaji temperature geofluida i masenog protoka radnog fluida na proizvodnju električne energije, kao i maksimalnog pritiska radnih fluida. Rezultat je pokazao da se proizvodnja energije povećava sa višom temperaturom geofluida zbog poboljšanog prenosa toplote. Izopetan je nadmašio n-pentan, što se pripisuje njegovim superiornim termodinamičkim svojstvima. CO_2 je pokazao bolje performanse kao geofluid od vode, naglašavajući njegovu superiornost, primećenu u povećanju proizvodnje energije. Jedinstvene karakteristike CO_2 omogućavaju efikasan prenos toplote na nižim temperaturama, što ga čini ekološki prihvatljivim i efikasnim izborom. Nasuprot tome, upotreba vode kao geofluida predstavlja neke implikacije za lokalne ekosisteme i vodne resurse. Iz perspektive životne sredine, CO_2 pokazuje veći potencijal za smanjenje uticaja na životnu sredinu, što je u skladu sa prelaskom na čistije izvore energije. Međutim, ekonomska razmatranja sugerišu kompromis, jer projekti CO_2 mogu dovesti do većih početnih troškova u poređenju sa sistemima zasnovanim na vodi. Regulatorni faktori i ekonomska izvodljivost, stoga, igraju ključnu ulogu u izboru geofluida za proizvodnju geotermalne energije.

Ključne reči: *Geofluid, radni fluid, ORC, obnovljiva energija*

Naučni rad
Rad primljen: 21.09.2023.
Rad prihvaćen: 07.10.2023.
Rad je dostupan na sajtu: www.idk.org.rs/casopis

Balakrishnan Latha[1]*, *Kaliyaperumal Kavitha*[1]
Susai Rajendran[2,3]

[1]*PG and Research Department of Chemistry, National College (Autonomous),Tiruchirappalli, Affiliated to Bharathidasan University, Tiruchirappalli, Tamil Nadu, India,* [2]*PG Department of Chemistry, Corrosion Research Centre, St. Antony's College of Arts and Sciences for Women, Dindigul, Affiliated to Mother Teresa Women's University, Kodaikanal, Tamil Nadu, India,* [3]*Centre for Nanoscience and Technology, Pondicherry University, Puducherry, India*

Scientific paper
ISSN 0351-9465, E-ISSN 2466-2585
https://doi.org/10.62638/ZasMat1005

Zastita Materijala 65 (1)
86 - 96 (2024

Inhibition of corrosion of mild steel in simulated oil well water by aqueous extract of *Hibiscus rosa-sinensis* flower

ABSTRACT

An aqueous extract of Hibiscus rosa-sinensis flower (HRF) has been used as corrosion inhibitor in controlling the corrosion of mild steel in simulated oil well water (SOWW). Weight loss method reveals that 10 % v/v of the extract offers 82 % inhibition efficiency (IE) to mild steel (MS) immersed SOWW. The mechanistic aspects of corrosion inhibitive effect have been investigated by polarization study and AC impedance spectra. Polarization study reveals that the mixed type of inhibitor in the presence of inhibitor system. The corrosion inhibition effect is confirmed by the increase in the linear polarization resistance value and decrease in the corrosion current value. The protective layer is formed on the metal surface is confirmed by the AC impedance spectra. This is confirmed by the fact that there is increase in charge transfer resistance value and decrease in the double layer capacitance value. The adsorption of inhibitor molecule obey Langmuir adsorption isotherm. The protective coating is characterized by FTIR spectroscopy. It confirms that the inhibitor has coordinated with ferrous ion the metal surface through the active principle component of β-sitosterol, quercetin and kaempferol-3-xylosylglucoside. The surface morphology has been investigated by scanning electron microscopy (SEM). Hence, aqueous extract of Hibiscus rosa-sinensis flower with simulated oil well water good corrosive inhibitive effect on pipeline made of mild steel.

Keywords: *Hibiscus rosa-sinensis, simulated oil well water, mild steel, corrosion inhibition, surface morphology, SEM*

1. INTRODUCTION

Corrosion normally occurs in oil and gas pipelines. Since the pipelines play the role of transporting oil and gas from the wellheads to the processing facilities, they are exposed to the continuous threat of corrosion, from the date of commissioning up to decommissioning or abandonment [1]. Almost any aqueous environment can promote corrosion, which occurs under numerous complex conditions in oil and gas production, processing and pipeline systems [2]. Internal corrosion in oil and gas industry is generally caused by water, carbon dioxide (CO_2) and hydrogen sulfide (H_2S) and also can be aggravated by microbiological activity [3]. One method used to reduce corrosion in the petroleum industry is corrosion inhibitors. The inhibitors must be put above a specific minimum concentration to obtain an optimal inhibition.

The plant extraction may become corrosion inhibitors due to the advantages of wide sources and biodegradation. It was previously reported that the extracts of *Napoleonaeaimperalis* [4], *Cardiospermumhalicacabum* leaf [5,6], *Tiliacordata* [7], *Morindacitrifolia* [8], *Acanthus montanus* [9] and *Calotropisprocera* [10] showed corrosion inhibition. Heteroatoms such as nitrogen (N), oxygen (O), sulfur (S) and phosphorus (P) can be used as adsorption centers of inhibitor molecules and these atoms also have become important features of efficient corrosion inhibitors. Anuratha et al have used the corrosion inhibition of carbon steel in low chloride media by an aqueous extract of *Hibiscus rosa-sinensis* [11]. Rajendran et al have studied the corrosion behaviour of aluminium in the presence of an aqueous extract of *Hibiscus rosa-sinensis*

*Corresponding author: Balakrishnan Latha
E-mail: susairajendran@gmail.com
Paper received: 24. 09. 2023.
Paper accepted: 03. 10. 2023.
Paper is available on the website: www.idk.org.rs/journal

[12], Desai have studied the *Hibiscus rosa-sinensis* leaves extracts used as corrosion inhibitors for mild steel in HCl [13]. However, to the best of our knowledge the aqueous extract of *Hibiscus rosa-sinensis* flower has not been investigated in SOWW medium for its anticorrosion properties.

Hibiscus rosa-sinensis (Figure 1) is a perennial ornamental woody plant; belong to Malvaceae family available throughout India. Various parts of this plant like roots, leaves and flowers have been known to possess medicinal properties like anti inflammatery, antifungal, anti-microbial, oral contraceptive, laxative, aphrodisiac, menorrhagicetc [14]. The aqueous extract of *Hibiscus rosa-sinensis* flower contain main active principle constituents such as β-sitosterol, quercetin and kaempferol-3-xylosylglucoside [15].

In the present study, the corrosion inhibitive properties of the aqueous extract of *Hibiscus rosa-sinensis* flower (HRF) in controlling corrosion of mild steel in SOWW solution have been investigated by weight loss and electrochemical study. The HRF extract of active principle constituents have been characterized by FTIR, with the formation of protective film formation against corrosion. The morphology of the mild steel surface was examined by SEM.

Figure 1. Hibiscus rosa-sinensis flower

Slika 1. Cvet Hibiscus rosa-sinensis

2. MATERIALS AND METHODS

Preparation of inhibitor

The aqueous extract of *Hibiscus rosa-sinensis* flower (HRF) were prepared by the method of soxhlet extraction. About 100 g of powdered plant of *Hibiscus rosa-sinensis* flower was uniformly packed into thimble and extracted with 1000 ml of double distilled water. The process of extraction continues till the solvent in siphon tube of the extractor becomes colourless. After the process of extraction, the extract was kept overnight for cooling and made up to 1000 ml with the same double distilled water to get 10 % (w/v) extract.

Preparation of simulated oil well water (SOWW)

In 100 mL of DD water, sodium chloride (3.5 g), calcium chloride (0.305 g) and magnesium chloride (0.186 g) are added. Just before experiment add 0.067 g sodium sulfide and 0.4 mL of concentrated hydrochloric acid to generate hydrogen sulfide gas to form a simulated oil well water containing 100 ppm of H_2S [16].

Preparation of mild steel (MS)

Mild steel specimens (0.0267 % S, 0.06 % P, 0.4 % Mn, 0.1 % C and the rest iron) of dimensions 1.0 cm x 4.0 cm x 0.2 cm were polished to a mirror finish and degreased with acetone.

Weight loss method

Mild steel specimens in triplicate were immersed in 100 ml of the simulated oil well water containing various concentrations of the inhibitor (aqueous extract of *Hibiscus rosa-sinensis* flower) for a period of one day. The weight of the specimens before and after immersion was determined using a Shimadzu balance, model AY62. The corrosion products were cleaned with Clarke's solution [17]. The corrosion rate were calculated using the following equation [18,19].

$$Corrosion\ rate = W/AT$$

Where

W = loss in weight (mg)

A = surface area of the specimen (dm^2)

T = period of immersion (days)

The corrosion rate is expressed in mdd units [mdd = mg/(dm^2)(day)]

The inhibition efficiency was calculated using the relation.

$$Inhibition\ efficiency = [(CR_1-CR_2)/CR_1] \times 100\ \%$$

Where

CR_1= corrosion rate in the absence of inhibitor

CR_2 = corrosion rate in the presence of inhibitor.

Electrochemical studies

In the present work, corrosion resistance of MS immersed in various test solutions were measured by polarization study and AC impedance spectra.

Polarization study

Polarization studies were carried out in a CHI-electrochemical work station with impedance model

660A. It was provided with iR compensation facility. A three electrode cell assembly was used. Mild steel was used as working electrode, platinum as counter electrode and saturated calomel electrode (SCE) as reference electrode. From polarization study, corrosion parameters such as corrosion potential (E_{corr}), corrosion current (I_{corr}), Tafel slopes, anodic=b_a and cathodic=b_c and linear polarization resistance (LPR) value were calculated.

AC Impedance spectra

The same instrument and set-up used for polarization study was used to record AC impedance spectra also. A time interval of 5 to 10 min was given for the system to attain a steady state open circuit model. The real part (Z') and imaginary part (-Z") of the cell impedance were measured in Ohms at various frequencies. AC impedance spectra were recorded with initial E(V) = 0, high frequency (1-10^5 Hz), low frequency (1 Hz), amplitude (V) = 0.005 and quiet time (s) = 2. From Nyquist plot the values of charge transfer resistance (R_t) and the double layer capacitance (C_{dl}) values were calculated.

FTIR spectra

FTIR spectra were recorded in a Perkin - Elmer "Spectrum Two" spectrophotometer. The film was carefully removed, mixed thoroughly with KBr made in to pellets and FTIR spectra were recorded.

Scanning electron microscopy (SEM)

The mild steel specimens immersed in various test solutions for one day were taken out, rinsed with double distilled water, dried and subjected to the surface examination. The surface morphology measurements of the mild steel surface were carried out by scanning electron microscopy (SEM) using CAREL ZEISS make model EVO-18.

3. RESULTS AND DISCUSSION

Pipelines made of MS are used to carry oil well water in petroleum industry. These pipes may undergo inner corrosion. To prevent corrosion, corrosion inhibitors are used. The corrosion resistance of MS in SOWW, has been evaluated by polarization study and AC impedance spectra. Surface morphology was analysed by scanning electron microscopy. Aqueous extract of HRF has been used as corrosion inhibitor.

Weight loss method

The corrosion rate of mild steel in SOWW is studied by weight loss method in the absence and presence of aqueous extract of *Hibiscus rosa-sinensis* flower (HRF) on immersion period of one day at 30°C and the percentage inhibition efficiency is calculated. Table 1 shows the variation of corrosion rate (mdd), inhibition efficiency (IE in %) and surface coverage (θ) with varying concentration of inhibitor (in % v/v). From the data, it is observed that corrosion rate is significantly lowered down in the presence of the inhibitor. The corrosion rate is found to be dependent on the concentration of the inhibitor. With the increase in concentration, the corrosion rate decreases gradually. The decrease in the corrosion rate is due to the presence of active phytochemicals.

Figure 2 shows the variation of corrosion rate (CR) with concentration of inhibitor (in % v/v) and the data reveals that inhibition efficiency increases with increase in the concentration of the inhibitor (HRF) in SOWW medium. The maximum inhibition efficiency of 82 % is noticed at 10 % v/v of the inhibitor concentration. The decreasing corrosion rate and increasing inhibition efficiency are attributed to the adsorption of inhibitor on the metal surface.

Table 1. The corrosion rate, inhibition efficiency and surface coverage of aqueous extract of HRF on MS in SOWW at room temperature (303K)

Tabela 1. Brzina korozije, efikasnost inhibicije i pokrivenost površine vodenog ekstrakta HRF na MS u SOWW na sobnoj temperaturi (303K)

Inhibitor (HRF % v/v)	Corrosion rate (CR) mdd	IE%	Surface coverage (θ)
0	15.55	-	-
2	6.53	58	0.580
4	5.44	65	0.650
6	4.35	72	0.720
8	3.11	80	0.800
10	2.80	82	0.820

The increase in the concentration increases the surface coverage due to adsorption which increases the active sites on the metal surface. Hence, the inhibition efficiency increases with increase in the concentration. The presence of lone pair of electrons on the hetero atoms of oxygen facilitates the formation of co-ordinate bonds with the metal and is responsible for corrosion inhibition. Most of the effective organic inhibitors used in petroleum industry have hetero atom such as O, N and S along with multiple bonds in their molecules through which they are adsorbed on the metal surface [20, 21].

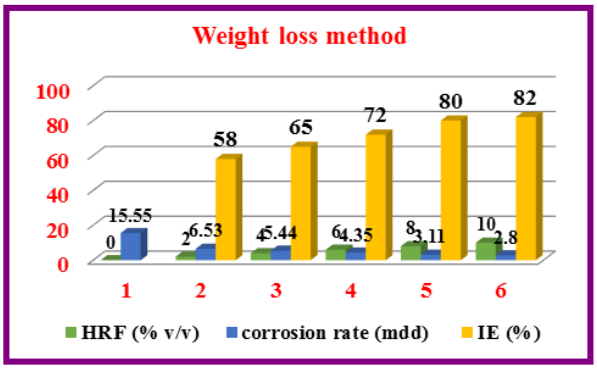

Figure 2. Column chart: HRF (% v/v), corrosion rate (mdd) and IE (%) of MS in SOWW medium in absence and presence of different concentrations of inhibitor (HRF)

Slika 2. Kolona grafikon: HRF (% v/v), brzina korozije (mdd) i IE (%) MS u SOWW medijumu u odsustvu i prisustvu različitih koncentracija inhibitora (HRF)

Adsorption isotherm

An adsorption isotherm gives the direct relationship between the corrosion inhibition efficiency with the degree of surface coverage at constant temperature for different concentrations of inhibitor solutions. The adsorption isotherm provides the basic information about the nature of interaction between the mild steel surface and inhibitor molecular constituents [22]. Adsorption of the corrosion inhibitor molecules occurs on the mild steel surface by the displacement of molecule of water adsorbed on the metal surface. Also, the adsorption depends on the temperature, chemical composition and constituents of inhibitor and the electrochemical potential at the metal-solution interface [23, 24].

Langmuir adsorption isotherm was proposed to account for the adsorption of the corrosion inhibitor molecules on the surface of metal. From the isotherm, the linear relationship between θ and concentration of inhibitor can be found.

Advantage of use of Langmuir adsorption isotherm

The Langmuir isotherm model is one of the most common and simple to use isotherms due to its effectiveness in low concentrations, exibility with computer simulations, and easy handling. The Langmuir adsorption isotherms predict linear adsorption at low adsorption densities and a maximum surface coverage at higher solute metal concentrations.

To specify the adsorption mode of *Hibiscus rosa-sinensis* flower extract molecules on the mild steel surface in the SOWW medium, the degree of surface coverage (θ) for different concentrations of inhibitor (2, 4, 6, 8 and 10 % v/v) at room temperature was found from the weight loss method. According to Langmuir adsorption isotherm, the following equation relates the surface coverage (θ) and inhibitor concentration, C.

$$C/\theta = 1/K_{ads} + C$$

The plot of Langmuir adsorption isotherm, C/θ vs C is shown in Figure 3. The ΔG^0_{ads} is calculated from the equation.

$$\Delta G^0_{ads} = -2.303\ RT \log (K_{ads} \times 55.55)$$

The values of adsorption parameters obtained from Langmuir adsorption includes free energy of adsorption (ΔG^0_{ads}), equilibrium constant (K_{ads}), coefficient of correlation (R^2), slope and intercept values are presented in Table 2. The R^2 value approaches unity. The value of standard free energy of adsorption is -8.905 kJmol^{-1} indicates the physical adsorption process. The negative sign indicates that the adsorption of the inhibitor (HRF) constituents on the metal is a spontaneous process and adsorption takes place very easily without requiring any extra energy. These observations indicates that the adsorption of inhibitor molecules on the metal surface obey the Langmuir adsorption isotherm [25, 26].

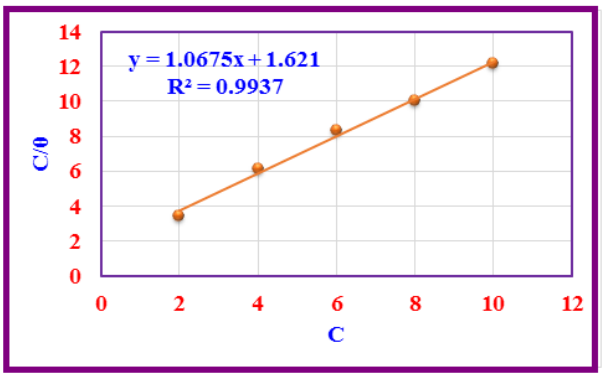

Figure 3. Langmuir adsorption isotherm for the inhibition effect of aqueous extract of HRF on mild steel corrosion in SOWW at room temperature (303 K)

Slika 3. Langmuir-ova adsorpciona izoterma za inhibicioni efekat vodenog ekstrakta HRF na blagu koroziju čelika u SOWW na sobnoj temperaturi (303 K)

Table 2. Adsorption parameters obtained from Langmuir adsorption isotherm for the corrosion inhibitive effect of aqueous extract of HRF on mild steel in SOWW

Tabela 2. Parametri adsorpcije dobijeni iz Langmuir-ove adsorpcione izoterme za inhibicijski efekat vodenog ekstrakta HRF na meki čelik u SOWW

R^2	Slope	Intercept	K_{ads}	ΔG^0_{ads}
0.9937	1.0675	1.621	0.617	-8.905

Electrochemical study

Analysis of polarization study

Polarization study is employed to confirm the formation of protective layer on the MS surface. If a protective layer is formed, the linear polarization resistance (LPR) value increases and the corrosion current (I_{corr}) value decreases. The polarization curves of MS immersed in different environments are shown in Figure 4 and 5.

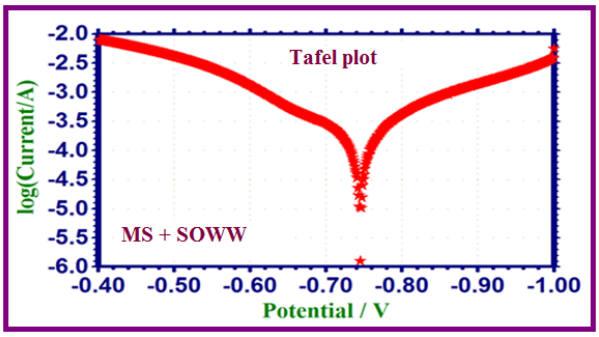

Figure 4. Polarization curves for corrosion of MS immersed in SOWW

Slika 4. Polarizacione krive za koroziju MS uronjenog u SOWW

Polarization parameters such as corrosion potential (E_{corr}) value, corrosion current (I_{corr}) value, linear polarization resistance (LPR) value and Tafel slopes (b_c = cathodic slope and b_a = anodic slope) are calculated from the polarization curves. The values are summarized in Table 3. It is noticed from the Table 3 that when mild steel is immersed in SOWW medium, the corrosion potential (E_{corr}) value is -745 mV vs SCE. The corrosion current (I_{corr}) value is 3.14 x 10^{-4} A/cm^2. The linear polarization resistance (LPR) value is 127 ohm cm^2.

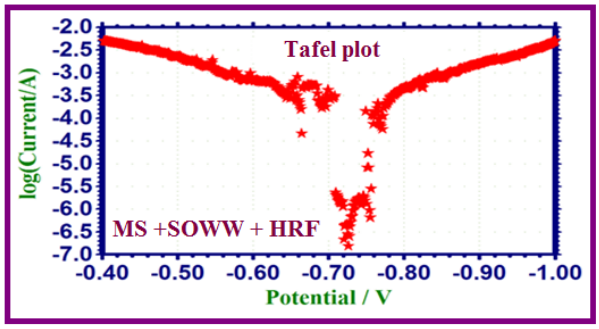

Figure 5. Polarization curve for corrosion of MS immersed in SOWW + 10 % v/v HRF

Slika 5. Kriva polarizacije za koroziju MS uronjenog u SOWW + 10 % v/v HRF

The addition of 10 % v/v of inhibitor (HRF) in SOWW medium the corrosion potential (E_{corr}) value is shifted from -745 to -726 mV vs SCE. This shift is very small. The displacement of E_{corr} is < 85 mV, hence the inhibitor can be classified as a mixed type inhibitor [27] controlling both anodic reaction and cathodic reaction by forming a protectivefilm [28, 29]. When 10 % v/v of HRF is added to the SOWW medium the linear polarization resistance (LPR) value increases from 127 to 662 ohm cm^2. The corrosion current (I_{corr}) value decreases from 3.14 x 10^{-4} to 4.93 x 10^{-6} A/cm^2. The results confirm that a protective layer is formed on the MS surface. Hence the corrosion of MS is controlled.

Table 3. Potentiodynamic polarization parameters of mild steel in SOWW in the absence and presence of aqueous extract of inhibitor (HRF)

Tabela 3. Potenciodinamički parametri polarizacije mekog čelika u SOWW u odsustvu i prisustvu vodenog ekstrakta inhibitora (HRF)

Concentration of aqueous extract of CHL (% v/v)	E_{corr} mV vs SCE	Tafel slope mV/decade		LPR Ohm cm^2	I_{corr} A/cm^2
		b_c	b_a		
0	-745	183	183	127	3.14 × 10^{-4}
10	-726	141	160	662	4.93 × 10^{-6}

Analysis of AC impedance spectra

AC impedance spectra provide information about the formation of protective layer on the MS. If a protective layer is formed on the MS surface, the charge transfer resistance (R_t) value increases; double layer capacitance (C_{dl}) value decreases and the impedance [log (z/ohm)] value enhances. The AC impedance spectra of MS immersed in SOWW medium in presence of inhibitor HRF are shown in Figure 6 and 7. The Nyquist plot and the Bodeplots are shown in Figure 6 and 7 respectively. The corrosion parameters, namely the charge transfer resistance (R_t), double layer capacitance value (C_{dl}) and impedance [log(z/ohm)] value are summarized in Table 4.

It is noticed from the Table 4 that when MS is immersed in SOWW, the charge transfer resistance (R_t) value is 17.435 ohm cm^2. The double layer capacitance (C_{dl}) value is 2.925 x 10^{-7} F/cm^2. The impedance [log (z/ohm)] value is 1.391 and the

phase angle value is 26.58°. In the presence of inhibitor HRF, the charge transfer resistance (R_t) value increases from 17.435 ohm cm^2 to 22.948 ohm cm^2. The double layer capacitance (C_{dl}) value decreases from 2.925x10^{-7} F/cm^2 to 2.223x10^{-7} F/cm^2. The impedance [log (z/ohm)] value increases from 1.391 to 1.936. The phase angle value increases from 26.58° to 28.95°. The results conclude that a protective layer is formed on the MS surface [11, 31, 32]. It restricts the flow of electrons from the MS to the medium. Hence corrosion of MS is controlled.

Table 4. Electrochemical impedance parameters of mild steel in SOWW in the absence and presence of aqueous extract of inhibitor (HRF)

Tabela 4. Parametri elektrohemijske impedanse mekog čelika u SOWW u odsustvu i prisustvu vodenog ekstrakta inhibitora (HRF)

Concentration of aqueous extract of HRF, (% v/v)	Nyquist plot		Bode plot	
	R_t, Ohm cm^2	C_{dl}, F/cm^2	Impedance [log(Z/Ohm)]	Phase angle, (°)
0	17.435	2.925 × 10^{-7}	1.391	26.58
10	22.948	2.223 × 10^{-7}	1.936	28.95

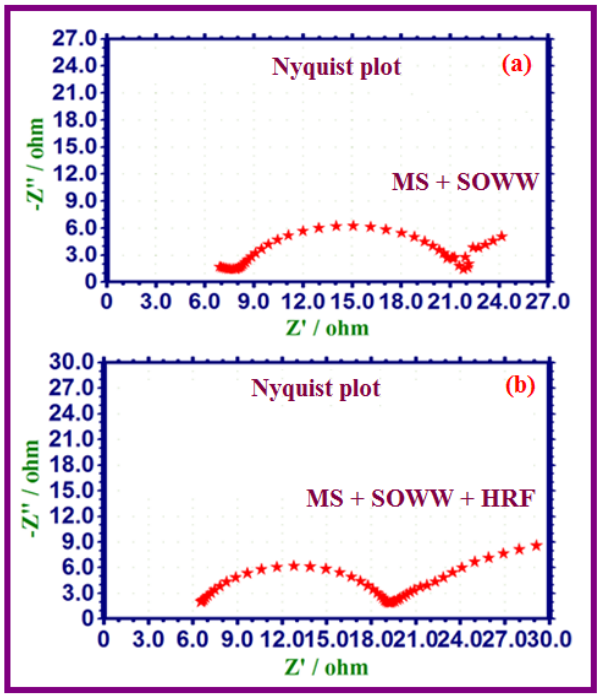

Figure 6. Nyquist plot of mild steel in different environments (a) SOWW without inhibitor (b) with 10 % v/v aqueous extract of inhibitor (HRF)

Slika 6. Nyquist-ov dijagram mekog čelika u različitim okruženjima (a) SOWW bez inhibitora (b) sa 10% v/v vodenog ekstrakta inhibitora (HRF)

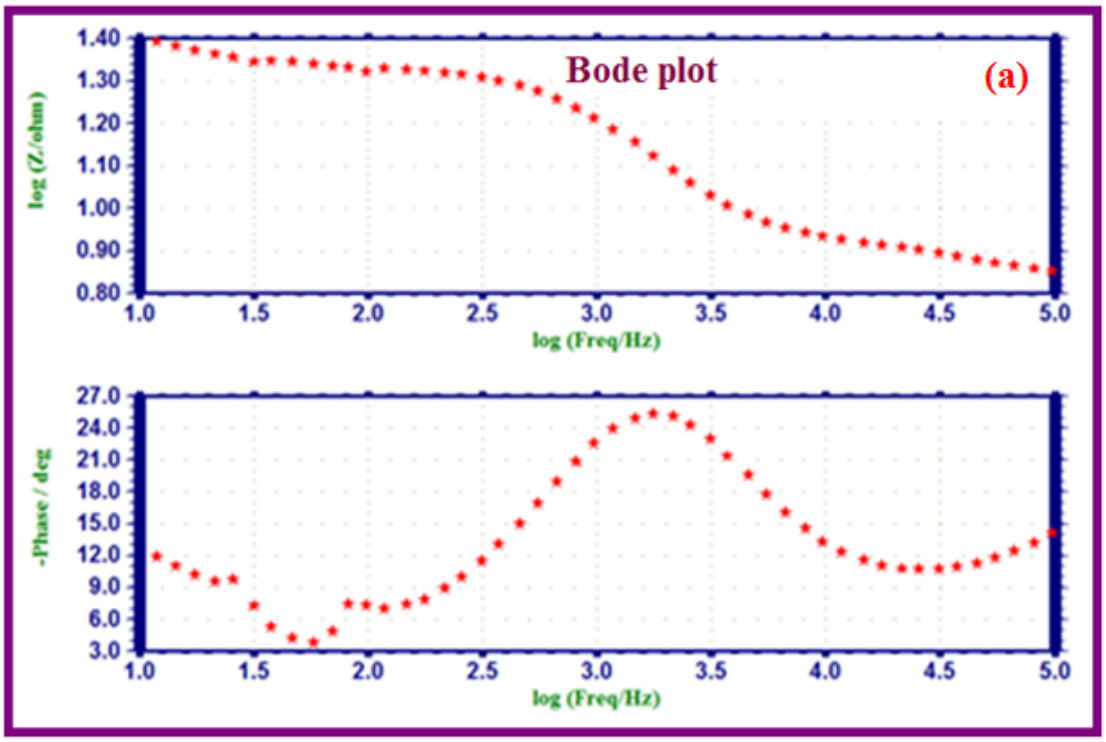

Figure 7a. Bode plots of mild steel in SOWW without inhibitor (blank)

Slika 7a. Bode-ovi dijagrami mekog čelika u SOWW bez inhibitora (prazno)

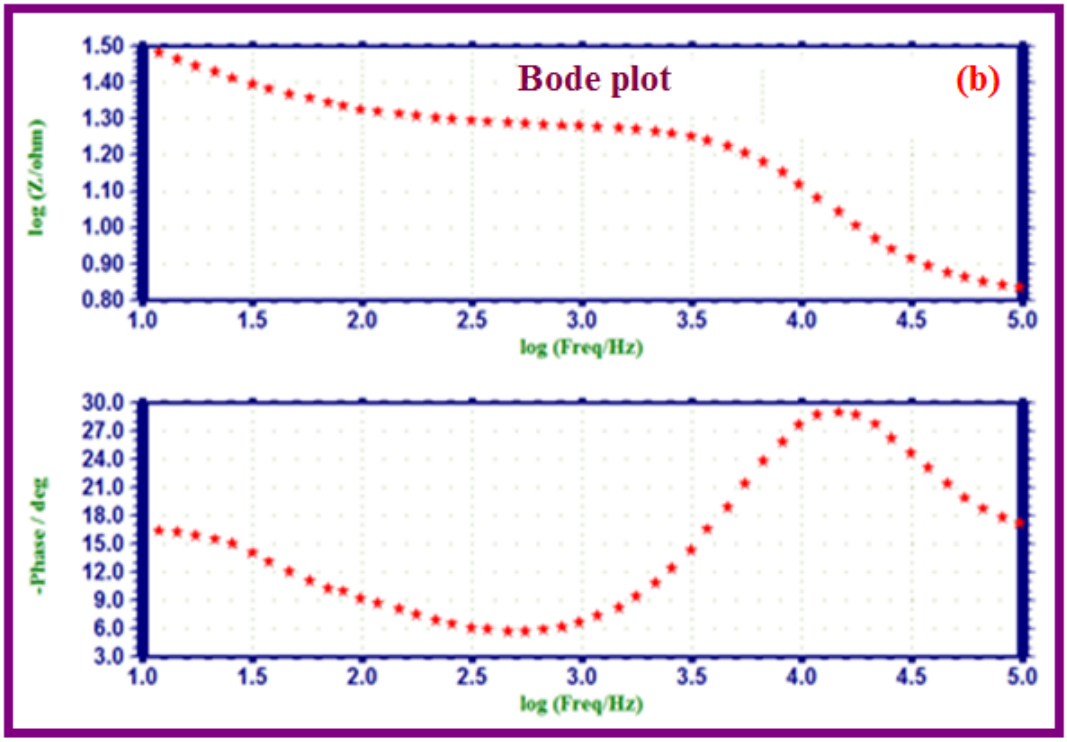

Figure 7b. Bode plots of mild steel in SOWW with 10 % v/v aqueous extract of inhibitor (HRF)

Slika 7b. Bode-ovi dijagrami mekog čelika u SOWW sa 10% v/v vodenog ekstrakta inhibitora (HRF)

Analysis of FTIR spectra

FTIR spectra have been used to analyse the protective film formed on the metal surface. A few drops of an aqueous extract of *Hibiscus rosa-sinensis* flower were dried on a glass plate. A solid mass was obtained. It was blended with KBr and converted into pellet. Its FTIR spectral pattern is recorded and given in Figure 8, the assignments are shown in Table 5. A broad band appears at 3423.09 cm^{-1} is attributed to -OH group. The band observed at 2924.60 cm^{-1} and 2855.20 cm^{-1} represents the aliphatic C-H stretching. The peak at 1637.75 cm^{-1} shows the presence of C=O (aromatic ketone) and aromatic ring (C=C) group. The peak at 1385.94 cm^{-1} has been assigned to CH bending frequency. The band 1244.85 cm^{-1} indicates the presence of C-O stretching group. The peak at 1069.75 cm^{-1} is assigned to C-O-C stretching vibration. The C-H out of plane bending (oop) absorbs at 899.80 cm^{-1} and 668.44 cm^{-1}.

The FTIR spectrum of the protective layer formed on the mild steel surface after immersion in the solution containing SOWW with 10 % v/v of inhibitor (HRF) solution is shown in Figure 9. The respective absorption frequencies are given in Table 5. The shift at 3423.09 cm^{-1} to 3382.19 cm^{-1} can be attributed to the presence of -OH stretching. The slight shift from 2924.60 cm^{-1} to 2925.10 cm^{-1} indicates the presence of C-H bond. The peak has shifted from 1637.75 cm^{-1} to 1629.76 cm^{-1} indicate the presence of C=O and C=C aromatic ring group.

Table 5. FTIR spectral data for the aqueous extract of HRF and the scratched film from mild steel surface after immersion in SOWW with 10 % v/v HRF

Tabela 5. FTIR spektralni podaci za vodeni ekstrakt HRF i izgrebani film sa površine mekog čelika nakon potapanja u SOWW sa 10 % v/v HRF

Stretching frequency, cm^{-1}		Various functional groups
Dried aqueous extract of HRF	Protective film formed on mild steel surface	
3423.09	3382.19	-OH stretching
2924.60	2925.10	-CH stretching
2855.20	-	-CH stretching
1637.75	1629.76	C=O/C=C stretching
1385.94	1454.39	-CH bending
1244.85	-	C-O stretching
1069.75	1022.37	C-O-C stretching
899.80	872.82	CH “oop”
668.44	688.46	CH “oop”
-	469.70	γ-Fe_2O_3

The C-H bending frequency has shifted from 1385.94 cm^{-1} to 1454.39 cm^{-1}. The frequency 1244.85 cm^{-1} for C-O group is disappeared. The C-O-C stretching frequency has shifted from 1069.75 cm^{-1} to 1022.37 cm^{-1}. The peak C-H "oop" bending shifted from 899.80 cm^{-1} to 872.82 cm^{-1} and 618.11 cm^{-1} to 694.82 cm^{-1}. The new absorption band at 469.70 cm^{-1} probably originates from the Fe^{2+}-*Hibiscus rosa-sinensis* flower complex formation. This shows that due to interaction between the metal and the active constituents present in the flower extract, there is a change in the chemical nature of the active constituents [33, 34].

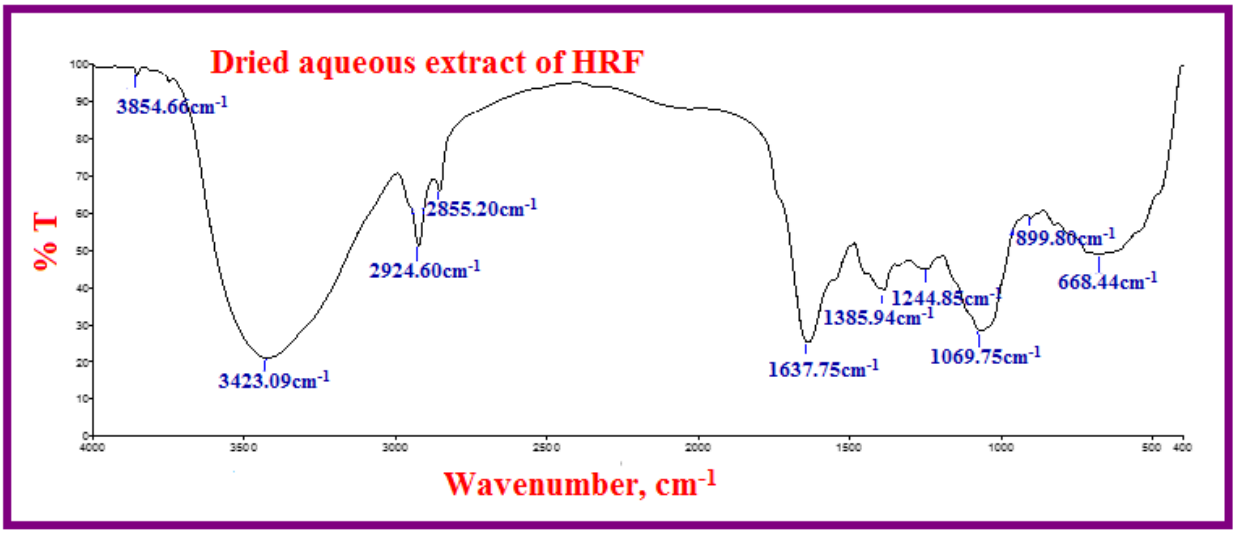

Figure 8. FTIR spectrum of dried aqueous extract of pure inhibitor (HRF)

Slika 8. FTIR spektar osušenog vodenog ekstrakta čistog inhibitora (HRF)

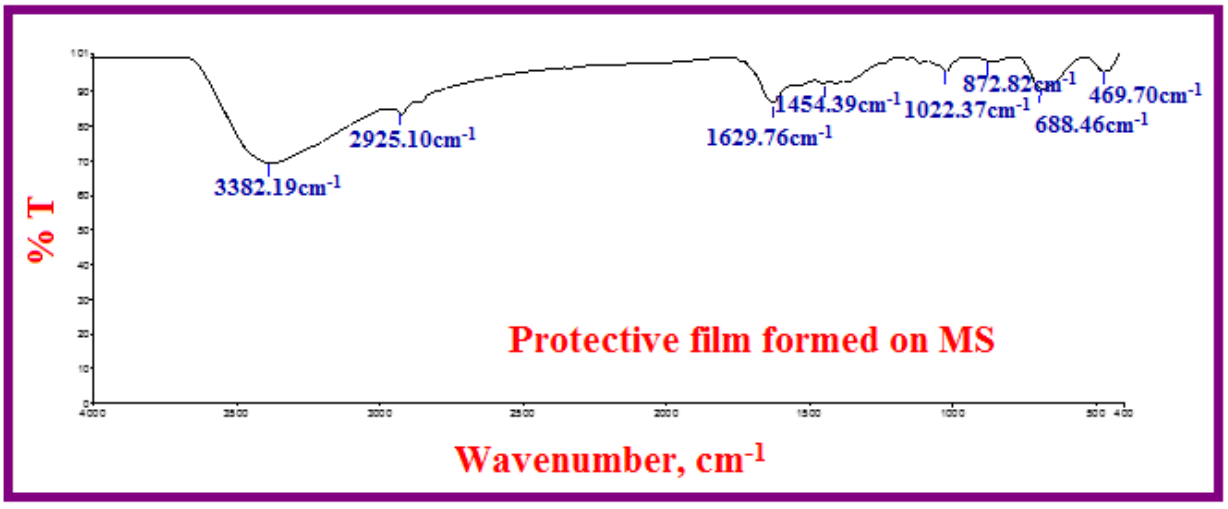

Figure 9. FTIR spectrum of scratched film from the mild steel surface after immersion in SOWW with 10 % v/v aqueous extract of inhibitor (HRF)

Slika 9. FTIR spektar izgrebanog filma sa površine mekog čelika nakon potapanja u SOWW sa 10% v/v vodenog ekstrakta inhibitora (HRF)

Analysis of SEM studies

SEM image is employed in the analysis of surface morphology of the specimen. The SEM images of MS in various environments are shown in Figure 10. The SEM image of polished MS is given in Figure 10a. The SEM image of polished MS immersed in SOWW is shown in Figure 10b. The SEM image of the MS immersed in SOWW in presence of inhibitor HRF are given in Figure 10c. The SEM images of polished MS are appeared to be smooth. The SEM image of the MS in SOWW environment is seemed to be rough. The noticeable

cavities are present on the MS surface. The SEM image of the MS in SOWW and inhibitor (HRF) are appeared to be significantly smooth than in the SOWW medium. Thus the SEM study reveals the MS surface is protected by the formation of non-porous smooth thin film in the presence of inhibitor (HRF)[35].

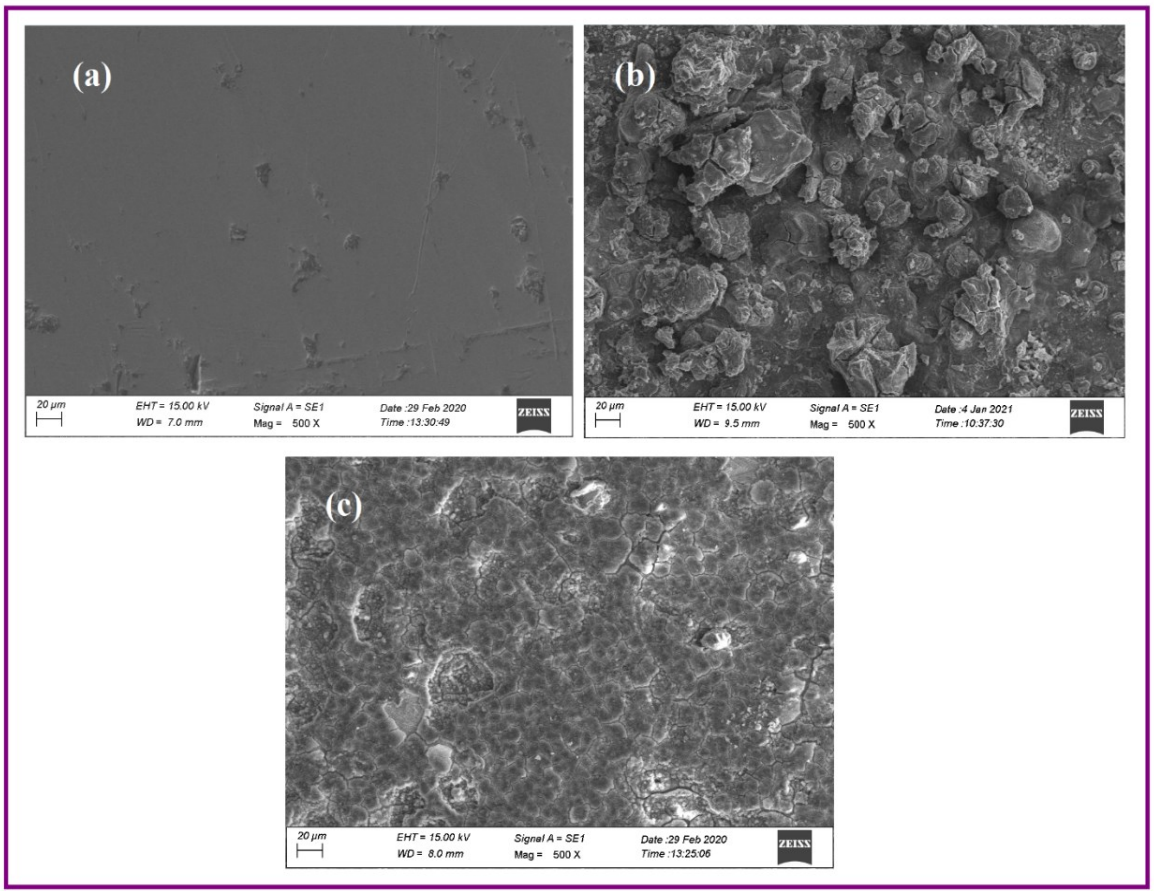

Figure 10. SEM micrographs of (a) Polished MS (b) MS immersed in SOWW (c) MS immersed in SOWW with 10 % v/v aqueous extract of HRF

Slika 10. SEM mikrografije (a) Poliranog MS (b) MS uronjenog u SOWW (c) MS uronjenog u SOWW sa 10% v/v vodenog ekstrakta HRF

Mechanism of corrosion inhibition

The extract of the flower contains many chemical constituents such as cyanidin, quercetin, hentriacontane, calcium oxalate, thiamine, riboflavin, niacin and ascorbic acidsThey adsorbed on the metal surface and form protective film on the metal surface and thus corrosion is controlled [36].

4. CONCLUSION

The following conclusions can be obtained from the results.

- The weight loss method reveals that 82 % inhibition efficiency is observed in controlling corrosion of mild steel in simulated oil well water containing corrosion of an aqueous extract of *Hibiscus rosa-sinensis* flower.
- Potentiodynamic polarization study shows that mixed type of inhibitor.
- AC impedance spectra reveal that protective film is formed on the metal surface.
- The presence of active principle component in the aqueous extract of HRF has been confirmed by FTIR spectra.
- The smoothness of the metal surface has been studied by SEM.

5. REFERENCE

[1] K.Tamalmani, H.Husin (2020) Review on Corrosion Inhibitors for Oil and GasCorrosion Issues, Applied Sciences, 10(10), 3389.

[2] L.T.Popoola, A.S.Grema, G.K.Latinwo, B.Gutti, A.S.Balogun (2013) Corrosion problems during oil and gas production and its mitigation, International Journal of Industrial Chemistry, 4(35), 1-15.

[3] M.N.Rahuma, B.Kannan (2014) Corrosion in Oil and Gas Industry: A Perspective on Corrosion Inhibitors, J. of Material Sciences and Engineering, 3(3), 110-119.

[4] L.N.Emembolu, O.D.Onukwuli, C.J.Umembamalu, C.O.Aniagor (2020) Evaluation of the corrosion inhibitory effect of NapoleonaeaImperalis leaf extract on mild steel in a 1.3 M H_2SO_4, medium, J. of Bio- and Tribo-Corrosion, 6(128), 1-15.

[5] I.Y.Suleiman, A.Kasim, S.R.Ochu (2019) Anti‑corrosion Properties of Ethanol Extract of Cardiospermumhalicacabum Leaf on Steel Pipelines in Acidic Environment, Journal of Bio- and Tribo-Corrosion, 5(65), 1-13.

[6] K.Kavitha, H.Benitasherine, S.Rajendran (2021) Cardiospermum halicacabum leaves extract as a green corrosion inhibitor for mild steel in simulated oil well water medium, International Journal of Corrosion and Scale Inhibition, 10(4), 1646–1660.

[7] A.S.Fouda, A.S.Abousalem, G.Y.EL-Ewady (2017) Mitigation of corrosion of carbon steel in acidic solutions using an aqueous extract of Tiliacordata as green corrosion inhibitor, International Journal of Industrial Chemistry, 8, 61–73.

[8] R.Kusumastuti, R.I.Pramana, J.W.Soedarsono (2017)The Use of MorindaCitrifolia as a Green Corrosion Inhibitor for Low Carbon Steel in 3.5% NaCl Solution, International Conference on Chemistry, Chemical Process and Engineering, 020012-1–020012-9.

[9] G.I.Udom, G.A.Cookey, A.Abia (2017) The Effect of Acanthus montanus Leaves Extract on Corrosion of Aluminium in Hydrochloric Acid Medium, Current Journal of Applied Science and Technology, 25(2), 1-11.

[10] A.El-A.S.Fouda, A.A.El-Hossiany, H.M.Ramadan (2017) Calotropisprocera plant extract as green corrosion inhibitor for 304 stainless steel in hydrochloric acid solution, Zastita Materijala, 58(4), 541 - 555.

[11] K.Anuradha,R.Vimala,B.Narayanasamy, J.A.Selvi, S.Rajendran (2008) Corrosion Inhibition of Carbon Steel in Low Chloride Media by an Aqueous Extract of Hibiscus rosa-sinensis Linn, Chemical Engineering Communications, 195, 352–366.

[12] S.Rajendran, J.Jeyasundari, P.Usha, J.A.Selvi, B.Narayanasamy, A.P.P.Regis, P.Rengan (2009) Corrosion Behaviour of Aluminium in the Presence of an Aqueous Extract of Hibiscus Rosa-sinensis, Portug.Electrochim.Acta, 27(2), 153-164.

[13] P.S.Desai (2015) Hibiscus rosa-sinensis (JASUD) leaves extracts used as corrosion inhibitors for mild steel in hydrochloric acid, European Journal of Pharmaceutical and Medical Research, 2(1),470-485.

[14] M.Goutam, D.K.Prabir,D.Pranjal, S.Akhsay, K. Shymodip, S.Pintu, M.Debasmita, S.Argha, N. Tarique, K.Chandan, R.C.Sangita (2018) Authentication and Photochemical Screening of Hibiscus Rosa Sinensis, International Journal of Research and Analytical Reviews, 5(4), 712u-718u.

[15] I.M.Khan, R.Rahman, A.Mushtaq,M.Rezgui (2017) Hibiscus rosa-sinensis L. (Malvaceae): Distribution, chemistry and uses, International Journal of Chemical and Biochemical Sciences, 12, 147-151.

[16] R.Geethanjali, S.Subhashini (2015) Investigation of Corrosion Inhibition Efficiency of Some Synthesized Water Soluble Terpolymers on N-80 Steel in HCl, NaCl and Simulated Oil Well Water, Portug. Electrochim. Acta, 33(2), 85-104.

[17] G.Wranglen (1986) Introduction to Corrosion and Protection of Metals, London: Chapman and Hall, p.236.

[18] S.S.Sawant, D.Khandeparker, A.Tulaskar, K. Venkat,A.Garg (1995) Corrosion and microfouling of copper and its alloys in a tropical marine waters of India (Mangalore), Indian Journal of Chemical Technollogy, 2, 322-326.

[19] K.Kavitha, H.B.Sherine, S.Rajendran (2021) Anti-corrosive properties of an aqueous extract of Chrysanthemum indicum flower, International Journal of Corrosion and Scale Inhibition, 10(2), 783–800.

[20] S.Muralidharan,S.V.Iyer (1997) The influence of N-heterocycles on corrosion inhibition and hydrogen permeation through mild steel in acidic solutions, Anti-Corrosion Methods and Materials, 44, 100.

[21] R. Saratha, S.V. Priya, P. Thilagavathy (2009) Investigation of Citrus aurantiifolia leaves extract as corrosion inhibitor for mild steel in 1 M HCl, E-Journal of Chemistry, 6(3), 785-795.

[22] E.A.Noor, A.H.Al-Moubaraki (2008) Thermodynamic study of metal corrosion and inhibitor adsorption processes in mild steel/1-methyl-4 [4'(-X)-styrylpyridinium iodides/hydrochloric acid systems, Materials Chemistry and Physics, 110, 145-154.

[23] H.Shao, J.Wang, Z.Zhang, J.Zhang, C.Cao (2003) The cooperative effect of calcium ions and tartrate ions on the corrosion inhibition of pure aluminum in an alkaline solution, Materials Chemistry and Physics, 77, 305-309.

[24] A.A.S.Begum, R.M.A.Vahith, V.Kotra, M.R.Shaik, A.Abdelgawad, E.M.Awwad, M.Khan (2021) Spilanthesacmella leaves extract for corrosion inhibition in acid medium, Coatings, 11(106), 1-23.

[25] O.F.Nwosu, E.Osarolube, L.A.Nnanna, C.S.Akoma, T.Chigbu (2014) Acidic corrosion inhibition of Piper guineense seed extract on Al alloy, American Journal of Materials Science, 4(4), 178-183.

[26] T.Sathiyapriya,G.Rathika (2019) Corrosion inhibition efficiency of human black hair extract on mild steel in 1M H_2SO_4 media, Indian Journal of Chemical Technology, 26, 216-223.

[27] H.M.A.El-Lateef, M.A.Abo-Riya,A.H.Tantawy (2016) Empirical and quantum chemical studies on the corrosion inhibition performance of some novel synthesized cationic gemini surfactants on carbon steel pipelines in acid pickling processes, Corrosion Science, 108, 94-110.

[28] M.Lebrini, F.Robert, H.Vezin, C.Roos (2010) Electrochemical and quantum chemical studies of some indole derivatives as corrosion inhibitors for C38 steel in molar hydrochloric acid, Corrosion Science, 52, 3367-3376.

[29] F.El-T.Heakal, M.A.Deyab, M.M.Osman, M.I. Nessim, A.E.Elkholy (2017) Synthesis and

assessment of new cationic Gemini surfactants as inhibitors for carbon steel corrosion in oilfield water, Journal of RSC Advances, 7, 47335-47352.

[30] A.SuriyaPrabha, K.Kavitha, H.BenitaSherine, S. Rajendran (2020) Inhibition of corrosion of mild steel in simulated oil well water by an aqueous extract of Andrographispaniculata, Indian Journal of chemical Technology, 27, 452-460.

[31] J.J.M.Praveena, J.A.Clara, S.S.Rajendran, A.J. Amalraj (2021) Inhibition of corrosion of mild steel in well water by an aqueous extract of soapnut (SapindusTrifoliatus), Zastita Materijala, 62(4), 277–290.

[32] P.Deivanayagam,S.Selvaraj (2018) Cardiospermum halicababum leaves extract as green inhibitor for corrosion of brass in 1.0N hydrochloric acid solution, International Journal for Research in Engineering Application and Management, 4(6), 292-298.

[33] M.A.Deyab, M.M.Osman, A.E.Elkholy,F.El-T.Heakal (2017) Green approach towards corrosion inhibition of carbon steel in produced oilfield water using lemongrass extract, Journal of RSC Advances, 7, 45241-45251.

[34] R.M.Silverstein, F.X.Webster, D.J.Kiemle (2005) Spectroscopic identification of organic compounds, John Wiley and Sons, seventh edition, 82, 106-115.

[35] I.Y.Suleiman, A.M.Sani, O.O.Clifford (2020) Characterization and corrosion behaviours of AISI 316 in hydrochloric environment at various concentrations, Zastita Materijala, 61(3), 220–228.

[36] P.Ruban, K.Gajalakshmi (2012) In vitro antibacterial activity of Hibiscus rosa-sinensis flower extract against human pathogens. Asian Pac J Trop Biomed. 2(5), 399-403. doi:10.1016/S2221-1691(12)60064-1.

IZVOD

INHIBICIJA KOROZIJE MEKOG ČELIKA U SIMULIRANOJ VODI IZ BUNARA VODENIM EKSTRAKTOM CVETA *Hibiscus rosa-sinensis*

Vodeni ekstrakt cveta Hibiscus rosa-sinensis (HRF) korišćen je kao inhibitor korozije u kontroli korozije mekog čelika u simuliranoj vodi iz bunara (SOWW). Metoda gubitka težine otkriva da 10% v/v ekstrakta nudi 82% efikasnost inhibicije (IE) za SOWW uronjen u meki čelik (MS). Mehanistički aspekti inhibicije korozije su istraženi proučavanjem polarizacije i spektra impedanse naizmenične struje. Studija polarizacije otkriva da je mešoviti tip inhibitora u prisustvu inhibitornog sistema. Efekat inhibicije korozije je potvrđen povećanjem vrednosti otpora linearne polarizacije i smanjenjem vrednosti struje korozije. Zaštitni sloj koji se formira na površini metala potvrđuju spektri impedanse naizmenične struje. Ovo potvrđuje činjenica da dolazi do povećanja vrednosti otpora prenosa naelektrisanja i smanjenja vrednosti kapacitivnosti dvostrukog sloja. Adsorpcija molekula inhibitora je podređena Langmuir-ovoj adsorpcionoj izotermi. Zaštitni premaz karakteriše FTIR spektroskopija. To potvrđuje da je inhibitor koordinirao sa jonima gvožđa na površini metala preko aktivne komponente b-sitosterola, kvercetina i kempferola-3-ksilozilglukozida. Morfologija površine je ispitana skenirajućim elektronskim mikroskopom (SEM). Dakle, vodeni ekstrakt cveta Hibiscus rosa-sinensis sa simuliranom vodom iz bunara ima dobar korozivni inhibitivni efekat na cevovode od mekog čelika.

Ključne reči: *Hibiscus rosa-sinensis, simulirana naftna bušotina, meki čelik, inhibicija korozije, morfologija površine, SEM.*

Naučni rad
Rad primljen: 24.09.2023.
Rad prihvaćen: 03.10.2023.
Rad je dostupan na sajtu: www.idk.org.rs/casopis

Yassine El Guerri[1], Bendaoud Mebarek[2], Mourad Keddam[3]*

[1]Research Laboratory of Industrial Technologies, University of Tiaret, Zaâroura, Tiaret, Algeria, [2]Laboratoire de Recherche en Intelligence Artificielle et Systèmes, University of Tiaret, Zaâroura, Tiaret, Algeria [3]Laboratoire de Technologie des Matériaux, Faculté de Génie Mécanique et Génie des Procédés, USTHB, El-Alia, Bab-Ezzouar, Alger, Algérie

Scientific paper
ISSN 0351-9465, E-ISSN 2466-2585
https://doi.org/10.62638/ZasMat1016
Zastita Materijala 65 (1)
97 - 109 (2024)

Confrontation of linear versus nonlinear approach in Fe_2B boride layer thickness predictions

ABSTRACT

Kinetic studies of boride layers focus on trying to accurately predict their thicknesses according to some variables using different approaches. In this paper, an approach that is reliant on a multilinear regression is investigated. In doing so, with an engineering perspective, temperature T and time t are used as the sole variables in predicting a boride layer thickness u. The approach uses experimental data from a boriding process performed on iron substrates of the XC38 steel. A comparison between the proposed linear model and a nonlinear one is seen afterward to scrutinize the results. That nonlinear approach is known as the diffusion model and is based on Fick's second law, where it uses more variables than the linear approach to estimate its predictions. Ultimately, the comparison elucidated that the use of a linear regression-based model can be an accurate engineering tool to identify boride layer thicknesses, but without interpolating the results outside the scope of the studied interval.

Keywords: *Multilinear regression / Linear regression / Boriding / Boride layer / Boron.*

1. INTRODUCTION

Different hardening processes have been envisaged since the revolution of industrial machining. These processes focus on surface treatments of tools and parts, enhancing wear resistance during use to further prolong lifespan. Nitriding, carbonizing, chromium plating, thermal spraying, chemical vapor deposition or physical vapor deposition coatings are some known processes. Boriding is one such process where significant advantages of mechanical properties are reached [1 - 3].

Boriding is widely spread over diverse fields like fittings, gear transmissions, milling and crushing technologies, extrusion techniques, stamping, tools, renewable energies, and others [4,5]. The process is also known as boronizing or boron coating, a thermo-chemical treatment carried out in solid, liquid or gaseous media, hence the naming of the processes. E.g., gas boriding, paste boriding, powder pack boriding process or others [1,5,6].

The most common one is the latter, and it is done by immersing parts in a boriding agent, where there are different boron sources (B4C, amorphous boron, ferroboron), activators ($NaBF_4$, KBF_4, NH_4Cl, Na_2CO_3, NiO) and diluents (SiC, SiO_2, Si_3N_4, Al_2O_3), then sealing them in a heat resistant steel furnace [5,7]. During the process, intermetallic compounds are formed between the boron and other elements, for instance, iron, chromium, nickel, vanadium, cobalt, molybdenum, tungsten, and titanium [8], depending upon the material processed. Borided materials range from cast iron, cast steel, and most steel grades to nickel-based alloys and specific materials such as stellite, except silicon and aluminum [9].

Each boriding process is founded upon the diffusion of boron atoms at high temperatures during a time period, resulting in either a monophase layer or a multiphase one [10,11]. This particular layer has multiple valuable properties, increased resistance to wear from abrasions [12], acids [13], oxidations [14], corrosions [15], erosions [16], and adhesions by decreasing friction [17,18]. Depending on the base material and other aspects, it also increases hardness to about 1000 or 2600 HV and even higher [19,20]. All those factors expand the service life of parts by improving their degradation resistance [21].

*Corresponding author: Yassine El Guerri
E-mail: yassine.elguerri@univ-tiaret.dz
Paper received: 25. 09. 2023.
Paper accepted: 23. 10. 2023.
Paper is available on the website: www.idk.org.rs/journal

Throughout the advancement of research and the increase of its expenditure, modeling the kinetics of that boride layer became predominantly essential. Doing so demanded the characterization of the required variables to predict the boride layer thickness with less cost and fewer experiments. Specific models were developed by researchers, and further investigations were carried out. Presenting a few, the parabolic growth law model [22], the alternative diffusion model [23], the Dybkov model [24], the integral model [25,26] and the diffusion model that is based on the second law of Fick [26-30]. All these models are nonlinear and have a common goal: to analyze the diffusion data by studying the kinetics of boride layer thicknesses.

In this study, data of a boronized XC38 steel substrate [28] is explored through an attempt to predict the growth of the Fe_2B boride layer thickness u with a linear-based model that uses engineering lenses, hence, needing the least variables possible, temperature T and time t. After getting the predicted results, they are compared with a nonlinear model presented by Mebarek *et al.* in previous research, the diffusion model [28]. This comparison allows us to see if not taking other variables, such as incubation time t_0, boron concentrations C and the diffusion coefficients D, into account can mislead or falsify predictions.

Primarily, the study begins by developing the theories that support both the nonlinear model of Mebarek *et al.* [28] and the proposed linear model. After that, calculating and illustrating the results, then comparing each model's results by assessing their errors with the experimental data. The purpose is to ascertain if using engineering lenses via a linear model can be considered in the studies of Fe_2B boride layer kinetics due to it needing fewer variables, thus, ease of use.

2. EXPERIMENTAL DATA

The linear approach can be of use from an engineering point of view and is validated through comparison with another nonlinear approach, the diffusion model, published previously by Mebarek *et al.* [27]. Both approaches use the same experiment results obtained from boronizing substrates of XC38 steel [29]. Moreover, the samples' composition is given in Table 1, and the thermochemical boriding experiments were carried out in liquid mediums composed of borax ($Na_2B_4O_7$) and 30 $wt.\%$ silicon carbide (SiC).

Table 1. Composition of the XC38 steel samples

Tabela 1. Sastav uzoraka od čelika XC38

Elements	C	Cr	Cu	Ni	Co	Si	Mn	Fe
[$wt.\%$]	≈0.38	<0.1	<0.05	≈0.045	≈0.17	≈0.34	≈0.67	balance

The experiments were performed at three different temperatures, 850, 950 and 1000 °C with three treatment times, two, four and six hours.

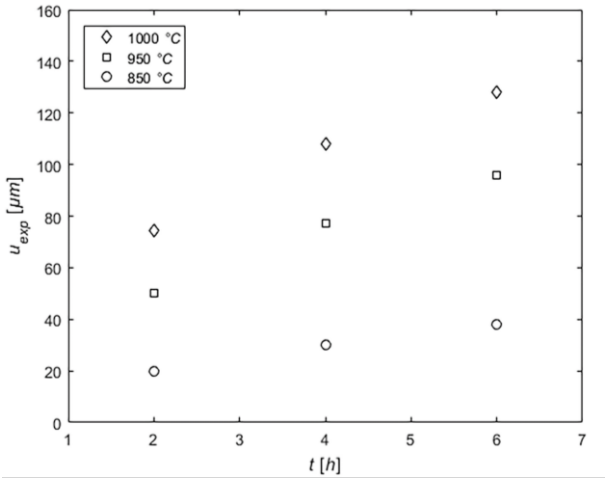

Figure 1. Boriding XC38 steel from 2 to 6 h on 850, 950 and 1000 °C

Slika 1. Boronizacija čelika XC38 u trajanju od 2 do 6 h na temperaturi 850, 950 i 1000 °C

By observations under an optical and electron microscope with sweeping, Fe_2B boride genesis was observed and different layer thicknesses were obtained depending on temperatures and treatment times, as illustrated in Figure 1.

3. MODELS

Diffusion model

The diffusion model is nonlinear and uses an approach presented by Mebarek *et al.* [28]. It is based on the equation of Fick used on semi-infinite media where different equations are summoned in order to characterize the growth rate constant k with which the model is established from experimental data. The boron concentration profile is illustrated in Figure 2, and described by the diffusion equation (1), the second law given by Fick.

$$\frac{\partial C_i}{\partial t} = D_i \frac{\partial^2 C_i}{\partial x^2} \qquad (1)$$

As all models have assumptions, this model's assumptions are given as follows:

- The flow of boron atoms is perpendicular to the sample surface, and the interface runs parallel to the sample surface.
- The growth of the position of the interface according to time is parabolic.
- The borided layer is thin compared to the thickness of the sample.
- The porosity effect does not exist on the surface of the material.
- The borided layer Fe_2B is formed instantly and immediately covers the surface (inexistence of the incubation time t_0).
- The diffusion coefficient is constant with composition.

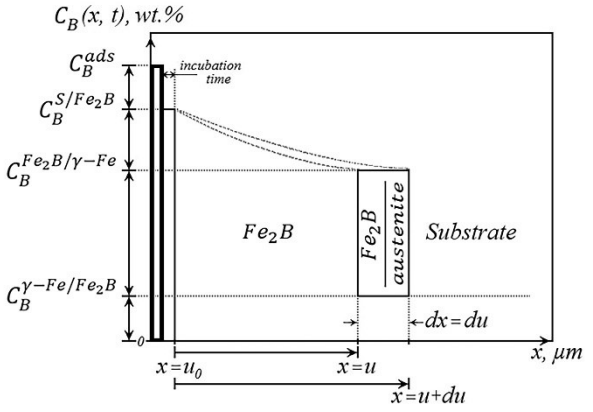

Figure 2. Boron concentration throughout the Fe_2B boride layer thickness

Slika 2. Koncentracija bora u celoj debljini sloja Fe_2B borida

The general solution of the first given equation for each phase i (Fe_2B and γ-Fe) is given as equation (2) which characterizes the general concentration equation:

$$C_i(x,t) = A_i + B_i erf\left(\frac{x}{2\sqrt{D_i t}}\right) \quad (2)$$

where

A_i and B_i constants

erf Gaussian error function

x boride layer thickness

The boride layer thickness u is simulated via a parabolic law of time t and the growth rate constant k whose value is unknown, as given in equation (3).

$$u_{sim} = k\sqrt{t} \quad (3)$$

The Boundary conditions of the study are:

At initial conditions and limits

$$C(x,0) = 0,$$

$$C(0,t) = C_B^{S/Fe_2B},$$

$$C(\infty,t) = 0.$$

At interface

$$C_{Fe_2B}(u_{sim},t) = C_B^{\frac{Fe_2B}{\gamma}-Fe},$$

$$C_{\gamma-Fe}(u_{sim},t) = C_B^{\gamma-Fe/Fe_2B}$$

where

C_B^{S/Fe_2B} at the sample surface

$C_B^{Fe_2B/\gamma-Fe}$ *and* $C_B^{\gamma-Fe/Fe_2B}$

in the interface of Fe_2B and γ-Fe.

Using equations (2), (3) and the boundary conditions, the concentrations of each phase i (Fe_2B and γ-Fe), are reached as follows:

$$C_{Fe_2B}(x,t) = C_B^{S/Fe_2B} + \frac{C_B^{Fe_2B/\gamma-Fe} - C_B^{S/Fe_2B}}{erf\left(\frac{k}{2\sqrt{D_{Fe_2B}}}\right)} erf\left(\frac{x}{2\sqrt{D_{Fe_2B}t}}\right) \quad (4)$$

$$C_{\gamma-Fe}(x,t) = \frac{C_B^{\gamma-Fe/Fe_2B}}{erfc\left(\frac{k}{2\sqrt{D_{\gamma-Fe}}}\right)} erfc\left(\frac{x}{2\sqrt{D_{\gamma-Fe}t}}\right) \quad (5)$$

The mass balance equation for the Fe_2B/γ-Fe interface is derived from the literature, equation (6):

$$W\frac{du_{sim}}{dt} = \Delta J_{x=u_{sim}} \quad (6)$$

where

$$W = \frac{1}{2}\left(C_B^{S/Fe_2B} - C_B^{Fe_2B/\gamma-Fe}\right) + \left(C_B^{Fe_2B/\gamma-Fe} - C_B^{\gamma-Fe/Fe_2B}\right)$$

$$\Delta J_{x=u_{sim}} = \left(J_{i_1} - J_{i_2}\right)_{x=u_{sim}}$$

$$J_i = -D_i\frac{\partial C_i(x,t)}{\partial x}$$

J_i represents the flow.

Using equations (3), (4) and (5) within equation (6) and by rearranging it, only the growth rate constant k remains as the sole non determined variable, as in equation (7):

$$f(k) = \frac{Wk}{2} + \frac{1}{\sqrt{\pi}} \left[\begin{array}{c} \left(C_B^{S/Fe_2B} - C_B^{Fe_2B/\gamma-Fe}\right)\sqrt{D_{Fe_2B}} \dfrac{exp\left(-\frac{k^2}{4D_{Fe_2B}}\right)}{erf\left(\frac{k}{2\sqrt{D_{Fe_2B}}}\right)} + \\ + \left(C_B^{Fe_2B/\gamma-Fe} - C_B^{\gamma-Fe/Fe_2B}\right)\sqrt{D_{\gamma-Fe}} \dfrac{exp\left(-\frac{k^2}{4D_{\gamma-Fe}}\right)}{erfc\left(\frac{k}{2\sqrt{D_{\gamma-Fe}}}\right)} \end{array} \right] \quad (7)$$

The rest of the parameters of equation (7) are: temperature T, treatment time t and activation energy Q found in the boron diffusivity D in each phase i and its concentration C. These parameters can be determined.

- For the Fe_2B phase, an estimation of the diffusivity of boron D in it has been attained through the Arrhenius relation for the diffusion process, equation (8):

$$u^2 = D_0 t \, exp\left(-\frac{Q}{RT}\right) \quad (8)$$

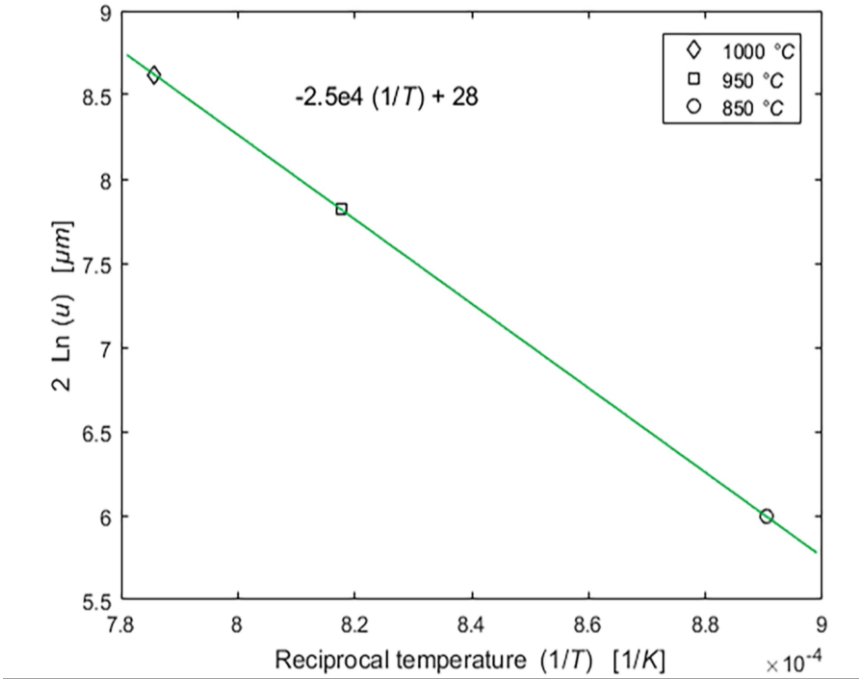

Figure 3. Reciprocal temperature dependence of the boride layer thickness formed after 2 h

Slika 3. Zavisnost debljine boridnog sloja formiranog nakon 2 h od vrednosti recipročne temperature

By linearizing the equation (8) and plotting it using 2 h of treatment time from experimental data as of Figure 3, the activation energy Q was deduced as 207.8 kJ.

Thus, a diffusivity of boron in the Fe_2B phase was attained as:

$$D_{Fe_2B} = 1.388 \cdot 10^{-4} \, exp\left(-\frac{207.8 \cdot 10^3}{RT}\right) [m^2 s^{-1}]$$

- For the γ-Fe phase, the diffusion coefficient found in reference [30] was used.

$$D_{\gamma-Fe} = 4.4 \cdot 10^{-8} \, exp\left(-\frac{91.51 \cdot 10^3}{RT}\right) [m^2 s^{-1}]$$

- As for the concentrations, they were taken from references [31] and [32].

$$C_B^{Fe_2B/\gamma-Fe} = 8.83 \; wt.\%$$
$$C_B^{\gamma-Fe/Fe_2B} = 35 \cdot 10^{-4} \; wt.\%$$

Incorporating all previously determined parameters into equation (7) and through nonlinear solving methods such as Newton-Raphson's numerical method by finding its root, in other terms, solving $f(k) = 0$, a positive value of the growth rate constant k can be determined. The calculated growth rate constant k is given in Table 2.

Table 2. Evolution of the calculated growth rate constant according to temperature

Tabela 2. Zavisnost izračunate konstante brzine rasta od temperature

$T\ [°C]$	750	800	850	900	950	1000	1050
$k\ [\mu m\ s^{-1/2}]$	0.1481	0.2275	0.3365	0.4800	0.6672	0.9037	1.1960

After having the growth rate constant k values, the approach of Mebarek *et al.* [28] proceeds to overcome the last assumption made earlier about the incubation time t_0 by exploiting a mathematical term that simulates it (incubation time), equation (9), using the difference between the simulated boride layer thickness u_{sim} and the experimental data u_{exp}.

Table 3 gives the values gotten of that simulated incubation time.

$$t_0(t,T) = \left(\frac{u_{sim} - u_{exp}}{k}\right)^2 \quad (9)$$

Table 3. The simulated incubation time values.

Tabela 3. Simulirane vrednosti vremena inkubacije.

$t_0\ [s]$	$T\ [°C]$	$t\ [h]$		
		2	4	6
	850	217.39	320.19	389.96
	950	65.56	14.07	6.35
	1000	5.27	0.22	25.67

After that, a unitless parameter was added to predict the boride layer thickness [28]. This parameter is identified as $B(T)$ and helps in taking the incubation time t_0 into consideration after estimating it depending on the temperature T as illustrated in Figure 4. Its equation (10) is given as:

$$B(T) = 1 - \sqrt{t_0/t} \quad (10)$$

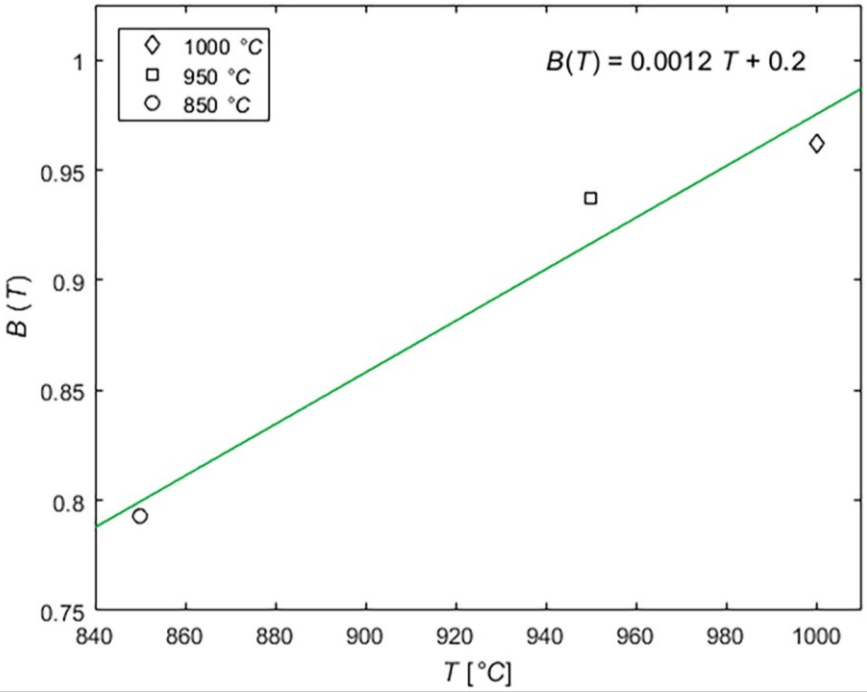

Figure 4. Evolution of parameter B in accordance with temperatures of 2 h

Slika 4. Zavisnost parametra B od temperature nakon 2 h

In the end, the equation (11) was used in this approach's predictions:

$$u_D = kB\sqrt{t} \quad (11)$$

Linear model

The proposed linear model utilizes a multilinear regression, also called multiple linear regression. Regressions are statistical techniques that employ numerous independent variables to forecast or determine the value of a dependent variable. Its general equation (12) is found in multiple literatures, such as [33]:

$$y = \beta_0 + \beta_1 x_1 + \beta_2 x_2 + \cdots + \beta_p x_p + \varepsilon \quad (12)$$

where

y the dependent or predicted variable

$x_1\ x_2\ \ldots\ x_p$ the independent variables

$\beta_0\ \beta_1\ \beta_2\ \ldots\ \beta_p$ regression coefficients

ε the model's error term (residual)

The multilinear regression is based on certain assumptions [34, 35]:

- Dependent and independent variables must have linear relationships.
- Non-collinearity; the independent variables are not highly correlated with each other.
- The variance of the residuals is constant.
- Independence of observation.
- Multivariate normality.

In this studied case, there are two variables, temperature and time. Thus, the equation (12) becomes equation (13):

$$y = \beta_0 + \beta_1 x_1 + \beta_2 x_2 + \varepsilon \quad (13)$$

These two variables have a nonlinear relationship, which doesn't satisfy the earlier assumptions. Furthermore, advanced multilinear regressions can overcome this issue by adding an interaction term [35] to the equation (13) between variables with nonlinear relationships. Resulting in a model having independent variables and an interaction term that adjusts the nonlinear relationship as in equation (14):

$$y = \beta_0 + \beta_1 x_1 + \beta_2 x_2 + \beta_3 x_1 x_2 + \varepsilon \quad (14)$$

where

$x_1 x_2$ represent the interaction term

4. COMPUTATIONS

The first nonlinear approach's calculations were done in reference [28]. Hence, this section is dedicated to the second one, the proposed linear model, the advanced multilinear regression.

Equating the boride layer thickness

Utilizing the equation (14) of the multilinear regression model, our approach's equation (15) becomes as follows:

$$u_i(T_i, t_i) = \beta_0 + \beta_1 T_i + \beta_2 t_i + \beta_3 T_i t_i \quad (15)$$

where

i represents the data points

u is the predicted boride layer thickness

T and t are the independent variables of temperature and time

$\beta_0\ \beta_1\ \beta_2\ \beta_3$ are the regression coefficients

This equation (15) is applied to all nine experimental data points given in Figure 1 gives nine equations.

Forming the matrixial system

The nine equations obtained from equation (15) are rewritten in a matrixial form, equation (16), for computing purposes [36] in order to facilitate calculations by using an automated computation that calculates any data.

$$U = X\,\beta \quad (16)$$

where

$$U = [\,u_i\,]$$

$$X = [\,1\ \ T_i\ \ t_i\ \ T_i t_i\,]$$

$$\beta = \begin{bmatrix} \beta_0 \\ \beta_1 \\ \beta_2 \\ \beta_3 \end{bmatrix}$$

$i = 1 : n$ while n represents the number of data points

U a vector column of the data boride layer thicknesses u

X a $(n \times 4)$ matrix of the independent variables and the interaction term

β a vector column of the regression coefficients

Resolving the system

The resolution of the matrixial system gives the regression coefficients and can either be done via a computing platform or mathematically [37] with the formula below:

$$\beta = (X'X)^{-1}\,X'\,U \quad (17)$$

After resolution, the obtained regression coefficients are given in Table 4.

Table 4. The obtained regression coefficients of the linear model

Tabela 4. Dobijeni koeficijenti regresije za linearni model

Coefficients $[10^{-3}]$	β_0	β_1	β_2	β_3
	-199000	245.2381	-46875	60.7143

Establishing the linear model

In the end, through the multilinear regression, the equation (18) of the linear approach is attained and helps to determine the boride layer thickness u depending upon any given temperature T in $°C$ and time t by hours.

$$u_L(T,t) = \beta_0 + \beta_1 T + \beta_2 t + \beta_3 T t \qquad (18)$$

where

u_L represents the boride layer thickness predicted using the regression

Assessing the errors

The comparison of the results was conducted using residuals, the mean absolute error (MAE) as of equation (19), the standard error of the estimate (SEE), equation (20) and the minimal and maximal errors.

$$MAE = \frac{1}{n}\sum_{i=1}^{n} | u_i - \bar{u} | \qquad (19)$$

$$SEE = \sqrt{\frac{\sum_{i=1}^{n}(u_i - \bar{u})^2}{n-2}} \qquad (20)$$

where

u_i denotes the predicted value

$\bar{u}$ the actual value

n the number of predictions

5. RESULTS AND DISCUSSIONS

Predicted boride layer thickness

The boride layer thickness's predictions u_{pre} were done initially via the diffusion model u_D then via the equation (18) attained after using the multilinear regression u_L. The results are given in Figure 5 and detailed in Table 5.

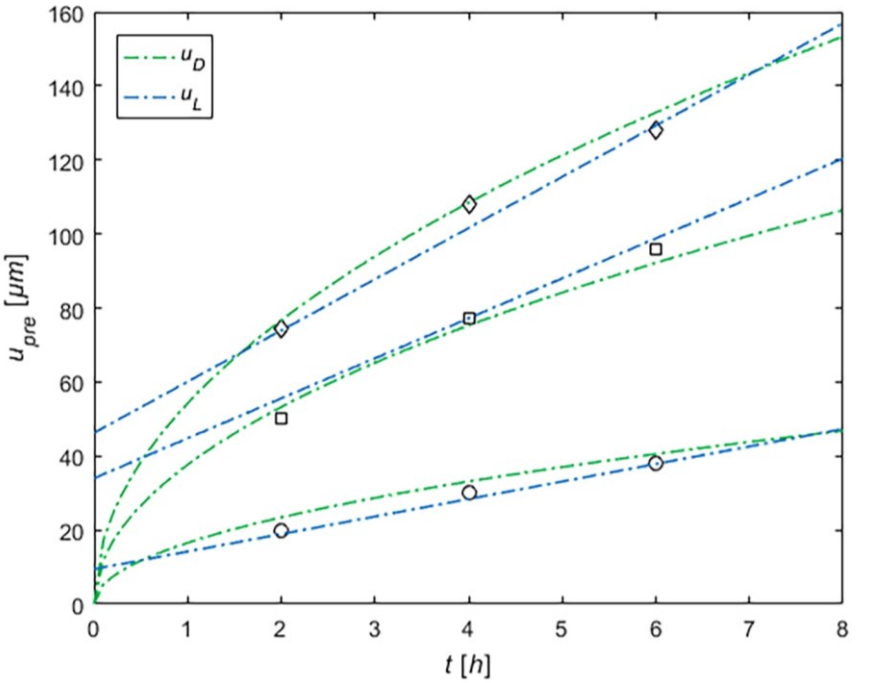

Figure 5. Predicted Fe_2B boride layer thicknesses of each model (Diffusion and Linear)

Slika 5. Predviđene debljine sloja Fe_2B borida za oba modela (difuzioni i linearni)

Figure 5 elucidates that the accuracy of the linear model before 2 h and after 6 h of treatment time is questionable, especially at the beginning of the experiment (0 h), where it is seen that they are unreasonable, having a boride thickness without even beginning the experiment.

Due to such observations, the results of the multilinear regression should not be considered if outside the scope of the studied interval, which was from 2 to 6 hours of treatment time.

Table 5. Predicted Fe_2B boride layer thicknesses values of each model (Diffusion and Linear)

Tabela 5. Predviđene vrednosti debljine sloja borida Fe_2B za oba modela (difuzioni i linearni)

u_{pre} [μm]	T [$°C$]	t [h]			Residuals		
		2	4	6			
u_D	850	23.41	33.11	40.55	3.41	3.11	2.55
	950	53.22	75.26	92.17	3.22	-1.74	-3.83
	1000	76.68	108.44	132.82	2.18	0.44	4.82
u_L	850	18.92	28.38	37.85	-1.08	-1.62	-0.15
	950	55.58	77.19	98.80	5.58	0.19	2.80
	1000	73.92	101.60	129.27	-0.58	-6.40	1.27

Nonetheless, as detailed in Table 5, even though the results of the multilinear regression aren't like those of the diffusion model, compared to the experimental data, they were more accurate in seven out of nine predictions. Subsequently, the approach can be conceivable in predicting boride layer thicknesses.

Comparing models

To better understand the accuracy of both approaches, a comparison between both predictions is made with what has been stated in the assessing errors section. The error comparisons were arranged in Table 6.

Ascertaining the results with known error formulas makes it clearer to see the accuracy of both models. Ending up with what's stated in Table 6, an insignificant difference of 0.04 between them in the standard error of the estimate (SEE) and a favorable mean absolute error (MAE) for the linear model over the nonlinear one by 0.62. The other differences concerning the minimal and maximal errors differed insignificantly by 0.29 and 1.58, respectively.

Table 6. Prediction errors of each model (Diffusion and Linear)

Tabela 6. Greške predviđanja za oba modela (difuzioni i linearni)

	u_D	u_L
MAE	2.81	2.19
SEE	3.46	3.50
$Min\ Err$	0.44	0.15
$Max\ Err$	4.82	6.40

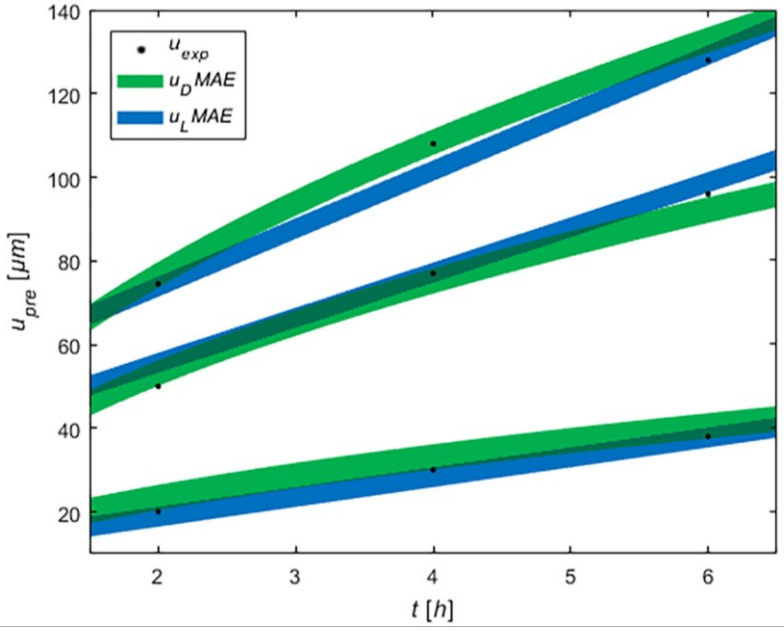

Figure 6. The mean absolute error (MAE) scope in each point for both models

Slika 6. Opseg srednje apsolutne greške (MAE) u svakoj tački za oba modela

To further see the meaning of the mean absolute error (MAE), equation (19), in both models, Figure 6 was established illustrating the scope of error according to it for each model on all nine predicted points, and it is observed that the nonlinear model had five over nine predictions out of the scope but nearing it, while the linear model had only three with two being quite far of the scope indicating that the nonlinear model is slightly more accurate but considering that the linear one uses lesser variables and doesn't consider the incubation time t_0, it can be said that it is still relatively precise in its other predictions.

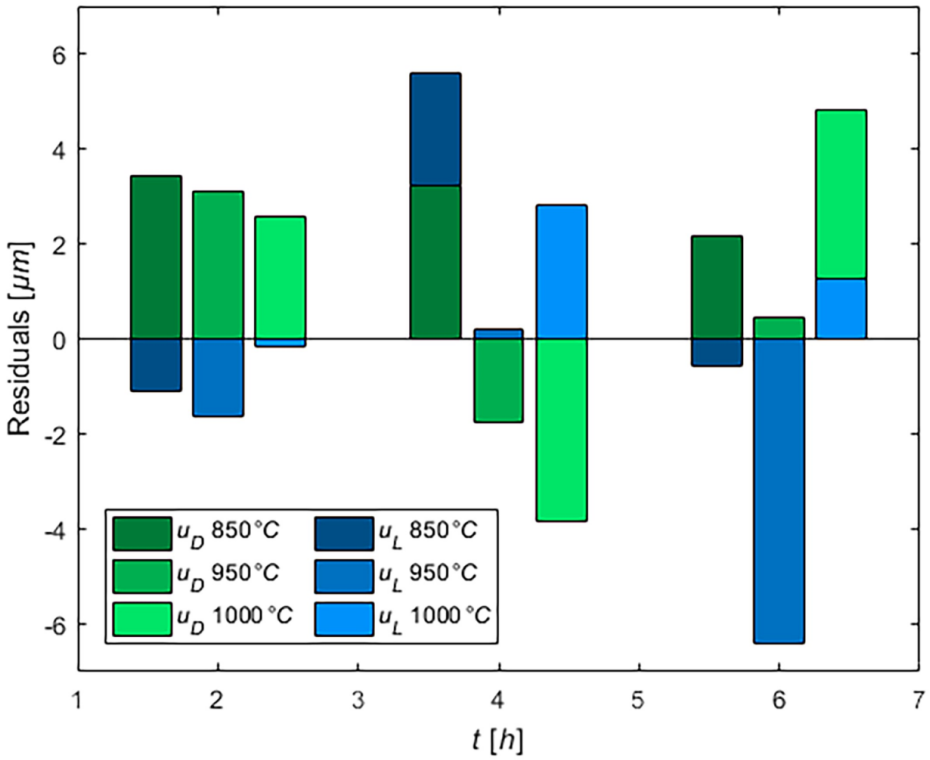

Figure 7. Predictions' residuals on both models

Slika 7. Odstupanja od predviđenih vrednosti za oba modela

Similar to Table 5, Figure 7 efficiently illustrates the resulted residuals from each model's predictions, where it is seen that; the linear model did poorly on two predictions, 4 and 6 h of treatment time at 850 and 950 $°C$ respectively. Nevertheless, it did predict all seven other predictions greater than the nonlinear model (diffusion model).

Additionally, having more negative residuals is better than positive ones because predicting a layer thickness less than its actual value is favored, and that was seen with the linear model contrary to the nonlinear one that had seven out of nine positive residuals, which is detrimental in certain boride layer thicknesses use cases.

With these insignificant differences and such low residuals and errors obtained, it can be stated that both approaches were quite nearing experimental data, making them both comparable and valid models in determining the Fe_2B boride layer thickness.

Iso-thickness diagram

Equation (18), plotted three-dimensionally, displays the obtained predictions of the boride layer thickness u_L as a function of temperature T and time t as a surface plot graphic, Figure 8.

Figure 8 unravels that the influence of temperature is more significant than that of time in the growth of the boride layer thickness. Nevertheless, to better grasp and identify the given predictions from that graphic, they are re-illustrated in Figure 9 as a two-dimensional plot renowned as the iso-thickness diagram.

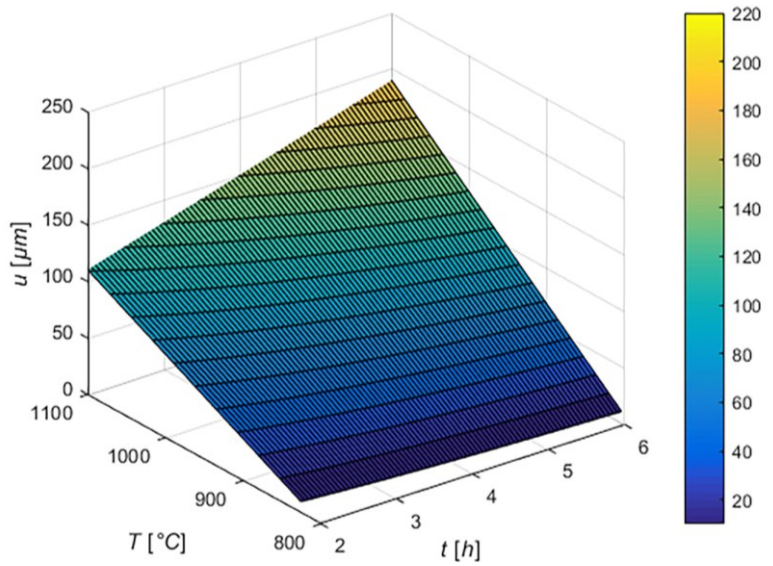

Figure 8. Three-dimensional predictions of the boride layer thickness by temperature and time

Slika 8. Trodimenzionalni prikaz predviđanja debljine boridnog sloja u zavisnosti od temperature i vremena

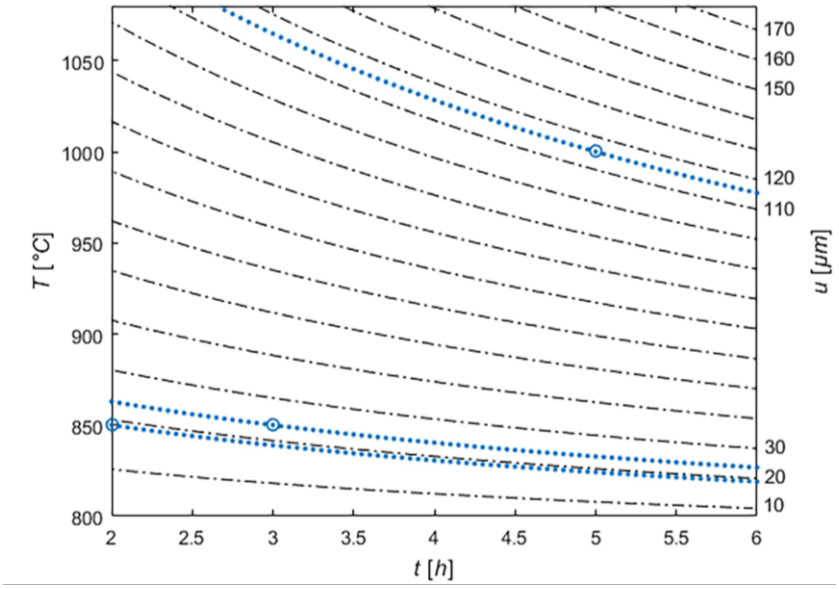

Figure 9. Iso-thickness diagram relating the boride layer thickness to the boriding parameters using the linear model

Slika 9. Dijagram izo-debljine kod linearnog modela koji povezuje debljinu boridnog sloja sa parametrima boronizacije

Table 7. Difference between graphical predictions and calculated ones

Tabela 7. Razlike između grafičkih predviđanja i izračunatih vrednosti

Temperature $[°C]$	850	850	1000
Time $[h]$	2	3	5
u_D $[\mu m]$	23.41	28.68	121.24
Calculated u_L $[\mu m]$	18.92	23.65	115.43
Graphical u_L $[\mu m]$	19	24	115

Other predictions of the boride layer thickness were estimated at 2, 3 and 5 h with a temperature of 850, 850 and 1000 $°C$, respectively. The results are encircled in the iso-thickness diagram within Figure 8 and given in Table 7.

As seen in Table 7, the boride layer thickness can be taken instantly graphically by means of the iso-thickness diagram, with a prediction of near 24 μm for a boriding done with 850 $°C$ for 3 hours, which is found if calculated using the linear regression model's equation (18) as 23.65 μm.

Consequently, the iso-thickness diagram is a valuable tool to instantly determine the temperature T and the treatment time t needed for any desired boride layer thickness u while considering the reading errors.

Alternatively, the same point predicted using the diffusion model, equation (11), gives a boride layer thickness of 28.68 μm, which is higher than what is predicted by the linear model (23.65 μm) but may highly be a higher value than what the actual one might be, and that is from the fact that was discovered in advance (the diffusion model has nearly all predictions over the actual experimental values), so it can therefore be assumed that the actual value may be close to one of them or may be between the predicted values of both models. Given the above, it can be supposed that the two models, linear and nonlinear, are relatively comparable.

6. CONCLUSION

With only two variables from experimental data (temperature and time), a linear-based model has been developed using an advanced multilinear regression, which gave advantageous estimations, making it, from an engineering point of view, a viable approach for Fe_2B boride layer thickness predictions.

Interpolating the predictions of a linear regression beyond the interval of the data sets may lead to detrimental predictions as interpreted, but conversely, exploiting them in the studied interval gave us predictions as accurate as the diffusion model, which was nonlinear and used more variables.

Even though nonlinear models have their advantages in the determination of other factors since they depend on numerous variables, sometimes simplifying things with a linear model can be convenient when the expenses of the research are limited, but keeping in mind that it is more on the practical side than that of a scientifical one.

One of the advantages of the linear model over the nonlinear one is that it often gives predictions that are nearer or inferior to the actual value, and that's favorable when it comes to predicting a layer thickness since expecting less and getting more is beneficial in the end, contrary to predicting a certain thickness and ending up with less which was more the case of the nonlinear model

An iso-thickness diagram is established to instantly identify the temperature and the treatment time required or convenient for any desired Fe_2B boride layer thickness.

While the results are representative of this specific experimental process mentioned and can't be extrapolated on other processes, it was determined that the approach is valid and further studies with it can be carried out on other substrates. Moreover, its potential regarding the kinetics of dual-phased boride layer (FeB and Fe_2B) is to be investigated.

7. REFERENCES

[1] R.A.García-León, J.Martínez-Trinidad, I.Campos-Silva (2021) Historical Review on the Boriding Process using Bibliometric Analysis, Springer, Transactions of the Indian Institute of Metals, 74, 541-557. doi.org/10.1007/s12666-020-02174-6

[2] M.Kulka (2019) Current Trends in Boriding Techniques, Springer, Cham, Switzerland. doi.org/ 10.1007/978-3-030-06782-3

[3] B.Bhushan (2001) Modern Tribology Handbook, Taylor & Francis, Boca Raton, USA. doi.org/ 10.1201/9780849377877

[4] J.L.Dossett, G.E.Totten (2013) Steel Heat Treating Fundamentals and Processes, Chapter Boriding (Boronizing), ASM International, Materials Park, Ohio, USA. doi.org/10.31399/asm.hb.v04a. 9781627081658

[5] Y.G.Gogotsi, R.A.Andrievski (1999) Materials Science of Carbides, Nitrides and Borides, Springer, NATO Science Series, Saint Pétersbourg, Russia. doi.org/10.1007/978-94-011-4562-6

[6] A.P.Tschiptschin, C.E.Pinedo (2022) Surface Hardening of Stainless Steel, Ambrish Singh, IntechOpen, London, UK. doi.org/10.5772/ intechopen.105036

[7] F.Xie, X.Ye, J.Cheng, L.Sun (2013) A Study on an Energy-saving and High-efficient Pack Boriding Technology for Tool and Die Steels, Elsevier, Physics Procedia, 50, 76-81. doi.org/10.1016/ j.phpro.2013.11.014

[8] E.J.Mittemeijer, M.A.Somers (2014) Thermochemical Surface Engineering of Steels, Improving Materials Performance, Elsevier, Woodhead Publishing, UK. doi.org/10.1016/C2013-0-16318-0

[9] J.R.Davis (2003) Surface Hardening of Steels: Understanding the Basics, ASM International, Materials Science, Ohio, USA. ISBN: 978-0-87170-764-2

[10] I.Campos-Silva, M.Ortiz-Domínguez, H.Cimenoglu, R.Escobar-Galindo, M.Keddam, M.Elías-Espinosa, N.López-Perrusquia (2011) Diffusion model for growth of Fe_2B layer in pure iron, Taylor & Francis, Surface Engineering, 27(3), 189-195. doi.org/10. 1179/026708410X12550773057820

[11] M.Keddam, S.M.Chentouf (2005) A diffusion model for describing the bilayer growth (FeB/Fe_2B) during the iron powder pack boriding, Elsevier, Appl. Surf.

Sci., 252(2), 393-399. doi.org/10.1016/ j.apsusc. 2005.01.016

[12] C. Martini, G. Palombarini, G. Poli, D. Prandstraller (2004) Sliding and abrasive wear behavior of boride coatings, Elsevier, Wear, 256(6), 608-613. doi.org/10.1016/j.wear.2003.10.003

[13] S.C. Singhal (1977) A hard diffusion boride coating for ferrous materials, Elsevier, Thin Solid Films, 45(2), 321-329. doi.org/10.1016/0040-6090(77) 90265-6

[14] R. Ramadoss, N Kumar, S. Dash, D. Arivuoli, A. K. Tyagi (2013) Wear mechanism of CrN/NbN superlattice coating sliding against various counterbodies, Elsevier, Int. J. Refract. Met. Hard Mater., 41, 547-552. doi.org/10.1016/j.ijrmhm. 2013.07.005

[15] P. A. Dearnley, K. L. Dahm, H. Çimenoğlu (2004) The corrosion-wear behaviour of thermally oxidized CP-Ti and Ti-6Al-4V, Elsevier, Wear, 256(5), 469-479. doi.org/10.1016/S0043-1648(03)00557-X

[16] S. Ma, J. Xing, P. Lyu, Y. Wang, G. Liu (2018) Multiphase interface structure induced erosion resistance of directional solidified Fe-B alloy in flow liquid zinc, Elsevier, Mat. Lett., 211, 281-284. doi.org/10.1016/j.matlet.2017.10.027

[17] R. Kara, F. Çolak, Y. Kayali (2016) Investigation of Wear and Adhesion Behaviors of Borided Steels, Springer, Transactions of the Indian Institute of Metals, 69(6), 1169-1177. doi.org/10.1007/s12666-015-0698-2

[18] E. Rabinowicz (1966) Friction and Wear of Materials 2nd Edition, J. Appl. Mech., 33(2), p. 479. ISBN: 978-0-471-83084-9

[19] M. Usta, I. Ozbek, M. Ipek, C. Bindal, A. H. Ucisik (2005) The characterization of borided pure tungsten, Elsevier, Surface and Coatings Technology, 194(2-3), 330-334. doi.org/10.1016/j.surfcoat.2004.06.042

[20] R. Carrera-Espinoza, U. Figueroa-López, J. Martínez-Trinidad, I. Campos-Silva, E. Hernández-Sánchez, A. Motallebzadeh (2016) Tribological behavior of borided AISI 1018 steel under linear reciprocating sliding conditions, Elsevier, Wear, 362-363, 1-7. doi.org/10.1016/j.wear.2016.05.003

[21] W. Fichtl (1981) Boronizing and its practical applications, Elsevier, Materials & Design, 2(6), 276-286. doi.org/10.1016/0261-3069(81)90034-0

[22] S. Ipek Ayvaz, I. Aydin (2020) Effect of the Microwave Heating on Diffusion Kinetics and Mechanical Properties of Borides in AISI 316L, Springer, Transactions of the Indian Institute of Metals, 73, 2635-2644. doi.org/10.1007/s12666-020-02072-x

[23] M. Keddam, P. Jurči (2021) Alternative Kinetic Model of Growth of Boride Layers on Steel AISI 316, Springer, Metal Science and Heat Treatment, 63, 430-436. doi.org/10.1007/s11041-021-00707-4

[24] V. I. Dybkov, W. Lengauer, P. Gas (2006) Formation of boride layers at the Fe-25% Cr alloy-boron interface. J Mater Sci, 41, 4948-4960. doi.org/10.1016/j.apsusc.2004.05.141

[25] M.Keddam (2004) A kinetic model for the borided layers by the paste-boriding process, Elsevier, Applied Surface Science, 236(1-4), 451-455. doi.org/10.1016/j.apsusc.2004.05.141

[26] Y.El Guerri, B. Mebarek, M. Keddam (2022) Impact of the diffusion coefficient calculation on predicting Fe_2B boride layer thickness, Sciendo, Koroze a Ochrana Materialu KOM - Corrosion and Material Protection Journal, 66, 25-35. doi.org/10.2478/kom-2022-0005

[27] B.Mebarek, M.Keddam, M. Kulka (2021) Simulation of the incubation time for the formation of (FeB/Fe_2B) bilayer on pure iron, Sciendo, Koroze a Ochrana Materialu KOM - Corrosion and Material Protection Journal, 65, 49-56. doi.org/10.2478/kom-2021-0006

[28] B. Mebarek, A. Benguelloula, A. Zanoun (2018) Effect of Boride Incubation Time During the Formation of Fe_2B Phase, Scielo, Materials Research 21(1), 1-7. doi.org/10.1590/1980-5373-MR-2017-0647

[29] S. A. Bouaziz, N. Boudaoud, A. Zanoun (2009) Thermochimical boriding of a C38 steel in molten salts containing borax-SiC, EDP Sciences, Matériaux et Techniques 97(4), 253-259. doi.org/10.1051/mattech/2009036

[30] B. Mebarek, S. A. Bouaziz, A. Zanoun (2012) Simulation model to study the thermochemical boriding of stainless steel “AISI 316” (X5CrNiMo17-12-2), EDP Sciences, Matériaux et Techniques, 100(2), 167-175. doi.org/10.1051/mattech/2012009

[31] M. Keddam, S. M. Chentouf (2005) A diffusion model for describing the bilayer growth (FeB/Fe_2B) during the iron powder-pack boriding, Elsevier, Applied Surface Science, 252(2), 393-399. doi.org/10.1016/j.apsusc.2005.01.016

[32] B. Hallemans, P. Wollants, J. R. Roos (1995) Thermodynamic assessment of the Fe-Nd-B phase diagram, Springer, Journal of Phase Equilibria, 16, 137-149. doi.org/10.1007/BF02664851

[33] G. K. Uyanık, N. Güler (2013) A Study on Multiple Linear Regression Analysis, Elsevier, Procedia - Social and Behavioral Sciences, 106, 234-240. doi.org/10.1016/j.sbspro.2013.12.027

[34] J. W. Osborne, E. Waters (2002) Four assumptions of multiple regression that researchers should always test, Practical Assessment, Research and Evaluation, 8, 1-5. doi.org/10.7275/r222-hv23

[35] P. Roback, J. Legler (2021) Beyond Multiple Linear Regression: Applied Generalized Linear Models and Multilevel Models in R, CRC Press, New York, USA. doi.org/10.1201/9780429066665

[36] S. Chatterjee, A. S. Hadi (1986) Influential Observations, High Leverage Points, and Outliers in Linear Regression, Statist. Sci., 1(3), 379-393. doi.org/10.1214/ss/1177013622

[37] K. M. Ramachandran, C. P. Tsokos (2021) Chapter 7 - Linear regression models, Mathematical Statistics with Applications in R, Elsevier, Academic Press. doi.org/10.1016/C2018-0-02285-9

IZVOD

POREĐENJE LINEARNOG I NELINEARNOG PRISTUPA ZA PREDVIĐANJE DEBLJINA Fe_2B BORIDNIH SLOJEVA

Kinetička ispitivanja boridnih slojeva su usmerena na pokušaje tačnog predviđanja debljine tih slojeva primenom nekih promenljivih uz korišćenje različitih pristupa. U ovom radu su primenjeni pristupi koji se zasnivaju na multilinearnoj regresiji. Pri tome, temperatura T i vreme t su jedine promenljive koje su korišćene u predviđanju debljine sloja borida u, što je značajno sa inženjerske tačke gledišta. Navedeni pristupi koriste eksperimentalne podatke iz procesa boriranja koji je izveden na uzorcima od čelika XC38. Urađeno je poređenje linearnog i nelinearnog modela da bi se odredila valjanost rezultata predviđanja. Nelinearni pristup je poznat kao model difuzije i zasnovan je na drugom Fikovom zakonu. Taj pristup koristi više promenljivih od linearnog pristupa za procenu debljine boriranog sloja. Kao zaključak, izvršeno poređenje je pokazalo da model zasnovanog na linearnoj regresiji može biti pouzdan inženjerski alat za određivanje debljine boridnih slojeva, bez ekstrapolacije rezultata izvan proučavanog opsega.

Ključne riječi: *Multilinearna regresija / Linearna regresija / boronizacija / Boridni sloj / Bor*

Naučni rad
Rad primljen: 25.09.2023.
Rad prihvaćen: 23.10.2023
Rad je dostupan na sajtu: www.idk.org.rs/casopis

Annamalai Selvam[1], Santiagu John Mary[1], Asirvatham Ajila[1],Devadoss Delinta[1], Vijayagopal Sribharathy[2], Senthamarai Kannan Muthukumaran[3]*

[1]Department of Chemistry, Loyola Institute of Frontier Energy (LIFE), Loyola College, Chennai-600 034, Tamil Nadu, India, [2]Department of Chemistry, Anna Adhars College for Women, Chennai-600 040, Tamil Nadu, India, [3]Department of Chemistry, Ramakrishna Mission Vivekananda College, Chennai-600 004, Tamil Nadu, India

Scientific paper
ISSN 0351-9465, E-ISSN 2466-2585
https://doi.org/10.62638/ZasMat1004

Zastita Materijala 65 (1)
110 - 125 (2024)

Electrochemical activities of Ni-Ti alloy in artificial blood plasma with Trigonella foenum graecum seeds

ABSTRACT

An investigation of the electrochemical behaviour of Ni-Ti alloy when exposed to artificial blood plasma (ABP) in the presence of 0.1 and 0.5 ppm of Trigonella foenum graecum (TFG) seeds for 1, 10, 20, and 30 days. Studies on AC impedance and polarisation have shown that a protective coating forms on the metal surface while inhibiting corrosion. The protective film has formed on the Ni-Ti implant alloy surface, the linear polarization resistance increased (LPR), and the corrosion current value (I_{corr}) decreased. The charge transfer resistant value (R_{ct}) and impedance value increase and the double-layer capacitance value decrease.The protective layers morphology and the elemental composition were analyzed by SEM/EDAX.The property of the protective film on the Ni-Ti alloy has been examined by atomic force microscope. The X-ray diffraction analysis has confirmed the nature of the apatite. The corrosion inhibition efficiency of Ni-Ti alloy in ABP in the presence of TFG seeds at various concentrations for different times was improved and protected.

Keywords:*Nickel-titanium, AFM, protective film, Nyquist plots, Bode plots*

1. INTRODUCTION

Nickel-Titanium alloy, known as nitinol, has been used in orthopedic and orthodontic applications because of its attractiveness and exceptional properties. It possesses super elasticity and shape memory effect. Due to its excellent biocompatibility, which is comparable with that of Ti, along with shape memory and super elasticity properties, Ni-Ti alloy draws more attention in biomedical applications than other metallic constituents [1]. The Ni-Ti SMAs are among the most popular SMAs for biomedical applications, including stents or medical and dental wires, due to the relative ease of formability and improved fracture and fatigue resistance compared with other commercial shape memory alloys [2]. The Ni-Ti alloys in the medical field provide significant advantages and new treatment options in various medical cases.

*Corresponding author: Annamalai Selvam
E-mail: selvamchemist@gmail.com
Paper received: 25. 09. 2023.
Paper accepted: 25. 10. 2023.
Paper is available on the website: www.idk.org.rs/journal

However, metallic ion release, particularly Ni release, still requires a more profound understanding for improved safety and biocompatibility of this class of alloys in the human body, especially for long-term treatments. The Ni release occurs as a result of the interaction of the alloy with tissue or body fluids. It depends on the alloy type, tissue or body fluid surrounding it, and the type and morphology of the possible oxide layers forming on the alloy. Each parameter affects how the alloy's chemical, mechanical, and surface properties change within the body, affecting the materials biocompatibility. Among these parameters, passive oxide layer formation is more critical in affecting the Ni release. Compared to Ni, Ti is chemically a more reactive metal and can easily segregate at the surface and form an oxide layer when exposed to atmospheric or aqueous conditions. Ti can form various oxides, including TiO, Ti_2O_3, and TiO_2 [3,4].The various metals and alloys have been used as biomaterials whose corrosion resistance has been investigated in artificial body fluids, various metals, and alloys such as Co-Cr-Mo alloys [5, 6], Cr-Ni stainless steel, Cr-Ni-Mo stainless steel [7]. According to reports, fenugreek has hypocholesterolemic, anti-diabetic, anti-cancer,

anti-microbial, and anti-parasitic properties [8]. The production of therapeutic medicines is due to the many compounds in fenugreek seeds and leaves.

In general, fenugreek contains three important constituents with medicinal value: (i) 4-hydroxy isoleucine, (ii) galactomannans, and (iii) steroidal saponins. These constituents have placed fenugreek among the most commonly recognized 'nutraceutical' or health food products [9]. The TFG seeds are helpful in heart disease and aphrodisiac and as a galactagogue promoting lactation [10]. Being a natural health product, it can treat and cure diseases, thus providing medical and health benefits. It has therefore been regarded as a possible nutraceutical [11]. This study was designed to investigate the effect of Ni-Ti alloy in artificial blood plasma in the presence of TFG seeds. This study reveals that the intake of TFG seeds containing Fenugreekine increases immunity. The various concentrations of seeds were prepared, and their inhibition efficiency of TFG in the artificial blood plasma for 1, 10, 20, and 30 days has been examined by Potentiodynamic polarization, AC impedance spectroscopy, SEM analysis, EDAX, AFM, and XRD techniques.

By directly giving some naturally occurring phytoproducts to diabetic patients to assist in controlling their blood sugar levels, it is possible to measure the corrosion activity of metal alloys under various environments. Trigonella foenum graecum seeds were employed in this investigation as an anti-diabetic.

2. MATERIALS AND METHODS

2.1. Materials

The metal specimen, Ni-Ti alloy composition Ti = 50.1, Ni = 40.2, and C = 9.7 wt. %. The chemical composition of artificial blood plasma was prepared in the laboratory, according to PN-EN ISO 10993-15 standard (g/l distilled water) was NaCl=6.8, $CaCl_2$=0.2, KCl=0.4, NaH_2PO_4=0.026, $NaHCO_3$=2.2, Na_2HPO_4=0.126, $MgSO_4$=0.1 [12]. The pH of artificial blood plasma was 7.4, used as an electrolyte in the electrochemical studies.

The Trigonella foenum graecum seeds were bought in the local market. The seed powder was weighed and dissolved in ethanol. Two different extracts were obtained, namely aqueous and ethanol extracts [13]. The different concentrations of these extracts were used for the experiment to characterize the nutrients which contain the hetero atoms, and π electrons act as suitable inhibitors.

2.2. Methods

A CHI660A workstation model was used in the electrochemical studies. The Tafel plot was obtained from potentiodynamic polarization studies as a potential versus log (i) plot. The corrosion potential (E_{corr}) and corrosion current (I_{corr}) were deduced from the Tafel plot.

The corrosion current is obtained using the Stern-Geary equation 1 [14].

$$Icorr = \frac{\beta a \times \beta c}{2.3\ Rp\ (\beta a \times \beta c)} \qquad \text{…..……..(1)}$$

where

β_a and β_c are the Tafel slopes of the anodic and cathodic part of Tafel plot and Rp is polarization resistance.

A polarization study was utilised to calculate the linear polarisation resistance (LPR), corrosion potential (E_{corr}), and corrosion current (I_{corr}) of ABP in the presence and absence of TFG seeds.

AC impedance spectra were recorded in the same instrument used for the polarization study, using the same type of three-electrode cell assembly.The charge transfer resistance (R_{ct}) values and double-layer capacitance (C_{dl}) were calculated. From the results, analyze the protective film formation on the Ni-Ti alloy surface and know the systematic aspects of corrosion resistance. AC impedance was achieved using the CHI660A.The impedance were recorded with initial E (v) = 0; low frequency (Hz) =10; high frequency (Hz) =1×10^5; amplitude (V) = 0.005 and quit time (s) = 2 [15].

2.3. Characterizations

Subsequently, the surface morphology of the protective film after exposure to ABP in the presence of TFG seeds of 0.5 ppm was characterized using SEM spectroscopy.EDAX spectra were used to accomplish the elemental composition of the Ni-Ti alloy surface in the presence and absence of TFG seeds.

However, more definite characterizations of Ni-Ti alloy surface morphology in the presence of TFG seeds in ABP solution will be performed with the use of some new atomic force microscopy and X-ray diffraction investigations.

3. RESULTS AND DISCUSSION

3.1. Trigonella foenum graecum seeds

TFG seeds were ground into powder and then defatted by petroleum ether. The different alkaloids, saponin, and flavonoids are to be found in TFG, but saponin is to be found to be a high-level concentration in the TFG [16]. Plant tissue cultures from seeds grown under optimal conditions have produced as much as 2% diosgenin with fewer quantities of gitongenin and trigogenin. The significant components of TFG seeds are high carbohydrates, proteins, flavonoids, alkaloids, saponin, free amino acids, glycosides,

mucilage, minerals, and much more [17]. Further investigations have shown its effectiveness in diminishing blood glucose levels, treating gastric abnormalities, on lowering cholesterol [18].

3.2. Potentiodynamic polarization study

A polarization study has been used to confirm the formation of a protective film on the alloy surface during the corrosion inhibition process. The protective film is formed on the Ni-Ti alloy surface, the linear polarization resistance increases (LPR), and the corrosion current value (I_{corr}) decreases. Figure 1 to 4 shows the polarization curves of Ni-Ti alloy exposed in ABP in the absence and presence of TFG seeds at various concentrations for various time intervals. (Table 1) embraces the corrosion parameters, specifically I_{corr}, E_{corr}, and LPR.

Table 1. Results of potentiodynamic polarization measurements for Ni-Ti alloy

Tabela 1. Rezultati merenja potenciodinamičke polarizacije za Ni-Ti leguru

Days	Alloy	System	E_{corr} mV vs. SCE	βc mV/decade	βa mV/decade	LPR ($\Omega.cm^2$)	I_{corr} (A/cm^2)
1 Day	Ni-Ti	ABP	-513	137	376	1.8789×10^{6}	2.331×10^{-8}
		ABP /TFG 0.1ppm	-693	131	386	1.9769×10^{6}	2.230×10^{-8}
		ABP /TFG 0.5ppm	-618	137	376	2.0478×10^{6}	2.085×10^{-8}
10 Days		ABP	-626	150	406	9.0947×10^{5}	5.250×10^{-8}
		ABP /TFG 0.1ppm	-579	150	270	1.3144×10^{6}	3.391×10^{-8}
		ABP /TFG 0.5ppm	-692	160	283	2.5225×10^{6}	1.668×10^{-8}
20 Days		ABP	-494	141	504	5.3967×10^{5}	8.900×10^{-8}
		ABP /TFG 0.1ppm	-570	148	304	1.4747×10^{6}	2.917×10^{-8}
		ABP /TFG 0.5ppm	-585	151	284	2.0936×10^{6}	2.073×10^{-8}
30 Days		ABP	-509	149	443	5.0664×10^{5}	9.620×10^{-8}
		ABP /TFG 0.1ppm	-615	166	286	1.7446×10^{6}	2.621×10^{-8}
		ABP /TFG 0.5ppm	-786	122	306	2.0997×10^{6}	1.816×10^{-8}

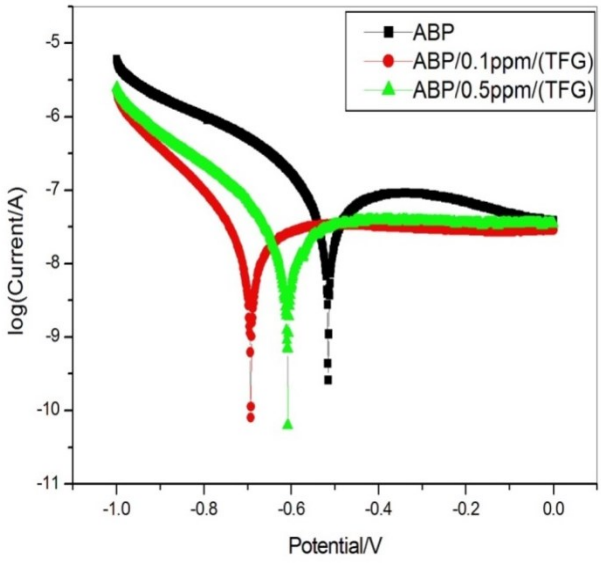

Figure 1. Polarization curves of Ni-Ti alloy exposed in ABP in the absence and presence of TFG seeds for 1 Day

Slika 1. Polarizacione krive legure Ni-Ti izložene u ABP u odsustvu i prisustvu semena TFG tokom 1 dana

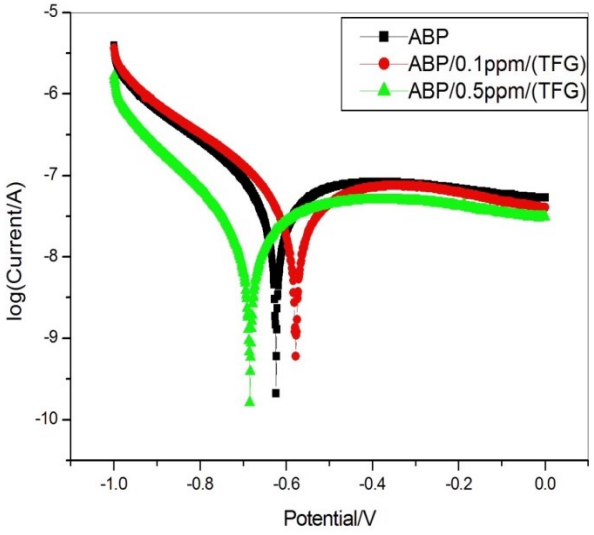

Figure 2. Polarization curves of Ni-Ti alloy exposed in ABP in the absence and presence of TFG seeds for 10 Days

Slika 2. Krive polarizacije legure Ni-Ti izložene u ABP u odsustvu i prisustvu TFG semena tokom 10 dana

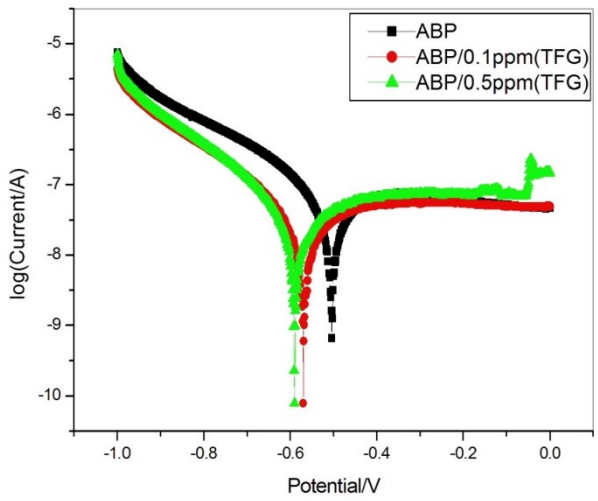

Figure 3. Polarization curves of Ni-Ti alloy exposed in ABP in the absence and presence of TFG seeds for 20 Days

Slika 3. Polarizacione krive legure Ni-Ti izložene u ABP u odsustvu i prisustvu TFG semena tokom 20 dana

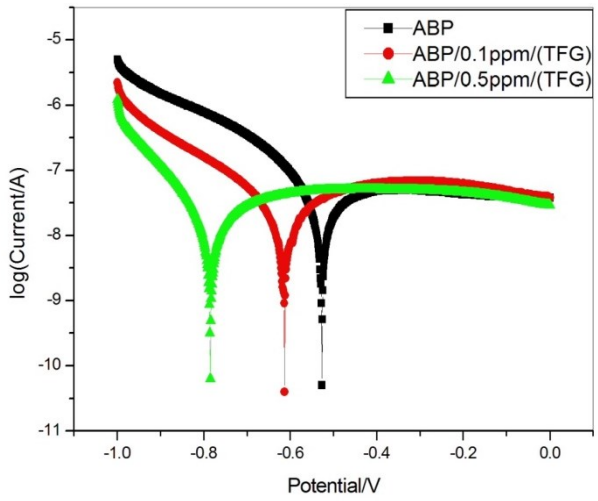

Figure 4. Polarization curves of Ni-Ti alloy exposed in ABP in the absence and presence of TFG seeds for 30 Days

Slika 4. Krive polarizacije legure Ni-Ti izložene u ABP u odsustvu i prisustvu TFG semena tokom 30 dana

The Ni-Ti alloy is immersed in ABP in the absence of TFG seeds for 1 day, the corrosion potential is -513 mV vs SCE, as shown in (Table 1). The LPR value is 1.8789×10^{6} ohm.cm^2, and the corrosion current (I_{corr}) is 2.331×10^{-8} A/cm^2. The Tafel slopes (b_c =137 mV/decade, b_a = 376 mV/decade). Similarly, when the Ni-Ti alloy is immersed in ABP in the presence of 0.1 ppm and 0.5 ppm of TFG seeds for 1 day, the potential corrosion shifts from -513 mV vs. SCE to -693 mV vs. SCE and -618 mV vs. SCE, as shown in (Table 1). The LPR value increases from 1.8789×10^{6} ohm.cm^2 to 1.9769×10^{6} ohm.cm^2 and 2.0478×10^{6} ohm.cm^2.The corrosion current (I_{corr}) value decreases from 2.331×10^{-8} A/cm^2 to 2.230×10^{-8} A/cm^2 and 2.085×10^{-8} A/cm^2. The Tafel slopes from (b_c= 137 mV/decade, ba = 376 mV/decade) to (b_c = 131 mV/decade, b_a = 386 mV/decade) and (b_c = 137 mV/decade, b_a = 376 mV/decade) indicate that the rate of change of corrosion current with potential is much higher during anodic polarisation than during cathodic polarisation.

The Ni-Ti alloy is immersed in ABP in the absence of TFG seeds for 10 days, the corrosion potential is -626 mV vs. SCE, as shown in (Table 1). The LPR value is 9.094×10^{5} ohm.cm^2 and the corrosion current (I_{corr}) is 5.250×10^{-8} A/cm^2. The Tafel slopes (bc =150 mV/decade, ba = 406 mV/decade).Similarly, when the Ni-Ti alloy is immersed in ABP in the presence of 0.1 ppm and 0.5 ppm of TFG seeds for 10 days, the potential corrosion shifts from -626 mV vs. SCE to -579 mV vs. SCE and -692 mV vs. SCE, as shown in (Table 1).The LPR value increases from 9.0947×10^{5} ohm.cm^2 to 1.3144×10^{6} ohm.cm^2 and 2.5225×10^{6} ohm.cm^2.The corrosion current (I_{corr}) decreases from 5.250×10^{-8} A/cm^2 to 3.391×10^{-8} A/cm^2 and 1.668×10^{-8} A/cm^2. The Tafel slopes from (bc = 150 mV/decade, ba= 406 mV/decade) to (bc=150 mV/decade, ba=270 mV/decade) and (bc =160 mV/decade, ba =283 mV/decade) indicate that the rate of change of corrosion current with potential is much higher during anodic polarisation than during cathodic polarisation. An oxide film is formed on the Ni-Ti alloy surface during anodic polarisation.

The Ni-Ti alloy is immersed in ABP in the absence of TFG seeds for 20 days, the corrosion potential is -494 mV vs. SCE, as shown in (Table 1).The LPR value is 5.3967×10^{5} ohm.cm^2, and the corrosion current (I_{corr}) is 8.900×10^{-8} A/cm^2. The Tafel slopes (bc =141 mV/decade, ba =504 mV/decade).Similarly, when the Ni-Ti alloy is immersed in ABP in the presence of 0.1 ppm and 0.5 ppm of TFG seeds for 20 days, the potential corrosion shifts from -494 mV vs. SCE to -570 mV vs. SCE and -585 mV vs. SCE, as shown in (Table 1).The LPR value increases from 5.3967×10^{5} ohm.cm^2 to 1.4743×10^{6} ohm.cm^2 and 2.0936×10^{6} ohm.cm^2. The corrosion current (I_{corr}) decreases from 8.900 10^{-8} A/cm^2 to 2.917×10^{-8} A/cm^2 and 2.073×10^{-8} A/cm^2. The Tafel slopes from

(bc =141 mV/decade, ba =504 mV/decade) to (bc =148 mV/decade, ba =304 mV/decade) and (bc =151 mV/decade, ba =284 mV/decade) indicate that the rate of change of corrosion current with potential is much higher during anodic polarisation than during cathodic polarisation. An oxide film is formed on the Ni-Ti alloy surface during anodic polarisation.

The Ni-Ti alloy is immersed in ABP in the absence of TFG seeds for 30 days, the corrosion potential is -509 mV vs. SCE, as shown in (Table 1). The LPR value is 5.0664×10^5 ohm.cm^2, and the corrosion current (I_{corr}) is 9.620×10^{-8} A/cm^2. The Tafel slopes (bc =149 mV/decade, ba = 443 mV/decade). Similarly, when the Ni-Ti alloy is immersed in ABP in the presence of 0.1 ppm and 0.5 ppm of TFG seeds for 30 days, the potential corrosion shifts from -509 mV vs. SCE to -615 mV vs. SCE and -786 mV vs. SCE, as shown in (Table 1). The LPR value increases from 5.0664×10^5 ohm.cm^2 to 1.7446×10^6 ohm.cm^2 and 2.0997×10^6 ohm.cm^2. The corrosion current (I_{corr}) decreases from 9.620×10^{-8} A/cm^2 to 2.621×10^{-8} A/cm^2 and 1.816×10^{-8} A/cm^2. The Tafel slopes from (bc=149 mV/decade, ba = 443 mV/decade) to (bc=166 mV/decade, ba =286 mV/decade) and (bc=122 mV/decade, ba =306 mV/decade) indicate that the rate of change of corrosion current with potential is much higher during anodic polarisation than during cathodic polarisation. An oxide film is formed on the Ni-Ti alloy surface during anodic polarisation.

The LPR rises, and the fall in corrosion current (I_{corr}) shows that the formation of a protective layer on the Ni-Ti implant alloy surface blocks the active sites and inhibits the corrosion, and weakens the rate of corrosion [19].

It is fascinating to note that the Ni-Ti in the presence of TFG seeds at 0.1 ppm and 0.5 ppm concentrations are immersed for 1, 10, 20 and 30 days, the rate of corrosion decreases, and the corrosion current also decreases, thereby showing in the LPR and I_{corr} values. This indicates that a compelling protective film is formed more on the alloy surface in the presence of TFG seeds for 30 days.

3.3. Analysis of Alternating Current impedance spectra

The equivalent circuit diagram of being immersed in ABP in the presence of 0.1 ppm and 0.5 ppm TFG seed concentrations for 1, 10, 20, and 30 days have shown in Figure 5 [20, 21]. The corrosion process is generally inhibited if the phase angle is greater than 45°.

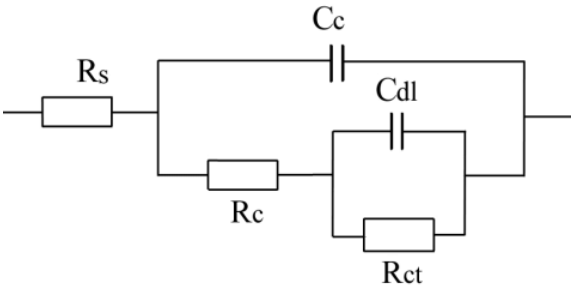

Figure 5. Equivalent circuit diagram

Slika 5. Ekvivalentna šema kola

R_{ct} = charge transfer resistance,

C_{dl} = double layer capacitance,

C_c = capacitance of the coating

The same kind of three-electrode cell assembly was utilised to record AC impedance spectra on the identical apparatus that was used for the polarisation investigation. At different frequencies, the cell impedance's real part Z' and imaginary part Z" were measured in ohms. Double layer capacitance (C_{dl}) and charge transfer resistance (R_t) values were computed.

$$R_t = (R_s + R_t) - R_s \quad .....(2)$$

where

R_t = total resistance

R_s = solution resistance

$$Cdl = \frac{1}{2\pi\ fmax\ Rct} \quad .....(3)$$

where

f_{max} = maximum frequency

The Ni-Ti alloy is immersed in ABP without TFG seeds for 1 day, the charge transfer resistance (R_{ct}) is 90 ohm.cm^2.The double layer capacitance (C_{dl}) is 1.766×10^{-8} F/cm^2, shown in (Table 2).The impedance value is 3.80 log (Z/ohm), as shown in (Figure 6(b)).The Bode phase graph shows the phase angle at 84°. Hence, the corrosion process is inhibited. When Ni-Ti alloy is immersed in ABP containing 0.1 ppm and 0.5 ppm of TFG seeds for 1 day, the R_{ct} value increases from 90 ohm.cm^2 to 180 ohm.cm^2 and 200 ohm.cm^2. The C_{dl} value decreases from 1.766×10^{-8} F/cm^2 to 8.83×10^{-9} F/cm^2 and 7.8×10^{-9} F/cm^2 shown in (Table 2).(Nyquist plots). The impedance increases from 3.80 log (Z/ohm) to 3.85 log (Z/ohm) and 3.95 log (Z/ohm), as shown in (Figure 6(b)). (Bode plots). The Bode-phase is shown between 82° and 83°. Hence corrosion is inhibited (Figure 6(c)).

Table 2. The fitted results of EIS using an equivalent circuit for the sample Ni-Ti alloy

Tabela 2. Prilagođeni rezultati EIS-a korišćenjem ekvivalentnog kola za uzorak Ni-Ti legure

Days	Alloy	System	Nyquist plot		Bode plot	
			$R_{ct}(\Omega.cm^2)$	$C_{dl}(F/cm^2)$	Impedance log(Z/ohm)	Phase angle (degrees)
1 Day	Ni-Ti	ABP	90	1.766×10^{-8}	3.80	84
		ABP/TFG 0.1 ppm	180	8.83×10^{-9}	3.85	82
		ABP /TFG 0.5 ppm	200	7.8×10^{-9}	3.95	83
10 Days		ABP	80	1.988×10^{-8}	3.90	85
		ABP /TFG 0.1 ppm	190	8.37×10^{-9}	4.15	80
		ABP /TFG 0.5 ppm	340	4.68×10^{-9}	4.35	65
20 Days		ABP	180	8.83×10^{-9}	3.95	81
		ABP /TFG 0.1 ppm	360	4.42×10^{-9}	4.0	84
		ABP /TFG 0.5 ppm	380	4.18×10^{-9}	4.05	86
30 Days		ABP	150	1.06×10^{-8}	3.95	80
		ABP /TFG 0.1 ppm	180	8.83×10^{-9}	4.20	76
		ABP /TFG 0.5 ppm	450	3.533×10^{-9}	4.40	84

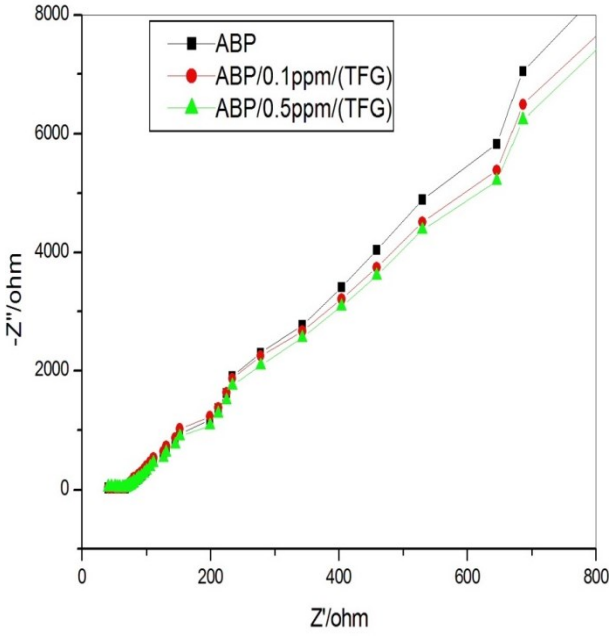

Figure 6(a). Nyquist plots of Ni-Ti alloy in ABP in the absence and presence of 0.1ppm and 0.5 ppm of TFG seeds for 1 day

Slika 6(a). Najkvistovi dijagrami legure Ni-Ti u ABP u odsustvu i prisustvu 0,1ppm i 0,5 ppm semena TFG tokom 1 dana

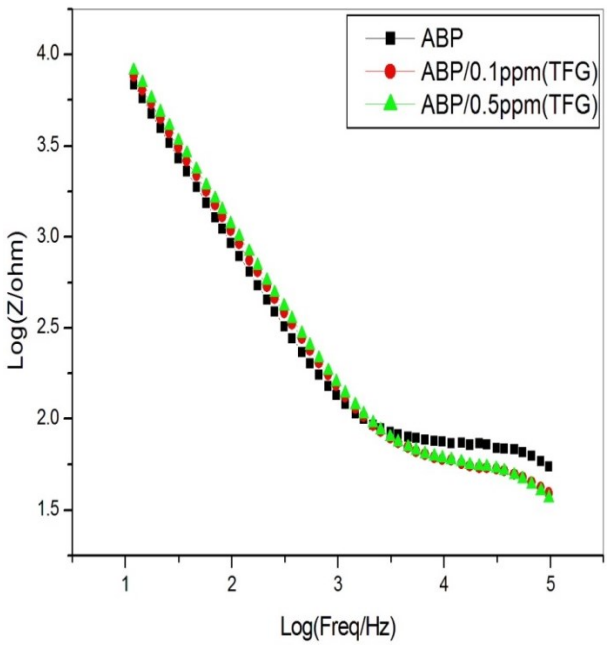

Figure 6(b). Bode plots of Ni-Ti alloy in ABP in the absence and presence of 0.1ppm and 0.5 ppm of TFG seeds for 1 day

Slika 6(b). Bodeovi dijagrami legure Ni-Ti u ABP u odsustvu i prisustvu 0,1 ppm i 0,5 ppm semena TFG tokom 1 dana

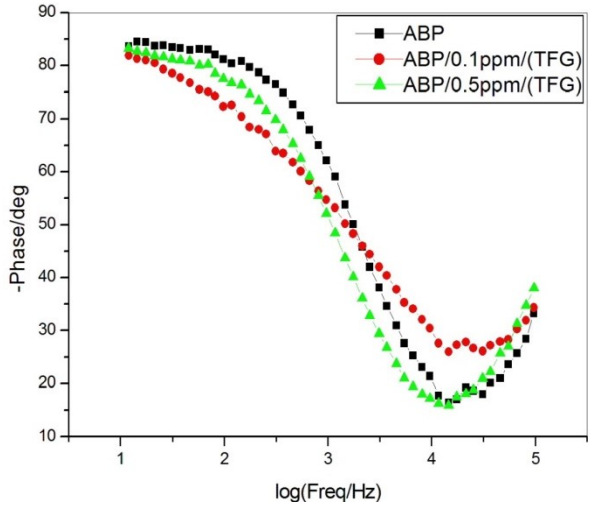

Figure 6(c). Bode plots of Ni-Ti alloy in ABP in the absence and presence of 0.1ppm and 0.5 ppm of TFG seeds for 1 day

Slika 6(c). Bodeovi grafikoni legure Ni-Ti u ABP u odsustvu i prisustvu 0,1 ppm i 0,5 ppm semena TFG tokom 1 dana

The Ni-Ti alloy is immersed in ABP without TFG seeds for 10 days, the charge transfer resistance (R_{ct}) is 80 ohm.cm^2. Therefore, the double layer capacitance (C_{dl}) is 1.988×10^{-8} F/cm^2 shown in (Table 2).The impedance value is 3.90 log (Z/ohm), as shown in (Figure 7(b)).The Bode phase graph shows the phase angle at 85°. Hence, the corrosion process is inhibited. When the Ni-Ti alloy is immersed in ABP containing 0.1 ppm and 0.5 ppm of TFG seeds for 10 days, the R_{ct} value increases from 80 ohm.cm^2 to 190 ohm.cm^2 and 340 ohm.cm^2.

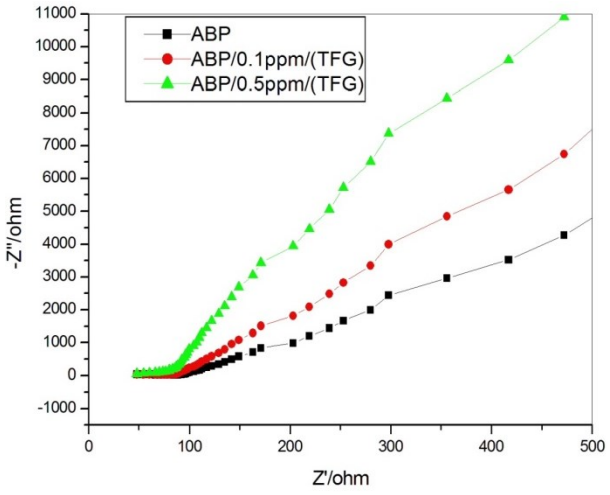

Figure 7(a). Nyquist plots of Ni-Ti alloy in ABP in the absence and presence of 0.1ppm and 0.5 ppm of TFG seeds for 10 days

Slika 7 (a). Najkvistovi dijagrami legure Ni-Ti u ABP u odsustvu i prisustvu 0,1ppm i 0,5 ppm semena TFG tokom 10 dana

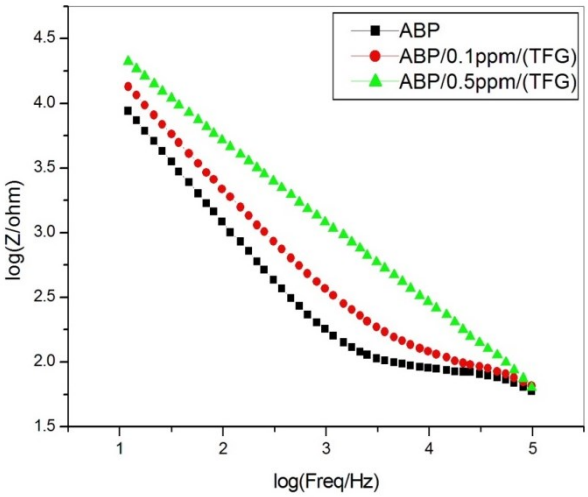

Figure 7(b). Bode plots of Ni-Ti alloy in ABP in the absence and presence of 0.1 ppm and 0.5 ppm of TFG seeds for 10 days

Slika 7(b). Bodeove grafike legure Ni-Ti u ABP u odsustvu i prisustvu 0,1 ppm i 0,5 ppm semena TFG tokom 10 dana

The C_{dl} value decreases from 1.988×10^{-8} F/cm^2 to 8.37×10^{-9} F/cm^2 and 4.68×10^{-9} F/cm^2 shown in (Table 2).(Nyquist plots). The impedance increases from 3.90 log (Z/ohm) to 4.15 log (Z/ohm) and 4.35 log (Z/ohm), as shown in (Figure (b)). (Bode plots). The Bode-phase is shown between 80° and 65°. Hence corrosion is inhibited (Figure 7(c)).

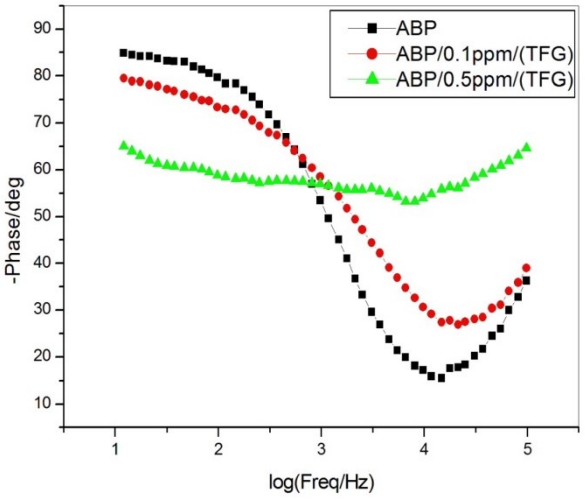

Figure 7(c). Bode plots of Ni-Ti alloy in ABP in the absence and presence of 0.1 ppm and 0.5 ppm of TFG seeds for 10 days

Slika 7(c). Bodeovi grafikoni legure Ni-Ti u ABP u odsustvu i prisustvu 0,1 ppm i 0,5 ppm semena TFG tokom 10 dana

The Ni-Ti alloy is immersed in ABP without TFG seeds for 20 days, the charge transfer resistance (R_{ct}) is 180 ohm.cm^2. The double layer capacitance (C_{dl}) is 8.83×10^{-9} F/cm^2, shown in

(Table 2).The impedance value is 3.95 log (Z/ohm), as shown in (Figure 8(b)). The Bode phase graph shows the phase angle at 81°. Hence, the corrosion process is inhibited. When Ni-Ti alloy is immersed in ABP containing 0.1 ppm and 0.5 ppm of TFG seeds for 20 days, the R_{ct} value increases from 180 ohm.cm^2 to 360 ohm.cm^2 and 380 ohm.cm^2. The C_{dl} value decreases from 8.83×10^{-9} F/cm^2 to 4.42×10^{-9} F/cm^2 and 4.18×10^{-9} F/cm^2, as shown in (Table 2).(Nyquist plots). The impedance value increases from 3.95 log (Z/ohm) to 4.0 log (Z/ohm) and 4.05 log (Z/ohm) shown in (Figure 8(b)). (Bode plots). The Bode-phase has shown the phase angle between 84° and 86°. Hence corrosion is inhibited (Figure 8(c)).

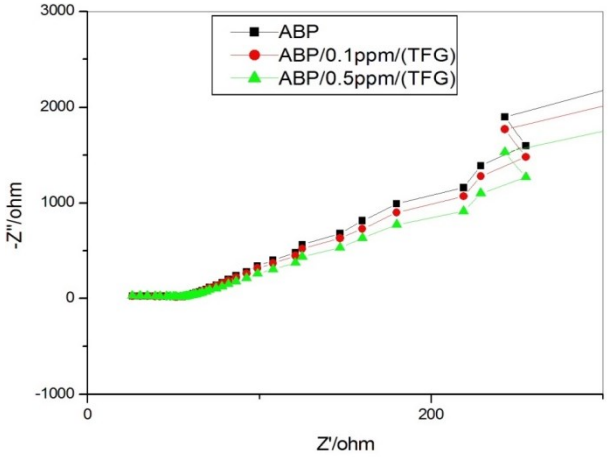

Figure 8(a). Nyquist plots of Ni-Ti alloy in ABP in the absence and presence of 0.1ppm and 0.5 ppm of TFG seeds for 20 days

Slika 8 (a). Najkvistovi dijagrami legure Ni-Ti u ABP u odsustvu i prisustvu 0,1 ppm i 0,5 ppm semena TFG tokom 20 dana

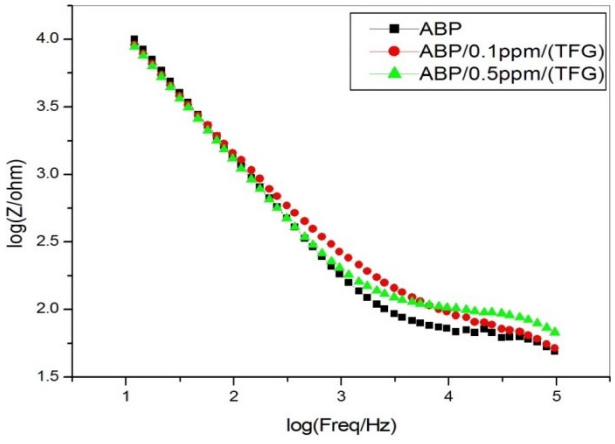

Figure 8(b). Bode plots of Ni-Ti alloy in ABP in the absence and presence of 0.1ppm and 0.5 ppm of TFG seeds for 20 days

Slika 8(b). Bodeove grafike legure Ni-Ti u ABP u odsustvu i prisustvu 0,1 ppm i 0,5 ppm semena TFG tokom 20 dana

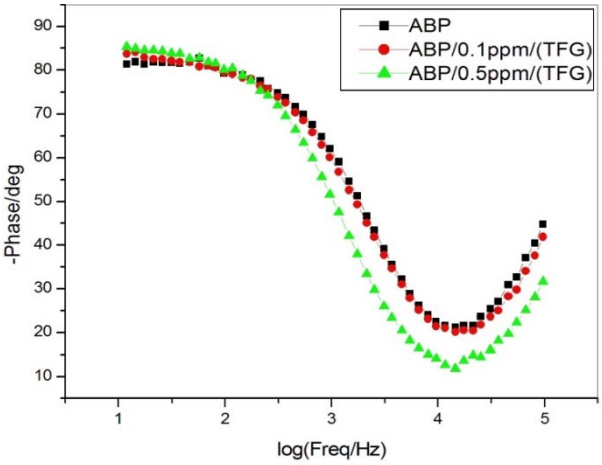

Figure 8(c). Bode plots of Ni-Ti alloy in ABP in the absence and presence of 0.1 ppm and 0.5 ppm of TFG seeds for 20 days

Slika 8(c). Bodeovi grafikoni legure Ni-Ti u ABP u odsustvu i prisustvu 0,1 ppm i 0,5 ppm semena TFG tokom 20 dana

The Ni-Ti alloy is immersed in ABP without TFG seeds for 30 days, the charge transfer resistance (R_{ct}) is 150 ohm.cm^2. The double layer capacitance (Cdl) is 1.06×10^{-8} F/cm^2, shown in (Table 2). The impedance value is 3.95 log (Z/ohm), as shown in (Figure 9(b)). The Bode phase graph shows the phase angle is 80°. So the corrosion process is inhibited. When Ni-Ti alloy is immersed in ABP containing 0.1 ppm and 0.5 ppm of TFG seeds for 30 days, the R_{ct} value increases from 150 ohm.cm^2 to 180 ohm.cm^2 and 450 ohm.cm^2.

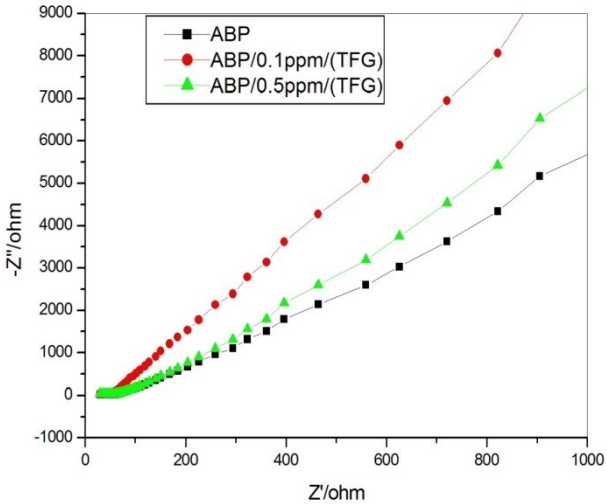

Figure 9(a). Nyquist plots of Ni-Ti alloy in ABP in the absence and presence of 0.1ppm and 0.5 ppm of TFG seeds for 30 days

Slika 9(a). Najkvistovi dijagrami legure Ni-Ti u ABP u odsustvu i prisustvu 0,1 ppm i 0,5 ppm semena TFG tokom 30 dana

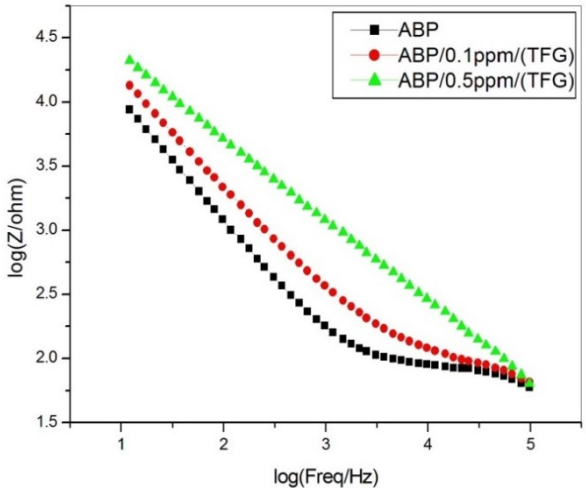

Figure 9(b). Bode plots of Ni-Ti alloy in ABP in the absence and presence of 0.1ppm and 0.5 ppm of TFG seeds for 30 days

Slika 9(b). Bodeove grafike legure Ni-Ti u ABP u odsustvu i prisustvu 0,1 ppm i 0,5 ppm semena TFG tokom 30 dana

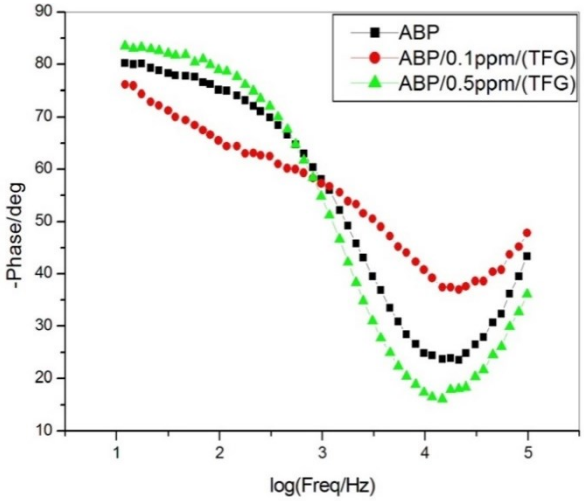

Figure 9(c). Bode plots of Ni-Ti alloy in ABP in the absence and presence of 0.1ppm and 0.5 ppm of TFG seeds for 30 days

Slika 9(c). Bodeovi grafikoni legure Ni-Ti u ABP u odsustvu i prisustvu 0,1 ppm i 0,5 ppm semena TFG tokom 30 dana

The C_{dl} value decreases from 1.06×10^{-8} F/cm^2 to 8.83×10^{-9} F/cm^2 and 3.533×10^{-9} F/cm^2, as shown in Table 2.(Nyquist plots). The impedance value increases from 3.95 log (Z/ohm) to 4.20 log (Z/ohm) and 4.40 log (Z/ohm), as shown in (Figure 9(b)). (Bode plots). The Bode-phase is shown between 76° and 84°. Hence, the corrosion is inhibited (Figure 9(c)).

From the results, the charge transfer resistant value (R_{ct}) and impedance value increase while the double-layer capacitance value decreases because double-layer capacitance is inversely related to charge transfer resistance [19].

The semi-circle diameter was significantly smaller in the absence of TFG seeds than in the presence of 0.1 ppm and 0.5 ppm of TFG seeds, as shown in Figure 6(a-d). The largest semi-circle diameter indicates the lowest corrosion rate, according to a comparison of the Nyquist diagrams for the three scenarios.

It is fascinating to note that the Ni-Ti alloys in the presence of TFG seeds at 0.1 ppm and 0.5 ppm concentrations are immersed for 1, 10, 20, and 30 days, the rate of corrosion decreases and the C_{dl} decreases, thereby showing in the R_{ct} increase. This indicates that a compelling protective film was formed more on the Ni-Ti alloy surface in the presence of TFG seeds for 30 days.

3.4. Scanning Electron Microscope

SEM micrographs of the surface are examined to understand the nature of the surface film in the absence and presence of inhibitors and the extent of the corrosion of Ni-Ti alloy [22, 23]. The SEM images of different magnifications (X500, X3.50K, and X2.00K) of Ni-Ti alloy specimens immersed in ABP in the absence and presence of additive systems are shown in Figure 10 a, b and c respectively.

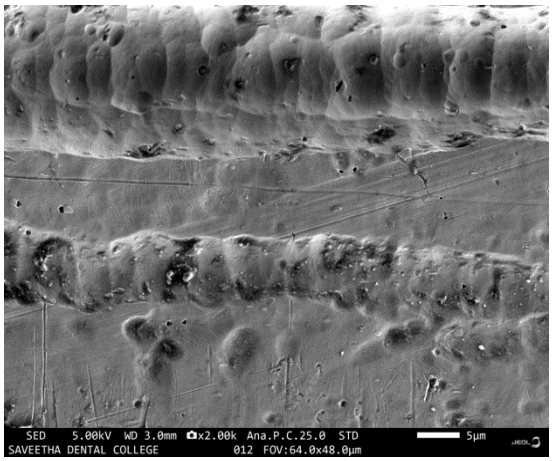

Figure 10 (a). SEM image of blank Ni-Ti alloy

Slika 10 (a). SEM slika polirane prazne legure Ni-Ti

The SEM proposes an illustrative demonstration of the Ni-Ti alloy surface. The SEM micrographs of the surface are examined. The SEM metaphors of blank Ni-Ti alloy are shown in Figure 10 (a) on the smooth surface of the alloy. This indicates the absence of corrosion products on the metal surface.The SEM metaphors of Ni-Ti alloy exposed in ABP have shown in Figure 10(b), designate the minor roughness of the alloy surface, which indicates the corrosion of Ni-Ti alloy in ABP (Figure 10(c)) shows that the presence of 0.5 ppm of TFG seeds in ABP at 30 days.

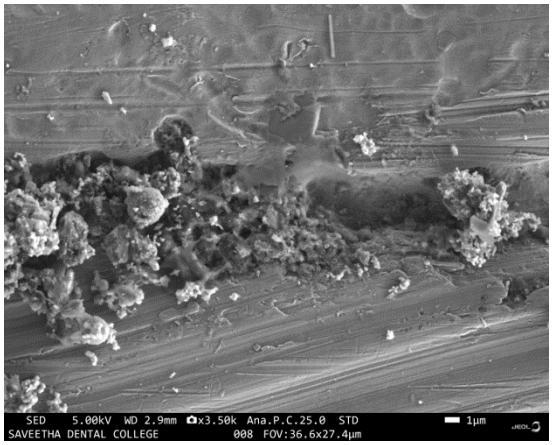

Figure 10 (b). SEM image of Ni-Ti alloy / ABP

Slika 10 (b). SEM slika legure Ni-Ti / ABP

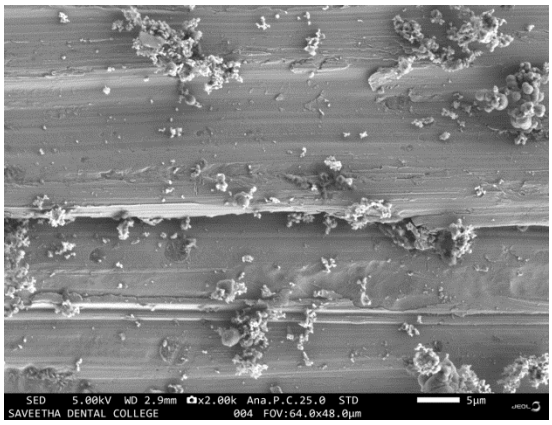

Figure 10 (c). SEM image of Ni-Ti alloy / ABP / TFG seeds

Slika 10 (c). SEM slika legure Ni-Ti / ABP / TFG semena

The surface coverage improvement is due to the formation of insoluble complexes on the alloy surface, which efficiently controls the dissolution of the Ni-Ti alloy.

3.5. Energy Dispersive Analysis of X-rays

The EDAX spectra were used to determine the elements present on the alloy surface before and after exposure to the inhibitor solution. The objective of this section was to confirm the results obtained from electrochemical measurements that a protective surface film of inhibitor is formed on the alloy surface. To achieve this, EDAX examinations of the alloy surface were performed in both the absence and presence of additive systems [24-27].

The EDAX spectrum of blank Ni-Ti alloy has shown in Figure 11(a) .The chemical compositions have shown Ni = 50.1, Ti = 40.2, and C = 9.7, respectively. The Ni-Ti alloy immersed in ABP containing 0.5 ppm of TFG seeds has shown in Figure 11(c). It shows the additional line characteristics for Na = 2.5, Ca = 7.8, P = 4.0, and Cl = 1.4. In addition, the intensity of the N = 25.2 signal is enhanced. The appearance of the Na and Ni signals and this enhancement in N and S are due to inhibitors (TFG seeds). These data show that the alloy surface is covered by P, N, Na, Cl, and Ca atoms have shown in Figure 11(c) demonstrates that, compared to those seen in ABP Figure 11(b), the Ni peaks seen in the presence of inhibitors are significantly decreased. The suppression of the Ni peaks occurs because of the overlying inhibitor film. This observation indicates the existence of an adsorbed layer of inhibitor that protects Ni-Ti alloy against corrosion. These results suggest that the N, P, Cl, Ca, and S atoms of TFG seeds have coordinated with Ni-Ti alloy complex. The anodic sites of the Ni-Ti alloy surface exhibit TFG seed complexes, while the cathodic sites of the alloy surface exhibit Ca atom precipitation in the form of superhydrophobic coatings.

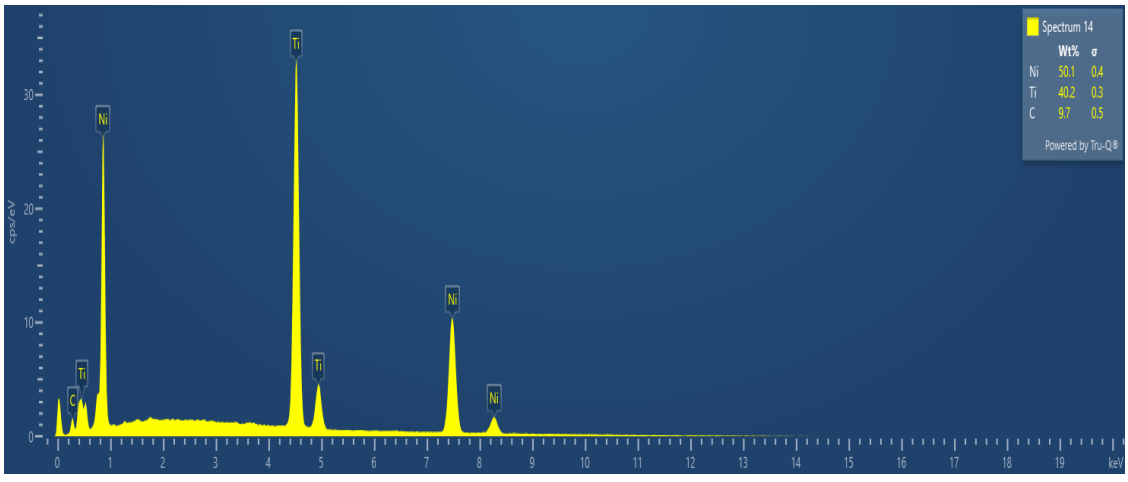

Figure 11 (a). EDAX of polished Ni-Ti alloy

Slika 11 (a.) EDAX od polirane legure Ni-Ti

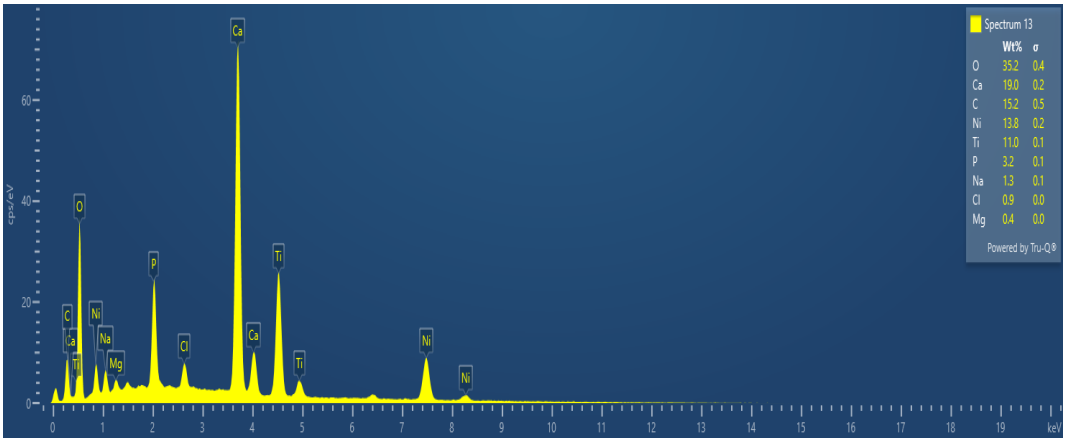

Figure 11 (b). EDAX of polished Ni-Ti alloy / ABP

Slika 11 (b). EDAKS od polirane legure Ni-Ti / ABP

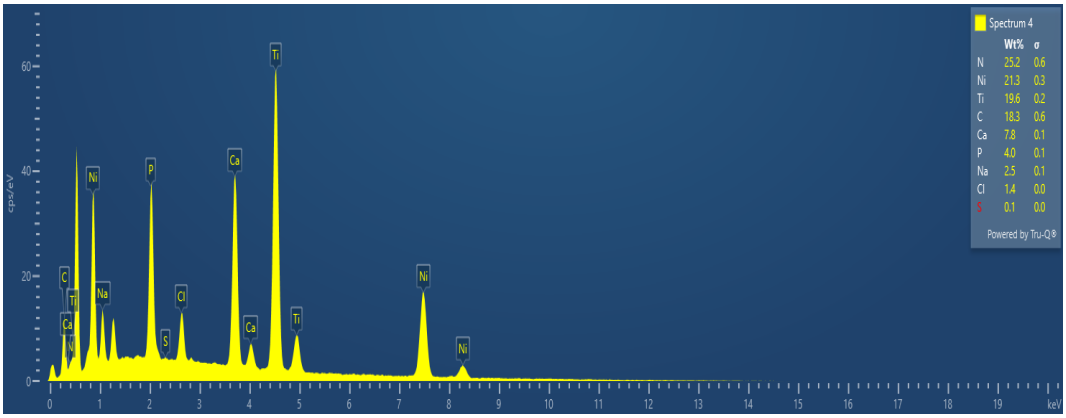

Figure 11 (c). EDAX of polished Ni-Ti alloy / ABP / TFG seeds

Slika 11 (c). EDAKS od polirane legure Ni-Ti / ABP / TFG semena

3.6. Atomic Force Microscope

Atomic force microscopy is a practical method for obtaining surface roughness data.AFM is becoming an accepted method of roughness investigation [26, 28].

The atomic force microscopy images were obtained with the help of AFM-Ntegra Prima, NTMDT, and Ireland incorporation. AFM instrument operating in contact mode in the air. The scan size of all the AFM images is 10 µm x 10 µm areas at a scan rate of 1 line/sec, and the scanning direction is horizontal. The varying scan rate depends upon the frequency and scanning area of the sample. AFM study is created for the best system of Ni-Ti alloy in TFG used as an inhibitor.

The analysis of an atomic force microscope (AFM) is a suitable method for collecting roughness indicators from various surfaces. The three-dimensional (3D) morphologies are present in the polished Ni-Ti alloy surface, the Ni-Ti alloy treated to artificial blood plasma, and 0.5 ppm of TFG at 30 days.

Table 3. AFM Analysis for Ni-Ti alloy exposed in the presence and absence of TFG seeds
Tabela 3. AFM analiza za Ni-Ti leguru izloženu u prisustvu i odsustvu TFG semena

Samples	RMS, (Sq) Roughness (nm)	Average, (Sa) Roughness (nm)	Maximum Peak-to peak valley Height, (nm)	Coefficient of Kurtosis (S_{ka})	Entropy	Surface Skewness (S_{sk})
Refined, Ni-Ti	20.95	15.30	430.64	6.74	9.55	0.088
ABP /Ni-Ti	46.16	28.16	648.3	18.26	10.34	2.94
ABP/Ni-Ti /TFG 0.5 ppm	54.26	39.87	860.86	9.48	10.11	1.30

AFM analysis was performed to attain the Average roughness (Sa), Root-mean-square roughness (Sq), and the maximum peak-to-peak valley (P-v) height values. These values for Ni-Ti alloy exposed in the different environments are summarized in Table 3.

Figure 12 (a) shows the surface topography of the polished Ni-Ti alloy surface. The Sa, Sq, and P-v height data for the refined Ni-Ti alloys are 15.30 nm, 20.95 nm, and 430.64 nm, correspondingly. These data designate the surface of Ni-Ti alloy as identical. The slight roughness discovered in the refined Ni-Ti alloy is due to atmospheric corrosion Figure 12(b) shows the pitting corrosion Ni-Ti alloy without Trigonella foenum-graecum engaged in ABP of Sa, Sq, and P-v data get for the refined Ni-Ti alloys is 28.16 nm, 46.16 nm, and 648.3 nm, correspondingly. These data designate the surface of Ni-Ti alloy with superior roughness to the refined Ni-Ti alloy.The Figure 12(c) shows the Ni-Ti alloy in ABP comprising 0.5 ppm of Trigonella foenum-graecum seeds. The data of Sa, Sq, and P-v height values for the refined Ni-Ti alloys are 39.87 nm, 54.26 nm, and 860.86 nm, correspondingly. These data designate that the surface of Ni-Ti alloy values is prominently high. These data also designate the surface of Ni-Ti alloy as superior roughness to the refined Ni-Ti alloy. These aspects authorize that the surface is smooth, and a strong shielding layer bounds the surface of the metal layer.

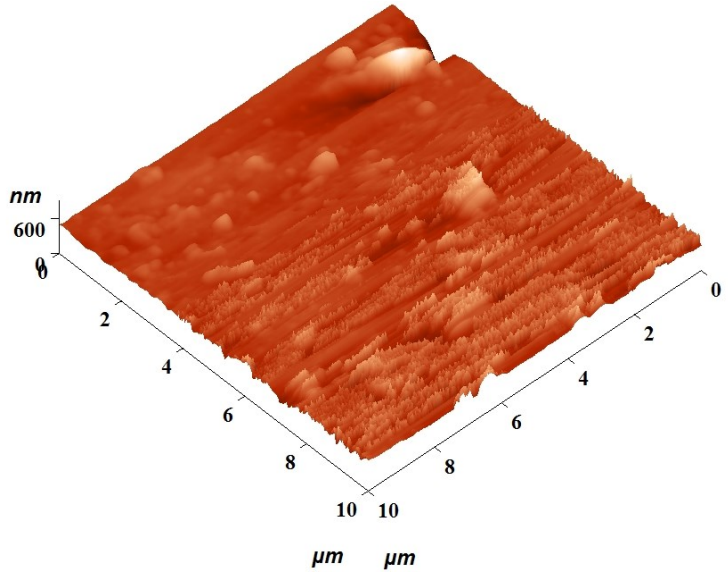

Figure 12 (a). AFM image of Ni-Ti alloy

Slika 12 (a). AFM slika legure Ni-Ti

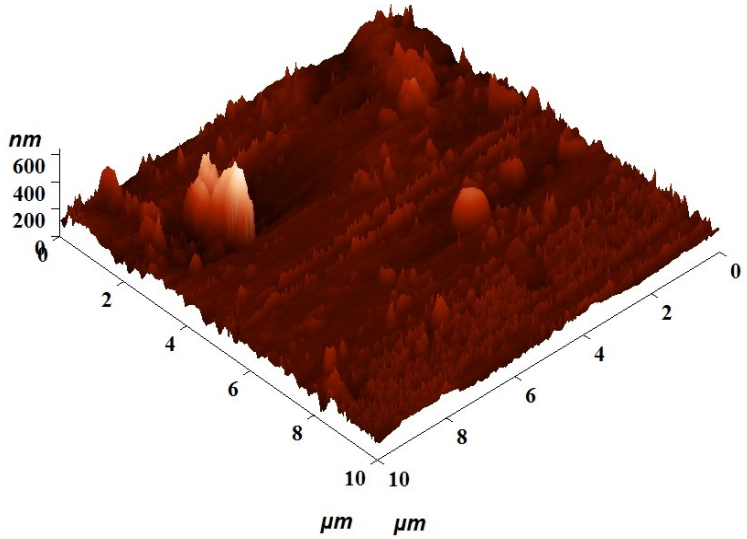

Figure 12 (b). AFM image of Ni-Ti alloy / ABP

Slika 12 (b). AFM slika legure Ni-Ti / ABP

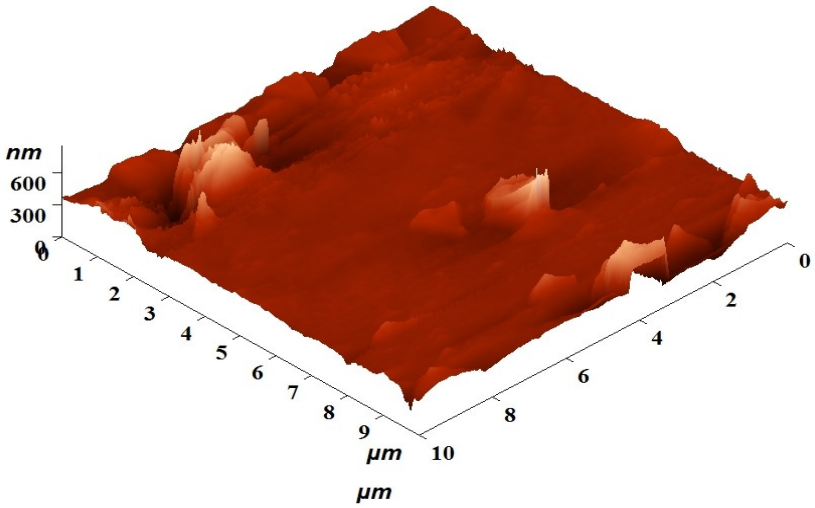

Figure 12 (c). AFM image of Ni-Ti alloy / ABP / TFG seeds

Slika 12 (c). AFM slika legure Ni-Ti / ABP / TFG semena

The entropy values for polished Ni-Ti alloy in ABP and Ni-Ti alloy in artificial blood plasma comprising 0.5ppm of TFG seeds decline progressively. It demonstrates that the Ni-Ti alloy corrosion resistance increases. Surface skewness (S_{sk}) is a statistical parameter to explain the amplitude distribution function, which indicates the probability that a profile of the surface has a certain height at any position. A surface with low skewness shows a porous surface with fairly deep valleys in a smoother plateau for refined Ni-Ti alloy. The Ni-Ti alloy exposed in ABP surfaces with high skewness shows the raised surface has relatively high spikes that bulge above a flatter average for Ni-Ti alloy exposed with TFG seeds engaged in ABP.Kurtosis is associated with the spikiness of the profile. The polished Ni-Ti alloy, Ni-Ti alloy in ABP, and Ni-Ti alloy in ABP comprising 0.5 ppm of TFG seeds, Kurtosis distribution, has few high peaks and low value comparatively flat surface. It is decided that the Ni-Ti alloy in ABP comprising 0.5 ppm of TFG seeds is more corrosion resistant than the polished Ni-Ti alloy and Ni-Ti alloy in ABP.

3.7. X-ray diffraction analysis

XRD patterns of the Ni-Ti alloy and Ni-Ti alloy in ABP in the presence of TFG seeds have shown in Figure 13(a) and Figure 13(b).It can be seen from XRD patterns that blank Ni-Ti alloy shows two prominent diffraction peaks between 20 and 80. The prominent peaks at 42.3 (110) and 77.5 (211) belong to the Ni-Ti phase [29].

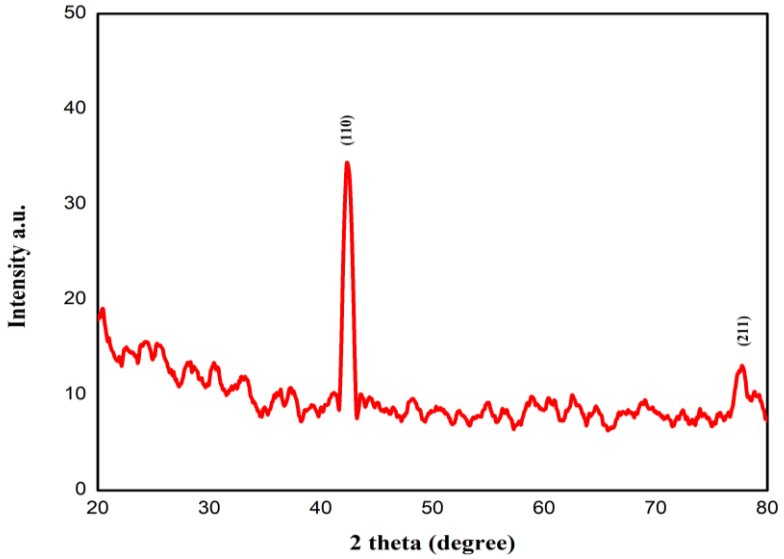

Figure 13 (a). XRD pattern of Ni-Ti alloy

Slika 13 (a). KSRD uzorak legure Ni-Ti

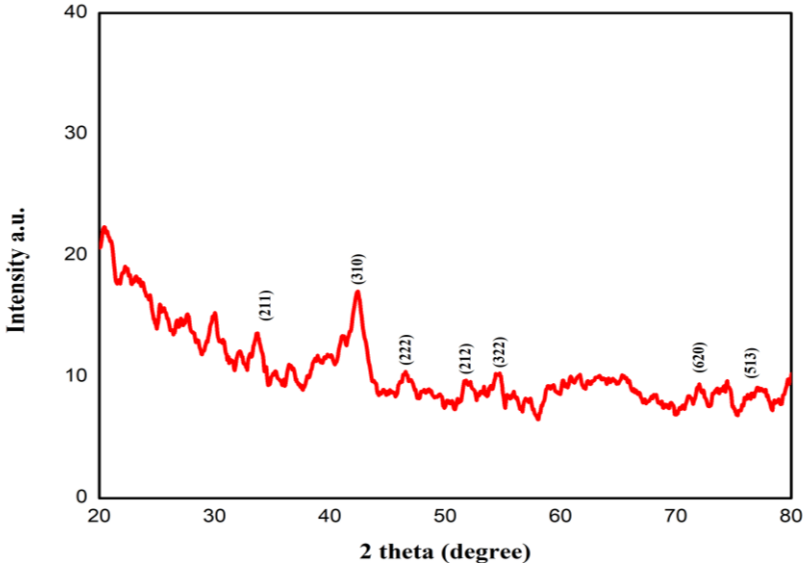

Figure 13 (b). XRD pattern of Ni-Ti alloy / ABP / TFG seeds

Slika 13 (b). KSRD uzorak legure Ni-Ti / ABP / TFG semena

After being immersed in TFG seeds implantation and anodization, a stable characteristic peak of rutile TiO_2 appears, as seen in their diffraction patterns in Figure 13(b). These results show the formation of a TiO_2 layer on the Ni-Ti Surface [30]. The HA on Ni-Ti alloy in ABP in the presence of TFG seeds was identified using an XRD investigation. As a result, the sample contains HA, as shown by the XRD analysis results in Figure 13(b).

The first three more significant peaks of intensity in the diffraction pattern of HA powder shown by XRD examination, the first three more significant peaks of intensity located between the angular zone $30 < 2\theta < 50$ were assigned corresponded to the Miller indices of 211, 310, and 222. Although such indexes are associated with HA, no isolated peaks with a lower intensity are present, indicating that crystallinity is not very high [31]. However, a comparison between the obtained HA XRD patterns and the JCPDS 09-432 file shows that HA powder obtained by the wet precipitation method represents the typical HA pattern [32].

4. CONCLUSION

It is fascinating to note that the Ni-Ti alloy in the presence of TFG seeds at 0.1 ppm and 0.5 ppm concentrations are immersed for 1, 10, 20 and 30 days, the rate of corrosion decreases, and the corrosion current also decreases, thereby showing in the LPR, $I_{corr,}$ C_{dl} and R_{ct} values. This indicates that a compelling protective film is formed on the alloy surface in the presence of TFG seeds. Thus, the polarisation study and AC impedance spectral study leads to the conclusion that the corrosion resistance of Ni-Ti alloys in ABP in the presence of TFG seeds of 0.1 ppm and 0.5 ppm for 1, 10, 20, and 30 days is in the following order:

30 days > 20 days > 10 days > 1 day

According to the description above, the 30 days of immersion operate as a more corrosion-resistant phase than other times because LPR increases while I_{corr} decreases, the rate of corrosion decreases and the C_{dl} decreases, thereby showing in the R_{ct} increase. This indicates that a compelling protective film was formed on the Ni-Ti alloy surface in the presence of TFG seeds.

The SEM has validated the superhydrophobic coatings surface morphology. EDAX has determined the elemental compositions of Ni-Ti alloys and ABP in the presence of TFG seeds. Using AFM and XRD, the topography and apatite formation complexes of the Ni-Ti alloy are investigated.

The electrochemical behaviour of Ni-Ti alloys in ABP was studied for 1, 10, 20, and 30 days, with and without TFG seeds. As a result of the discussions above, the anticorrosive coating layer of the alloy is formed for an increasing number of days. In addition, the alloys hydroxyapatite layer is formed for an increased number of immersion days. As a result of the preceding discussions, we conclude that ingesting any of the Trigonella foenum-graecum for a person with Ni-Ti alloy implanted will strengthen their immune system and create an anticorrosive layer. These Ni-Ti alloys underwent the observed electrochemical modifications.

5. REFERENCES

[1] M.A.Siyah, R.Moradian, I.Manouchehri (2019) Electrochemical impedance spectroscopy (EIS) study of modified SS316L using radio frequency sputtering Ti6Al4V coating in ringer solution, Anti-Corrosion Methods and Materials., 66(1), 27-33. https://doi.org/10. 1108/ ACMM-05-2018-1929.

[2] M.Gojic, L.Vrsalovic, S.Kozuh, D.Cubela, S. Gudic (2012) Microstructure and corrosion properties Ni-Ti alloy after electrochemical testing in 0.9% NaCl solution, Zaštita materijala., 53(4), 345-351. (http://idk. org.rs/wp-content/uploads/ 2013/12/ ZM_ 53_4_345.pdf.)

[3] S.A.Fadlallah, N.El-Bagoury, S.M.G.El-Rab, R.A.Ahmed, G.El-Ousamii (2014) An overview of Ni-Ti shape memory alloy: Corrosion resistance and antibacterial inhibition for dental application, J. of Alloys and Compounds., 583, 455-464. https://doi.org/ 10.1016/j.jallcom. 2013.08.029.

[4] S.A.Shabalovskaya, G.C.Rondelli, A.L.Undisz, J.W. Anderegg, T.D.Burleigh, M.E.Rettenmayr (2009) The electrochemical characteristics of native Nitinol surfaces, Biomaterials., 30(22), 3662-3671. https://doi.org/10.1016/j.biomaterials. 2009.03.034.

[5] F.Stergioudi, C.A.Vogiatzis, E.Pavlidou, S. Skolianos, N.Michailidis (2016) The corrosion resistance of porous NiTi biomedical alloy in simulated body fluids, Innovative Materials and Structures., 25(9), 095024. http://dx.doi.org/10. 1088/0964-1726/25/9/095024.

[6] T.Hu, C.Chu, Y.Xin,S.Wu, K.W.Yeung, P.K. Chu (2010) Corrosion products and mechanism on NiTi shape memory alloy in a physiological environment, Journal of Materials Research., 25(2), 350-358. https://doi.org/ 10.1557/JMR. 2010.0051.

[7] T.Hu, Y.C. Xin, S.L.Wu, C.L.Chu, J.Lu, L.Guan, P.K.Chu (2011) Corrosion behaviour on orthopedic Ni-Ti alloy with nanocrystalline/amorphous surface, Materials Chemistry and Physics., 126(1-2), 102-107. https://doi.org/10.1016/j.matchemphys. 2010. 11.061.

[8] S.Acharya, A.Srichamroen, S.Basu, B. Ooraikul, T.Basu (2006) Improvement in the nutraceutical properties of fenugreek (Trigonella foenum-graecum L.), Songklanakarin J. Sci. Technol., 28(1), 1-9. (https://www.thaiscience. info/journals/Article/SONG/10462627.pdf.)

[9] M.Aasim, F.S.Baloch, A.Bakhsh, M. Sameeullah, K.M.Khawar (2018) Biotechnological approaches for genetic improvement of fenugreek (Trigonella foenum-graceum L.) Biotechnological Approaches for Medicinal and Aromatic Plants Conservation, Genetic Improvement and Utilization., p.417-444. https://doi.org/10.1007/978-981-13-0535-1_19.

[10] D.Tiran, (2003) The use of fenugreek for breastfeeding women. Complementary Therapies in Nursing and Midwifery., 3(9), 155-156. http://dx. doi.org/ 10.1016%2FS1353-6117(03) 00044-1.

[11] E.K.Kalra (2003) Nutraceutical definition and introduction, Aaps Pharmsci., 5(3), 27-28. https://doi.org/10.1208/ps050325.

[12] W.Kajzer, A.Krauze, W.Walke, J.Marciniak (2008) Corrosion behavior of AISI 316L steel in artificial body fluids, Journal of Achievements in Materials and manufacturing engineering., 31(2), 247-253. (https://www.researchgate.net/profile/AnitaKajzer/publication/268808675_Kajzer_Krauze_Walke_Marciniak_Journal_of_Achievements_in_Materials_and_Manufacturing_Engineering/links/54772a190cf2a961e48240bd/Kajzer-Krauze-Walke-Marciniak-Journal-of-Achievements-in-Materials-and-Manufacturing-Engineering.pdf, 01.12.2008.)

[13] G.A.Petropoulos (2002) Fenugreek: the genus Trigonella., CRC Press. https://doi.org/10.4324/ 9780203217474.

[14] F.R.García-Galvan, S.Fajardo, V.Barranco, S.Feliu (2021) Experimental apparent stern–geary coefficients for AZ31B Mg alloy in physiological body fluids for accurate corrosion rate determination, Metals,, 11(3), 391. https://doi.org/10.3390/ met11030391.

[15] A.C.C.Mary, S.Rajendran, H.Al-Hashem, R.J. Rathish, T.Umasankareswari, J.Jeyasundari (2015) Corrosion resistance of mild steel in simulated produced water in presence of sodium potassium tartrate, Int. J. Nano Corr. Sci. Eng., 1, 42-50. (https://www.researchgate.net/profile/Susai-Rajendran/publication/272834126_Corrosion_Resistance_Of_Mild_Steel_In_Simulated_Produced_Water_In_Presence_Of_Sodium_Potassium_Tartrate/links/54f1c2650cf2f9e34eff053d/Corrosion-Resistance-Of-Mild-Steel-In-Simulated-Produced-Water-In-Presence-Of-Sodium-Potassium-Tartrate.pdf.)

[16] V.Singh, A.N.Garg (2006) Availability of essential trace elements in Indian cereals, vegetables, and spices using INAA and the contribution of spices to daily dietary intake, Food Chemistry., 94(1),81–89. doi:10.1016/j.foodchem.2004.10.053 .

[17] K.Srinivasan (2006) Fenugreek (Trigonella foenum-graecum) A review of health beneficial physiological effects, Food reviews international., 22(2), 203–224. https://doi.org/10.1080/ 87559120600586315.

[18] P.Ojha, P.Prajapati, T.B.Karki (2018) Soaking and germination effect on bioactive components of fenugreek seeds (Trigonella foenum graecum L.), International Food Research Journal., 25(2), 690-694. http://www. ifrj.upm.edu.my/.

[19] S.John Mary, G.Puthlibai, P.Kathiravan, J.Mano Deepa, A.Selvam (2021) Electrochemical behavior of Ni-Ti (Super-elastic) alloy in the artificial saliva in the presence of Phexin, Materials Today Proceedings., pp. 36, 878–882. https://doi.org/ 10.1016/j.matpr. 2020. 07.022.

[20] E.Castaneda, J.G.Gonzalez-Rodriguez, J.Colin, M.A.Neri-Flores (2010) Electrochemical behavior of Ni-Al-Fe alloys in simulated human body solution, Journal of Solid State Electrochemistry., 14, 1145-1152. https://doi.org/10. 1007/ s10008-009-0941-z

[21] S.John Mary, S.Rajendran (2013) Corrosion Behaviour of SS316L in Artificial Blood Plasma in the Presence of Amoxicillin, Portugaliae Electrochimica Acta., 31(1), 33-40. doi: 10.4152/ pea. 201301033.

[22] S.R.Paital, N.B.Dahotre (2009) Calcium phosphate coatings for bio-implant applications Materials performance factors and methodologies, Materials Science and Engineering: R: Reports., 66(1-3), 1-70. https://doi.org/10. 1016/ j.mser.2009.05.001.

[23] V.A.Brigitta, C.Thangavelu, S.Rajendran (2019) Effects of tablet on orthodontic wire made of SS 316L alloy in Artificial Saliva, International J. of Research and Analytical Reviews., 6,1000-1005. (https://www.researchgate.net/profile/SusaiRajendran/publication/332303320_Effects_of_Tablet_on_Orthodontic_Wire_made_of_SS316L_Alloy_in_Artificial_Saliva/links/5cacdf00458515cd2b0d266c/Effects-of-Tablet-on-Orthodontic-Wire-made-of-SS316L-Alloy-in-Artificial-Saliva.pdf.)

[24] A.Abdal-Hay, H.A.Fouad, B.Alshammari, K.A. Khalil (2020) Biosynthesis of bonelike apatite 2D nanoplate structures using fenugreek seed extract, Nanomaterials., 10(5), 919. https://doi. org/ 10. 3390/ nano10050919.

[25] M.A.Hussein, M.Kumar, R.Drew, N.Al-Aqeeli (2017) Electrochemical corrosion and in vitro bioactivity of nano-grained biomedical Ti-20Nb-13Zr alloy in a simulated body fluid, Materials., 11(1), 26-35. http://dx. doi.org/10. 3390/ ma11010026.

[26] R.Nagalakshmi, L.Nagarajan, R.J.Rathish, S.S. Prabha, N.Vijaya, J.Jeyasundari, S.Rajendran (2014) Corrosion resistance of SS316L in artificial urine in presence of D-glucose, Int. J. Nano. Corr. Sci. Engg., 1(1), 39-49. (https://www.researchgate.net/profile/SusaiRajendran/publication/272743214_Corrosion_Resistance_Of_SS316l_In_Artificial_Urine_In_Presence_Of_D-Glucose/links/54ecaa6f0cf27fbfd7713d7d/Corrosion-Resistance-Of-SS316l-In-Artificial-Urine-In-Presence-Of-D-Glucose.pdf.)

[27] Y.C.Hong, D.H.Shin, S.C.Cho, H.S.Uhm (2006) Surface transformation of carbon nanotube powder into super-hydrophobic and measurement of wettability, Chem.Phys.Lett., 427(4–6), 390-393. doi:10.1016/j.cplett.2006.06.033.

[28] J.C.Souza, S.L.Barbosa, E.A.Ariza, M.Henriques, W.Teughels, P.Ponthiaux, J.P.Celis, L.A. Rocha (2015) How do titanium and Ti6Al4V corrode in the fluoridated medium as found in the oral cavity? An in vitro study, Materials Science and Engineering: C., 47, 384-393. https://doi. org/10.1016/j.msec. 2014.11.055.

[29] P.Kowalski, B.Losiewicz, T.Goryczka (2015) Deposition of chitosan layers on Ni-Ti shape memory alloy, "Archives of Metallurgy and Materials"., 1, 171-176. http://dx.doi.org/10.1515/ amm-2015-0027.

[30] S.Viswanathan, L.Mohan, P.Bera,C.Anandan (2016) Effect of oxygen plasma immersion ion implantation on the formation of nanostructures over Ni–Ti alloy, RSC advances., 6(78), 74493-74499. https://doi.org/10.1039/ C6RA11541A.

[31] D.Malina, K.Biernat, A.Sobczak-Kupiec (2013) Studies on the sintering process of synthetic hydroxyapatite, Acta Biochimica Polonica., 60(4), 851-855. https://pubmed.ncbi.nlm. nih.gov/ 24432345/.

[32] L.D.Guillen-Romero, M.T.Oropeza-Guzman, E.A. Lopez-Maldonado, A.L.Iglesias, J.A.Paz-Gonzalez, T.Ng, E.Serena-Gomez, L.J.Villarreal-Gomez (2019) Synthetic hydroxyapatite and its use in bioactive coatings, Journal of applied biomaterials & functional materials., 17(1), 2280800018817463. https://doi.org/10.1177/2280800018817463

IZVOD

ELEKTROHEMIJSKE AKTIVNOSTI Ni-Ti LEGURE U VEŠTAČKOJ KRVNOJ PLAZMI SA SEMENOM TRIGONELLA *Foenum graecum*

Istraživano je elektrohemijsko ponašanje legure Ni-Ti kada je izložena veštačkoj krvnoj plazmi (ABP) u prisustvu 0,1 i 0,5 ppm semena Trigonella foenum graecum (TFG) tokom 1, 10, 20 i 30 dana. Studije o impedansi i polarizaciji naizmenične struje su pokazale da se zaštitni premaz formira na površini metala dok sprečava koroziju. Zaštitni film je formiran na površini legure Ni-Ti implantata, povećan je otpor linearne polarizacije (LPR), a vrednost struje korozije (Icorr) je smanjena. Vrednost otpornosti na prenos naelektrisanja (Rct) i vrednost impedanse se povećavaju, a vrednost kapacitivnosti dvoslojnog sloja se smanjuje. Morfologija zaštitnih slojeva i elementarni sastav analizirani su pomoću SEM/EDAX. Svojstvo zaštitnog filma na leguri Ni-Ti ispitano je atomskim mikroskopom. Analiza difrakcije rendgenskih zraka je potvrdila prirodu apatita.Efikasnost inhibicije korozije legure Ni-Ti u ABP u prisustvu TFG semena u različitim koncentracijama za različito vreme je poboljšana i zaštićena.

***Ključne reči**: Nikl-titanijum, AFM, zaštitni film, Nyquist dijagrami, Bodeovi dijagrami*

Naučni rad
Rad primljen: 25.09.2023.
Rad prihvaćen: 25.10.2023.
Rad je dostupan na sajtu: www.idk.org.rs/casopis

*Avani Kumar Upadhyay[1,2], Manjeet Singh Goyat[3, 4,]**

[1]Department of Mechanical Engineering, School of Engineering, University of Petroleum & Energy Studies, Dehradun, Uttarakhand, India, [2]CAD Department, Tendemloop Technologies Pvt. LTd., Bangalore, Karnataka, India, [3]Department of Applied Science, School of Engineering, University of Petroleum & Energy Studies, Dehradun, Uttarakhand, India, [4]Smart Materials, Mads Clausen Institute, University of Southern Denmark, Sønderborg, Denmark

Review paper
ISSN 0351-9465, E-ISSN 2466-2585
https://doi.org/10.62638/ZasMat1038

Zastita Materijala 65 (1)
126- 142 (2024

A review on improved physical and thermal properties of oxide nanoparticles reinforced epoxy composites

ABSTRACT

Epoxy resins are well-known because of their desirable thermal and mechanical characteristics in a variety of fields, including the automotive, construction, and aerospace sectors. However, the inherent brittle nature of highly cross-linked epoxy resins generally leads to weakness in resisting the formation of cracks and their movement. The brittleness of the epoxy resins is one of the major obstacles inhibiting its use at a wider scale. Therefore, many researchers focused on reinforcement of epoxy resins by different types of nanostructures including carbon nanotubes (CNTs), organic/inorganic nanofillers to provide higher strength, without diminishing other essential thermo-physical characteristics of the nanocomposites. Most of the review articles focused on the CNT-reinforced epoxy composites and very limited review articles are available that focus on the oxide nanofiller reinforced epoxy composites. In this review article, epoxy nanocomposites reinforced with alumina (Al_2O_3), titania (TiO_2), silica (SiO_2), and zirconia (ZrO_2) nanoparticles have been investigated. The influence of the oxide nanoparticles in modifying the physical and thermal properties of the epoxy nanocomposites has been presented, compared, and critically analysed to optimize the performance of epoxy nanocomposites.

Keywords: *Oxide nanofiller; glass transition temperature; physical properties; thermal properties; thermal degradation*

1. INTRODUCTION

Since the beginning of human civilization, it has been desired to combine different types of inexpensive materials to efficiently increase the performance of various types of commodity materials. Beginning with the most primitive composite material, which was composed of straw and mud, and progressing all the way up to the most cutting-edge composite materials, which are utilized in the fabrication of body components for spacecraft, several advancements in the form of the composite material have been sought for and accomplished. To make a material that has better qualities in comparison to its component materials, composites have the advantage of combining the advantageous features of their constituent materials, which is one of the benefits of using composites.

With the commercialization of polymers, numerous research interests have been drawn for the expansion of polymer-based nanocomposite because of the distinctive characteristics of these composites. These properties include low cost, good exterior, exceptional resistance to chemicals, good manufacturability, material design flexibility, large strength/weight, and balanced mechanical performance[1–3]. By selecting combinations of parts that are appropriate, it is even possible to adapt and maximize the qualities of polymer composite materials. The polymer nanocomposites have better thermal, mechanical, and electrical capabilities at low loading, and higher gas barrier qualities while maintaining clarity, improved dimensional stability, and many other desirable characteristics [4,5]. Only the well-dispersed nanofillers without significant clustering in a polymer matrix can improve the physical and mechanical properties of the resulting polymer nanocomposite up to a great extent.

One of the most known thermosetting polymers used as the base matrix to produce polymer nanocomposites is epoxy adhesive. Epoxy resins

*Corresponding author: Manjeet Singh Goyat
E-mail: msgoyat@ddn.upes.ac.in
Paper received: 27. 09. 2023.
Paper accepted: 25. 10. 2023.
Paper is available on the website: www.idk.org.rs/journal

are having huge industrial utilization in the structural, aerospace, automotive, electronics and sportswear. Additionally due to high cross-linking capacity, epoxy composites are naturally brittle, leading to poor resistance to crack initiation and growth [6]. One of the key goals of researchers is to develop an epoxy that has a greater level of toughness, without compromising other essential features like as its thermo-physical and mechanical characteristics that are highly sought in a variety of structural applications.

To develop structural nanocomposites, many scientists investigate the reinforcement of inorganic nanoparticles apart from organic nanoparticles in the epoxy and other polymeric resins. To attain isotropic physical, thermal, and mechanical properties, nanoparticles are frequently used for reinforcing epoxy nanocomposites due to their high specific surface area and less hindrance to the cross-linking density of the epoxy resin. The cost of nanocomposites has always been a matter of great concern for few years (Fig. 1). The expensive raw materials and manufacturing processes made it difficult to use them for each automotive and aerospace application yet the mass production of the components can help in reducing the cost [7–9].

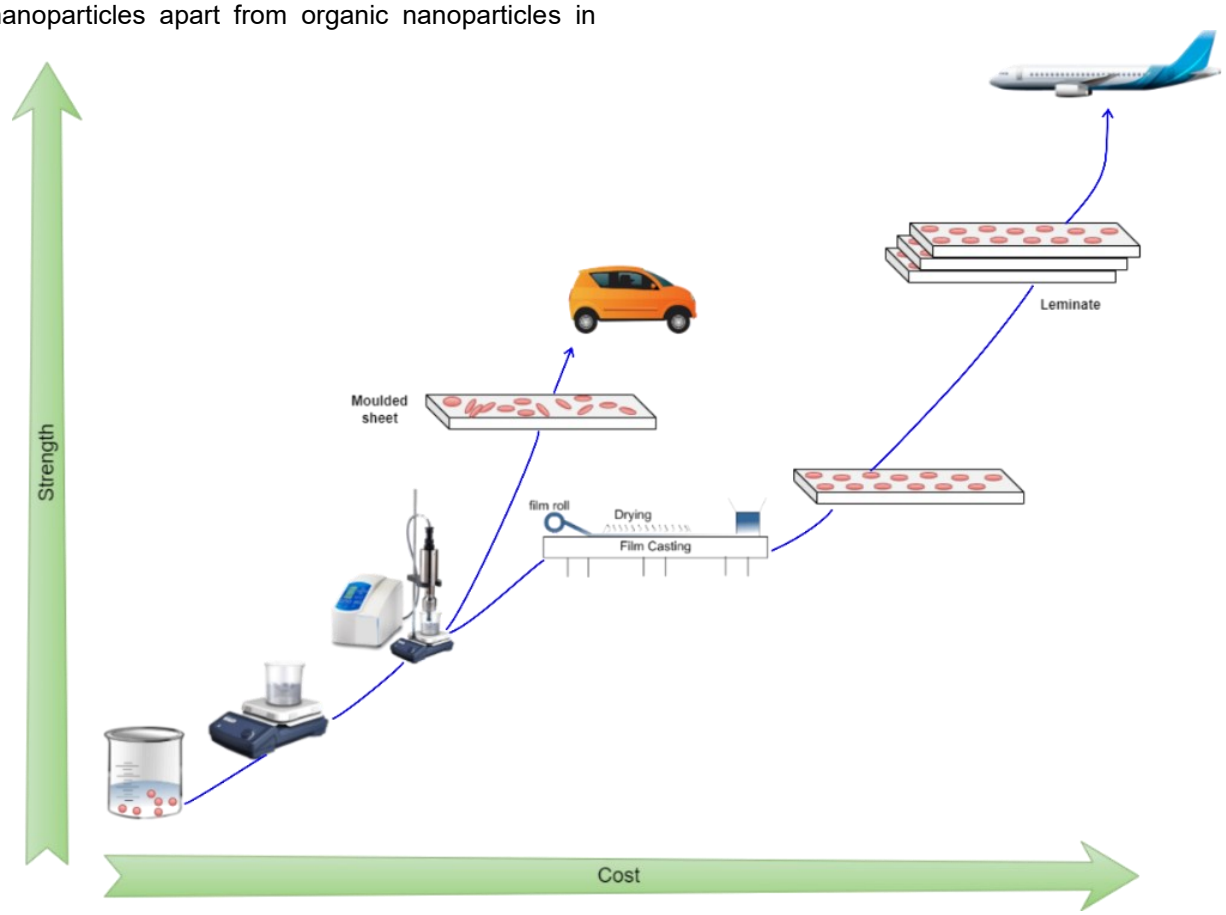

Figure 1. Relative performance and cost profiles in nanocomposite manufacturing [7]

Slika 1. Relativne performanse i profili troškova u proizvodnji nanokompozita [7]

The presence of fillers with a high specific surface area contributes to the formation of a substantial interface within the composite, assuming that the modifiers are adequately disseminated throughout the matrix. The enhancement of toughness and strength in structural ceramics and polymers has been the subject of investigation, with findings indicating considerable improvements when nanoparticles are used as building blocks, as compared to microparticles[10,11]. Furthermore, the interaction of nanoparticles and base matrix is contingent upon the surface structure, geometry, and surface chemistry of the particles, exerting a significant impact on the creation of the interface. Nanoparticles have a somewhat lower degree of matrix deformation restriction in comparison to microparticles due to their enhanced integration into the polymer microstructure, which is facilitated by their proximity to molecular dimensions. The

potential impact of nanoparticles on the deformation processes of polymers at the micro or nanoscale may be anticipated based on their strong interactions with the matrix.

Extensive research has been conducted on integrating nanofillers with both low and high aspect ratios. This integration has shown promise in enhancing the toughness of polymers, as well as improving key properties like wear-resistance and electrical resistivity. Reports indicate that epoxy reinforced with Ag nanoparticles helps stabilize temperature, whereas carbon black mixed in epoxy base generates reheating properties suitable for applications involving higher voltages. Moreover, the incorporation of organoclay into epoxy results in remarkable dampness and air resistance attributes, contingent upon the specific varity of clay used [12,13]. Notably, the inclusion of aluminium hydroxide particles has been observed to enhance the flame-retardant characteristics of polyvinyl chloride. Recent research highlights the remarkable potential of hybrid fillers like $Mg(OH)_2$/lignin when added to poly(vinyl chloride) matrices. This addition significantly enhances thermal stability, demonstrating an approximate threefold increase compared to unfilled polymers [14].

In recent times, there has been a significant focus on the use of rigid spherical oxide nano-particles as fillers, as seen by the attention they have garnered in several studies[15-25]. The incorporation of stiff spherical oxide nanoparticles into epoxy glue results in a comparatively lower degree of impediment during the cross-linking process. Multiple studies have previously shown that the integration of oxide nanofiller into thermosetting plastic matrices is an efficient method for enhancing their thermo-mechanical capabilities, while still maintaining other crucial features such as T_g (glass transition temperature) and stiffness. However, the most commonly used four types of oxide nanoparticles such as Al_2O_3 [11,22,26–31], TiO_2 [20,21,25,30-42], SiO_2 [23, 31, 43–46] and ZrO_2 [15,17,47–49] are extensively utilized for reinforcing epoxy matrix to attain noteworthy alterations in its T_g, thermo-physical properties. On different occasions, the mixing of alumina nanoparticles in epoxy shows increment or decrement or no change in the T_g of the resulting nanocomposites. However, on the addition of silica nanoparticles in epoxy resin, no significant effect on T_g of the epoxy resin is reported, however, Young's modulus, fracture toughness, and fracture energy showed a noteworthy improvement [10]. This irregular pattern in T_g might be mostly due to a variety of reasons like nanoparticle size, amount, and dispersion scenario in the polymer matrix. Further, the reported studies lack a unified and systematic approach to the development of nanocomposites. Additional crucial variables like tacticity, cross-linking density and molecular weight of the nanocomposite may have a substantial influence on enhancing the material characteristics. Hence, it is important to investigate the thermo-mechanical characteristics of the epoxy matrix when supplemented with oxide nanoparticles, considering their size, quantity, and dispersion within the matrix, since these factors significantly impact the diverse toughening methods.

The full use of the distinctive influence of oxide nanofillers in enhancing the characteristics of the nanocomposite may be achieved by effective dispersion within a polymer matrix. The distribution conditions and uniform microstructure of nanofiller have a major impact on the mechanical performance. The dispersion process used for introducing nanoparticles into the polymer matrix is a crucial step in attaining the required material properties. In order to get a uniform dispersion, a range of dispersion techniques, including shear mixing [47], solution mixing [50], mechanical stirring [51] and melt mixing [52] have been utilized to incorporate nanofiller in the epoxy base. In recent years, ultrasonic cavitation has gained global recognition as a method for dispersing oxide nanoparticles in epoxy adhesives. This technique is favoured due to its convenient processing and its effectiveness in dispersing individual nanoparticles inside semi-viscous liquids[53]. The phenomenon of ultrasonic cavitation does not provide a uniform dispersion of ultrasonic energy throughout the whole of the material. Furthermore, it has been shown that the ultrasonic cavitation approach has reduced efficacy in dispersing a large concentration of nanoparticles, often above 3 wt% [33]. The challenges need the refinement and enhancement of the ultrasonic vibration procedure. Nevertheless, a recently documented pioneering method known as ultrasonic dual mixing (UDM), such as the combination of ultrasonication and mechanical mixing, presents a more favourable prospect for ensuring comprehensive contact between the entire material and the ultrasonic probe. This technique allows for a gradual exposure to ultrasonic energy, thereby maximizing its benefits while minimizing any potential degradation of the base material [22].

The primary emphasis of this article is to examine the role of oxide nanoparticles in improving the physical and thermal properties of epoxy composites.

2. POLYMER NANOCOMPOSITES

Polymer nanocomposite represent a significant class of hybrid organic/inorganic nanofiller reinforced materials containing inorganic nanofillers in shape of nanotubes, nano sheets and nanoparticles dispersed uniformly in a polymer-based matrix [54]. The variation in different physiognomies of a polymer, including crystalline structure, entanglement, mobility of polymer chain and density can considerably impact the characteristics of polymer nanocomposites even at low nanoparticle concentration compared to typical micro particles [55]. The distinctive characteristics of nanofillers are a result of their reduced size, often ranging from 1-100 nm. This reduction in size results in a substantial increase in surface area to nanoparticle volume. The dispersion state and microstructural homogeneity of nanofillers have a considerable impact on the mechanical and thermal characteristics of polymeric matrices that are reinforced with them [46].

Polymer nanocomposites are typically developed using either thermosetting or thermoplastic polymeric materials as the matrix [41,56,57]. Epoxy adhesives are the most commonly utilized thermosetting polymer because of their versatility in different industries, including the automotive, aerospace, paint and coatings, and electrical instrumentation sectors[58–60]. Epoxy adhesives are inexpensive, strong, and resistant to a wide range of chemicals and conditions. In addition, epoxy adhesives may be utilized to attach with various materials including plastic, rubber, ceramic, wood and glass, [61] etc. Epoxies have good sealing characteristics and can quickly fill gaps [62]. While epoxy adhesives do have several benefits, such as those already discussed, their brittleness prevents them from being used in complex constructions. Water absorption studies were published to evaluate the coefficient of diffusion, maximum moisture absorption, and T_g of epoxy [63], but these results do not yet provide a complete picture of the combined degradable action of moisture and temperature on epoxy. When it comes to fracture propagation resistance and hardness, epoxy adhesives fall short [30,64]. To find solutions, scientists from all around the globe have experimented with several nanofillers.

3. NANOFILLERS FOR POLYMER NANOCOMPOSITES

Numerous studies have extensively investigated polymer nanocomposites using various matrices such as polyamide-6 [65], polystyrene [66], polyetherimide [67], epoxy [68,69] along with diverse nanofillers like montmorillonite clay $CaCO_3$, TiO_2, Ag, Al_2O_3, carbon nanotubes and SiO_2 [39,46,70-73]. This study focuses on examining epoxy adhesive as the chosen polymer matrix.

Rigid spherical oxide nanoparticles as fillers have garnered huge attraction in recent studies [29,45,74]. Due to their excellent mechanical characteristics, chemical inactivity, sustainability at high temperature, and economical [15,20,22,35, 73, 75]. Oxide nanoparticles (alumina, titania, zirconia etc.) have been considered as prospective nanofillers for the industrial applications. Furthermore, because of their low aspect ratio ~1, spherical oxide nanoparticles provide less hindrance to the cross-linking of the polymer when mixed into the epoxy. Furthermore, the spherical oxide nanoparticles prevent premature failure and keep the matrix transparent. But nanoparticles attract each other due to their high surface area to volume ratio and attractive electrostatic forces (van der Waals force) resulting in agglomeration. Because the van der Waals forces become one of the strongest forces in the range of 1-10 nm. The agglomeration of nanofillers in the matrix is highly undesirable to obtain the enhancement in various properties of the developed nanocomposites [45], because, the agglomeration of nanoparticles restricts their interaction with the matrix. One of the most difficult parts of making nanoparticulate-epoxy composites with enhanced characteristics due to the challenge of homogeneous dispersion of nanoparticles in the epoxy matrix.

4. PROPERTIES OF NANOPARTICULATE-EPOXY COMPOSITES

The enhancement of properties of polymer nanocomposites can be achieved using the homogeneous dispersion of numerous types of nanoparticles in a polymer matrix. According to reports, a significant enhancement in the T_g of the bulk epoxy matrix may be attained by using a relatively small quantity of Al_2O_3, TiO_2, and SiO_2 nanoparticles [30,33,76]. However, it has been shown that the epoxy matrix supplemented with oxide nanoparticles exhibits varying behaviors in terms of increased, decreased [77], or insignificant changes in T_g [78]. Hence, it is important to acquire the knowledge about precise variation of the T_g in epoxy matrices supplemented with oxide nanoparticles. The mechanical properties of the material are also heavily influenced by the dispersion state and microstructural uniformity of the nanoparticles [46]. The integration of nanoparticles into the polymer matrix by dispersion is a crucial procedure to get the required material

characteristics. The simultaneous integration of oxide nanoparticles into the epoxy matrix results in the reinforcement of epoxy matrix that can lead the enhancement of physical and mechanical properties of the matrix. The increased potential for contact between nanoparticles and the epoxy matrix is attributed to the large surface area to volume ratio [79]. The introduction of nanoparticles into the polymer matrix has the potential to impact the morphological structure of the resulting nanocomposite, hence affecting its thermo-physical, mechanical, tribological, and fracture properties [74].

Numerous parameters, including nanoparticle type, concentration, size, surface chemistry, dispersion scenario in the matrix, and immobilized particle-matrix interface, contribute to the morphological architectural shift caused by the presence of nanoparticles [79,80]. To enhance the thermo-physical characteristics of nanocomposites, a strongly immobilized particle-matrix boundary and uniformly distributed nanofiller play a primary role [81]. But a surge in nanofiller concentration in polymeric base beyond a threshold value leads to a decline in the thermo-physical characteristics due to the dominance of particle-particle interaction and thereby significant agglomeration.

4.1. Influence of Oxide Nanofiller on T_g

The oxide nanofiller such as Al_2O_3, TiO_2, ZrO_2 and SiO_2 nanoparticles are considered as prospective candidates to increase the several important characteristics of polymer nanocomposites. Many studies are reported for TiO_2 nanoparticles reinforced polymer composites to improve photocatalytic activity, thermal, viscoelastic, and mechanical properties [40,42,66,82–84]. The mixing of TiO_2 nanoparticles in the epoxy resin can increase the T_g of the resulting nanocomposite [33]. The reported enhancement in T_g for TiO_2-epoxy nanocomposites is different for a different size, content, and surface characteristics of TiO_2 nanoparticles as well as the difference in epoxy matrix properties and preparation techniques used to develop nanocomposites [30,33,38]. The reported maximum improvement in T_g for TiO_2-epoxy nanocomposite containing 1 wt% of TiO_2 nanoparticles (5 nm) is about 11 ^oC [33].

It is also verified that a significant enhancement in T_g can be attained by mixing low content of Al_2O_3 nanoparticles [30]. However, it has been shown that the Al_2O_3 nanoparticles reinforced epoxy exhibits inconsistent behavior, with T_g either increasing, decreasing [85], or not changing [86]. The maximum reported improvement in T_g for Al_2O_3-epoxy nanocomposite containing 5 wt% of Al_2O_3 nanoparticles (10-30 nm) is about 12 ^oC [87].

The ZrO_2 nanoparticles have a good capability to enhance the various characteristics of the epoxy matrix. But, the ZrO_2 nanoparticles are extensively studied for anticorrosion coatings [88-90] and wear-resistant materials [48] because of their high strength, high fracture toughness. Zirconia nanofiller work as virtuous heat resister due to their high resistivity against heat [90]. Only limited literature is available on ZrO_2 nanoparticle reinforcement. Numerous investigation have revealed that the inclusion of ZrO_2 nanofillers inside the polymer base has the potential to enhance the glass transition temperature (T_g) [47,91]. The maximum reported improvement in T_g for ZrO_2-epoxy nanocomposite containing a high content of 8 vol% of ZrO_2 nanoparticles (12 nm) is about 8 ^oC [47].

The observed elevation in glass transition temperature (T_g) is often ascribed to a reduction of motion of polymer chain sections inside the epoxy base, which may be related to the interaction between the matrix and nanoparticles. Only well-dispersed nanoparticles into the epoxy base can restrict the polymer chain flexibility. This is possible in two ways: (i) the generation of high interface area due to nanoparticle-matrix interaction, which can change the local dynamics of the matrix, and (ii) the very small nanoparticle surface-to-surface distance, which can limit the polymer chain segment movement. The possibility of restriction to the polymer chain segment movement is significantly increased if the nanoparticles are well dispersed in the epoxy and have a robust adhesion amongst the nanoparticles and surrounding polymer base [30]. The local fragmented mobility of matrix chain can be predicted by evaluating the fragmented relaxation period or T_g of loaded and unloaded nanocomposite. Adding oxide nanoparticles can affect the T_g of nanocomposite in three ways i.e., increase, decrease, or no change (Fig. 2). This mainly depends on the filler matrix interfacial interactions. Strong filler matrix bonding (electrostatic, covalent, H-bond) of wetted particle will leads to increase in T_g whereas large space between filler and matrix at the interface of unwetted particles is responsible for decrease in T_g [92]. Further T_g will remain unaffected due to shaky interface formation. Bansal et al. [93] studied the comparability between PNC (polymer nanocomposite) and thin polymer films. They suggested that polymer segment between two particles is analogous to a thin film of an equivalent thickness (equal to interparticle spacing).

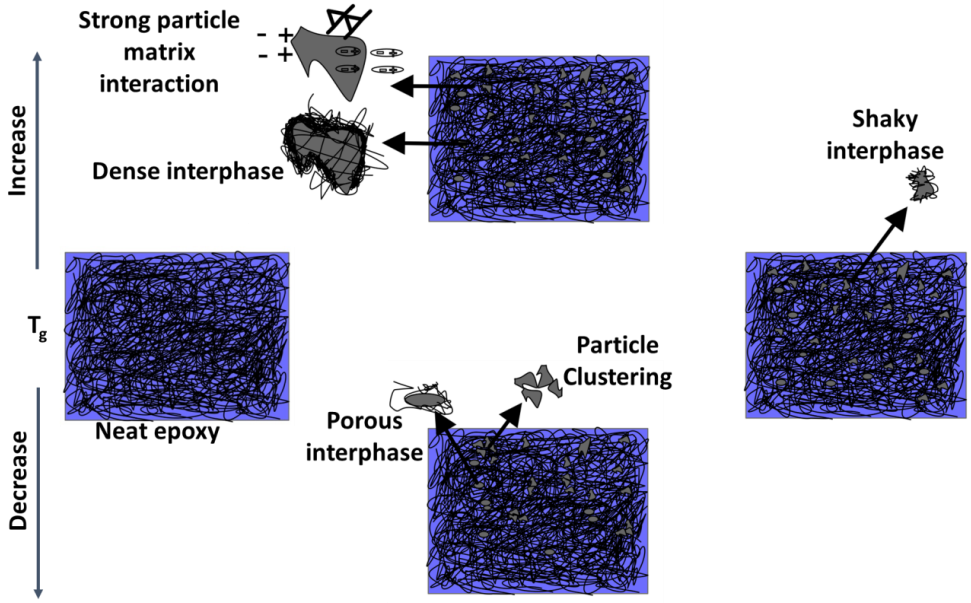

Figure 2. Schematic diagram showing mechanism of increasing, decrease and no alteration in glass transition temperature (T_g)

Slika 2. Šematski dijagram koji pokazuje mehanizam povećanja, smanjenja i bez promene temperature staklastog prelaza (T_g)

The incorporation of oxide nanoparticles in the epoxy matrix may work as extra virtual nodes for epoxy chain network, thereby resulting in the enhanced T_g [33]. Furthermore, the nanofiller may work as physical cross-linkers [30] leading to the enhanced cross-linking density of the resulting nanocomposite, and increased cross-linking density results in the enhanced T_g. Another possibility of an increase in T_g because of the development of a huge share of the restrained epoxy at the nanoparticle-matrix boundary. It is anticipated that the rise in T_g would exhibit a direct relationship with the surface area of the nanoparticle. Specifically, as the particle size decreases, the surface area increases, hence intensifying the constriction effect on the epoxy resin networks. Therefore, the restriction effect on polymer chain segment movement increases with the content along with decreasing particle size [30]. The reduction in T_g seen in systems with high nanoparticle content may be attributed to two primary factors. Firstly, the adhesion of polymer resin on the exterior of the nanofillers can cause a change in the non-stoichiometric mixture. The T_g of the epoxy-amine system is reduced due to its non-stoichiometric nature, resulting in a noticeable fall in T_g [94,95]. One potential factor is the non-uniform dispersion of nanoparticles inside the base matrix, which may be attributed to the prevalence of inter-nanofiller attraction forces [38]. This occurrence leads to particle agglomeration, resulting in a reduction in crosslinking density and subsequently a fall in the T_g.

In recent reports, an enhancement in T_g values is observed due to an increase in TiO_2 nanoparticle concentration (0.5 to 10 wt.%) in epoxy as depicted by DSC. Though at high nanofiller concentration (~20 wt%) descent in T_g values are found (Fig. 3a). 10 wt.% TiO_2-epoxy nanocomposite showed a maximum increment of ~ 27% in T_g [96]. The effect of the SiO_2 nanoparticle content on T_g is exhibited in Fig. 3b. The increased T_g values seen in SiO_2-epoxy nanocomposites fabricated using the sol-gel technique may be credited to the constrained movement of epoxy chain segments [97]. Kumar et al. [98] examined the consequence of mixing ZrO_2 nanofiller on the thermomechanical characteristics of epoxy nanocomposite. Authors revealed that increasing ZrO_2 content (up to 4 wt.%) enhances the T_g (Fig. 3c). The phenomenon described is attributed to the adhesion of epoxy atoms onto the boundary of nanofillers, resulting in a low movement of epoxy atoms. Dorigato et al. [91] investigated the improvement in epoxy adhesives with calcined zirconia nanoparticles and obtained the trends of DSC and DMTA tests of T_g for various zirconia epoxy nanocomposites. The values of T_g obtained from the peak of tan δ in dynamic mechanical thermal analysis (DMTA) testing were consistently greater compared to those obtained

from differential scanning calorimetry (DSC) tests. The graph illustrates a non-monotonic trend in T_g as the zirconia concentration increases, with the greatest rise seen at a filler level of 1 vol%. The statement aligns well with the interpretations made by Dean et al. [99]. Yazman et al. [100] examined the outcomes of Al_2O_3 on the T_g of epoxy nanocomposite in his more recent study. Authors found that adding Al_2O_3 (up to 1.5 wt.%) into epoxy matrix provides around a 15% improvement in the T_g (Fig. 3d).

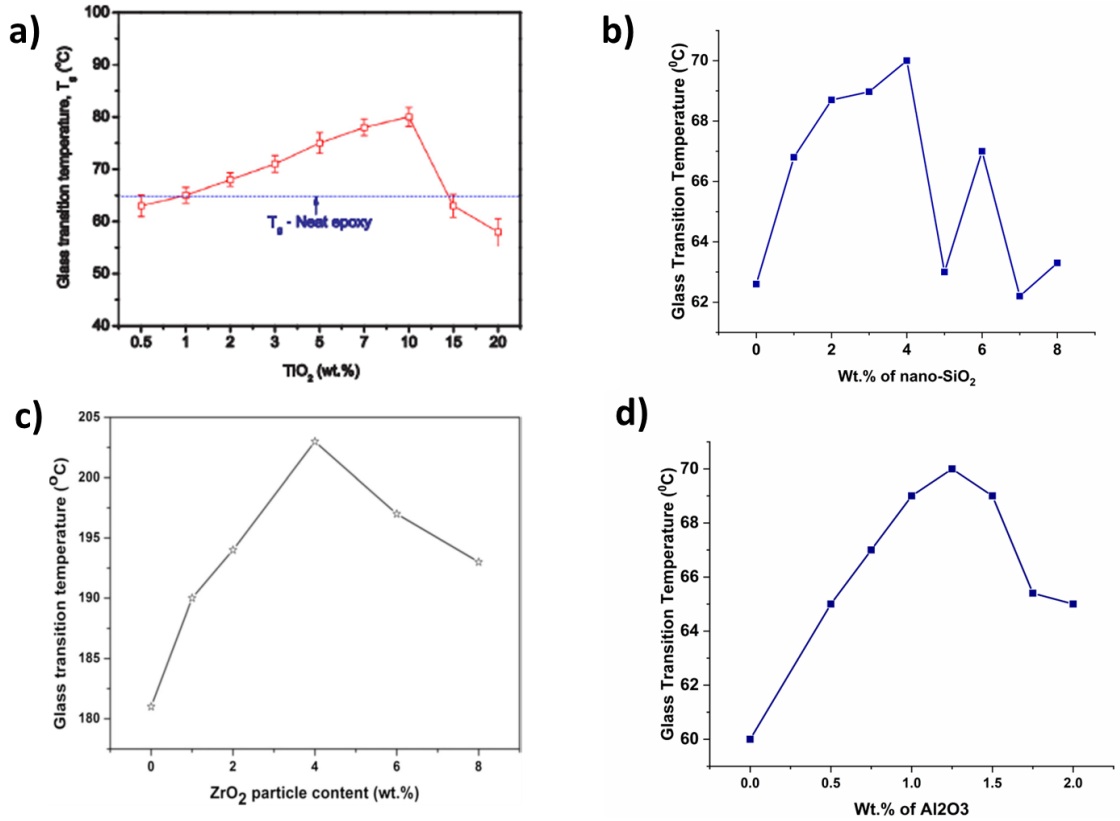

Figure 3. Variation T_g with respect to (a) wt% of TiO_2 [96] (b) wt% of SiO_2 (c) wt% of ZrO_2 [98] (d) wt% of Al_2O_3

Slika 3. Varijacija T_g u odnosu na (a) tež.% TiO_2 [96] (b) tež.% SiO_2 (c) tež.% ZrO_2 [98] (d) tež.% Al_2O_3

Reduced epoxy chain segment movement, high cross-linking density, and dense interphase formation were the reported reasons for the same. The observed drop in T_g with increasing filler amounts may be attributed to the simultaneous occurrence of two opposing processes. The potential for an increase in the chain blocking effect is anticipated with the rise in nanoparticle concentration. In a recent study, Wang et al. [101] conducted an investigation into the influence of functionalized Titania nanoparticles on the physical characteristics of the epoxy nanocomposite. Functionalization of nanoparticles was performed by adding a silane coupling agent. The authors revealed that adding TiO_2 will reduce the molecular chain mobility results in an increment in the T_g. An increment of 43% in T_g is reported at 5 wt% nanofiller. Strong interface formation was found to be a major cause of restricted molecular chain movement. Li et. al.[102] considered the influence of adding mesoporous TiO_2 in the epoxy composite electrolyte on electrochemical and mechanical performance. The authors presented that mixing mesoporous TiO_2 destroys the ordered molecular chain of polymer and promotes cross-linking. This happened due to the interaction of TiO_2 with the polar groups of the polymer chain resulting in a decrement in the reorganization of the polymer chain. The authors concluded that adding TiO_2 content up to 6 wt% will increase the compression strength of the composite by 60%. In addition, the use of TiO_2 nanofiller served as a thermal barrier, hence enhancing the heat insulation properties. Marotta et. al. [103] conducted a study on the curing behavior, mechanical characteristics, and thermal properties of nanocomposites consisting of epoxy and TiO_2. According to the authors' findings, the incorporation of nano TiO_2 results in a reduction in the enthalpy of the curing process and induces a shift of the reaction towards a higher temperature. Furthermore, the literature provides an explanation

for the dual impact of TiO_2 incorporation, namely, the reduction in the reaction volume of epoxy anhydride and the formation of a novel interaction between TiO_2 and epoxy. These effects together result in a decrease in the degree of crosslinking within the polymer matrix. The literature has shown that there is a reduction in the T_g and a little increase in the mechanical characteristics of the composite. The experimental and predictive investigation conducted by Papanicolaou et al. [104] examined the impact of TiO_2 nanoparticles and microparticles on the flexural strength of epoxy nanocomposites. Composites were prepared by magnetic stirring. SEM images revealed that the formation of micro aggregates is inevitable in the mixing of micro TiO_2. Nano TiO_2 particles showed better particle distribution in the matrix. The authors revealed that adding nano TiO_2 will decrease the flexural modulus for all strain rates applied. This happened due to the delayed cross-linking and creation of filler matrix interface. Nano TiO_2 in limited weight fraction (up to 1%) produces a plasticization effect which produces the rubber-like property in the composite.

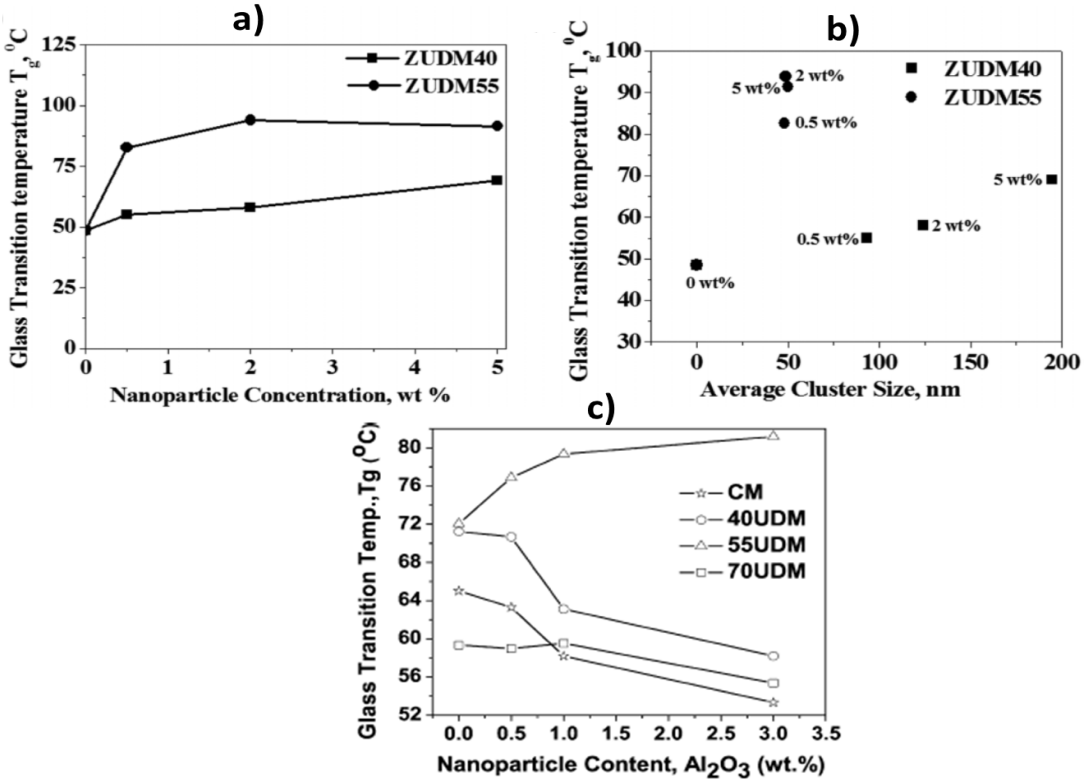

Figure 4. Graphical representation of deviation of T_g for Neat epoxy along with ZUDM40 and ZUDM55 nanocomposite with variation of (a) nanofiller wt% and (b) mean agglomerate dimension. (c) variation of T_g with wt.% of Al_2O_3 at variable UDM parameter; ZUDM40: ZrO_2 / epoxy nanocomposite fabricated by ultrasonication amplitude of 40%; ZrO_2: zirconium dioxide; ZUDM55: ZrO_2/epoxy nanocomposite developed by ultrasonication amplitude of 55% [17]; 40UDM is UDM at vibration of 40% amplitude; 55UDM is UDM processed at 55% amplitude; 70UDM is UDM processed at 70% amplitude [22]

Slika 4. Grafički prikaz devijacije Tg za Neat epoksid zajedno sa nanokompozitom ZUDM40 i ZUDM55 sa varijacijama (a) težinskih % nanopunila i (b) srednje dimenzije aglomerata. (c) varijacija Tg sa tež.% Al2O3 pri promenljivom UDM parametru; ZUDM40: ZrO_2/epoksidni nanokompozit proizveden ultrazvučnom amplitudom od 40%; ZrO_2: cirkonijum dioksid; ZUDM55: ZrO_2/epoksidni nanokompozit razvijen ultrazvučnom amplitudom od 55% [17]; 40UDM je UDM pri vibraciji od 40% amplitude; 55UDM je UDM obrađen na 55% amplitude; 70UDM je UDM obrađen pri 70% amplitude [22]

In another study [17], a variation of T_g with nanoparticle content and average cluster size for ZrO_2-epoxy nanocomposites is shown in Fig. 4a and b respectively, developed by ultrasonication amplitude at 40% (ZUDM40) and 55% (ZUDM55). The monotonically increasing T_g trend is found in ZUDM40 up to 5 wt%. Figure 4c demonstrates that the inclusion of ZrO_2 nanoparticles with a cluster size ranging from 40–50 nm leads to a notable increase in the T_g of ZUDM55. Conversely, a marginal alteration in T_g was observed when incorporating ZrO_2 nanoparticles with a larger

average cluster size in ZUDM40. This suggests that higher levels of processing hinder the reduction in T_g at higher particle concentrations. The enhancement of T_g resulting from the addition of 20–30 nm ZrO_2 nanoparticles can be credited to the robust adhesion amongst the nanofiller and the epoxy, which restricts the molecular mobility of the epoxy material under thermal conditions.

The study reveals that comparable patterns may be seen in composites with Al_2O_3 particles with a size of less than 25 nm, embedded in epoxy resin using an advanced ultrasonic dual mixing (UDM) technique. The present research examines the disparity in T_g seen in nanocomposites fabricated by two distinct methods: conventional mixing (CM) and ultrasonic dispersion and mixing (UDM). The investigation focuses on nanocomposites with varying amplitudes of 40%, 55%, and 70%. The UDM has shown optimal outcomes, such as a 26% enhancement in T_g, when operated at an amplitude of 55%, as seen in Figure 3(c). The primary objective of incorporating particles into a polymer matrix is to enhance the cross-linking process by impeding the movement of the epoxy atoms. Nevertheless, the amplification of amplitude by 70% leads to the occurrence of excessive heat, which subsequently results in the breaking of polymer chains and therefore decreases the T_g values [22].

Table 1 summerises the results of recent publications about T_g of oxide nanoparticles reinforced epoxy adhesive.

Table 1. Summary of T_g of oxide nanofiller-epoxy composites
Tabela 1. Rezime Tg kompozita oksidnih nanopunila i epoksida

Development process	Oxide nanofiller				T_g of neat epoxy adhesive (°C)	T_g of nano-composite (°C)	Variation (%)	Ref.
	Type	Diameter (nm)	Concentration					
			(wt.%)	(vol.%)				
Mechanical stirring with heating	TiO_2	25	5		81	116	43	[101]
Ultrasonic cavitation	TiO_2	5	1	-	118	129	9	[33]
Bead-Mill	TiO_2	300	-	8	170	172	0.1	[30]
Shear Mixing & ultrasonic cavitation	TiO_2	50		3	49	52	6	[38]
Optimized ultra-sonication process	TiO_2	~48	10	-	-	-	27	[96]
Ultrasonicated dual mixing	TiO_2	30	1	-	78	82	5	[105]
Ultrasonicated dual mixing	TiO_2 (hybrid)	30	1	-	79	97	23	[106]
Mechanical mixing/ultrasonication	Al_2O_3	78	2	-	59	62	5	[107]
Ultrasonication	Al_2O_3	20	1.25	-	60	70	17	[100]
Planetary centrifugal mixing	Al_2O_3	30	1	-	84	104	23	[108]
Mechanical mixing	Al_2O_3	35	2.5	-	70	78	11	[109]
Mechanical stirring	Al_2O_3	10-30	-	5	83	95	15	[87]
Bead-Mill	Al_2O_3	13	-	5	170	185	9	[30]
Shear mixing	Al_2O_3	45	20	-	112	112	0	[78]
Mechanical mixing and ultrasonication	ZrO_2	45	6	-	61	68	11	[110]
Ultrasonic dual mixing	ZrO_2	30	4	-	181	204	13	[98]
Ultrasonication	ZrO_2	45	6	-	61	70	15	[111]
Ultrasonic dual mixing	ZrO_2	25	2	-	49	94	92	[17]
Mechanical stirring	ZrO_2	15	-	1	50	55	10	[91]
Torus Mill	ZrO_2	12	-	8	100.3	108	8	[47]
Ultrasonication	SiO_2	30	4	-	152	164	8	[112]
Ultrasonication	SiO_2	14	4	-	82	112	36	[113]
Mechanical mixing	SiO_2	270	5	-	228	239	5	[114]
Ultrasonication	SiO_2	15	4	-	62	70	11	[97]
Sonication	SiO_2	100	40	-	~125	~87	-30	[81]

4.2. Effect of Oxide Nanoparticles on Thermal Stability

The use of thermal analysis techniques to assess the thermal deterioration of materials has significant importance in estimating their longevity and durability. The primary weight reduction of epoxy adhesives based on DEGBA typically takes place within the temperature range of 370-420 °C, mostly as a result of the breakdown of the bisphenol-A [115,116]. The degradation event encompasses a series of sequential steps, including chain scission, char production or carbonization, and char stabilization [117]. As the thermal stability of oxide nanoparticles is very high due to their ceramic nature, therefore in the case of nanoparticulate-epoxy composites, the thermal degradation also follows the same trend as mentioned above for epoxy matrix. Thermal stability of nanocomposites is usually evaluated considering three factors: (1) decomposition temperature (determined from weight loss % of the material with respect to the increase in temperature), (2) activation energy for degradation, and (3) Integral procedural decomposition temperature (IPDT). Several studies have shown improvements in the thermal stability of epoxy matrices with the inclusion of oxide nanoparticles such as TiO_2, Al_2O_3, SiO_2, and ZrO_2. [49,115,118]. A significant increase in decomposition temperature, the activation energy of decomposition, and IPDT has been reported for TiO_2-epoxy and Al_2O_3-epoxy nanocomposites [33,113]. However, a slight improvement in the thermal immovability is reported for ZrO_2-epoxy nanocomposites [49]. The better thermal sustainability of nanoparticulate-epoxy nanocomposites may be credited to the consistent distribution of nanofillers inside the underlying epoxy. The distribution of nanofillers throughout the epoxy base and the presence of a well-defined filler-epoxy boundary contribute to the formation of a heat flow barrier. This barrier is primarily credited to the thermal inertness of oxide nanofillers [115]. The retardant effects of the resultant nanocomposites on heat flow are enhanced as the nanoparticle concentration increases. The quantity of particles has a positive correlation with the concentration of nanoparticles. The augmentation of particle content, coupled with notable clustering, results in a reduction of the cross-linking density. Thermosetting polymers often exhibit a comparatively high degree of cross-linking density, resulting in elevated decomposition temperatures [33]. The optimization of cross-linking density occurs when the epoxy matrix is maintained at its full stoichiometry. Once the stoichiometry of the epoxy resin is disrupted by the introduction of external TiO_2, Al_2O_3, SiO_2, and ZrO_2 nanoparticles, above a critical threshold [49,115,118,119]. the crosslink density diminishes. Consequently, a reduction in crosslink compactness results in reduction in the decomposition temperature.

The observed rise in the activation energy for the disintegration of the nanocomposites may be attributed to the significant structural changes that occur, particularly when the nanoparticles are uniformly dispersed inside the epoxy matrix. In instances when nanoparticles are effectively disseminated inside a matrix, the phenomenon of limitation to random chain scission is intensified due to the greater number of impediments that impede the transport of heat and oxygen through the matrix. However, exceeding a critical threshold of nanoparticle concentration has a negative impact on the activation energy of breakdown.

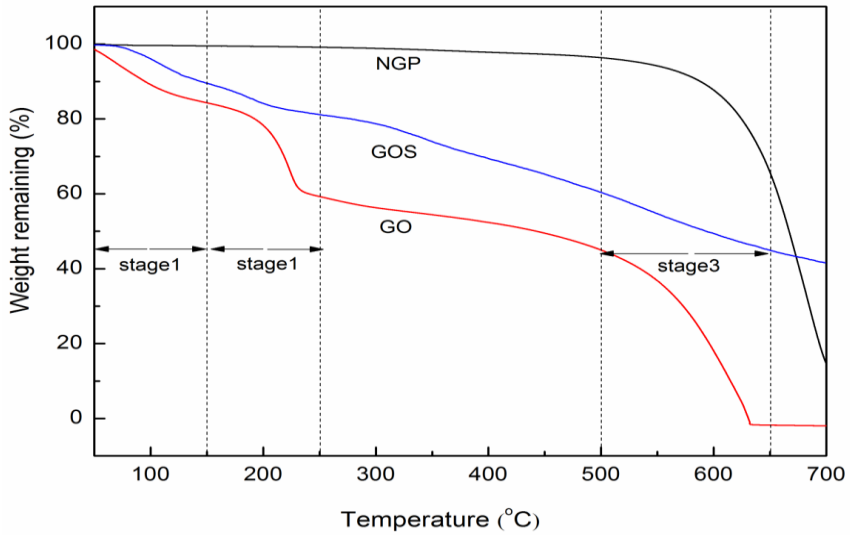

Figure 5. Wt.% v/s Temperature plot of epoxy nanocomposite [121]

Slika 5. Grafik tež. % u odnosu na temperaturu epoksidnog nanokompozita [121]

The relationship between the change in IPDT and the increase in nanoparticle content within the epoxy matrix often differs from that seen for the activation energy of these nanocomposites. The disparity in the physical characteristics of activation energy and the IPDT [120] may account for this phenomenon. The concept of activation energy pertains to the rapid breakdown procedure of the epoxy atom chain, with the exclusion of the early decomposition and char yield creation. On the other hand, the IPDT encompasses the whole constancy of the samples, counting the beginning, rapid decay, and closing char formation stages. The observed trend of increasing IPDT in oxide nanoparticulate-epoxy composites with more nanofiller loading may be credited to this factor. Thus, the inclusion of TiO_2 nanofiller in the epoxy matrix results in better thermal resistivity compared to the neat epoxy adhesive. The introduction of the Al_2O_3 and ZrO_2 nanoparticles into the epoxy resin also enhances thermal resistance because these particles work as virtuous insulators to the heat flow through the matrix [90]. The better thermal resistance by the ZrO_2 nanoparticle may further be supported by their good attachment with the epoxy matrix [30].

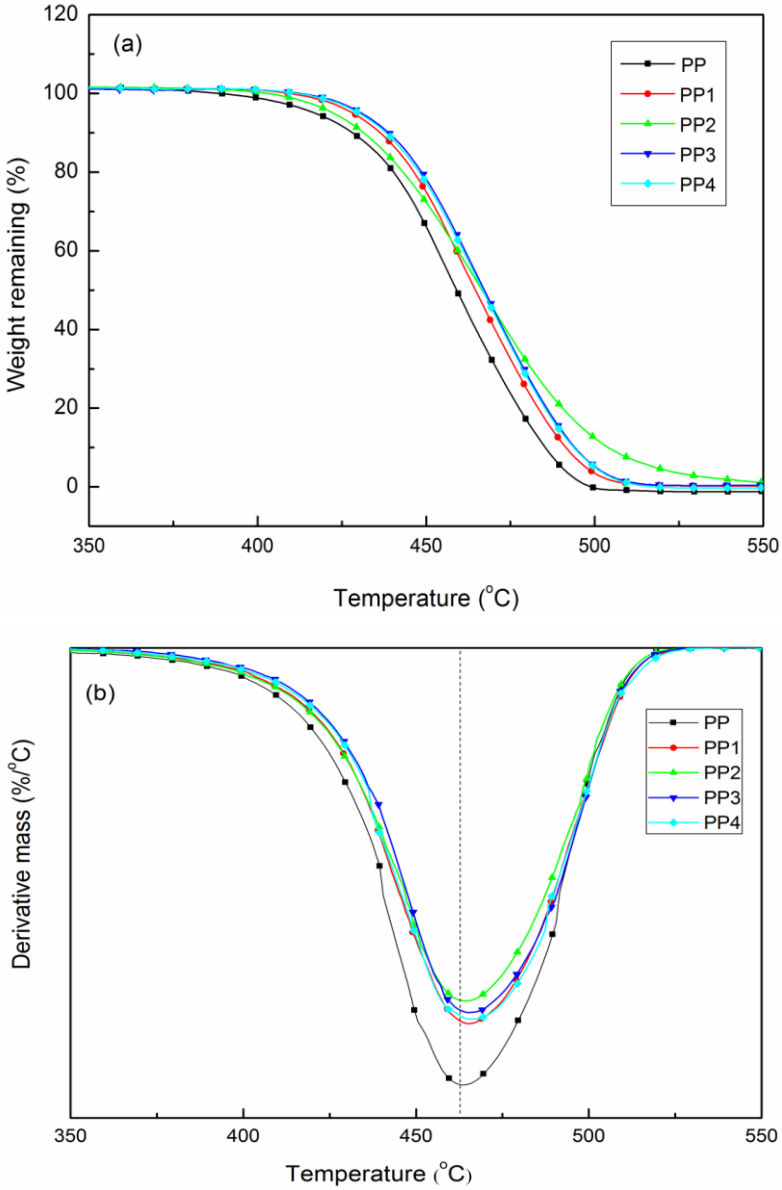

Figure 6. Wt.% vs Temperature plot of epoxy nanocomposite and DTG (b) thermograms wt. loss % vs temperature [121]

Slika 6. Grafik tež.% u odnosu na temperaturu epoksidnog nanokompozita i DTG (b) termogram mas. gubitak % u odnosu na temperaturu [121]

The thermal breakdown curves of natural graphite powder (NGP), graphene oxide (GO), and graphene-SiO_2 hybrids (GOS) were investigated by Bian et al. [121] as seen in Figure 5. The findings indicate that the degradation of GOS exhibits similarities to that of GO, but with a slower degradation rate and a greater accumulation of residual GOS characteristics. This may be attributed to the incorporation of SiO_2. The incorporation of graphene oxide sheets (GOS) into polymer nanocomposites contributes to the enhancement of their thermal characteristics. Figure 6 depicts the thermogravimetric analysis (TGA) and derivative thermos-gravimetric (DTG) curves of hybrid polypropylene/graphene oxide silicon dioxide (PP/GOS) nanocomposites including varying concentrations of graphene oxide SiO_2 (GOS) [121]. The maximum decomposition temperature is found to increase from 454^0C to 462.4^0C for pure PP to GOS/PP (0.5 wt%) nanocomposite respectively.

5. CONCLUSIONS

The performance of oxide nanoparticulate reinforced epoxy nanocomposites is dependent on a wide variety of parameters. These parameters include the category of epoxy resin, size, the type, concentration, and shape of oxide nanofillers, as well as the interface between the nanofillers and the base polymer matrix. The manifold enhancement in the physical, thermal and mechanical properties of polymer nanocomposites can only be achieved if nanoparticles are uniformly dispersed (up to a maximum cluster of 2 to 3 particles) without significant clustering in viscous polymer matrix (epoxy matrix). Multiple processing techniques were used in the past for dispersing nanofillers in the epoxy like polymer matrix. Each method of disagglomerating nanoparticles has its own set of advantages and disadvantages, however, the ultrasonic dual mode mixing approach found out very promising for dispersing nanofillers in polymer matrices even up to the size of individual nanoparticles.

The research results that have been published so far are still insufficient to exhibit a direct link between the physical characteristics of nanoparticulate-epoxy composites and their thermal properties. Because in some cases, all three trends observed using the same nanoparticle with different dispersion scenario in polymer matrix. Based on the dispersion scenario, the physical and thermal properties may increase, decrease and remain unchanged. This has happened because of the way of physical adsorption of polymer layer on the nanoparticle surface. From an industrial perspective, the creation of a more sophisticated material also necessitates the existence of a direct link between the process and the material. To get the most possible advantage from the nanoparticulate-epoxy composites, it is obligatory to do more research in this direction.

Acknowledgements

M.S. Goyat acknowledges the funding by Science and Engineering Research Board (SERB), Department of Science & Technology (DST), India, project number SUR/2022/005356.

6. REFERENCES

[1] V.K. Thakur, M.K. Thakur, R.K. Gupta (2017) Hybrid polymer composite materials: Structure and chemistry.Editor Elsevier, book, p.356

[2] I. Erukhimovich, M.O. de la Cruz (2004) Phase equilibria and charge fractionation in polydisperse polyelectrolyte solutions, 45, 1390–1398. doi: 10.1002/polb.

[3] L. Hsu, C. Weder, S.J. Rowan (2011) Stimuli-responsive, mechanically-adaptive polymer nanocomposites. J. Mater. Chem., 21(9), 2812–22. doi: 10.1039/C0JM02383C.

[4] J. Guo, J. Long, D. Ding, Q. Wang, Y. Shan, A. Umar, X. Zhang, B.L. Weeks, S. Wei, Z. Guo (2016) Significantly enhanced mechanical and electrical properties of epoxy nanocomposites reinforced with low loading of polyaniline nanoparticles. RSC Adv., 6(25), 21187–92. doi: 10.1039/C5RA25210E.

[5] P. Chammingkwan, K. Matsushita, T. Taniike, M. Terano (2016) Enhancement in mechanical and electrical properties of polypropylene using graphene oxide grafted with end-functionalized polypropylene. Materials (Basel)., 9(4), 240-248. doi: 10.3390/ma9040240.

[6] J. Bin Dai, H.C. Kuan, X.S. Du, S.C. Dai, J. Ma (2009) Development of a novel toughener for epoxy resins. Polym. Int., 58(7), 838–845. doi: 10.1002/pi.2604.

[7] A.K. Naskar, J.K. Keum, R.G. Boeman (2016) Polymer matrix nanocomposites for automotive structural components. Nat. Nanotechnol., 11(12), 1026–30. doi: 10.1038/nnano.2016.262.

[8] V.B. Mohan, K. Lau, D. Hui, D. Bhattacharyya (2018) Graphene-based materials and their composites: A review on production, applications and product limitations. Compos. Part B Eng., 142, 200–220. doi: 10.1016/j.compositesb.2018.01.013.

[9] G. Mittal, K.Y. Rhee, V. Mišković-Stanković, D. Hui (2018) Reinforcements in multi-scale polymer composites: Processing, properties, and applications. Compos. Part B Eng., 138,122–139. doi: 10.1016/j.compositesb.2017.11.028.

[10] P. Dittanet, R.A. Pearson (2012) Effect of silica nanoparticle size on toughening mechanisms of filled epoxy. Polymer (Guildf)., 53(9), 1890–905. doi: 10.1016/j.polymer.2012.02.052.

[11] I. Ozsoy, A. Demirkol, A. Mimaroglu, H. Unal, Z. Demir (2015) The influence of micro- And nano-

filler content on the mechanical properties of epoxy composites. Stroj. Vestnik/Journal Mech. Eng., 61(10), 601–609. doi: 10.5545/sv-jme.2015.2632.

[12] A. Jelić, M. Sekulić, M. Travica, J. Gržetić, V. Ugrinović, A.D. Marinković, A. Božić, M. Stamenović, S. Putić (2022) Determination of Mechanical Properties of Epoxy Composite Materials Reinforced with Silicate Nanofillers Using Digital Image Correlation (DIC). Polymers (Basel)., 14(6), 1255. doi: 10.3390/polym14061255.

[13] A. Jelić, A. Marinković, M. Sekulić, S. Dikić, V. Ugrinović, V. Pavlović, S. Putić (2021) Design of halloysite modification for improvement of mechanical properties of the epoxy based nanocomposites. Polym. Compos., 42(5), 2180–92. doi: 10.1002/pc.25967.

[14] Ł. Klapiszewski, J. Tomaszewska, K. Skórczewska, T. Jesionowski (2017) Preparation and characterization of eco-friendly Mg(OH)2/lignin hybrid material and its use as a functional filler for poly(vinyl chloride). Polymers (Basel)., 9(7), 258-265. doi: 10.3390/polym9070258.

[15] S. Halder, P.K. Ghosh, M.S. Goyat (2012) Influence of ultrasonic dual mode mixing on morphology and mechanical properties of ZrO2-epoxy nanocomposite. High Perform. Polym., 24(4), 331–341. doi: 10.1177/0954008312440714.

[16] P.K. Ghosh, M.S. Goyat, D. Mishra, R. Nagori (2012) Physical and Mechanical Properties of Epoxy-Nanoparticulate Composite Adhesive. Adv. Mater. Res., 585, 297–300. doi: 10.4028/www.scientific.net/AMR.585.297.

[17] S. Halder, M.S. Goyat, P.K. Ghosh (2016) Morphological, structural, and thermophysical properties of zirconium dioxide-epoxy nanocomposites. High Perform. Polym., 28(6), 697–708. doi: 10.1177/0954008315595275.

[18] A. Hooda, M.S. Goyat, R. Gupta, M. Prateek, M. Agrawal, A. Biswas (2017) Synthesis of nano-textured polystyrene/ZnO coatings with excellent transparency and superhydrophobicity. Mater. Chem. Phys., 193, 447–452. doi: 10.1016/j.matchemphys.2017.03.011.

[19] T. Prasad, S. Halder, M.S. Goyat, S.S. Dhar (2016) Morphological dissimilarities of ZnO nanoparticles and its effect on thermo-physical behavior of epoxy composites. Polym. Compos., 39(1), 135-145. doi: 10.1002/pc.23914.

[20] M.S. Goyat, S. Rana, S. Halder, P.K. Ghosh (2018) Facile fabrication of epoxy-TiO 2 nanocomposites: A critical analysis of TiO 2 impact on mechanical properties and toughening mechanisms. Ultrason. Sonochem., 40, 861–73. doi: 10.1016/j.ultsonch.2017.07.040.

[21] M.S. Goyat, P.K. Ghosh (2017) Impact of ultrasonic assisted triangular lattice like arranged dispersion of nanoparticles on physical and mechanical properties of epoxy-TiO 2 nanocomposites. Ultrason. Sonochem., 42, 141-154. doi: 10.1016/j.ultsonch.2017.11.019.

[22] M.S. Goyat, S. Ray, P.K. Ghosh (2011) Innovative application of ultrasonic mixing to produce homogeneously mixed nanoparticulate-epoxy composite of improved physical properties. Compos. Part A Appl. Sci. Manuf., 42(10), 1421–31. doi: 10.1016/j.compositesa.2011.06.006.

[23] S. Haldera, P.K. Ghosh, M.S. Goyat, S. Ray (2013) Ultrasonic dual mode mixing and its effect on tensile properties of SiO2-epoxy nanocomposite. J. Adhes. Sci. Technol., 27(2), 111–124. doi: 10.1080/01694243.2012.701510.

[24] S. Halder, T. Prasad, N.I. Khan, M.S. Goyat, S. Ram Chauhan (2017) Superior mechanical properties of poly vinyl alcohol-assisted ZnO nanoparticle reinforced epoxy composites. Mater. Chem. Phys., 192, 198–209. doi: 10.1016/ j.matchemphys.2016.12.055.

[25] P.K. Ghosh, A. Pathak, M.S. Goyat, S. Halder (2012) Influence of nanoparticle weight fraction on morphology and thermal properties of epoxy/TiO2 nanocomposite. J. Reinf. Plast. Compos., 31(17), 1180–8. doi: 10.1177/0731684412455955.

[26] L.L. Zhai, G.P. Ling, Y.W. Wang (2008) Effect of nano-Al2O3 on adhesion strength of epoxy adhesive and steel. Int. J. Adhes. Adhes., 28(1–2), 23–28. doi: 10.1016/j.ijadhadh. 2007.03.005.

[27] A. Omrani, L.C. Simon, A.A. Rostami (2009) The effects of alumina nanoparticle on the properties of an epoxy resin system. Mater. Chem. Phys., 114(1), 145–50. doi: 10.1016/ j.matchemphys. 2008.08.090.

[28] L. Zhai, G. Ling, J. Li, Y. Wang (2006) The effect of nanoparticles on the adhesion of epoxy adhesive. Mater. Lett., 60(25–26), 3031–3. doi: 10.1016/j.matlet.2006.02.038.

[29] B. Wetzel, F. Haupert, M.Q. Zhang (2003) Epoxy nanocomposites with high mechanical and tribological performance. Compos. Sci. Technol., 63(14), 2055–67. doi: 10.1016/S0266-3538(03)00115-5.

[30] B. Wetzel, P. Rosso, F. Haupert, K. Friedrich (2006) Epoxy nanocomposites–fracture and toughening mechanisms. Eng. Fract. Mech., 73(16), 2375–98.

[31] R.K. Nayak, A. Dash, B.C. Ray (2014) Effect of Epoxy Modifiers (Al2O3/SiO2/TiO2) on Mechanical Performance of epoxy/glass Fiber Hybrid Composites. Procedia Mater. Sci., 6, 1359–64. doi: 10.1016/j.mspro.2014.07.115.

[32] K. Kumar, P.K.K. Ghosh, A. Kumar (2016) Improving mechanical and thermal properties of TiO2-epoxy nanocomposite. Compos. Part B Eng., 97, 353–60. doi: 10.1016/j.compositesb. 2016.04.080.

[33] A. Chatterjee, M.S. Islam (2008) Fabrication and characterization of TiO2-epoxy nanocomposite. Mater. Sci. Eng. A, 487(1–2), 574–85. doi: 10.1016/j.msea.2007.11.052.

[34] Y. Zhou, E. White, M. Hosur, S. Jeelani (2010) Effect of particle size and weight fraction on the flexural strength and failure mode of TiO2 particles reinforced epoxy. Mater. Lett., 64(7), 806–9. doi: 10.1016/j.matlet.2010.01.016.

[35] B. Bittmann, F. Haupert, A.K. Schlarb (2011) Preparation of TiO2/epoxy nanocomposites by ultrasonic dispersion and their structure property

relationship. Ultrason. Sonochem., 18(1), 120–126. doi: 10.1016/j.ultsonch.2010.03.011.

[36] B. Bittmann, F. Haupert, A.K. Schlarb (2012) Preparation of TiO2epoxy nanocomposites by ultrasonic dispersion and resulting properties. J. Appl. Polym. Sci., 124(3), 1906–11. doi: 10.1002/app.34493.

[37] H.A. Al-Turaif (2010) Effect of nano TiO2 particle size on mechanical properties of cured epoxy resin. Prog. Org. Coatings, 69(3), 241–6. doi: 10.1016/j.porgcoat.2010.05.011.

[38] I. a Al-ajaj, M.M. Abd, H.I. Jaffer, A. Materials (2013) Mechanical Properties of Micro and Nano TiO 2 / Epoxy Composites. Int. J. Mining, Metall. Mech. Eng., 1(2), 2–6.

[39] C.B. Ng, B.J. Ash, L.S. Schadler, R.W. Siegel (2001) A study of the mechanical and permeability properties of nano-and micron-TiO2, filled epoxy composites. Adv. Compos. Lett., 10(3), 101–11. doi: 10.1177/096369350101000301.

[40] G. Xian, R. Walter, F. Haupert (2006) A synergistic effect of nano-TiO2 and graphite on the tribological performance of epoxy matrix composites. J. Appl. Polym. Sci., 102(3), 2391–400. doi: 10. 1002/app.24496.

[41] P. Carballeira, F. Haupert (2010) Toughening effects of titanium dioxide nanoparticles on TiO 2/epoxy resin nanocomposites. Polym. Compos., 31(7), 1241–6. doi: 10.1002/pc.20911.

[42] C. Guan, C.L. Lü, Y.F. Liu, B. Yang (2006) Preparation and characterization of high refractive index thin films of TiO2/epoxy resin nanocomposites. J. Appl. Polym. Sci., 102(2), 1631–6. doi: 10.1002/app.23947.

[43] H. Zhang, Z. Zhang, K. Friedrich, C. Eger (2006) Property improvements of in situ epoxy nanocomposites with reduced interparticle distance at high nanosilica content. Acta Mater., 54(7), 1833–42. doi: 10.1016/j.actamat.2005.12.009.

[44] A.J. Kinloch, J.H. Lee, A.C. Taylor, S. Sprenger, C. Eger, D. Egan (2003) Toughening structural adhesives via nano- and micro-phase inclusions. J. Adhes., 79(8–9), 867–73. doi: 10.1080/00218460309551.

[45] Y. Zheng, Y. Zheng, R. Ning (2003) Effects of nanoparticles SiO2 on the performance of nanocomposites. Mater. Lett., 57(19), 2940–4. doi: 10.1016/S0167-577X(02)01401-5.

[46] M.Z. Rong, M.Q. Zhang, Y.X. Zheng, H.M. Zeng, K. Friedrich (2001) Improvement of tensile properties of nano-SiO2/PP composites in relation to percolation mechanism. Polymer (Guildf)., 42(7), 3301–4. doi: 10.1016/S0032-3861(00)00741-2.

[47] R. Medina, F. Haupert, A.K. Schlarb (2008) Improvement of tensile properties and toughness of an epoxy resin by nanozirconium-dioxide reinforcement. J. Mater. Sci., 43(9), 3245–52. doi: 10.1007/s10853-008-2547-8.

[48] R. V. Kurahatti, A.O. Surendranathan, S. Srivastava, N. Singh, A. V. Ramesh Kumar, B. Suresha (2011) Role of zirconia filler on friction and dry sliding wear behaviour of bismaleimide nanocomposites. Mater. Des., 32(5), 2644–9. doi: 10.1016/j.matdes.2011.01.030.

[49] Y. Hu, G. Gu, S. Zhou, L. Wu (2011) Preparation and properties of transparent PMMA/ZrO2 nanocomposites using 2-hydroxyethyl methacrylate as a coupling agent. Polymer (Guildf)., 52(1), 122–9. doi: 10.1016/j.polymer.2010.11.020.

[50] A. Olad, M. Barati, S. Behboudi (2012) Preparation of PANI/epoxy/Zn nanocomposite using Zn nanoparticles and epoxy resin as additives and investigation of its corrosion protection behavior on iron. Prog. Org. Coatings, 74(1), 221–7. doi: 10.1016/j.porgcoat.2011.12.012.

[51] G. Das, N. Karak (2009) Epoxidized Mesua ferrea L. seed oil-based reactive diluent for BPA epoxy resin and their green nanocomposites. Prog. Org. Coatings, 66(1), 59–64. doi: 10.1016/j.porgcoat. 2009.06.001.

[52] D. Wu, L. Wu, J. Wang, Y. Sun, M. Zhang (2011) Effect of epoxy resin on the thermal behaviors and viscoelastic properties of poly(phenylene sulfide). Mater. Chem. Phys., 128(1–2), 274–82. doi: 10.1016/j.matchemphys.2011.03.015.

[53] Y. Liu, D.L. Duan, S.L. Jiang, S. Li (2015) Preparation and its cavitation performance of nickel foam/epoxy/SiC co-continuous composites. Wear, 332–333, 979–87. doi: 10.1016/j.wear.2014. 12.025.

[54] R. DaganI (1992) Nanostructured Materials Promise To Advance Range of Technologies. Chem. Eng. News, 70(47), 18–24. doi: 10.1021/cen-v070n047.p018.

[55] M.Z. Rong, M.Q. Zhang, Y.X. Zheng, H.M. Zeng, R. Walter, K. Friedrich (2001) Structure–property relationships of irradiation grafted nano-inorganic particle filled polypropylene composites. Polymer (Guildf)., 42(1), 167–83. doi: 10.1016/S0032-3861(00)00325-6.

[56] P.K. Ghosh, S.K. Nukala (2008) Characteristics of adhesive joints of metals using inorganic particulate composite adhesives. Trans. Indian Inst. Met., 61(4), 307–17. doi: 10.1007/s12666-008-0044-z.

[57] C. Zhang, X. Bai, X. Lian, Y. Dou, H. Liu (2011) Study on morphology and mechanical properties of PMMA-based nanocomposites containing POSS molecules or functionalized SiO2 particles. High Perform. Polym., 23(6), 468–76. doi: 10.1177/0954008311417023.

[58] R.R. Tummala, E.J. Rymaszewski, Y.C. Lee (1989) Microelectronics Packaging Handbook. J. Electron. Packag., 111(3), 241-249. doi: 10.1115/1.3226540.

[59] Q. Yao, J. Qu (2002) Interfacial versus cohesive failure on polymer-metal interfaces in electronic packaging - Effects of interface roughness. J. Electron. Packag. Trans. ASME, 124(2), 127–34. doi: 10.1115/1.1459470.

[60] F.L. Jin, X. Li, S.J. Park (2015) Synthesis and application of epoxy resins: A review. J. Ind. Eng. Chem., 29, 1–11. doi: 10.1016/j.jiec.2015.03.026.

[61] S.H. Goodman (1998) Epoxy Resins. Handbook of Thermoset Plastics, pp. 193–268.

[62] J. Murphy (2001) Additives for Plastics Second Edition. Elsevier Science Ltd.

[63] G. Viana, M. Costa, M.D. Banea, L.F.M. da Silva (2017) Behaviour of environmentally degraded epoxy adhesives as a function of temperature. J. Adhes., 93(1–2), 95–112. doi: 10.1080/00218464. 2016.1179118.

[64] P. Rosso, L. Ye (2007) Epoxy/silica nanocomposites: Nanoparticle-induced cure kinetics and microstructure. Macromol. Rapid Commun., 28(1), 121–6. doi: 10.1002/marc. 200600588.

[65] L. Liu, Z. Qi, X. Zhu (1999) Studies on nylon 6/clay nanocomposites by melt-intercalation process. J. Appl. Polym. Sci., 71(7), 1133–8. doi: 10.1002/ (SICI)1097-4628(19990214)71:7<1133::AID-APP 11>3.0.CO;2-N.

[66] Z. Wang, G. Xie, X. Wang, Z. Zhang (2006) Rheology and dispersion behavior of high-impact polystyrene/ethylene-vinyl acetate copolymer/TiO2 nanocomposites. J. Appl. Polym. Sci., 100(6), 4434–8. doi: 10.1002/app.23713.

[67] J. Bijwe, J. Indumathi, A.K. Ghosh (2002) On the abrasive wear behaviour of fabric-reinforced polyetherimide composites. Wear, 253(7–8), 768–77. doi: 10.1016/S0043-1648(02)00169-2.

[68] I. Stewart, A. Chambers, T. Gordon (2007) The cohesive mechanical properties of a toughened epoxy adhesive as a function of cure level. Int. J. Adhes. Adhes., 27(4), 277–87. doi: 10.1016/ j.ijadhadh.2006.05.003.

[69] A.J. Kinloch, A.C. Taylor (2006) The mechanical properties and fracture behaviour of epoxy-inorganic micro- and nano-composites. J. Mater. Sci., 41(11), 3271–97. doi: 10.1007/s10853-005-5472-0.

[70] C.-M. Chan, J. Wu, J.-X. Li, Y.-K. Cheung (2002) Polypropylene/calcium carbonate nanocomposites. Polymer (Guildf)., 43(10), 2981–92. doi: 10.1016/S0032-3861(02)00120-9.

[71] M. Shanthi, M. Gupta, A.E.W.E.W. Jarfors, M.J.J. Tan (2011) Synthesis, characterization and mechanical properties of nano alumina particulate reinforced magnesium based bulk metallic glass composites 528(18), 6045–50. doi: 10.1016/j.msea.2011.03.103.

[72] A. Gautam, S. Ram (2010) Preparation and thermomechanical properties of Ag-PVA nanocomposite films. Mater. Chem. Phys., 119(1–2), 266–71. doi: 10.1016/j.matchemphys. 2009. 08.050.

[73] P. Pötschke, A.R. Bhattacharyya, A. Janke (2004) Carbon nanotube-filled polycarbonate composites produced by melt mixing and their use in blends with polyethylene. Carbon N. Y., 42(5–6), 965–9. doi: 10.1016/j.carbon.2003.12.001.

[74] M. Imanaka, Y. Takeuchi, Y. Nakamura, A. Nishimura, T. Iida (2001) Fracture toughness of spherical silica-filled epoxy adhesives. Int. J. Adhes. Adhes., 21(5), 389–96. doi: 10.1016/S0143-7496(01)00016-1.

[75] A. Mondal, S. Ram (2003) Al3+-stabilized c-ZrO2 nanoparticles at low temperature by forced hydrolysis of dispersed metal cations in water. Solid State Ionics, 160(1–2), 169–81. doi: 10.1016/S0167-2738(03)00130-9.

[76] T. Mahrholz, J. Stängle, M. Sinapius (2009) Quantitation of the reinforcement effect of silica nanoparticles in epoxy resins used in liquid composite moulding processes. Compos. Part A Appl. Sci. Manuf., 40(3), 235–43. doi: 10.1016/j.compositesa.2008.11.008.

[77] S. Singha, M.J. Thomas (2008) Reduction of permittivity in epoxy nanocomposites at low nano-filler loadings. Annual Report - Conference on Electrical Insulation and Dielectric Phenomena, CEIDP, IEEE, pp. 726–9.

[78] S. Zhao, L.S. Schadler, R. Duncan, H. Hillborg, T. Auletta (2008) Mechanisms leading to improved mechanical performance in nanoscale alumina filled epoxy. Compos. Sci. Technol., 68(14), 2965–75. doi: 10.1016/j.compscitech.2008.01.009.

[79] S. Wu, M.D. Soucek (2000) Crosslinking of acrylic latex coatings with cycloaliphatic diepoxide. Polymer (Guildf)., 41(6), 2017–28. doi: 10.1016/S0032-3861(99)00370-5.

[80] M. Xiong, G. Gu, B. You, L. Wu (2003) Preparation and characterization of poly(styrene butylacrylate) latex/nano-ZnO nanocomposites. J. Appl. Polym. Sci., 90(7), 1923–31. doi: 10.1002/app.12869.

[81] Y. Sun, Z. Zhang, K.S. Moon, C.P. Wong (2004) Glass transition and relaxation behavior of epoxy nanocomposites. J. Polym. Sci. Part B Polym. Phys., 42(21), 3849–58. doi: 10.1002/polb.20251.

[82] J. Yin, H. Chen, Z. Li, X. Qian, J. Yin, M. Shi, G. Zhou (2003) Preparation of PS/TiO2 core-shell microspheres and TiO 2 hollow shells. J. Mater. Sci., 38(24), 4911–6. doi: 10.1023/B: JMSC. 0000004413.69813.04.

[83] N. Hebestreit, J. Hofmann, U. Rammelt, W. Plieth (2003) Physical and electrochemical characterization of nanocomposites formed from polythiophene and titaniumdioxide. Electrochim. Acta, 48(13), 1779–88. doi: 10.1016/S0013-4686 (02) 00783-1.

[84] G. Xian, Z. Zhang, K. Friedrich (2006) Tribological properties of micro- And nanoparticles-filled poly(etherimide) composites. J. Appl. Polym. Sci., 101(3), 1678–86. doi: 10.1002/app.22578.

[85] S. Singha, M.J. Thomas (2008) Dielectric properties of epoxy nanocomposites. IEEE Trans. Dielectr. Electr. Insul., 15(1), 12–23. doi: 10.1109/T-DEI.2008.4446732.

[86] H. Zhao, R.K.Y. Li (2008) Effect of water absorption on the mechanical and dielectric properties of nano-alumina filled epoxy nanocomposites. Compos. Part A Appl. Sci. Manuf., 39(4), 602–11. doi: http://dx.doi.org/ 10.1016/ j.compositesa.2007.07.006.

[87] C.H. Chen, J.Y. Jian, F.S. Yen (2009) Preparation and characterization of epoxy/γ-aluminum oxide nanocomposites. Compos. Part A Appl. Sci. Manuf., 40(4), 463–8. doi: 10.1016/j.compo-sitesa.2009.01.010.

[88] S. Kozhukharov, G. Tsaneva, V. Kozhukharov, J. Gerwann, M. Schem, T. Schmidt, M. Veith (2008)

Corrosion Protection Properties of Composite Hybrid Coatings With Involved Nanoparticles of Zirconia and Ceria. Chem. Technol., 43 SRC-, 54, 73–80.

[89] G. Gusmano, G. Montesperelli, M. Rapone, G. Padeletti, A. Cusmà, S. Kaciulis, A. Mezzi, R. Di Maggio (2007) Zirconia primers for corrosion resistant coatings. Surf. Coatings Technol., 201(12), 5822–8. doi: 10.1016/j.surfcoat.2006.10.036.

[90] J.F. Quinson, C. Chino, A.M. De Becdelievre, C. Guizard, M. Brunel (1996) Deformation capability and protective role of zirconia coatings on stainless steel. J. Mater. Sci., 31(19), 5179–84. doi: 10.1007/BF00355922.

[91] A. Dorigato, A. Pegoretti, F. Bondioli, M. Messori (2010) Improving epoxy adhesives with zirconia nanoparticles. Compos. Interfaces, 17(9), 873–92. doi: 10.1163/092764410X539253.

[92] M.A. Kashfipour, N. Mehra, J. Zhu (2018) A review on the role of interface in mechanical, thermal, and electrical properties of polymer composites. Adv. Compos. Hybrid Mater., 1(3), 415–39. doi: 10.1007/s42114-018-0022-9.

[93] A. Bansal, H. Yang, C. Li, K. Cho, B.C. Benicewicz, S.K. Kumar, L.S. Schadler (2005) Quantitative equivalence between polymer nanocomposites and thin polymer films. Nat. Mater., 4(9), 693–8. doi: 10.1038/nmat1447.

[94] H. Miyagawa, L.T. Drzal (2004) Thermo-physical and impact properties of epoxy nanocomposites reinforced by single-wall carbon nanotubes. Polymer (Guildf)., 45(15), 5163–70. doi: 10.1016/j.polymer.2004.05.036.

[95] G.R. Palmese (1991) The interphase in thermosetting composites:Ph.D.Thesis, Newark, Delaware: University of Delaware Dept..

[96] M.S. Goyat, S. Rana, S. Halder, P.K. Ghosh (2018) Facile fabrication of epoxy-TiO2 nanocomposites: A critical analysis of TiO2 impact on mechanical properties and toughening mechanisms. Ultrason. Sonochem., 40(June 2017), 861–73. doi: 10.1016/j.ultsonch.2017.07.040.

[97] S.K. Singh, D. Singh, A. Kumar, A. Jain (2020) An Analysis of Mechanical and Viscoelastic Behaviour of Nano-SiO2 Dispersed Epoxy Composites. Silicon, 12(10), 2465–77. doi: 10.1007/s12633-019-00335-x.

[98] K. Kumar, P.K. Ghosh, A. Kumar, O. Singh (2021) Enhanced Thermomechanical Properties of ZrO2 Particle Reinforced Epoxy Nanocomposite. J. Mater. Eng. Perform., 30(1), 145–53. doi: 10.1007/s11665-020-05350-3.

[99] D. Dean, R. Walker, M. Theodore, E. Hampton, E. Nyairo (2005) Chemorheology and properties of epoxy/layered silicate nanocomposites. Polymer (Guildf)., 46(9), 3014–21. doi: 10.1016/j.polymer.2005.02.015.

[100] Ş. Yazman, M. Uyaner, F. Karabörk, A. Akdemir (2021) Effects of nano reinforcing/matrix interaction on chemical, thermal and mechanical properties of epoxy nanocomposites. J. Compos. Mater., 55(28), 4257–72. doi: 10.1177/00219983211037059.

[101] S. Wang, S. Yu, J. Li, S. Li (2020) Effects of functionalized nano-TiO2 on the molecular motion in epoxy resin-based nanocomposites. Materials (Basel)., 13(1), 163. doi: 10.3390/ma13010163.

[102] S. Li, H. Jiang, T. Tang, Y. Nie, Z. Zhang, Q. Zhou (2018) Improved electrochemical and mechanical performance of epoxy-based electrolytes doped with mesoporous TiO2. Mater. Chem. Phys., 205, 23–8. doi: 10.1016/j.matchemphys.2017.10.075.

[103] A. Marotta, N. Faggio, V. Ambrogi, A. Mija, G. Gentile, P. Cerruti (2021) Biobased furan-based epoxy/TiO2 nanocomposites for the preparation of coatings with improved chemical resistance. Chem. Eng.J.,406,127107 doi:10.1016/j.cej.2020.127107.

[104] G.C. Papanicolaou, A.E. Manara, L.C. Kontaxis (2020) Experimental and prediction study of displacement-rate effects on flexural behaviour in nano and micro TiO2 particles-epoxy resin composites. Polymers (Basel)., 12(1), 22. doi: 10.3390/polym12010022.

[105] A. Kumar, K. Kumar, P.K. Ghosh, K.L. Yadav (2018) MWCNT/TiO2 hybrid nano filler toward high-performance epoxy composite. Ultrason. Sonochem., 41, 37–46. doi: 10.1016/j.ultsonch.2017.09.005.

[106] Nitesh, A. Kumar, S. Saini, K.L. Yadav, P.K. Ghosh, A. Rathi (2022) Morphology and tensile performance of MWCNT/TiO2-epoxy nanocomposite. Mater. Chem. Phys., 277, 125336. doi: 10.1016/j.matchemphys.2021.125336.

[107] M. Ozen, G. Demircan, M. Kisa, A. Acikgoz, G. Ceyhan, Y. Işıker (2022) Thermal properties of surface-modified nano-Al2O3/Kevlar fiber/epoxy composites. Mater. Chem. Phys., 278, 125689. doi: 10.1016/J.MATCHEMPHYS.2021.125689.

[108] M. Liang, K.L. Wong (2017) Study of Mechanical and Thermal Performances of Epoxy Resin Filled with Micro Particles and Nanoparticles. Energy Procedia, 110, 156–61. doi: 10.1016/J.EGYPRO.2017.03.121.

[109] J.P.B. de Souza, J.M.L. dos Reis (2015) A thermomechanical and adhesion analysis of Epoxy/Al2O3 nanocomposites. Nanomater. Nanotechnol., 5(1), 1–7. doi: 10.5772/60938.

[110] S. Kumar Singh, D. Gunwant, A. Vedrtnam, A. Kumar, A. Jain (2022) Synthesis, characterization, and modelling the behavior of in-situ ZrO2 nanoparticles dispersed epoxy nanocomposite. Eng. Fract. Mech., 263, 108300. doi: 10.1016/j.engfracmech.2022.108300.

[111] S.K. Singh, A. Kumar, A. Jain (2018) Effect of nanoparticles dispersion on viscoelastic properties of epoxy-zirconia polymer nanocomposites. IOP Conf. Ser. Mater. Sci. Eng., 18, 100591 doi: 10.1088/1757-899X/330/1/012001.

[112] J. Zheng, X. Zhang, J. Cao, R. Chen, T. Aziz, H. Fan, C. Bittencourt (2021) Behavior of epoxy resin filled with nano-SiO2 treated with a Eugenol epoxy silane. J. Appl. Polym. Sci., 138(14), 1–11. doi: 10.1002/app.50138.

[113] S.K. Singh, A. Kumar, A. Jain (2021) Mechanical and viscoelastic properties of SiO2/epoxy nanocomposites post-cured at different

temperatures. Plast. Rubber Compos., 50(3), 116–26. doi: 10.1080/14658011.2020.1840203.
[114] A. Zotti, S. Zuppolini, A. Borriello, M. Zarrelli (2020) Thermal and mechanical characterization of an aeronautical graded epoxy resin loaded with hybrid nanoparticles. Nanomaterials, 10(7), 1–14. doi: 10.3390/nano10071388.
[115] S.J. Park, F.L. Jin (2004) Thermal stabilities and dynamic mechanical properties of sulfone-containing epoxy resin cured with anhydride. Polym. Degrad. Stab., 86(3), 515–20. doi: 10.1016/j.polymdegradstab.2004.06.003.
[116] W.S. Wang, H.S. Chen, Y.W. Wu, T.Y. Tsai, Y.W. Chen-Yang (2008) Properties of novel epoxy/clay nanocomposites prepared with a reactive phosphorus-containing organoclay. Polymer (Guildf)., 49(22), 4826–36. doi: 10.1016/j.polymer. 2008.08.019.
[117] V. Babrauskas (2004) Plastics flammability handbook: Principles, regulations, testing, and approval,. Fire Saf. J., 39(6), 525–7. doi: 10.1016/j.firesaf.2004.02.005.
[118] S.M. Khaled, R. Sui, P.A. Charpentier, A.S. Rizkalla (2007) Synthesis of TiO2 - PMMA nanocomposite: Using methacrylic acid as a coupling agent. Langmuir, 23, 3988–95. doi: 10.1021/la062879n.
[119] B.B. Johnsen, A.J. Kinloch, R.D. Mohammed, A.C. Taylor, S. Sprenger (2007) Toughening mechanisms of nanoparticle-modified epoxy polymers. Polymer (Guildf)., 48(2), 530–41. doi: 10.1016/j.polymer.2006.11.038.
[120] B. Guo, D. Jia, C. Cai (2004) Effects of organo-montmorillonite dispersion on thermal stability of epoxy resin nanocomposites. Eur. Polym. J., 40(8), 1743–8. doi: 10.1016/j.eurpolymj.2004.03.027.
[121] J. Bian, Z.J. Wang, H.L. Lin, X. Zhou, W.Q. Xiao, X.W. Zhao (2017) Thermal and mechanical proper¬ties of polypropylene nanocomposites reinforced with nano-SiO2 functionalized graphene oxide. Compos. Part A Appl. Sci. Manuf., 97, 120–7. doi: 10.1016/j.compositesa.2017.01.002.

IZVOD

PREGLED POBOLJŠANIH FIZIČKIH I TERMIČKIH SVOJSTAVA EPOKSIDNIH KOMPOZITA OJAČANIH NANOČESTICAMA OKSIDA

Epoksidne smole su dobro poznate zbog svojih poželjnih termičkih i mehaničkih karakteristika u raznim oblastima, uključujući automobilsku, građevinsku i avio-industriju. Međutim, inherentna krhka priroda visoko umreženih epoksidnih smola generalno dovodi do slabosti u otpornosti na stvaranje pukotina i njihovo kretanje. Krhkost epoksidnih smola je jedna od glavnih prepreka koja sprečava njihovu upotrebu u širem obimu. Zbog toga su se mnogi istraživači fokusirali na ojačavanje epoksidnih smola različitim tipovima nanostruktura uključujući ugljenične nanocevi (CNT), organska/neorganska nanopunila da bi se obezbedila veća čvrstoća, bez umanjivanja drugih bitnih termo-fizičkih karakteristika nanokompozita. Većina članaka za pregled fokusiranih na epoksidne kompozite ojačane CNT-om, a dostupni su vrlo ograničeni članci za pregled koji se fokusiraju na epoksidne kompozite ojačane oksidnim nanopunilima. U ovom preglednom članku istraženi su epoksidni nanokompoziti ojačani nanočesticama glinice (Al_2O_3), titanija (TiO_2), silicijum dioksida (SiO_2) i cirkonijum (ZrO_2). Uticaj nanočestica oksida u modifikaciji fizičkih i termičkih osobina epoksidnih nanokompozita je predstavljen, upoređen i kritički analiziran u cilju optimizacije performansi epoksidnih nanokompozita.

Ključne reči: *oksidni nanopunjač; temperatura prelaska stakla; fizička svojstva; termička svojstva; termička degradacija*

Pregledni rad
Rad primljen: 27.09.2023.
Rad prihvaćen: 25.10.2023.
Rad je dostupan na sajtu: www.idk.org.rs/casopis

*Aryan Boora, Bhavna Rohilla, Priya Malik, Supriya Sehrawat, Sushma Kumari, Anisha Sharma, Kirti Dahiya, Surender Duhan**

Advanced Sensors Lab, Department of Physics, Deenbandhu Chhotu Ram University of Science and Technology, Murthal, Haryana,India

Scientific paper
ISSN 0351-9465, E-ISSN 2466-2585
https://doi.org/10.62638/ZasMat1011

Zastita Materijala 65 (1)
143 - 150 (2024)

Impact of annealing on structural and optical properties of sol-gel derived samarium silica nanocomposites

ABSTRACT

The pursuit of finely tuned material properties has driven the exploration of annealing strategies in the context of Samarium Silica Nanocomposites (Sm-SiO_2 NCs) synthesized through the sol-gel route. This study unveils novel insights into the influence of optimized annealing protocols on the structural and functional evolution of these advanced nanocomposites. Through meticulous experimentation, we establish that controlled temperature annealing plays a pivotal role in tailoring the microstructure and properties of Sm-SiO_2 NCs. The judicious manipulation of annealing parameters, including temperature duration, and atmosphere, orchestrates distinct transformations in the composite architecture. Field emission microscopy and structural analysis reveal that precise annealing promotes the consolidation of nanoscale domains, leading to improved crystallinity and enhanced connectivity between samarium species and the silica matrix. Moreover, the annealing-induced modifications extend beyond structural aspects to influence functional properties, an increase in crystallite size was observed from 15 nm to 43 nm as an effect of annealing. Our findings illustrate a remarkable enhancement in luminescence intensity as a consequence of optimized annealing, showcasing the potential for tailored photonic applications. These revelations are supported by a comprehensive suite of analytical techniques, including X-ray diffraction, Fourier transform infra red,\Field emission with Energy dispersive x-ray and photoluminescence spectroscopy. The synthesis-annealing synergy not only advances our fundamental understanding of nanocomposite evolution but also furnishes a pathway towards designing multifunctional materials with precision-engineered attributes.

Keywords: *Nanocomposites, Sol-Gel Route, annealing strategies, microstructural evolution, functional enhancements*

1. INTRODUCTION

In the pursuit of tailoring material properties at the nanoscale, the synthesis and optimization of multifunctional nanocomposites have gained substantial attention due to their potential applications in a wide array of fields. Among these, the coupling of rare earth elements with silica matrices has emerged as a compelling avenue for engineering advanced materials with tailored optical, magnetic, and catalytic properties [1-3]. The integration of Samarium Silica Nanocomposites (Sm-SiO_2 NCs) stands as a representative example, where the deliberate incorporation of samarium species into a silica matrix has shown remarkable potential for applications ranging from photonics to biomedicine. The sol-gel technique has emerged as a versatile and robust approach for fabricating nanocomposites with controlled compositions and morphologies [4,5]. In this context, the role of post-synthesis thermal treatments, particularly annealing, has garnered attention as a strategic tool for refining the properties of these nanocomposites. Annealing involves subjecting the synthesized materials to controlled elevated temperatures for a specified duration, often in controlled atmospheres [6,7]. Through this process, it is possible to induce structural rearrangements, phase transitions, and modifications in physicochemical properties that can be harnessed to enhance the functionality of the resulting nanocomposites [8-10].

This study delves into the realm of optimized annealing strategies for Sm-SiO_2 NCs prepared via the sol-gel route. The motivation behind investigating annealing stems from its potential to exert

*Corresponding author: Surender Duhan
Email: surender6561@gmail.com
Paper received: 28. 09. 2023.
Paper corected: 11.11.2023.
Paper accepted: 16. 11. 2023.
Paper is available on the website: www.idk.org.rs/journal

profound influence over the microstructure and properties of these nanocomposites [11,12]. By judiciously manipulating the annealing parameters, such as temperature, duration, and gas atmosphere, it becomes possible to drive controlled transformations that impact the arrangement of samarium species within the silica matrix. Consequently, these controlled changes in structure lead to corresponding enhancements in properties, such as photoluminescence intensity and magnetic behavior. The interplay between sol-gel synthesis and annealing presents an intriguing avenue for tailoring nanocomposite characteristics with precision [13-15]. Through a systematic exploration of annealing strategies, a deepened understanding of the structure-property relationships in Sm-SiO_2 NCs can be achieved. This investigation not only contributes to fundamental knowledge about nanocomposite evolution but also holds the potential to drive the development of innovative applications that capitalize on the synergistic effects of sol-gel synthesis and optimized annealing.

The annealing procedure plays a pivotal role in determining the final properties of the investigated Samarium Silica Nanocomposites prepared by the Sol-Gel method. In the subsequent sections of this paper, we present our findings on the influence of various annealing protocols on the structural and functional attributes of Sm-SiO_2 NCs. Through a combination of advanced characterization techniques, we unveil the intricate changes induced by annealing and underscore the potential of this approach for precise property engineering in nanocomposites.The study demonstrates that controlled temperature annealing is pivotal in tailoring the microstructure and properties of Sm-SiO_2 NCs. Optimized annealing protocols, including temperature, duration, and atmosphere, lead to distinct transformations in the composite architecture. This includes improved crystallinity, enhanced connectivity between samarium species and the silica matrix, and a remarkable enhancement in luminescence intensity. The findings highlight the significance of the annealing process in achieving precise property engineering in nanocomposites, advancing their potential applications in various fields.

2. MATERIALS AND METHODS

2.1. Materials

The materials employed for the preparation of Sm_2O_3-SiO_2 nanocomposites consisted of Tetraethyl orthosilicate, hydrochloric acid (HCl), nitric acid (HNO_3), samarium oxide and ethanol, all of which were acquired from Sigma Aldrich. Distilled water was utilized exclusively for all experiments conducted.

2.2. Methods

Using the sol-gel methodology, a silica gel doped with Sm was produced through refluxing highly pure chemicals. A mixture of tetraethoxysilane, ethanol, and deionized water was combined with hydrochloric acid, which acted as a catalyst. For the gel preparation, the molar ratios of starting solutions were adjusted as follows: 0.38:0.162:0.0923:0.031 for H_2O:C_2H_5OH:HCl:TEOS. Notably, all glass samples were doped with 6% Sm_2O_3. The inclusion of samarium oxide in the early stages of the process involved dissolving samarium oxide in nitric acid under elevated temperatures, yielding a clear white solution [16,17]. This resulting precipitate was then incorporated into the previously prepared solution. Following filtration, the solutions were stirred for a duration of 2h at room temperature, resulting in homogeneous solutions. Subsequently, these solutions were poured into various molds and placed in a drying oven set at 100°C. Gelation was evident approximately four days later. The aging process ensued, contributing to further contraction and solidification of the gel. The doped samples exhibited a glassy yellow hue due to the presence of samarium. To obtain powdered forms of the doped samples, a pestle and mortar were employed [18]. The resultant powder samples were subjected to sintering in a muffle furnace across temperature ranges of 780°C, 980°C, and 1180°C.

2.3. Characterizations

Characterizing the structural, morphological, and functional changes induced by optimized annealing strategies is pivotal to unravel the intricate interplay between thermal treatment and the properties of Samarium Silica Nanocomposites (Sm-SiO_2 NCs) synthesized via the sol-gel route. The characterization efforts provide a comprehensive understanding of how controlled annealing influences the evolution of these advanced nanocomposites. The characteristic diffraction peaks of samarium oxide and silica are meticulously tracked using RIGAKU XRD diffractometer. Energy-dispersive X-ray spectroscopy (EDS) coupled with FESEM allows for elemental mapping, facilitating the visualization of elemental distribution across the nanocomposite. Photoluminescence spectroscopy (PL) serves as a probing tool for assessing the impact of optimized annealing on the luminescent properties of Sm-SiO_2 NCs. FTIR has been used in order to trace out the functional groups attached herein with silica species.

3. RESULTS AND DISCUSSION

3.1. Crystallographic structure

The X-ray diffraction (XRD) analysis was conducted on samarium oxide-doped silica powder that underwent calcination at various temperatures (ranging from 780°C to 1180°C) for different durations as depicted in Fig.1. Interestingly, the XRD pattern of the powder subjected to calcination at 780°C for 3 h did not exhibit distinct reflection peaks, implying the material remained in an amorphous state. This outcome suggests that even after 3h of annealing well below the binary oxides' melting point, there was no discernible effect on altering the amorphous phase of the Sm_2O_3–SiO_2 composite. Upon increasing the calcination temperature to 980°C and maintaining it for 3 h, a pronounced transformation in the reflection pattern became evident. Notably, two prominent reflections emerged at angles 2θ of 28.22° and 32.75°. The broader peak centered around 2θ of 19.86° could be attributed to the (101) reflection of the cristobalite structure, as per the JCPDS file no. 39-1425. The presence of the cristobalite phase suggests the persistence of water molecules within the sample. Conversely, the sharp peak is plausibly associated with the (222) reflection of the cubic Sm_2O_3–SiO_2 phase. Notably, the application of heat treatment at 1180°C for 6 h led to a reduction in the number of pores and their interconnectivity, resulting in a substantial alteration of the amorphous phase [1, 9].

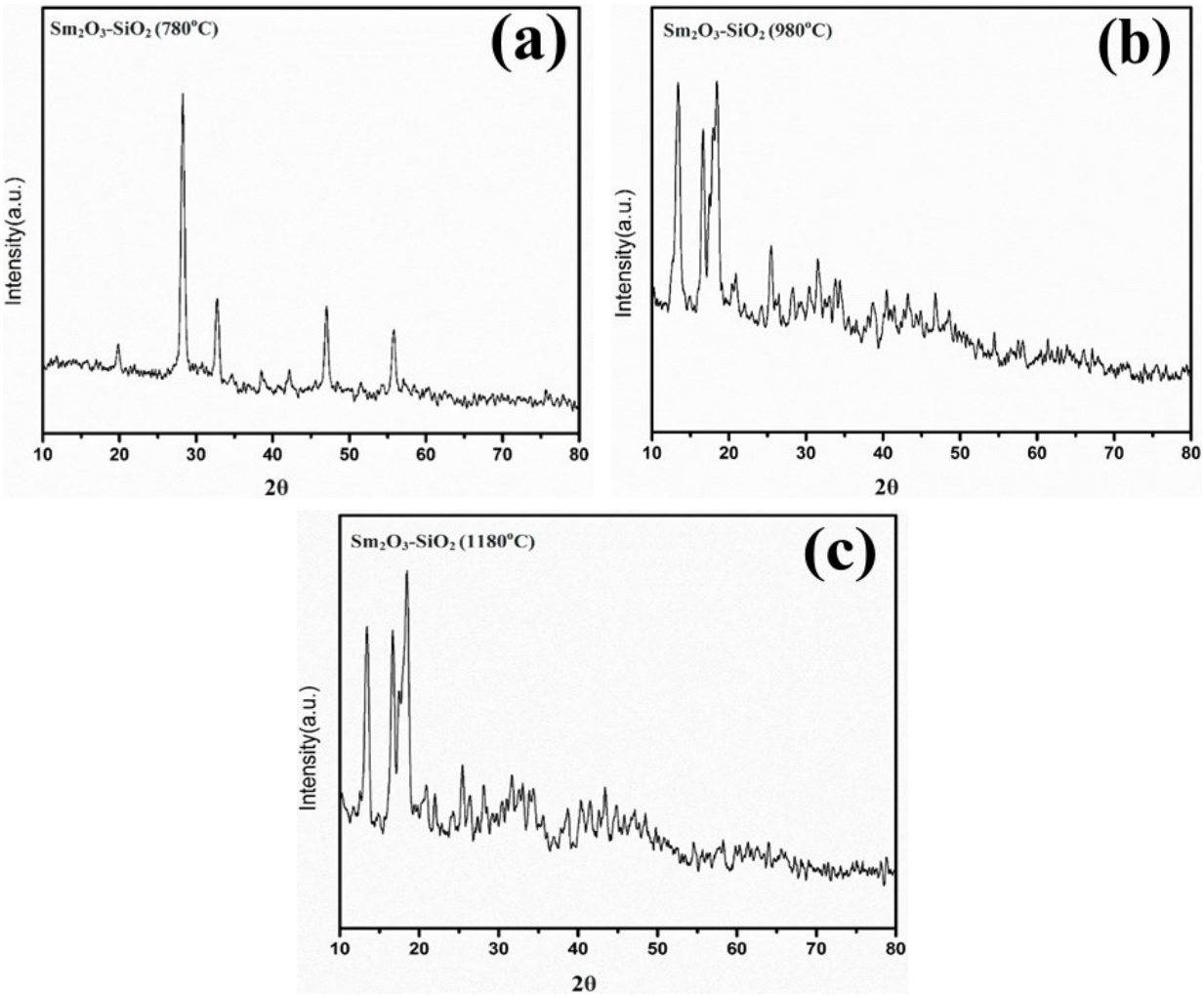

Figure 1. XRD pattern of annealed samples at (a) 780°C , (b) 980°C, (c) 1180°C

Slika 1. XRD grafik žarenih uzoraka na (a) 780°C, (b) 980°C, (c) 1180°C

It's noteworthy to mention that previous investigations did not reveal such significant reflections in the high Sm_2O_3 loaded sample annealed at 1000°C. However, annealing the sample at 780°C under vacuum conditions did yield a faint reflection. The narrower diffraction pattern around 28.22° was employed to calculate the mean crystallite size using the Scherrer formula, yielding

a size of 15 nm (with d=3.16 Å and a=10.94 Å). These outcomes suggest that during prolonged annealing for sintering, the crystallite size increases to 43 nm due to nanoparticle coalescence. These findings collectively indicate that low-temperature heat treatment (780-1180°C) combined with extended annealing duration enhances both the crystallinity and the size of the nanocomposites [6, 18]. These patterns not only ascertain the crystalline phases present but also reveal potential phase transitions triggered by annealing. The shift in peak positions, intensities, and widths unveils subtle changes in crystallographic parameters, shedding light on the arrangement of samarium species within the silica matrix.

3.2. FTIR

The FTIR transmittance spectra, spanning a range of 4000–500 cm^{-1}, vividly illustrate the effects of heat treatment on the doped samples. Notably, when subjected to a temperature of 980°C, distinctive bands emerge at 540, 800, 1629, and 1040 cm^{-1}. These bands find assignment in the symmetrical stretching vibration of Si–O–Si bonds, the vibrational mode of the ring structure of SiO_2 tetrahedra, the characteristic stretching mode Si–OH inherent to the gel structure, the TO mode originating from the asymmetric stretching vibration of Si–O–Si bonds, and the bending modes linked with water adsorbed onto the silica surface, respectively as shown in Fig. 2 [19, 20].

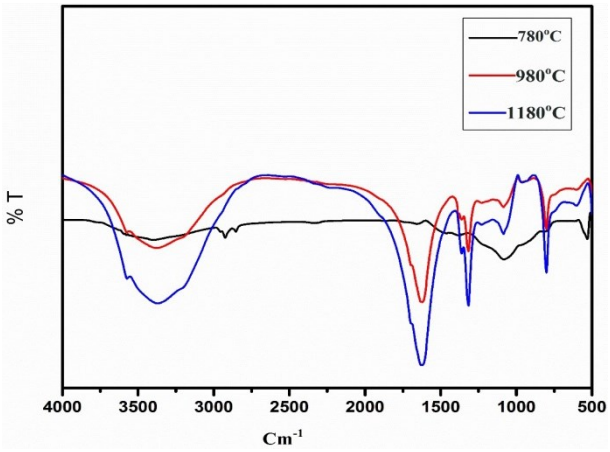

Figure 2. FTIR spectra of samarium silica nanocomposites

Slika 2. FTIR spektar nanokompozita samarijuma silicijum dioksida

In the lower frequency range of the FTIR spectra, a robust band centered around 1629 cm^{-1} is attributed to the Sm–OH bond. The intriguing facet lies in the transformation brought about by elevated temperature heat treatment, where the extended sintering process converts Sm–OH into the cubic Sm_2O_3 phase. Adding to this intrigue, the TO mode of Si–O–Si experiences a subtle shift towards higher wave numbers as the calcination temperature climbs to 1180°C during a 6 h treatment. The results obtained from FTIR analysis synergistically reinforce the findings deduced from X-ray diffraction (XRD) data [21]. The FTIR spectral shifts and distinctive bands align with the structural changes and transformations identified through XRD, collectively providing a robust validation of the dynamic alterations that transpire in the doped samples under varying heat treatment conditions [10].

3.3. Morphology of Sm_2O_3–SiO_2 nanoparticles

Field Emission Scanning Electron Microscopy (FESEM) coupled with Energy-Dispersive X-ray (EDX) analysis has unveiled profound insights into the microstructural and compositional changes exhibited by samarium-doped silica samples subjected to annealing at varying temperatures – 780°C, 980°C, and 1180°C as shown in Fig. 3 [15,21]. These observations provide a comprehensive picture of how heat treatment at different temperatures influences the morphology and elemental distribution within the composite material [2].

Annealing at 780°C: At this relatively lower annealing temperature, FESEM images reveal a predominantly agglomerated morphology of the doped silica particles. These clusters appear moderately porous, and the surface texture exhibits a level of irregularity. The particle sizes appear within the nanoscale range, with subtle variations attributed to agglomeration tendencies. The relative elemental composition reflects the intended composition of the composite as shown in Fig. 4.

Annealing at 980°C: Upon elevating the annealing temperature to 980°C, a noticeable transformation in the microstructure becomes evident. FESEM images portray a refined particle arrangement, with reduced agglomeration and a more uniform distribution. The surface texture appears smoother, with indications of enhanced particle connectivity.

Annealing at 1180°C: At the highest annealing temperature of 1180°C, FESEM images exhibit a further evolution in the microstructure. The particle agglomerations are significantly mitigated, leading to a more dispersed arrangement. The particle surfaces appear smoother and more homogenous, with indications of reduced porosity.

EDX analysis reaffirms the consistent presence of samarium, silicon, and oxygen. Interestingly, quantitative analysis of elemental proportions reflects a marginal change, potentially indicating subtle shifts in elemental diffusion due to the elevated annealing temperature.

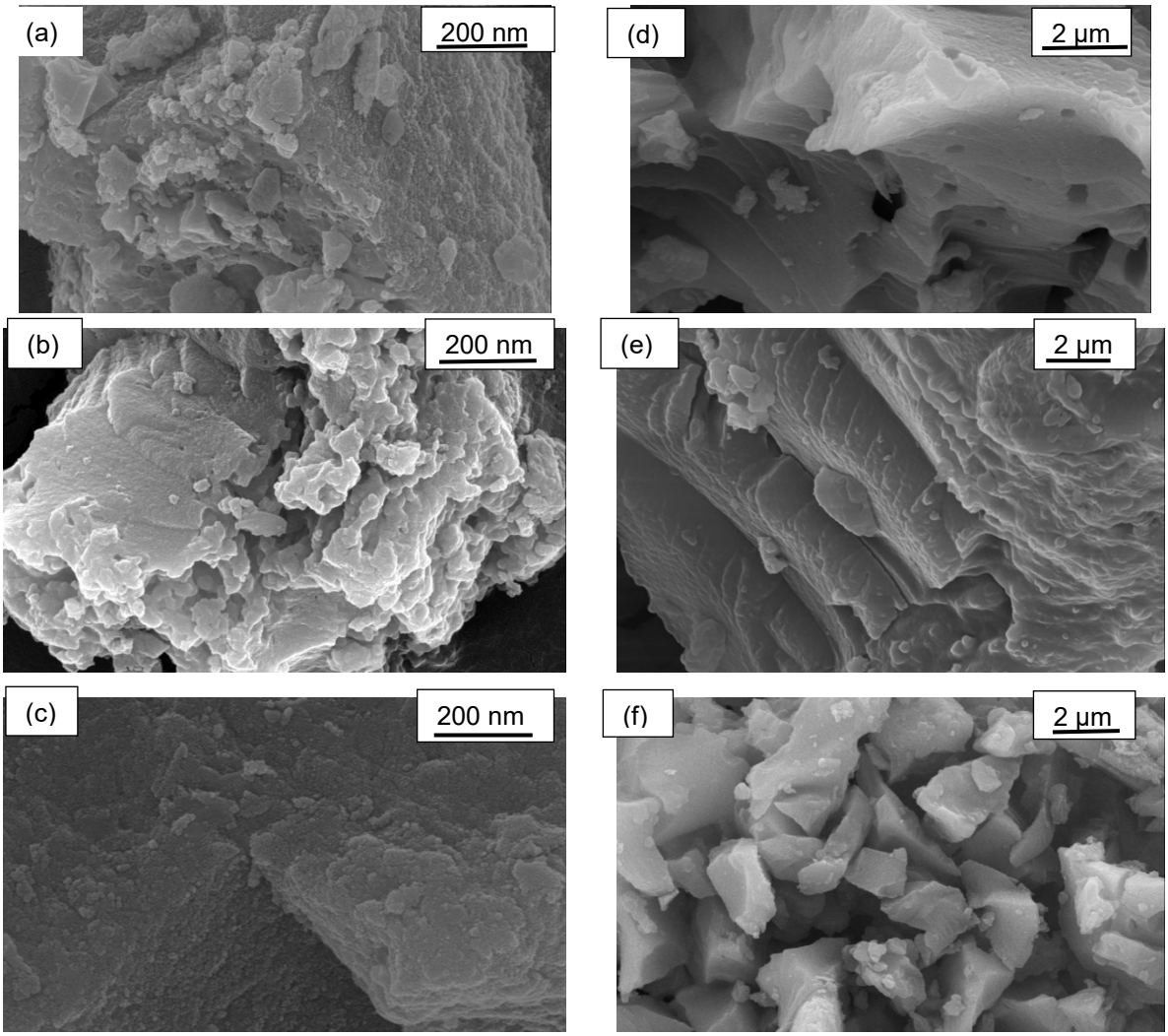

Figure 3. FESEM images of samarium silica nanocomposites annealed at 780°C, 980°C and 1180°C respectively; (a,b,c) at 200 nm scale and (d,e,f) at 2 µm scale

Slika 3. FESEM slike nanokompozita samarijum silicijum dioksida žarenih na 780 ^{0}C, 980^{0}C i 1180^{0}C respektivno; (a,b,c) na skali od 200 nm i (d,e,f) na skali od 2 µm

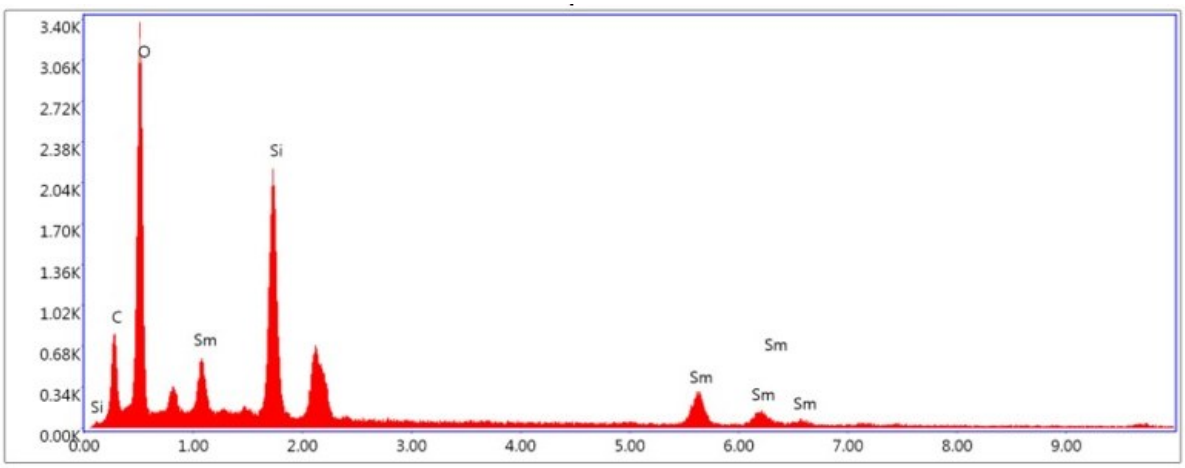

Figure 4. EDX spectra of samarium silica nanocomposites

Slika 4. EDX spektri nanokompozita samarijuma silicijum dioksida

Collectively, the FESEM images and EDX analyses illustrate a compelling narrative of structural refinement and compositional stability as the annealing temperature increases from 780°C to 1180°C [16]. The observed trends in morphology and elemental distribution bear significant implications for tailoring the material properties, influencing applications in catalysis, photonics, and beyond.

3.4. Photoluminiscence study

The presented Fig. 5 encapsulates the Photoluminescence (PL) spectra of typical powdered Sm_2O_3-SiO_2 samples, each undergoing distinct annealing conditions in ambient air. The samples are subjected to temperatures of 780°C (3 h), 980°C (3 h), and 1180°C (6 h). Notably, all spectra showcase continuous and broad luminescent patterns, characterized by a distinctive peak centered around 618 nm. This luminescence is attributed to the presence of samarium crystallites, despite the influence of concentration quenching [22, 23].

Of particular interest is the intriguing interplay between temperature and PL intensity. As the temperature is elevated, there is a discernible elevation in PL intensity. This phenomenon is attributed to the augmentation of nonradiative processes, which in turn diminish the efficacy of radiative recombination [24-26]. This relationship underscores the intricate balance between temperature-induced processes that either enhance or hinder the luminescence efficiency within the Sm_2O_3-SiO_2 samples.

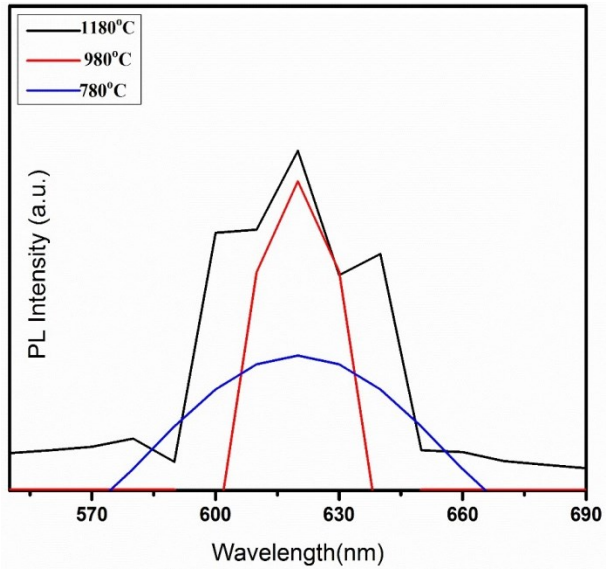

Figure 5. FTIR spectra of samarium silica nanocomposites

Slika 5. FTIR spektri nanokompozita samarijuma silicijum dioksida

4.CONCLUSIONS

The investigation has illuminated substantial alterations in both structural and functional attributes. Annealing-induced crystalline phase transitions and enhanced ordering underscore the pivotal role of temperature in shaping the material's architecture. Concurrently, the significant modifications in photoluminescence behavior emphasize the nuanced interplay between annealing and functional properties. One limitation may be the specific conditions chosen for annealing, as variations in temperature and duration could yield different results. Additionally, the research may focus on a particular aspect of the material properties, leaving room for exploration of other potential characteristics. Furthermore, the applicability of the findings in real-world scenarios or industrial settings may need further investigation. As for the future scope, expanding the research to encompass a broader range of annealing conditions and exploring diverse applications of Samarium Silica Nanocomposites could enhance the comprehensiveness of the study. Additionally, investigating potential synergies with other materials or incorporating advanced characterization techniques may open new avenues for understanding and optimizing the properties of these nanocomposites.

This study underscores the potential of annealing as a versatile tool for engineering tailored material characteristics. The synergy between sol-gel synthesis and annealing offers a promising avenue for creating advanced nanomaterials with finely tuned properties. As nanoscience advances, the insights garnered here contribute to the evolving landscape of material design, fostering opportunities for innovative applications across diverse technological domains.

Acknowledgements

Bhavna Rohilla and Aryan Boora, express gratitude to the University Grants Commission (UGC) for their support in funding the research through the Junior Research Fellowship (JRF) program, with reference number 221610112839 and 221610122664 respectively. The authors are thankful to Department of Science and Technology for providing support and facilities for the research work under FIST grant (Senction order no. and Date) SR/FST/PS-1/2018/32.

5. REFERENCES

[1] A.Aslam, M.Farrukh, S.Karim (2019) Sensitization of Sm/SnO2 SiO2 Nanocomposite with Zwitterionic Surfactant for Enhanced Photocatalytic Performance under Sunlight. *Russian Journal of Physical Chemistry A*, *93*(8), 1610-1619.

[2] G.Veloso, R.Ferreira, W.Roberto, S.N.Silva (2023) Development of core-shell nanocomposites containing iron oxide, silica and samarium for potential application in cancer treatments involving brachytherapy and magnetic hyperthermia. *REM-International Engineering Journal*, *76*, 177-186.

[3] S.Gadale, V.Rokade, S.Waghmode (2020) Synthesis, Characterization of Nd Doped Silica Nanocomposites and its Photocatalytic Activity. *Journal of Advanced Scientific Research*, *11*(04 Suppl 9), 72-77.

[4] D.Lei, W.Zhang, H.Li (2022) Tetrabutylammonium hydroxide mediated sol-gel synthesis of samarium titanate to enhance photocatalytic activity. *Materials Research Bulletin*, *154*, 111935.

[5] B.Han, N.Chen, D.Deng, S.Deng, I.Djerdj, Y.Wang (2015) Enhancing phosphate removal from water by using ordered mesoporous silica loaded with samarium oxide. *Analytical Methods*, *7*(23), 10052-10060.

[6] M.Zahedi, S.Hassanzadeh-Tabrizi, A.Saffar-Teluri, (2018) Sol-gel synthesis and luminescence properties of Ba2SiO4: Sm3+ nanostructured phosphors. *Ceramics International*, *44*(9), 10169-10174.

[7] D.Lei, W.Zhang, H. Li (2022) Tetrabutylammonium hydroxide mediated sol-gel synthesis of samarium titanate to enhance photocatalytic activity. *Materials Research Bulletin*, *154*, 111935.

[8] A.Boora, S.Duhan, V.Kumar (2023) Novel highly flexible room temperature humidity sensor based on mesoporous NiO/TUD-1 hybrid nanocomposite. *Journal of Materials Science*, 58, 15421-15437.

[9] Y.Zou, J.He, Z.Tang, L.Zhu, F.Liu (2020) Structural and mechanical properties of styrene–butadiene rubber/silica composites with an interface modified in-situ using a novel hindered phenol antioxidant and its samarium complex. *Composites Science and Technology*, *188*, 107984.

[10] K.Michailovska, I.Indutnyi, P.Shepeliavyi, M. Sopinskyy, V.Dan'ko, Z.Tsybrii, D.Maziar (2023) Formation of silicon nanocomposites by annealing of (SiO x/Sm) n multilayers: luminescence, Raman and FTIR studies. *Applied Nanoscience*, 13(11), 7187-7194.

[11] K.Dawngliana, S.Rai (2022) Linear and nonlinear and optical properties of Sm3+ co-doped alumino-silicate glass prepared by sol-gel method. *Journal of Non-Crystalline Solids*, *598*, 121929.

[12] A.Danks, S.Hall, Z.J.Schnepp (2016) The evolution of 'sol–gel'chemistry as a technique for materials synthesis. *Materials Horizons*, *3*(2), 91-112.

[13] J.Junaidi, W.Sulistiani, Y.Efridahniar, I.Pratiwi, I.Firdaus, P.Manurung, P.Karo (2023) Synthesis and Characterization of Ag/SiO2 Nanocomposite Based on Rice Husk Silica Using Sol-Gel Method. *Journal of Nano Research*, *78*, 31-42.

[14] D.Bokov, A.Turki Jalil, S.Chupradit, W.Suksatan, M.Javed Ansari, I.Shewael, E.Kianfar (2021) Nanomaterial by sol-gel method: synthesis and application. *Advances in Materials Science and Engineering*, *2021*, 1-21.

[15] B.Bhavna, S.Duhan (2023) Modification of mesoporous SBA-16 with cobalt doping for outstanding humidity sensor at room temperature. *Journal of Porous Materials*, 31(1), 1-14.

[16] A.Boora, S.Sehrawat, S.Duhan (2023) Smart Materials for Smart Manufacturing. In *Handbook of Smart Manufacturing*, CRC Press, p.109-137.

[17] M.Jamdar, Z.Heydariyan, A.Alzaidy, E.Dawi, M.Salavati-Niasari (2023) Eco-friendly auto-combustion synthesis and characterization of SmMnO3/Sm2O3/Mn2O3 nanocomposites in the presence of saccharides and their application as photocatalyst for degradation of water-soluble organic pollutants. *Arabian Journal of Chemistry*, *16*(12), 105342.

[18] B.Bhavna, A.Boora, M.Goyat, S.Duhan (2023) Exploring 2D Hexagonal WO3/COK-12 Nanostructures for Efficient Humidity Detection. *Materials Advances*, 4, 5785-5796.

[19] E.Poonia, M.Dahiya, V.Tomer, K.Kumar, S.Kumar, S.Duhan (2018) Humidity sensing behavior of tin-loaded 3-D cubic mesoporous silica. *Physica E: Low-dimensional Systems and Nanostructures*, *101*, 284-293.

[20] Y.Chen, W.Cai, W.Wang, A.Chen (2019) Preparation, characterization, and application of dendritic silica-supported samarium-doped ceria nanoparticles in ultra-precision polishing for silica films. *Journal of Nanoparticle Research*, *21*, 1-14.

[21] V.Tomer, S.Devi, R.Malik, S.Duhan (2016) Mesoporous materials and their nanocomposites. *Nanomaterials and Nanocomposites: Zero-to Three-Dimensional Materials and Their Composites*,e-book, p. 223-254.

[22] E.Campos-Zuñiga, I.Alonso-Lemus, IV.Agarwal, J.Escorcia-García (2019) Sol-gel synthesis for stable green emission in samarium doped borosilicate glasses. *Ceramics International*, *45*(18), 24052-24059.

[23] M.Zaid, H.A.Sidek, R.El-Mallawany, K.Almasri, K.Matori. (2020) Synthesis and characterization of samarium doped calcium soda–lime–silicate glass derived wollastonite glass–ceramics. *Journal of materials research and technology*, *9*(6), 13153-13160.

[24] M.Raju, R.Rao, N.Vijayan, P.Azeem (2021) A novel orange-red Sm3+-doped CaSiO3 nanostructured phosphor derived from agro food waste materials for white light applications. *Ceramics International*, *47*(19), 26704-26711.

[25] V.Tomer, S.Duhan (2016) Ordered mesoporous Ag-doped TiO 2/SnO 2 nanocomposite based highly sensitive and selective VOC sensors. *Journal of Materials Chemistry A*, *4*(3), 1033-1043.

[26] M.Rahuma, B.Kannan (2014) Corrosion in Oil and Gas Industry: A perspective on Corrosion Inhibitors. *J. Of Material Sciences and Engineering*, 3(3), 110-119.

IZVOD

UTICAJ ŽARENJA NA STRUKTURNA I OPTIČKA SVOJSTVA NANOKOMPOZITA OD SAMARIJUM SILICIJUM DIOKSIDA DOBIJENIH SOL-GELOM

Potraga za fino podešenim svojstvima materijala dovela je do istraživanja strategija žarenja u kontekstu nanokompozita samarijum silicijum dioksida (Sm-SiO_2 NCs) sintetizovanih putem sol-gel puta. Ova studija otkriva nove vidike u uticaj optimizovanih protokola žarenja na strukturnu i funkcionalnu evoluciju ovih naprednih nanokompozita. Kroz pedantno eksperimentisanje, ustanovljeno je da žarenje na kontrolisanoj temperaturi igra ključnu ulogu u prilagođavanju mikrostrukture i svojstava Sm-SiO_2 NCs. Razumna manipulacija parametrima žarenja, uključujući trajanje temperature i atmosferu, orkestrira različite transformacije u kompozitnoj arhitekturi. Emisiona mikroskopija i strukturna analiza otkrivaju da precizno žarenje promoviše konsolidaciju domena nanorazmera, što dovodi do poboljšane kristalnosti i poboljšane povezanosti između vrsta samarijuma i matriksa silicijum dioksida. Štaviše, modifikacije izazvane žarenjem se protežu izvan strukturnih aspekata kako bi uticale na funkcionalna svojstva, uočeno je povećanje veličine kristalita sa 15nm na 43nm kao efekat žarenja. Naši nalazi ilustruju značajno poboljšanje intenziteta luminiscencije kao posledicu optimizovanog žarenja, pokazujući potencijal za prilagođene fotonske aplikacije. Ova otkrića su podržana sveobuhvatnim paketom analitičkih tehnika, uključujući difrakciju rendgenskih zraka, infracrvenu Furijeovu transformaciju, emisiju polja sa energetski disperzivnom rendgenskom spektroskopijom i fotoluminiscentnom spektroskopijom. Sinergija sinteze i žarenja ne samo da unapređuje naše fundamentalno razumevanje evolucije nanokompozita, već takođe pruža put ka dizajniranju multifunkcionalnih materijala sa precizno projektovanim atributima.

Ključne reči: *nanokompoziti, sol-gel ruta, strategije žarenja, mikrostrukturna evolucija, funkcionalna poboljšanja*

Naučni rad
Rad primljen: 28.09.2023.
Rad korigovan: 11.11.2023.
Rad prihvaćen: 16.11.2023.
Rad je dostupan na sajtu: www.idk.org.rs/casopis

Yashna Anthony, Veena Ragupathi*

Centre of Clean Energy and Nanoconvergence (CENCON), Department of Chemistry, Hindustan Institute of Technology and Science, Padur, Chennai, India

Scientific paper
ISSN 0351-9465, E-ISSN 2466-2585
https://doi.org/10.62638/ZasMat1002

Zastita Materijala 65 (1)
151 - 157 (2024)

Superior electrochemical performance of SnSe-PPy nanocomposites for supercapacitor application

ABSTRACT

Recently, Metal chalcogenides have received considerable interest in the field of energy storage devices. In this work, tin selenide-polypyrrole (SnSe-PPy) nanocomposite has been synthesized by hydrothermal method and its supercapacitive behavior is investigated. The synthesized SnSe-PPy nanocomposite is analysed by X-ray diffraction (XRD), Fourier transform infrared spectroscopy (FTIR), Scanning electron microscopy (SEM) and electrochemical characterisation. XRD confirms the existence of orthorhombic SnSe, and the FTIR result reveals the presence of polypyrrole. The supercapacitive behavior of SnSe-PPy nanocomposite is studied by cyclic voltammetry and galvanostatic charge-discharge studies. SnSe-PPy nanocomposite delivers the specific capacitance of 223 F g^{-1} at 10 mV sec^{-1}. The addition of polypyrrole increases the conductivity of the material and improves its supercapacitive behavior.

Keywords: *Tin selenide, polypyrrole, supercapacitor, specific capacity, cycle life*

1. INTRODUCTION

The global economy is severely affected by energy crises and environmental degradation problems. Energy production mainly depends on the combustion of fossil fuels, which produce greenhouse gas emissions and pollution. Therefore, generating effective storage devices that produce clean and sustainable energy is essential. In this perspective, batteries, fuel cells, and supercapacitors are effectively utilized as electrochemical energy storage devices [1,2]. In batteries, chemical energy is converted into electrical energy through a process called a redox reaction. Fuel cells work similar to batteries, but chemical energy from fuel is converted into electrical energy. In this context, a supercapacitor (SC) is a promising energy storage device that fills the gap between conventional capacitors and batteries [3,4]. SCs provide higher power outputs than batteries and store more energy than capacitors.

Benefiting from the better characteristics of supercapacitors such as high power density and long-term stability, it is extensively used in electric motors, wind turbines, MP3 players and Regenerative braking [5,6]. Mostly, Supercapacitors are used alone or in conjunction with other energy storage technology [7-9]. In supercapacitors, the electrode stores charges by the non-faradic and faradaic processes. Supercapacitors are classified into four types: (i) electrolytic double layer (EDLC), (ii) pseudo, (iii) hybrid and (iv) battery-type capacitors [10]. Among all, the pseudo supercapacitors have gained significant attention due to their exceptional features like high power density and enhanced cycle life.

Generally, using appropriate electrode materials with nanostructured architecture improves the electrochemical performance and efficiency of SCs [11,12]. The electrode material can be made from a variety of materials [12]. Carbon-based materials are used in EDLCs and transition metal oxides (RUO_2, TiO_2, ZnO, GeO_2), metal chalcogenides (SnS, MOS_2, WS_2, MoSe), conducting polymers (polyaniline (PANI), polypyrrole (PPy), poly cetylene (PA), polythiophene (PTH)) are used in Pseudo-capacitors [13-15].

In recent years, Metal chalcogenides have drawn significant interest, and tin selenides (SnSe) is gaining popularity due to their diverse application like thermoelectric, sensors, solar cells, and energy storage [16-18]. Manoj Kumar et al. reviewed the

*Corresponding author: Yashna Anthony
E-mail: rveena@hindustanuniv.ac.in
Paper received: 28. 09. 2023.
Paper accepted: 27. 11. 2023.
Paper is available on the website: www.idk.org.rs/journal

physical properties of tin-selenide material, such as phases, defects, growth mechanisms, deposition methods, and the various possible applications. Due to their favourable bandgap and absorption coefficient, these materials have gained significant attention in photovoltaic and optoelectronic applications [19]. However, among other metal chalcogenides, very few works have been published on the supercapacitive behavior of SnSe. Zhang et al. fabricated 2D, tin selenide nanodisks and nanosheets, and SnSe nanodisk delivered the specific capacitances of 168 F g^{-1}, and SnSe nanosheet yielded 228 F g^{-1} [20]. In general, the addition of conducting polymers, especially Polypyrrole (PPy), improves the electrochemical performance of metal chalcogenides by the providing necessary surface area, which improves the charge storage capacity. Yang Huang et al. demonstrated various synthesis procedures to fabricate PPy nanostructures [21]. Polypyrrole has promising properties such as high conductivity, stability, large surface area, and low equivalent series resistance, and these properties are essential to fabricating efficient supercapacitors.

Hence, in this study, to enhance the electrochemical performance of tin selenide, polypyrrole is incorporated, and SnSe–PPy nanocomposites have been prepared using a hydrothermal method. The supercapacitive behavior of SnSe–PPy nanocomposites is investigated.

2. MATERIALS AND METHODS

2.1. Materials

Tin (II) chloride dihydrate ($SnCl_2 \cdot 2H_2O$) was purchased from Merck Life Science Private Limited Mumbai. Selenium, pyrrole, hydrogen hydrazine, potassium hydroxide, Sodium hydroxide pellets, and ethanol were purchased from Sigma Aldrich.

2.2. Synthesis of Polypyrrole (PPy)

The synthesis of polypyrrole (PPy) was carried out using the chemical polymerization method. 3 g of dodecyl benzene sulphonic acid (50 ml) was added to the 0.1 M ferric chloride solution (50 ml). Following this, 0.1 M of pyrrole was added dropwise to the mixed solution at 5°C for 4 h. After the polymerization process was complete, the obtained polypyrrole was washed with distilled water to remove residual reactants and by-products. Finally, the washed PPy was dried at 60°C to get the final PPy material. This process involves the formation of a polymer from a monomer, where the monomer pyrrole underwent oxidative polymerization in the presence of a dopant, dodecyl benzene sulphonic acid, and an oxidant, ferric chloride hexahydrate.

2.3. Synthesis of SnSe-PPy nanocomposite

The hydrothermal method was adopted to synthesize SnSe-PPy nanocomposite materials. To synthesize SnSe-PPy nanocomposites, 2.6 grams of $SnCl_2.H_2O$, 0.1 grams of selenium and 10 wt% polypyrrole were added to 100 ml of distilled water and stirred at room temperature for 2 h. Then, the NaOH (0.01M) solution, followed by hydrogen hydride solutions, was added to the precursor's solution and stirred for 6h. The solution was transferred to an autoclave and heated at 100°C for 8 h. The resulting blackish-brown colour solution was centrifuged at 3000 RPM. At last, the powder was washed with distilled water and dried at 60°C in the oven. Fig. 1 represents the synthesis of SnSe-PPy nanocomposite by hydrothermal method.

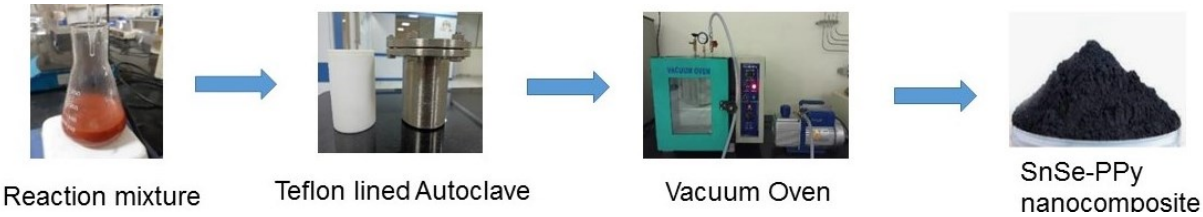

Figure 1. Synthesis of SnSe-PPy nanocomposite

Slika 1. Sinteza SnSe-PPi nanokompozita

2.4. Characterizations

The X-ray diffraction (XRD) characterization was carried out using an X-ray diffractometer (BRUKER USA D8 Advance, Davinci). Fourier transform infrared spectroscopy (FTIR) measurements were performed using Nicolet iS50 within the operating range of 400- 4000 cm^{-1}. The FTIR sample is prepared by adding 200 mg of anhydrous potassium bromide with 2 mg of the sample. Then the mixture was pelletized with a pressure of 10 k Pa cm^2. The morphology of the material was analysed using a VEGA3 TESCAN scanning electron microscope.

2.4.1. Electrochemical Characterization

The electrochemical characterizations were carried out using a VersSTAT-3 electrochemical workstation. The three-electrode configuration is

used to perform the supercapacitive behavior of SnSe-PPy nanocomposite. The working electrodes were prepared by mixing an 80:10:10 ratio of active material, carbon black and polyvinylidene difluoride (PVDF) respectively. The slurry was then coated onto a stainless steel current collector with a 1x1 cm² area and dried overnight at 90°C. The weight of the electrode material coated on the SS electrode was kept constant at approximately 1mg for all electrochemical measurements. Pt foil and Ag/AgCl were used as a counter and reference electrode. 2M KOH solution was used as an electrolyte.

3. RESULT AND DISCUSSIONS

X-ray diffraction pattern of pure PPy is shown in Fig. 2a, and the result reveals a broad pattern in the range 2θ = 20° and 30°, which indicates the formation of amorphous PPy [22].

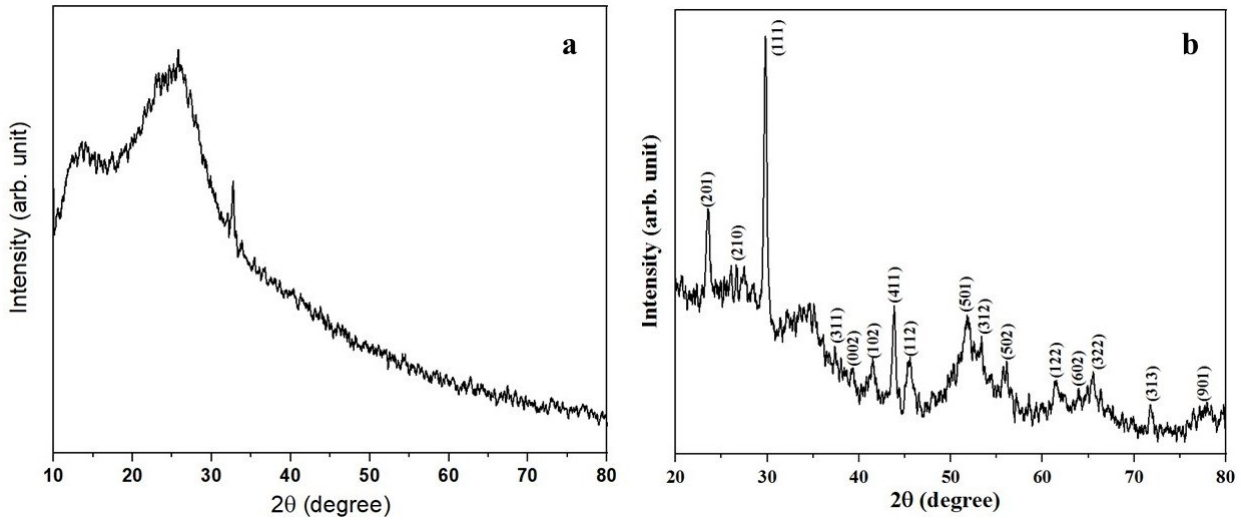

Figure 2. (a&b) XRD diffraction pattern of polypyrrole (PPy) and SnSe-PPy nanocomposite

Slika 2. (a&b) XRD difrakcioni uzorak polipirola (PPi) i nanokompozita SnSe-PPi

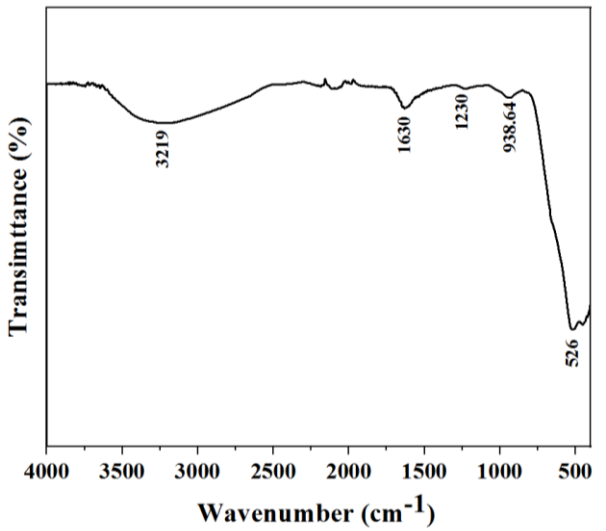

Figure 3. FTIR spectrum of SnSe-PPy nanocomposite

Slika 3. FTIR spektar SnSe-PPi nanokompozita

Fig. 2b reveals the XRD pattern of hydro-thermal-derived SnSe-PPy materials. The X-ray diffraction pattern exhibits two theta peaks at 23.41°, 30.12°, 41.54°, 51.67°, 65.38°, and 61.46° corresponding to the (201), (111), (102), (601), (203), and (122) planes respectively. The XRD results confirm the existence of the orthorhombic phase of SnSe. The lattice parameter values 'a', 'b', and 'c' were calculated and are found to be a = 11.057 Å, b= 4.164 Å, c= 4.604 Å which is well matched with the JCPDS data (89-0236). No predominant peak corresponding to polypyrrole was observed.

The chemical structures of SnSe-PPy nano-composite were studied by the FTIR technique. FTIR Spectra of SnSe-PPy material are shown in Fig. 3. The peak that appeared at 526 cm^{-1} corresponds to SnSe vibration. The characteristic peak of polypyrrole is observed at 1630 cm^{-1}, 939 cm^{-1}, 1230 cm^{-1} and 3219 cm^{-1}. The peak at 1630 cm^{-1} attributes C=C vibration modes. The peaks at 939 and 1230 cm^{-1} ascribe to C-H wagging and C-N bonds, respectively. The occurrence of the broad peak at 3219 cm^{-1} is attributed to N-H stretching vibrations in the pyrrole ring [23].

The electrochemical properties of electrode materials are significantly influenced by their surface morphology and specific surface area. The size and shape of the SnSe- PPy material were analyzed by scanning electron microscope.

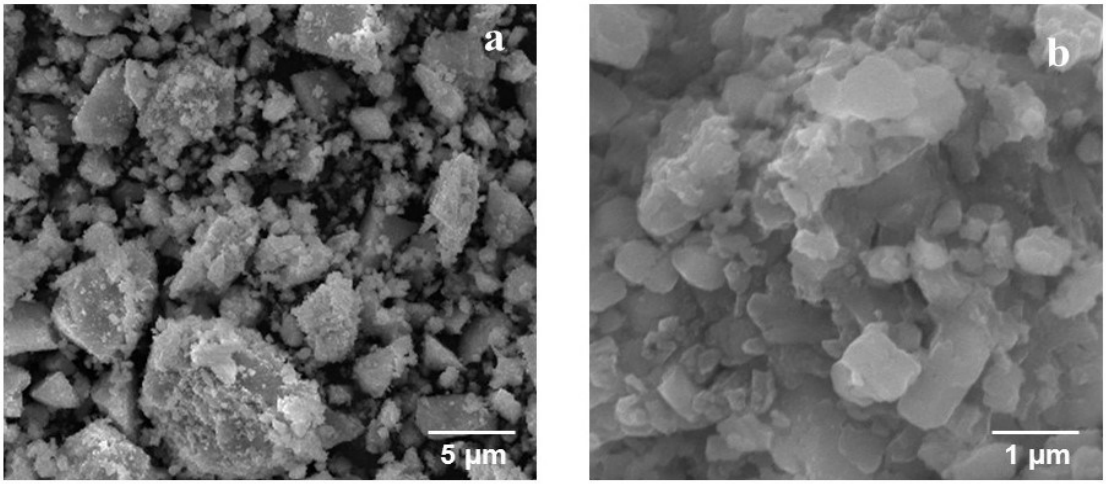

Figure 4. (a & b) SEM images of SnSe-PPy nanocomposite

Slika 4. (a i b) SEM slike SnSe-PPi nanokompozita

The morphology of SnSe-PPy nanoparticles was recorded using SEM, and the images are shown in Fig. 4 (a & b). The magnified SEM image (Fig. 4b) illustrates the presence of agglomerated triangle and spherical shape particles with an average size of 100 nm to 500 nm.

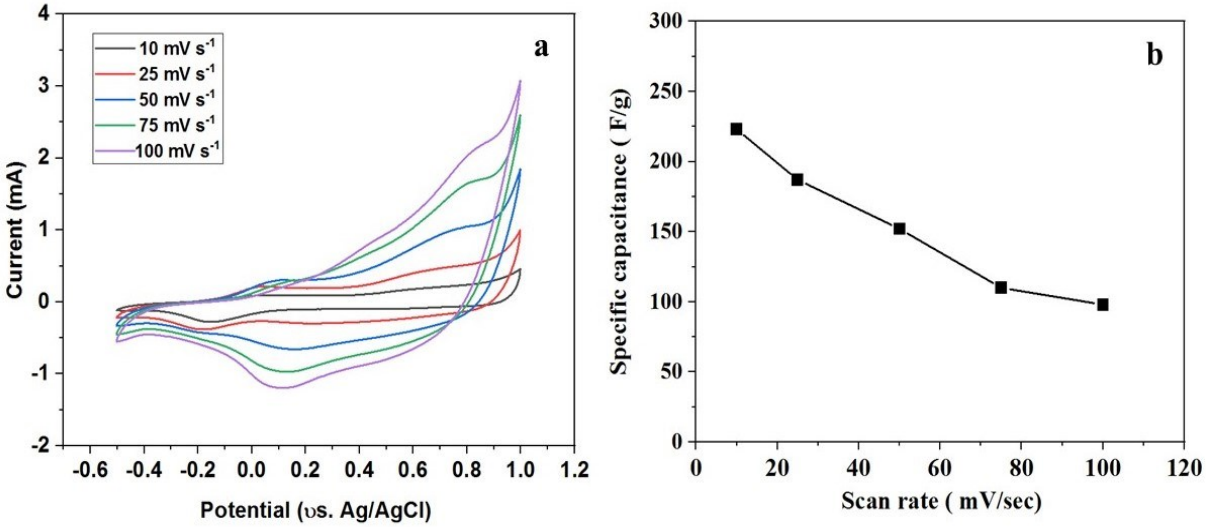

Figure 5. a) Cyclic voltammogram and b) specific capacitance versus scan rate

Slika 5. a) Ciklični voltamogram i b) specifična kapacitivnost u odnosu na brzinu skeniranja

The Cyclic Voltammetry (CV) technique is utilized to investigate the redox properties and reversibility of SnSe-PPy nanocomposites as shown in Fig. 5a. The CV measurements were performed at the scan rates of 10, 25, 50, 75, and 100 mV s^{-1} and potential window of -0.4 V to 1 V. The negative and positive current regions detected in the CV curves indicate the cathodic reduction and anodic oxidation processes. The CV result confirms the existence of reversible reaction ($Sn^{2+} \leftrightarrow Sn^{4+}$) in SnSe-PPy nanocomposites [20]. The CV results exhibit the faradaic behavior of SnSe-PPy material.

The increase of integral current area shows the enhancement of the capacitive behavior of SnSe-PPy electrodes. When the scan rate increases, the area under the CV curve also increases, indicating that there is an outstanding capacitive behavior [24].

The equations below were used to calculate the special capacitance of SnSe-PPy electrodes.

$$Cs = \frac{\int I\, dt}{m\vartheta}$$

where

C_s is the specific capacitance of the SnSe-PPy electrodes

m is the amount of active material,

ϑ is the scan rate and I is the Integral current.

The calculated specific capacitance values are 223, 187, 152, 110 and 98 F g^{-1} at the scan rates of 10, 25, 50, 75 and 100 mV s^{-1} respectively (Fig. 5b). At a scan rate of 10 mV s^{-1}, an exceptionally high capacitance of 223 F g^{-1} was observed. However, at faster scan rates, only the material's outer surface can participate in the capacitive process with the electrolyte ions, leading to less utilization of the electroactive material.

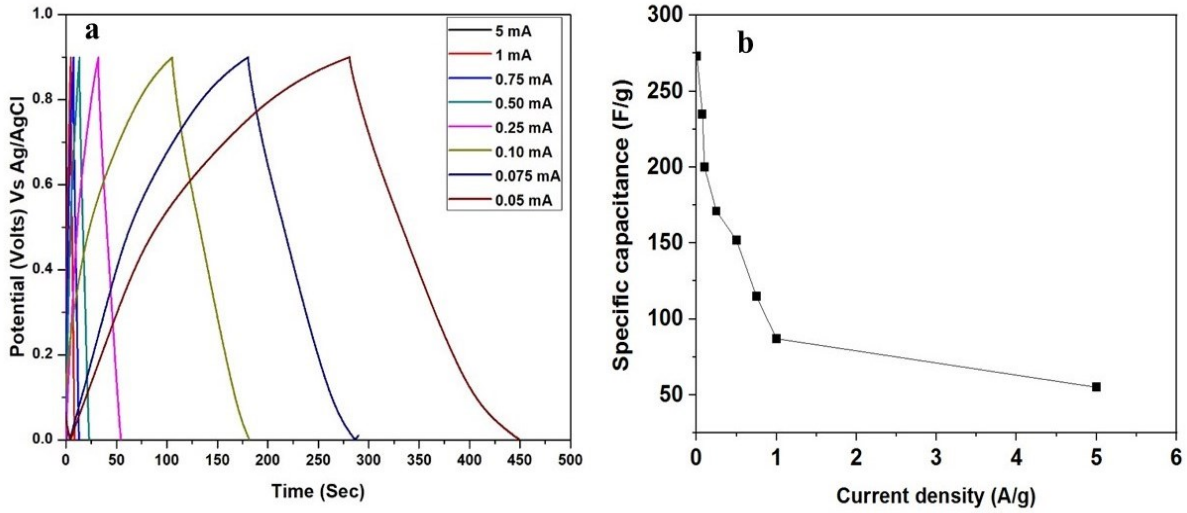

Figure 6. a) Galvanostatic charge discharge measurements, b) Specific capacitance versus current densities

Slika 6. a) Merenja galvanostatskog pražnjenja, b) Specifični kapacitet u odnosu na gustinu struje

Fig. 6a shows the galvanostatic charge-discharge (GCD) curves for SnSe-PPy nanocomposite electrodes at different current densities. The specific capacitance Cs is calculated from the GCD curve using the following equation,

$$Cs = \frac{I\Delta t}{m\Delta V}$$

The specific capacitance versus current densities is shown in the Fig. 6b**.** The calculated specific capacitance at different current densities of 0.05, 0.075, 0.10, 0.25, 0.50, 0.75, 1 and 5 mA are 273, 235, 200, 171, 152, 115, 87 and 55 F g^{-1} respectively.

At a current density of 0.05 mA, the electrode exhibits a maximum specific capacitance of 273 F g^{-1}. It is usual for supercapacitors to experience a reduction in capacitance at relatively higher current densities due to the faster discharge rate compared to lower current densities [25]. The incorporation of polypyrrole enhances the electrical conductivity and improves the electrochemical performance of SnSe-PPy nanocomposite.

Electrochemical impedance spectra of the SnSe-PPy electrode are measured in the range of 100 kHz to 0.01 Hz and shown in Fig. 7. The semicircle at a high frequency range indicates the charge transfer process at the electrode - electrolyte interface. On the Nyquist plot, the point where the semicircle intersects the real axis shows the solution resistance (Rs) and charge transfer resistance (R_{ct}) [26,27].

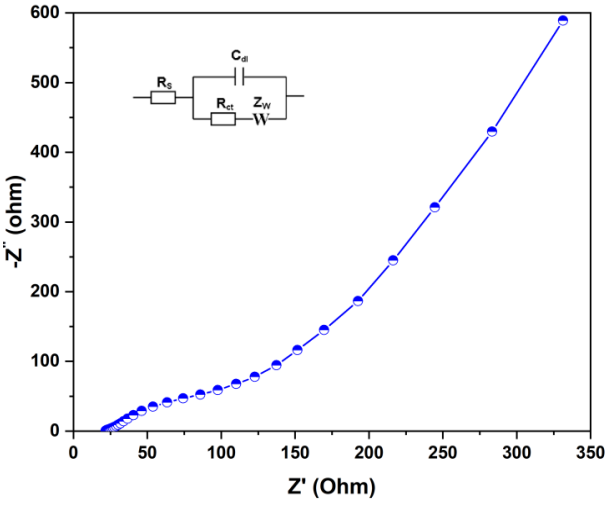

Figure 7. Nyquist plot of SnSe-PPy electrode

Slika 7. Nyquist-ov dijagram SnSe-PPi elektrode

The inset Fig. 7 displays the equivalent circuit diagram (Randle circuit)**.** The diagonal line in the low-frequency range denotes Warburg impedance, which is associated with the diffusion of ions from the electrolyte to the surface of the electrode**.** The

Nyquist plot shows a straight line in the low-frequency area and a quasi-semicircle in the high-frequency region. These patterns are related to the mass transfer and charge transfer processes, respectively.

The equivalent circuit comprises various parameters, including the bulk resistance (R_s), charge transfer resistance (R_{ct}), C_{dl}, which denotes the pseudo capacitance, and Warburg parameter (W). The solution resistance (R_s) is 21 Ω, and the charge transfer resistance (R_{ct}) is 46.25 Ω.

4. CONCLUSIONS

In this work, SnSe-PPy nanocomposites are synthesized by the hydrothermal method and the supercapacitive behavior of SnSe-PPy nanocomposites is investigated. XRD confirms the formation of orthorhombic SnSe. The SEM image shows agglomerated triangle-shaped particles. The SnSe-PPy electrode delivers the specific capacitance of 273 Fg^{-1} at 0.05 mA. The incorporation of polypyrrole enhances the electrical conduction and improves the electrochemical performance of SnSe-PPy nanocomposite. However, scalable synthesis and optimization of polypyrrole quantity has been required for commercial application.

Acknowledgements

Veena Ragupathi acknowledges the research funding from the Science and Engineering Research Board (SERB), Govt. of India under TARE – SERB (No.TAR/2019/000125).

5. REFERENCES

[1] A. Dutta, S. Mitra, M. Basak, T. Banerjee (2023) A comprehensive review on batteries and supercapacitors: Development and challenges since their inception, Energy Storage., 5, e339.

[2] S. Badwal, S. Giddey, C. Munnings, A. Bhatt, A. Hollenkamp (2014) Emerging electrochemical energy conversion and storage technologies, Front. Chem., 2, 79, 1-28.

[3] W. Zuo, R. Li, C. Zhou, Y. Li, J. Xia, J. Liu (2017) Battery-Supercapacitor Hybrid Devices: Recent Progress and Future Prospects, Adv. Sci., 4, 1600539, 1-29.

[4] M. Winter, R.J. Brodd (2004) What Are Batteries, Fuel Cells, and Supercapacitors?, Chem. Rev., 104, 4245-4270.

[5] V. Ragupathi, P. Panigrahi, G.S. Nagarajan (2023) Review—Supercapacitor Active Material from Recycling, ECS J. Solid State Sci. Technol.,12, 24001.

[6] M.E. Şahin, F. Blaabjerg, A. Sangwongwanich (2022) A Comprehensive Review on Supercapacitor Applications and Developments, Energies.,15, 674, https://doi.org/10.3390/en15030674

[7] S.M. Benoy, M. Pandey, D. Bhattacharjya, B.K. Saikia (2022) Recent trends in supercapacitor-battery hybrid energy storage devices based on carbon materials, J. Energy Storage., 52,104938.

[8] A.Townsend, C.Martinson, R.Gouws, D. Bessarabov (2021) Effect of supercapacitors on the operation of an air-cooled hydrogen fuel cell, Heliyon., 7, e06569.

[9] Q. Xun, S. Lundberg, Y. Liu (2021) Design and experimental verification of a fuel cell/supercapacitor passive configuration for a light vehicle, J. Energy Storage., 33, 102110. https://doi.org/10.1016/j.est.2020.102110

[10] M.A.Mohd Abdah, N.H.N.Azman, S. Kulandaivalu, Y. Sulaiman (2019) Review of the use of transition-metal-oxide and conducting polymer-based fibres for high-performance supercapacitors, Mater. Des., 186, 108199. https://doi.org/10.1016/j.matdes.2019.108199

[11] B.K. Saikia, S.M. Benoy, M. Bora, J. Tamuly, M. Pandey, D. Bhattacharya (2020) A brief review on supercapacitor energy storage devices and utilization of natural carbon resources as their electrode materials, Fuel., 282, 118796.

[12] S.Rajagopal, R.M.Ibrahim, D.Velev (2022) Electrode Materials for Supercapacitors in Hybrid Electric Vehicles: Challenges and Current Progress, Condens. Matter., 7, 6, 1-33.

[13] Z.S. Iro, C. Subramani, S.S. Dash (2016) A Brief Review on Electrode Materials for Supercapacitor, Int. J. Electrochem Sci., 11,10628-10643, doi: 10.20964/2016.12.50

[14] M.Z. Ansari, S.A. Ansari, S.-H. Kim (2022) Fundamentals and recent progress of Sn-based electrode materials for supercapacitors: A comprehensive review, J. Energy Storage., 53, 105187.

[15] M. Vandana, S. Veeresh, H. Ganesh, Y.S. Nagaraju, H. Vijeth, M. Basappa, H. Devendrappa (2022) Graphene oxide decorated SnO2 quantum dots/polypyrrole ternary composites towards symmetric supercapacitor application, J. Energy Storage., 46, 103904.

[16] W. Shi, M. Gao, J. Wei, J. Gao, C. Fan, E. Ashalley, H. Li, Z. Wang (2018) Tin Selenide (SnSe): Growth, Properties, and Applications, Adv. Sci., 5, 1700602.

[17] M.R. Burton, S. Mehraban, D. Beynon, J. McGettrick, T. Watson, N.P. Lavery, M.J. Carnie (2019) 3D Printed SnSe Thermoelectric Generators with High Figure of Merit, Adv. Energy Mater., 9, 1900201.

[18] J. Kang, L. Wang, L. Zhang (2023) Discrete card-shaped bimetallic selenides as anode materials for sodium ion batteries with excellent long cycle stability, J. Solid State Chem., 323, 124014.

[19] M. Kumar, S. Rani, Y. Singh, K. Gour, V.N. Singh (2021) Tin-selenide as a futuristic material: properties and applications, RSC Adv., 11, 6477.

[20] C. Zhang, H. Yin, M. Han, Z. Dai, H. Pang, Y. Zheng, Y.-Q. Lan, J. Bao, J. Zhu (2014) Two-

Dimensional Tin Selenide Nanostructures for Flexible All-Solid-State Supercapacitors, ACS Nano., 8, 3761.

[21] Y. Shi, L. Pan, B. Liu, Y. Wang, Y. Cui, Z. Bao, G. Yu (2014) Nanostructured conductive polypyrrole hydrogels as high-performance, flexible supercapacitor electrodes, J. Mater. Chem. A., 2, 6086-6091.

[22] S. Shrikrushna, J. Kulkarni (2015) Influence of Dodecylbenzene Sulfonic Acid Doping on Structural, Morphological, Electrical and Optical Properties on Polypyrrole/3C-SiC Nanocomposites, J. Nanomed. Nanotechnol., 6, 5, 1000313.

[23] M.U. Shariq, A. Husain, M. Khan, A. Ahmad (2021) Synthesis and characterization of polypyrrole/ molybdenum oxide composite for ammonia vapour sensing at room temperature, Polym. Polym. Compos., 29, S989.

[24] B. Pandit, L.K. Bommineedi, B.R. Sankapal (2019) Electrochemical engineering approach of high performance solid-state flexible supercapacitor device based on chemically synthesized VS2 nanoregime structure, J. Energy Chem., 31, 79-88.

[25] C. Tian, Q. Lu, S. Zhao (2019) Monodispersed and hierarchical silica@manganese silicate core–shell spheres as potential electrodes for supercapacitor, J. Solid State Chem., 277, 475-483. https://doi.org/10.1016/j.jssc.2019.07.006

[26] B. Pandit, B. Sankapal, P. Koinkar (2019) Novel chemical route for CeO2/MWCNTs composite towards highly bendable solid-state supercapacitor device, Sci. Rep., 9, 5892-5905. doi: 10.1038/ s41598-019-42301-y

[27] B. Pandit, C.D. Jadhav, P.G. Chavan, H.S. Tarkas, J. V Sali, R.B. Gupta, B.R. Sankapal (2020), Two-Dimensional Hexagonal SnSe Nanosheets as Binder-Free Electrode Material for High-Performance Supercapacitors, IEEE Trans. Power Electron., 35, 11344-11351. doi: 10.1109/TPEL. 2020.2989097

IZVOD

SUPERIORNE ELEKTROHEMIJSKE PERFORMANSE SNSE-PPY NANOKOMPOZITA ZA PRIMENU U SUPERKONDENZATORIMA

Nedavno su metalni halkogenidi dobili značajno interesovanje u oblasti uređaja za skladištenje energije. U ovom radu hidrotermalnom metodom je sintetizovan nanokompozit kalaj selenid-polipirol (SnSe-PPi) i ispitano je njegovo superkapacitivno ponašanje. Sintetizovani SnSe-PPi nanokompozit je analiziran rendgenskom difrakcijom (XRD), infracrvenom spektroskopijom Furijeove transformacije (FTIR), skenirajućom elektronskom mikroskopom (SEM) i elektrohemijskom karakterizacijom. XRD potvrđuje postojanje ortorombičnog SnSe, a FTIR rezultat otkriva prisustvo polipirola. Superkapacitivno ponašanje SnSe-PPi nanokompozita je proučavano cikličnom voltametrijom i studijama galvanostatskog pražnjenja. SnSe-PPi nanokompozit isporučuje specifičan kapacitet od 223 F g^{-1} pri 10 mV sec^{-1}. Dodatak polipirola povećava provodljivost materijala i poboljšava njegovo superkapacitivno ponašanje.
***Ključne reči**: Kalaj selenid, polipirol, superkondenzator, specifični kapacitet, životni vek.*

Naučni rad
Rad primljen: 28.09.2023.
Rad prihvaćen: 27.11.2023.
Rad je dostupan na sajtu: www.idk.org.rs/casopis

Vaishali Bhavsar[1,2], Deepti Tripathi[2]*

[1]Applied Sciences and Humanities Department SAL College of Engineering, SAL Education, Gujarat Technological University, Ahmedabad, Gujarat, India, [2]Department of Physics, School of Sciences, Gujarat University, Ahmedabad, Gujarat, India

Scientific paper
ISSN 0351-9465, E-ISSN 2466-2585
https://doi.org/10.62638/ZasMat1001

Zastita Materijala 65 (1)
158 - 168 (2024

Tuning low frequency dielectric properties of flexible ternary polymer blend film reinforced with bio- ionic liquid for the application in green electronics

ABSTRACT

Biofriendly conducting polymeric blends and composites exhibiting high dielectric constant and dielectric loss are promising for applications as sensors, actuators, microwave absorbing materials, fuel cells and biomedical applications. A great deal of work is reported on using fillers such as conductive nanomaterials, bio ceramics, carbon nanotubes, graphene etc in blends of Polyvinylchloride, Polyvinylpyrrolidone, Polymethylmethacrylate, Polyvinyl alcohol with conducting polymer Polypyrrole, Polyaniline for enhancing their conductivities, tailoring dielectric and electrical, thermal and surface properties of such polymeric materials. However, appropriate dispersion of such fillers in polymeric matrices remains technically challenging. In this regard, bio-ionic liquids have emerged as a novel class of materials and their combination with specific polymer blends opens the possibility to develop smart novel materials with different morphologies. Present work aims to explore the low frequency dielectric properties exhibited by free standing, flexible, biofriendly/biodegradable ternary polymer blend film of Polyvinylchloride-Polyvinylpyrrolidone-Polypyrrole reinforced with choline acetate. The detailed analysis of low frequency dielectric properties authenticates that addition of choline acetate result in modifying the dielectric properties of ternary polymer blend film.. The harmlessness of these films was confirmed from disk diffusion test indicating their benign nature towards (Escherichia coli) (CFT073) and (Bacillus subtilis). Therefore, the developed films can potentially be used for various scale multifunctional dielectric and electrical applications working in close contact with living matter, green electronics and various health monitoring systems.

Keywords: *Bio ionic liquid, choline acetate, polyvinylchloride, polyvinylpyrrolidone, polypyrrol*

1. INTRODUCTION

The emergence of the green soft organic electronics has directed to the search of methods that combine the electrical properties of the materials with flexibility, bio-friendliness and bio-degradability [1-5]. Such soft biocompatible polymeric materials (blends and composites) have many advantageous properties and find a great deal of application in food packaging, textile, tissue engineering applications, sensors, actuators, electromagnetic shielding, biomedical implants and other biomedical and electronic applications [5-9].

The "soft" nature of polymeric materials enables better mechanical compatibility with human body than other traditional electronic materials and opens up options to design them to be used as mechanically flexible substrates often required for thin film electronics and medical implants. However, the hindrance is that polymeric materials usually have very low conductivity compared with inorganic counterparts. In this regard, the use of conducting polymers in areas of electronics and biomedical sciences is also of immense interest. In addition, biofriendly polymeric materials (blends and composites) exhibiting high dielectric constant and dielectric loss are promising for applications as sensors, actuators, microwave absorbing materials and many more [10]. Researchers working in the field of polymers have blended a variety of bio-compatible polymers such as *Polyvinylchloride (PVC), Polyvinylpyrrolidone (PVP), Polymethylmethacrylate (PMMA), Polyvinyl*

*Corresponding Author: Vaishali Bhavsar
Email: vaishali.b.bhavsar@gmail.com
Paper received: 28. 09. 2023.
Paper corected: 25.11.2023.
Paper accepted: 02. 12. 2023.
Paper is available on the website: www.idk.org.rs/journal

alcohol (PVA) [11-15] and doped such blends with conducting polymer (ppy, pani) for enhancing conductivities, tailoring their dielectric, electrical, optical, thermal and surface properties, [6,16,17]. In addition fillers such as conductive nanomaterials, bioceramics, carbon nanotubes, graphene etc are incorporated in such blends of insulating and conducting polymers for enhancing their dielectric properties, but appropriate dispersion of such fillers in polymeric matrices remains technically challenging [15,18-20]. Therefore, there is an unmet need for the development of biofriendly, biodegradable polymer materials with highly tunable dielectric, electrical and physical properties. In this regard employment of bio ionic liquids in the fabrication of polymer composites is a favourable approach as they exhibit enhanced biocompatibility and low toxicity profiles [21,22]. Reinforcing bio- ionic liquid in polymeric matrix serves as promising alternative in the field of electronics due to their high thermal stability, ionic conductivity and solubility and miscibility with many compounds such as organic, inorganic, and polymeric materials and can provide an advantage because of their responsive chemical structure, which has both large cations and anions that are weakly coordinated. These ions can interact with organic or inorganic fillers and biocompatible polymers. The existence of intermolecular interactions can have synergistic effect on polymer, and consequently improve the interfacial link between the filler and the polymer matrix [10].The combination of bio-ionic liquids with specific polymer blends opens the possibility to develop novel materials with different morphologies such as films, gels, membranes, fibers, with tailored functionality [23].

Having known this, not much of work is reported on preparing and studying bio-ionic liquid reinforced polymer blend film. Present work aims to bridge this gap and explore the properties exhibited by free standing, flexible, bio-friendly/bio-degradable bio-ionic liquid reinforced ternary polymer blend film. In our previous work we have reported optical and electrical properties of ternary polymer blend film of PVC- PVP (taken in ratio 1:1) doped with different weight percentage concentration(10%, 30%, and 50%) of conducting polymer Polypyrrole (PPy). The results indicate that PPy doped PVC-PVP blend films with tuneable optical, electrical and dielectric properties can be potential material for use in photonic biosensors, solar cell and optoelectronics field [24]. Present work aims at understanding and investigating the effect of reinforcing choline acetate (two different concentrations 0.5 gm and 1.5 gm) in PVC-PVP-50%PPy on low frequency dielectric properties of base matrix and how the dielectric properties can be tuned by such reinforcement. Despite all the constituents of the prepared polymer films are individually established as harmless materials but when combined the whole film has to be tested for biological effects as well. Therefore to confirm the biofriendliness and harmlessness of the prepared bio-ionic liquid reinforced ternary polymer blend film, we exclusively carried out the disk diffusion test [2,21,25].

Over all analysis of the studies carried out shows that the presence of bio-ionic liquid choline acetate resulted in enhancement of dielectric constant and ac conductivity in low frequency region. The disk diffusion test shows that the polymer blend film of PVC-PVP-50%PPy exhibited almost negligible development of inhibition ring where as the blend film of PVC-PVP-50%PPy reinforced with choline acetate showed no ring of inhibition indicating their benign nature towards Gram-negative bacteria (*Escherichia coli*) (CFT073) and gram positive bacteria (*Bacillus subtilis*). Therefore the developed flexible biofriendly ternary polymer blend film of PVC-PVP-50%PPy reinforced with appropriate amount of bio-ionic liquid choline acetate with high dielectric constant, low loss factor and high ac conductivity can potentially be used for various scale multifunctional dielectric and electrical applications working in close contact with living matter, green electronics and various health monitoring systems in biomedical field.

2. MATERIALS AND METHODS

2.1. Materials

Conducting polymer, polypyrrole (PPy) has numerous applications in a variety of different fields [26-28]. Polyvinylpyrrolidone (PVP), a water-soluble polar polymer, is known to have a growing pharmaceutical and biomedical importance [29]. However, films made of PVP alone are not practically so useful as they become quite brittle on aging resulting into their poor processability. To make PVP films amenable, here it is proposed to blend it with Polyvinyl Chloride (PVC) which has good resistance to weathering, offers good biocompatibility and possess excellent mechanical strength [17,30,31]. In present work, PVP supplied by Loba Chemie having an average molecular weight of 40,000 gm/mol was blended with PVC.

Polyvinyl Chloride (PVC) with average molecular weight 62,000 gm/mol) supplied by Sigma Aldrich was used as an insulating matrix. Pyrrole monomer supplied by Spectrochem, India, was used as received. Tetrahydrofuran purchased from HPLC was used as solvent and anhydrous ferric chloride purchased from Otto Chemicals, was used as oxidant for polymerization of pyrrole

monomer. Choline-based ionic liquids have gained much interest due to their enhanced biocompatibility [32,33]. Choline bio-ionic liquids have shown a potential in applications where low environmental and biological impact is critical [21]. It is also important to note when considering the biodegradability of materials, that choline based ionic liquids can be decomposed by microorganisms [2]. In present work, choline acetate with molecular formula $C_7H_{17}NO_3$ and molecular weight of 163.21 procured from Sigma Aldrich was used.

2.2. Methods

Free standing films of ternary blend film was prepared by solution cast technique. The solution containing PVC-PVP in ratio 1:1 with 50% weight concentration of pyrrole monomer and 0.5 gm of choline acetate was carefully poured in petri dish and allowed to dry for 48 hours in dark place under normal temperature and pressure, so that the solvent evaporates slowly. The films were then gently pulled from the petri dish. The oxidative polymerization of the Py monomer in matrix was carried out by technique called mixing oxidative polymerization [34,35]. Similarly, PVC-PVP-50% PPy film with 1.5gm of choline acetate was prepared. The films were kept in a desiccator until use.

2.3. Characterization

Polymer morphology is a microscale property that is largely dictated by the amorphous or crystalline portions of the polymer chains and their influence on each other. The morphology of PVC-PVP-50%PPy films reinforced with different weight percentage concentrations of choline acetate were examined using Scanning Electron Microscope (SEM) (ZEISS) (Model: Merlin VP Compact) supplied by Carl Zeiss. Low frequency dielectric data were obtained using Agilent precision LCR meter E4980A with solid test fixture (Model No: 16451B) having electrodes of 0.5cm in diameter 0.5cm. The parallel capacitance and parallel resistance were measured in the frequency range of 20Hz to 2MHz at room temperature. The dielectric constant (ε′) and dielectric loss (ε″) and ac conductivity were evaluated. In order to assess the harmlessness of ternary polymer blend films of PVC-PVP-50% PPy with and without choline acetate, the disk diffusion method [2,21] was carried out. The assessment was done towards an uropathogenic strain of Gram-negative bacteria (*Escherichia coli*) (CFT073) and gram-positive bacteria (*Bacillus subtilis*). For this Lysogeny broth agar served as the substrate for bacterial growth and the bacterial suspension was smeared on its surface. The films were cut into 5x5mm size and were placed on the surface of the inoculated agar with sterilized forceps. The plates were incubated at 37^0C. The plates were observed after 48 hrs and 72 hrs and each time they were photographed to assess the development of inhibition rings.

3. RESULTS AND DISCUSSION

3.1. Morphological analysis

The information on microstructural evolution of PPy in PVC-PVP film and morphology of PVC-PVP-50%PPy blend films was obtained from SEM measurements. The micrograph for ternary polymer blend film of PVC-PVP-50%PPy is shown in Figure 1.

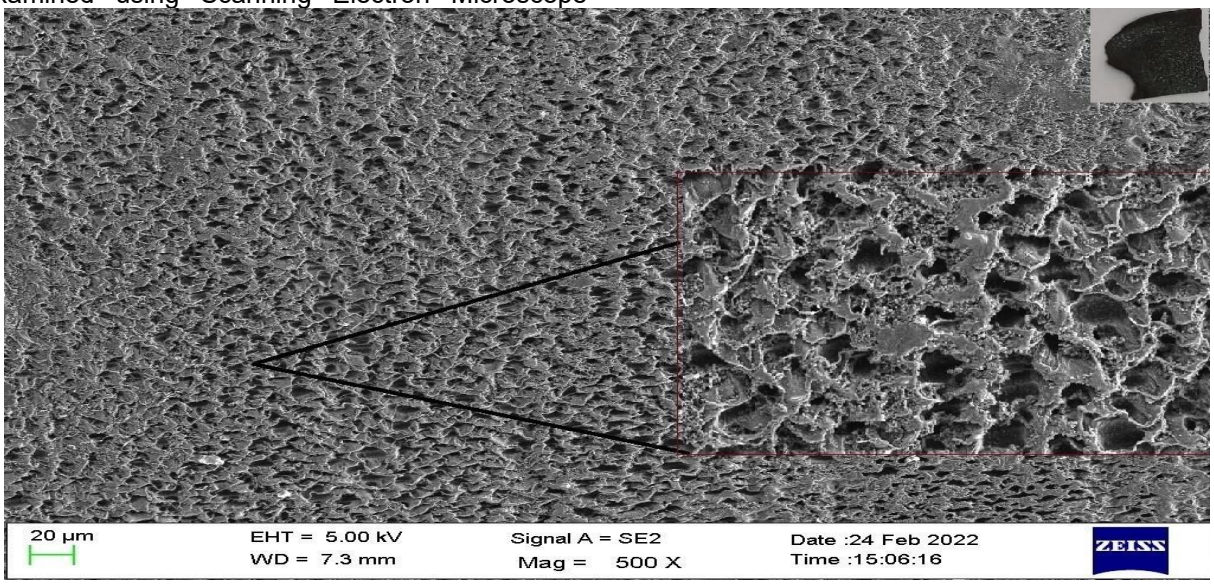

Figure 1. SEM image of PVC-PVP-PPy ternary blend film with 50% weight concentration of PPy (inset shows magnified view). (a)Photographic image of film

Slika 1. SEM slika PVC-PVP-PPi ternarnog mešanog filma sa koncentracijom od 50% težine PPi (umetak prikazuje uvećan prikaz). (a) Fotografska slika filma

The micrograph (Fig. 1) displayed macro granular structure formed by aggregation of small globular structures which are typical cauliflower type confirming the presence of PPy in ternary blend film of PVC-PVP-50%PPy. The SEM image of PVC-PVP-50%PPy ternary blend film shows dense porous network structure. The presence of this porous network indicated that if these ternary polymer blend films are reinforced with some filler, then it could result in enhancing a conducting network thereby modifying its dielectric and electrical properties.

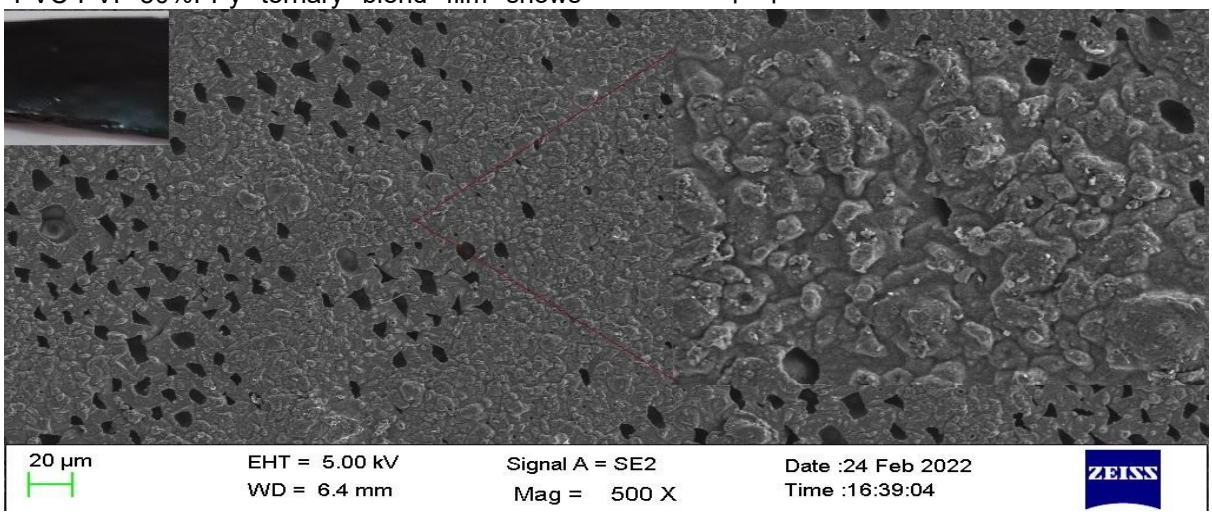

Figure 2. SEM image of Choline acetate (0.5gm) reinforced PVC-PVP-50%PPy Film (inset shows the magnified view) (b)Photographic image of film

Slika 2. SEM slika holin acetatom (0,5 g) ojačanog PVC-PVP-50%PPi filma (umetak prikazuje uvećani prikaz) (b) Fotografska slika filma

By reinforcing the ternary polymer blend with lower concentration (0.5gm) of choline acetate, the microstructure of pristine ternary polymer blend films shows a significant change. The SEM image shows (Fig. 2) clear formation of micropores of different sizes.. which serve as high energy sites and as a consequence, the enhancement in interconnecting network is formed leading to an increase in conductivity. The micrograph also shows expanded regions of globular morphology. The photographic image of this film exhibited smooth surface (Fig.2 (b)) as compared to that of pristine ternary polymer blend film [36].

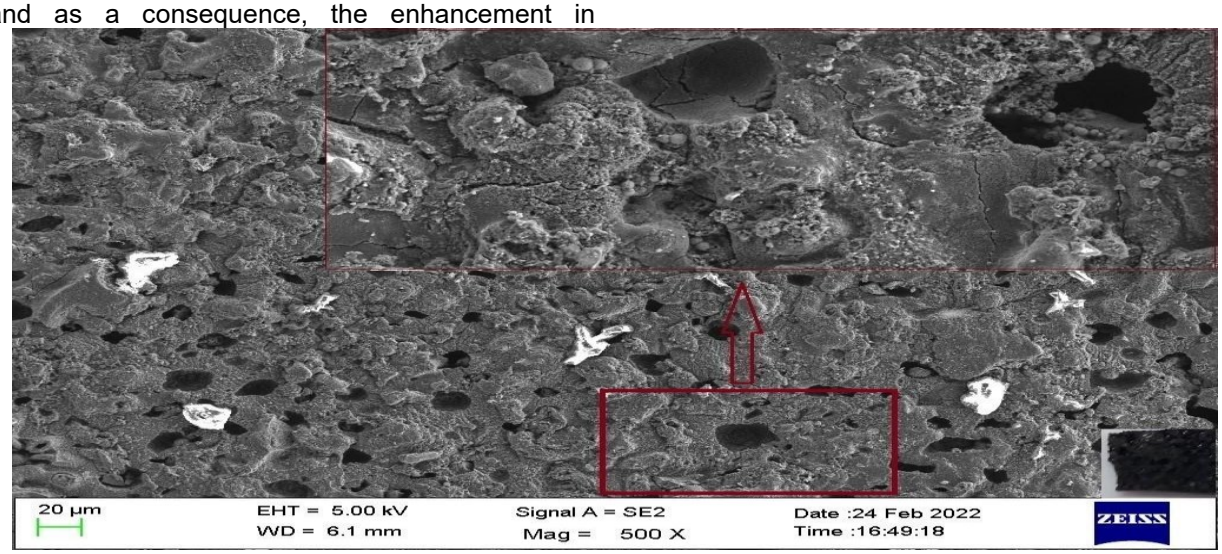

Figure 3. SEM image of Choline acetate (1.5gm) reinforced PVC-PVP-50%PPy Film (inset shows the magnified view) (c)Photographic image of film

Slika 3. SEM slika holin acetatom (1,5 g) ojačanog PVC-PVP-50%PPi filma (umetak prikazuje uvećani prikaz) (c) Fotografska slika filma

However, in the case of reinforcing higher concentration (1.5 gm) of choline acetate in ternary polymer blend, the morphology of the hybrid sample totally changed. The photographic image (Fig. 3 (c)) and the SEM micrograph exhibited rough surface.

Moreover, the surface cracks (encircled in SEM image) and bumps were also observed in the SEM image of ternary polymer blend film with higher concentration of choline acetate. The microgranular aggregations can be seen to be formed but they were not uniformly distributed [37]. It was noteworthy that ternary polymer blend film with lower concentration (0.5 gm) of choline acetate was more efficiently inserted in the film than higher concentration (1.5 gm) and resulted in to a film formation with smooth surface, dominant presence of amorphous content and enhanced flexibility of the films, which may play an important role in the electrical conductivity exhibited by this film [38].

3.2. Dielectric analysis

In order to acquire information on the characteristics of ionic and molecular interaction in polymeric materials, dielectric analysis can be used. In present work, the dielectric properties of PVC-PVP-50%PPy ternary polymer blend film is investigated in low frequency (100 Hz to 2 MHz) region. In addition the effect of reinforcing PVC-PVP-50%PPy ternary polymer blend film with two various concentrations of bio-ionic liquid choline acetate on its dielectric properties is also investigated.

Complex Permittivity Spectra

Frequency dependent variation in dielectric constant (ε′), for ternary polymer blend film of PVC-PVP-50%PPy with different concentration (0.5 gm and 1.5 gm) of Choline acetate is shown in Fig. 4. The large change in ε′ of choline acetate reinforced ternary polymer blend films as opposed to pristine ternary polymer blend film is ascribed to the presence of additional ions as charge carriers and thus the polarizability of the films with choline acetate reinforced shoot up [39]. The diminution in ε′ values in the high frequency region is attributed to the fact that if the rotational motion of the dipoles is not sufficiently faster so as to attain equilibrium with rapidly changing fields, then relaxation of dipoles occur resulting in decrease in ε′ values. As observed the ε' values for choline acetate reinforced PVC-PVP-50%PPy ternary blend film were quite high in the low frequency region which is owing to the dominant contribution of electrode polarization effect over bulk material properties. This effect is observed due to accumulation of ions near electrode surfaces and contributes to the formation of electric double layers when the duration of reversal of applied alternating electric field is slow [40].The appreciable increase in ε' values of these biofriendly choline acetate reinforced ternary polymer blend film suggests that they possible can be used as controllable dielectric material in the design and fabrication of simple functional circuits used in several biodegradable electronic devices in biomedical field as demonstrated in the literature [15]. Therefore, the studied biofriendly films can be dielectrically tuned as per required range for various electrical applications by varying the frequency of exciting field [14].

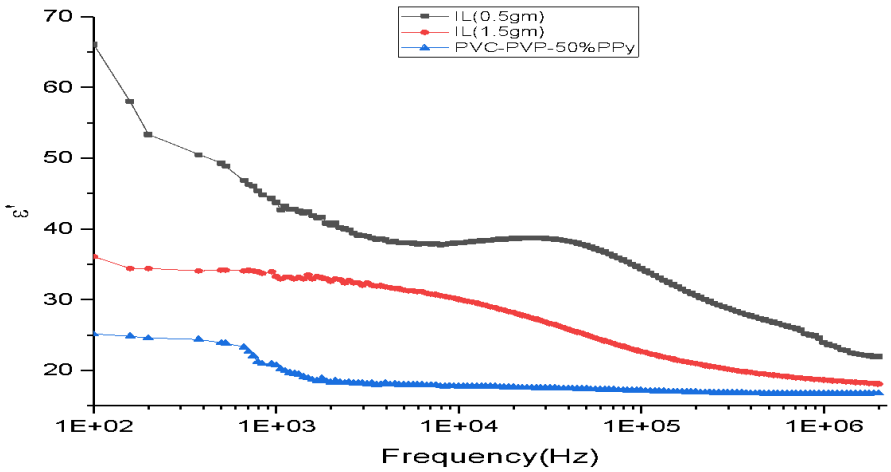

Figure 4. Variation in ε' with frequency for ternary blend films

Slika 4. Varijacija u ε' sa frekvencijom za filmove sa ternarnom mešavinom

Loss tangent

Dissipation factor or loss tangent (tan δ) is the measure of applied energy converted into heat and gets dissipated from the material. Frequency dependent variation of loss tangent (tanδ) for all the films is shown in Figure 5. It can be easily observed that the loss factor of ternary polymer blend film has increased after reinforcing choline acetate in the films. The loss tangent spectra of choline acetate reinforced ternary polymer blend films exhibited well defined relaxation peaks which are attributed to the higher flexibility of polymer chains.

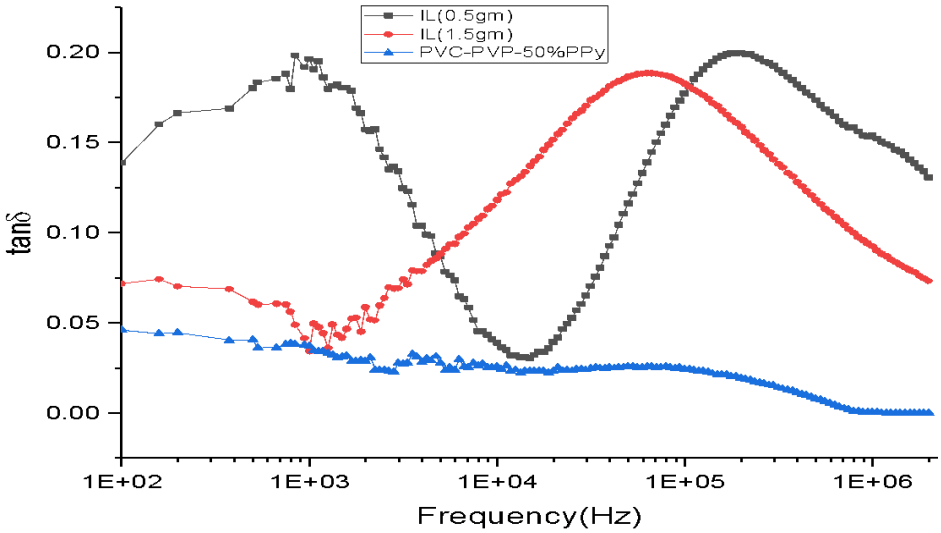

Figure 5. Variation in tand with frequency for Choline Acetate reinforced PVC-PVP-50%PPy film

Slika 5. Varijacija u tand sa frekvencijom za PVC-PVP-50%PPi film ojačan holin acetatom

The loss tangent spectra of choline acetate reinforced ternary polymer blend film exhibited peaks which is the consequence of dielectric relaxation process associated with the presence of heterogeneities in the samples [36]. Appearance of relaxation peak in higher frequency region observed for low concentration of choline acetate reinforced film can be attributed to the fast segmental motion coupled with mobile ions. Relaxation peak appearing in the intermediate frequency region for high concentration of choline acetate reinforced film is the consequence of dipolar and interfacial polarization effects [36]. Thus, the addition of an appropriate amount of bio-ionic liquid, choline acetate may slacken the segmental packing in the chains, thereby increasing free volume for dipolar relaxation to occur. Here, the tan δ values for all the ternary polymer blend films were reported to be less than 0.2, which is desirable for a material to avoid energy loss due to power dissipation.

AC conductivity analysis

The electrical conductivity measurement is a well rooted technique in analysing the properties of charge accumulation at the electrode-polymer interface and ion transport in polymer films. The dielectric conductivity sums overall dissipative effects, which may represent the conductivity caused by migrating charge carriers and related to an energy loss associated with a frequency dependence. For a dielectric, conductivity is a complex quantity which is given as

$$\sigma * = \sigma' + \sigma''$$

Where

σ' is the real part of conductivity

σ'' the imaginary part

The variation of real part of complex conductivity also known as the AC conductivity (σ′) of pristine and choline acetate reinforced PVC-PVP-50%PPy ternary blend films with frequency is shown in Fig. 6. For all the ternary polymer blend films the σ′ values increase by about four orders of magnitude when the frequency changes by four orders (i.e., from 10^2Hz to 10^6 Hz) as can be noted from this figure.

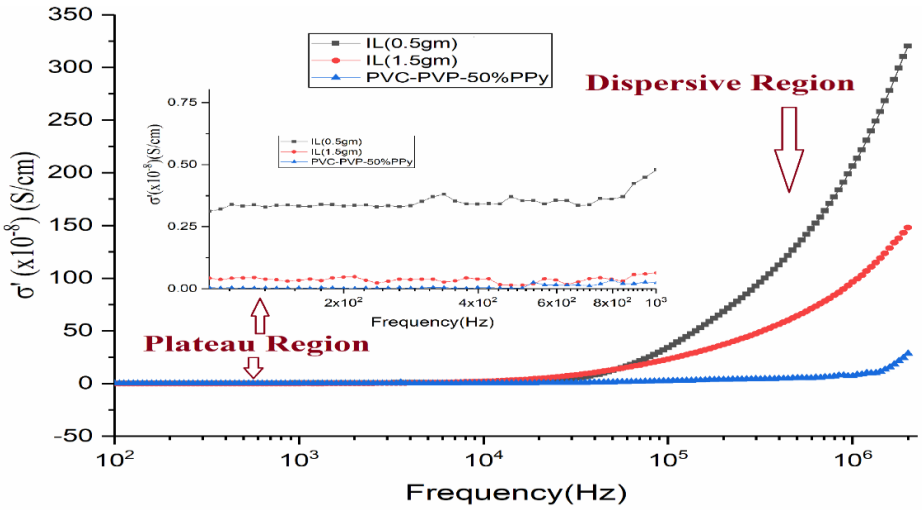

Figure 6. Variation in σ′ with frequency for ternary polymer blend film with and without choline acetate

Slika 6. Varijacija u σ′ sa frekvencijom za film mešavine ternarnog polimera sa i bez holin acetate

A close look at the σ' spectra for all the films show two distinct regions (i) a low frequency plateau region *i.e.* frequency independent behaviour (ii) dispersion in higher frequency region *i.e.* frequency dependent behaviour. The transition from frequency in-dependent σ' values to the frequency dependent values observed in these films signals the onset of conductivity relaxation phenomenon [41,42]. In low frequency region, more and more charge accumulation occurs at the electrode-polymer interfaces which lead to decrease in number of mobile ions and eventually result in low values of conductivity (Fig. 3- inset) [43].The high frequency dispersive region points towards a bulk relaxation phenomenon taking place which provides information about the migration of trapped ions related with AC conductivity [44]. Herein, the conductivity is high owing to the increased mobility of charge carriers. Additionally, these σ′ plots of the investigated bio-ionic liquid reinforced ternary polymer blend films validate that their σ′ values at 100 Hz are of the order of 10^{-10} S/cm which is enhanced to 10^{-6} S/cm at 2MHz. Bio-ionic liquid choline acetate produces a slight plasticizing effect leading to chain motion and high ion conductivity [45]. However, the enhancement is much more pronounced for lower concentration (0.5gm) of choline acetate in PVC-PVP-50%PPy in the entire measured frequency window.

The ternary polymer blend film with higher concentration (1.5 gm) of choline acetate exhibited σ' values less than that for low concentration in the entire experimental frequency range which could be due to the influence of ion pairs, ion triplets and the ion aggregations formed which reduces the overall mobility and the number of effective charge carriers [36,45].This variation makes it evident that these biofriendly choline acetate reinforced ternary polymer blend films are materials of appreciable electrical conductivity over the four orders of magnitude broad frequency window, and therefore, they can serve as flexible-type biofriendly material in developing the biofriendly electronic devices in the biomedical and green electronics fields.

3.3. Assessment of harmlessness of bio-ionic liquid reinforced film

For the prepared choline acetate reinforced polymer films to be used as flexible biofriendly harmless [21] polymeric material in the biomedical and green electronics field, microorganisms are excellent candidates, because of their environmental and industrial impact, and the robustness of the toxicity assays.

Ternary polymer blend film without choline acetate did not exhibit any inhibition zone (Fig. 7). However, the films with choline acetate reinforced also did not exhibit any inhibition zone. What draws our attention is that the ternary films reinforced with choline acetate show a rapid growth of bacteria (Fig. 7 (a) and (b)) on the film as compared to pristine ternary polymer blend film. The benign nature of choline acetate reinforced polymer films towards *E.coli* bacteria have been reported in literature [21] which supports our observations. In present case, the ternary polymer blend film with higher concentration (1.5 gm) of choline acetate exhibited maximum bacterial growth. To sum up, we can say that as such ternary polymer blend film with and without choline acetate are benign towards *E. coli* and *Bacillus*

Subtilis, however ternary polymer blend film with higher concentration of choline acetate is more benign towards these bacteria which shows that the films under study are harmless and can be used as biofriendly polymer film in the field of green electronics and biomedical industry [46].

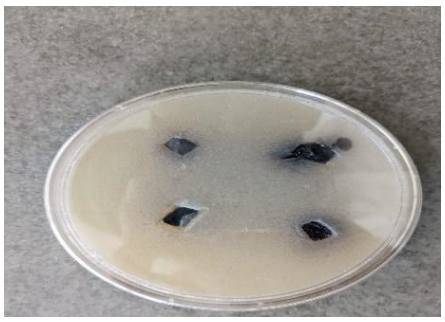

(a)

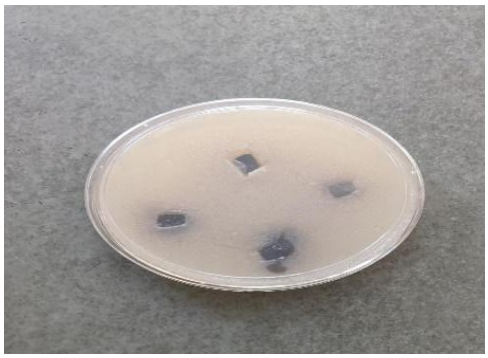

(b)

Figure 7. Results for disk diffusion test of E. coli and Bacillus Subtilis assay for ternary polymer blend films. (a) observation after 22 hours and (b) observation after 72 hours. Positions: 1-PVC-PVP-PPy, 2- PVC-PVP-PPy-IL(0.5gm), 3- PVC-PVP-PPy-IL(1.5gm)

Slika 7. Rezultati testa disk difuzije E. coli i Bacillus Subtilis testa za ternarne filmove mešavine polimera. (a) posmatranje posle 22 sata i (b) posmatranje posle 72 sata. Pozicije: 1-PVC-PVP-PPi, 2- PVC-PVP-PPi-IL(0,5gm), 3- PVC-PVP-PPi-IL(1,5gm)

4. CONCLUSIONS

Morphological characterization, low frequency dielectric properties, biological impact of ternary polymer blend film of PVC-PVP-50%PPy reinforced with two different (0.5gm and 1.5gm) concentrations are thoroughly investigated and described herein.The morphological study i.e. SEM images show that, the microstructure of pristine ternary polymer blend films shows a significant change on reinforcing it with various concentrations of choline acetate. Strong physical interactions and networking between choline acetate and matrix of ternary polymer blend resulted in enhancement in flexibility of the blend film which is favorable feature for the flexible green electronics and biomedical applications.

The dielectric study revealed that there is significant improvement of ion-dipolar interaction and ion-dipolar ordering in the film with addition of bio-ionic liquid. The increase in ε' values for choline acetate (0.5gm) reinforced PVC-PVP-50% PPy ternary blend film is about 16% at 100Hz and 4% at 2MHz. Choline acetate reinforced ternary polymer blend film with high values of ε' and low values of loss factor suggest that they possibly can be used as controllable dielectric material in the design and fabrication of simple functional circuits used in several biodegradable electronic devices in the biomedical field. The study of biological impact of ternary polymer blend film with and without choline acetate reveal their benign nature towards E. coli and Bacillus Subtilis, however ternary polymer blend film with higher concentration of choline acetate is more benign towards these bacteria.

To summarize, PVC-PVP-50%PPy ternary polymer blend film reinforced with appropriate amount of bio-ionic liquid choline acetate hold much promising modifications in structural, morphological, mechanical, and dielectric properties. More importantly the benign nature exhibited by these films towards E.coli and Bacillus Subtilis suggest that they can potentially be used for various scale multifunctional dielectric and electrical applications working in close contact with living matter, green electronics and various health monitoring systems in biomedical field.

Acknowledgements (Optional)

Experimental facilities developed using financial assistance provided through DST-FIST (Level-I) and DRS (SAP) program have been utilized to carry out this work and it is gratefully acknowledged. Authors are thankful to Prof. P. N. Gajjar, Head, Department of Physics, School of Science, Gujarat University, Ahmedabad and Prof. V. A. Rana, Department of Physics, School of Science, Gujarat University, Ahmedabad for help extended to take LCR measurements and for his constant encouragement. Authors are thankful to Dr. Mukesh Ranjan and . Shri K. P. Sooraj, Institute of Plasma Research, Gandhinagar, Gujarat, for extending their support for taking SEM images. Authors are thankful to Dr. Riddhi Trivedi, SAL Institute of Pharmacy, SAL Education, Ahmedabad,Gujarat for help extended to carry out disk diffusion test.

5. REFERENCES

[1] A.F.Ahmad *et al. (2020)* Biodegradable Poly (lactic acid)/Poly (ethylene glycol) Reinforced Multi-Walled Carbon Nanotube Nanocomposite Fabrication, Characterization, Properties, and Applications, *Polymers*, 12, 427-449.

[2] F.Elhi *et al. (2020)* Electromechanically active polymer actuators based on biofriendly choline ionic liquids, *Smart Mater. Struct.* 29, 055021, doi: 10.1088/1361-665X/ab7f24.

[3] Y.Wu *et al. (2016)* Green and biodegradable composite films with novel antimicrobial performance based on cellulose , *Food Chem.*, 197, 250–256, doi: 10.1016/j.foodchem.2015.10.127.

[4] V.Rathi, V.Panwar, G.Anoop, M.Chaturvedi, K. Sharma, B.Prasad (2019) Flexible, Thin Composite Film to Enhance the Electromagnetic Compatibility of Biomedical Electronic Devices, *IEEE Trans. Electromagn. Compat.*, 61, 1033–1041, doi: 10.1109/TEMC.2018.2881267.

[5] L.Wang, Z.Ma, Y.Zhang, H.Qiu, K.Ruan, J.Gu (2022) Mechanically strong and folding-endurance $Ti_3C_2T_x$ MXene/PBO nanofiber films for efficient electromagnetic interference shielding and thermal management, *Carbon Energy*, 4, 200–210, doi: 10.1002/cey2.174.

[6] D.Suman, N.Karna, B.P.Sahoo (2019) Development of Poly (vinylidene fluoride) and Polyaniline blend with high dielectric permittivity, excellent electromagnetic shielding effectiveness and Ultra low optical energy band gap: Effect of ionic liquid and temperature, *Polymer*, 181, 121759, doi: 10.1016/j.polymer.2019.121759.

[7] A.A.Shamsuri, R.Daik (2015) Application of ionic liquids and their mixtures for preparation of advanced polymer blends and composites: a short review, Rec. Adv. in Matr. Sci., 40, 45-59.

[8] A.Gupta, M.Jain, M.Kumari, S.K.Tripathi (2021) Electrical, electrochemical and structural studies of a chlorine-derived ionic liquid-based polymer gel electrolyte, *Beilstein J. Nanotechnol.*, 12, 1252–1261, doi: 10.3762/bjnano.12.92.

[9] K.-W. Yeung, C.-Y.Tang, W.-C.Law, G.C.-P.Tsui, X. Xie (2021) Development of ionic liquid-based electroactive polymer composites using nanotechnology, *Nanotechnol. Rev.*, 10, 99–116, doi: 10.1515/ntrev-2021-0009.

[10] A.A.Shamsuri, S.N.A.Md. Jamil, K.Abdan (2021) A Brief Review on the Influence of Ionic Liquids on the Mechanical, Thermal, and Chemical Properties of Biodegradable Polymer Composites, *Polymers*, 13, 2597, doi: 10.3390/polym13162597.

[11] S.B.Aziz, M.F.Z. Kadir, M.H.Hamsan, H.J.Woo, M. A. Brza (2019) Development of Polymer Blends Based on PVA:POZ with Low Dielectric Constant for Microelectronic Applications. *Sci. Rep.*, 9, 13163, doi: 10.1038/s41598-019-49715-8.

[12] L.Wang, C.Liu, S.Shen, M.Xu, X.Liu (2020) Low dielectric constant polymers for high speed communication network, *Adv.Ind.Eng.Polym.Res.*, 3, 138–148, doi: 10.1016/j.aiepr.2020.10.001.

[13] K.Qian, R.Qiao, S.Chen, H.Luo, D.Zhang (2020) Enhanced permittivity in polymer blends *via* tailoring the orderliness of semiconductive liquid crystalline polymers and intermolecular interactions *J. Mater. Chem.C*, 8, 8440–8450, doi: 10.1039/ D0TC00766H.

[14] R.J.Sengwa, P.Dhatarwal (2021) PVA/MMT and (PVA/PVP)/MMT hybrid nanocomposites for broad-range radio frequency tunable nanodielectric applications, *Mater. Lett.*, 299, 130081, doi:10. 1016/j.matlet.2021.130081.

[15] P.Dhatarwal, R.J.Sengwa (2020) Structural and dielectric characterization of (PVP/PEO)/Al2O3 nanocomposites for biodegradable nanodielectric applications, *Adv. Compos. Hybrid Mater.*, 3, 344–353, doi: 10.1007/s42114-020-00168-y.

[16] S.Jha, V.Bhavsar, K.P.Sooraj, M.Ranjan, D. Tripathi (2021) Investigation of the effect of *in-situ* grown PPy on low frequency dielectric properties and other properties of PVA-PVP blend film, *J. Adv. Dielectr.*, 11, 2150020, doi: 10.1142/ S2010135X2150020X.

[17] S.H.Deshmukh, D.K.Burghate, V.P.Akhare, V.S. Deogaonkar, P.T.Deshmukh, M.S.Deshmukh (2007) Electrical conductivity of polyaniline doped PVC-PMMA polymer blends, *Bull. Mater. Sci.*, 30, 51–56, doi: 10.1007/s12034-007-0009-6.

[18] I.Noshadi *et al. (2017)* Engineering Biodegradable and Biocompatible Bio-ionic Liquid Conjugated Hydrogels with Tunable Conductivity and Mechanical Properties, *Sci. Rep.*, 7, 4345-4363, doi: 10.1038/s41598-017-04280-w.

[19] S.Ahmad, S.Ahmad, S.A.Agnihotry (2007) Synthesis and characterization of in situ prepared poly (methyl methacrylate) nanocomposites, *Bull. Mater. Sci.*, 30, 31–35, doi: 10.1007/s12034-007-0006-9.

[20] M.Faisal, S.Khasim (2013) Electrical Conductivity, Dielectric Behavior and EMI Shielding Effectiveness of Polyaniline-Yttrium Oxide Composites, *Bull. Korean Chem. Soc.*, 34, 99–106, doi: 10.5012/ bkcs.2013.34.1.99.

[21] F.Elhi *et al. (2020)* Understanding the Behavior of Fully Non-Toxic Polypyrrole-Gelatin and Polypyrrole-PVdF Soft Actuators with Choline Ionic Liquids, *Actuators*, 9, 40-57, doi: 10.3390/ act9020040.

[22] E.L.Bennett, C.Song, Y.Huang, J.Xiao (2019) Measured relative complex permittivities for multiple series of ionic liquids, *J. Mol. Liq.*, 294, 111571, doi: 10.1016/j.molliq.2019.111571.

[23] D.M.Correia *et al. (2020)* Ionic Liquid–Polymer Composites: A New Platform for Multifunctional Applications, *Adv. Funct. Mater.*, 30, 1909736, doi: 10.1002/adfm.201909736.

[24] V.Bhavsar, D.Tripathi (2020) Study of biocompatible polymer blend films with tuneable band gap, *Indian*

J of Pure and App Phy. 58, 795-803, http://nopr.niscpr.res.in/handle/123456789/55602.

[25] L.Xue *et al.(2013)* Choline acetate enhanced the catalytic performance of Candida rogusa lipase in AOT reverse micelles, *Colloids Surf. B Biointerfaces*, 105, 81–86, doi: 10.1016/j.colsurfb. 2012.12.050.

[26] E.Håkansson, A.Amiet, A.Kaynak (2006) Electromagnetic shielding properties of polypyrrole/polyester composites in the 1–18GHz frequency range, *Synth. Met.*, 156, 917–925, doi: 10.1016/j.synthmet.2006.05.010.

[27] D.D.Ateh, H.A.Navsaria, P.Vadgama (2006) Polypyrrole-based conducting polymers and interactions with biological tissues, *J. R. Soc. Interface*, 3, 741–752, doi: 10.1098/rsif.2006.0141.

[28] R.Balint, N.J.Cassidy, S.H.Cartmell (2014) Conductive polymers: Towards a smart biomaterial for tissue engineering, *Acta Biomater.*, 10, 2341–2353, doi: 10.1016/j.actbio.2014.02.015.

[29] A.Rawat, H.K.Mahavar, S.Chauhan, A.Tanwar, P. Singh (2012) Optical band gap of polyvinylpyrrolidone/polyacrilamide blend thin films, *Indian J of Pure and App Phy*., 50,100-104, https://www.semanticscholar.org/paper/Optical-band-gap-of-blend-thin-films-Rawat-Mahavar/2cecd86c7d3cb376ae43a69092772dbd7a908766

[30] D.Mondal *et al (2013)* Effect of poly(vinyl pyrrolidone) on the morphology and physical properties of poly(vinyl alcohol)/sodium montmorillonite nanocomposite films, *Prog. Nat. Sci.Mater.Int.*, 23, 579–587, doi: 10.1016/j.pnsc.2013.11.009.

[31] M.Altenhofen da Silva, M.G.Adeodato Vieira, A.C. Gomes Maçumoto, M.M.Beppu (2011) Polyvinylchloride (PVC) and natural rubber films plasticized with a natural polymeric plasticizer obtained through polyesterification of rice fatty acid, *Polym. Test.*, 30, 478–484, doi: 10.1016/j.polymertesting.2011.03.008.

[32] D.-J.Tao, Z.Cheng, F.-F.Chen, Z.-M.Li, N.Hu, X.-S. Chen (2013) Synthesis and Thermophysical Properties of Biocompatible Cholinium-Based Amino Acid Ionic Liquids, *J.Chem.Eng.Data*, 58, 1542–1548, doi:10.1021/je301103d.

[33] B.L.Gadilohar, G.S.Shankarling (2017) Choline based ionic liquids and their applications in organic transformation, *J.Mol.Liq.*, 227, 234–261, doi: 10.1016/j.molliq.2016.11.136.

[34] V.Bhavsar, D.Tripathi (2017) Study of attenuation of microwaves by PPy-Doped PVC films, *Polym. Eng. Sci.*, 57, 89–94, doi: 10.1002/pen.24388.

[35] H.R.Hafiz (1996), Aspects on the percolation and conduction behavior in polypyrrole-poly (vinyl chloride) composite, *Polym. Bull.*, 37, 647–654,, doi: 10.1007/BF00296611.

[36] S.Jayanthi (2019) Studies on ionic liquid incorporated polymer blend electrolytes for energy storage applications, *Adv. Compos. Hybrid Mater.*, 2, 351–360, doi: 10.1007/s42114-019-00102-x.

[37] P.-H.Wang, T.-L.Wang, W.-C.Lin, H.-Y.Lin, M.-H. Lee, C.-H.Yang (2018) Crosslinked Polymer Ionic Liquid/Ionic Liquid Blends Prepared by Photopolymerization as Solid-State Electrolytes in Supercapacitors, *Nanomaterials*, 8, 225-242, doi: 10.3390/nano8040225.

[38] M.Ravindar Reddy, A.Mallikarjun, M.J.Reddy, A. R.Subrahmanyam, M.V.Reddy (2021) Investigation of morphology and transport properties of Na^+ ion conducting PMMA:PEO hybrid polymer electrolyte, *J. Polym. Eng.*, 41, 654–659, doi: 10.1515/polyeng-2020-0346.

[39] K.Subramaniam, A.Das, D.Steinhauser, M.Klüppel, G.Heinrich (2011) Effect of ionic liquid on dielectric, mechanical and dynamic mechanical properties of multi-walled carbon nanotubes/ polychloroprene rubber composites, *Eur.Polym.J.*, 47, 2234–2243, doi: 10.1016/j.eurpolymj. 2011. 09.021.

[40] S.Choudhary, R.J.Sengwa (2016) Structural dynamics and ionic conductivity of amorphous type plasticized solid polymer electrolytes, *APPL PHYS*, 54, 159-169.

[41] A.Yussuf, M.Al-Saleh, S.Al-Enezi, G.Abraham (2018) Synthesis and Characterization of Conductive Polypyrrole: The Influence of the Oxidants and Monomer on the Electrical, Thermal, and Morphological Properties, *Int. J. Polym. Sci.*, 2018, ID 4191747, doi: 10.1155/2018/4191747.

[42] M.D.Migahed, M.Ishra, T.Fahmy, A.Barakat (2004) Electric modulus and AC conductivity studies in conducting PPy composite films at low temperature, *J.Phys.Chem.Solids*, 65, 1121–1125, doi: 10.1016/j.jpcs.2003.11.039.

[43] A.Gupta, A.Jain, S.K.Tripathi (2021) Structural, electrical and electrochemical studies of ionic liquid-based polymer gel electrolyte using magnesium salt for supercapacitor application, *J. Polym. Res.*, 28, 235, doi: 10.1007/s10965-021-02597-9.

[44] O.Gh.Abdullah, R.R.Hanna, H.T.Ahmed, A.H. Mohamad, S.A.Saleem, M.A.M.Saeed (2021) Conductivity and dielectric properties of lithium-ion biopolymer blend electrolyte based film, *Results Phys.*, 24,104135, doi: 10.1016/j.rinp.2021.104135.

[45] P.Wang, P.Xu, Y.Zhou, Y.Yang, Y.Ding (2018) Effect of MWCNTs and P[MMA-IL] on the crystallization and dielectric behavior of PVDF composites, *Eur. Polym. J.*, 99, 58–64, doi: 10.1016/j.eurpolymj.2017.12.003.

[46] D.A.Nasrallah, M.A.Ibrahim (2022) Enhancement of physico-chemical, optical, dielectric and anti-microbial properties of polyvinyl alcohol/ carboxymethyl cellulose blend films by addition of silver doped hydroxyapatite nanoparticles, *J. Polym. Res.*, 29, 86, doi: 10.1007/s10965-022-02943-5.

IZVOD

PODEŠAVANJE NISKOFREKVENTNIH DIELEKTRIČNIH SVOJSTAVA FLEKSIBILNOG TERNARNOG FILMA MEŠAVINE POLIMERA OJAČANOG BIOJONSKOM TEČNOŠĆU ZA PRIMENU U ZELENOJ ELEKTRONICI

Bioprijateljske polimerne mešavine i kompoziti koji pokazuju visoku dielektričnu konstantu i dielektrične gubitke obećavaju za primene kao senzori, materijali koji apsorbuju mikrotalase, gorivne ćelije i biomedicinske aplikacije. Izveštava se o korišćenju punila kao što su provodljivi nanomaterijali, biokeramika, ugljenične nanocevi, grafen itd. u mešavinama polivinilhlorida, polivinilpirolidona, polimetilmetakrilata, polivinil alkohola sa provodljivim polimerom polipirol polianilin za poboljšanje njihove tanilo-električne provodljivosti, dielektrične provodljivosti, i svojstva površine takvih polimernih materijala. Međutim, odgovarajuća disperzija takvih punila u polimernim matricama ostaje tehnički izazov. U tom smislu, bio-jonske tečnosti su se pojavile kao nova klasa materijala i njihova kombinacija sa specifičnim mešavinama polimera otvara mogućnost za razvoj pametnih novih materijala sa različitim morfologijama. Ovaj rad ima za cilj da istraži niskofrekventne dielektrične osobine koje pokazuje slobodno stojeći, fleksibilni, bioprijateljski/biorazgradivi ternarni polimerni film mešavine polivinilhlorid-polivinilpirolidon-polipirol ojačan holin acetatom. Detaljna analiza niskofrekventnih dielektričnih svojstava potvrđuje da dodavanje holin acetata rezultira modifikacijom dielektričnih svojstava ternarnog filma mešavine polimera. Bezopasnost ovih filmova potvrđena je testom difuzije diska koji ukazuje na njihovu benignu prirodu prema (Escherichia coli) (CFT073) i (Bacillus subtilis). Stoga se razvijeni filmovi potencijalno mogu koristiti za različite multifunkcionalne dielektrične i električne aplikacije koje rade u bliskom kontaktu sa živom materijom, zelenom elektronikom i raznim sistemima za praćenje zdravlja.

Ključne reči: *Biojonska tečnost, holin acetat, polivinilhlorid, polivinilpirolidon, polipirol*

Naučni rad
Rad primljen: 28.09.2023.
Rad korigovan: 25.11.2023.
Rad prihvaćen: 02.12.2023.
Rad je dostupan na sajtu: www.idk.org.rs/casopis

*Shree H.K. Ranjin, Nidhi Pathak, Charu Lata Dube**

School of Nano Sciences, Central University Gujarat, Gandhinagar, Sector, India

Scientific paper
ISSN 0351-9465, E-ISSN 2466-2585
https://doi.org/10.62638/ZasMat1037

Zastita Materijala 65 (1)
169 - 175 (2024

Photocatalytic degradation of textile dye with titanium (IV) doped tungsten oxide nanoparticles

ABSTRACT

Water pollution from textile industries is a major concern with respect to the availability of clean drinking water. The removal of textile (organic) dyes through photocatalytic degradation with pure WO_3 and titanium (IV) doped tungsten oxide [Ti (IV)-WO_3] nanospheres were studied under visible light. The WO_3 and Ti (IV)-WO_3 nanospheres were synthesized via microwave-assisted method at microwave power of 160 W for the duration of 20 mins. The as synthesised WO_3 and Ti (IV)-WO_3 nanospheres were characterized for their structural, microstructural, and spectroscopic properties by using powder X-ray diffraction (XRD), UV–Visible (UV-Vis) spectroscopy, Fourier-transform infrared spectroscopy (FTIR), Scanning electron microscopy (SEM) and High-resolution transmission electron microscopy (HR-TEM). The X-ray diffractograms confirmed the formation of highly pure WO_3 and Ti (IV)-WO_3 nanospheres. The average crystallite size of WO_3 and Ti (IV)-WO_3 nanospheres were calculated as 53.37 nm and 35.24 nm respectively using Debye Scherrer equation. The bandgap of Ti (IV)-WO_3 was found to be decreased to 2.5 eV from 3.2 eV (WO_3) respectively. It can be deduced that Ti (IV)-WO_3 can be utilized as efficient visible light (λ>420 nm) driven photocatalyst as the bandgap was < 3 eV. The agglomerated spherical nanoparticles were seen for WO_3 and Ti (IV)-WO_3 in the HR-TEM images. The photocatalytic activity of textile dye was analyzed by UV-Vis spectrophotometer under visible light. The photocatalytic organic dye degradation was investigated. The enhanced photocatalytic activity of titanium (IV) doped tungsten oxide (10 wt%) was observed to be ~100% in 100 mins. This makes titanium (IV) doped tungsten oxide nanospheres, a potential nanomaterial for water purification.

***Keywords**: Photocatalytic degradation, organic dyes, microwave assisted method, photocatalytic activity*

1. INTRODUCTION

In contemporary world, water pollution has a far-reaching negative consequence in the ecosystem. The harmful effluents in water includes broadly organic and inorganic wastes such as dyes, pharmaceutical ingredients, pesticides, fertilizers, heavy metal ions, metal oxides and metal complexes etc. Several industries such as the textiles, paper, chemicals, fertilizers, pesticides, metal-plating, batteries, food processing, refineries and pharma industries are the source of uncontrolled water pollution [1].

The release of textile dyes (organic pollutants) into the water bodies through textile industries increase the biochemical and chemical oxygen demand (BOD and COD), reduce the growth of the plant, enter the food chain, and may further lead to toxicity, mutagenicity, and carcinogenicity [2]. Hence, several methods have been adopted for the purification of waste water.

The water purification through photocatalysis of dye degradation is highly researched area by several researchers [3,4]. Photocatalysis technique involves, usage of a suitable photocatalyst which degrades the harmful contaminants into simple mineral acids, carbon dioxide and hydrogen in a very short period in the presence of near UV / Visible light [5,6]. Photocatalysts are the solids which accelerate the reaction rate in the presence of light without undergoing any permanent chemical change throughout the reaction [7]. Among the photocatalysts, the visible-light-driven

*Corresponding author: Charu Lata Dube
E-mail: charulata.dube@cug.ac.in
Paper received: 27. 09. 2023.
Paper accepted: 13. 12. 2023.
Paper is available on the website: www.idk.org.rs/journal

photocatalysts are extensively utilized for the photochemical induced reactions. The photocatalytic efficiency of photocatalysts under visible light can be enhanced by direct and effective method of band gap regulation. The dopant (cations), into the lattice of the semiconductors alters the band structure of the semiconductors, resulting in the formation of narrow bands which are localized above the valence bands (VB) in the semiconductors which ultimately extend the visible light absorption [8].

The tungsten oxide (WO_3) finds a wide range of applications in photocatalysis which makes it an important semiconductor [9]. It is found that in visible light region, the reduction potential of WO_3 electrons is low as it possesses a low level of conduction band (CB) which enables WO_3 to have low photocatalytic efficiency [10]. The doping of cations such as titanium (Ti^{+4}) ions into the WO_3 lattice will alter its band gap structure and resulting in shift in absorption towards the visible light region.

The particles size of atoms, molecules, or ions, determines the formation of a substitutional solid solution. It is known that the stability of the solid solution depends upon the lesser difference in the particle sizes, and so is the higher solubility of the solution, which is determined by the crystal structure stability [11]. Due to similarity between W^{+6} and Ti^{+4} ionic radii, W-O and Ti-O bond lengths, and WO_3 and TiO_2 crystal structures, Ti^{+4} replaces W^{+6} in the WO_3 lattice. Although W^{+6} and Ti^{+4} have different valences, when Ti (IV) dopes in WO_3, the valence difference between the two causes a finite solid solution to develop [12].

The current research work, describes the synthesis of WO_3 and Ti (IV) doped WO_3 nanospheres through a microwave assisted method for the degradation of Rhodamine B (RhB) dye. Dye degradation efficiency of synthesized photocatalysts were investigated at different concentrations of the dopant [Ti (IV) ions] in the visible light region.

2. EXPERIMENTAL DETAILS

2.1. Materials

Sodium tungstate ($Na_2WO_4.H_2O$, 99%), titanium dioxide (TiO_2, 98%), rhodamine B dye ($C_{28}H_{31}ClN_2O_3$, 96%), nitric acid (HNO_3, 96%) are purchased from Merck. Analytical grade chemicals and reagents are used in purified form. Distilled water (DI) water used, is filtered by a Millipore Milli-Q Integral Water Purification System (Millipore Corp.) throughout the complete experiment.

2.2. Preparation of pure WO_3

A dissolution of 6 g of $Na_2WO_4.H_2O$ in 70 ml of distilled water was prepared and stirred for 15 mins. Addition of a specific concentration of HNO_3, to maintain the pH~1 of the solution. HNO_3 acts as a precipitating agent. The solution turned light yellow in color after the addition of HNO_3, this solution was transferred to a microwave oven (Samsung 28L, MC28A5013AK/TL) and was processed under 160 W for 20 mins. The preparation of WO_3 is expressed in the equation 1 (Eq.1) [13]. A precipitate was obtained in the end of the reaction. DI water was used for washing the precipitate, after centrifugation. The product was kept for drying at 80° C for 12 h in hot air-drying oven. After calcination at 600° C for 5 h, the final product was dried and stored.

2.3. Preparation of Ti (IV) doped WO_3

6 g of $Na_2WO_4.H_2O$ and different molar ratio (2, 5, 10 and 20 wt%) of TiO_2 were dissolved in 70 ml of DI water. Stirring of the solution for 15 mins with addition of suitable amount of HNO_3 to maintain the pH~1 of the solution was performed. A light-yellow color of the solution was obtained after the addition of HNO_3 and was processed in microwave oven under 160 W for 20 mins. The preparation of Ti (IV) doped WO_3 is expressed in the equation 2 (Eq.2). DI water was used for washing the precipitate, after centrifugation. The product was dried at 80° C for 12 h in hot air-drying oven. Further after calcination at 600° C temperature for 5 h, the product was stored.

$$Na_2WO_4 + 2HNO_3 \rightarrow WO_3 + 2NaNO_3 \quad (1)$$

$$Na_2WO_4 + 2HNO_3 + xTi^{+4} \rightarrow xTi{:}WO_3 + +2NaNO_3 \quad (2)$$

2.4. Characterization

The pure WO_3 and Ti (IV) doped WO_3 nanoparticles were characterized for their structural and morphological properties and were investigated for their photocatalytic activity. The X-ray diffractograms of the samples were recorded with X-ray diffractometer (XRD, D8 Advance, Bruker, Germany) with Cu Kα X-ray radiation source in 1.5456 Å at 40 kV and 40 mA over the 2θ range of 10-80° with a scan rate of 0.1 sec/step. The morphological studies were performed with a 180 kV High resolution transmission electron microscope (HR-TEM) (JEOL JEM-2100 TEM, Tokyo, Japan). The TEM samples were prepared on carbon-coated copper grids, followed by drying in air. The optical properties were analyzed with Fourier transform infrared spectrophotometer (FTIR, Perkin Elmer Spectrum 65 series, Massachusetts, United States) in the range of 400-4000 cm^{-1} and Ultraviolet-Visible spectrophoto-

meter (UV, Shimadzu UV1800 ENG 240V) in the spectral range of 300–800 nm.

2.5. The photodegradation of rhodamine B (RhB) dye

The photocatalytic dye degradation efficiency of both pure WO_3 nanospheres and Ti (IV)-WO_3 nanospheres were determined by using a 200 W incandescent bulb as a visible light source for the degradation of RhB in aqueous solution. The photocatalyst (90 mg of photocatalyst [Ti (IV)-WO_3] was added to RhB aqueous solution ($1x10^{-5}$ M) in a conical flask at 25° C. Stirring of solution was done for 30 mins in dark condition for equilibrium adsorption and desorption. The photocatalytic tests were carried out at different intervals of time by taking 3 ml of suspension each time followed by centrifugation (6000 rpm, 5 mins). The degraded RhB concentration was measured using obtained photocatalyst and supernatant after centrifugation. The concentrations of RhB were measured with the UV-Visible spectrophotometer.

3. RESULTS AND DISCUSSIONS

3.1. XRD analysis

The X-ray diffractograms of WO_3 and Ti (IV)-WO_3 are shown in Fig.1.The XRD peaks in Fig.1(a) at 23°, 23.5°, 24.3° correspond to the WO_3 phase with (002), (020) and (200) planes, respectively (JCPDS File No. 01-072-1465) [14]. The Fig.1(a) shows XRD pattern of pure WO_3 and the XRD patterns of Ti (IV)-WO_3 with doping of Ti (IV) as 2, 5, 10, 20 wt% are shown in Fig.1(b), 1(c), 1(d) and 1(e), respectively. The average crystallite size of WO_3 nanospheres is calculated as ~ 53.3 nm using Debye Scherrer equation (Eq.3).

$$d = K\frac{\lambda}{\beta\, Cos\,\theta} \qquad (3)$$

Where

d average crystallite size,

K shape constant (0.9),

λ wavelength (1.54 Å),

β full width at half maxima,

θ Bragg's angle of respective peaks.

The doping of Ti (IV) is confirmed with the peak values obtained at 25.2°, 37.7º, 48.1°, 55.1º, and 62.7. The obtained 2θ values confirm the presence of TiO_2 anatase phase with characteristic peak at 25.2°, corresponding to the (101) plane in Fig.1(b, c, d, e) (JCPDS File No. 75-1537) [15]. The increment in the Ti (IV) concentration led to increase in the intensity of the peak at 25.2° gradually (marked in the Fig.1 with black ellipse). The obtained XRD patterns explain that with the increase in the dopant concentration of Ti (IV) above 10 wt%, a separate phase of TiO_2 appears, which indicates that the Ti (IV) ions is doped in the lattice of WO_3 crystal structure to form a finite solid solution.

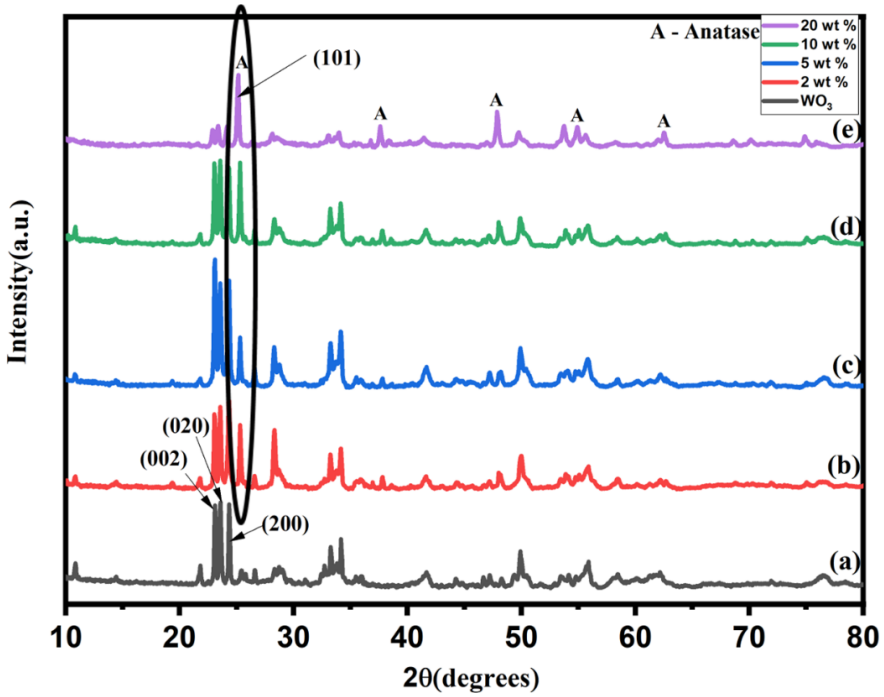

Figure 1. X- ray diffractogram of (a) pure WO_3, (b) 2 wt% Ti (IV)-WO_3, (c) 5 wt% Ti (IV)-WO_3, (d) 10 wt% Ti (IV)-WO_3, (e) 20 wt% Ti (IV)-WO_3 nanoparticles

Slika 1. Rendgenski difraktogram (a) pure WO_3, (b) 2 wt% Ti (IV)-WO_3, (c) 5 wt% Ti (IV)-WO_3, (d) 10 wt% Ti (IV)-WO_3, (e) 20 wt% Ti (IV)-WO_3 nanočestice

3.2. HR-TEM analysis

The corresponding HR-TEM morphology of pure WO_3 and Ti (IV)-WO_3 is shown in Fig.2. Fig.2(a) corresponds to the morphology of pure WO_3 which is nano-spherical in nature with average size of nanoparticles ~5.29 nm. Fig.2(b) represents the similar nano-spherical morphology of Ti (IV)-WO_3 nanoparticles. The HR-TEM images illustrate that WO_3 nanoparticles size is unaffected by the doping of Ti (IV) cations into the lattice. A reduction in the size of the nanoparticles (average size~4.4 nm) is observed after doping of Ti (IV) ions. In addition, doping of titanium may reduce agglomeration of nanoparticles, Fig.2(b) [16].

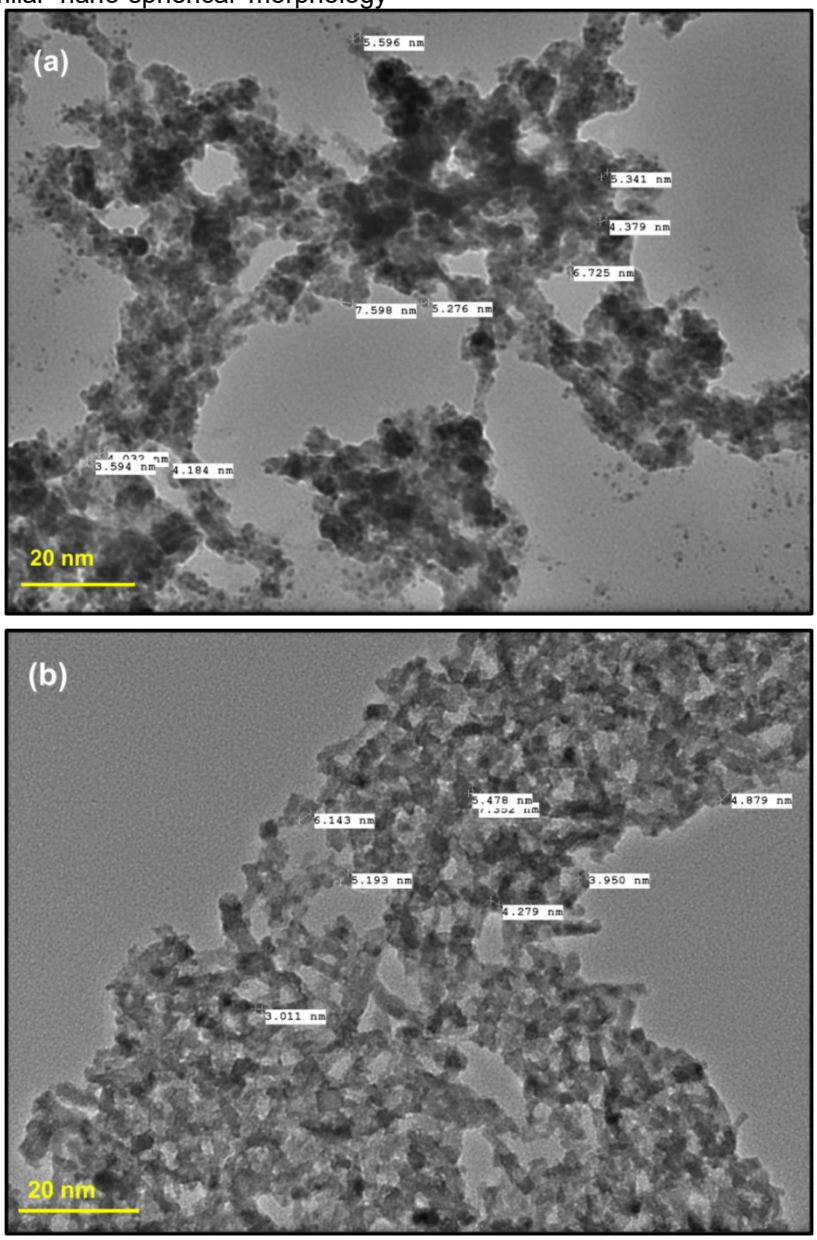

Figure 2. HR-TEM images of (a) pure WO_3 and (b) Ti (IV)-WO_3 nanoparticles

Slika 2. HR-TEM slike (a) pure WO_3 and (b) Ti (IV)-WO_3 nanočestice

3.3. FTIR analysis

The FTIR analysis is performed for pure WO_3 and Ti (IV)-WO_3 nanoparticles. Fig.3 represents the FTIR spectrum of (a) pure WO_3 (2.74×10^{-1} M), (b) 2 wt%, (c) 5 wt%, (d) 10 wt%, (e) 20 wt % Ti (IV)-WO_3 nanoparticles, respectively. The FTIR spectra of WO_3 exhibits peaks at 620 cm^{-1} (W-O stretching) and 831 cm^{-1} (W-O-W bending) as shown in Fig.3(a). Fig.3(b), (c), (d) and (e) represents the absorption peak at 528 cm^{-1} and a small shoulder peak at 1401 cm^{-1} corresponding to the Ti-O-Ti bending and stretching modes, respectively.

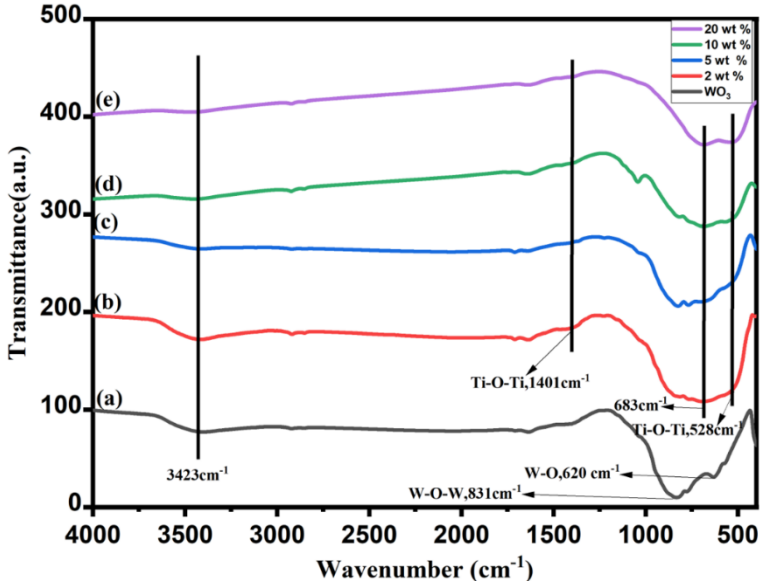

Figure 3. FTIR spectra of (a) pure WO_3, (b) 2 wt% Ti (IV)-WO_3, (c) 5 wt% Ti (IV)-WO_3, (d) 10 wt% Ti (IV)-WO_3, (e) 20 wt% Ti (IV)-WO_3 nanoparticles

Slika 3. FTIR spektar (a) pure WO_3, (b) 2 wt% Ti (IV)-WO_3, (c) 5 wt% Ti (IV)-WO_3, (d) 10 wt% Ti (IV)-WO_3, (e) 20 wt% Ti (IV)-WO_3 nanočestica

The presence of Ti (IV) ions into the lattice of WO_3 is confirmed. The peak broadening with reduction in WO_3 peak intensities is observed with the Ti (IV) ions doping into the lattice of WO_3, Fig.3(b). In Fig.3(e), the appearance of broad peak ~681cm^{-1} distinctly (with the increase in concentration of Ti (IV) ions) can be attributed to the Ti–O–Ti bonds formed in the TiO_2 lattice [17]. This indicates that the Ti (IV) ions is doped in the lattice of WO_3 crystal structure to form a finite solid solution, supporting XRD results. Additionally, the peak observed at ~3423 cm^{-1} is corresponding to hydroxyl group of O-H stretching vibration [18].

3.4. Photocatalytic Degradation study

The photocatalytic performance is examined by photo catalytically degradation of an aqueous solution of RhB dye. The absorption spectra of RhB aqueous solution (1x10^{-5} M, 150 ml) with degradation by 90 mg of photocatalyst (Ti (IV)-WO_3) under the exposure of 200 W tungsten bulb is shown in Fig.4(a).

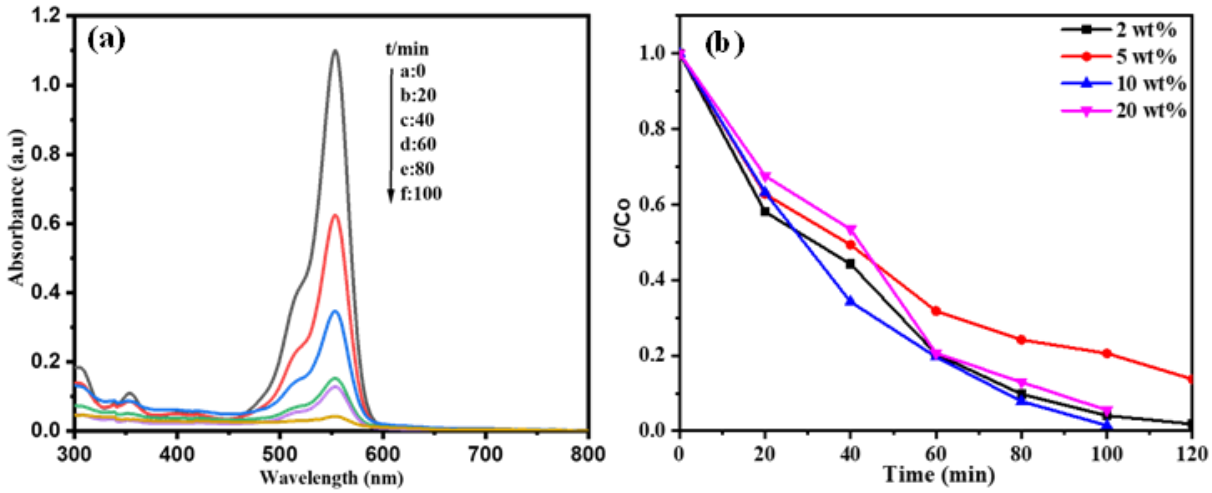

Figure 4.(a) Absorption spectrum of RhB solution with 10 wt% Ti (IV) -WO_3 (b) Photodegradation of RhB with 2 wt%,5 wt%,10 wt% and 20 wt% Ti(IV)-WO_3 photocatalysts

Slika 4. (a) Spektar apsorpcije rastvora RhB sa 10 wt% Ti (IV) -WO_3 (b) Fotodegradacija RhB sa 2 tež%, 5 tež%, 10 tež% i 20 tež% Ti(IV)-WO_3 fotokatalizator

The absorption peak at 550 nm was obtained, corresponding to the absorption of RhB molecules [19]. The rapid decrease in the intensity of the absorption peak was observed with the continuous exposure time and the disappearance in the peak is observed after 100 mins. In the presence of visible light, a series of comparative experiments were performed, to investigate the influence of concentration of Ti (IV) ions. It was observed from Fig.4(a) that in the absence of any photocatalyst, RhB is almost not degraded. It was observed that the photocatalytic efficiency is almost 100% with 120 mins of visible light irradiation in 2 wt% Ti (IV)-WO_3.

The degradation efficiency reduced to ~86% after 120 mins of visible light irradiation with 5 wt% Ti (IV)-WO_3. The doping of 10 wt% Ti (IV)-WO_3 exhibits good photocatalytic activity and dye degradation efficiency reaches almost 100% in 100 mins of visible light irradiation. However, an excess amount of Ti (IV) ions in WO_3 results in decrease of degradation efficiency of ~94% in 100 mins of light irradiation. Thus, it can be inferred that 20 wt% doped Ti (IV)-WO_3 nanoparticles exhibits a low photocatalytic efficiency than its 10 wt% doped counterpart within 100 mins. Therefore, excessive doping of Ti (IV) ions is not preferable [20].

Hence, the above results reveal that the photocatalytic activity of Ti (IV) doped WO_3 nanoparticles is improved in comparison to the pure WO_3 photocatalyst. The optimized percentage of Ti (IV) dopant is 10 wt%. Although, the amount of Ti (IV) with 20 wt%, the photocatalytic activity of the Ti (IV) doped WO_3 photocatalyst decreases.

4. CONCLUSION

In summary, we reported a facile method for synthesis of pure WO_3 nanospheres and Ti (IV)-WO_3 nanospheres. The doping of Ti (IV) ions reduced the band gap of WO_3 to form additional impurity states in the band structure of WO_3. The presence of Ti (IV) ions into the lattice of WO_3 was confirmed with several characterizations performed. The morphology of Ti (IV)-WO_3 as nanospheres confirmed that doping had no effect on the morphology of WO_3 nanoparticles. The photocatalytic activity obtained of Ti (IV)-WO_3 nanoparticles proved that the photocatalytic efficiency improved with the doping of Ti (IV) ions. This research suggests a suitable route for the synthesis of photocatalysts in short time with enhanced properties. The improved visible light driven photocatalytic activity of Ti (IV)-WO_3 nanoparticles paves a way for its application in the water purification.

Acknowledgements

The authors are grateful to the Central Instrumentation Facility (CIF), Central University of Gujarat (CUG), Gandhinagar, Gujarat, India for providing necessary research facilities and support. Ms. Shree Ranjini H.K. thankfully acknowledges Dr. Charu Lata Dube the for conceptualizing the work. Ms. Shree Ranjini H.K. acknowledges Ms. Nidhi Pathak and Ms. Ritu Kumari Pilania for their guidance and scientific discussion during the work.

5. REFERENCES

[1] R.Gusain, K.Gupta, P.Joshi, O.P.Khatri (2019) Adsorptive removal and photocatalytic degradation of organic pollutants using metal oxides and their composites: A comprehensive review, Advances in colloid and interface science, 272, 102009.

[2] B.Lellis, C.Z.Fávaro-Polonio, J.A.Pamphile, J.C. Polonio (2019) Effects of textile dyes on health and the environment and bioremediation potential of living organisms, Biotechnology Research and Innovation, 3(2), 275-290.

[3] M.Saeed, M.Muneer, A.U.Haq, N.Akram (2022) Photocatalysis: An effective tool for photo-degradation of dyes—A review, Environmental Science and Pollution Research, p.1-19.

[4] A.Rafiq, M.Ikram, S.Ali, F.Niaz, M.Khan, Q.Khan, M.Maqbool (2021) Photocatalytic degradation of dyes using semiconductor photocatalysts to clean industrial water pollution, J. of Industrial and Engineering Chemistry, 97, 111-128.

[5] M.Elangovan, S.M.Bharathaiyengar, J.Ponnan Ettiyappan (2021) Photocatalytic degradation of diclofenac using TiO_2-CdS heterojunction catalysts under visible light irradiation, Environmental Science and Pollution Research, 28, 18186-18200.

[6] H.Yuan, Y.Zhu, Q.Xu (2020) Research Progress of Bi-Based Catalysts for Photocatalytic Oxidation of VOCs, Hans Journal of Chem. Engin. and Techn., 10(2), 73-81.

[7] N.A.Rajpurohit, K.Bhakar, M.Nemiwal, D.Kumar (2022) Design and synthesis of hybrid nanostructures for sustainable energy and environmental remediation, Arabian Journal of Geosciences, 15, 1-16.

[8] C.Feng, S.Wang, B.Geng (2011) Ti (iv) doped WO_3 nanocuboids: fabrication and enhanced visible-light-driven photocatalytic performance, Nanoscale, 3(9), 3695-3699.

[9] F.Heshmatpour, F.S.Seyed Atashi (2023) Synthesis and characterization of iron-based spinel nanoparticles with different coatings and their ability in photocatalytic degradation of methylene blue, J. of Applied Chemistry, 18(68), 9-28.

[10] T.L.Nguyen, V.D.Quoc, T.L.Nguyen, T.T.T.Le, T.K.Dinh, P.H.Nguyen (2021) Visible-Light-Driven SO_4^{2-}/TiO_2 Photocatalyst Synthesized from Binh Dinh (Vietnam) Ilmenite Ore for Rhodamine B Degradation, J. of Nanomaterials, 2021, 1-13.

[11] U.Aarthi, D.Shukla, S.Rengaraj, K.S.Babu (2020). Ordered to defect fluorite structural transition in Ce_{1-}

$_xNd_xO_{2-\delta}$ system and its influence on ionic conductivity, J. of Alloys and Compounds, 838, 155534.
[12] K.Yin, Y.Shen (2020) Theoretical insights into CO_2 hydrogenation to HCOOH over $Fe_xZr_{1-x}O_2$ solid solution catalyst, Applied Surface Science, 528, 146926.
[13] N.Moghni, H.Boutoumi, H.Khalaf, N.Makaoui, G.Colón (2022) Enhanced photocatalytic activity of TiO_2/WO_3 nanocomposite from sonochemical-microwave assisted synthesis for the photodegradation of ciprofloxacin and oxytetracycline antibiotics under UV and sunlight, J. of Photochemistry and Photobiology A: Chemistry, 428, 113848.666.
[14] H.Ijadpanah-Saravy, M.Safari, A.Khodadadi-Darban, A.Rezaei (2014) Synthesis of titanium dioxide nanoparticles for photocatalytic degradation of cyanide in wastewater, Analytical Letters, 47(10), 1772-1782.
[15] I.A.De Castro, J.A.De Oliveira, E.C.Paris, T.R. Giraldi, C.Ribeiro (2015) Production of heterostructured TiO_2/WO_3 Nanoparticulated photocatalysts through a simple one pot method, Ceramics International, 41(3), 3502-3510.
[16] C.H.Su, C.Y.Su, Y.F.Lin (2015) Microstructural characterization and field emission properties of tungsten oxide and titanium-oxide-doped tungsten oxide nanowires, Materials Chemistry and Physics, 153, 353-358.
[17] B.Singaram, J.Jeyaram, R.Rajendran, P. Arumugam, K.Varadharajan (2019) Visible light photocatalytic activity of tungsten and fluorine codoped TiO_2 nanoparticle for an efficient dye degradation, Ionics, 25, 773-784.
[18] J.Y.Zhang, I.W.Boyd, B.J.O'sullivan, P.K.Hurley, P.V.Kelly, J.P.Senateur (2002) Nanocrystalline TiO_2 films studied by optical, XRD and FTIR spectroscopy, J. of Non-Crystalline Solids, 303(1), 134-138.
[19] S.A.Singh, G.Madras (2013) Photocatalytic degradation with combustion synthesized WO_3 and WO_3TiO_2 mixed oxides under UV and visible light, Separation and Purification Technology, 105, 79-89.
[20] İ.Ç.Davaslıoğlu, K.V.Özdokur, S.Koçak, Ç.Çırak, B.Çağlar, B.B.Çırak, F.N.Ertaş (2021) WO_3 decorated TiO_2 nanotube array electrode: Preparation, characterization and superior photoelectrochemical performance for rhodamine B dye degradation, J. of Molecular Structure, 1241, 130673.

IZVOD

FOTOKATALITIČKA DEGRADACIJA TEKSTILNE BOJE SA NANOČESTICAMA VOLFRAM OKSIDA DOPOVANIM TITANIJUMOM (IV)

Zagađenje vode iz tekstilne industrije predstavlja veliku zabrinutost u pogledu dostupnosti čiste vode za piće. Uklanjanje tekstilnih (organskih) boja fotokatalitičkom degradacijom sa čistim VO_3 i titanijumom (IV) dopiranim volfram oksidom [Ti (IV)-VO_3] nanosferama je proučavano pod vidljivom svetlošću. Nanosfere VO_3 i Ti (IV)-VO_3 su sintetizovane metodom uz pomoć mikrotalasa pri mikrotalasnoj snazi od 160V u trajanju od 20 minuta. Sintetizovane nanosfere VO_3 i Ti (IV)-VO_3 su okarakterisane po svojim strukturnim, mikrostrukturnim i spektroskopskim osobinama korišćenjem difrakcije rendgenskih zraka na prahu (XRD), UV-Visible (UV-Vis) spektroskopije, Fourier-transform infracrvene spektroskopije (FTIR), skenirajuća elektronska mikroskopija (SEM) i transmisiona elektronska mikroskopija visoke rezolucije (HR-TEM). Rendgenski difraktogrami potvrdili su formiranje visoko čistih nanosfera VO_3 i Ti (IV)-VO_3. Prosečna veličina kristalita VO_3 i Ti (IV)-VO_3 nanosfera je izračunata kao 53,37 nm i 35,24 nm respektivno korišćenjem formule Debie Scherrer. Utvrđeno je da je pojasni razmak Ti (IV)-VO_3 smanjen na 2,5 eV sa 3,2 eV (VO_3) respektivno. Može se zaključiti da se Ti (IV)-VO_3 može koristiti kao efikasan fotokatalizator koji pokreće vidljiva svetlost (l>420 nm), pošto je pojas bio < 3eV. Aglomerirane sferične nanočestice su viđene za VO_3 i Ti (IV)-VO_3 na HR-TEM slikama. Fotokatalitička aktivnost tekstilne boje je analizirana UV-Vis spektrofotometrom pod vidljivom svetlošću. Istražena je fotokatalitička organska degradacija boje. Uočeno je da je povećana fotokatalitička aktivnost volfram oksida dopiranog titanijumom (IV) (10 tež.%) ~100% za 100 minuta. Ovo čini nanosfere volfram oksida dopirane titanijumom (IV), potencijalnim nanomaterijalom za prečišćavanje vode.

Ključne reči: *fotokatalitička degradacija, organske boje, mikrotalasna metoda, fotokatalitička aktivnost*

Naučni rad
Rad primljen: 27.09.2023.
Rad prihvaćen: 13.12.2023.
Rad je dostupan na sajtu: www.idk.org.rs/casopis

UPUTSTVO ZA PRIPREMU RADA

Radovi u casopisu Zastita materijala se objavljuju samo na engleskom jeziku.

Radi ujednačavanja izgleda radova, koji se objavljuju u časopisu ***Zaštita materijala*****,** autori se moraju pridržavati uputstva za pripremu radova. Rukopisi u kojima ova uputstva nisu poštovana biće odbijeni bez recenzije. Urednik zadržava pravo da formatiranje rada uskladi sa standardima časopisa. Tekst rukopisa treba da bude u jednoj koloni, a formatiranje teksta što jednostavnije, zato što će se veći deo formatiranja prilikom obrade rukopisa ukloniti i zameniti. Treba, međutim, koristiti podebljana slova (*bold*), kurziv (*italic*), superskripte, subskripte itd. Za obradu teksta treba koristiti program MS Word, format .doc, font Arial sa proredom 1,5. Na stranicama formata A4 margine treba da budu: gornja i donja 3 cm, leva i desna 2,2 cm. Treba numerisati sve redove i sve strane rukopisa.

Kompletan rukopis treba da sadrži: naslov, izvod (apstrakt, na srpskom i engleskom jeziku), ključne reči (na srpskom i engleskom jeziku), uvod, eksperimentalni deo, rezultate, diskusiju, zaključak, reference, tabele i slike. Pozicije slika i tabela treba obeležiti u tekstu (slike i tabele ne treba inkorporirati u datoteku koja sadrži rukopis; oni se dostavljau kao posebne datoteke u odgovarajućim formatima). Nazivi slika ispisuju se ispod slika, a nazivi tabela iznad tabela. Na kraju rukopisa iza slika i tabela, na posebnoj strani treba dati spisak naziva slika i tabela po redu navođena u manuskriptu. **Nazivi slika i tabela daju se na srpskom i engleskom jeziku.**

Kako bi se izbegle nepotrebne gramatičke i pravopisne greške, autorima radova napisanih na engleskom jeziku savetujemo da prilikom pisanja koriste funkcije "spell-check" i "grammar-check".

Naslov treba da bude jasan sam po sebi i ne preterano dugačak (ne više od 15 reči, Arial *bold*, velika slova veličine 14). Puno ime autora (ime i prezime – Arial *bold-italic*, veličina slova 12) navodi se ispod naslova. Afilijacija i kompletna poštanska adresa autora navode se odmah ispod punog imena autora (Arial, *italic*, veličina slova 11). Kada rad ima više od jednog autora, svako ime treba obeležiti arapskom cifrom u superskriptu, a autora za korespondenciju treba obeležiti zvezdicom (*) iznad imena. Takođe, puno ime i e-mail adresu autora za korespodenciju treba napisati u fusnoti na prvoj stranici rukopisa.

Izvod, ne bi trebalo da bude duži od 250 reči (10–15 redova; Arial, *italic*, veličina slova 11) i trebalo bi da sadrži kratak pregled metoda i najvažnije rezultate rada, tako da se može koristiti prilikom indeksiranja u referentnim periodičnim publikacijama i bazama podataka. U izvodu ne treba navoditi reference.

Ključne reči (pojmovi, geografske lokacije, rezultati; Arial, *italic*, veličina slova 11) se navode u posebnom redu na kraju izvoda. Ključne reči moraju biti relevantne za temu i sadržaj rada. Dobar izbor ključnih reči preduslov je za ispravno indeksiranje rada u referentnim periodičnim publikacijama i bazama podataka.

NAPOMENA: Radovi se objavljuju samo na engleskom jeziku izuzev onih delova radova koji moraju da budu prikazani na engleskom i srpskom jeziku.

Uvod (Arial, veličina slova 12) treba da sadrži ciljeve rada i kratak pregled relevantnih prethodnih istraživanja, izbegavajući pri tom detaljan pregled literature i rezultata.

Eksperimentalni deo (Arial, veličina slova 12) trebalo bi da sadrži dovoljno detalja da bi se obezbedila reprodukcibilnost eksperimenata. Metode koje su opisane u već objavljenim publikacijama ne treba opisivati u radu, već samo treba navesti relevantne reference i opisati one elemente koji se razlikuje u odnosu na objavljene metode i postupke.

Rezultati i diskusija (Arial, veličina slova 12) ne bi trebalo da sadrže ono što se već nalazi u tabelama i na slikama. Rezultati bi trebalo da budu jasni i koncizni. Diskusija treba da objasni značaj rezultata istraživanja, a ne da ih ponavlja ili opisuje. Treba izbegavati detaljno navođenje objavljene literature i raspravu o istoj.

Zaključak (Arial, veličina slova 12) treba da sadrži samo pregled osnovnih naučnih doprinosa rada. Treba predstaviti samo glavne zaključke do kojih se došlo na osnovu rezultata. U zaključku ne treba navoditi reference.

Formule, simboli i skraćenice. Formule bi trebalo kucati kurzivom (preporučujemo Equation Editor of Microsoft Office 2003) i trebalo bi da budu navedene i obeležene u samom rukopisu, osim ako ne zahtevaju neko posebno formatiranje. Formule treba numerisati sa desne strane, između zagrada:

$$a^3 = 3M / 4N \qquad (1)$$

Pozivanje na jednačinu/jednačine u tekstu: (jed. 1) ili jednačine (1-4) itd.

Složenije hemijske formule trebalo bi prikazati kao slike.

Skraćenice treba definisati prilikom prvog pominjanja u izvodu i u glavnom delu teksta; treba ih navoditi dosledno, uvek na isti način, od početka do kraja teksta.

Tabele i ilustracije treba suštinski da doprinesu boljem razumevanju i tumačenju rezultata rada. Slike, crteži i druge ilustracije treba da budu jasni i dobrog kvaliteta.
Ilustracije moraju biti u jednom od sledećih formata:
•TIFF (ili JPEG): u boji ili sivim tonovima (polutonovima), od minimum 300 dpi.
•TIFF (ili JPEG): crno-beli linearni crteži, od minimum 1000 dpi.
•TIFF (ili JPEG): kombinacije linearnih crteža i površina u boji, odnosno sivim tonovima (polutonovima), od minimum 500 dpi.

Molimo vas ne činite:

• uz rukopis dostavljati ilustracije optimizovane za korišćenje na ekranu (npr, GIF, BMP, Pict, WPG); one obično imaju nisku rezoluciju i mali raspon boja;
• dostavljati ilustracije koje imaju rezolucije manje od gore navedenih;
• dostavljati ilustracije nesrazmerno velikih dimenzija u odnosu na format rukopisa.

Legende za tabele i slike treba dostaviti uz rukopis, ali ih ne treba inkorporirati u tekst. Slike treba označiti kao "Sl." (Sl. 1) i numerisati arapskim brojevima prema redosledu kojim su navedene u tekstu. Mesta za tabele i slike treba jasno naznačiti u rukopisu. Nazivi slika ispisuju se ispod slika, a tabela iznad tabela. Na kraju rukopisa iza slika i tabela, na posebnoj strani treba dati spisak naziva slika i tabela po redu navođena u manuskriptu, na oba jezika - srpskom i engleskom.

Zahvalnica/Acknowledgements treba da se nalazi u posebnom odeljku na kraju članka, a ispred spiska referenci.

Reference. Spisak referenci, navedenih na jeziku na kom su objavljene, treba da sadrži **samo** radove koji su citirani u tekstu. Citirani radovi navode se u listi referenci po redosledu citiranja u tekstu. U tekstu se broj reference navodi u uglastim zagradama, [ ]. Kod radova koji su prihvaćeni za objavljivanje ali još uvek nisu dobili paginaciju treba staviti napomenu „u štampi“ ili „in press“.

Primeri navođenja referenci su dati u nastavku:

Navođenje radova: [1] I.Ilić, M.Sokić, N.Vučković, V.Matković (2005) Electrochemical process of obtaining glucose**,** Tehnika, 56(3), 9-14.

Ostali časopisi i novine: [1] S. Petrović, Washington Post, 4 Okt. 2005, p. 6

Navođenje knjige: [1] M.Jaić, R.Živanović-Trbojević (2000) Wood finishing, Technical Press, Belgrade.

Citiranje knjiga na CD-ROM i DVD: [1] M.Petrović (2002) Opšta hemija [CD-ROM]; Nolit, Beograd.
[2] G.Jakšić (2002) Analitička hemija [DVD]; Nolit, Beograd.

Čapter u knjizi: [1] M. Stojanovic, Č.Lačnjevac, Z.Lopičić (2012) Corrosion and Corrosion Behavior of depleted uranium, knjiga Corrosion and Protection of Materials, Izdavač ITNMS, Belgrade, pp 223-281.

Navođenje simpozijuma/skupa: [1] M.Petrović, M.Stojanović, M.Mihajlović (2013) 16. YUCORR, Tara, Serbia, proceedings, p.235-242.
[2] M.Pavić, K.Stojanović, M.Mihić (2013) 16. CORR, Beograd, Serbija [CD-ROM];

Doktorske teze: [1] S. Petrović, Modelovanje transporta zagađujućih materija u aluvijalnim sedimentima reke Dunav, doktorska teza, Univerzitet u Novom Sadu, jun 2011.

Patenti: [1] **P.**Wait (1989), Device for Elementary Analyses. USA Patent, No. *123456*.

Tekst sa Web site: [1] M.Arslanagić, S.Kandic - Maglajlić (2011) Manual for the source of scientific papers (http://www.efsa.unsa.ba/ef/docs/handbooks/ manual_economic_web.pdf, 01.12.2013.)
[2] Međunarodna unija za čistu i primenjenu hemiju*, http://www.iupac.org/dhtml_home.html (24 April 2005).*

Proverite da li su sve reference navedene u tekstu navedene i u spisku referenci (i obrnuto).

NAPOMENA:

- **Recenzija i objavljivanje radova su besplatni.**
- **Autorima će PDF datoteka koja sadrži njihov prihvaćeni rad biti poslata besplatno, elektronskom poštom. Štampana verzija sveske u kojoj se nalazi prihvaćeni rad besplatno će biti dostavljena autoru za korespondenciju.**
- **Elektronska verzija rada biće dostupna na internet stranici časopisa, www.idk.org.rs/casopis, i može se koristiti u skladu sa uslovima licence Creative Commons Attribution 4.0 International license (https://creativecommons.org/licenses/by/4.0/)**

UREĐIVAČKI ODBOR
Časopis ZAŠTITA MATERIJALA

MANUSCRIPT PREPARATION

Authors must follow the instructions for authors strictly, failing which the manuscripts would be rejected without review. Editor reserves the right to adjust the formatting style to conform to the standards of the journal. The text layout should be in single-column format. Keep the layout of the text as simple as possible. Most formatting codes will be removed and replaced on processing the manuscript. However, do use bold face, italics, subscripts, superscripts etc. The manuscript should be written in Microsoft Word format.doc, font Arial with 1.5 spacing. On the pages of the manuscript size A4 margins should be: top and bottom 3 cm, left and right 2.2 cm. Add the line numbering and page numbers.

The complete manuscript should contain the title, abstract, keywords, introduction, experimental part, results, discussion, conclusion, references, drawings, tables and pictures. Mark the position of figures and tables in the text. Each figure must have a title below the figure and each table must have a title above the table. Figure and table captions should be listed at the end of the manuscript.

To avoid unnecessary errors, it is strongly advised to use the "spell-check" and "grammar-check" functions of your word processor.

Title should be clear, not too long but explanatory (no more than 15 words; Arial bold, all caps, 14 points). The full name(s) of the author(s) (first name, then last name, in Arial bold 12 points) should be written below the title. The affiliation(s) and complete postal address(es) of the author(s) should be provided immediately after the full name of the authors and written with Arial 11 points. When the paper has more than one author, their names should be followed by a mark (Arabic numeral) as superscript; for the corresponding author, an asterisk symbol should be added using *Word_Insert_Reference_Footnote_Symbol* sequence. Also, the full and e-mail addresses of the corresponding author should be provided in the footer of the first page.

Abstract, not exceeding 250 words (10-15 lines), written in Arial, 11 points, italic, should contain a short review of the method and the most important results of work, so that its original text can be used in referential periodicals and databases. Do not include citations in the Abstract.

Keywords (concepts, locations, results) written with Arial 11 points, italic, are listed in a separate line at the end of the abstract. Keywords should be relevant to the topic and content of the paper. An accurate list of keywords will ensure correct indexing of the paper in referential periodicals and databases.

Introduction, written in Arial, 12 points, should include the objectives of the work and provide an adequate background, avoiding a detailed literature survey or a summary of the results.

Experimental, written in Arial, 12 points – provide sufficient detail to allow the work to be reproduced. Methods already published should be indicated by a reference: only relevant modifications should be described.

Results and Discussion written in Arial, 12 points, should not contain what has been already explained by tables and figures. Results should be clear and concise. Discussion should explore the significance of the results of the work, not repeat them. Avoid extensive citations and discussion of published literature.

Conclusion written in Arial 12 points should contain only essential contributions made to science. The main conclusions drawn from results should be presented. Do not include citations in this section.

Formulae, symbols and abbreviations. Formulae will be typeset in Italics (preferably with the Equation Editor of Microsoft Office 2003) and should be written or marked as such in the manuscript, unless they require a different styling. The formulae should be numbered on the right side, between brackets:

$$a^3 = 3M / 4N \qquad (1)$$

Always refer in the text to the Equations as (Eq. 1), Eqs. (1-4) etc. Complex Chemical Formulae should be presented as Figures.

Abbreviations should be defined when first mentioned in the abstract and in the main body of the text and ensure consistency of abbreviations throughout the article.

Tables and figures should essentially contribute to better understanding and interpretation of the results. Photos, drawings and other illustrations should be clear and of good quality. The acceptable image formats include:

- TIFF (or JPEG): Color or grayscale photographs (halftones), keep to a minimum of 300 dpi.

- TIFF (or JPEG): Bitmapped (pure black & white pixels) line drawings, keep to a minimum of 1000 dpi.TIFF (or JPEG): Combinations bitmapped line/half-tone (color or grayscale), keep to a minimum of 500 dpi.

Please do not:

• Supply files that are optimized for screen use (e.g., GIF, BMP, PICT, WPG); these typically have a low number of pixels and limited set of colors;

• Supply files that are too low in resolution;

• Submit graphics that are disproportionately large for the content.

Table and Figure titles, should accompany the manuscript and **should not be inserted** in the text. **Illustrations** should be labeled "**Fig.**", **(Fig.1),** and numbered consecutively in Arabic numerals in the order in which they are referred to in the text.

Places for tables and figures should be clearly indicated in the manuscript.

Each figure must have a title below the figure and each table must have a title above the table. Figure and table captions should be listed at the end of the manuscript.

Acknowledgements. Include acknowledgements in a separate section at the end of the article before the references.

References. The list of References should only include works that are cited in the text. References are listed in the order in which they appear in the text. Citation in the text is done by specifying the number of references in square brackets, in the original language. Papers which have been accepted for publication should be included in the list of references with the name of the journal and the specification "in press".

Examples of citations are given below:

Journal papers: [1] I.Ilić, M.Sokić, N.Vučković, V.Matković (2005) Electrochemical process of obtaining glucose**,** Tehnika, 56(3), 9-14.

Nonscientific Journals and Newspapers: [1] S. Petrović, The Washington Post,Oct 4, 2005, p. 6

Books: [1] M.Jaić, R.Živanović-Trbojević (2000) Wood finishing, Technical Press, Belgrade.

Chapter in the Books: [1] M.Stojanovic, C.Lacnjevac, Z.Lopičic (2012) Corrosion and Corrosion Behavior of depleted uranium, book Corrosion and Protection of Materials, ITNMS, Belgrade, pp 223-281.

Recommended formats for CD-ROM and DVD books:

[1] M.Petrović (2002) General Chemistry [CD-ROM]; Nolit, Belgrade.

[2] G.Jakšić (2002) Analitical Chemistry [DVD]; Nolit, Belgrade.

Symposium/Congress: [1] M.Petrović, M.Stojanović, M.Mihajlović (2013) 16. YUCORR, Tara, Serbia, proceedings, p.235-242.

[2] M.Pavić, K.Stojanović, M.Mihić (2013) 16. CORR, Belgrade, Serbia [CD-ROM];

Patents: [1] **P.**Wait (1989), Device for Elementary Analyses. USA Patent, No. *123456*.

Text from the Web site: [1] M.Arslanagić, S.Kandic - Maglajlić (2011) Manual for the source of scientific papers (http://www.efsa.unsa.ba/ef/docs/handbooks /manual_economic_web.pdf, 01.12.2013.)

[2] International Union of Pure and Applied Chemistry, *http://www.iupac.org/dhtml_home.html* (April 24, 2005).

Please ensure that every reference cited in the text is also present in the reference list (and vice versa).

NOTE:

- **Review and publications are free of charge.**
- **The authors will be provided with a .pdf file containing the paper, via e-mail, free of charge. A hard copy of the journal issue is sent to the corresponding author for free.**
- Copies of papers available on the website of the journal can be used in accordance with the **Creative Commons Attribution 4.0 Internationa license (https://creativecommons.org/licenses/by/4.0/)**

EDITORIAL BOARD
MATERIAL PROTECTION